

UNIVERSITY OF BIRMINGHAM

DEVELOPMENT OF AN OPTICAL DEVICE FOR THERAPEUTICS AND DIAGNOSTICS IN NEUROTRAUMA

by

ANDREW ROBERT STEVENS

A thesis submitted to the University of Birmingham for the degree of

DOCTOR OF PHILOSOPHY

Neuroscience, Trauma and Ophthalmology

Institute of Inflammation and Ageing

College of Medical and Dental Sciences

University of Birmingham

April 2024

UNIVERSITY OF
BIRMINGHAM

University of Birmingham Research Archive

e-theses repository

This unpublished thesis/dissertation is copyright of the author and/or third parties. The intellectual property rights of the author or third parties in respect of this work are as defined by The Copyright Designs and Patents Act 1988 or as modified by any successor legislation.

Any use made of information contained in this thesis/dissertation must be in accordance with that legislation and must be properly acknowledged. Further distribution or reproduction in any format is prohibited without the permission of the copyright holder.

© Copyright by ANDREW ROBERT STEVENS, 2024

All Rights Reserved

Abstract

Neurotrauma (traumatic injury to the brain or spinal cord) is a global health challenge and major cause of death and disability. Pharmacological therapies, typically targeting single receptors or pathways, have thus far proven unable to significantly affect the multitude of pathophysiological mechanisms required to promote effective repair. Photobiomodulation (PBM) is a therapeutic approach using red/near-infrared light to promote recovery after injury by mitigating neuroinflammation and preventing neuronal apoptosis. Whilst there is growing evidence for the efficacy of PBM in neurotrauma, two key translational barriers exist: (1) the ability to deliver effective doses transcutaneously to injured tissue within the CNS of humans is severely limited; and (2) there is no currently available means to monitor the therapeutic response to PBM in order to optimise dose delivery. As such, this thesis seeks to develop a medical device which can address these barriers: an implant, composed of optical fibres, which is capable of both delivering PBM directly to injured tissue; and monitor the response to therapy using Raman spectroscopy (RS).

A systematic review of the literature identified key components of effective PBM in traumatic brain injury (TBI): use of 660 nm or 810 nm wavelengths; short duration of treatment; and early implementation post-injury. Using an experimental rat model of spinal cord injury (SCI), 660 nm PBM (24.4 mW/cm^2, 60 s, daily for 7 days) was shown to improve functional recovery, lesion size and axonal regeneration after SCI, and delivery of PBM using an implantable device improved early expression of regeneration-associated proteins. Raman spectral differences were identified between injury conditions. Using a rat model of mild TBI, 810 nm transcranial PBM was superior to 660 nm PBM, alone and in combination (20.0 mW/cm^2, 120 s, daily

for 3 days), and resulted in improvements in functional recovery. PBM reduced astrocyte and microglial activation after TBI, and treatment was identifiable by spectral biomarkers monitored using RS. Investigation of the mechanisms of PBM demonstrated that 660 nm PBM reduces neuroinflammation in microglia *in vitro*. Transcriptomics and pathway analysis of 660 nm PBM vs no treatment in the injured spinal cord demonstrated significant upregulation of regeneration associated pathways, and downregulation of key apoptotic genes. This was accompanied by reduced transcription of mitochondrial components and ribosomal transcription, supporting a metabolic mechanism for PBM which leads to neuroprotective and restorative effects. Development of prototype devices demonstrated that effective doses of PBM can be delivered to the brain and spinal cord, using optical fibres integrated into clinically-feasible implantation methods. Lensing and spatial distribution of fibres improved PBM distribution to maximise the volume of injured tissue exposed to treatment.

The work presented here demonstrates proof-of-concept for implantable PBM delivery, with monitoring of effect using RS. Beneficial effects have been demonstrated in both TBI and SCI, and the doses to achieve these effects are deliverable using the developed prototype. RS has been demonstrated as a suitable tool to identify biomarkers associated with successful and effective PBM therapy. This supports the subsequent development of a full device prototype, suitable for use in first-in-human study, toward the translation of this device for clinical trials.

For Freya

Acknowledgements

I would like to express my sincere appreciation for the support, mentorship and guidance given by my supervisors, Prof. Antonio Belli and Prof. Zubair Ahmed. For all your encouragement and reassurance; for the advice and teaching; for supporting the (countless) grant applications; for giving me the opportunity; thank you. True to your word, you got me through it.

The concept for the medical device was developed by Mr David Davies, Prof. Will Palin and Dr Mohammed Hadis. I am very grateful that they had confidence in me to continue their work on the project, and for the support they have offered throughout my studies. I would also like to thank Mr Davies for convincing me to take on this project, and for his encouragement, ideas and endless enthusiasm. I would also like to thank Prof. Palin and Dr Hadis, along with Prof. Mike Milward, for welcoming me into their laboratory and research group, and for offering their expertise, equipment and training which made the work in this thesis possible.

This work would not have been possible without research funding, and I extend my sincere thanks to the following organisations for their financial support: National Institute for Health Research (Surgical Reconstruction and Microbiology Research Centre); Royal College of Surgeons of England (Roberta Swan Surgical Research Fellowship); The Wellcome Trust (Translational Development Fund); Medical Research Council (Impact Accelerator Account); Midland Neuroscience Teaching and Research Fund; University of Birmingham Research Development Fund; and Celentyx Ltd for their support via an industry secondment.

Over the course of the last three years, I have been fortunate to meet many colleagues and collaborators from across the University of Birmingham, to whom I would also like to express my gratitude, for their support and assistance with this project. To name but a few, from neuropharmacology, I would like to thank Prof. Nick Barnes and Jamie Cowley for their support in using their microglial model. For their support with Raman spectroscopy, I would like to thank Dr Liam Kelleher, as well as Prof. Pola Goldberg Oppenheimer and her group, particularly Clarissa Stickland and Georgia Harris. I would also like to thank all of my colleagues from Neuroscience and Ophthalmology, for their support and encouragement during my studies. I am especially grateful to Abhinav Thareja for the time he spent teaching and assisting with my laboratory work, and to Dr Valentina Di Pietro for her help and expertise in RNA extraction and transcriptomics. Thank you also to Alice Phillips, Freya Godfrey and Freya Anderson for their contributions to this work during their projects in the laboratory. I would also like to express sincere thanks to the staff of the University of Birmingham Biomedical Services Unit for their assistance throughout this project.

To my parents, Bob and Sharon, thank you for everything. I promise this is the last one. To my family and friends, thank you for tolerating my complaining, for occasionally feigning interest in lasers, and for just being there. Lastly, to my wife, Freya, for making this possible, and for making it fun. How you put up with me at the best of times, let alone through this, I will never know. If each word of this thesis were a "thank you" that I owe to you, it wouldn't be enough.

Contents

Abstract **i**

Acknowledgements **v**

Contents **vii**

List of Figures **xvii**

List of Tables **xxv**

List of Acronyms **xxvii**

List of Terms **xxxix**

Publications and Collaborative Working Declaration **xliii**

1 Introduction **1**

1.1 Neurotrauma 2

1.2 Traumatic brain injury 2

1.2.1 Importance 2

1.2.2 Classification 3

1.2.3 Pathophysiology 4

1.2.4 Clinical management 5

1.3 Spinal cord injury 7

1.3.1 Importance 7

1.3.2 Classification . . . 7
1.3.3 Pathophysiology . . . 9
1.3.4 Clinical management . . . 11
1.4 Repair after neurotrauma . . . 12
1.4.1 Overview . . . 12
1.4.2 Molecular and cellular responses to neurotrauma . . . 12
1.4.3 Approaches to promoting neuroprotection and neuroregeneration . . . 24
1.5 Photobiology . . . 28
1.5.1 Photons . . . 29
1.5.2 Photons in biological tissues . . . 29
1.5.3 Photobiological interactions . . . 34
1.6 Photobiomodulation . . . 35
1.6.1 History . . . 36
1.6.2 Parameters and radiometry . . . 37
1.6.3 Medical applications . . . 37
1.6.4 Photobiomodulation in neurotrauma . . . 39
1.6.5 Translational barriers . . . 39
1.7 Raman spectroscopy . . . 40
1.8 Pilot data . . . 42
1.9 Premise and device concept . . . 47
1.10 Hypothesis . . . 50
1.11 Aims and objectives . . . 50

2 Literature Review **53**

2.1 Introduction . . . 53
2.2 Aims . . . 54
2.3 Methods . . . 54
2.3.1 Study selection . . . 55
2.3.2 Data extraction . . . 56

2.3.3 Synthesis of results . . . 56
2.3.4 Risk of bias . . . 56
2.3.5 Statistical analysis . . . 56
2.4 Results . . . 57
2.4.1 Human studies . . . 57
2.4.2 Animal studies . . . 59
2.4.3 Meta-analysis . . . 61
2.4.4 Neurological severity score . . . 62
2.4.5 Lesion size . . . 65
2.4.6 Alternative functional outcomes . . . 66
2.4.7 Histological outcomes . . . 68
2.4.8 Mechanistic outcomes . . . 68
2.4.9 Experimental factors . . . 72
2.4.10 Risk of bias assessment . . . 72
2.5 Discussion . . . 72
2.5.1 Establishing an optimum modality . . . 73
2.5.2 Establishing an optimum dose . . . 75
2.5.3 Establishing an optimum dose regimen . . . 75
2.5.4 Establishing an optimum delivery technique . . . 76
2.5.5 Establishing the translational effect in humans . . . 77
2.5.6 Establishing a mechanism . . . 78
2.5.7 Risk of bias . . . 79
2.5.8 Controls . . . 80
2.5.9 Photobiomodulation parameter reporting . . . 80
2.5.10 Limitations . . . 80
2.5.11 Future directions . . . 82
2.5.12 Conclusion . . . 82

3 PBM/RS in SCI **83**

3.1 Introduction . . . 83

3.1.1 Dose *in vitro* . . . 86

3.1.2 Dose *in vivo* . . . 88

3.1.3 Delivery . . . 92

3.1.4 Aims . . . 92

3.2 Materials and methods . . . 93

3.2.1 *In vitro* methods . . . 93

3.2.2 *Ex vivo* methods . . . 97

3.2.3 Physical analysis methods . . . 98

3.2.4 *In vivo* spinal cord injury . . . 99

3.2.5 *In vivo* administration of photobiomodulation therapy . . . 101

3.2.6 Functional assessments . . . 102

3.2.7 Immunohistochemistry . . . 103

3.2.8 Microscopy and image analysis . . . 104

3.2.9 Quantification of regenerating axons . . . 104

3.2.10 Quantification of GAP43^{+} DRGN . . . 105

3.2.11 Evaluation of the glial scar . . . 105

3.2.12 Raman spectroscopy . . . 105

3.2.13 Statistical analysis . . . 106

3.3 Results . . . 107

3.3.1 Serum withdrawal model of injury in primary cell culture of dorsal root ganglion neurons . . . 107

3.3.2 *In vitro* dose delivery calibration . . . 107

3.3.3 Photobiomodulation is neuroprotective in an *in vitro* model of spinal cord injury . . . 107

3.3.4 Photobiomodulation increases neurite outgrowth in an *in vitro* model of spinal cord injury . . . 109

3.3.5 Photobiomodulation can be delivered in effective doses transdermally in an *in vivo* model of spinal cord injury . . . 110
3.3.6 Photobiomodulation can be delivered in effective doses invasively in an *in vivo* model of spinal cord injury . . . 124
3.3.7 *Post mortem* Raman spectroscopy is feasible for injury site spectral analysis in an *in vivo* model of spinal cord injury . . . 126
3.3.8 Photobiomodulation increases expression of regeneration associated proteins in an *in vivo* model of spinal cord injury: a pilot study . . . 127
3.3.9 An implant for delivery of photobiomodulation to the injured spinal cord is feasible *in vivo* . . . 127
3.3.10 Invasive and transcutaneous photobiomodulation improve early histological outcomes in an *in vivo* model of spinal cord injury . . . 128
3.3.11 Photobiomodulation improves neuroregeneration in an *in vivo* model of spinal cord injury . . . 129
3.3.12 Photobiomodulation reduces lesion size in an *in vivo* model of spinal cord injury . . . 129
3.3.13 Photobiomodulation improves functional outcomes in an *in vivo* model of spinal cord injury . . . 130
3.3.14 *Post mortem* Raman spectroscopy detects injury progression in an *in vivo* model of spinal cord injury . . . 130
3.4 Discussion . . . 144
3.4.1 Dosing . . . 144
3.4.2 Mechanism . . . 147
3.4.3 Delivery . . . 148
3.4.4 Raman spectroscopy . . . 150
3.4.5 Limitations . . . 151
3.5 Conclusion . . . 153

4 PBM/RS in TBI **155**

4.1 Introduction 155
4.1.1 Selection of a suitable model of traumatic brain injury 157
4.1.2 Selection of photobiomodulation parameters for traumatic brain injury . 160
4.1.3 Raman spectroscopy in traumatic brain injury 160
4.1.4 Objectives 160
4.2 Materials and methods 161
4.2.1 *Ex vivo* cadaveric modelling and profilometry 161
4.2.2 Weight drop model of mild traumatic brain injury 162
4.2.3 Application of photobiomodulation 162
4.2.4 Functional outcome assessments 163
4.2.5 Tissue processing 163
4.2.6 Staining of histological samples 164
4.2.7 Image acquisition and analysis 164
4.2.8 Raman spectroscopy 164
4.2.9 Statistical analysis 165
4.3 Results 166
4.3.1 Effective doses of 660 and 810 nm photobiomodulation to the brain are achievable via transcutaneous administration in an *in vivo* model of traumatic brain injury 166
4.3.2 Photobiomodulation improves functional recovery after traumatic brain injury 171
4.3.3 Photobiomodulation reduces astrocyte activation in the acute phase after traumatic brain injury 172
4.3.4 Photobiomodulation reduces microglial activation in the acute phase after traumatic brain injury 172
4.3.5 Photobiomodulation modestly reduces extracellular matrix deposition after traumatic brain injury 172

4.3.6 Photobiomodulation reduces expression of cleaved caspase-3 in the acute phase after traumatic brain injury . . . 173
4.3.7 Raman spectroscopy discriminates between injury states after traumatic brain injury . . . 184
4.4 Discussion . . . 200
4.4.1 Wavelength selection . . . 200
4.4.2 Delivery method . . . 201
4.4.3 Mechanism . . . 201
4.4.4 Raman spectroscopy . . . 202
4.4.5 Limitations . . . 203
4.5 Conclusion . . . 203

5 Mechanisms of PBM 205

5.1 Introduction . . . 205
5.1.1 Mechanisms of photobiomodulation . . . 205
5.1.2 Objectives . . . 210
5.2 Materials and methods . . . 211
5.2.1 Induced monocyte-derived microglia cell culture . . . 211
5.2.2 Application of photobiomodulation to iMDM . . . 212
5.2.3 Cytokine release quantification . . . 215
5.2.4 iMDM immunofluorescence . . . 215
5.2.5 iMDM imaging and image analysis . . . 216
5.2.6 DRGN serum transfer model . . . 216
5.2.7 DRGN preconditioning model . . . 217
5.2.8 Cell lysis and protein extraction . . . 217
5.2.9 BDNF ELISA . . . 218
5.2.10 *In vivo* model . . . 218
5.2.11 Transcriptomics . . . 218
5.2.12 Tissue extraction and RNA purification . . . 218

5.2.13 WT-seq and analysis . . . 219
5.2.14 Statistical analysis . . . 220
5.3 Results . . . 220
5.3.1 Induced monocyte-derived microglia model . . . 220
5.3.2 DRGN cell culture model . . . 224
5.3.3 *In vivo* spinal cord injury model . . . 225
5.3.4 Transcriptomics . . . 230
5.4 Discussion . . . 245
5.4.1 Neuroinflammation and glial activation . . . 245
5.4.2 Glial activation and the glial scar . . . 247
5.4.3 Preconditioning . . . 248
5.4.4 Paracrine signalling . . . 248
5.4.5 Extracellular matrix deposition . . . 249
5.4.6 Transcriptomics . . . 249
5.4.7 Limitations . . . 251
5.4.8 Future directions . . . 251
5.4.9 Conclusions . . . 252

6 Device Development **253**
6.1 Introduction . . . 254
6.1.1 Delivery methods of photobiomodulation . . . 254
6.1.2 Objectives . . . 255
6.2 Materials and methods . . . 256
6.2.1 Beam characterisation . . . 256
6.2.2 Prototype design and rendering . . . 256
6.2.3 Optical phantom . . . 257
6.2.4 Porcine tissue modelling . . . 257
6.2.5 Optical sources and fibres . . . 258
6.2.6 Thermal imaging . . . 258

6.2.7 Statistical analysis . . . 260
6.3 Results: Brain interface . . . 261
6.3.1 Original prototype . . . 261
6.3.2 Rendering material . . . 263
6.3.3 Fibre coupling . . . 267
6.3.4 Exit geometry . . . 270
6.3.5 Fibre modifications . . . 274
6.3.6 Lensing . . . 278
6.3.7 Fibre recess . . . 278
6.3.8 Fibre diameter and numerical aperture . . . 282
6.3.9 Diffuser . . . 285
6.3.10 Light source . . . 285
6.3.11 Spatial fibre orientation . . . 289
6.3.12 Optimal design features . . . 295
6.3.13 Summary . . . 295
6.4 Results: Spinal cord interface . . . 297
6.4.1 Fibre diameter . . . 298
6.4.2 Multiple fibres . . . 299
6.4.3 Fibre orientation . . . 299
6.4.4 Summary . . . 303
6.5 Discussion . . . 305

7 General Discussion **309**
7.1 Key findings . . . 309
7.2 Interpretations . . . 310
7.2.1 Efficacy of photobiomodulation . . . 310
7.2.2 Mechanisms of photobiomodulation . . . 310
7.2.3 Raman spectroscopy . . . 311
7.2.4 Devices . . . 313

7.3 Limitations 314
7.4 Recommendations 316
7.4.1 Photobiomodulation 316
7.4.2 Raman spectroscopy 317
7.4.3 Device development 318

8 Conclusions **321**

Bibliography **323**

A RS in TBI Review **387**

B Pilot Data **411**

C Antibodies **431**

D TBI Immunofluorescence Supplementary Images **433**

E Additional Raman Spectroscopy Analysis **457**

F WT-seq **465**

G Cranial Transmission **467**
G.1 Introduction 467
G.2 Methods 467
G.3 Results 468
G.4 Discussion 469

H PPIE **475**
H.1 Traumatic brain injury device 475
H.2 Spinal cord injury device 479

List of Figures

1.1 Intracranial pressure monitoring 6

1.2 Gross anatomy of axial section of spinal cord 8

1.3 Spinal cord tracts 9

1.4 Incomplete spinal cord injury syndromes 10

1.5 Acute phase of CNS trauma 15

1.6 Excitotoxicity in neurotrauma 16

1.7 Mitochondrial dysfunction in neurotrauma 18

1.8 Acute and chronic phases of glial scar formation 23

1.9 Photobiological interactions across the EM spectrum 30

1.10 Absorption spectra of water and haemoglobin 32

1.11 Schematic of absorption and scatter through a media 34

1.12 Pilot data: hippocampal slice PBM dosing 43

1.13 Pilot data: hippocampal slice PBM duration 44

1.14 Pilot data: hippocampal slice PBM region 45

1.15 Pilot data: hippocampal slice Raman spectroscopy 46

1.16 Schematic of device concept 48

1.17 Transcranial and implantable PBM devices 49

2.1 Systematic review flow chart 58

2.2 Meta-analysis of neurological severity score 62

2.3 Meta-analysis of lesion size 66

2.4 Risk of bias assessment for pre-clinical studies 73

3.1 Timeline of pathophysiology in traumatic SCI 85
3.2 Traumatic SCI models 90
3.3 Primary cell culture of DRGN 94
3.4 BioTHOR device 96
3.5 Optomechanics and beam characterisation 99
3.6 Thoracic spine anatomy with laminectomy site 100
3.7 Dorsal column crush model of traumatic SCI 101
3.8 Implantable PBM *in vivo* 102
3.9 DRGN serum withdrawal model 108
3.10 *In vitro* LED array 111
3.11 Neuroprotection in DRGN 112
3.12 Neurite outgrowth in DRGN 114
3.13 tcPBM and iPBM schematic 115
3.14 Thor LX2 transcutaneous profilometry 116
3.15 Thor LX2 transcutaneous thermography 117
3.16 MD-III laser transmission values 119
3.17 MD-III laser transmission beam profilometry 120
3.18 MD-III transcutaneous thermography 122
3.19 Temporal transcutaneous thermography 123
3.20 Implantable PBM device 125
3.21 Implant profiling 131
3.22 Implant profiling in cadaveric model 132
3.23 Implant thermography 133
3.24 Pilot Raman spectroscopy in a cadaveric model 134
3.25 *In vivo* pilot of transcutaneous PBM 135
3.26 *In vivo* implantation of PBM device 136
3.27 Early axonal regeneration at SCI site with implantable and transcutaneous PBM 137

3.28 Upregulation of GAP43 within DRGN with implantable and transcutaneous PBM 138
3.29 Axonal regeneration at SCI site with transcutaneous PBM 139
3.30 Axonal quantification rostral and caudal to SCI site with transcutaneous PBM . 140
3.31 Glial scar size quantification after SCI with transcutaneous PBM 141
3.32 Functional recovery with transcutaneous PBM after SCI 142
3.33 Raman spectroscopy of SCI site 143
3.34 1660 cm^{-1} peak intensity after SCI 144

4.1 Timeline of pathophysiology in TBI 156
4.2 Pre-clinical models of TBI 159
4.3 PBM application procedure 163
4.4 Brain areas imaged 165
4.5 Cadaveric profiling of transcranial 660 and 810 nm PBM 168
4.6 FLIR images of thermal profiling of transcranial 660 and 810 nm PBM 169
4.7 Temporal plots of thermal profiling of transcranial 660 and 810 nm PBM 170
4.8 Photobiomodulation improves functional outcome after traumatic brain injury . 171
4.9 PBM reduces immunofluorescence of GFAP 3 days post-injury 174
4.10 Immunofluorescence of GFAP 4 weeks post-injury 176
4.11 Immunofluorescence of CD11b 3 days post-injury 178
4.12 Immunofluorescence of extracellular matrix proteins 3 days post-injury 180
4.13 Immunofluorescence of extracellular matrix proteins 4 weeks post-injury 182
4.14 PBM reduces expression of cleaved caspase-3 after TBI 183
4.15 Merged Raman spectra after TBI 185
4.16 Quantitative analysis of peak intensities of Raman spectra 186
4.17 Extended spectra of treatment, injury and control groups 187
4.18 PCA of peak intensities of extended Raman spectra after TBI (treatment vs injury vs control) 188
4.19 PCA of peak intensities of extended Raman spectra after TBI (injury vs control) 190
4.20 PCA of peak intensities of Raman spectra after TBI (treatment vs injury) 192

4.21 Fingerprint region spectra (means) of treatment, injury and control groups . . . 193
4.22 PCA of fingerprint region means of mapped Raman spectroscopy after TBI (treatment vs injury vs control) . . . 194
4.23 PCA of fingerprint region means of mapped Raman spectra after TBI (injury vs control) . . . 196
4.24 PCA of fingerprint region means of mapped Raman spectra after TBI (treatment vs injury) . . . 198

5.1 Bespoke 96 well plate illumination device . . . 213
5.2 Plate illumination map . . . 214
5.3 iMDM immunofluorescence . . . 222
5.4 TNF-α release from iMDM after PBM . . . 222
5.5 Immunofluorescence images of iMDM after PBM . . . 223
5.6 iMDM CTCF and cell counts . . . 224
5.7 iMDM preconditioning . . . 225
5.8 DRG serum transfer and preconditioning . . . 226
5.9 BDNF concentrations of cell lysates . . . 226
5.10 Cleaved caspase-3 immunofluorescence in DRG 3 days post-SCI . . . 228
5.11 ECM and glial activation marker immunofluorescence in injury site 3 days post-SCI . . . 229
5.12 WT-seq differentially expressed genes with PBM . . . 232
5.13 k-means analysis of effect of PBM . . . 233
5.14 Pathway analysis using g:profiler . . . 234
5.15 GO and KEGG pathway analysis . . . 235
5.16 Neuron projection morphogenesis pathways . . . 236
5.17 Ribosomal pathway . . . 237
5.18 NADH (ubiquinone) pathway . . . 238
5.19 Calcium signalling pathways . . . 238
5.20 Top 20 upregulated genes . . . 239

5.21 Top 20 downregulated genes . . . 240
5.22 Top 20 regeneration associated genes . . . 241
5.23 Top 20 apoptosis associated genes . . . 242
5.24 Additional key differentially expressed genes with selected gene families . . . 243

6.1 PBM delivery devices . . . 256
6.2 Optical phantom cast . . . 258
6.3 Optical phantom profiling . . . 259
6.4 Calculating emissivity . . . 260
6.5 Original cranial bolt profiling . . . 262
6.6 Thermography of original bolt through moulds . . . 264
6.7 Thermography of original bolt in cadaveric model . . . 265
6.8 Bolt prototypes in differing rendering materials . . . 266
6.9 Profiling of bolt prototypes in differing rendering materials . . . 266
6.10 Beam profile images of bolt prototypes using fibre coupling . . . 268
6.11 Profilometry of bolt prototypes using fibre coupling . . . 269
6.12 Exit geometry designs . . . 271
6.13 Conical exit and flat geometry profilometry . . . 272
6.14 Punch, concave and conical exit geometry profilometry . . . 273
6.15 Fibre tip modification profilometry . . . 275
6.16 Exit geometry modification with leaky fibres profilometry . . . 276
6.17 Combined effect of fibre tip modification and conical exit geometry . . . 277
6.18 Bolt design with PMMA lens . . . 278
6.19 Beam distribution with plano-convex lens . . . 279
6.20 Fibre recess profilometry . . . 280
6.21 Beam distribution with plano-convex lens . . . 281
6.22 Fibre core diameter . . . 283
6.23 Fibre core diameter beam profilometry . . . 284
6.24 Effect of a diffuser . . . 286

6.25 Effect of a biconcave lens 287
6.26 Effect of light source type 288
6.27 CAD drawing of Lampshade V01 289
6.28 Lampshade V01 versus straight fibre orientation 290
6.29 CAD drawing of Lampshade V02 291
6.30 Lampshade V02 versus straight fibre orientation 292
6.31 Lampshade V01 versus Lampshade V02 293
6.32 Beam profilometry of Lampshade V01, V02 and straight fibre orientations . . . 294
6.33 Lampshade V02 bolt in skull 296
6.34 Spinal device schematics 298
6.35 Spinal probe: effect of fibre diameter 300
6.36 Spinal probe: effect of multiple fibres 301
6.37 Spinal probe: effect of fibre orientation 302
6.38 Implantation of a spinal fibre optic 304
6.39 PBM delivery devices (with developed implants) 305

D.1 GFAP 3 dpi Cg1. Cg2, Fr2 434
D.2 GFAP 3 dpi Fr1, HL, FL 435
D.3 GFAP 3 dpi cc, PV-CPu 436
D.4 GFAP 4 wpi Cg1 437
D.5 GFAP 4 wpi Cg2 438
D.6 GFAP 4 wpi Fr2 439
D.7 GFAP 4 wpi Fr1 440
D.8 GFAP 4 wpi HL 441
D.9 GFAP 4 wpi FL 442
D.10 GFAP 4 wpi cc 443
D.11 GFAP 4 wpi PV-CPu 444
D.12 CD11b/CD68 3 dpi Cg2, Cg1, Fr2 445
D.13 CD11b/CD68 3 dpi Fr1, HL, cc 446

D.14 CD11b/CD68 3 dpi PVA, PV-CPu, Ch 447
D.15 Laminin/Fibronectin Cg2 448
D.16 Laminin/Fibronectin Cg1 449
D.17 Laminin/Fibronectin Fr2 450
D.18 Laminin/Fibronectin Fr1 451
D.19 Laminin/Fibronectin HL 452
D.20 Laminin/Fibronectin cc 453
D.21 Laminin/Fibronectin Ch 454
D.22 Laminin/Fibronectin PV-CPu 455

E.1 Fingerprint region of individual spectra from treatment, injury and control groups458
E.2 PCA of individual fingerprint region spectra from mapped Raman spectroscopy after TBI (treatment vs injury vs control) 459
E.3 PCA of individual fingerprint region spectra from mapped Raman spectroscopy after TBI (injury vs control) 461
E.4 PCA of individual fingerprint region spectra from mapped Raman spectroscopy after TBI (treatment vs injury) 463

G.1 Scalp and skull transmission of PBM 469
G.2 Scalp, skull and brain transmission of PBM 470
G.3 D4σ distribution of transmitted PBM 471
G.4 Correlation of transmission of PBM through brain and an optical phantom . . . 472
G.5 Profilometry of transmission of PBM through brain and an optical phantom . . 474

List of Tables

1.1 ASIA grade and functional outcome 8

1.2 Neuroprotective/neurorestorative trials in TBI 26

1.3 Neuroprotective/neurorestorative trials in SCI 27

1.4 Summary of radiometry terminology 38

2.1 Summary table of included pre-clinical studies 60

2.2 Dosing regimens of included pre-clinical studies 64

2.3 Subgroup analysis for neurological severity score 65

2.4 Risk of bias assessment for clinical studies 74

3.1 PBM dosing of DRGN 87

3.2 Summary table of included pre-clinical SCI *in vivo* studies 91

3.3 MD-III laser calibration 118

3.4 MD-III transcutaneous transmission values 119

3.5 Implantable fibre optic probe transmission 126

5.1 Summary of discussed gene terms and functions 244

C.1 Antibody clones used 432

G.1 Cranial transmission of 660 nm light 471

List of Acronyms

5-ALA 5-aminolavulanic acid. 35

5-FDU 5-fluoro-2-deoxyuridine. 95, 109, 113, 147

ADDA 5 (1-[2-(1-adamantyl)ethoxy]-3-(3,4-dihydro-2(1H)-isoquinolinyl)-2-propanol). 206

Akt protein kinase B. 210

AMPA α-amino-3-hydroxy-5-methyl-4-isoxazole propionate. 16

ANOVA analysis of variance. 106, 165, 220, 260

ASIA American Spinal Injury Association. 7, 8

ATP adenosine triphosphate. 5, 17, 18, 68, 69, 78, 79, 83, 87, 88, 206, 208, 209, 231, 250, 311

AUC area under the curve. 98, 106, 165

Bax Bcl2 (B-cell lymphoma 2) associated X protein. 22, 70

BBB blood-brain barrier. 4, 5

Bcl-2 B-cell lymphoma 2. 22, 70

BDNF brain-derived neurotrophic factor. 14, 70, 71, 78, 79, 87, 208, 209, 218, 220, 225, 226, 249

BINT blast-induced neurotrauma. 59, 70

BrdU bromodeoxyuridine. 70, 71

BSA bovine serum albumin. 94, 95, 104

BW beam-walking. 163, 171, 200

CA cornu Ammonis. 43, 70, 78

CAD computer-aided design. 256, 262, 263, 266, 268, 289, 291

CAM cell adhesion molecules. 249

CAM computer aided manufacture. 256

cAMP cyclic adenosine monophosphate. 206, 209, 210, 250

caspase cysteinyl aspartic proteinases. 22

CBF cerebral blood flow. 71

CCI controlled cortical impact. 49, 59, 158, 159

CCO cytochrome c oxidase. 17, 31, 36, 37, 79, 83, 148, 200, 206

CD cluster of differentiation. 14, 86, 172, 179, 201, 211, 246

CI confidence interval. 8

CNS central nervous system. xvii, 1, 2, 5, 9, 12–15, 17, 19–22, 24, 28, 39, 42, 47, 48, 50, 84, 86, 149, 150, 152, 201, 205, 211, 212, 253–255, 305, 310, 313, 317, 322

COX cyclooxygenase. 231, 311

CRASH corticosteroid randomisation after significant head injury. 25

CREB cAMP response element-binding protein. 87, 209

CSF cerebrospinal fluid. 6, 21, 25, 75, 77

CSPG chondroitin sulphate proteoglycans. 21, 150, 247

CT computerised tomography. 3

CTCF corrected total cell fluorescence. 216, 223, 224

CW continuous wave. 61, 62, 68, 73, 74, 87

DAI diffuse axonal injury. 3, 158

DAPI 4,6-diamidino-2-phenylindole. 71, 95, 96, 104, 108, 113, 139

DCC dorsal column crush. 89, 97, 99, 100, 118, 127–130, 139–141, 144, 218, 219, 232, 239–243

DCX double cortin. 71

DEGs differentially expressed genes. 230, 232, 237, 238, 243

DG dentate gyrus. 43, 71

DMEM Dulbecco's Modified Eagle Medium. 107, 108, 113, 217, 224, 226

DNA deoxyribonucleic acid. 19

dpi days post injury. 70, 105, 128, 147, 150, 151, 164, 171, 172, 175, 179, 181, 185, 201, 247, 314, 315, 433

DRG dorsal root ganglia. 93, 94, 103, 105, 128, 225, 228

DRGN dorsal root ganglion neurons. xviii, xxv, 86–88, 93–96, 101, 107–109, 111, 113, 115, 127, 128, 135, 138, 147, 148, 209, 211, 216–218, 224–226, 228, 248, 249

ECM extracellular matrix. 13, 21, 201, 211, 218, 227, 249

EGF epidermal growth factor. 13

ELISA enzyme-linked immunosorbent assay. 215, 218

EM electromagnetic. xvii, xxxix, xl, 28–31, 35, 38

ER endoplasmic reticulum. 209, 250

ERK extracellular signal-regulated kinases. 87, 209

ETC electron transport chain. 17–19, 36, 83, 206

FBS foetal bovine serum. 107, 113, 115, 224

FDR false discovery rate. 219, 220, 230, 232–235, 239–243

FGF fibroblast growth factor. 14, 208

FLIR Forward Looking InfraRed. 98, 99, 120, 122, 123, 126, 258

FOV field of view. 134

FWHM full width at half maximum. 38, 61, 111, 120

GAGE generally applicable gene-set enrichment. 219, 230

GAP43 growth associated protein 43. x, 104, 105, 127–129, 135, 137–139, 144

GCS Glasgow coma scale. 3

GFAP glial fibrillary acidic protein. 20, 69, 172, 175, 177, 201, 227, 229, 245–248

GLAST glutamate-aspartate transporter. 16

GLT-1 glutamate transporter-1. 16

GO gene ontology. 219, 220, 230, 233–235, 237, 238

HCA hierarchical cluster analysis. 166, 189, 191, 193, 195, 197, 199, 460, 462, 464

HIF1A hypoxia inducible factor 1 subunit alpha. 148

Iba1 ionised calcium binding adaptor molecule 1. 220, 221, 227, 229

ICP intracranial pressure. 4–6, 12, 25, 47, 157, 254, 255

IFNγ interferon gamma. 15

IGF-1 insulin-like growth factor 1. 14

IL-1α interleukin-1 alpha. 20

IL-1β interleukin-1 beta. 14, 20

IL-10 interleukin-10. 14

IL-6 interleukin-6. 14, 20

ILs interleukins. 13

iMDM induced monocyte-derived microglia. 212, 220–224, 245, 251

iPBM invasive photobiomodulation. 128, 136–138, 144, 146, 148, 149, 152

IR infrared. 29

ISNCSCI International Standards for Neurological Classification of Spinal Cord Injury. 7

ISP intraspinal pressure. 25

JAK janus kinases. 201, 210

KEGG Kyoto encyclopedia of genes and genomes. 219, 220, 230, 233–235, 238

KO knock-out. 59

Lcn2 lipocalin-2. 201, 210

LED light-emitting diode. xviii, 57, 61, 92, 95, 111, 146, 212, 254, 285, 288, 295, 306, 319

LFP lateral fluid percussion. 59, 158, 159

LGIC light-gated ion channels. 36

LLLT low-level laser (or light) therapy. 35

LPS lipopolysaccharide. 220–225, 245, 246

MAG myelin-associated glycoprotein. 21, 23

MAP2 microtubule-associated protein 2. 69

MAPK mitogen-activated protein kinases. 209

MBP myelin basic protein. 15, 69

MMP mitochondrial membrane potential. 79, 206, 208, 209

MMPs matrix metalloproteinases. 13

mPTP mitochondrial permeability transition pore. 18

MRI magnetic resonance imaging. 57

MSC mescenchmyal stem cells. 77

MTT 3-(4, 5-dimethylthiazolyl-2)-2, 5-diphenyltetrazolium bromide. 208

MWM Morris water maze. 66, 67, 69, 76

NA numerical aperture. 101, 110, 124, 125, 132, 269, 272, 275–277, 279, 280, 282–284, 286, 287, 290, 292, 293, 295, 298, 300–302, 306

NADH nicotinamide adenine dinucleotide hydrogen. 17, 230, 238, 311

NC3Rs National Centre for the Replacement Refinement and Reduction of Animals in Research. 93, 161, 211

NEST NeuroThera Effectiveness and Safety Trials. 39, 54, 81

NFκB nuclear factor kappa-light-chain-enhancer of activated B cells. 20, 148, 210

NF-200 neurofilament 200. 105, 128, 129, 138, 140, 218, 228

NGF nerve growth factor. 14, 208

NgR Nogo receptor. 23

NICE The National Institute for Health and Care Excellence. 38, 317

NIR near-infrared. 28, 31

NIRS near-infrared spectroscopy. 33

NMDA N-methyl-d-aspartate. 16, 209, 231, 250

NO nitric oxide. 18, 19, 79, 87, 206, 207, 209

Nogo-A neurite outgrowth inhibitor-A. 21, 23

NOS nitric oxide synthase. 18, 87, 207, 250

NPLT nano-pulsed laser therapy. 61, 67–70, 74

NPrC neural progenitor cells. 208

NSS neurological severity score. xvii, 61–63, 65, 68, 69, 74, 80, 160

NTF neurotrophic factor(s). 23, 24

OCT optimal cutting temperature [compound]. 103, 163

OGD oxygen-glucose deprivation. 208

OMgp oligodendrocyte myelin glycoprotein. 21, 23

OPC oligodendrocyte progenitor cells. 247

P/S penicillin/streptomycin. 94, 95, 217

p75^{NTR} p75 neurotrophin receptor. 23

PA-1 plasminogen activator 1. 13

PBM photobiomodulation. xvii–xix, xxv, 1, 2, 28, 35–40, 42, 43, 46–51, 53–57, 59, 61, 62, 65, 67–73, 75–84, 86–89, 92, 93, 100, 102, 105, 107, 109, 111, 113, 115, 116, 118, 120, 126–130, 135–141, 144–153, 155, 157–164, 168–173, 175, 177, 179, 181–185, 189, 193, 195, 199–212, 216–232, 239–243, 245–256, 265, 303, 305–307, 309–311, 313–319, 321, 322, 433, 460, 464, 467, 469–471, 473, 474

PBMC peripheral blood mononuclear cells. 211

PBS phosphate buffered saline. 95, 103, 104, 127, 134, 215–217

PbtO2 partial pressure of brain tissue oxygen. 6, 47, 254

PCA principal component analysis. xix, xx, xxiii, 165, 166, 184, 189, 191, 193, 195, 197, 199, 200, 202, 312, 313, 457, 460, 462, 464

PCR polymerase chain reaction. 251

PDGF platelet-derived growth factor. 13

PI3K phosphoinositide 3-kinases. 210

PKA protein kinase A. 209

PLA polylactic acid. 256, 257, 261, 263, 266, 267, 270, 271, 274, 278, 299

PMMA polymethyl methacrylate. xxi, 278–281

PN peroxynitrite. 19

PNS peripheral nervous system. 2, 86

PPIE patient and public involvement and engagement. xlvii, 475

PPV positive predictive value. 8

PRISMA Preferred Reporting Items for Systematic Reviews and Meta-analyses. 54, 57, 58

PW pulsed wave. 61, 62, 68, 73, 74, 203

R/NIR red/near-infrared. 28, 33, 37, 55, 76, 79, 205, 257

Raf rapidly accelerated fibrosarcoma. 209

RAP regeneration associated protein. 128, 144, 148, 149, 151, 153, 309, 321

Ras rat sarcoma virus. 209

RNA ribonucleic acid. 218, 219, 315

RNS reactive nitrogen species. 18, 19

ROCK Rho-associated protein kinase. 23

ROI region of interest. 127, 134, 164, 218, 259

ROS reactive oxygen species. 10, 13, 16, 18, 19, 36, 69, 79, 83, 87, 207, 209

RPQ Rivermead post-concussion questionnaire. 57

RS Raman spectroscopy. 1, 2, 34, 40–43, 47, 48, 50, 51, 83, 93, 126, 155, 157–161, 202, 203, 253, 309, 311–313, 315, 318, 321, 322

SCI spinal cord injury. xviii, 1, 2, 7–12, 14, 22, 24, 25, 39, 47, 49–51, 53, 75, 83, 84, 86, 89, 90, 92, 93, 105, 118, 124–126, 139, 144, 147–153, 155, 160, 201, 203, 208, 210, 218, 225, 232, 245–250, 253, 254, 295, 306, 307, 309–311, 313, 316, 321

SD standard deviation. 56, 61, 111, 168, 266, 269, 272, 273, 275–277, 279, 280, 283, 286–288, 290, 292, 293, 300–302

SEM standard error of the mean. 56, 61, 108, 113, 115, 137, 138, 142, 222–224, 226, 228, 229, 471

SERS surface-enhanced Raman scattering. 41

SKiNET self-optimising Kohonen index network. 318

SMA SubMiniature version A. 97, 102, 258, 267–269, 272, 273, 275–277, 279, 280, 283, 286–288, 290, 292, 293, 300–302

STAT3 signal transducer and activator of transcription 3. 20, 70, 86, 148, 201, 210

strep-HRP horseradish peroxidase conjugated streptavidin. 215

SVZ subventricular zone. 71

SYRCLE Systematic Review Center for Laboratory Animal Experimentation. 56, 73, 79

TBI traumatic brain injury. 1–6, 9, 11, 12, 18, 24, 25, 36, 39, 42, 47–51, 53–55, 57, 59, 67–74, 77–79, 81, 82, 84, 146, 147, 155, 157–162, 164, 171–173, 184, 185, 189, 191, 193, 195, 197, 199–203, 208, 247–249, 253, 254, 295, 306, 307, 309–312, 314, 316, 317, 321, 460, 462, 464, 468, 471

tcPBM transcutaneous photobiomodulation. 127–130, 137–142, 144, 146, 148, 149

TGFβ transforming growth factor beta. 13

TNFα tumour necrosis factor alpha. 14, 20, 215, 220–222, 225, 245, 246, 309

tpi teeth per inch. 161

Trk tropomyosin receptor kinase. 23

TRP transient receptor potential (channels). 36, 207

TUJ1 neuron-specific antibody to class III β-tubulin. 71

UV ultraviolet. 28, 29, 124

UVB ultraviolet B. 35

VEGF vascular endothelial growth factor. 13

WD weight drop. 59, 158, 159

WGMT wire grip and motion test. 66, 67

wpi weeks post-injury. 172, 177, 182, 248, 315, 433

WT wild-type. 59

List of Terms

abscopal effect Effects of locally administered radiant energy elicited at a remote anatomical site which was not exposed to radiant energy. 77

absorption The capture of photonic energy by matter. 29

anisotropic scattering Scattering of light that is not equally probable to be in any direction; that is that there is different scatter dependent on the direction. 33

average irradiance The radiant power received per unit area (W/cm^2). 38

beam area Area of a beam perpendicular to the beam axis, derivative of D in a circular beam by $\pi(D/2)^2$ (cm^2). 38

beam diameter Diameter of a line perpendicular to, and intersecting the beam axis. 38

biphasic effect Two discretely differing biological effects from a stimulus when delivered at lower vs higher levels. 36

chromophore A molecule or compound which is able to absorb specific wavelengths of light. 31

coherent A light source (or beam) which emits (or transmits) photons of the same phase and wavelength. 37

continuous wave An EM wave with constant amplitude. 37

D4σ A measure of beam width. Calculated from the mean of 4x the standard deviation of the distributed beam intensity along x and y axes. 37, 38

elastic scattering Scattering of light where the energy (and wavelength) of the scattered photon is identical to that of the incident photon. 32

exposure time Duration of radiant exposure. 38

full width at half maximum The width of a curve where it is at exactly half its maximal peak. 37

inelastic scattering Scattering of light where the energy (and wavelength) of the scattered photon differs to that of the incident photon. 34

isotropic scattering Scattering of light that is equally probable to be in any direction. 33

phase The alignment of completion of a full cycle of an oscillating wave. 37

polarisation The geometric orientation of oscillation of transverse waves. 37

power (radiant flux) Energy transmitted by EM radiation per unit time (W or J/s). 38

pulse frequency The number of pulse cycles completed in a second (Hz). 38

pulsed wave An EM wave with varying amplitude delivered in repeated pulses at a given frequency. 37

radiant energy Energy transmitted by EM radiation (J). 38

radiant exitance The radiant power emitted per unit area (W/cm^2). 38

radiant exposure/fluence Energy transmitted by EM radiation per unit area (J/cm^2). 38

reciprocity The concept that delivery of lower radiant power over a longer time period is equivalent to delivery of higher radiant power over a shorter time period, where the total transmitted energies are equal. 37, 146

reflection Elastic collision of light onto a surface which results in light "bouncing" off of the surface, where the angle of reflection away from the surface is equal to the angle of incident light onto it. 29

refraction A change in direction in the propagation of light, as it passes from one media to another, dependent on the refractive index of each material. 29

scattering Where light is forced to deviate in trajectory. 29

wavelength Distance (nm) between two corresponding points on a waveform. 38

PUBLICATIONS AND COLLABORATIVE WORKING DECLARATION

Due to the collaborative nature of this project, some work performed in part by other researchers has been included in this thesis. Similarly, over the course of its production, some of the work in this thesis has been published in peer-reviewed journals. For transparency, a declaration of any results generated through collaborative work, and any material used which has been published by the thesis author, is given below. All illustrations and schematic diagrams were created by the thesis author.

Introduction

Sections of this chapter, either adapted or *verbatim*, have been published in peer-reviewed journals:

A.R. Stevens, A. Belli, Z. Ahmed. Neurotrauma - From Injury to Repair: Clinical Perspectives, Cellular Mechanisms and Promoting Regeneration of the Injured Brain and Spinal Cord. *Biomedicines* 2024, 12, 643. doi: 10.3390/biomedicines12030643.

A.R. Stevens, M. Hadis, M. Milward, Z. Ahmed, A. Belli, W. Palin, D.J. Davies. Photobiomodulation in Acute Traumatic Brain Injury: A Systematic Review and Meta-Analysis. *J Neurotrauma* 2023, Feb;40(3-4):210-227. doi: 10.1089/neu.2022.0140.

A.R. Stevens, C. Stickland, G. Harris, Z. Ahmed, P. Goldberg Oppenheimer, A. Belli, D.J. Davies. Raman Spectroscopy as a Neuromonitoring Tool in Traumatic Brain Injury: A Systematic Review and Clinical Perspectives. *Cells* 2022 Apr 5;11(7):1227. doi: 10.3390/cells11071227.

D.J. Davies, M. Hadis, V. Di Pietro, G. Lazzarino, M. Forcione, G. Harris, **A.R. Stevens**, W.C. Soon, P. Goldberg Oppenheimer, M. Milward, A. Belli, W. Palin. Photobiomodulation reduces hippocampal apoptotic cell death and produces a Raman spectroscopic "signature". *PLoS ONE* 2022 17(3): e0264533. doi: 10.1371/journal.pone.0264533.

Literature review

This chapter has been published in the Journal of Neurotrauma:

A.R. Stevens, M. Hadis, M. Milward, Z. Ahmed, A. Belli, W. Palin, D.J. Davies. Photobiomodulation in Acute Traumatic Brain Injury: A Systematic Review and Meta-Analysis. *J Neurotrauma* 2023 Feb;40(3-4):210-227, doi: 10.1089/neu.2022.0140.

The systematic review was performed by the thesis author, with second searches and validation performed by Zubair Ahmed. Minimal contributions to narrative were added by co-authors.

PBM/RS in SCI

The work in this chapter has been published in the peer-reviewed journal, Bioengineering and Translational Medicine:

A.R. Stevens, M. Hadis, A. Phillips, A. Thareja, M. Milward, A. Belli, W. Palin, D.J. Davies, Z. Ahmed. Implantable and transcutaneous photobiomodulation promote neuroregeneration and recovery of lost function after spinal cord injury *Bioeng Transl Med* 2024;e10674, doi: 10.1002/btm2.10674.

Elements of this chapter were possible through collaborative working. Work described was performed by the thesis author, with the following contributions from collaborators: acquisition

of Raman spectra was performed by Clarissa Stickland; analysis of functional outcomes was performed with the assistance of Prof. Zubair Ahmed; dorsal column crush surgeries were performed by Prof. Zubair Ahmed; functional outcomes were assessed by two observers, the thesis author and Abhinav Thareja.

PBM/RS in TBI

Elements of this chapter have been published in the peer-reviewed journal, Biomedicines:

A.R. Stevens, A. Belli, Z. Ahmed. Neurotrauma—From Injury to Repair: Clinical Perspectives, Cellular Mechanisms and Promoting Regeneration of the Injured Brain and Spinal Cord. *Biomedicines* 2024, 12(3), 643, doi: 10.3390/biomedicines12030643.

Aspects of this chapter were possible through collaborative working. Work described was performed by the thesis author, with the following contributions from collaborators: acquisition of Raman spectra was performed with the assistance of Liam Kelleher; weight drop modelling was (in part, in addition to the majority performed by the thesis author) performed by Prof. Zubair Ahmed and Dr Valentina Di Pietro; functional outcomes were assessed by two observers, the thesis author and Abhinav Thareja.

Mechanisms of PBM

Aspects of this chapter were possible through collaborative working. Work described was performed by the thesis author, with the following contributions from collaborators: preparation of induced microglial cultures was performed by Jamie Cowley.

Device development

All work described in this chapter was performed by the thesis author.

General discussion

Some included discussion in this chapter has been adapted from work written by the thesis author which has been published in a peer-reviewed journal:

A.R. Stevens, C. Stickland, G. Harris, Z. Ahmed, P. Goldberg Oppenheimer, A. Belli, D.J. Davies. Raman Spectroscopy as a Neuromonitoring Tool in Traumatic Brain Injury: A Systematic Review and Clinical Perspectives. *Cells* 2022 Apr 5;11(7):1227. doi: 10.3390/cells11071227.

Conclusions

All narrative in this chapter was written by the thesis author.

Appendix A: RS in TBI

This paper has been published in a peer-reviewed journal:

A.R. Stevens, C. Stickland, G. Harris, Z. Ahmed, P. Goldberg Oppenheimer, A. Belli, D.J. Davies. Raman Spectroscopy as a Neuromonitoring Tool in Traumatic Brain Injury: A Systematic Review and Clinical Perspectives. *Cells* 2022 Apr 5;11(7):1227. doi: 10.3390/cells11071227. The systematic review was performed by the thesis author, with second searches and validation performed by Zubair Ahmed. Minimal contributions to narrative were added by co-authors.

Appendix B: Pilot data

This paper has been published in a peer-reviewed journal:

D.J. Davies, M. Hadis, V. Di Pietro, G. Lazzarino, M. Forcione, G. Harris, **A.R. Stevens**, W.C. Soon, P. Goldberg Oppenheimer, M. Milward, A. Belli, W. Palin. Photobiomodulation reduces hippocampal apoptotic cell death and produces a Raman spectroscopic "signature". *PLoS ONE* 2022 17(3): e0264533. doi: 10.1371/journal.pone.0264533.

Appendix C: Antibodies

All narrative in this chapter was written by the thesis author.

Appendix C: TBI immunofluorescence supplementary images

All imaging in this chapter was performed by the thesis author.

Appendix D: Additional Raman spectroscopy analysis

All analysis in this chapter was performed by the thesis author.

Appendix D: WT-seq

The description of the methodology in this chapter was provided by Qiagen (Holden, Germany), whom performed the WT-seq.

Appendix E: Cranial transmission

All experiments and analysis in this chapter were performed by the thesis author.

Appendix E: PPIE

The reports of these patient and public involvement and engagement (PPIE) meetings were collated by Laura Nice/Jenny Needham as summaries of meetings where projects were presented by the thesis author.

Chapter 1

INTRODUCTION

This thesis is centred on the development of a medical device for the acute treatment of the central nervous system (CNS) after traumatic injury: traumatic brain injury (TBI) and spinal cord injury (SCI). The overarching aim is to develop a device which uses photobiomodulation (PBM): the application of light for therapeutic purposes, to promote neural regeneration and neuroprotection after neurotrauma. The device also incorporates a diagnostic optical technique, Raman spectroscopy (RS), as a label-free method for *in vivo* tissue analysis. The work in this thesis aims to address the translational barriers which have hitherto prevented successful clinical translation of PBM and RS in neurotrauma. As such, this work seeks to:

1. identify and elucidate these barriers;
2. propose solutions;
3. demonstrate pre-clinical evidence for the efficacy and utility of these solutions;
4. further the understanding of the mechanisms of PBM; and
5. develop medical technology which can feasibly interface with the CNS to deliver PBM in humans.

Chapter 1 introduces the clinical and biological contexts of TBI and SCI, and summarises the scientific and technological concepts of the optical technologies employed, along with the

overarching hypothesis, aims and objectives of the thesis. Chapter 2 presents the prior literature in the area of PBM in TBI. Chapter 3 presents work to optimise the dosing and delivery methods of PBM using *in vitro* and *ex vivo* models and applies these with RS analysis using an *in vivo* model of SCI. Chapter 4 performs *ex vivo* PBM dose delivery optimisation, followed by application of PBM and RS in an experimental model of TBI. Chapter 5 uses a variety of models to further explore and delineate the mechanism(s) of PBM in neurotrauma. To support the onward translation of this device concept, feasibility for technological application in humans is demonstrated in Chapter 6 by developing functioning prototypes for application of optical technologies to the injured CNS via an optical interface. Chapter 7 discusses the findings and limitations of this work in context of the wider literature, and proposes future directions for the development of this device. Chapter 8 presents the conclusions of the thesis.

1.1 Neurotrauma

Trauma, a physical injury resulting from external force, is ubiquitous across geographical and societal groups. Whilst many body tissues are capable of significant biological and functional repair, the human CNS is not. Neuronal cells of the CNS do not replicate to replace cells lost after injury, and, in contrast to the peripheral nervous system (PNS), surviving neurons are not capable of regeneration of axons.[1] Due to the unique and profound functions of the CNS, the ramifications of such injury without recovery are of enormous significance; to individuals, their families and to wider society. Amongst several possible and valid definitions of neurotrauma, the present thesis will consider neurotrauma as: “traumatic injury to the brain or spinal cord”.

1.2 Traumatic brain injury

1.2.1 Importance

TBI is a significant global health challenge with no disease-modifying treatment shown to improve outcomes. A principle cause of morbidity and mortality in young adults, incidence

of TBI in Europe is estimated at 1012 cases per 100 000 people per year, and 939 per 100 000 globally.[2,3] TBI disproportionately affects low to middle income countries and is a significant financial burden to economies worldwide: the total annual cost globally is estimated in the region of £47 billion.[4,5] Risk of suffering TBI is present across society, and injuries are often sustained through road traffic collisions, falls or assault. A wide range of life-changing sequelae may result from injury, including: motor and sensory deficits; cognitive dysfunction; impaired consciousness; depression; behavioural change; and increased mortality including increased risk of suicide.[6–10] These consequences are as yet untreatable beyond supportive therapy in the acute setting, and rehabilitative therapy thereafter.[11]

1.2.2 Classification

TBI is typically stratified by either symptomatic severity or anatomical measures. The clinical presentation of a patient can be used to stratify severity based on the Glasgow coma scale (GCS),[12] where a GCS score of 13-15 is mild; 9-12 is moderate; and ≤8 is severe.[13] The duration of loss of consciousness or of post-traumatic amnesia can also be used to classify injury severity.[14] Anatomical measures can be used, for example to classify TBI by location of haemorrhage, presence of diffuse axonal injury (DAI), or by a the presence/absence of multiple variables as in the computerised tomography (CT) derived Marshall or Rotterdam grading systems.[15,16] Emerging alternative stratification tools, for example using immunohistochemical markers, are in early research phases and not in widely accepted practice.[17]

The differences in outcomes, management and pathophysiology vary enormously across this spectrum of injury sub-types. Though termed "mild" TBI (also termed concussion), the long term consequences can be of severe impact to quality of life and ability to function.[6–10] Mild TBI accounts for up to 90% of TBI, and persistent symptoms occur in up to one third. Severe TBI is invariably a life-changing injury, with mortality rates as high as 40%, and often results in long-term significant disability.[6]

1.2.3 Pathophysiology

The damage resulting from trauma to the brain is typically considered in two parts: primary and secondary. Primary brain injury is sustained from the immediate event of trauma itself, whilst 'secondary brain injury' occurs after injury, due to a variety of adverse sequelae resulting in further cell death and damage.[18] Though primary injury may be modifiable (through personal and public health measures to reduce incidence and severity of injuries), acute medical care interventions typically focus on mitigation of secondary injury mechanisms as modifiable targets to improve patient outcomes.[19]

Secondary injury to neural tissue can occur through a broad variety of mechanisms, spanning cellular, systemic and anatomical processes. On a cellular level, mitochondrial dysfunction after injury can result in metabolic failure and oxidative stress, which have a role in the propagation of injury and triggering apoptotic cell death after TBI, with associated effects on long-term function.[20,21] "Metabolic crisis" is a phenomonenon in TBI which results in severe metabolic dysfunction despite adequate provision of metabolic substrates.[22] Neuroinflammatory processes, whilst essential for wound healing and restoration of the blood-brain barrier (BBB), contribute to harmful propagation of injury into the penumbra (areas of brain with lesser injury, surrounding an injury focus).

The initial injury, and ensuing necrosis, results in dysregulated release of neurotransmitters (such as glutamate).[23] Their activation of local synapses leads to uncontrolled regional depolarisation, known as excitotoxicity. Locally this can compound metabolic dysfunction, and result in regional dysregulated cellular activation (cortical spreading depolarisation) or global seizures.[24,25]

Development of cerebral oedema and expansion of surgical mass lesions result in increasing intracranial pressure (ICP). Due to the fixed volume of the intracranial space, expansion of intracranial contents results in increasing intracranial pressure (ICP), as first described in the Monro-Kellie hypothesis.[26] This can result in a variety of harmful sequelae, and is the prevailing cause of mortality in the early phase after TBI. Anatomically, this can lead to compression (and obfuscation *in extremis*) of arteries, cranial nerves and ultimately brain parenchyma. Where this

includes compromise of the delicate structures of the brainstem, including regions of respiratory control, mortality rates are high. Increasing ICP also results in global compromise of cerebral blood flow, with unfavourable effects on brain oxygenation and provision of essential metabolites (predominantly glucose), which further propagate cellular dysfunction after injury.

Whilst the pathophysiology of TBI has been subject of many years of scientific research, the processes which propagate neural damage after injury are not fully elucidated. More recent observations have been attributed to support emerging hypotheses of further injury mechanisms. For example, damage to the BBB through injury may result in dysregulated entry of systemic molecules into the CNS, such as pro-inflammatory cytokines. Similarly, dysregulated release of adenosine triphosphate (ATP) from damaged neuronal cells has been hypothesised to contribute to increased neuroinflammation and cellular apoptosis.[27]

1.2.4 Clinical management

Whilst there is growing understanding of the pathophysiological mechanisms of TBI, the opportunities to measure and correct these processes are limited. Contemporary therapeutic paradigms in severe TBI are predominantly based on the monitoring of ICP, informing clinical decision making to offer intervention for correction and normalisation of these indices as supportive measures.[28]

ICP monitoring is performed using a temporarily implantable fibre optic probe, which is placed within brain parenchyma to a depth of 1.5-2.0 cm. This probe connects externally to a transducer and user interface, and real-time pressure readings can be presented to the clinician. The procedure to implant an ICP probe requires a hole (typically 2.7 mm) to be drilled through the skull, and an opening in the dura and cortex is made via sharp puncture. The entry point is typically at Kocher's point (an anatomical point 11 cm posterior to the nasion in the mid-pupillary line). A plastic self-tapping, hollow bore "bolt" is screwed into the burr hole to house and secure the ICP wire (Fig. 1.1).

Acute management of TBI is predominantly targeted at control of ICP alongside general supportive intensive care and management of other traumatic injuries.[28] Therapeutic interven-

tion to reduce ICP uses: (1) patient head positioning; (2) therapeutic hypocapnia; (3) sedation and paralysis; (4) osmotic therapy; (5) diversion of cerebrospinal fluid (CSF); (6) barbiturate coma; and (7) decompressive craniectomy.

Since the establishment of ICP monitoring as standard-of-care in TBI, additional monitoring capabilities have been integrated with an ICP probe into cranial access to increase the scope of the "bolt" paradigm (Fig. 1.1). This has seen greatest success with the introduction of partial pressure of brain tissue oxygen (PbtO2) monitoring, and to a lesser extent with microdialysis probes.[29–31] The extent to which the inclusion of these technologies provides information which is of value for clinical decision making is yet to be conclusively determined,[28–31] and as such they are variably implemented. Despite this, early investigations of PbtO2 monitoring have shown a trend toward lower mortality with its use, and it has been included in TBI guidelines for ensuring adequate cerebral oxygenation during hyperventilation therapy.[28,29]

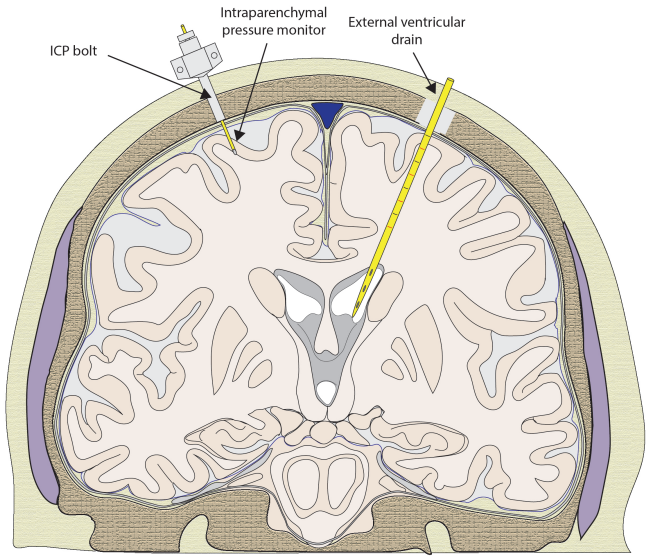


Figure 1.1: Schematic diagram of a coronal section of the head, with an intraparenchymal pressure monitor (with bolt) and external ventricular drain *in situ*. Both devices may be used to measure pressure from their respective compartments via a transducer. Intraparenchymal pressure monitors are typically inserted to a 1.5-2.0 cm depth via a 2.7 mm burr hole. External ventricular drains typically require 5.0-6.0 cm insertion depths to reach the lateral ventricle, often via a 1.4 cm burr hole.

1.3 Spinal cord injury

1.3.1 Importance

Traumatic SCI is damage to the spinal cord sustained by mechanical trauma, resulting in a deficit in neurological function.[32] Injuries affect people across society and the globe with a bimodal age distribution. Injury may occur from falls, road traffic collisions, or sporting accidents, and less commonly from assaults and penetrating or blast injuries.[33] SCI is of increasing prevalence, with 2500 new cases occurring each year in the UK alone,[34] resulting in additional lifetime costs of around £2.8 billion each year.[34,35] The lifelong disabilities caused by SCI are typically profound: loss of motor and sensory function, loss of bladder, bowel and sexual function, as well as neuropathic pain and, in some cases tetraplegia and loss of respiratory function.[32] Whilst some recovery can be anticipated in incomplete injuries through rehabilitation, the loss of function sustained in SCI is typically permanent, as the spinal cord has no innate capacity for repair.[36]

1.3.2 Classification

SCI is most commonly classified using the American Spinal Injury Association (ASIA) impairment scale.[37] This classifies injury based on neurological impairment, measured by a thorough and standardised International Standards for Neurological Classification of Spinal Cord Injury (ISNCSCI) clinical examination.[37] This identifies whether an injury is "complete" (*i.e.* no preservation of any neurological function below the level of injury) or "incomplete" (*i.e.* partial preservation of motor, sensory or sacral function below the level of injury) as well as identifying the neurological level of injury (the lowest (most caudal) spinal cord segment with intact neurological function). Both neurological level of injury and injury severity indicate prognosis for functional outcome.[38] Severity of injury has been correlated with likelihood of recovery of ability to walk independently, with complete injury (ASIA A) associated with the lowest probability of independent ambulation (Table 1.1).[39,40]

The spinal cord is a complex structure, composed of grey matter (unmyelinated) and white

Table 1.1: Table to show likelihood of independent ambulation after one year (positive predictive value (PPV)) with 95% confidence interval (CI) based on ASIA impairment scale classification. Based on van Middendorp *et al.*, 2011.[39,40]

ASIA grade	PPV	95% CI
A	8.3%	5.2–12.6
B	39.4%	27.6–52.2
C	61.8%	50.0–72.8
D	97.3%	92.2–99.4

matter (myelinated). Three columns can be recognised as structures of the cord which run bilaterally in a rostro-caudal plane: the dorsal, ventral, and lateral columns (Fig. 1.2). Within these columns are more focal tracts, categorised as ascending (afferent/sensory), descending (efferent/motor) and mixed (Fig. 1.3). SCI can be classified by spinal cord regions damaged/affected by the injury. SCI can be complete (with all tracts affected) or incomplete (with some tracts preserved).[41,42] The regions affected and corresponding clinical presentations of incomplete SCI syndromes are shown in Fig.1.4. Similarly, the variety of pre-clinical models for the study of traumatic SCI result in differing neurological deficits dependent on the anatomical location of injury (discussed further in Chapter 3).

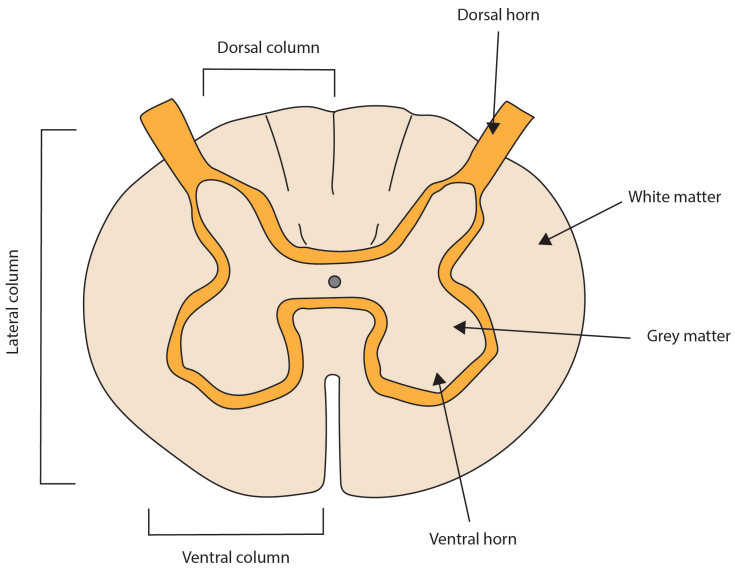


Figure 1.2: Schematic diagram of an axial cross section of spinal cord, with labelled dorsal (posterior); lateral; and ventral (anterior) column on the left side (structures exist bilaterally).

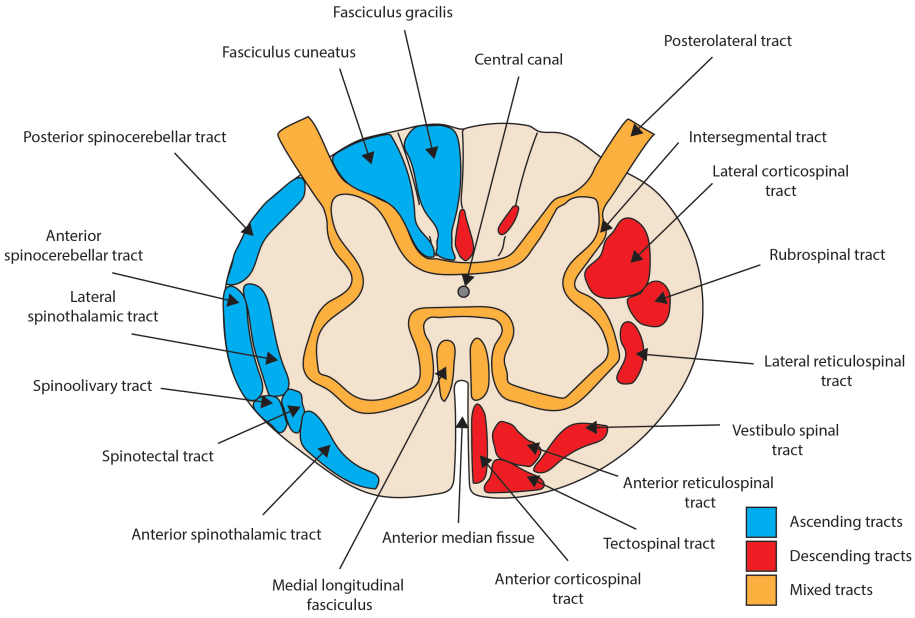


Figure 1.3: Schematic diagram of an axial cross section of spinal cord, with labelled ascending, descending and mixed tracts (structures exist bilaterally).

1.3.3 Pathophysiology

The pathophysiological phenomena of SCI, as an acute traumatic insult to the tissues of the CNS resulting in swelling within an enclosed and fixed bony/dural space, hold many similarities to those described above for TBI. Similarly, the injury mechanisms can be considered as "primary" (occurring directly from trauma) and "secondary" (as subsequent events and consequences following the primary injury).[32,38,43] Primary injury can result from direct spinal cord trauma (from penetrating objects or primary blast trauma) or, more commonly in civilian settings, from mechanical force and pressure from fracture and/or dislocation of the surrounding spinal column. Bony displacement, fragments, or the resultant haemorrhage can all mediate primary injury.[32,38,43] Though primary injury typically occurs at the time of the trauma, the primary *neuronal* injury can be delayed from the index traumatic event: trauma which compromises the mechanical stability of the spinal column can result in delayed mechanical injury to the spinal cord only after weight-bearing.[32,43]

The initial trauma to the spinal column and spinal cord commences a complex cascade of secondary injury mechanisms as seen in TBI.[32,38] In the acute post-injury phase, vascular or

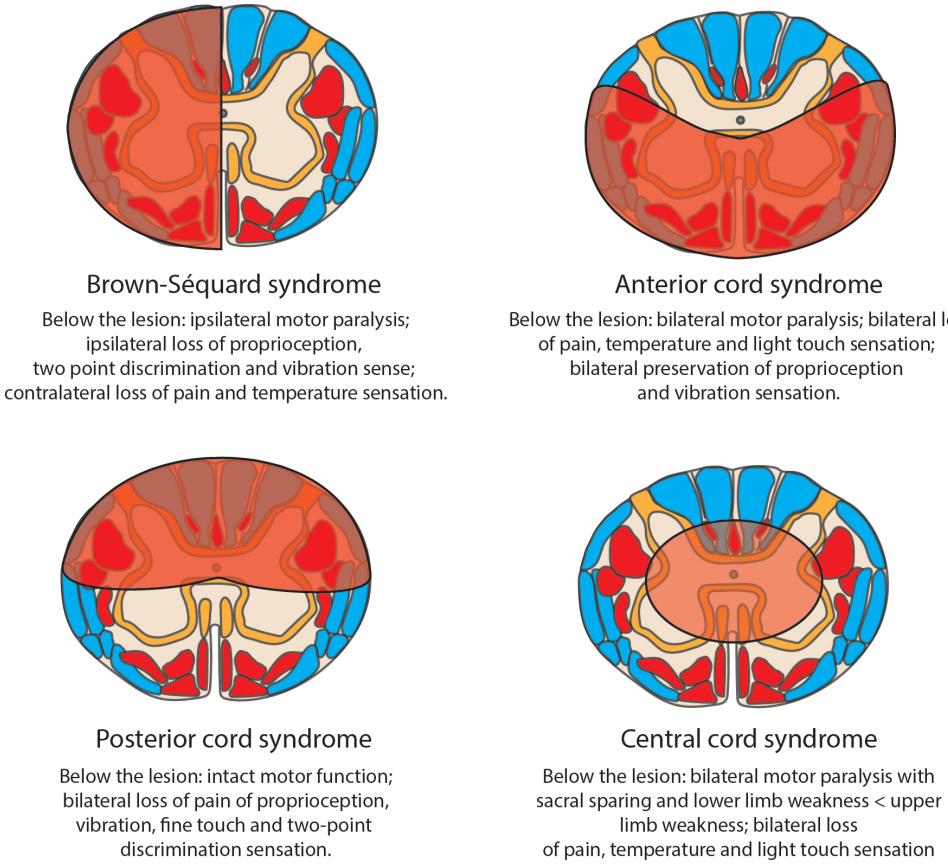


Figure 1.4: Schematic diagram of four classically described incomplete SCI syndromes with brief descriptions of their typically associated clinical features. Damaged regions are denoted in translucent red. Motor tracts = opaque red; sensory tracts = blue. Brown-Séquard syndrome (hemisection of the cord) can occur following trauma, particularly penetrating injuries, or from expansion of tumours. Anterior cord syndrome can occur during trauma, or from ischaemia. Posterior cord syndrome typically follows posterior spinal artery occlusion. Central cord syndrome is a cervical SCI which can occur after a hyperextension injury with pre-existing cervical stenosis.

bony injury can compromise arterial supply to spinal cord, resulting in prolonged ischaemia and ongoing neuronal injury, whilst resultant haemorrhage can cause direct pressure effects with compressive results on local tissue.[32,38] Dysregulated necrotic release of neurotransmitters such as glutamate from neurons and astrocytes can result in excitotoxicity, intracellular calcium influx and ultimately cell death via apoptosis or necrosis, accompanied by sodium influx resulting in oedema.[32,38,44,45] Release of reactive oxygen species (ROS) and free radicals from necrotic or dysfunctional cells can result in oxidative stress and lipid peroxidation.[43,46] Metabolic failure further contributes to this ionic and oxidative disturbance.[46,47] Damage to the blood-spinal cord

barrier disturbs its protective function and allows unregulated migration of inflammatory cells and cytokines into the area to perpetuate the local inflammatory response, contributing to local spinal cord oedema which can in turn result in further damage.[32,48,49]

In the sub-acute phase, there is ongoing apoptotic activation within and surrounding the umbra of the injury site.[50,51] Growth cone collapse and aborted axonal regeneration, alongside demyelination and continuation of the inflammatory response which initiates to glial scar formation.[1,36,52] In the chronic phase, cavitation and maturation of the glial scar occur, alongside degeneration and regression of remaining axons.[38]

1.3.4 Clinical management

In further similarity to TBI, current therapeutic paradigms for SCI focus primarily on the mitigation and prevention of secondary damage, particularly via mechanical and hypoxic damage.[32,43] Initial assessment and management follows Advanced Trauma Life Support guidelines and involves resuscitation for maintenance of spinal perfusion pressure.[32,53,54] Immobilisation of the spinal column for resuscitation is recommended where possible to avoid additional damage through mechanical effects of instability.[55] More definitive management of bony instability is typically achieved via fixation, accompanied (where indicated) by bony decompression of the spinal cord.[32,56–59] Alongside the supportive management of blood pressure dysregulation (through neurogenic shock, orthostatic hypotension and autonomic dysreflexia) targeted blood pressure regulation and augmentation to optimise spinal cord perfusion is also a common feature of contemporary management.[60,61] Management beyond these targeted therapies is supportive, managing the complications of injury and promoting functional recovery through physical therapies and rehabilitation.[32]

1.4 Neuroprotection and regeneration after trauma

1.4.1 Overview

The general principles of promoting survival and repair of the CNS after traumatic injury can be considered across both TBI and SCI. CNS neurons do not regenerate once lost, and typically enter apoptosis or a senescent state after injury. Lost or dysfunctional neurons cannot be replaced through proliferation. The resulting immediate cell loss and damage (primary injury) from the direct effect of the trauma is not modifiable once sustained. As such, current interventions in neurotrauma care aim to mitigate secondary injury. In TBI, optimisation of ICP decreases early mortality and mitigates pressure induced brain injury. In SCI, spinal decompression and fixation may mitigate propagation of secondary injury through pressure effects; or prevent subsequent mechanical injury through bony instability. Despite intense research into neuroprotection and neuroregeneration however, no therapeutic intervention is presently available in clinical practice which improves functional outcomes through promoting survival or repair of neurons after injury. Long-term rehabilitation may improve functionality, facilitated through neural plasticity and use of physical aids, to improve function. However, the capacity for functional recovery by these means are extremely limited at present, particularly in severe injuries, owing largely to the innate failure of the CNS to repair or regenerate neurons.[1]

1.4.2 Molecular and cellular responses to neurotrauma

CNS responses to injury can be categorised into three phases, which are not entirely distinct but represent the principal processes occurring over general time periods after injury:[62]

1. Acute phase (0-3 days post-injury)
2. Subacute phase (3-14 days post injury)
3. Chronic/consolidation phase (14 days onwards post-injury)

Acute phase

Haemorrhage Alongside direct traumatic injury to neural tissue and necrosis of directly damaged cells, the index traumatic event results in damage to local blood vessels leading to haemorrhage into the injury site.[32] This, if of large volume, can result in direct compressive effects, but also results in the delivery of cytokines, blood-derived immune cells (lymphocytes, neutrophils, macrophages), clotting factors and growth factors into the injured neural tissue, usually excluded by the blood-CNS barrier. Activation of the coagulation cascade and platelet degranulation results in the release of transforming growth factor beta (TGFβ) and platelet-derived growth factor (PDGF).[63]

Inflammatory cascade The presence of TGFβ and proinflammatory mediators activates the inflammatory cascade, directly and indirectly via chemokine release (activating migrated blood-derived immune cells (macrophages, neutrophils, lymphocytes) and resident glia (microglia, astrocytes)) (Fig. 1.5). This activation potentiates the inflammatory response, releasing further TGFβ, as well as interleukins (ILs) and epidermal growth factor (EGF). Local chemokines also result in tissue remodelling via upregulation of matrix metalloproteinases (MMPs) and plasminogen activator 1 (PA-1). Whilst the initial neuroinflammatory response is triggered during this acute phase, the immune response persists throughout these three phases.[64]

To an extent, leucocyte activation is favourable in traumatic injury for the restoration of blood-CNS barrier integrity, wound sterilisation and debridement. Neutrophils sterilise the wound of foreign pathogens by phagocytosis, with release of inflammatory mediators, MMPs and ROS. Monocytes deposit extracellular matrix (ECM) and initiate angiogenesis via release of vascular endothelial growth factor (VEGF). Macrophages and resident microglia have a multi-faceted role with favourable effects (mitigating local excess neurotransmitters from necrotic release, tissue remodelling, growth factor release) and unfavourable effects (myelin phagocytosis, demyelination, astrogliosis).

Populations of microglia, the resident macrophage of the CNS, demonstrate a biphasic response after trauma, with peaks within acute/sub-acute as well as chronic consolidation

phases.[62,64,65] However, of greater importance than microglial presence/proliferation to the favourable or unfavourable environment post-injury, is the phenotype. It has been traditionally understood that microglia may become polarised to an M1 phenotype (pro-inflammatory) or M2 phenotype (anti-inflammatory, pro-repair)[62,66–68] in a similar manner to the model which describes phenotypic switching for circulating macrophages. According to this dichotomous model, microglia in the M1 state are understood to release pro-inflammatory cytokines/chemokines, including TNFα, IL-6 and IL-1β and increase surface expression of CD16, CD32, CD40 and CD86 (Fig. 1.5). Conversely, M2 phenotype microglia increase expression of CD163 and CD206, producing anti-inflammatory mediators (IL-10), growth factors (IGF-1, FGF) and neurotrophic factors (NGF, BDNF).[68,69] However, recent advances in the understanding of microglia and their behaviour *in vivo* has led to increased recognition of a complex and heterogeneous range of microglial phenotypes across a variety of conditions.[70] A diverse set of transcriptional states, reflecting a multitude of functional modes, have been identified in microglial populations *in vivo*. As such, microglial functional reactivity in response to injury microenvironments is likely to represent a much broader range of states than a simple M1 or M2 phenotype. As such, the previously described M1 and M2 "phenotypes" are likely to each represent a wide range of functional possibilities, which may not be wholly "pro-" or "anti-" inflammatory.[70,71] Furthermore, in addition to well-characterised inhibitors/mediators of inflammation, there is increased recognition of microglial-neuronal crosstalk mechanisms such as via direct synaptic interfaces, extracellular vesicles and communication via gap junctions. Together these suggest a complex and pivotal role of microglia in neurotrauma pathophysiology.[72]

(Monocyte-derived) macrophages exhibit similar phenotypes to microglia, with corresponding pro- and anti-inflammatory roles within the CNS after injury. Pro-inflammatory phenotypic switching of macrophages in SCI has been related to presence of extracellular myelin,[73] present in abundance in the context of axonal disruption within white matter. Macrophages, alongside microglia, debride myelin and other cellular debris by phagocytosis, performed mainly by macrophages in the lesion core and by microglia within the penumbra. Foam macrophages, formed by macrophage uptake of lipid from myelin, can result in additional damage once

formed.[62] Influx of peripherally circulating T-lymphocytes similarly can promote microglial activation through release of IFNγ[74] and perpetuate increased permeability of the blood-CNS-barrier through release of perforin.[75] Conversely, T-cell responses to myelin basic protein (MBP) have been associated with chaperoned microglial phenotype shifting toward pro-repair functions.[76]

Compromise of the blood-CNS barrier Loss of integrity of the blood-CNS barrier from the immediate trauma, sustained by the molecular activity described above by T-lymphocytes amongst other mechanisms, permits continued compromise of the exclusion of the CNS from the blood-derived immune cells and circulating inflammatory mediators, which in turn sustains the neuroinflammatory response and contributes to developing oedema (Fig. 1.5).

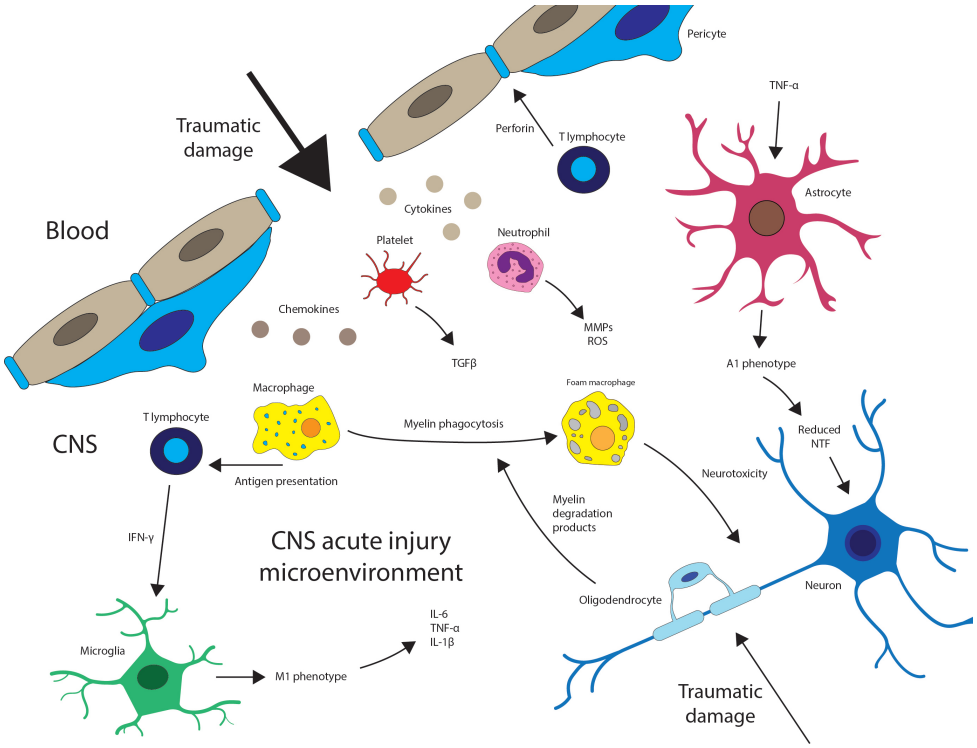


Figure 1.5: Schematic diagram of the acute phase of injury, following compromise of the blood CNS barrier and entry of blood-derived cells and signalling proteins, detailing pro-inflammatory signalling leading to microglial/astrocytic phenotypic changes.

Excitotoxicity Excitotoxicity results from increased and uncontrolled release of excitatory neurotransmitters after trauma, principally glutamate.[18,64] Glutamate release from damaged axons in the spinal cord and pre-synaptic terminals in the brain results in accumulation within the injury micro-enivronment,[23] compounded later by impaired reuptake due to decreased astrocytic expression of glutamate transporters GLAST and GLT-1.[77] Glutamate activate AMPA and NMDA receptors, which permit influx of cations (K^+, Na^+, Ca^{2+}) and depolarisation, with excessive activation resulting in intracellular Ca^{2+} accumulation, compromising mitochondrial function,[18] contributing to ROS production and activating apoptotic pathways (Fig. 1.6).

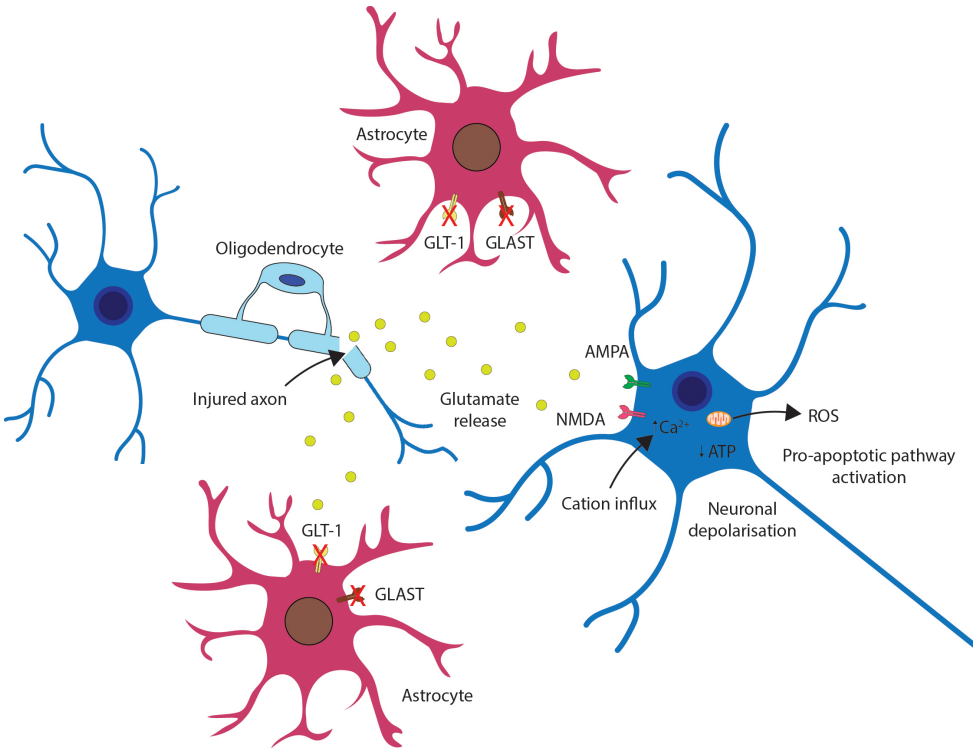


Figure 1.6: Schematic diagram of the excitotoxicity resulting from uncontrolled glutamate release from severed pre-synaptic axons, perpetuated by downregulation of astrocytic capacity for scavenging free glutamate.

Oedema Oedema in neurotrauma is a significant mechanism of secondary injury propagation, which occurs through three mechanisms. Cytotoxic oedema is a result of failure of ATP-dependent Na^+-K^+ pumps (particularly in astrocytes), resulting in accumulation of Na^+ (and

consequently, water via aquaporin channels[78,79]) within the cell. Ionic oedema follows, with diffusion of Na^+ ions across the intact blood-CNS barrier into the extracellular space to replenish those sequestered intracellularly by cytotoxic oedema. Vasogenic oedema occurs through the influx of water and solutes across a compromised blood-CNS barrier (particularly large proteins such as albumin) into the interstitium of the CNS.

Mitochondrial dysfunction Maintenance of normal mitochondrial function is integral to cellular energetics and metabolism, and thereby all cellular function. As shown in Figure 1.7, the inner mitochondrial membrane is the site of the electron transport chain (ETC), which performs ATP synthesis via aerobic respiration, and is integral to the process of oxidative phosphorylation, alongside the citric acid cycle. Briefly, the ETC is a series of four protein complexes which transfer electrons to create an electrochemical gradient which enables the function of ATP synthases. These complexes are:

1. Complex I - type I nicotinamide adenine dinucleotide hydrogen (NADH) dehydrogenase
2. Complex II - succinate dehydrogenase
3. Complex III - $CoQH_2$-cytochrome c reductase
4. Complex IV - cytochrome c oxidase (CCO)

Integral to this pathway are also NADH, ubiquinone and cytochrome c, which facilitate electron transport into and along the ETC, permitting the transmembrane transport of H^+ ions, creating the required electrochemical gradient. CCO is notable here, as its copper and haem components permit the absorption of photonic energy into the ETC, and is a central site of photochemical reactions within eukaryotes.[80–83]

Mitochondrial dysfunction after neurotrauma is a mechanism of secondary injury across cell types, with exquisite effects on the neuron due to its high metabolic demands. Rises in intracellular Ca^{2+}, typically due to excitotoxicity or oxidative stress, act as an initiator to mitochondrial crisis. Mitochondrial Na^+/Ca^{2+} exchange channels activity permits Ca^{2+} entry into the

mitochondria, with rising intra-mitochondrial calcium leading to opening of the mitochondrial permeability transition pore (mPTP), mitochondrial oedema and swelling, loss of mitochondrial membrane potential and severe disruption of ATP synthesis.[84–86] This membrane damage results in release of mitochondrial proteins such as cytochrome c, Ca^{2+} and ROS into the cytosol, which in turn can trigger apoptosis.[86] Additionally, upregulation in activity of nitric oxide synthase (NOS) and increase in nitric oxide (NO) production can independently impair ETC function.[86]

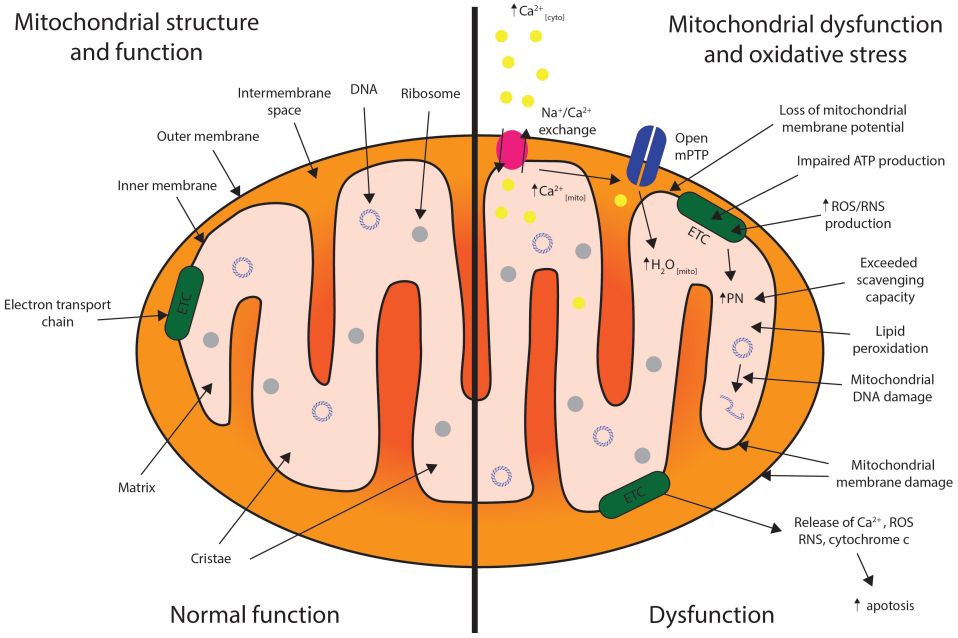


Figure 1.7: Schematic diagram of mitochondrial structure and normal function (left); and dysfunction after trauma (right). Dysfunction here is triggered by rising cytosolic Ca^{2+} ($Ca^{2+}{}_{cyto}$), resulting in increased mitochondrial Ca^{2+} ($Ca^{2+}{}_{mito}$). This opens mPTP channels and intramitochondrial oedema, loss of mitochondrial membrane potential, impaired ATP production, increase ROS/RNS production and release of mitochondrial pro-apoptotic proteins into the cytosol.

Mitochondrial dysfunction, as a failure of oxidative phosphorylation despite substrate availability in response to the adverse environment of injury, is one component of a wider metabolic failure in the acute/sub-acute phase of neurotrauma, particularly recognised in TBI.[87–91] Alongside this intrinsic energetic failure of normal metabolism, hyperglycolosis occurs whereby there is a deduction in oxygen consumption relative to the overall metabolic rate, leading to an increase in the production of lactate.[88] This excess, and correspondingly an increase in the lac-

tate/pyruvate ratio, is associated with poor outcome and has been termed "metabolic crisis".[87] This association with poor outcome suggests that metabolic failure has a prominent contribution to the propagation of secondary injury,[91] and is a key pathophysiological facet to correct through current and prospective therapeutic intervention. Such primary metabolic failure may be further compounded by a relative lack of substrate (as in hypoglycaemia) or of oxygen (as in ischaemia), which may occur regionally or globally, as a consequence of other secondary injury cascades within the CNS, or the systemic effects of trauma.

Oxidative stress Oxidative stress in a biological system results from an imbalance of production of oxidants, and the capacity to scavenge and neutralise them (via enzymatic activity (such as superoxide dismutase) or antioxidants (such as vitamin C or E)).[92] Whilst oxidative phosphorylation is an essential cellular process, it is the most prevalent source of reactive oxygen species (ROS) production. Examples of ROS include: hydrogen peroxide (H_2O_2); hydroxyl radicals (OH, a free radical); and superoxide (O_2^-, an anion radical). Furthermore, reactive nitrogen species (RNS) such as nitric oxide (NO) also act as oxidising agents,[93] interacting with ROS to produce a range of reactive species[94] such as peroxynitrite (PN). Whilst ROS/RNS have physiological functions, such as regulating cardiovascular function and neurotransmission in the case of NO, dysregulation of ROS/RNS can lead to cascading oxidative damage to proteins and lipids, including DNA, and therefore a fine homeostasis of the redox balance of the microenvironment is required.

Dysfunctional mitochondrial activity results in abnormal release of ROS or free radicals. In states such as neurotrauma, where ROS and RNS production is confluent, production far outstrips any antioxidant/scavenger capacity.[84,86] Mitochondrial production of NO, and electron leakage from the ETC combine to produce superoxide radicals (O_2^-), resulting in the formation of PN. PN, OH, O_2^- and other potent oxidising agents propagate mitochondrial damage via lipid peroxidation, leading to mitochondrial DNA damage,[84,90] illustrated in Figure 1.7. This mediates further disruption of the mitochondrial integrity, allowing release of ROS resulting in destruction of cellular structures, proteins and lipids; triggering apoptotic pathways, release of

pro-inflammatory mediators; and perpetuating secondary injury.[64]

Sub-acute phase

Axonal sprouting Initial early axonal sprouting of damaged neurons after injury can be observed in the early sub-acute phase after injury. This is later aborted, as the early modest release of neurotrophic factors after injury is not sustained, and the generation of a non-permissive injury microenvironment via other mechanisms inhibits any remaining drive for growth from residual neurotrophic factors. This is in contrast to peripheral nervous system injury, where Schwann cells produce a consistent and graded concentration of neurotrophic factors to support axonal regeneration.[95,96]

Astrocyte activation Astrocytes, the multifunctional support cell of the CNS, become activated after traumatic injury, resulting in their proliferation within the lesional area and transformation to "reactive" astrocytes (astrogliosis) and upregulate expression of glial fibrillary acidic protein (GFAP).[97] Reactive astrocytes have a range of functional states, and astrocytosis has been recognised to range vastly in its severity based on molecular characteristics,[98,99] Despite such heterogeneity, astrocyte biology is commonly described based on two characterised phenotypes: A1 pro-inflammatory/neurotoxic astrocytes; and A2 anti-inflammatory/pro-survival astrocytes (akin to the phenotypic polarisation of reactive microglia).[18,62,100,101] A1 astrocytes are formed via activation of the nuclear factor kappa-light-chain-enhancer of activated B cells (NFκB) pathway (induced by microglial secretion of IL-1α and TNFα) and exhibit a neurotoxic phenotype which triggers neuronal and oligodendrocyte cell death[101,102] (Fig. 1.5). Expression of component C3 is used to identify A1 astrocytes.[62] A2 astrocytes were initially identified as being polarised by ischaemic injury and are specifically induced via TNFα/IL-1β/IL-6 mediated activation of the signal transducer and activator of transcription 3 (STAT3) pathway.[100,103,104] Scar formation via A2 astrocytes can create a more permissive environment for regeneration through an astroglial scar,[105] with recognised roles of A2 astrocytes in increasing availability of neurotrophins.[102] A2 astrocytes may be identified by their specific expression of the cell surface

receptor S100A10.[62] Similarly to that described for microglia, the A1/A2 polarity has been recently recognised as a reductive description of a complex range of biological responses.[99,106] Whilst A1/A2 may be understood terminology for a generalised set of astrocytic reactive behaviours, it should be appreciated that each of these states represent a much broader continuum of molecular and functional characteristics.[98,99]

Initiation of a glial scar Immediately after injury, a lesion core is formed through haemorrhage as a collection of non-neuronal cells, blood products, CSF and serous fluid which accumulate through the damaged blood-CNS barrier. Astrocytes migrate to the periphery of this core lesion site and begin to form a network of tightly connected peripheral processes to surround and corral the lesion core to effect a physical barrier between the lesion core and the penumbral neural tissue.[62] Fibroblasts (cells which form connective tissue) from dura and/or blood; and pericytes (endothelial cells of capillary networks and blood-CNS barrier interfaces) also migrate to this zone and proliferate.[62,107]

Upon forming a network, astrocytes, pericytes and fibroblasts begin to form an extracellular matrix (ECM), with secretion of laminin, collagen (type IV), fibronectin and chondroitin sulphate proteoglycans (CSPG) which form the molecular meshwork of the glial scar.[62,97] Whilst the presence of the glial scar, particularly the presence of CSPG, forms both a physical barrier and non-permissive chemical microenvironment. In contrast, the presence of an ECM appears necessary for axonal regeneration with matrix proteins such as laminin acting as an intercellular skeleton, as total scar suppression impairs stimulated axonal regeneration.[105]

Demyelination Acute damage to myelin can occur either by direct damage to the myelin sheath itself (alongside axonal injury) or due to damage to the supporting oligodendrocyte from which the myelin is derived.[18,64,108] This damaged myelin also contributes to this non-permissive microenvironment, via release of inhibitory proteins myelin-associated glycoprotein (MAG), neurite outgrowth inhibitor-A (Nogo-A) and oligodendrocyte myelin glycoprotein (OMgp). Akin to the mechanisms by which neurons are lost after trauma, oligodendrocytes and their associated myelin can undergo continued damage during the subacute and chronic phases post-

injury: via excitotoxicity, oxidative stress, inflammatory cytokines and necrotic proteolytic enzymes. The role of lymphocytes in immune amplification is favourable for the response to pathogens, however they form endogenous myelin reactive lymphoctes, initiating immune-driven demyelination which potentiates CNS damage.[109] Furthermore, oligodendrocytes appear dependent on neuronal survival, and axonal degeneration and neuronal apoptosis result in further loss of oligodendrocytes.[108]

Consolidation phase

Apoptosis Triggered by a variety of stimuli in the post-injury tissue environment, loss of CNS cells can persist in the chronic phase after injury to apoptosis. Apoptosis, as a controlled process of programmed cell death, contrasts with the disordered events of necrosis which are typical of immediate traumatic cell death in the acute phase.[110] Apoptosis may occur either as an intracellular (intrinsic) stress response, mediated by Bcl-2/Bax pathways, or due to extracellular factors (extrinsic) in response to a variety of local cell signalling molecules.[50,110–112] Intrinsic pathways to apoptosis may be triggered via a variety of the discussed mechanisms, including mitochondrial dysfunction, oxidative stress, lipid peroxidation and excitotoxicity.[110] Intrinsic and extrinsic pathways activate a series of intracellular signalling pathways mediated by the cysteinyl aspartic proteinases (caspase) family. Caspases can be grouped into "initiator" caspases (Caspase-8, 9, 10) and "executioner" caspases (Caspase-3, 6, 7), some with activity across both functions (Caspase-2).[112,113]

Consolidation of the glial scar Consolidation of the glial scar during the chronic phase after injury creates a continual inhibitory environment for regeneration of severed axons. In SCI, cavitation may expand as inflammatory cells remove non-viable tissue, and an expanding zone of apoptosis, degeneration and demyelination can occur.[114] The acute and consolidation phases of glial scar formation are illustrated in Fig.1.8.

Aborted axonal regeneration In the non-permissive milieu of the tissue microenvironment post-injury, perpetuated by the consolidation of the glial scar, there is a combination of an

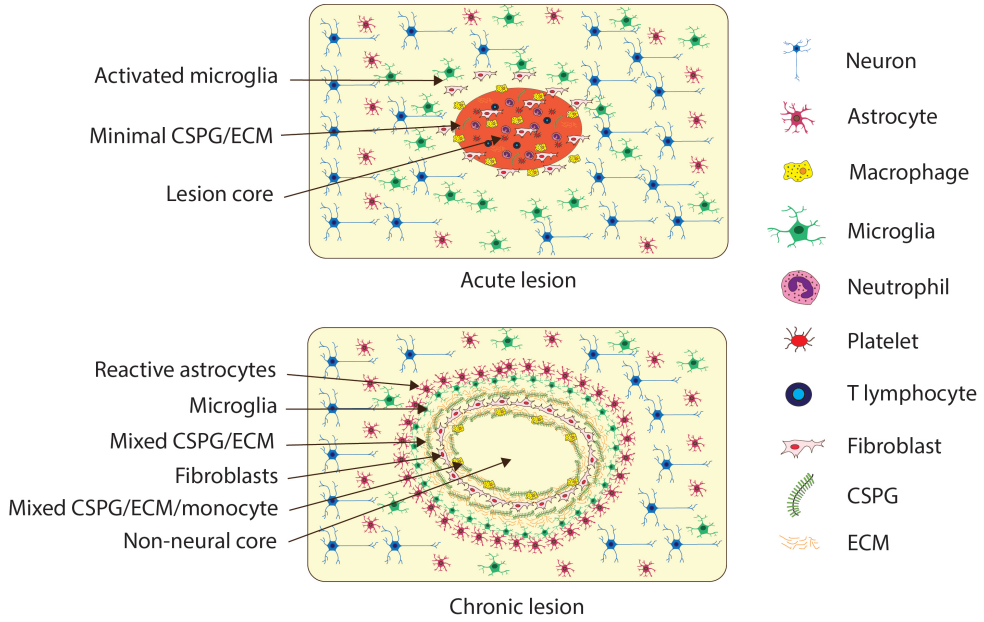


Figure 1.8: Schematic diagram of the acute phase (top) and chronic/consolidation phase (bottom) of glial scar formation and cavitation, with description of cellular properties of layers from the lesion core to the penumbral neural tissue.

abudance of inhibitory factors and scarcity of neurotrophic factors. Low concentrations of neurotrophins are insufficient to promote or maintain axonal regeneration in the context of the non-permissive factors.[95,96] Myelin-derived inhibitory factors continue to contribute to the collapse of the axonal growth cone. MAG, Nogo-A and OMgp bind to the Nogo receptor (NgR) complex and activate an intracellular pathway mediated by Rho-A and Rho-associated protein kinase (ROCK).[18] Via their respective receptors, non-myelin-derived signalling molecules such as ephrins[115] and semaphorins (semaphorin 3A[116]) also converge on this pathway to inhibit cofilin activity and promote growth cone collapse.[18,117]

Neurotrophins act predominantly at the tropomyosin receptor kinase (Trk) receptor family (A/B/C) via various intracellular signalling pathways.[118–120] The transmembrane protein $p75^{NTR}$ can interact directly with low affinity to NTFs, or potentiate NTF affinity at Trk receptors or binding of pro-neurotrophins at the sortilin receptor.[118] Co-activity of $p75^{NTR}$ in the presence of NTFs mitigates its activity in the NgR complex, reducing the effect of inhibitory signals.

1.4.3 Approaches to promoting neuroprotection and neuroregeneration

The pathophysiological mechanisms described above contribute significantly to the failure of the CNS to survive and regenerate after injury. The key features that may support a great understanding of neuronal regeneration include:

1. Insufficient and unsustained provision of NTF after injury.
2. Neuronal/glial apoptosis.
3. Formation and consolidation of a glial scar.
4. Release of local inhibitory factors from migrating and resident immune and glial cells.
5. Collapse of growth cones of regenerating axons.
6. Rarity of establishing functional reconnections with targets distal to the injury.

Effective therapies to improve functional neurological recovery therefore need to address two broad pathophysiological mechanisms: (1) the propagation of secondary injury via the multitude of mechanisms which contribute to further cell loss and the creation of a microenvironment which is strongly inhibitory of regeneration; and (2) promotion of axonal regeneration and establishment of functional reconnections. A multitude of approaches have been explored in pre-clinical and clinical studies in therapeutic attempts to mitigate damage (neuroprotection) and/or promote repair (neuroregeneration) after traumatic injury to the CNS, through means to intervene with the pathophysiological mechanisms, but none have yet demonstrated sufficient benefits to be accepted in clinical practice.

Methylprednisolone is an example of such a therapy which is neither proven nor widely accepted. The original publication of the National Acute Spinal Cord Injury Study (NASCIS2) in 1990 resulted in widespread implementation of methylprednisolone therapy in SCI on the basis of unclear and inconsistent results, and its inclusion in clinical guidelines has been conflicting in the period since.[121,122] More recent attempts to validate any beneficial effect in SCI have not provided conclusive evidence.[75,122,123] Administration of methylprednisolone in TBI has

been demonstrated in the CRASH trial to increase risk of two week mortality.[124] There is current interest in the early administration of gabapentinoids to promote functional recovery after SCI.[125,126] Despite some encouraging results from early human studies, this is yet to be confirmed in appropriately powered prospective randomised-controlled trials.[127–130]

Following the establishment of ICP control as a therapeutic target in severe TBI,[28] intraspinal pressure (ISP) and spinal perfusion have been areas of growing interest in SCI research. Direct pressure monitoring with targeted therapy, perfusion pressure optimisation and dural decompression (expansion duroplasty) have been proposed to mirror the pressure-directed surgical care in TBI.[131–133] Study is presently ongoing to assess the potential therapeutic benefits of expansion duroplasty in the acute phase after SCI, with the rationale of creating additional intraspinal volume than bony decompression alone, in order to permit post-injury oedema and limit local pressure effects.[134] Based on a similar rationale, lumbar drainage of CSF has been proposed as a strategy to achieve more favourable intraspinal pressure with some early success in pre-clinical studies.[135]

To address the urgent need for therapeutics beyond ICP targeted therapies, emerging therapeutic approaches targeting a variety of pathophysiological processes in neurotrauma are the focus of much current pre-clinical research, comprehensively described elsewhere.[18,36,62,136] Despite the identification of many promising neuroprotective and neurorestorative pre-clinical strategies in animal models, few of these have reached translation to study in large clinical trials, and none reported have thus far demonstrated significant functional benefits. These are summarised in Table 1.2 (for TBI) and in Table 1.3 (for SCI). [i]

[i]This summary table has not included studies with the intention of neuroprotection primarily by improving control of ICP or ISP, as these approaches do not represent a direct neuroprotective strategy. Notable examples include the RESCUE-ICP study[137] and the EUROTHERM3235 study.[138]

Table 1.2: Table demonstrating recent neuroprotective/neurorestorative strategies for TBI deployed in large (n > 100) clinical studies (Phase III randomised controlled trials) with details and study outcomes.

Intervention	**Intended mechanism**	**Study details**	**Outcome**
Citicoline[139]	Endogenous compound with pleiotropic neuroprotective effects	1,213 patients randomised to 90 days' enteral citocoline versus placebo	No improvement in functional or cognitive status at 30, 90, and 180 days
Dexanabinol[140]	Non-psychotropic cannabinoid derivative compound with pleiotropic neuroprotective effects	846 patients randomised to 150 mg intravenous dexanabinol within 6 h of injury versus placebo	No improvement in functional or status at 6 months post-injury
Erythropoeitin[141]	Glycoprotein hormone with pleiotropic cytokine-like neurocytoprotective effects	606 patients randomised to weekly subcutaneous injections of 40,000 units of erythropoetin for up to three doses (first up to 24 h post-injury), versus placebo	No difference in levels of severe neurological dysfunction at 6 months post-injury
Magnesium sulfate[142]	Electrolyte associated with reductions in excitotoxicity and cortical spreading depolarisations	499 patients randomised to a 5 day course of two doses of magnesium sulphate commencing within 8 h of injury versus placebo	No significant difference in high-dose group on primary (composite functional) outcome. Group in lower magnesium intervention arm had significantly worse outcome
Methylprednisolone[143]	Mitigate inflammation	10,008 patients randomised to 48 h infusion of methylprednisolone versus placebo within 8 h of injury	Methylprednisolone was associated with an increased risk of death or severe disability at 6 months post-injury and the trial was terminated early
Progesterone[144]	Pleiotropic neuroprotective effects which include inhibition of inflammation, reduction of apoptosis and prevention of excitotoxicity	1,195 patients randomised to 120 h infusion of progesterone (0.7 mg/kg) versus placebo	No clinical benefit for improvement of outcomes at 3 or 6 months

Table 1.3: Table demonstrating recent neuroprotective/neurorestorative strategies for SCI deployed in large (n > 100) clinical studies (Phase III randomised controlled trials) with details and study outcomes.

Intervention	**Intended mechanism**	**Study details**	**Outcome**
Gacyclidine[145]	Naturally occurring molecules in nerve cell membranes with neuroprotective effects	228 patients randomised to one of three doses of gacyclidine versus placebo within 2 h injury followed by another dose within 4 h	Trend toward improvement in motor function but no statistically significant difference after one year
GM-1 ganglioside[146]	Naturally occurring molecules in nerve cell membranes with neuroprotective effects	760 patients randomised to either low or high dose Sygen or placebo within 72 h of injury	No significant difference in motor or sensory recovery. Combined with conflicting evidence from other smaller studies there is still no convincing evidence to support a beneficial effect
Methylprednisolone[75,121–123]	Mitigate inflammation, inhibits lipid peroxidation and stabilises neuronal membranes	Multiple RCTs comparing methylprednisolone infusion versus control	Conflicting evidence across studies, but overall consensus is that methylprednisolone does not result in improvements in functional outcome, with significant potential for harmful side effects
Naloxone[121]	Endogenous hormone with pleiotropic neuroprotective effects	487 patients randomised to naloxone (25 mg/mL), within 8 h versus placebo (and methylprednisolone, described above)	No significant difference in functional outcome at 6 weeks or 6 months post-injury
Tirilazad mesylate[146]	Steroid analogue, inhibits lipid peroxidation and stabilises neuronal membranes	499 patients randomised to either tirilazad mesylate for 48 hr (2.5 mg/kg) versus two dose regimes of methylprednisolone	Recovered motor function at rates similar to or slightly higher than patients who received 24 hr methylprednisolone

Future directions

Whilst molecular targets and novel approaches hold some promise for promoting repair and recovery after neurotrauma, pharmacological methods typically target single receptors and effect discrete pathways within the complex and multifaceted pathophysiology of the CNS after injury. Interventional studies continue to investigate novel targets and approaches but have thus far failed to prove efficacious in improving functional outcomes.[18,62,147,148] Efforts to improve future outcomes from neurotrauma therefore urgently focus upon opportunities to intervene with the breadth of harmful cellular mechanisms, including monitoring their progression to provide targeted treatment. Therefore exploration of alternative methods to target multiple mechanisms of injury propagation may yield novel effective interventions which may offer a step-change in management opportunities. The following section introduces photobiological interactions, and specifically photobiomodulation (PBM), as a potential solution to this problem.

1.5 Photobiology

PBM is the application of photons from the ultraviolet (UV), visible and near-infrared (NIR) region of the electromagnetic (EM) spectrum to biological tissue for the purpose of therapeutic advantage, restoration of function or enhancement of physiology.[149] Whilst cellular absorption of photons from this broad region of the EM spectrum has been shown to elicit discernible biological responses, red/near-infrared (R/NIR) light (600-1100 nm) is the most commonly applied spectrum for the intention of beneficial effects. At its core, PBM is the application of photons as a carrier of energy into a biological system to elicit some favourable effect. The effects of PBM are highly dependent on the amount of photonic energy delivered to tissue over a given time period and anatomical area/volume. This section is an introduction to the scientific principles which underly the delivery, parameters and biological effects of PBM.

1.5.1 Photons

A photon is a subatomic particle that constitutes a package (or quantum) of EM radiation. A single photon conveys a discrete amount of EM radiation and together are massless particles which travel in waves. The energy of a photon is inversely proportional to the wavelength,[150] and can be calculated with equation:

$$E = hf = \hbar\omega = \frac{hc}{\lambda}$$

where E = energy; h = Planck's constant ($h = 6.63 \times 10^{-34}$); f = frequency; $\hbar$ = reduced Planck's constant (Dirac constant); $h/2\pi$; ω = angular frequency; and c = speed of light.

The properties of photons differ significantly based on these variables, particularly wavelength. On this basis, wavelength ranges are categorised into segments of the EM spectrum: gamma rays; X rays; UV; visible light; infrared (IR) light; microwaves and radio waves (Fig. 1.9). These variables result in a variety of effects when photons interact with biological systems.

1.5.2 Photons in biological tissues

The behaviour of light which is incident on biological tissue exhibit key phenomena: reflection, refraction, absorption and scattering[150, 151ii].

Reflection Reflection is an elastic collision of light onto a surface which results in light "bouncing" off of the surface, where the angle of reflection away from the surface is equal to the angle of incident light onto it. This is described in the law of reflection:[150, 151]

$$\theta_i = \theta_r$$

where θ_i = incident angle and θ_r = reflected angle.

[ii] Other specific effects exist, such as fluorescence and opalescence, which are not discussed here.

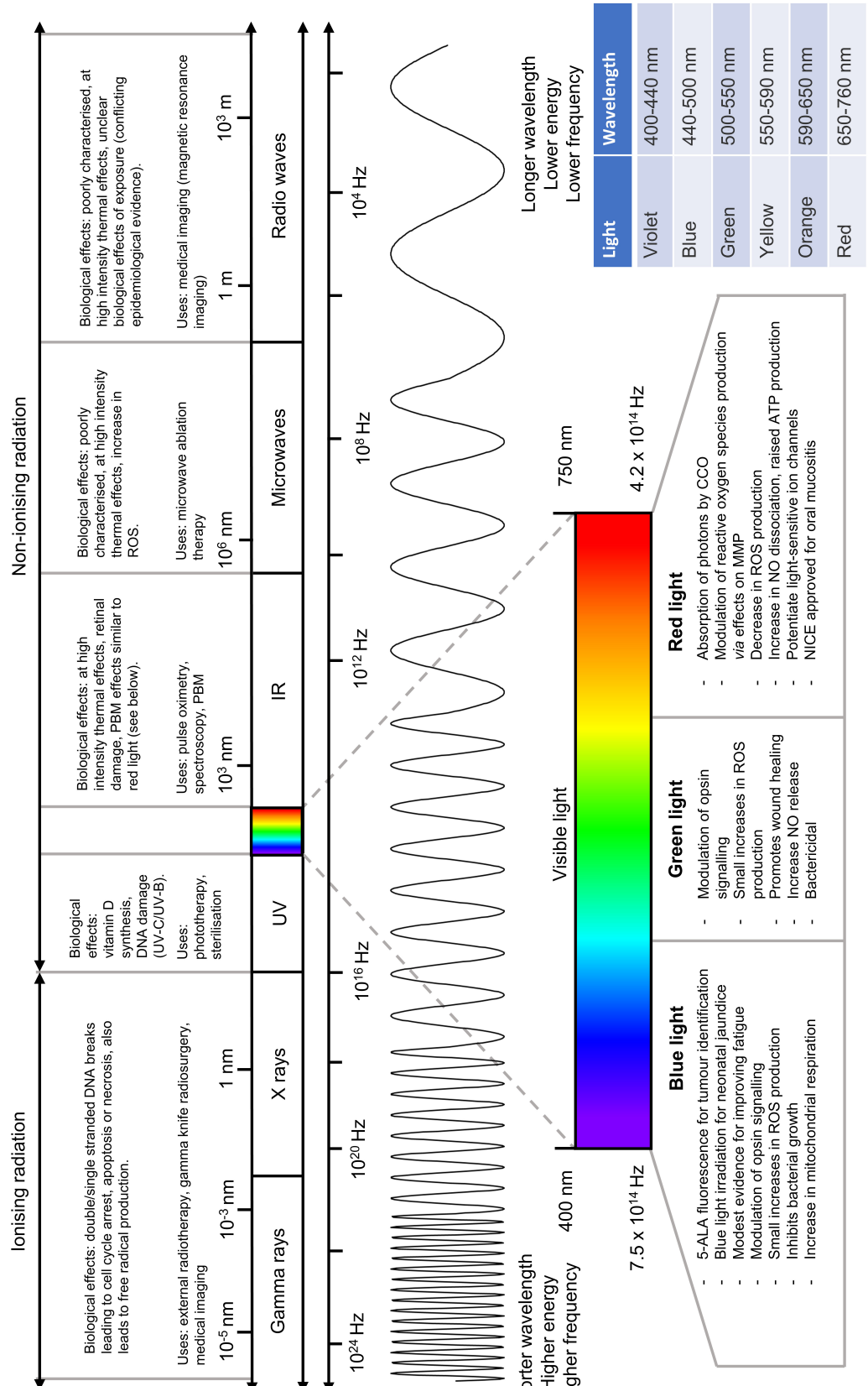


Figure 1.9: Schematic diagram representing the EM spectrum, with descriptions of the photobiological interactions and medical applications of sections of the spectrum.[149,152–159]

Refraction Refraction is a change in direction in the propagation of light, as it passes from one media to another, dependent on the refractive index of each material. This is described in Snell's law:[150,151]

$$n_1 sin\theta_1 = n_2 sin\theta_2$$

where n_1 = refractive index of media 1, θ_1 = incident angle, n_2 = refractive index of media 2, and θ_1 = refracted angle.

Absorption Absorption of a photon is dependent on the presence of a chromophore, a molecule or compound which is able to absorb specific wavelengths of light. The term "chromophore" is specific to absorption in the visible part of the EM spectrum (400-700 nm), though is also commonly used to describe absorption in the NIR part of the spectrum. Chromophores are abundant in biological tissue.[150] Haemoglobin (with differing absorption properties dependent on its oxy-/deoxy-haemoglobin state); water; myoglobin; melanin; cytochrome c; cytochrome c oxidase (CCO); and lipids are all important chromophores in biological tissue optics.[iii]

The optical properties of a given compound for absorption can be described by the absorption coefficient (μ_a): the probability of absorption per unit pathlength (in cm^{-1}):.[150,151]

$$\mu_a = C\epsilon$$

where C = molar concentration (M or mol/L) of the chromophore and ϵ = the molar extinction coefficient (or molar absorptivity) (cm^{-1}/M)

For multiple chromophores within a tissue, the combined μ_a may be calculated with equation:

$$\mu_a = \sum C_i \epsilon_i$$

Figure 1.10 demonstrates the significant shifts in absorbance across the EM spectra for the most prominent chromophores in human tissue: water and haemoglobin. Applications of optics to live biological tissue typically use wavelengths within the "optical window" between 650-

[iii] Particular substances (fluorophores), after absorption of light, may emit light of a different (usually longer) wavelength.

1350 nm, where both water and haemoglobin absorption values are sufficiently low to permit tissue penetration beyond only superficial layers.[160]

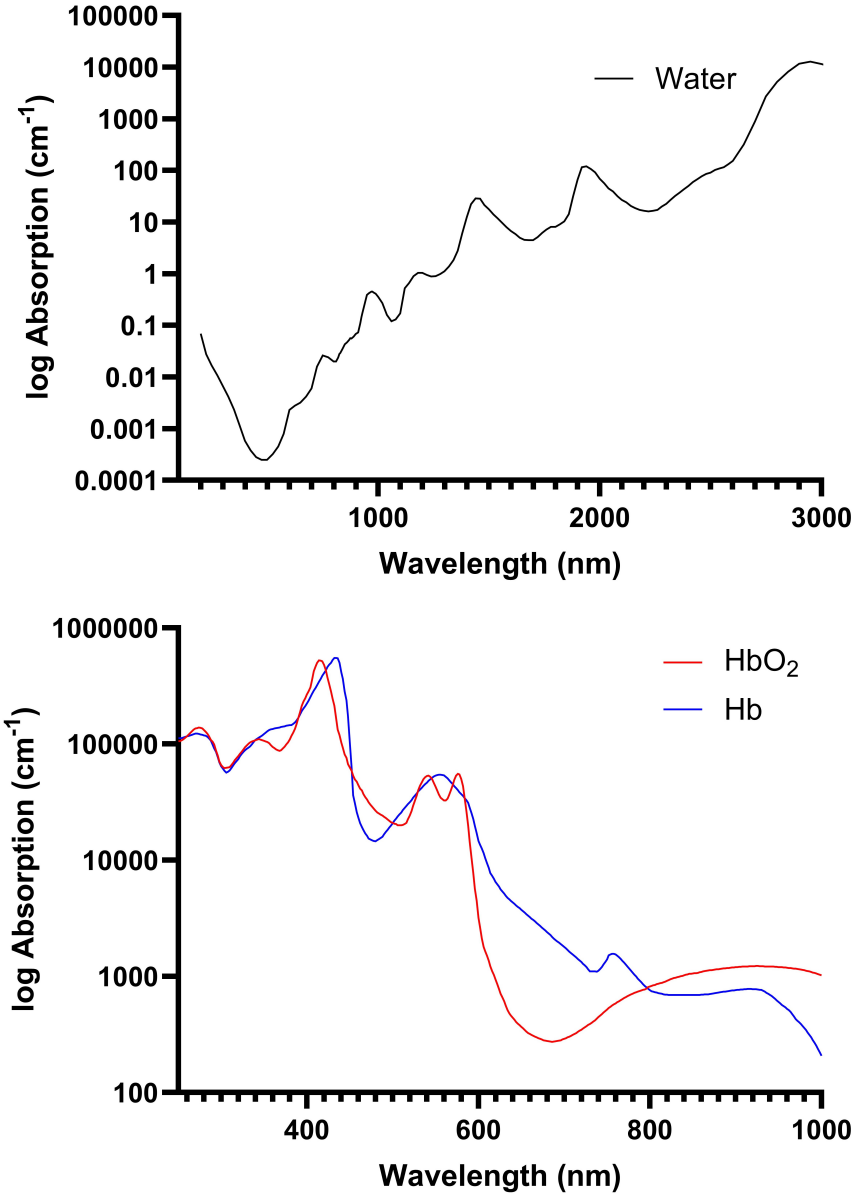


Figure 1.10: Absorption spectra of water and haemoglobin. Spectra plotted from open access optical absorbance data for water[161] and haemoglobin.[162]

Scattering Alternatively, photons can be scattered by particles within tissue: forced to deviate trajectory. This refers to elastic scattering, where the energy (and wavelength) of the scattered

photon is equal to that of the incident photon. This may be isotropic scattering or anisotropic scattering. The probability of [elastic] scattering per unit pathlength (μ_s) can be calculated using equation:

$$\mu_s = \sigma_s N$$

where σ_s is the scattering surface area of an individual particle (in cm^2) and N is the number density (or concentration) of the particles (in cm^{-3}). σ_s may be calculated using equation:

$$\sigma_s = Q_s A_s$$

where Q_s is the scattering efficiency and A_s is the cross section of the particle.

Light propagation through tissue The ability for photons to cause biological effects is dependent on absorption of photons by a chromophore (see the "First Law of Photochemistry below). For superficial tissues with incident light upon the surface, this is a more frequent event than tissues at depth as absorption and scattering through tissue exponentially attenuates the intensity of a light source (the number of photons) reaching any given depth. A schematic of absorption and scatter is given in Figure 1.11. The overall attenuation of light intensity[iv] travelling through tissue can be calculated using the equation described as Beer-Lambert's Law:

$$I = I_0 e^{-(\mu_a + \mu_s)L}$$

where I is resultant intensity, μ is molar absorptivity, I_0 is the incident intensity, and L is the pathlength (thickness of the media).

The absorption and scattering properties of biological tissues to R/NIR photons have been utilised through optical diagnostic technologies in recent decades. The differing absorption properties of oxy- and deoxy-haemoglobin permit cerebral near-infrared spectroscopy (NIRS), with R/NIR optical sources placed on the scalp with scattered photons returning to nearby

[iv] Equation 1.5.2e does not account for the propagation of scattered light forward to depth L. Due to anisotropic scattering, the total resultant intensity at depth L would be increased by "forward" scattered photons.

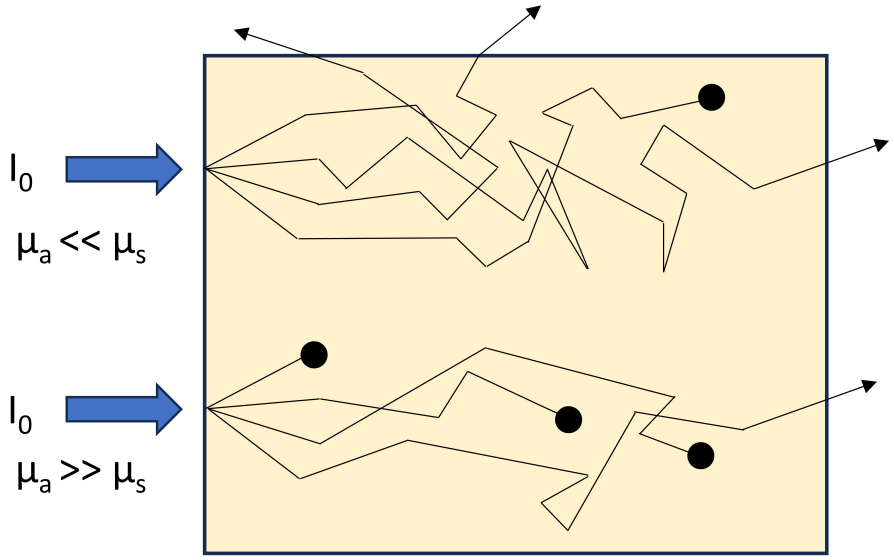


Figure 1.11: Schematic representation of the paths of photons where absorption predominates ($\mu_a >> \mu_s$) and where scatter predominates ($\mu_a << \mu_s$). I_0 denotes incident intensity. I_1 is resultant intensity (not shown). For clarity, effects of reflectance/refraction not shown. Adapted from Bigio and Fantini, 2016.[150]

detectors.[163] A related technology, Raman spectroscopy (RS), uses the Raman effect of inelastic scattering of light. In contrast to elastic scatter, inelastic scatter emits a photon of differing energy to the incident photon. This event is much rarer than elastic scatter but offers highly specific information on the molecular bonds present in a material or tissue. This is discussed in further detail in Section 1.7.

1.5.3 Photobiological interactions

Photobiological interactions can be understood as photochemical reactions in a biological system, thereby adhering to the same fundamental principles. The Grotthuss–Draper law (also known as the "First Law of Photochemistry" or the "Principle of Photochemical Activation") states that light must be absorbed by the system in order to effect a photochemical reaction. As an example from biological systems, the process of photosynthesis requires photosynthetic pigments in chlorophyll to absorb a photon to achieve a state of electron excitation to effect the subsequent

chemical reaction. The "Second Law of Photochemistry", the Stark-Einstein law, states that one photon is absorbed by each molecule of the reacting substance.

The concept of the biological effect of photons from across the EM spectrum is well established for a variety of human physiological processes. Retinal photoreceptors convert incident photons into neuronal signals, and photons in the ultraviolet B (UVB) part of the EM spectrum are integral in the biological synthesis of cholecalciferol (vitamin D). Medical applications of photobiological interactions are also commonplace in modern practice. Photons with short wavelength and high energy (gamma rays) are administered as radiotherapy or gamma knife radiosurgery. The use of 5-aminolavulanic acid (5-ALA), preferentially taken up by high-grade glioma tissue, and converted to protoporphyrin IX which fluoresces under violet-blue (405 nm) light, has become central in oncological neurosurgery to maximise resection margins.[164] Figure 1.9 summarises the key biological effects and medical applications of photons from across the EM spectrum.

As described in Figure 1.9, many photobiological interactions result in ablative or damaging effects on tissue, either by direct photobiological interactions or via indirect mechanisms such as local thermal effects from water absorption (Fig. 1.10) and subsequent tissue heating.[149,152–159] In contrast, PBM is a key phenomenon whereby application of photons may elicit a direct effect on cells which is beneficial to their function or survival.

1.6 Photobiomodulation

Otherwise termed low-level laser (or light) therapy (LLLT), PBM employs relatively low power output from an optical source, which have been identified to elicit favourable biological effects, in contrast to ablative applications of light which typically administer high energy levels to discrete areas. These observations are in keeping with the pharmacological concept of hormesis[165] (or more historically the Arndt–Schulz "rule"): a phasic biological response with varied effects of stimulation or inhibition, relative to increasing doses of applied substance/stressor/condition. Whilst this concept is not ubiquitous to all substances/stressors/conditions, it appears applicable

to PBM, in that there have been number of observations of a biphasic effect of PBM.[80,166–169]

In order for light to affect a biological system, a photon must be absorbed by a chromophore (see the First Law of Photochemistry; subsection 1.5.3). One proposed mechanism of PBM is based on the chromophore activity of CCO, as this complex of the ETC readily absorbs such light energy.[82,83] This has numerous downstream effects within the mitochondria via stabilisation of mitochondrial membrane potential,[170] which averts the overproduction of ROS by dysfunctional mitochondria, reducing local oxidative stress.[171] Via modulation of apoptotic pathways,[172–175] cell survival is increased. PBM has also been demonstrated to reduce microglia activation after TBI, and ameliorate the local inflammatory response.[176] Pre-clinical studies on the efficacy of PBM in acute TBI have generated positive results, utilising moderate or severe models of TBI in rodent species, with promising results in an early clinical study.[177] In addition to CCO, light-gated ion channels (LGIC) such as transient receptor potential (channels) (TRP) have been implicated as potential further chromophores of the PBM effect. A wider review of the mechanisms of PBM in neurotrauma is given in subsection 5.1.1.

1.6.1 History

The discovery of the effect of PBM is owed to the invention of the laser.[149] A laser is a light emitting device, based on the stimulation of electrons in an optical media to a higher energy state by an energy source, resulting in the subsequent emission of photons on their return to the ground state. After amplification through repeated passes through a gain medium (achieved in a space between two mirrors), a coherent light source is achieved, emitting photons of the same phase and wavelength. The term laser arose as an acronym of a short description of this function: light amplification by stimulated emission of radiation. This effect was first described in 1958 by Townes and Schawlow,[178] with the demonstration of the first functioning ruby laser in 1960 by Maiman.[179]

The potential for carcinogenic effects of laser light were investigated in 1968 by Endre Mester.[180] Using a murine model, the dorsal surface was shaved and a low-level ruby laser was administered to the skin, alongside a control group. Whilst there was no evidence of oncogenesis

in the animals treated with the ruby laser, it was noted that the hair growth in the laser group exceeded that of the control group, resulting in a hypothesis of a beneficial metabolic biological effect. The following decades of research in this field have sought to understand, optimise and apply this effect in a range of medical conditions.

1.6.2 Parameters and radiometry

The parameters of light delivery to tissue for PBM therapy is critical to its efficacy; with effects of delivery variability comparable to that of dose delivery in pharmaceutical terms. The key radiometric variables of light delivery involve light of a specific wavelength; with delivery of a specific energy; delivered to a specific area of tissue; over a given time. Selected wavelengths for PBM are typically between 600-1100 nm,[82] as a range in which absorbance and scatter by tissue is minimised relative to wavelengths outside this window, and as such permits some penetrance beyond the incident tissue surface. Within this range, wavelengths between 700-780 nm are less favoured due to lower absorbance by CCO; a central chromophore for the PBM effect. This constrains many applications of PBM to R/NIR light, which is the principal range considered in this thesis. However, it is noteworthy that applications of blue/green visible light for PBM is a considerable field in itself, with differing mechanisms and effects.[154]

Table 1.4 provides key explanations of the core terminology used in these radiometric descriptions of PBM parameters. Further definitions are available in the glossary (continuous wave; pulsed wave; full width at half maximum; D4σ; polarisation; phase; reciprocity; coherent).

For PBM, average irradiances delivered to target tissues are typically in the region of 2.5-200 mW/cm^2, with exposure durations between 30 seconds and one hour. Radiant energy typically ranges from 1-5 J/cm^2, with suppressive effects observed with higher exposures.[82,182]

1.6.3 Medical applications

The scientific and clinical interest in such contexts has a broad evidence base with efficacy shown in clinical trials for some conditions, particularly in: dermatological pathology,[183,184] wound healing,[185,186] cancer-related lymphoedema[187] and, most notably, in oral inflammatory

Table 1.4: Summary table of radiometry terminology used in the measurement and reporting of PBM parameters. * there are several accepted means for defining D: D4σ; knife edge width (20/80 or 10/90); full width at half maximum (FWHM); D86 and $1/e^2$. This thesis uses $D4\sigma$. Table adapted from Hadis *et al.*, 2016.[181]

Terminology	Definition	Unit
wavelength (γ)	Distance between two corresponding points on a waveform	nm
pulse frequency (ν)	The number of pulse cycles completed in a second	Hz
radiant energy (Q)	Energy transmitted by EM radiation	J
radiant exposure/fluence (H)	Energy transmitted by EM radiation per unit area	J/cm^2
power (radiant flux) (ϕ)	Energy transmitted by EM radiation per unit time	W (J/s)
beam diameter (D)	Diameter of a line perpendicular to, and intersecting the beam axis*	cm
beam area (A)	Area of a beam perpendicular to the beam axis, derivative of D in a circular beam by $\pi(D/2)^2$	cm^2
average irradiance (E)	The radiant power received per unit area	W/cm^2
radiant exitance (M)	The radiant power emitted per unit area	W/cm^2
exposure time (t)	Duration of radiant exposure	s

conditions such as oral mucositis, for which it is approved by The National Institute for Health and Care Excellence (NICE).[188,189] PBM has also shown promise in pre-clinical studies for burns.[190,191] Common to this group of pathological applications are the superficial nature of the target tissue: skin, immediate subcutaneous tissue or the oral cavity. These are eminently amenable to direct access via an externally placed optical source, with sufficient tissue penetrance in these superficial layers to achieve relevant and consistent PBM doses.

In recent years, interest in PBM therapy has grown rapidly across a broad range of disorders, including: chronic obstructive pulmonary disease (COPD);[192] type 2 diabetes mellitus (T2DM);[193] chronic kidney disease (CKD);[194] rheumatoid arthritis (RA);[195] acute viral infection;[196] bone fractures/bone repair;[197,198] and tendinopathies.[199] This compounding interest

has also included a variety of neurological conditions, such as: multiple sclerosis (MS);[200] stroke;[80] neurodegenerative diseases (Alzheimer's, Parkinson's);[80,201–205] psychiatric disorders (depression, anxiety);[80,206,207] retinal disease;[208,209] stroke;[80,210] trigeminal neuralgia;[211] chemotherapy induced peripheral neuropathy;[212] and most pertinently, neurotrauma.[80,83,213]

1.6.4 Photobiomodulation in neurotrauma

A comprehensive review of the literature of the applications of PBM in TBI is available in Chapter 2, and previous literature on the application of PBM in SCI is discussed in Chapter 3 and elsewhere.[213] Optimal dosing parameters are discussed in Chapters 3/4; the mechanisms of PBM are described in Chapter 5; and the delivery of PBM to the CNS is considered in Chapter 6.

1.6.5 Translational barriers

Whilst early pre-clinical results have supported the possibility of a beneficial effect of PBM therapy in TBI and SCI, realising these effects in clinical settings has proven challenging. The study of transcutaneous PBM in small mammals has demonstrated beneficial effects, yet such non-invasive delivery methods in large mammals produces only a small fraction of the energy transmission at the level of the target (CNS) tissue. The efficacy of PBM in ischaemic stroke had been considered promising, culminating in a phase III randomised controlled trial - the NEST-3 study.[210] However, the study failed to demonstrate efficacy and was terminated early, with its failure blamed on several parameters in the study design including variables for dosing, which were poorly established and not characterised (including irradiance (both surface and after tissue penetration)), time of initiation post-injury was inappropriate, and the therapeutic course duration was insufficient.[83,214]

Three key barriers represent significant challenges in the translation of PBM in neurotrauma:

1. Effective and optimum photon delivery to CNS tissue in adult humans is challenging.[214,215] The thickness of bone, and thickness, vascularity and variable pigmentation

of the skin/subcutaneous tissue heterogeneously and significantly impair the transmission of photons to neural tissue. As such, currently available techniques are not able to safely achieve doses within the effective range.

2. If sufficient transmission were achieved, the heterogeneity between subjects render control of accurate light dose delivery impossible without a means of accurately personalising or monitoring dose delivery.

3. Due to deficiencies in the understanding of the mechanism and optimal dosing parameters of PBM, it is not yet possible to ascertain a regimen of treatment to be translated.

1.7 Raman spectroscopy

Raman spectroscopy (RS) is a molecular monitoring technique, dependent on the inelastic scatter of photons detectable after excitation from a monochromatic light source. RS has gained interest in medical applications as a sensitive, label-free optical monitoring modality, capable of detecting molecular change in real-time.[216–218] Key to the suitability of RS is its non-destructive nature: it permits accurate tissue interrogation at a molecular level without compromising tissue integrity. RS has, in recent years, developed a growing interest for a number of potential medical diagnostic applications.[217] These include: the diagnosis of atherosclerotic plaques during endovascular cardiac interventions; diagnosis of inflammatory bowel disease during endoscopy; and cancer diagnosis in a number of organs and tissue types.

RS is the technique in which light, inelastically scattered from an excited molecule, is exploited for information on the molecule's structure. Upon excitation by a monochromatic light source (e.g. a laser), electrons in a molecule are excited, inducing a dipole. The dipole interacts with the light, and can hereafter be distinctly categorised as follows: elastic (Rayleigh) scattering and inelastic (Stokes and anti-Stokes) scattering. The Raman effect is observed through inelastic scatter, in which the scattered light has either a higher or lower energy than that of the laser. For the light to have a higher energy, as in anti-Stokes scattering, the molecule will have been in an excited state prior to being exposed to light. As the molecule relaxes to its ground state,

the emitted photon has more energy in comparison to the photon emitted from the laser. Most molecules, however, are found in their ground state at room temperature, making this event unlikely. For this reason, usually only Stokes scattering is considered. Stokes scattering consists of a ground state molecule being raised to a higher energy state as a result of exposure to the laser. The molecule returns to an energy state above the ground state: as such, the emitted photon has a lower energy value than that of the laser. RS data acquired is expressed as a function of the Raman wavenumber, the shift being the difference between the induced light and the scattered light. Each Raman shift is distinct due to the specific molecular vibration each molecule will have, dependent on the number of atoms present, bond lengths, atoms present, etc. The differences recorded provide each molecule a unique, label-free fingerprint, no matter the concentration of sample present and is non-destructive, making RS a powerful tool and compatible with use *in vivo*.

The primary limitation of RS lies in its inherently weak nature. The number of photons inelastically scattered is comparatively small relative to elastically scattered light. This means that the signal is easily overwhelmed by fluorescence, especially from organic molecules. To counter this, the lasers used tend to lie in the near-infrared range, the industrial standard being 785 nm, which allows for the least fluorescence without compromising on the resolution. Other approaches to improve outputs have been to take advantage of nanoscale features of surfaces such as gold or copper to chemically and electromagnetically enhance the sample. This is known as surface-enhanced Raman scattering (SERS) and is considered as the most effective way to increase the Raman signal. SERS's requirement for the sample to be placed on a specialised surface, however, limits its use to *ex vivo* applications.

RS has been subject of growing interest in pre-clinical studies for identification and study of a number of pathophysiological mechanisms. For example, RS has been used to detect oxidative stress induced inflammation in human endothelial cells;[219] excitotoxicity in epithelial cells;[220] and tracking of mitochondrial function.[221] Raman techniques have been utilised in brain injury models, demonstrating consistent RS spectral changes in response to injury, including: rat ischaemia-reperfusion injury;[222] biochemical change in post-traumatic stress disorder rat

models;[223] and radiation damage to brain in mice.[224] RS has been used in the identification of pathognomic biochemical alterations in a number of neurodegenerative disorders in pre-clinical studies,[225] and identification of neoplasia in cerebral tissue.[226] RS has found applications and interest in neuro-oncological surgery in recent years.[183,227–236] For rapid intraoperative diagnosis of excised tissue, interest has grown in Raman histology: use of Raman microscopy with deep convolutional neural networks for rapid and accurate prediction of tissue diagnosis for use in the operating theatre.[237] The application of RS for intraoperative differentiation of normal brain tissue and glioma tissue demonstrates a proof-of-concept for monitoring applications in the human brain,[235] but the exploration of this in the context of TBI has been limited. For a comprehensive introduction to RS and its application in TBI, see Appendix A.

1.8 Pilot data

The principle of delivery of both invasive PBM and RS to the CNS conceptually require the same fundamental device: an interface between optical fibres and the brain or spinal cord. These optical fibres can then be externally connected to lasers sources or spectrometer detectors to permit the different optical device functions. As outlined above, PBM has the potential to improve the conditions of the CNS after injury, and RS may be able to detect differences in injury severity and possibly responses to therapeutics. It is on this basis that pilot experiments were performed to explore a potential relationship between the effects of PBM and the signal gained by RS. The experiments described here were performed by David Davies and colleagues. [v] The full methodology and results of this investigation are given in its published form in Appendix B.

Using hippocampal slice cultures from the adult Sprague-Dawley rat, apoptosis was quantified using NucView 488 Caspase-3.[238] To optimise the dose of PBM in this model, PBM was delivered for 1 min using 3x average irradiance levels (LT1 = 21.3 mW/cm^2, LT2 = 42.4 mW/cm^2, LT3 = 85.0 mW/cm^2) (Fig. 1.12). 42.4 mW/cm^2 produced the greatest reduction in apoptosis in comparison to control (ambient light treated) groups. Using 42.4 mW/cm^2 again,

[v] The author of this thesis was involved in the analysis and writing of this work, and has been published in PLoS ONE.[238]

dose duration (1 min, 2 min, 3 min) was explored (Fig. 1.13, demonstrating that 1 min resulted in the most significant decrease in apoptosis. Analysis based on hippocampal region showed that the effect was most significant in cornu Ammonis (CA) 1 and 2 regions (the most metabolically active regions in comparison to dentate gyrus (DG)) (Fig. 1.14). RS of the live hippocampal slices after 3 and 5 days in culture (with or without daily PBM treatment) demonstrated a clear and significant shift in the 1660 cm^{-1}/1440 cm^{-1} peak ratios at each therapeutic interval, suggesting this may be feasible as a means of monitoring the therapeutic response to PBM.

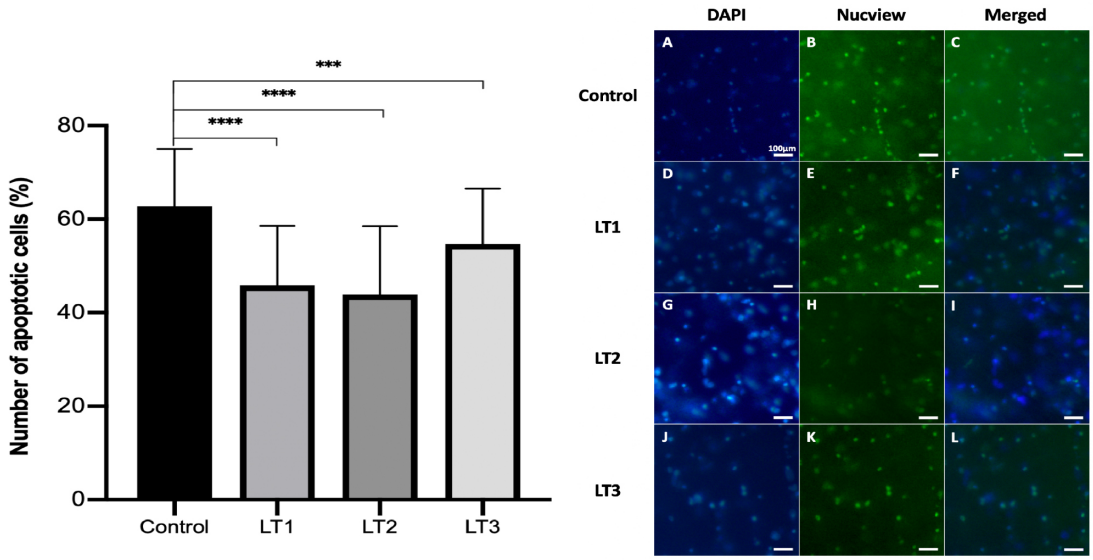


Figure 1.12: Effect of irradiance - Percentage of apoptotic cells in each group, LT1 = 21.3 mW/cm^2, LT2 = 42.4 mW/cm^2, LT3 = 85.0 mW/cm^2. **** = $p < 0.0001$, *** = $p < 0.001$, ** = $p < 0.01$, error bars = SD. DAPI = 4', 6-diamidino-2-phenylindole.

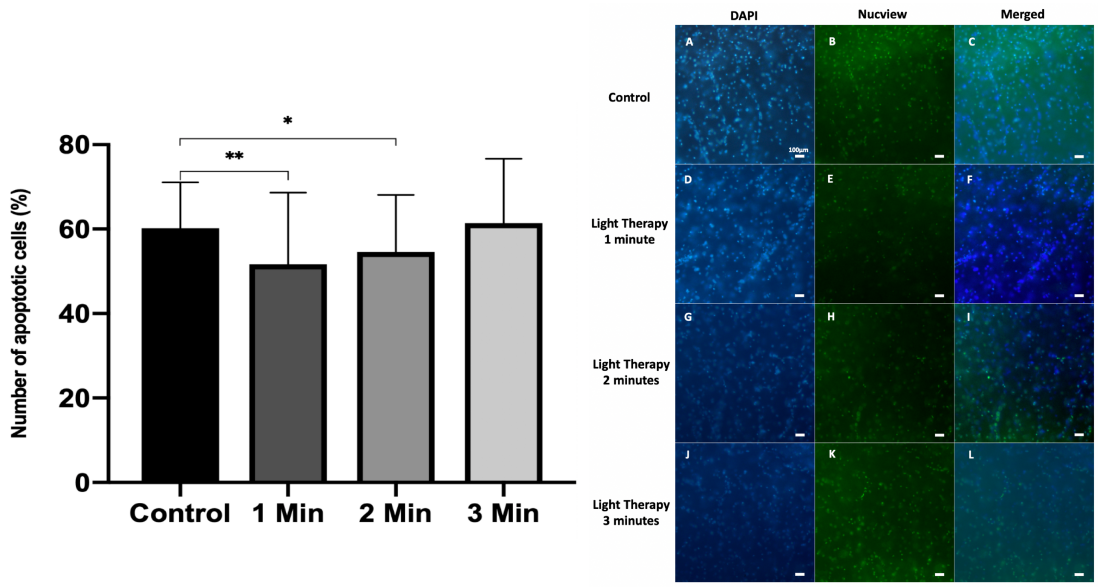


Figure 1.13: Percentage of apoptotic cells in response to varying light therapy durations, either 1, 2 or 3 min per day over 5 days, with LT2 (42.4 mW/cm^2). ** = $p < 0.01$, * = $p < 0.05$, error bars = SD. DAPI = 4', 6-diamidino-2-phenylindole.

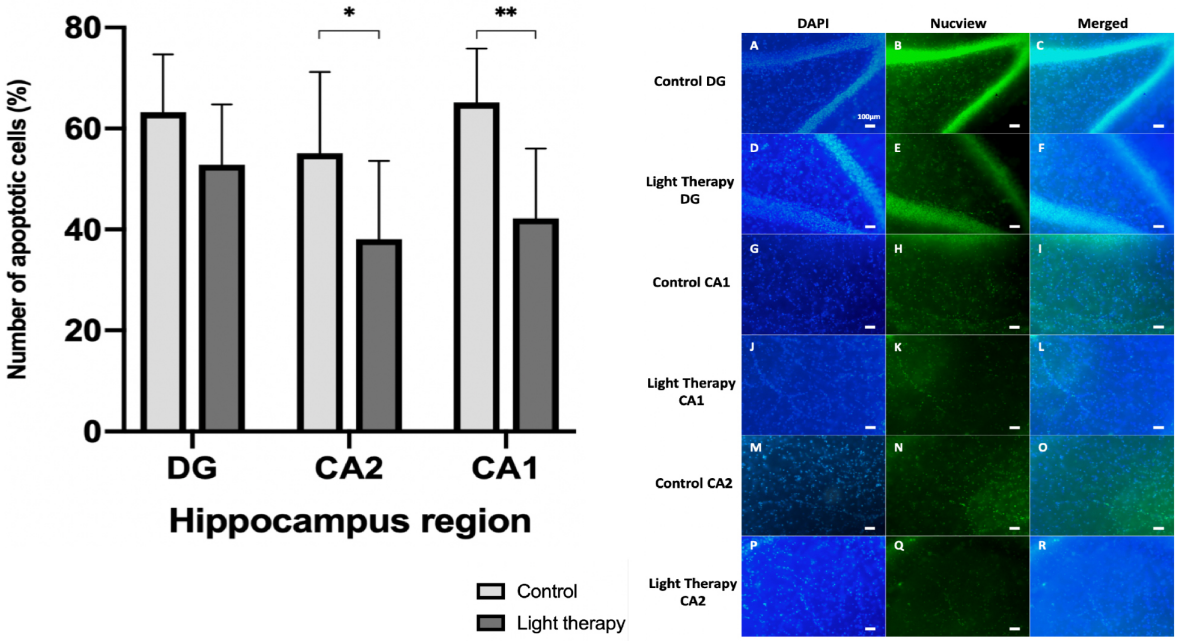


Figure 1.14: Differential effect of LT2 (42.4 mW/cm^2) on the individual hippocampal regions observed. LT2 = 660 nm irradiation for 2 min per day over a 5 day culture period. ** = p < 0.01, * = p < 0.05, error bars = SD. CA1 = cornu Ammonis 1, CA2 = cornu Ammonis 2, DG = dentate gyrus, DAPI = 4', 6-diamidino-2-phenylindole

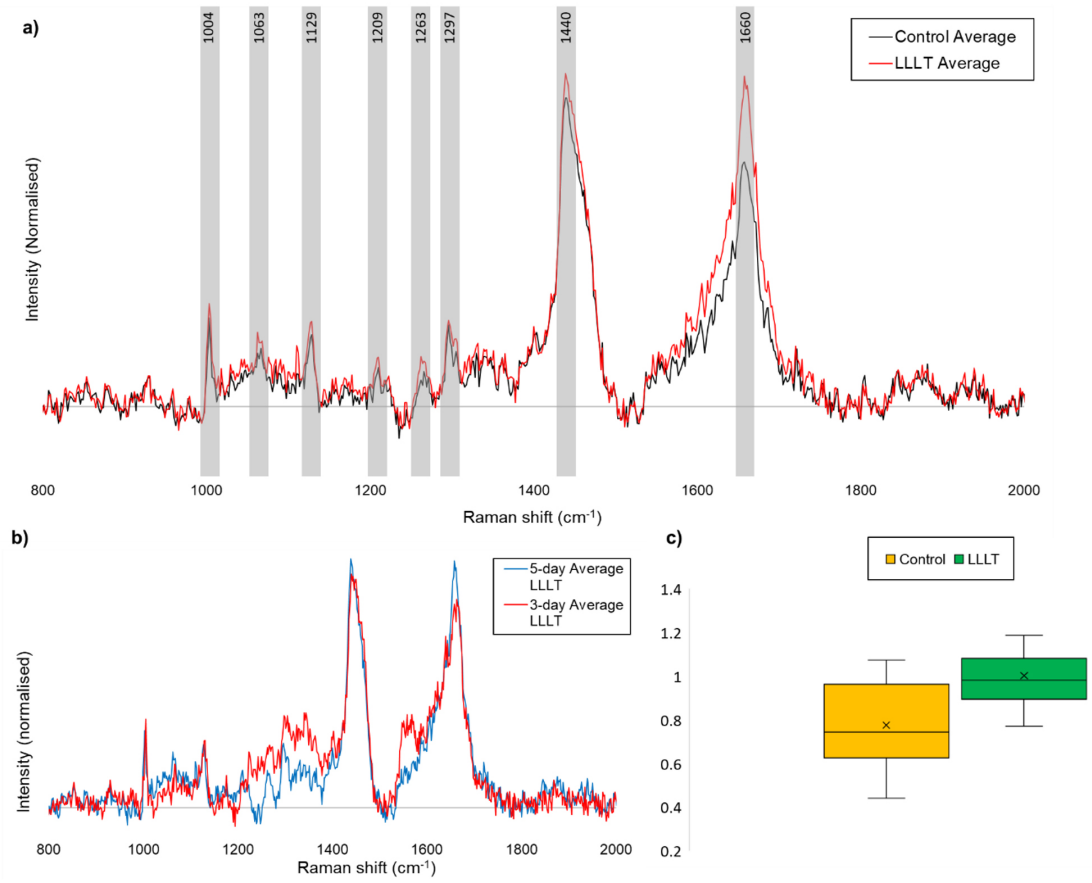


Figure 1.15: a) Comparative figure of average control and average PBM Raman spectra, normalised, illustrating the changes in average intensity of the 1440 and 1660 cm^{-1} peaks, and highlighting the assigned, characteristic peaks of rat hippocampus. b) Comparative figure of normalised Raman spectra from average 3-day PBM samples and average 5-day PBM samples, no significant difference was observed between the 1660 cm^{-1}/1440 cm^{-1} peak ratios at each therapeutic interval (p = 0.4). c) Box and Whisker plot illustrating the increase in average peak intensity ratio of 1660 cm^{-1}/1440 cm^{-1}, increasing from 0.774 for control samples to 1.002 for PBM samples (p = 0.0204).

1.9 Premise and device concept

Previous techniques in neurotrauma have employed inadequate PBM delivery at a neuronal level owing to their transcutaneous application, (due to absorption and scatter in superficial tissue) resulting in severely limited delivery and insufficient energy doses to the injurious target site. The quantity of transmitted light is highly variable, which renders the study of optimum dosing challenging, and there are no means to confirm the beneficial effect or personalise the delivery parameters. To address these challenges, toward a translatable device, this thesis seeks to develop a novel method of direct (invasive) PBM delivery for both TBI and SCI.

Direct application achieves up to 20-fold greater light delivery than transcutaneous application of photobiomodulation (PBM),[239] with the further advantage of offering superior reproducibility of delivered photons reaching the target tissue between individuals. An invasive optical device also offers additional opportunities to utilise spectroscopic methods for monitoring tissue responses to PBM. Given the biphasic effect of PBM therapy,[166] real-time monitoring and dose adjustment feedback would be highly advantageous to permit personalisation of dose based on injury burden and biochemical cellular responses. As such, this thesis will also develop the concept that RS could provide such feedback to inform a closed-loop stimulation-monitoring system via a CNS-optical interface, which may permit a dose-feedback loop to be established via a single device, as conceptualised by the pilot data above.

The concept of invasive neuromonitoring is well established in severe TBI, given the prevalence of invasive intraparenchymal ICP monitoring, and growing implementation of PbtO2 monitoring.[28] Similarly in SCI, there is increasing recognition of invasive monitoring devices, and surgical approaches to the injured spinal column for bony decompression and stabilisation are already commonplace. These principles, established in clinical practice, offer opportunities for the inclusion of additional invasive device technologies in acute severe neurotrauma, without significant additional risk burden to patients. For example in TBI, the concept of this invasive PBM device is that such intracranial access to permit the standard of care (twist drill craniostomy) can be readily adapted to permit the application of an optical technology system.

The overarching aim of the presented work is to develop an implantable device which

establishes an optical interface with the CNS. The proposed devices should be capable of: delivering direct-to-brain/spinal cord PBM stimulation; (2) monitoring the therapeutic effect and injury burden via optical spectroscopy; and (3) integrate into current "standard-of-care" invasive neuromonitoring modalities.[28] A conceptual device schematic is given in Figure 1.16.

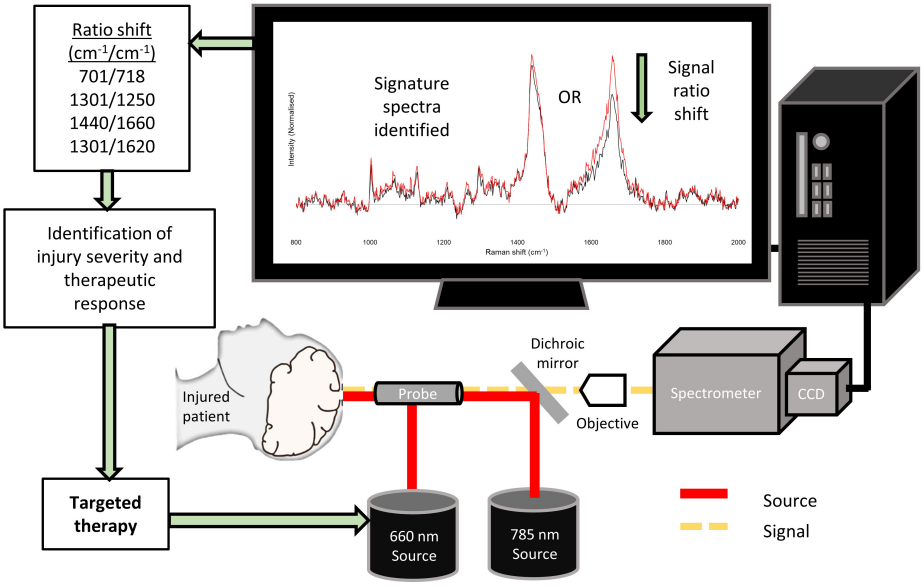


Figure 1.16: Schematic representation of the concept of utilising PBM therapy with RS neuromonitoring in a closed loop system to optimise therapeutic dosing. CCD = charge-coupled device, 660 nm source represents a PBM source, 785 nm source represents a Raman laser source.

The device concept described in Figure 1.16 is reliant upon the favourable effects of PBM being achievable through direct application to the injurious tissue, though this is not an evidenced position. Therefore, demonstrating the efficacy of *direct* PBM in neurotrauma, in comparison to transcutaneous delivery, is an objective of this thesis. A schematic of the concept of implantable PBM devices for CNS injury is shown in Figure 1.17.

Demonstration of the efficacy of direct PBM in TBI via an implant is technically challenging. Whilst this has clear advantages to improve transmittance to the brain surface (Fig. 1.17), invasive application of PBM to the human brain, given the diffuse nature of a typical injury, is likely to require complex or multiple implants to achieve delivery of relevant effective doses of PBM.

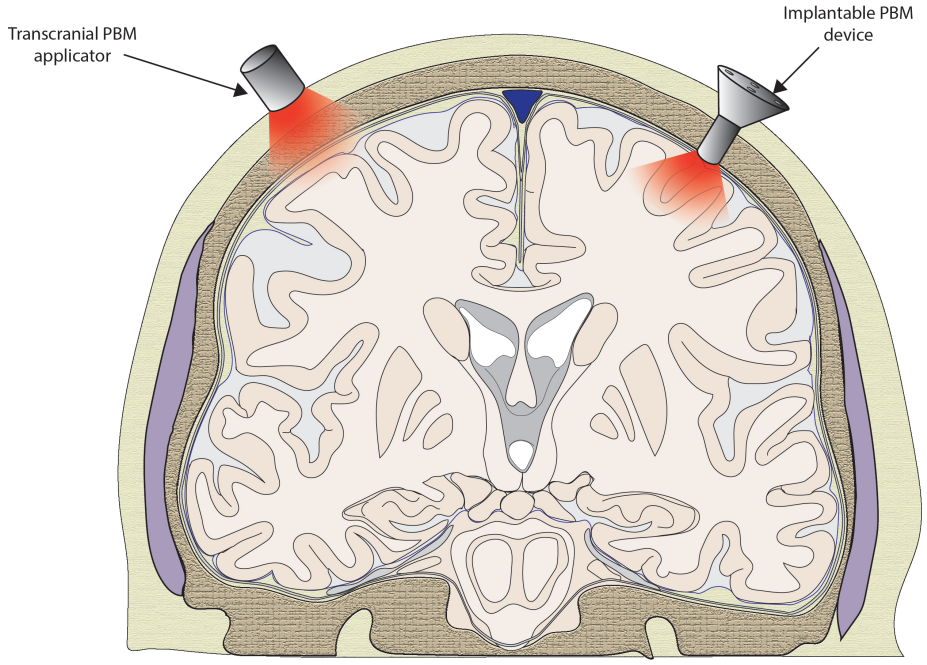


Figure 1.17: Schematic diagram of a coronal section through the head showing the concept of transcranial and implantable PBM delivery devices.

Replication of this in a small mammal model for initial pre-clinical evidence is challenging. Restriction to a focal TBI model, such as CCI may overcome the necessity for diffuse PBM distribution, but there remains a significant technical challenge of ethically and reproducibly siting an implantable optical device stably and directly over the cerebral cortex. In contrast, SCI is typically a focal injury, and siting a device securely over the dorsum of a small mammal model with a protrusion toward the spinal cord is posited as a more stable and reproducible experimental paradigm.

Utilising a SCI model holds further advantages. Firstly, SCI and TBI have several important pathophysiological features in common, and demonstrating the efficacy of direct PBM in SCI would also support efficacy in TBI. Secondly, use of an SCI model, if proven efficacious, would provide evidence for a second important clinical application for this device concept, and would provide additional support for the onward development of the overall device concept toward both clinical applications. As such, developing pre-clinical evidence in this thesis will focus

initially in Chapter 3 on SCI. A model of TBI will then be used in Chapter 4 to further explore optimal wavelengths for PBM, as well as the concept of using RS to monitor therapeutic efficacy. Improved understanding of the mechanism of PBM will benefit translational potential, and will be explored in Chapter 5. Chapter 6 will describe the development of prototype devices for both the brain and spinal cord, as this is the eventual goal of the device concept.

1.10 Hypothesis

The primary hypothesis of this work is that **direct delivery of PBM via an implantable device is an effective and translatable therapeutic strategy in neurotrauma that will promote neuroprotection and neuroregeneration**. The secondary hypothesis is that RS is a suitable technique for monitoring the injured CNS, including monitoring the response to therapeutics such as PBM.

1.11 Aims and objectives

The overarching aims of this thesis are to:

1. Investigate the efficacy of direct delivery of PBM via an implantable device in neurotrauma.
2. Optimise dosing strategies of PBM in neurotrauma.
3. Develop the understanding of the mechanism of PBM in neurotrauma.
4. Investigate the utility of RS neuromonitoring for identification of neurotrauma injury and treatment states.
5. Develop translational devices capable of invasive delivery of PBM in humans.

The specific objectives of this thesis are to:

1. Identify optimal dose parameters of PBM for direct delivery to promote repair after SCI.

2. Develop a methodology to deliver these optimal dose parameters via invasive and non-invasive routes to the injured spinal cord in a pre-clinical model of SCI.

3. Investigate and compare the effects of direct and transcutaneous PBM after SCI in a pre-clinical model.

4. Investigate the utility of RS neuromonitoring for identification of injury and treatment states after SCI.

5. Develop matched delivery methods for 660 nm and 810 nm PBM by transcranial route in an experimental model of TBI.

6. Investigate and compare the effects of 660 nm and 810 nm PBM after TBI in a pre-clinical model.

7. Investigate the utility of RS neuromonitoring for identification of injury and treatment states after TBI.

8. Improve the understanding of the mechanism(s) by which PBM affects outcomes after neurotrauma.

9. Develop proof-of-concept implantable medical devices capable of delivering PBM in a clinical setting in the acute phase after traumatic injury to the brain/spinal cord.

Chapter 2

LITERATURE REVIEW OF PHOTOBIOMODULATION IN TRAUMATIC BRAIN INJURY

This chapter provides a systematic review and meta-analysis of the evidence for the application of PBM in acute TBI.[i] [ii]

2.1 Introduction

The application of PBM in the field of TBI has gathered interest and scientific evidence in the last decade. The application of PBM as a therapeutic intervention for the injured brain has taken two principal forms: (1) in the acute setting post-injury, intended as a neuroprotective/neurorestorative therapy; and (2) in the rehabilitative setting in the chronic phase post-injury, for the purpose of improving symptomatology or neurocognitive/neuropsychological function. Pre-clinical studies on the efficacy of PBM in acute TBI have generated positive results, utilising moderate or severe models of TBI in rodent species,[81] with promising results in an early clinical study.[177] The methodology, outcome measures and hypothesised mechanisms in chronic

[i] This chapter has been published in the Journal of Neurotrauma.[240]

[ii] A previous systematic review has been performed to summarise the evidence relating to PBM in SCI.[213] Summary of this evidence is provided in Chapter 3.

contexts differ greatly from acute applications, and as such, the chronic/rehabilitative phase of TBI recovery is beyond the scope of this literature review, reflecting the focus of this thesis of utilising PBM as a therapy for acute neurotrauma.

The efficacy of PBM in ischaemic stroke had too been considered promising.[81] Such promise culminated in a phase III randomised controlled trial - the NEST-3 study which did not demonstrate efficacy and was terminated early.[210] However, the study design has stimulated criticism,[80] the themes of which represent ongoing scientific "unknowns" in PBM research. The optimal variables of dosing are yet to be established, including irradiance (both surface and after tissue penetration), time of initiation post-injury, optimal duration of therapeutic course, and optimal brain regions for irradiance. Formally establishing the evidence base in TBI is essential for informing future directions in both pre-clinical, translational and clinical research, to minimise the risk of future clinical PBM studies in TBI using suboptimal parameters.

2.2 Aims

This systematic review and meta-analysis seek to comprehensively identify and summarise the scientific literature on the use of PBM in acute TBI. The variables of PBM implemented in identified studies will be analysed with respect to the observed outcomes.

2.3 Methods

A systematic review of the literature was performed on 4th October 2021 following the methodology of the Cochrane Handbook for Systematic Reviewers and presented in accordance with the Preferred Reporting Items for Systematic Reviews and Meta-analyses (PRISMA) guidelines.[241] Systematic searches were performed independently in duplicate. The following databases were searched, from their respective inception to 4th October 2021: Medline, Embase, Cochrane Central, Scopus, Google Scholar and Web of Science. Reference lists of pertinent articles on the topic were hand-searched for suitable articles. Reference lists of identified articles for inclusion were also hand-searched for suitable articles. An example search strategy for Medline is given

below:

1. Exp Low-Level Light Therapy
2. Photobiomodulation.mp
3. Exp Phototherapy/
4. Phototherapy.mp
5. Low level laser therapy.mp
6. 1 or 2 or 3 or 4 or 5
7. Exp Brain Injuries, Traumatic/
8. Exp Craniocerebral Trauma/
9. Head injury.mp
10. 7 or 8 or 9
11. 6 and 10

2.3.1 Study selection

Studies were independently screened for inclusion by two reviewers (A.R.S., and Z.A.). Initial screening based on title and abstract were performed, followed by full text screening. Eligibility for study inclusion was defined as: use of PBM therapy (red/near-infrared (R/NIR)) in acute TBI. Any methodology was accepted, and studies involving *in vitro/in vivo* animal or human subjects were included. Studies which only reported computational modelling methods were excluded. Articles were excluded where blue or white light therapy were used, and where PBM was used in chronic or rehabilitative phase of injury. Conference abstracts were excluded to avoid duplicate reporting where insufficient detail was available to in abstracts to identify such cases; where full manuscripts were available for conference proceedings, these were screened against included manuscripts to exclude duplicate reporting.

2.3.2 Data extraction

Data were extracted from included reports using a piloted form. Data extracted from pre-clinical studies included; species and injury model used, number of replicates, PBM therapy variables (wavelength, irradiance, timing, doses, light source, delivery site), outcomes, and findings of any mechanistic sub-studies. Data were extracted for meta-analysis for neurological severity score and lesion size indices, and other functional and histological outcomes were extracted for narrative presentation. Where data were not directly reported as values, values were extrapolated from published figures. From clinical studies, patient characteristics, PBM therapy variables, any comparator used, outcome measures and outcomes were recorded.

2.3.3 Synthesis of results

This systematic review presents a combination of meta-analysis and narrative presentation of available data. Specific outcome measures were deemed suitable for meta-analysis where $n \geq 3$ studies had presented data (either directly or suitable for accurate extrapolation) in this regard. Remaining outcomes reported in included articles will be presented in tabular and narrative form without statistical analysis.

2.3.4 Risk of bias

Risk of bias in individual studies was assessed using Systematic Review Center for Laboratory Animal Experimentation (SYRCLE)'s tool for assessing risk of bias,[242] and overall risk of bias was determined as low, moderate or high for each included article. For clinical trials, Cochrane Risk of Bias tool with overall risk of bias determined via design quality assessment as good, fair or poor for each included article.[243]

2.3.5 Statistical analysis

Data for meta-analysis were extracted as mean, standard deviation (SD) and *n* number. Where standard error of the mean (SEM) were presented, SD was calculated using SEM and *n* number.

Review Manager 5.4.1 (Cochrane Collaboration, 2022) was used for meta-analysis. Effect size was calculated with a 95% confidence interval, using a standardised mean difference model due to heterogenous data reporting. A fixed effects model was used, and where heterogeneity was calculated by chi-square test as $\geq$ 50%, a random effects model was used.

2.4 Results

The search strategy identified 1,784 records, with 1,459 remaining after removal of duplicates, leaving 93 full-text articles which were assessed for eligibility against the inclusion/exclusion criteria after abstract screening. 18 studies met the criteria for inclusion, with 17 pre-clinical studies being conducted in animal models,[168,172–174,176,244–255] and one clinical study using human participants.[177] The full PRISMA flow chart for search results is shown in Figure 2.1.

2.4.1 Human studies

The review identified a single study of PBM in acute TBI in human participants. Figuero Longo *et al.*, 2020[177] randomised 68 patients with moderate TBI to receive either sham therapy or transcranial PBM within 72 hours of injury. The PBM therapy application used an 810 nm LED array within a custom helmet, with reported average irradiance to the scalp of 36 mW/cm^2 for 20min applications. The authors calculated that their system provides a surface energy of 1.3 J/cm^2 per session based on cadaveric modelling. Patients received 3 x 20 min sessions, at least 12 hours apart. 28 patients received at least one PBM session, and were evaluated for diffusion magnetic resonance imaging (MRI) outcomes Rivermead post-concussion questionnaire (RPQ) in comparison to control group. There were significant changes in radial diffusivity, mean diffusivity and fractional anisotropy at the late subacute stage between PBM and sham groups, though not for axial diffusivity or other time points. RPQ scores were somewhat improved in PBM group versus sham, though not of statistical significance, though it is noteworthy that the study is not appropriately powered to identify significance for functional outcomes.

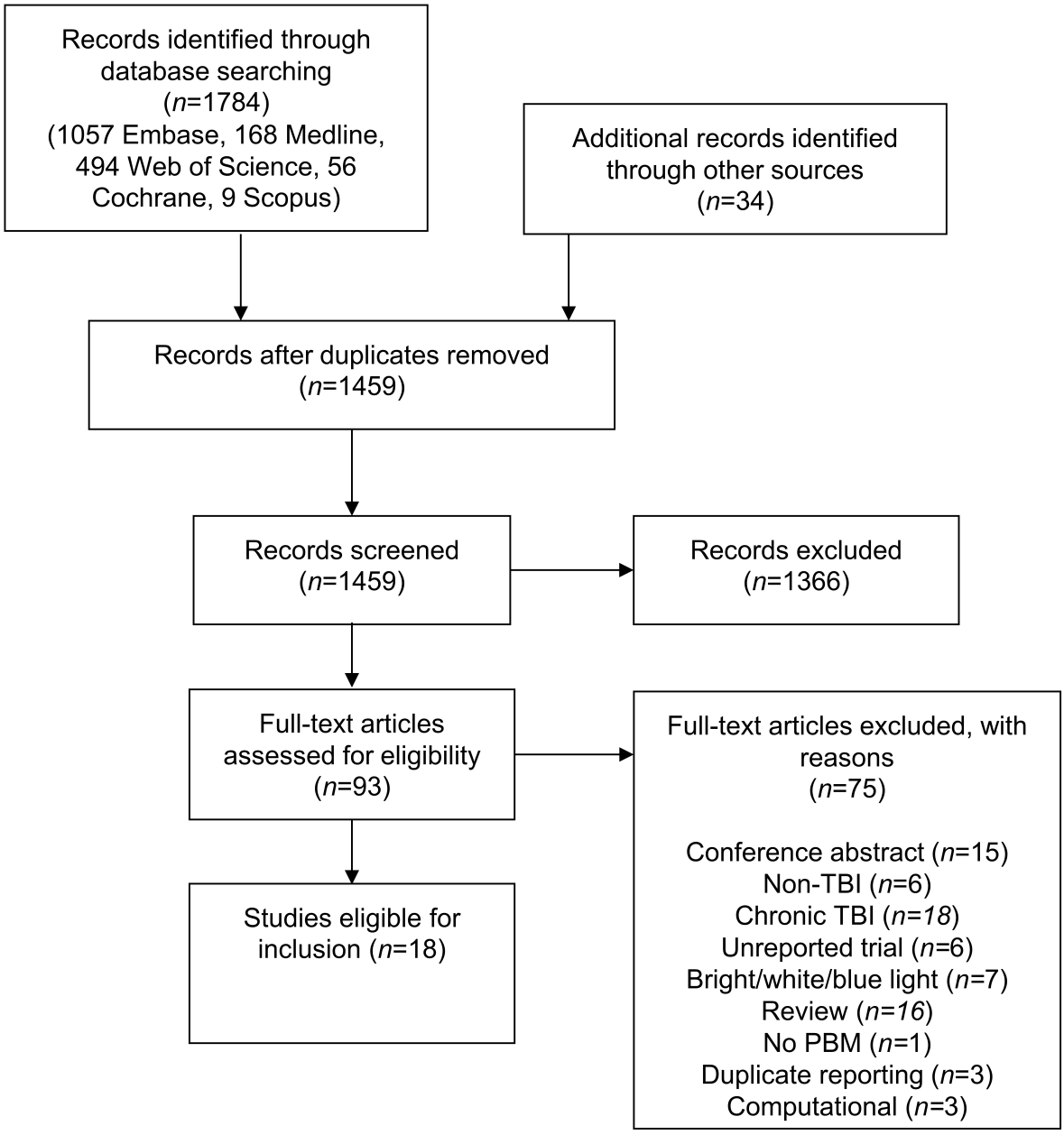


Figure 2.1: PRISMA flow chart of systematic review process

2.4.2 Animal studies

We identified 17 studies of PBM in animal models of TBI[168, 172–174, 176, 244–255] (Table 2.1). All studies used an *in vivo* model of TBI, with one study using neuronal cell cultures as an additional model.[245] Four studies used rats,[172, 173, 250, 253] one study used a transgenic (X-1 knock-out (KO)) mouse[249] and 13 used wild-type (WT) mice.[168, 174, 176, 244–248, 251, 252, 254] Seven studies used controlled cortical impact (CCI) models,[168, 174, 176, 244, 247, 248, 253] six used weight drop weight drop (WD)[246, 251, 252, 254, 255] (one in a repeated TBI model[172]), two used controlled scalp impact,[245, 249] one open lateral fluid percussion (LFP),[250] and one blast-induced neurotrauma (BINT).[173]

Table 2.1: Caption on next page

	Species	TBI model	Severity	λ (nm)	Administration site	Mode	Source	Average irrad. (mW/cm^2)	Cortical irrad. (mW/cm^2)	Exposure time (min)	Energy (J/cm^2) per dose	Cortical energy (J/cm^2) per dose	First dose post-injury (hours)	Total doses (regimen)
Ando et al., 2011	Mouse	CCI	Severe	810	Scalp (over craniotomy)	CW, 10 Hz, 100 Hz	Laser	50	3-7.5	12	36	*	4	1
Dong et al., 2015	Mouse	Scalp impact	Moderate	810	Scalp	10 Hz	Laser	150	8.9	4	36	1.8 to 2.5	4	1
Esenaliev et al., 2018	Rat	Closed BINT	Mild to moderate	808	Scalp	NPLT (20 Hz)	Laser	*	*	5	*	300	1	1
Giacci et al., 2014	Rat	Open LFP	Mild	670, 830	Scalp (over craniotomy)	CW	LED	*	*	30	28.4 / 22.5	*	0	7 (OD)
Khuman et al., 2012	Mouse	CCI	Not stated	800	Cortex or scalp over craniotomy	CW	Laser	250, 500, 1000	*, 250, 500, 1000	2, 7	30, 60, 105, 120, 210	*, 30, 60, 105, 120, 210	1 or 4	1
Oron et al., 2007	Mouse	Skull WD	Mild	808	Skull	CW	Laser	*	10 or 20	2	*	1.2-2.4	4	1
Oron et al., 2012	Mouse	Skull WD	Mild to moderate	808	Skull	CW, 100 Hz, 600 Hz	Laser	21	10	2	2.52	1.2	4, 6 or 8	1
Quirk et al., 2012	Rat	CCI	Moderate	670	Scalp (over craniotomy)	CW	LED	50	*	5	15	*	Not stated	6 or 20 (BD)
Shemesh et al., 2022	Mouse	Scalp WD	Severe	810	Cortex	CW	Laser	50	50	15	45	45	0.16	1
Wu et al., 2010	Mouse	Skull WD	Moderate to severe	660, 810, 980	Scalp	CW	Laser	150	*	4	36	*	4	1
Wu et al., 2012	Mouse	Skull WD	Moderate to severe	665, 730, 810, 980	Scalp	CW	Laser	150	*	4	36	*	4	1
Xuan et al., 2013	Mouse	CCI	Severe	810	Scalp (over craniotomy)	CW	Laser	25	*	12	18	*	4	1/3/14 (OD)
Xuan et al., 2014	Mouse	CCI	Moderate to severe	810	Scalp (over craniotomy)	CW	Laser	25	*	12	18	*	4	1/3 (OD)
Xuan et al., 2015	Mouse	CCI	Severe	810	Scalp (over craniotomy)	CW	Laser	50	*	12	36	*	4	1/3 (OD)
Xuan et al., 2016	Mouse	CCI	Severe	810	Scalp (over craniotomy)	CW	Laser	25	*	12	18	*	4	3/14 (OD)
Yang et al., 2020	Rat	Skull WD (repeat)	Mild	808	Scalp	CW	Laser	350	25	2	*	*	2	15 (OD)
Zhang et al., 2014	Mouse (X-1 KO)	Scalp impact	Mild	810	Scalp	10 Hz	Laser	150	Not stated	4	36	1.8-2.5	4	1

Table 2.1: Summary table of included pre-clinical studies. BINT = blast-induced neurotrauma; CCI = controlled cortical impact; CW = continuous wave; LFP = lateral fluid percussion; OD = once a day; BD = twice a day; PW = pulsed wave; WD = weight drop; λ = wavelength; * denotes where a protocol has been used but irradiance parameters have not been presented.

The available reported PBM variables for therapeutic regimens are given in Table 2.1, with all used permutations of a variable given (where a study has used multiple therapeutic regimens). Notably, 15 studies used a wavelength in the 800-810 nm region, either alone or in comparison with another wavelength, with two studies not using a wavelength in this region[250,253] (using 670 or 830 nm). full width at half maximum (FWHM) values were not reported. Two studies used a light-emitting diode (LED),[250,253] 15 employing a laser source. Two studies delivered PBM directly to the cortical surface of the lesion site[176,254] with 15 studies applying the source to skull or scalp. Four studies used a pulsed wave (PW) source,[244,245,249,252] alone or in combination with continuous wave (CW), one used nano-pulsed laser therapy (NPLT),[173] and 12 used CW alone. One study used PBM in combination with metabolic substrates,[245] 16 using PBM alone. All studies commenced PBM within 8 hours of injury. Ten studies used PBM protocols with a single dose of PBM,[173,244–246,249–252,254,255] with seven using alternative and additional course duration up to 15 days.[172]

2.4.3 Meta-analysis

Two outcomes were sufficiently reported in the included studies to permit robust meta-analysis: neurological severity score (NSS) and lesion size. NSS was predominantly reported as baseline NSS (± SD/SEM) and end-point NSS (± SD/SEM). Insufficient detail was available in any included study, or in the wider literature, to calculate or infer the ΔSD, and so the end-point NSS was used in a standardised mean difference model.

2.4.4 Neurological severity score

Meta-analysis was performed for the nine studies reporting NSS values in PBM and control groups.[168,172,174,244,246–249,251,252,255] Given the frequent use of sub-study groups based on varying therapeutic protocols, a total of 28 therapeutic protocols from across nine studies are included in the analysis shown in Figure 2.2. Overall, effect size is -1.55 [-2.10, -1.01] in favour of PBM versus control ($p < 0.00001$, I^2 82%).

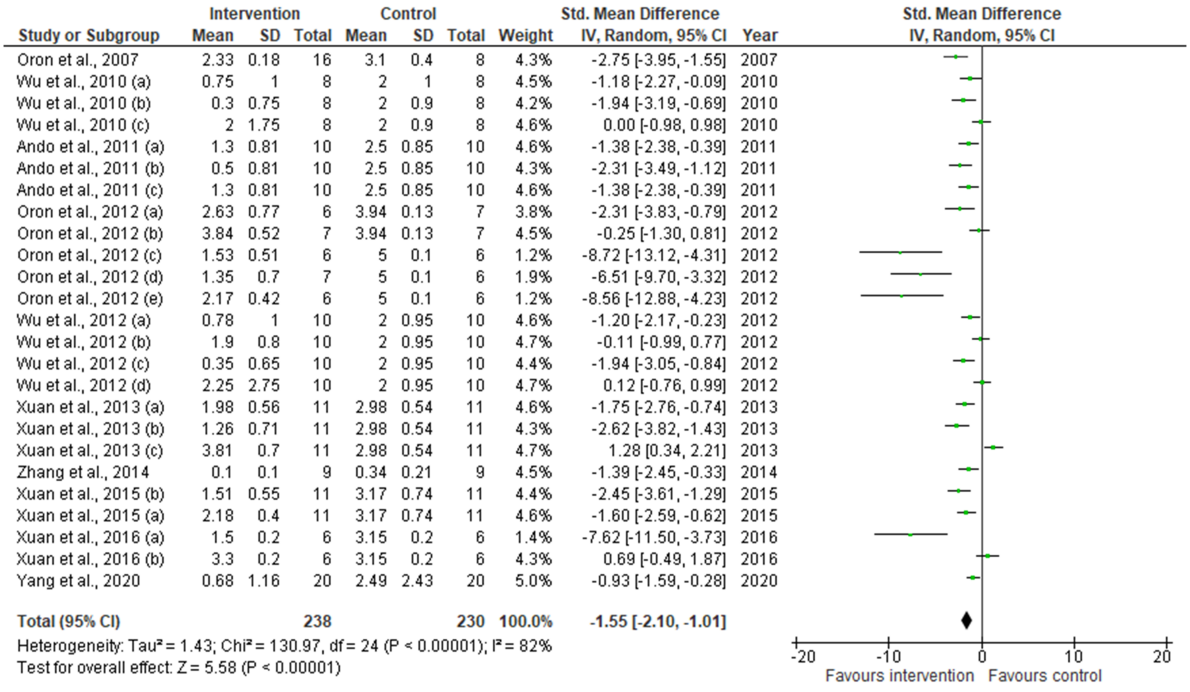


Figure 2.2: Forest plot of end neurological severity score (standardised mean difference).[168,174,244,246–249,251,252,255] NSS at 28 days with exception of Yang *et al.*, 2020,[172] Zhang *et al.* 2014[249] (both 14 days), and Oron *et al.*[252] (c-e) (27 days). Control total value includes duplicates from varying test conditions compared with single control group.

Given the heterogeneity of therapeutic regimens employed, both inter- and intra- article, sub-group analysis was performed based on distinct variables: CW vs PW, wavelength of PBM, timing of first dose post-injury, total number of doses and incident energy per dose (calculated for cortical surface energy) (Table 2.3). Both continuous and pulsed wave PBM have statistically significant effects on NSS. Ando *et al.*, 2011 reported statistically significant advantage of PW at 10 Hz over CW, but not of PW at 100 Hz.[244] Wavelengths in the region of 665/810 nm are

associated with positive effects, but not 730/980 nm. A first dose after 4 hours post-injury or a course of treatment with >3 doses were not effective, and all energy values were associated with reduced NSS. Dosing regimens for sub-studies and therapeutic protocols included in meta-analysis are described in Table 2.2, and subgroup analysis in Table 2.3.

Table 2.2: Caption on next page.

	f	λ (nm)	Average irradiance (mW/cm^2)	Average irradiance (cortex) (mW/cm^2))	Exposure (minutes)	Administration	First dose post-injury (hours)	Doses	Brief results of intervention versus control
Oron et al., 2007[251]	CW	808	10 or 20	0.899	2	Skull	4	1	Improved NSS at 28 days ($p < 0.05$)
Wu et al., 2010 (a)[255]	CW	665	150	*	4	Scalp*	4	1	Improved NSS ($p < 0.05$) and lesion size ($p < 0.05$)
Wu et al., 2010 (b)[255]	CW	810	150	9.39	4	Scalp*	4	1	Improved NSS ($p < 0.05$) and lesion size ($p < 0.01$)
Wu et al., 2010 (c)[255]	CW	980	150	9.39	4	Scalp*	4	1	No effect on NSS at 28 days
Ando et al., 2011 (a)[244]	CW	810	50	5.25	12	Scalp*	4	1	Improvement of NSS at 28 days
Ando et al., 2011 (b)[244]	10 Hz	810	50	5.25	12	Scalp*	4	1	Most effective for improvement of NSS at 28 days ($p < 0.001$) and lesion size ($p < 0.01$)
Ando et al., 2011 (c)[244]	100 Hz	810	50	5.25	12	Scalp*	4	1	Improvement of NSS at 28 days
Khuman et al., 2012 (a)[176]	CW	800	500	0.5	2	Cortex	1	1	No effect on lesion size at 14 days ($p = 0.12$)
Oron et al., 2012 (a)[252]	CW	808	21	10	2	Skull	6	1	Improvement of NSS at 28 and 56 days ($p < 0.05$)
Oron et al., 2012 (b)[252]	CW	808	21	10	2	Skull	8	1	No effect on NSS at 56 days
Oron et al., 2012 (c)[252]	CW	808	21	10	2	Skull	4	1	Improvement of NSS at 56 days ($p < 0.001$) and lesion size ($p < 0.01$)
Oron et al., 2012 (d)[252]	100 Hz	808	21	10	2	Skull	4	1	Improvement of NSS at 56 days ($p < 0.001$) and lesion size ($p < 0.01$)
Oron et al., 2012 (e)[252]	600 Hz	808	21	10	2	Skull	4	1	Improvement of NSS at 56 days ($p < 0.001$)
Wu et al., 2012 (a)[246]	CW	665	150	*9.39	4	Scalp	4	1	Improvement of NSS at 28 days ($p < 0.05$)
Wu et al., 2012 (b)[246]	CW	730	150	*9.39	4	Scalp	4	1	No effect on NSS at 28 days
Wu et al., 2012 (c)[246]	CW	810	150	9.39	4	Scalp	4	1	Improvement of NSS at 28 days ($p < 0.001$)
Wu et al., 2012 (d)[246]	CW	980	150	9.39	4	Scalp	4	1	No effect on NSS at 28 days
Xuan et al., 2013 (a)[247]	CW	810	25	2.63	12	Scalp*	4	1	No effect on NSS or lesion size at 28 days
Xuan et al., 2013 (b)[247]	CW	810	25	2.63	12	Scalp*	4	3	Improvement of NSS at 28 days ($p < 0.001$) and lesion size ($p <0.01$)
Xuan et al., 2013 (c)[247]	CW	810	25	2.63	12	Scalp*	4	14	Improvement of lesion size at 28 days ($p <0.01$)
Giacci et al., 2014 (a)[250]	CW	670	0.02	*<1	30	Scalp*	0	7	No effect on lesion size at 7 days
Giacci et al., 2014 (b)[250]	CW	830	0.01	*<1	30	Scalp*	0	7	No effect on lesion size at 7 days
Xuan et al., 2015 (a)[248]	CW	810	50	3.13	12	Scalp*	4	1	Improvement of NSS at 28 days ($p < 0.05$)
Xuan et al., 2015 (b)[248]	CW	810	50	3.13	12	Scalp*	4	3	Improvement of NSS at 28 days ($p < 0.001$)
Zhang et al., 2014[249]	10 Hz	810	150	8.85	4	Scalp	4	1	NSS at day 7 significantly reduced ($p < 0.001$)
Xuan et al., 2016(a)[168]	CW	810	25	2.63	12	Scalp*	4	3	Improved NSS versus control and 14 day treatment duration ($p <0.001$)
Xuan et al., 2016 (b)[168]	CW	810	25	2.63	12	Scalp*	4	14	Improved NSS versus control at week 7 ($p < 0.01$) and week 8 ($p <0.001$) post-injury
Yang et al., 2020[172]	CW	808	350	25	2	Scalp	2	15	Improved NSS throughout protocol ($p < 0.05$)

Table 2.2: Dosing regimens of included pre-clinical studies and sub-studies included in meta-analyses. Scalp$*$ denotes scalp administration over craniotomy. # = data not available, cortical irradiance calculated/extrapolated using transmittance penetration data (Ando et al., 2011[244] where λ = 800-810 nm). $*$ data not available and incalculable. f = frequency; CW = continuous wave; PW = pulsed wave; NSS = neurological severity score.

Table 2.3: Subgroup analysis for endpoint neurological severity score. Subgroups stratified from those in Figure 2.2 and Table 2.1. NSS at 28 days with exception of Yang et al., 2020,[172] Zhang et al., 2014[249] (both 14 days), Oron et al., 2012 (c-e) (27 days).[252] CW = continuous wave; PW = pulsed wave, $*$ = heterogeneity not applicable due to small sample size. Energy per dose at cortical surface is calculated where not reported by respective study as described in Table 2.2 caption.

Variable (n interventional animals)	Effect size [95% CI]	p-value	I^2 for heterogeneity (p value)
Mode			
CW (220)	-1.31[-1.88, -0.73]	< 0.00001	82% (< 0.00001)
PW (42)	-2.94 [-4.48, -1.39]	0.0002	79% (0.0006)
Wavelength			
660-670 nm (18)	-1.19 [-1.91, -0.47]	0.001	0% (0.98)
730 nm (10)	-0.11 [-0.99, 0.77]	0.81	$*$
800-815 nm (216)	-1.93 [-2.59, -1.26]	< 0.00001	83% (< 0.00001)
980 nm (18)	0.06 [-0.59, 0.72]	0.85	0% (0.86)
First dose timing post-injury			
$\leq$ 4 hours (249)	-1.60 [-2.18, -1.02]	< 0.00001	83% (< 0.00001)
> 4 hours (13)	-1.20 [-3.22, 0.81]	0.24	79% (0.03)
Number of treatments			
$\leq$3 (217)	-1.81 [-2.36, -1.27]	< 0.00001	77% (<0.00001)
>3 (45)	0.31 [-1.18, 1.80]	0.69	88% (0.0003)
Energy per dose at cortical surface			
0 E $\leq$ 1 (J/cm^2) (16)	-2.75 [-3.95, -1.55]	< 0.00001	$*$
1 < E $\leq$ 2 (J/cm^2) (101)	-2.77 [-4.33, -1.21]	0.0005	90% (< 0.00001)
2 < E $\leq$ 3 (J/cm^2) (95)	-1.12 [-1.68, -0.55]	0.0001	67% (0.001)
E < 3 (J/cm^2) (50)	-1.36 [-1.90, -0.83]	< 0.00001	26% (< 0.00001)

2.4.5 Lesion size

Ten studies reported outcomes of lesion size at study endpoint, encompassing 21 therapeutic protocols. Overall effect size was -1.55 in favour of PBM, [-2.19, -0.95] (p < 0.00001, I^2 = 75%). Standardised mean difference was used due to heterogeneity in reported effect and measurement techniques. Forest plot for lesion size across included studies is illustrated in Figure 2.3. Dosing

regimens for sub-studies and therapeutic protocols included in meta-analysis are described in Table 2.2.

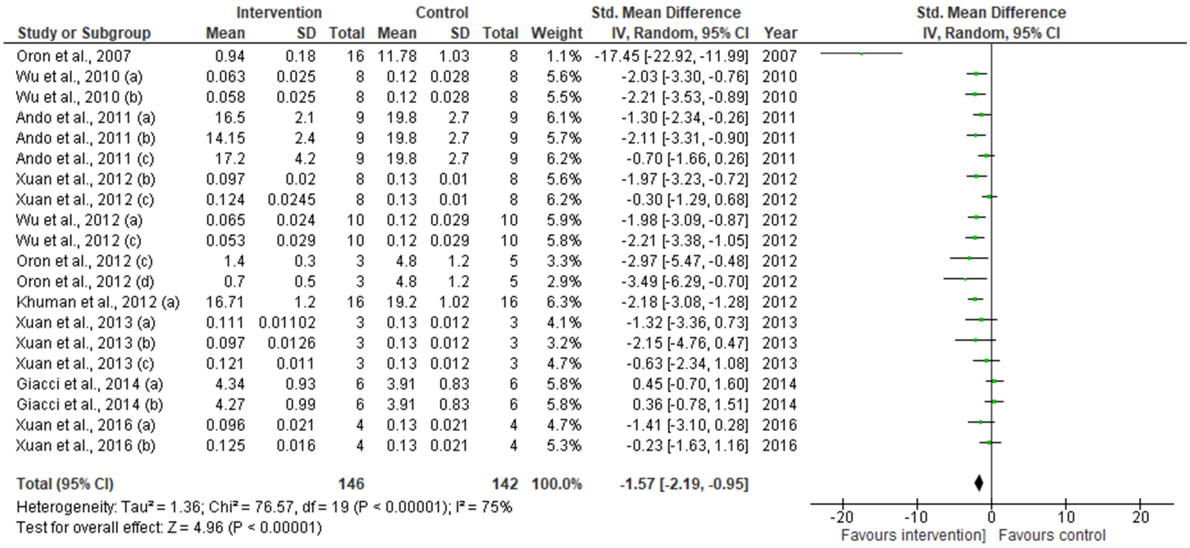


Figure 2.3: Forest plot of lesion size (histologically or radiologically determined).[168, 244, 246–248, 250–252, 255] Values at 28 days post-injury with exception of Oron et al., 2012[252] (56 days), Khuman et al., 2012[176] (14 days) and Giacci et al., 2014[250] (7 days). Control total value includes duplicates from varying test conditions compared with single control group.

2.4.6 Alternative functional outcomes

Morris water maze (MWM) was an outcome measure used in n = 5 studies.[168, 173, 174, 176, 245] However, there was significant heterogeneity between training schedules, timing of testing post-injury (varying from 7 to 55 days post-injury), the use of hidden platform, visible platform and probe trials. As such, these were not deemed suitable for meta-analysis and the findings of individual studies for MWM will be described in the narrative below. Similarly, other functional outcomes were used by studies with varying frequency: forced swim test (n = 1),[244] tail suspension test (n = 1),[244] wire grip and motion test (WGMT) (n = 2),[174, 247] rotarod score (n = 1),[250] bilateral asymmetry test (n = 1),[250] beam balance scores (n = 1),[173] nose poke tasks (n = 1),[253] open field, elevated plus maze, Y maze and fear conditioning (all n = 1),[172] and discussed

below.

Khuman *et al*., 2012[176] performed MWM trials, with inclusion of probe trials and analysis of progressive improvement. Statistically significant improvements in outcomes were mixed, though 60 J/cm^2 delivered either transcranially or directly for a single administration demonstrated a statistically significant improvement versus controls in all measured MWM domains. All PBM groups versus controls exhibited greater progressive improvement ($p < 0.0001$). Administered directly, 60, 120 and 210 J/cm^2 but not 30 or 105 J/cm^2 resulted in MWM hidden platform latency improvements, and 60 and 120 J/cm^2 elicited probe trial improvements. Single dose transcranial administration of 60 J/cm^2 resulted in improvements in all MWM domains if given 1 hour after injury, but not after 4 hours or daily for 7 days. Esenaliev *et al*., 2018 used NPLT in a blast induced neurotrauma (BINT) model. NPLT was demonstrated to improve MWM ($p < 0.05$) at 7 days post-injury, though this effect was not observed on subsequent days' MWM testing.

Xuan *et al*., 2016[168] also used the MWM test at 22 and 49 days post injury. Groups with TBI receiving 3x daily PBM treatments at day 22 demonstrated significant improvements in latency scores for both platform and probe trials, compared to TBI controls ($n = 6$, $p < 0.05$ and 0.01 respectively). The effect was not significant at day 49 though the effect was still observed, and the group receiving 14 days of treatment had results similar to TBI controls at both timepoints post-injury. Giacci *et al*., 2014 found no significant differences between control, 670 nm and 830 nm treatments at 7 days post-injury in rotarod score or in the bilateral asymmetry test contralateral vs ipsilateral latency.[250] Xuan *et al*., 2013[247] used a WGMT and showed no statistically significant improvement in vestibular function in any treatment group. Xuan *et al*., 2014[174] utilised the WGMT at 7, 14, 21 and 28 days post-TBI using single or triple doses of PBM (810 nm, 25 mW/cm^2, 12 min transcranial). The authors demonstrated statistically significant improvements in WGMT performance in both single ($p < 0.05$) and triple ($p < 0.001$) doses at 28 days post-injury, with significant improvements recognised also at 14 and 21 days in PBM versus control. Khuman *et al*. 2012,[176] also found no improvement on motor recovery in a stationary wire grip test. Esenaliev *et al*., 2018[173] used transcranial NPLT in

a blast induced neurotrauma (BINT) model. NPLT was demonstrated to improve beam-balance test scores on day 1 post-injury ($p < 0.01$), beam walk test scores on day 1 and 2 post-injury ($p < 0.001$ and < 0.05 respectively), not observed at later time points. Quirk *et al*., 2012,[253] (670 nm, 50 mW/cm^2, 5 min exposure time, daily exposure for 72 h) found some improvements in movement domains (nose poke tasks) though not all, and their functional testing was limited to this assessment. Ando *et al*., 2011[244] found statistically significant improvements in the forced swim test (for depression) in the group receiving PW 10 Hz ($p < 0.05$) at 28 days post-injury, and significant improvements in the tail suspension test for anxiety and depression in both PW 10 Hz and PW 100 Hz at 28 days post-injury. CW groups did not demonstrate statistically significant improvements in these domains. Yang *et al*., 2020[172] performed more extensive functional assessments in their repeated TBI model. Open field (mobility), elevated plus maze (anxiety), Y maze (spatial memory) and fear conditioning testing all demonstrated statistically significant improvements attributable to PBM administration after repeated closed TBI.

2.4.7 Histological outcomes

Wu *et al*., 2012[246] marked fractional defects on morphometric brain sections with H&E staining, and identified that 665 and 810 nm LLLT resulted in statistically significant reductions in numbers of mean fractional defect areas ($p < 0.05$ and < 0.01 respectively, $n = 10$ per group).

2.4.8 Mechanistic outcomes

Metabolic activity

Ando *et al*., 2011[244] performed ATP fluorometric assay for specimens immediately after laser exposure versus control, finding no significant differences between control and intervention arms. However, a trend suggested a mild increase of cortical ATP content with 10 Hz PW treatment, correlating with this as the treatment condition with greatest effect on improving NSS and lesion size. Zhang *et al*., 2014,[249] though principally using W-1 KO mice, performed ATP assay on WT mice with and without LLLT after mTBI, demonstrating that at 24 h after injury there was

a significant increase in cortical ATP levels with LLLT ($p < 0.001$, $n = 6$ per group). Dong *et al*., 2015,[245] included LLLT therapy to cultured SH-SY5Y neuronal cells in varying conditions. They report that hypoxia (induced by CoCI2) related cell death was significantly reduced by exposure to 3-10 J/cm^2 LLLT at 2 h post-exposure to hypoxia, with increasing survival with increasing energy or exposure periods (up to 10 J/cm^2 x3). The effect was augmented with the addition of mitochondrial substrates to the media (glucose/lactate/pyruvate). They further demonstrated that this increased survival with LLLT exposure correlated with suppression of lactate level at 0-18hr, increase in ATP level, reduction in reactive oxygen species (ROS) level and increase in mitochondrial membrane potential. In an *in vivo* model of hypoxia (using cortical topical oxyrase) they reported complete prevention of hypoxia related hippocampal tissue loss due to Oxyrase in the presence of LLLT.

Neuroinflammation

Khuman *et al*., 2012[176] performed quantitative analysis of microglial activation. 60 J/cm^2 resulted in a significant reduction in activated microglia compared to control treatment ($p = 0.03$, $n = 4$/group). Khuman *et al*., 2012[176] also found no significant difference between treatment and control for: magnitude of brain oedema at 24 h, brain tissue loss or protein nitrosylation. Yang *et al*., 2020[172] also found that PBM lowered MAP2 dispersion, increased MBP and reduced cleaved Tau, with the authors concluding that PBM attenuates axonal injury after repeated TBI. Yang *et al*., 2020[172] found that PBM was associated with attenuated astrogliosis at the lesion site, and attenuated the increases of IBA1 and IL-1B associated with pro-inflammatory shifts post-injury. PBM associated elevation of IL-10, in combination with reduction of IL-1B was attributed by the authors to a shift from "pro-inflammatory" to "anti-inflammatory" phenotypes after exposure to PBM. NPLT-treated rats (Esenaliev *et al*., 2018[173]) demonstrated lower CD68+ microglial cells (marker of microglial activation). Xuan *et al*., 2016[168] stained for glial fibrillary acidic protein (GFAP) in multiple brain areas in their study using 3/14 day PBM courses post-injury. Whilst the 14 day course did not correlate with functional improvements (MWM, NSS), the 3 day course did improve these outcomes. Both 3/14 day courses were associated with reduced

GFAP staining in all tested brain areas at 56 days post-injury, to a similar extent.

Apoptotic markers

Quirk *et al*., 2012,[253] performed Western blotting on tissue extracts from four brain regions in TBI and sham ± PBM administration. Glutathione levels, vastly increased in injury site versus same brain area in sham, were not significantly changed in the lesion site with the application of PBM. However, they identified a statistically significant reduction in Bcl2 (B-cell lymphoma 2) associated X protein (Bax) levels (pro-apoptotic protein) after application of PBM compared with controls. Levels of B-cell lymphoma 2 (Bcl-2) (anti-apoptotic marker) were also significantly increased after PBM compared with no therapy. B-actin levels were not significantly altered. Esenaliev *et al*., 2018[173] in their transcranial BINT model found that at 3 dpi in injured cortical neurons (Fluoro-Jade C negative) from rats exposed to NPLT had lower expression of Bax, caspase-3 and signal transducer and activator of transcription 3 (STAT3), with higher levels of BDNF expression. This effect was not observed on 7 dpi. Similarly, NPLT-treated rats showed lower immunofluorescence with caspase-3 staining on 3 dpi, with no observed immunofluorescence at 7 dpi. Similarly, Yang *et al*., 2020[172] also found a significant and marked reduction in cytosolic caspase-3 and caspase-9 associated with PBM administration after repeated closed head injury. Xuan *et al*., 2014[174] found significant reductions in caspase-3 expression at day 4 post-injury in both single ($p < 0.05$) and triple ($p < 0.01$) treatment regimens versus control.

Neuronal damage and proliferation

Yang *et al*., 2020[172] in PBM treated rats after repeated closed head injury, found that synaptic degradation was prevented by PBM based on expression of synaptophysin and spinophilin in hippocampal cornu Ammonis (CA)1 region. NPLT-treated rats (Esenaliev *et al*., 2018[173]) demonstrated higher cell proliferation in the subgranular zone (bromodeoxyuridine (BrdU) immunohistochemistry). Xuan *et al*., 2013[247] demonstrated statistically significant reduction in degenerating neurons in 3 day treatment regimen specimens through Fluoro-Jade C staining

compared with sham treatment (n = 8, $p < 0.05$). Xuan *et al.*, 2013[247] also showed statistically significant increases in BrdU staining (proliferating cells) with 3 day treatment vs sham (n = 8, $p < 0.001$). Xuan *et al.*, 2014[174] found significant increases in BrdU/DAPI ratio in hippocampal dentate gyrus (DG) at day 7 post-injury in both single ($p < 0.01$) and triple ($p < 0.001$) treatment regimens versus control, and at day 28 post-injury (single ($p < 0.05$) and triple ($p < 0.01$)) . Similar results were also shown for neurogenic subventricular zone (SVZ) and in perilesional tissue all at 7 and 28 days post-TBI. Xuan *et al.*, 2014[174] found significant increases in PBM treated specimens versus control in microtubule-associated migration protein double cortin (DCX) suggestive of presence of maturing neurons. DCX/DAPI ratio in DG and perilesional tissue was increased in treated subjects at 7 and 28 days, and in SVZ at 7 but not 28 days. Xuan *et al.*, 2014[174] also performed staining using neuron-specific antibody to class III β-tubulin (TUJ1) (expressed in differentiating neural progenitor cells) at 7 and 28 days post-injury in PBM and control specimens, finding an association between increased TUJ1/4,6-diamidino-2-phenylindole (DAPI) ratio and PBM treatment at both timepoints in both DG and SVZ. Xuan *et al.*, 2015[248] demonstrated a transient upregulation in brain-derived neurotrophic factor (BDNF) at day 7 post-injury in DG and SVZ, not observed in the perilesional region. The lesion and SVZ at 28 days post-injury showed upregulation of Synapsin-1, suggestive of synaptogenesis.

Cerebral blood flow

Shemesh *et al.*, 2022[254] used a terminal anaesthesia model, with TBI and subsequent craniotomy for dual-wavelength speckle contrast imaging with 20 min of baseline data, delivery of PBM directly, and a further 20 min of data taken. Measures of cerebral blood flow (CBF), saturation and overall oxygen consumption increased in animals receiving PBM therapy versus control.

2.4.9 Experimental factors

Transmittance

Ando *et al.*, 2011[244] performed profiling of the laser power transmission to brain tissue for each of their treatment protocols, measuring transmission through scalp alone, and skull and scalp. Using this data, they calculated an approximation of irradiance to cortical surface based on the dimensions of overlying scalp/skull in their model. Oron *et al.*, 2007[251] similarly used cadaveric mouse tissue to simulate their protocol with a power meter positioned within the cranium to directly measure transmitted irradiance. Shemesh *et al.*, 2022[254] also directly measured power outputs to calculate incident dose at the "sample plane" (cortical surface in their direct delivery model with a 200 mW output source at 20 cm from cortex).

Temperature

Khuman *et al.*, 2012,[176] recorded temperature changes in their model of direct application of PBM to the cortical surface: PBM treatment "increased brain temperature by 0.2 ± 0.1 °C (30 J/cm^2), 2.5 ± 0.4 °C (60 J/cm^2), and 4.1 ± 0.3 °C (120 J/cm^2), over the 2 min application period. In the transcranial protocol, LLLT (60 J/cm^2) increased brain temperature by 1.8 ± 0.1 °C. The authors reported that brain temperature returned to baseline within 3–5 min.

2.4.10 Risk of bias assessment

Risk of bias assessment for the included human clinical study is presented in Table 2.4, with overall study quality determined as "Fair". Overall risk of bias for animal studies was high across most studies, as illustrated in Figure 2.4.

2.5 Discussion

This systematic review presents a comprehensive summary of the available literature on the use of PBM therapy in the context of acute TBI. The meta-analysis, though limited in its scope due

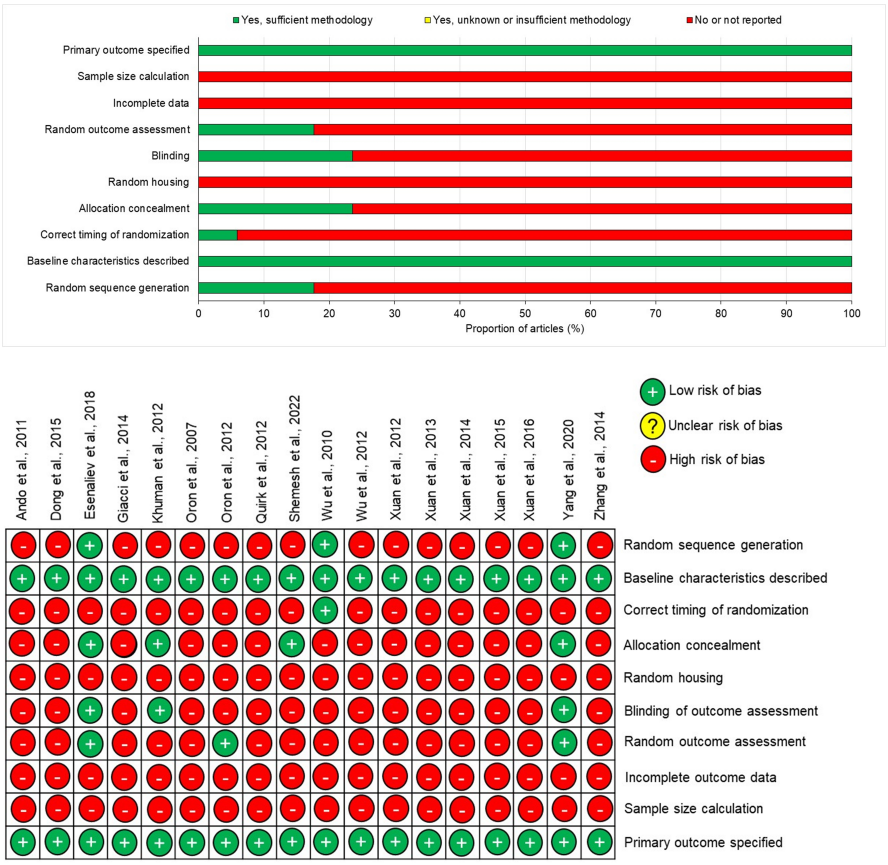


Figure 2.4: Risk of bias analysis for the included pre-clinical studies using the SYRCLE tool

to literature heterogeneity, combined with supplementary narrative summary, presents clear and robust data of the therapeutic benefit of PBM in pre-clinical models on functional, histological and radiological TBI outcomes. The presented data on specific mediators amalgamates a broad variety of mechanistic insights into the action of PBM in TBI. Subgroup analysis based on variables of PBM parameters also offers an important quantitative summary toward establishing the translational potential for PBM.

2.5.1 Establishing an optimum modality

The subgroup analysis presented in this review identified that the available evidence supports both CW and PW as therapeutic modes of dose administration. The greater effect size of PW is suggestive that there may be an advantage to this approach, though this analysis is not able to

Table 2.4: Risk of bias assessment for clinical studies, based on Cochrane RoB tool[243]

	Randomisation	Deviations from intended interventions	Missing outcome data	Measurement of outcome	Selective reporting	Overall
Figueiro Longo et al., 2020[177]	Low	High	Low	Some concerns	Low	Fair

draw conclusions on the relative merits of PW in comparison to CW. Both approaches generated an effect size favouring intervention with statistical significance. It is noteworthy however that Ando *et al.*, 2011[244] compared CW with PW (10 Hz) and PW (100 Hz) and found PW 10 Hz the most effective, with a statistically significant further improvement of outcomes compared with CW. Oron *et al.*, 2012 too found that PW at 100 Hz was associated with improved NSS recovery at 56 days post-injury compared with CW.[252] The application and mechanistic effect of pulsed wave light delivery is not fully understood and warrants further well controlled studies.

Given the presence of one paper in the literature describing the technique, insufficient evidence on the application of NPLT in TBI is available to draw conclusions as to its efficacy, particular in comparison with CW/PW.

The subgroup analysis also identifies a clear dichotomy amongst the used wavelengths: wavelengths in the region of 665 and 810 nm corelated with therapeutic effect, and wavelengths in the region of 730 and 980 nm did not. This apparent failure of 730/980 nm wavelengths to elicit detectable therapeutic benefit in *in vivo* models of TBI has two potential explanations: (1) 730/980 nm do not elicit the same phototherapeutic and biochemical effects at a cellular level in TBI; (2) penetrance of 730/980 nm photons to the target tissue is impaired in comparison with other wavelengths. These potential causes of therapeutic failure are not able to be informed by the current available evidence identified here. Longer wavelengths penetrate further, however 980 nm light has increased levels of absorption by water and oxygenated haemoglobin than the shorter wavelengths,[256] which may in part explain this phenomenon. A further consideration is that no included study reported full width at half maximum value; a measure of the bandwidth of a light source at 50% capacity (though spectral transmittance was reported by Giacci *et al.*,

2014[250] for their SCI model). As such, it is not possible to evaluate whether sources outside the emission maxima of 660 and 810 nm may have included these peaks.

2.5.2 Establishing an optimum dose

In the subgroup analysis on overall dose, all three subgroups of dose demonstrated efficacy with statistical significance. The optimal dose is a subject of much debate in PBM research which has not been resolved with wide-ranging and thorough reviews from across the large body of PBM literature in multiple tissue types.[257] The well-established "biphasic dose response" of PBM creates potential problems of both under- and overdosing of target tissue.[166,167] The Hamblin laboratory have argued that greater mitochondrial concentration (as in cerebral tissue) is more likely to respond favourably to relatively low levels of fluence, and have a greater propensity for failure due to overdose.[257] However, the doses delivered at any depth within cerebral tissue due to impedance from scalp, skull, periosteum, dura, cerebrospinal fluid (CSF), blood (and brain itself) is greatly attenuated even in rodent tissue: this issue is amplified in larger mammals such as humans.[258] Delivery varies further on factors such as skull thickness, differing between species, patients and anatomical locations. In the absence of subject-specific complex computational modelling, even establishing "the dose" reaching the target tissue is difficult, more so if attempting to resolve this to discrete anatomical locations within the organ. Study therefore on "the optimum dose" is an even greater challenge.

2.5.3 Establishing an optimum dose regimen

Subgroup analysis has also demonstrated clearly that two key factors in the PBM dosing regimen should be considered. Firstly, the time to initial dose is of great importance: the therapeutic effect appears to be lost or greatly diminished when first dose administration is given more than around six hours post-injury in rodent models. Furthermore, the beneficial effects of PBM appear to be lost where repeated administrations are given on a daily basis over a number of days, though the optimum duration of a treatment course cannot be established from the current literature. Xuan *et al.*, 2013[247] examined this directly, and showed that in their model the

efficacy increased with 3x vs 1x doses, but any derived benefit was lost if the course continued to 14x doses. Whilst direct comparative data is limited to this study, Yang *et al*., 2020 found considerable therapeutic benefits, particularly in functional outcomes, with doses given over a 15 day course.

2.5.4 Establishing an optimum delivery technique

The specifics of delivery varied greatly between studies using a transcranial delivery method. PBM parameters (irradiance, fluence and exposure time), positioning factors (direct to skull, direct to scalp, or a specified distance from the scalp) and specimen factors (underlying durotomy/craniotomy/closed surgical wound) all have considerable effects on the dose delivery to the target tissue.

The included results are not able to inform conclusions regarding the potential benefits of varying specifics of a transcranial application method, nor inform conclusions on the benefits of either direct or transcranial application of PBM. Only one study used both direct and transcranial approaches (Khuman *et al*., 2012[176]) and they were not directly compared. Dosing at 60 J/cm^2 60-80 min post-injury were concluded by the authors as the main factors in eliciting functional improvements in MWM testing, with this dose performing best in either direct or transcranial administration. Administered directly, 60/120/210 J/cm^2 but not 30/105 J/cm^2 resulted in MWM hidden platform latency improvements, and 60/120 J/cm^2 elicited probe trial improvements. Across all MWM outcomes, 60 J/cm^2 given at 60-80 min post-injury, whether delivered directly or transcranially were deemed to elicit similar modest improvements (though direct statistical comparison was not presented). The remaining outcomes were not significantly improved by any PBM regimen tested in this study. Whilst this review has principally considered the incident energy exposure to injured target tissue (i.e. delivery to neural/glial cells), there is growing interest in the systemic effects of PBM. Given the low penetrance of R/NIR light to the brain from external application, it has been hypothesised that transcranial PBM has contributory effects from photon absorption in superficial tissues (scalp with its rich vascularity, skull with calvarial bone marrow).[259,260] PBM directed to the tibia in a mouse model of Alzheimer's

disease has been shown to activate mescenchmyal stem cells (MSC)[261] with neuroprotective effect. Calvarial bone marrow niches have interfaces with CSF, which is a possible conduit for activated MSCs from skull in transcranial PBM.[262]

Further to this, PBM application to anatomically distant sites has been observed to result in therapeutic effects in neurological disorders. Termed the ”abscopal effect”, therapeutic action distant to irradiated tissue has been recognised in radiotherapy since 1953,[263,264] and more recently considered in PBM.[265] Research in Parkinson's disease has identified therapeutic benefit for improvement of clinical signs in a short series of patients receiving PBM to the abdomen and neck,[203] with similar benefits to those observed with transcranial delivery.[202] In animal models however, direct stimulation appears to carry greater benefit.[204,205] The mechanism for this is not known, but has been proposed as activation of remote immune and stem cells which become systemically active after PBM.[204] It is noteworthy here that the deep brain target in Parkinson's disease (substantia nigra) receives significantly attenuated doses in humans, even with transcranial application.

2.5.5 Establishing the translational effect in humans

This review has focused on the acute phase of injury. The applications of PBM in patients with TBI in clinical studies is however much more broad when considering chronic or rehabilitative contexts and has been well summarised elsewhere.[255,260] This systematic review identified one study reporting the application of PBM in acute TBI in human subjects. Whilst the study was not sufficiently powered to detect any functional benefit, this study provides some evidence of a physiological effect of transcranial PBM through radiological outcomes. Whether this will translate to clinically relevant effects should be the subject of further study, but Figuero Longo and colleagues[177] were able to demonstrate a favourable safety profile to support further study. Similarly to the presented pre-clinical literature, the included clinical study raises issues with regard to measurement and reporting of delivered dose. Data on fluence at a cortical level was not presented. Furthermore, the total number of doses received by enrolled patients varied and was not transparently reported nor considered in the data analysis. For this reason, the overall

quality of the study was deemed "fair", and consideration for dose, dose regimen and dose delivery should be a key consideration in the planning of further clinical trials of PBM in TBI.

2.5.6 Establishing a mechanism

Through presentation of molecular sub-studies from the included literature, this review has illustrated the broad range of potential therapeutic mechanisms of PBM in TBI. A full discussion of the complex and not fully elucidated mechanism of PBM is beyond the scope of this review, however there are key themes observed from the included articles. In summary, PBM therapy in acute TBI appears to correlate with: (1) increases in ATP levels;[244,245,249] (2) reduction in reactive oxygen species;[245] (3) increase in mitochondrial membrane potential;[245] (4) reduction in microglial activation/astrogliosis;[172,173,176] (5) reduction of pro-inflammatory mediators;[168] (6) reduction in apoptotic markers;[172–174,253] (7) decreased neuronal degeneration;[172,247] (8) increased cell proliferation and maturation;[174,247] and (9) increased cerebral blood flow.[254] Given the heterogeneity of PBM parameters and injury models, it cannot be concluded whether such mechanisms are specific to a particular PBM parameter/injury interaction or representative of a broad mechanism of effect which is common to PBM modalities in acute TBI. However, the presence of beneficial effects on multiple discrete TBI pathophysiological processes is encouraging for its prospective translational benefit.

This systematic review has identified multiple studies reporting reduction in neural degeneration in TBI after PBM, reducing hippocampal (cornu Ammonis (CA)1) synaptic degradation[172] and reducing degenerating neurons.[247] There is also significant evidence to support neurogenic and synaptogenic activity stimulated by PBM.[173,174,247] Included articles have identified increased subgranular cell proliferation;[173] increased hippocampal, SVZ and perilesional cell proliferation,[247];[174] and neuronal maturation and differentiation of neuronal progenitor cells.[174] Upregulation of BDNF post-PBM has been correlated with increased expression of Synapsin-1, with the authors concluding that early BDNF upregulation may mediate synaptogenesis in later (28 days post-injury) recovery phase.[248] In the wider literature, BDNF upregulation has been observed in PBM treated animal models of Alzheimer's disease, and has been pro-

posed as a neuroprotective mechanism for PBM.[266] Similarly, increased neurogenesis[267,268] and synaptogenesis[267] has been observed in occlusive and pro-thrombotic rat stroke models after PBM treatment. Upregulation of BDNF expression with PBM has also been demonstrated in an organotypic hippocampal slice model[269] and a methanol-induced toxicity occipital cortex damage model.[270]

Whilst the accumulated evidence presented here offers insights into potential downstream pathways mediating the therapeutic effects of PBM in acute TBI, understanding of an overall mechanism of action for R/NIR light on injured brain tissue remains incomplete. Integral to photobiological interaction, photons must be absorbed by a biological molecule to elicit an effect, i.e. a chromophore. cytochrome c oxidase (CCO) has been understood as a primary chromophore of PBM,,[271,272] with photon energy resulting in the dissociation of nitric oxide (NO),[273] increasing MMP and ATP production, and modulating ROS production.[270] Whilst there is a clear role of the mitochondria in mediating the biological effects of PBM, the specific role of CCO has not been fully confirmed. A novel mechanism disparate to CCO has recently emerged for 980 nm light: activating heat or light sensitive calcium ion channels.[274] It remains possible, or even likely, that there are further chromophores which contribute to the wide-ranging biological effects of PBM, with discrete and unidentified downstream mechanisms, with specific chromophores related to wavelength of PBM.

2.5.7 Risk of bias

The risk of bias across the included animal studies was found to be generally high. In most cases, reporting of factors as per SYRCLE guidelines were not adhered to. All studies described baseline characteristics and had clear primary outcomes; however, randomisation and blinding were overlooked by the majority of studies. To ensure replicable and robust data to inform the ongoing direction of PBM research in TBI, adherence to such guidelines is strongly encouraged for future studies.

2.5.8 Controls

Included studies in this review have used control procedures which include the equivalent restraint required to facilitate PBM, but without its application. However, it is arguable that this is an inadequate control: application of a broadband light source at equivalent irradiance would be a more robust approach. An ideal source would elicit similar transient temperature changes to a PBM source, in order to control also for this secondary effect of PBM therapy and would robustly identify that wavelength-specific doses of incident light are the beneficial factor. A typical broadband source would deliver a fraction of its energy in the form of wavelengths of therapeutic interest. Such wavelengths could also be filtered. If exploring such options as controls, spectral irradiance should be comprehensively measured and presented in the study reporting.

2.5.9 Photobiomodulation parameter reporting

The detail with which PBM parameters were employed and reported in each study and sub-study varied greatly. Average irradiance and exposure time were reported across studies, but reporting of results of cadaveric modelling with direct measurement of transmitted PBM was infrequent. No study presented data from computational modelling of dose delivery or distribution. This enhances difficulties in the between-study comparison of efficacy: variability lies not only in PBM parameters but also in the transmission of those parameters to the target tissue. This is a salient and common shortcoming of much of the PBM literature.[181] The accurate reporting of radiometry in future studies should be prioritised.

2.5.10 Limitations

There are a number of limitations for this study. Due to heterogeneity in the included studies' selection of outcome measure, the meta-analysis is not comprehensive in scope and is able to represent only a subsection of the literature. Furthermore, due to common outcome measure preference within laboratories, high availability of NSS data or lesion size data is inherently

biased toward a selective pool of publications. A narrative review on PBM in TBI and stroke[83] from the Hamblin laboratory presents an excellent summary of the available data, with outputs categorised by research group. Subgroup analyses were performed here to maximise the value of meta-analysis by providing some insight into the efficacy of varying PBM parameters. This however is not entirely robust given the inclusion of only a single study in some sub-groups, and conclusions should be guarded with that consideration. Similarly, the statistical component of the meta-analysis cannot account for the duplicate appearance of control groups as though they were independent, where a single control group is common across multiple sub-studies where the data is taken from a single paper. As described above, PBM parameter reporting varied in its quality, and in some instances the dose for PBM parameters was calculated based on available beam transmittance data, and may not be entirely representative of the "true" figure which was not directly measured in the reported data.

This review does not comprise the available evidence for applications of PBM in chronic TBI, though a review summarising this data is available in the literature.[81] The study of chronic TBI is predominantly in case reports[275–278] or short case series[279–282] from human applications, in contrast to the evidence in acute TBI which is predominantly in animal models. This is likely attributable to the availability of replicable acute TBI models in animals (in contrast to chronic TBI models), and the practical logistics of patient recruitment in chronic (versus acute) TBI contexts. An ongoing randomised controlled trial for chronic TBI patients is likely to provide more robust evidence on the efficacy.[282] In contrast, applications of PBM in patients with stroke have predominantly been in the acute setting (NEST studies[210,283,284]) and there is little quality evidence for applications in the chronic rehabilitative phase post-ischaemic stroke.[285] Whilst some comparisons between pathologies (TBI, stroke) and time-points (acute, chronic) can be considered, the mechanisms, pathophysiology, interventional goals and outcome measures are discrete and specific, supporting the focused nature of this systematic review and meta-analysis.

2.5.11 Future directions

This study, in accordance with previous work,[257] has identified parameter heterogeneity and incomplete reporting as factors which impede accurate conclusions to be taken from PBM literature reviews. Accurate and comprehensively reported radiometry should be prioritised in future work, in order for clearly established dose delivery to target tissue to be compared between studies.[181] Given the lack of a well-established therapeutic dose window in TBI, accurate representation of dose delivery for comparison with outcome measures is key to advancing this knowledge. Transcranial approaches to PBM have a clear benefit in animal models, as illustrated here, but PBM delivery via this route is inherently impeded by the thickness of scalp and skull when translating this approach to humans. Thorough clarification of the effective dose window will be invaluable, alongside computational simulation, in determining whether this approach is the optimal route for clinical practice, or whether more elaborate or novel approaches may improve delivery and functional outcomes.[239,286–290]

2.5.12 Conclusion

This review has provided clear evidence of the beneficial effects of PBM in acute TBI. Whilst specific parameters for optimum effect cannot be determined, the literature supports: wavelength selection in the regions of 665 or 810 nm; minimising time to first treatment; and limited total applications of daily PBM. Included studies comprising mechanistic considerations support the hypotheses that PBM reduced cellular apoptosis, reduced microglial activation and neuroinflammation, attenuated neuronal degeneration, promoted neurogenesis/synaptogenesis and modulated metabolism. Precise radiometry reporting in the literature for the purposes of comparability between studies is encouraged for future work. Whilst clinical data in acute TBI is limited to a single study, a considered approach toward study protocols should be taken in order to ensure that further clinical study is utilising optimal parameters and is conducted to a high standard.

Chapter 3

INVESTIGATION OF PHOTOBIOMODULATION AND RAMAN SPECTROSCOPY IN SPINAL CORD INJURY

This chapter investigates the efficacy of transcutaneous/implantable PBM delivery and the utility of RS feedback using an experimental model of SCI.

3.1 Introduction

This chapter investigates the application of the PBM device concept in SCI. PBM is the application of light for the purposes of therapeutic benefit.[82] PBM acts principally at a mitochondrial level, with photon absorption by the photoacceptor of the ETC, CCO.[149,270,271,291] This results in a modulation of mitochondrial membrane potential, reduced production of ROS and increased availability of ATP.[240,260,292] Via undefined mechanisms, this mitochondrial initiator process triggers multiple favourable downstream pathways: mitigating apoptosis, neuronal damage and neuroinflammation; and promoting neuronal regeneration.[182,188,238,259,260,271,293] Previous lit-

erature exploring therapeutic applications of PBM has established evidence for its efficacy in a variety of topical (dermatological or oral) applications, where administration of photons with metered dosing can be achieved with precision due to direct-to-tissue delivery.[184,186,188] Beyond this, there is growing interest in the application of PBM to pathologies of deeper anatomical structures, including the CNS,[238,293–295] particularly as a therapy for neurotrauma: TBI and SCI.[213,240] As such, there is considerable potential for PBM to address multiple pathophysiological events in the secondary injury cascade which follows SCI, shown in Figure 3.1.

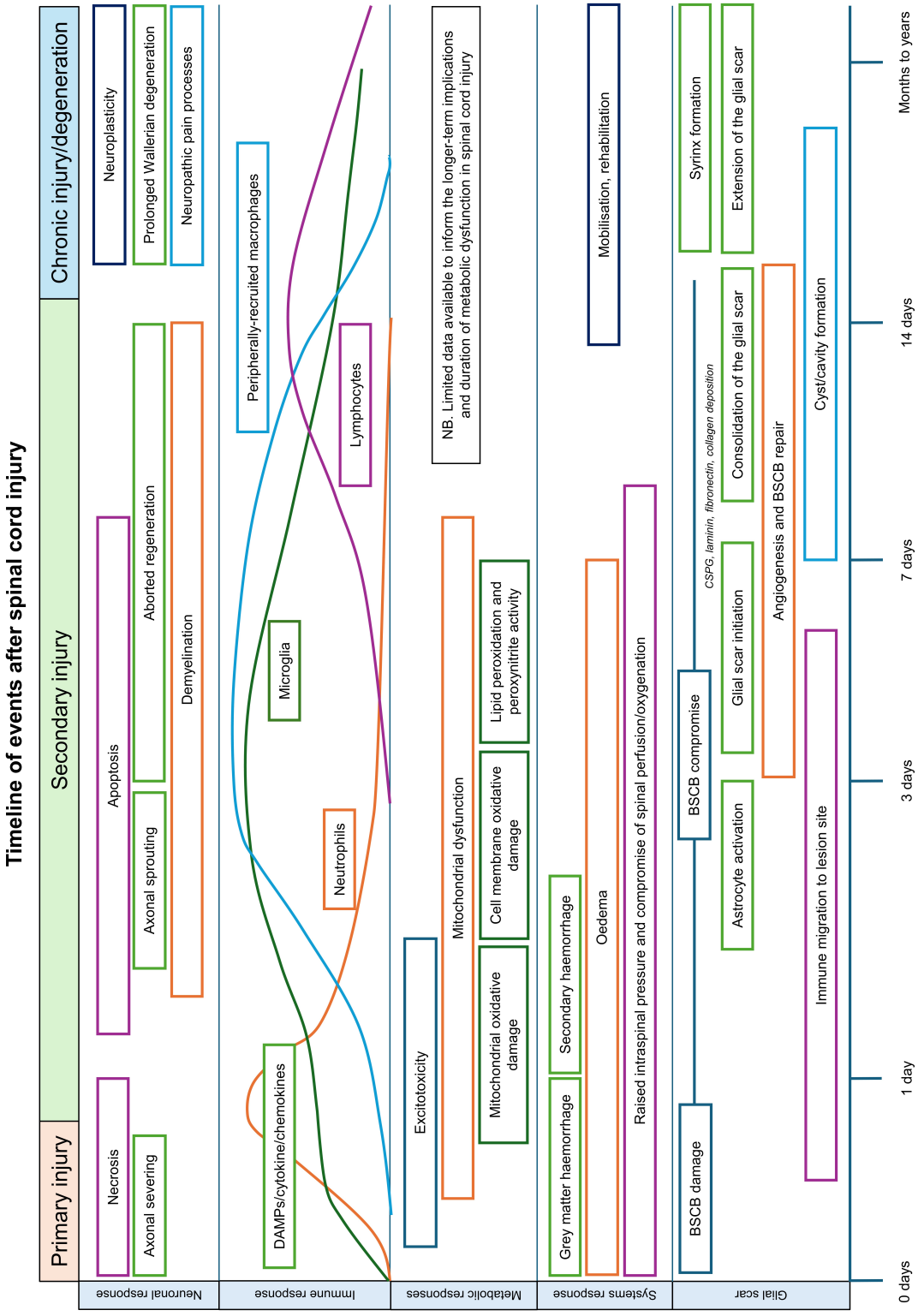


Figure 3.1: Schematic representation of a timeline of pathophysiology in traumatic SCI. BSCB = blood-spinal cord barrier; CSPG = chondroitin sulphate proteoglycans. Combined from multiple sources.[296–302]

The efficacy of PBM in improving functional and histological outcomes in rodent models of SCI has been demonstrated using transcutaneous application methods,[303–310] demonstrating favourable mechanisms of PBM. These include: attenuation of activation of pro-inflammatory phenotypes amongst macrophages/microglia/astrocytes;[43,308,309,311] reducing neuroinflammation through interleukin (IL4, IL6) regulation;[305,306] reducing CD68 expression;[307] STAT3 inhibition;[308,309] and mitochondrial regulation.[265] Whilst these results are encouraging of a positive biological effect, the translational potential of PBM is limited by the challenge of delivering effective and reliable doses transcutaneously to the injured CNS in humans, primarily due to the thickness of the overlying superficial tissue. PBM offers neuroprotection in rodent models of Parkinson's disease when delivered via an implant, as well as transcranially and remotely, although the optimum method of delivery remains unclear.[204,205,265,312,313] Direct delivery of PBM to the CNS has also been demonstrated as a feasible and safe method in a porcine SCI model,[314,315] adding further support to this approach. Direct delivery offers a more feasible translational prospect for effective dose delivery to target tissue in humans, though the relative efficacies of invasive and transcutaneous delivery methods are yet to be established.[312]

3.1.1 Dose *in vitro*

Toward the study of the invasive application of PBM *in vivo*, it is first paramount to establish the optimal dose parameters *in vitro*. Previous work in our laboratory has demonstrated that *in vitro* study of dorsal root ganglion neurons (DRGN) using a serum withdrawal model of cellular stress is a reliable means of optimisation of therapeutic dosing strategies for neuroprotective and neurorestorative therapies.[316] It is recognised that DRGN are not wholly CNS neurons (as they are pseudounipolar neurons with projections both into the CNS and into the PNS). However, extensive previous validation has been performed using this *in vitro* model for dosing studies, and successful demonstration of neuroprotection and neurite outgrowth using DRGN cell culture with serum withdrawal has been shown previously to be a strong indicator of success in an *in vivo* model of SCI.[316–318]

Table 3.1: Dosing regimes and outcomes of previously published journal articles reporting the application of PBM to DRGN. CW = continuous wave.

Article	Description	Wavelength	Mode	Average irradiance	Exposure time	Energy	Outcome
Burland *et al.*, 2014[319]	Primary cell culture DRGN from adult mice with or without sciatic nerve injury	645 nm	CW	11.3 mW/cm^2	240 s	2.72 J/cm^2	1.6 fold increase in neurite growth acceleration with PBM (both axotomised and non-injured)
Zheng *et al.*, 2015[320]	Primary cell culture DRGN from adult Sprague-Dawley rats	658 nm	CW	11.1 mW/cm^2	180/540/1440 s	2/6/16 J/cm^2	6 J/cm^2 PBM increases NO production, peaking 1 h after exposure, and 2/6 J/cm^2 increased NOS concentration
Wang *et al.*, 2014[321]	Primary cell culture DRGN from adult Sprague-Dawley rats	657 nm	CW	18 mW/cm^2	1166 s	21 J/cm^2	6 J/cm^2 Reduced extracellular ATP content after PBM due to upregulation of ecto-ATPases
Yan *et al.*, 2017[322]	Primary cell culture DRGN from neonatal Sprague-Dawley rats	632.8 nm	CW	12.7 mW/cm^2	42-300 s	0.5-3.8 J/cm^2	PBM increased BDNF mRNA levels aqnd neurite outgrowth, optimally at 1.9 J/cm^2, likely mediated by Ca^{2+}-triggered ERK/CREB pathway
Zheng *et al.*, 2021[310]	Primary cell culture DRGN from juvenile and adult mice in an oxidative stress model	808 nm	CW	2 mW/cm^2	440 s	0.88 J/cm^2	6 J/cm^2 PBM reduced ROS concentrations, increased neuronal survival and axonal regeneration

A broad variety of PBM parameters have been applied in neuronal cells *in vitro*, across multiple cell types.[323] Cellular responses to PBM vary considerably dependent on the cell type,[321] therefore optimisation in spinal neuronal culture models is preferable. A small body of literature has described the application of PBM in primary cell culture of DRGN, which is summarised in Table 3.1. The range of described effective average irradiance values is between 2-18 mW/cm^2, with exposure times from 42-1440 s resulting in delivery between 0.5-21 J/cm^2. Lower energy parameters within this range were more associated with survival and neurite outgrowth,[310,319,322] whilst higher values resulted in reduction in extracellular ATP concentrations. This is in keeping with observations on the general principles of the biphasic responses to PBM: lower levels of exposure are stimulating (for applications such as protection and repair); whilst higher levels of exposure are inhibitory (for applications such as pain management).[80] Broadly, this favourable range aligns with the effective parameters for protection against apoptosis described in Appendix B, and support the use of this range as an appropriate array of parameters to utilise in the first instance.

3.1.2 Dose *in vivo*

The biomechanics of SCI in humans varies greatly owing to a complex array of variables, often in association with the type of force exerted by the varying deformation of the surrounding spinal column during (or persisting/occurring after) the injurious event. Various experimental injury methodologies have sought to replicate this *in vivo*.[38,324] These are summarised below, with examples illustrated in Figure 3.2.

- Compression (affecting modifiable anatomical regions as shown in Figure 3.2): this is typically performed using either aneurysm clips,[325] calibrated forceps[316] or an inflatable balloon catheter;[326]
- Contusion: controlled impact to the spine or spinal cord by mechanical impact by a weight or driven by pressure;[38,324]

- Transection: complete disconnection, usually via sharp dissection, of rostro-caudal segments, either partial (often hemisection[327]) or complete cord transection;[328]
- Distraction: application of tension force along the axis of the spinal cord;[38,324]
- Dislocation: displacement of one vertebra against an adjacent vertebra, resulting in shear force along the axis of the spinal cord.[38,324]

Whilst a variety of models is valuable for the study of differing responses to SCI subtypes, this can impede the relevance of findings made through use of any one discrete model. For example, whilst cord hemisection (Fig. 3.2) closely mirrors the Brown-Séquard syndrome described in humans 1.4, this phenomenon after traumatic injury is rare and usually only observed occasionally after stab injury. A focal compression model (dorsal column crush (DCC)) has been selected for use here, as it has the advantage of representing common elements of severe injury found clinically (disruption of blood-spinal cord barrier, axonal cleavage, astrogliosis and scarring), and also permitting clinically-relevant functional outcome assessments including locomotor and sensory recovery.[114,316,329–331]

A wide range of doses have described as demonstrating beneficial effects in promoting recovery after SCI in the previous literature.[303–310] Extrapolated from heterogenous dosimetry reporting, prior studies describing the efficacy of PBM in SCI have utilised average irradiances at between 0.2-1070 mW/cm^2, with a range of fluences per treatment of 0.03-95.34 J/cm^2 using either wavelengths from 660, 810, or 905 nm regions.[303–310] Accordingly, the duration of treatment has also varied, with dose durations varying from 45-3600 s. As such, determination of effective dosing for *in vivo* studies here will be determined based on results of *in vitro* dose optimisation. A full summary of previously published evidence from studies applying PBM in an SCI model *in vivo* is given in Table 3.2.

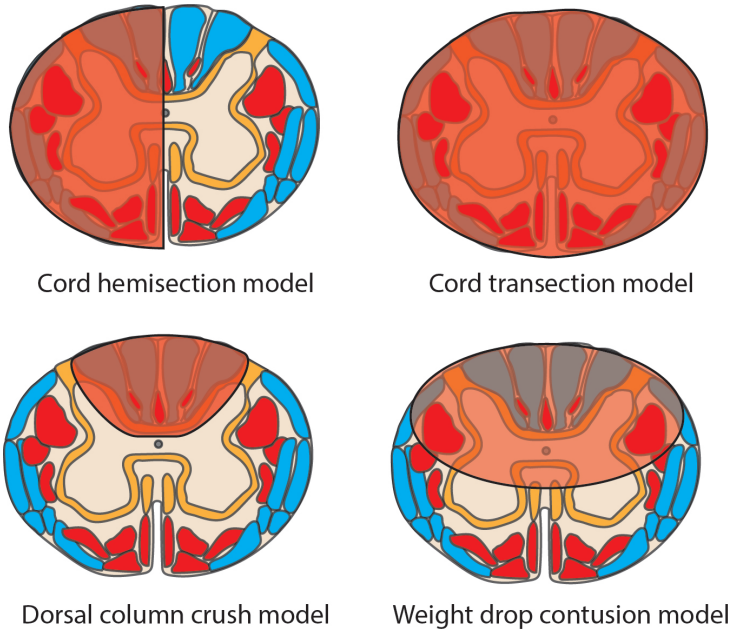


Figure 3.2: Schematic diagram of four pre-clinical SCI models used in the literature to replicate the conditions of traumatic injury. Damaged regions are denoted in translucent red. Motor tracts = opaque red; sensory tracts = blue.

Table 3.2: Caption on next page

	Species	SCI model	λ (nm)	Delivery	Mode	Source	Average irrad. (mW/cm^2)	Exposure time (min)	Energy per dose (J/cm^2)	First dose post-injury (min)	Total doses	Outcome
Byrnes et al., 2005[332]	Rat	Hemisection	810	Transcutaneous	CW	Laser	530	50	1590	15	14	Improved axonal regeneration and function
Ando et al., 2013[295]	Rat	Contusion	808	Direct intraoperative	CW	Laser	8	20	9.6	Immediate	5	Improved function and reduced lesion size
Giacci et al., 2014[250]	Rat	Contusion	670/830	Transcutaneous	CW	LED	*	30	28.4/22.6	*	*	No significant difference
Veronez et al., 2016[306]	Rat	Impactor	808	Transcutaneous	CW	Laser	1070	2.3/3.5/4.6	500/750/1000	15	7	Improved function, reduced lesion size, reduced CD-68
Song et al., 2017[304]	Rat	Bilateral compression	810	Transcutaneous	CW	Laser	530	50	1590	15	14	Improved function, neuronal survival, reduced inflammation
Mojarad et al., 2018[305]	Rat	Clip compression	660	Transcutaneous	CW	Laser	819	0.75	0.5	Immediate	7/14	Reduced hyperalgesia and IL-6
Svobodova et al., 2018[333]	Rat	Balloon compression	808/905	Transcutaneous	CW/PW (10Hz)	Laser	*	9	*	15	10	Improved function, reduced hyperalgesia, increased M2 macrophages
Wang et al., 2021[334]	Rat	Bilateral compression	808	Transcutaneous	CW	Laser	530	50	1590	15	14	Improved function, neuronal survival, reduced cavity size
Wang et al., 2021b[335]	Rat	Bilateral compression	808	Transcutaneous	CW	Laser	*	60	*	Immediate	14	Improved function, neuronal survival, reduced inflammation
Ma et al., 2022[308]	Mouse	Bilateral compression	808	Implant	CW	Laser	50	50	125	*	*	Improved function with inhibition of neurotoxic macrophages
Zhu et al., 2022[336]	Rat	Bilateral compression	808	Implant	CW	Laser	500	60	1800	*	*	Improved function, neuronal survival, increased ATP production
Ju et al., 2023[337]	Mouse	Vertical compression	808	Implant	CW	Laser	50	50	150	*	*	Improved neuronal survival and functional recovery
Zhang et al., 2023[337]	Rat	Bilateral compression	810	Implant	CW	Laser	*	60	*	Immediate	14	Reduced neuropathic pain, reduced astrocyte and microglial activation, decreased expression of CXCL10

Table 3.2: Summary table of pre-clinical studies with application of PBM after SCI. CW = continuous wave; LFP = lateral fluid percussion; PW = pulsed wave; λ = wavelength * denotes where parameters were not available. It is notable that given average irradiance/energy values are those quoted by the authors at the level of delivery (i.e. either at skin level for transcutaneous application, or cord surface level for implantable application).

3.1.3 Delivery

The concept of indwelling optical devices have been described infrequently in previous works in the brain and spinal cord (discussed in greater depth in Chapter 6).[43,312,314,338] Specifically, Liang and colleagues[43,314,338] have described a device using an axially diffusing optical fibre, sited in parallel to the spinal cord.

Based upon these works, three potential solutions may be considered:

1. A fibre optic probe, with or without a diffuser tip, orientated toward or fixed adjacent to, the injury site (at a perpendicular/obtuse angle), connected to an external light source;

2. A fibre optic probe, altered for diffusion along its length, orientated in parallel with the injury site, connected to an external light source;

3. An LED light source, orientated toward or fixed adjacent to, the injury site (at a perpendicular/obtuse angle), connected to an external power source[i].

3.1.4 Aims

A key factor in demonstrating the potential efficacy of an implantable PBM device in neurotrauma is to demonstrate that it is non-inferior to the established pre-clinical benefits derived by transcutaneous delivery methods. As such, the overarching aim of this chapter is to demonstrate that invasive delivery of PBM at optimum doses after SCI promotes neurorestoration equivalent to that achieved by transcutaneous administration. To this end, this chapter aims to:

1. Optimise PBM dosing parameters in an *in vitro* model of injury;

[i]Whilst internal power sources are possible, via a solid state battery and LED driver, the technological miniaturisation required to achieve this is inappropriate for a proof-of-concept phase.

2. Develop methods for delivering these parameters invasively and non-invasively in an *in vivo* model of SCI;

3. Validate these methods using cadaveric modelling;

4. Assess the validity of utilising RS for *ex vivo* injury site analysis after *in vivo* SCI;

5. Compare the efficacy of invasive and non-invasive PBM in an *in vivo* model of SCI;

6. Assess the efficacy of PBM for promoting functional and histological recovery after SCI;

7. Determine the utility of RS in assessing the spinal cord in order to monitor injury severity and treatment responses.

3.2 Materials and methods

All animal procedures were licensed by the UK Home Office and approved by the University of Birmingham's Animal and Ethical Review Board. Surgeries were carried out in strict accordance with the guidance of the UK Animals Scientific Procedures Act, 1986. Power calculations using the National Centre for the Replacement Refinement and Reduction of Animals in Research (NC3Rs) Experimental Design Assistant was used to determine sample sizes and all animals were randomly assigned to treatment groups, masked to the experimenters until analysis was complete.

3.2.1 *In vitro* methods

Primary cell culture of dorsal root ganglion neurons

Primary cell cultures of DRGN were performed as detailed in previous publications.[316–318] Adult (170-220 g) Sprague-Dawley rats (Charles River) were sacrificed by exposure to rising concentrations of CO_2 with confirmation of permanent cessation of circulation. Pairs of dorsal root ganglia (DRG) (T4-L7) were immediately removed (within 40 min of death) and placed into Neurobasal-A medium (1X) (Invitrogen) at 4-8 °C (Fig. 3.3). DRG were transferred through

two changes of fresh Neurobasal-A at 4-8 °C to remove any blood or debris, then incubated in a humidified chamber at 37 °C and 5% CO_2 for 2 h in Neurobasal-A containing 0.125% collagenase (Sigma).

Following incubation, DRG in collagenase media were transferred to 10 ml Neurobasal-A to dilute the collagenase. Excess solution was removed, and the DRG were resupended in 2 ml supplement Neurobasal-A (with B27 supplement, L-glutamine and 1% penicillin/streptomycin (P/S) solution. The resulting solution was triturated with successive gauges of pipette tips to homogenise the media. The resulting homogenate was centrifuged through 15% BSA at 120 g for 10 min at ambient temperature. The supernatant was discarded and the pellet was resuspended in a media containing soybean trypsin inhibitor (Gibco) and DNase I (Sigma). DRGN were counted using a haemocytometer and Trypan Blue solution.

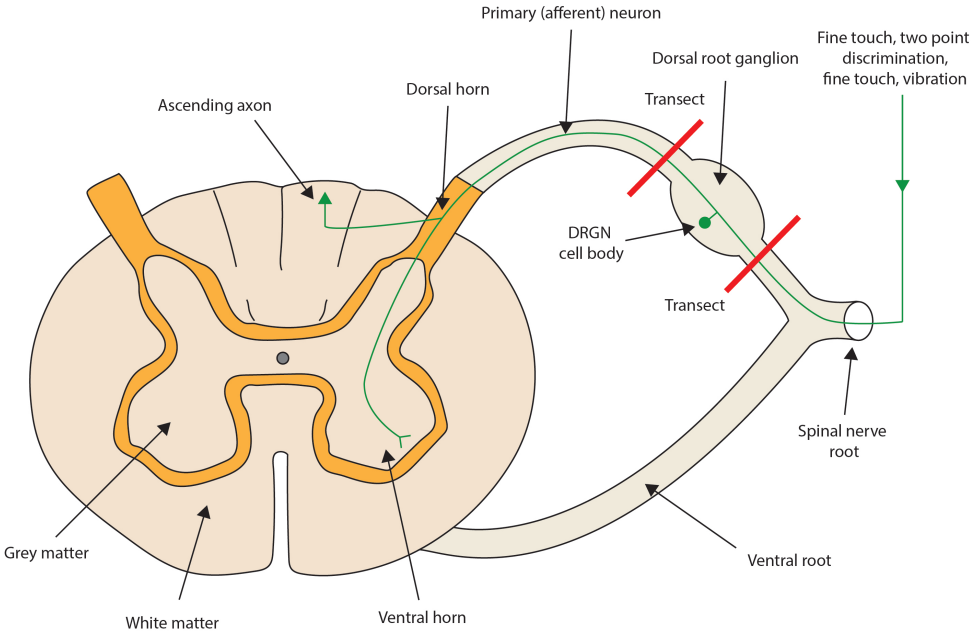


Figure 3.3: Schematic diagram of a cross section of spinal cord, with dorsal horn forming a dorsal root and dorsal root ganglion, containing primary (afferent) cell bodies of the DRGN. Red lines demonstrate points for microscissor transection to permit removal of the DRG. Unilateral DRG and spinal root shown here, though these are bilateral and at each spinal level in the thoracolumbar spine.

Sterile 8-well glass chamber slides (BD Biosciences, Oxford, UK) were prepared with 100 μg/ml poly-D-lysine (Sigma) for 1 h, followed by 20 μg/ml laminin (Sigma) for a further 1 h.

Dissociated DRGN were plated into chamber slides at 500 cells per well. DRGN were plated with 500 μl per well of Dulbecco's modified eagle medium (DMEM) (Invitrogen) containing 10% fetal bovine serum (FBS) and 1% P/S (both Invitrogen). Following 20-24 h incubation, the medium was replaced with DMEM and 1% P/S: with or without 10% FBS serum. To control for extraneous light exposure, plates were lightly covered with aluminium foil for incubation. To assess the effect of suppression of non-neuronal cell proliferation, cultures were performed in the presence or absence of 5-fluoro-2-deoxyuridine (5-FDU) (Sigma), at a final concentration of 30 μm in culture media where included.[316,339]

Photobiomodulation treatment for primary cell culture

Photobiomodulation was delivered as single daily doses, every 20-24 h, commencing within 15 min of serum withdrawal. 660 nm light was delivered with a calibrated variable power 660 nm LED array light source (BioTHOR device, Thor Photobiomedicine) (Fig. 3.4). 8 well plates were placed above the light source, mounted on a bespoke diffuser, to directly irradiate the base of the plate. The device was calibrated for a spectrum of voltage and current outputs, measuring the wavelength and absolute irradiance values delivered to the cell culture plane.

Immunocytochemistry

Cultures were fixed for 10 min using 4% formaldehyde, followed by 3x PBS washes. Cells were blocked for 10 min with 1M PBS containing 3% BSA and 0.1% Triton-X-100, followed by incubation with primary antibody for 1 h at RT, diluted in 1M PBS with 3% BSA. Plates were washed and incubated with secondary antibody for 1 h before mounting in Vectamount with DAPI (2B Scientific).

Microscopy and image analysis: immunocytochemistry

Immunostained slides were viewed under a fluorescent microscope with images captured using a mounted Axiocam HRc camera (all Carl Zeiss, Welwyn-Garden City, UK). Image capture and analysis were performed by an investigator blinded to the treatment conditions. To determine

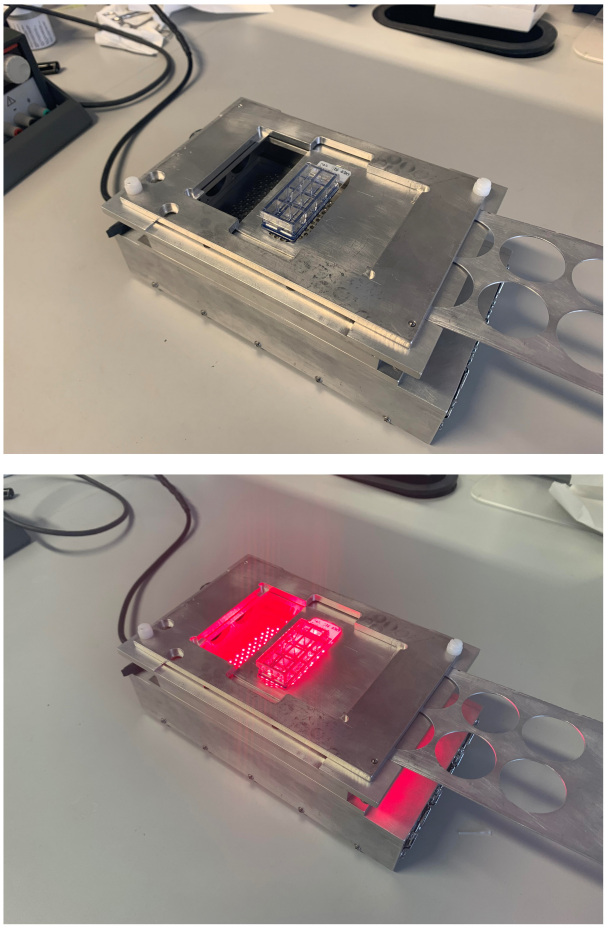


Figure 3.4: Top: BioTHOR device with diffuser and 8 well plate in treatment position, with device in "off" mode. Bottom: as above, in "on" mode.

cell viability, wells were divided into nine equal sections and one image taken per section. Viable DRGN were identified with βIII-tubulin and DAPI co-staining. To measure neurite outgrowth, after immunostaining for βIII-tubulin, images were taken of 30 randomly selected DRGN per well. The length of the longest neurite and number of branch points of the longest neurite were measured using NeuronJ (ImageJ[340]), and the number of DRGN with neurites were recorded. For each condition, at least 180 DRGN were analysed for neurite outgrowth parameters.

3.2.2 *Ex vivo* methods

Cadaveric modelling

To model the *in vivo* transmission of 660 nm light in both invasive and non-invasive administration models, cadaveric modelling was performed. Adult Sprague-Dawley rats (170-220 g, n = 6, male:female 1:1) were sacrificed by exposure to increasing concentrations of CO_2. After sacrifice, the procedure for DCC was performed as described below. For all cadavers, an anterior approach was then performed with midline thoracotomy, laparotomy and total evisceration from thoracic and abdominal compartments. An anterior approach corpectomy (T6-T10) was performed, and spinal cord divided at T5/6 and T10/11, with the intervening spinal cord removed. This approach exposed the laminectomy site from the anterior aspect. To record spectral irradiance, the fibre tip was positioned within the corpectomy site at the mid-point of the spinal canal (in the anterior-posterior plane). For beam profiling, the camera was focused on this plane.

Photobiomodulation administration *ex/in vivo*

For transcutaneous delivery, two devices were trialled: LX2 75 mW 660 nm Laser Therapy System with manufacturer supplied probe (Thor Labs); and an MDL-III 800 mW calibrated source. In both cases, the device was placed in direct contact with skin overlying the injury site and orientated toward the laminectomy site. As described below, for *in vivo* experiments MDL-III 800 mW was used.

For invasive delivery of 660 nm light , a calibrated 660 nm coherent laser source (MDL-III-660-FC-800 mW, CNI Co., Ltd., China) was used. The source was coupled to a rotary joint patch cable (FT200EMT) via an SMA-SMA mating sleeve (ADASMAB3), coupled to the implant (both Thor Labs, USA). Implants were fabricated using three components: 200 μm 0.39 NA 1 mm diffusion tip catheter (CFDSB10); implant guide (OGL-5); and phosphor bronze split mating sleeve (ADAL4-5) (all Thor Labs, USA). Individual components were cleaned using 70% ethanol and allowed to air dry in a sterile cabinet. Once dry, components were fixed

together using a commercially available cyanoacrylate, and allowed to cure at room temperature under ambient lighting for 24 h. After curing, implants were sterilised using ultraviolet light in a UVP CL-3000 (Analytik-Jena) cabinet, for 3x 10 min with 120 ° rotation between each cycle.

3.2.3 Physical analysis methods

Beam characterisation

Beam characterisation was performed with an SP620 camera and BeamGage Standard software (6.17), (both Ophir Photonics, Germany). Neutral density filters were used where required to optimise characterisation within the tolerances of the SP620 to avoid sensor saturation (ND1/2, Ophir Photonics, Germany). Linear calibration was performed, and ambient light calibration was performed using the Ultracal function of the integrated BeamGage software. $D4\sigma$ values were derived from beam diameters using the integrated Autoaperture function. For direct beam profiling the SP620 camera focused onto a target screen (LMR2/M, Thor Labs, USA) at a specified distance from the emitting fibre.

Power calibration values were derived through two methods. For spectral irradiance, spectrometry was acquired with a USB4000 spectrometer coupled to a 200 μm fibre with a CC-3 cosine corrector for an inlet aperture of 3900 μm (all OceanOptics, Germany). The spectrometer was calibrated using a standard halogen light source (DH-2000, OceanOptics, Germany). Spectral irradiance was calculated via AUC integration calculation (Excel, Microsoft, USA). Where aperture or sensitivity range of spectrometer system were not compatible with measurement, power values were acquired with PD300R-3W power meter (10 mm aperture, used with manufacturer supplied removable filter) and StarLab 3.0 software (all Ophir Photonics, Germany). An example of the set up used is shown in Figure 3.5.

Thermal imaging

For thermal imaging of the temperature changes associated with light administration, an AX5 (Teledyne FLIR LLC, Oregon, USA) camera was focused onto the tissue in contact with the

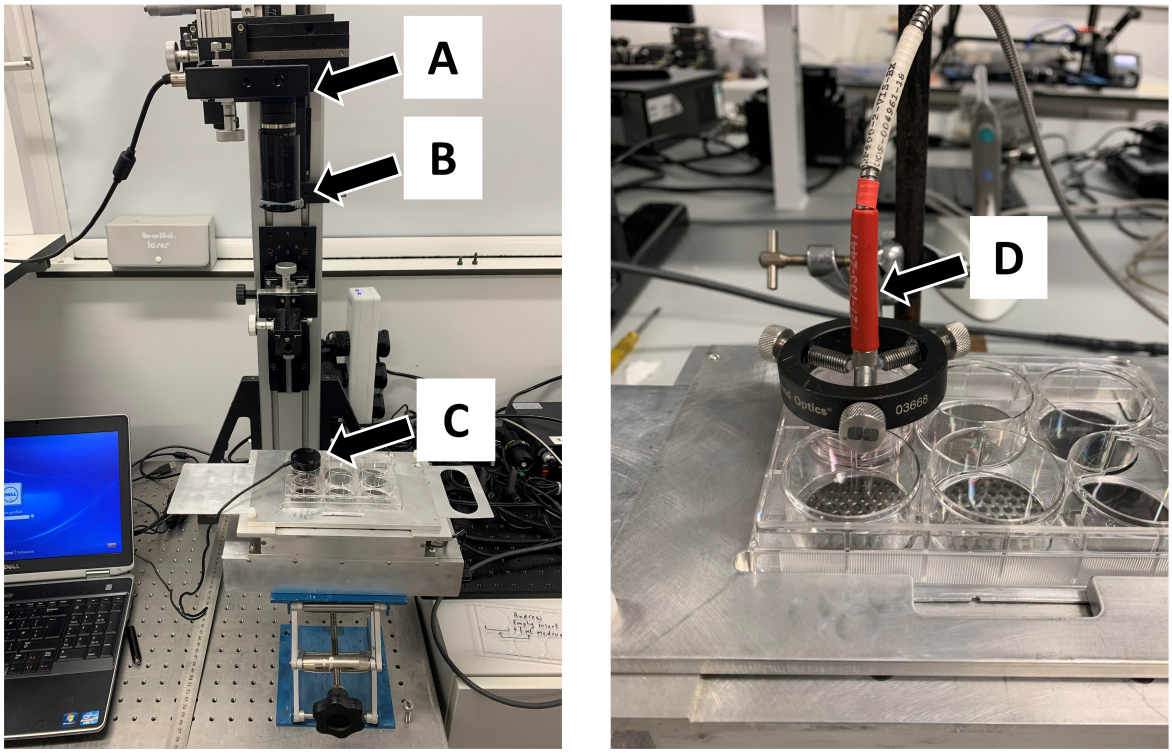


Figure 3.5: Left: Optomechanics equipment with positioned six well plate on BioTHOR device. SP620 beam profilometry camera (A) and optical filter unit (B), with PD300R-3W power meter fitted into well (C). Right: USB4000 spectrometer (D) coupled to a 200 μm fibre with a CC-3 cosine corrector positioned at base of six well plate on BioTHOR device.

highest irradiance from a given source. Image capture and thermal profiling was performed using FLIR ResearchIR (Teledyne FLIR). Animal tissue was assigned an emissivity of 0.95, probes were assigned an emissivity of 0.90.

3.2.4 *In vivo* spinal cord injury

Dorsal column injury model was performed as described elsewhere.[114,316,329–331] Adult Sprague-Dawley rats (190-250 g, n = 50, male:female 1:1, Charles River, UK) were anaesthetised using inhalational 5% isofluorane with 1.8 l/min O_2 after administration of intraperitoneal buprenorphine, with anaesthesia maintained using 2.5% isofluorane. A posterior approach to the spinal column, partial laminectomy and dorsal column crush (DCC) were performed at thoracic level 8 (T8). The dorsal skin was shaved and a 2.5 cm dorsal skin incision was made, with dorsal

fascia incised to expose the muscle. T8 was identified anatomically, and the muscle was divided from the spinous process of T8 bilaterally. A partial laminectomy was performed using bone rongeurs to expose the spinal cord (Fig. 3.6). The midline was identified, and a 1 mm depth and width DCC was performed, centred on the midline using modified watchmaker's forceps calibrated to a 1 mm width. The surgical wound was closed with 4-0 vicryl (Ethicon, New Jersey, USA) in layers (dorsal muscle, skin) in the non-invasive group. For invasively delivered PBM, the surgical wound was closed with inclusion of an implant. The tip of the catheter was positioned directly overlying the injury site from posterior (Fig. 3.8). Implants were secured using heat-sterilised surgical glue around the laminectomy site without contact with the spinal cord. The implant was further secured to the dorsal muscle and skin using 4-0 vicryl. For "sham" procedures, all steps were completed with the exception of the DCC. Post-operative analgesia was given (intraperitoneal buprenorphine) at 4 h and 18 h post-procedure. For all procedures using implants, visual confirmation was made during dissection that the implant remained intact and correctly positioned.[ii]

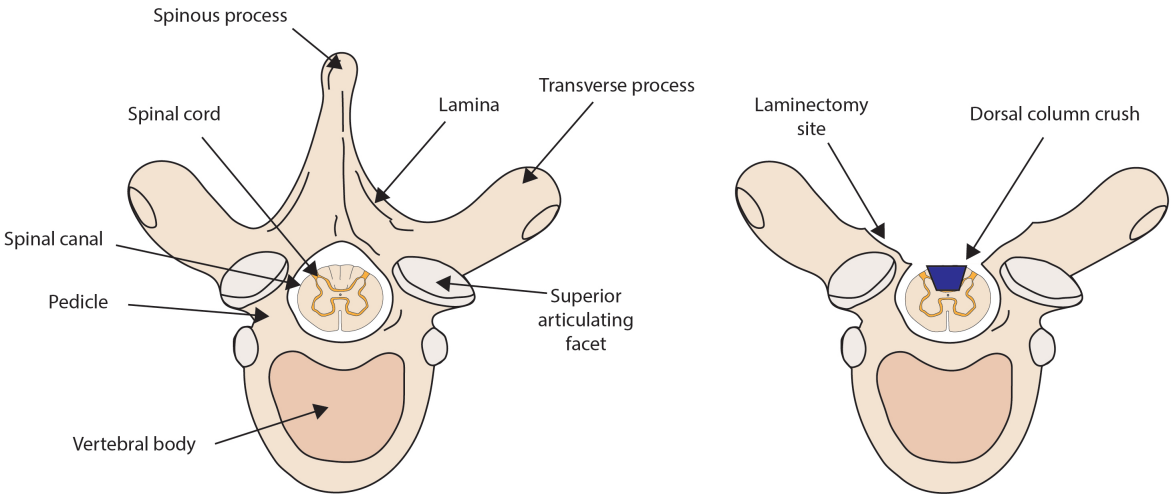


Figure 3.6: Schematic diagram of a thoracic vertebra in axial section, intact (left) and after laminectomy and dorsal column crush model (right).

[ii] *In vivo* DCC modelling was performed by Zubair Ahmed.

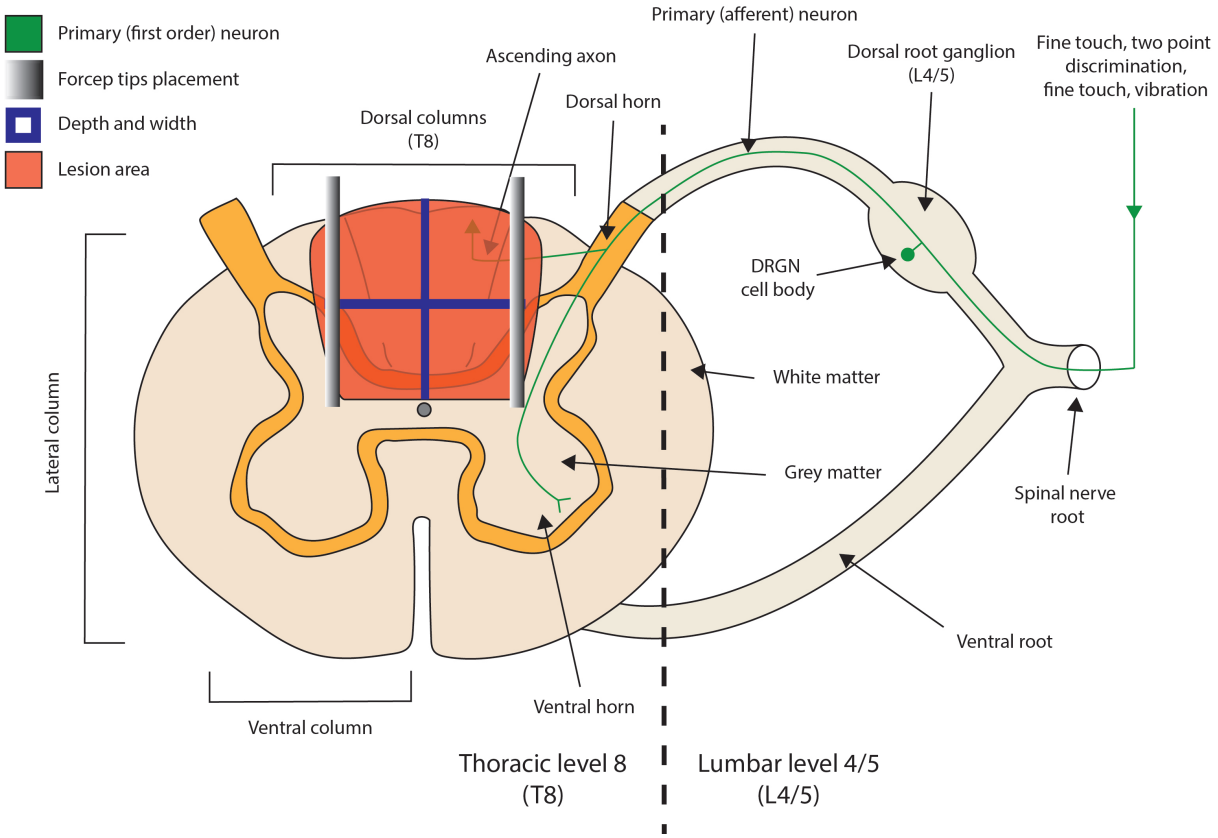


Figure 3.7: Schematic diagram of a dorsal column crush model used replicate the conditions of traumatic injury. Grey lines identify the site of forceps tip insertion, to a depth and width of 1 mm (in blue). The resulting damaged region is denoted in translucent red. The damaged zone (at T8, left side of image) includes the rostral axonal projections of DRGN at L4/L5 (right side of image), which ascend in the dorsal column.

3.2.5 *In vivo* administration of photobiomodulation therapy

For invasive delivery of 660 nm light, implants were fabricated using three components: 200 μm 0.39 NA 10 mm diffusion tip catheter (CFDSB10); implant guide (OGL-5); and phosphor bronze split mating sleeve (ADAL4-5) (all Thor Labs, New Jersey, USA). Individual components were cleaned using 70% ethanol and allowed to air dry in a sterile cabinet. Once dry, components were fixed together using a commercially available cyanoacrylate (Loctite), and allowed to cure at room temperature under ambient lighting for 24 h. After curing, implants were sterilised using ultraviolet light in a sterilisation cabinet, for 3x 10 min with 120 ° rotation between each cycle. For treatments calibrated 660 nm coherent laser source (MDL-III-660-FC-800 mW, CNI Co., Ltd., China) was used. The source was coupled to a rotary joint patch cable (FT200EMT) via an

SMA-SMA mating sleeve (ADASMAB3), coupled to the implant (both Thor Labs). The first treatment was given 15 min post-injury whilst the animal remained anaesthetised. Subsequent doses were given every 20-24 h, for either 3 days or 7 days, and connection to the external source was achieved by mild manual restraint. Dose was calibrated to deliver 24.42 mW/cm^2 at the level of the spinal cord, as developed and validated in this chapter.

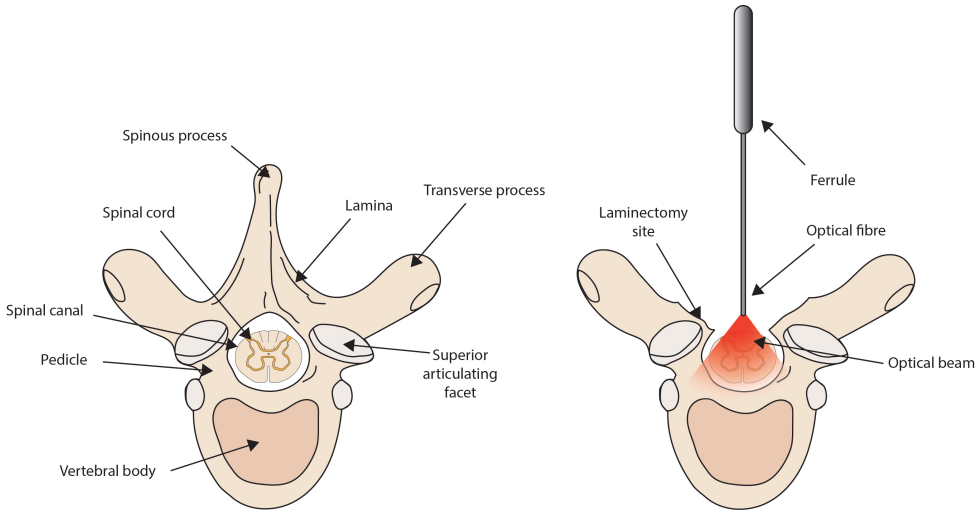


Figure 3.8: Schematic diagram of a thoracic vertebra in axial section, intact (left) and after laminectomy and implantable PBM device (right).

For transcutaneous delivery an MDL-III 800 mW calibrated source (as above) coupled to a FG550UEC Custom Fibre Bundle (Thor Labs). The diffuser tip of the probe was placed in direct contact with skin overlying the injury site (immediately lateral to the skin incision, and in line with T8 in the rostro-caudal plane) and orientated toward the laminectomy site. As above, the first treatment was given 15 min post-injury whilst the animal remained anaesthetised. Subsequent doses were given every 20-24 h, for either 3 days or 7 days, with probe positioning achieved by mild manual restraint.

3.2.6 Functional assessments

All functional assessments were recorded in duplicate by two blinded investigators. In the event of discrepancy, a mean of the two scores was used. Horizontal ladder crossing was performed as described previously.[316,329] Prior to surgery, rats were habituated and trained to cross the

horizontal ladder. The ladder is composed of two clear Perspex sheets, with 30 randomly distributed "rungs" (3 mm diameter plastic rods) inserted to create a horizontal ladder with irregularly spaced steps. On each trial, the ladder rungs were rearranged to prevent a learning effect. Three attempts were given to cross the ladder, with no time limit imposed. Each step with a hind limb was recorded as a "step" (successful landing and push off of each rung) or a "slip" (a missed step, unstable landing or failed push off). For analysis, a step:slip ratio was used as a mean of three repetitions per week.

Tape sensing and removal test was also performed as described elsewhere.[316,329] A 1 cm x 1 cm square of laboratory adhesive tape was adhered to the palmar surface of the left hindpaw, and the animal was returned to a cage with a plastic floor. Animals were observed for 90 s, with "sensing" recorded after localisation to the paw with intent to remove the tape, and "removal" recorded after successful removal of the entire piece of tape. Failure to sense or remove the tape after a full 90 s was recorded as a failure, and the piece of tape was removed by an investigator. Trials were performed on one occasion per animal, weekly for 6 weeks, after habituation prior to the index injury.

3.2.7 Immunohistochemistry

At 3 days or 6 weeks post-injury, animals were sacrificed by exposure to increasing concentrations of CO2 with confirmation of permanent cessation of the circulation. Immediately after death, animals were perfused with 4% paraformaldehyde by exposure of the heart and cannulation of the left ventricle. After fixation, tissues for immunohistochemistry were dissected: a 1.5 cm segment of spinal cord centred on T8; 0.5 cm lengths of spinal cord rostral (T7) and caudal (T9) to the injury site segment;[114,331] and L4/5 pairs of dorsal root ganglia (DRG). Tissues were post-fixed in 4% paraformaldehyde for 2 h, and washed in 1x PBS three times. Cryoprotection was achieved using increasing concentrations of sucrose solution (10, 20, 30%) before embedding in optimal cutting temperature [compound] (OCT) (Avantor, Pennsylvania, United States) and storage at -80 °C until use.

Sagittal sections of T8 lesion sites were taken in 15 μm slices using a cryostat (OTF,

Bright Instruments, UK). The entire tissue sample was cut and numbered, to allow the central section (at the lesion site epicentre) to be selected for analysis. Tissue sections were adhered to charged slides (SuperFrost +, Fisher Scientific, USA) and stored at -28 °C until use. After defrosting at room temperature, slides were washed in 1M PBS and permeabilised in a solution containing 0.1% Triton-X-100. After further washing in 1M PBS, tissue sections were blocked in a solution containing 0.5% BSA and 0.1% Triton-X-100. Sections were then incubated with primary antibody (anti-growth associated protein 43 (GAP43) raised in mouse, 1:400, Sigma; anti-laminin raised in rabbit, 1:400, Sigma) diluted in a solution containing 0.5% BSA and 0.01% Tween-20. Incubation was performed overnight at 4 °C. After incubation, slides were washed in PBS before incubation with secondary antibody (anti-mouse labelled with Alexa Fluor 488, 1:400, Sigma; anti-rabbit labelled with Alexa Fluor 594, 1:400, Sigma) for 1 h at room temperature. Slides were washed before mounting coverslips with Vectamount with DAPI (2B Scientific, UK). Antibody clones used are summarised in Table C.1.

3.2.8 Microscopy and image analysis

Immunostained slides were viewed under a fluorescent microscope with images captured using a mounted Axiocam HRc camera (all Carl Zeiss, Welwyn-Garden City, UK). Image capture and analysis were performed by an investigator blinded to the treatment conditions.[341] After image capture (taken at 20x magnification, approximately 50-200 images per tissue section), composite images were rendered using Photoshop (Adobe, USA) via the Photomerge function. Image processing and axonal counts were performed using ImageJ (National Institutes of Health, Bethesda, Maryland, USA).[340]

3.2.9 Quantification of regenerating axons

For axon quantification, in previous experience from our laboratory, cholera B toxin tracer methods are not effective in identification of regenerating axons in rat models.[330] As such, GAP43 immunoreactivity was used in sagittal midline T8 injury site sections as previously described.[114,316,329–331] Using the sagittal slices from the centre of the injury site at the midline,

the entire 15 mm section was imaged at 20x magnification, with a composite image rendered using Photoshop. Using ImageJ,[340] the rostro-caudal centre of the lesion was identified based on laminin co-staining, and markers were placed at intervals rostral and caudal to the epicentre. GAP43$^+$ immunoreactivity in rostro-caudally orientated linear streaks were counted where they intersected a line drawn perpendicular to each distance marker, to the requisite depth of the injury.[316,329,342] As these are ascending neurons, these axonal counts for each distance are presented as a percentage of the maximum number of GAP43$^+$ axons identified at the furthest observed distance (caudal) to the lesion site.

3.2.10 Quantification of GAP43$^+$ DRGN

For DRG sections, five images were taken from each specimen at 10x magnification. An investigator blinded to the treatment conditions took images from the maximal regions of GAP43 immunoreactivity including one image from each of the DRG (L4/5 bilateral DRG). After image acquisition, background removal and autothresholding was performed in ImageJ[340] for both GAP43 (Alexa Fluor 488) and NF-200 (Alexa Fluor 594). Cell counts for each image were performed and expressed as a ratio.

3.2.11 Evaluation of the glial scar

Using the central sagittal slices (2 x 15 μm slices per animal) of the injury site, laminin staining was evaluated using ImageJ.[340] After image scaling, the extent of laminin staining and cavitation were traced manually. Where cavitation extended beyond laminin immunoreactivity, this area was included. Within this region of interest, after background removal and autothresholding, average density was measured within ImageJ.[340,343]

3.2.12 Raman spectroscopy

For Raman spectroscopy analysis, tissues were collected 3 dpi after SCI, with groups receiving either 810 nm PBM (as described above) or sham treatment. The control (uninjured) group had

laminectomy alone. After the treatment protocol, animals were sacrificed as described above. Immediately post mortem, T8 was exposed via extended laminectomies T6-T0. A benchtop Renishaw InVia system was used to acquire Raman signal in a line map along the midline centred upon the lesion core (785 nm, 50% power output, 1 s exposure, 10 accumulations extended spectral scan in two repeated centred on 690 and 1610 cm^{-1}). Spectra were processed and merged using Spectragryph (merging across two centred scans from each specimen; baseline correction; smoothing) and peak intensities and AUC values were extracted from individual spectra using the integrated analytical functions.[iii]

3.2.13 Statistical analysis

Statistical analysis was performed using Prism 9.2.0 (GraphPad, California, USA). Shapiro-Wilk analysis was performed to test for normal distribution. For parametric data: t-test was used for comparison between two groups (using paired t-test for paired *in vitro* data); for comparison between more than two groups, one-way ANOVA was used with post-hoc Dunnett's method (using row-matching for paired *in vitro* data). Mixed effects models were used to assess functional outcomes, using R[344] (www.R-project.org) (described in detail elsewhere[329]). Tape sensing and removal tests were analysed by linear mixed modelling using *pbkrtest* and the Kenward-Roger method. Binomial generalised linear mixed models were used to assess horizontal ladder crossing tests, with models fitted using *lme4* with *glmer* function, with parametric bootstrap to calculate p value.

[iii] Raman spectral acquisition was performed by Clarissa Stickland, from specimens prepared by the thesis author.

3.3 Results

3.3.1 Serum withdrawal model of injury in primary cell culture of dorsal root ganglion neurons

The serum withdrawal model of injury in cultured DRGN, with serum withdrawal 24 h after primary cell culture, produced 68% cell loss at 120 h (Fig. 3.9). This represents a more significant cell loss than comparable studies,[316] however this is likely attributable to the additional injury burden of removal of culture vessels from incubation every 20-24 h to administer ambient/PBM light.

3.3.2 *In vitro* dose delivery calibration

A custom PBM delivery device was calibrated to deliver a range of average irradiances to DRGN in culture in an 8-well glass chamber slide (Fig. 3.10). The calibrated average irradiance values were in increments between 3.7 mW/cm^2 and 130.6 mW/cm^2 (Fig. 3.10 A/C), with wavelength ranging from 658.5 to 662.2 (Fig. 3.10 B/C) and even distribution across each well (Fig. 3.10 D). Slides were either exposed to (a) control therapy with background broadband laboratory light (Fig. 3.10 E) or (b) 660 nm PBM at a given setting (Fig. 3.10 F) under a bespoke foil lined cover to exclude background light (not pictured).

3.3.3 Photobiomodulation is neuroprotective in an *in vitro* model of spinal cord injury

The range of PBM average irradiances were used to determine the optimum value for improving DRGN cell viability in culture in a serum withdrawal model. DRGN were allowed to habituate in the presence of FBS for 24 h, before commencing a five day culture regime either with FBS (DMEM + Serum) or without FBS (DMEM). The spectrum of average irradiances of PBM was delivered daily (every 20-24 h) for 1 min per dose in Figure 3.11 A). Optimum DRGN viability after five days was observed with administration of 11 mW/cm^2, associated with an increase in

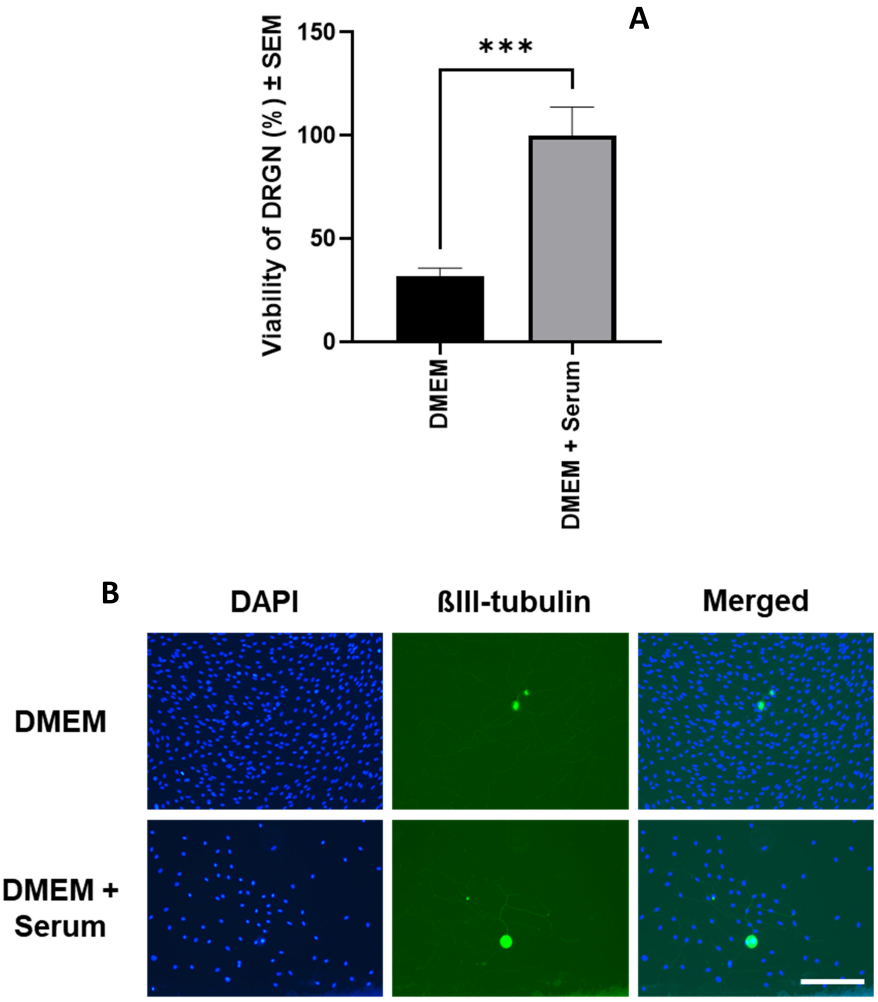


Figure 3.9: Serum withdrawal model of DRGN cell culture results in 68% cell loss at 5 days. A: viability of DRGN at 120 h post serum withdrawal (DMEM alone) was 31.9% ± 4.0 in comparison with continued culture with 10% fetal bovine serum (100% ± 13.8). n = 3, *** = $p < 0.001$, error bars denote SEM. B: βIII-tubulin and DAPI co-staining for DRGN identification. Scale bar = 250 μm.

cell viability of 45% (from 33.6% to 78.6%) compared with DMEM (plus ambient light) ($p < 0.0001$). A discernible dose-response difference is shown across the remaining irradiances, with 11 mW/cm^2 demonstrating a statistically significant difference from 131 mW/cm^2 ($p < 0.05$).

Optimum time exposure effects on cell viability were tested using 11 mW/cm^2. All culture plates were exposed to daily 10 min intervals outside the incubator (shielded from ambient light),

during which time they received either a duration (according to variable stated) of PBM therapy or 1 min ambient light exposure (Fig. 3.11 B). A plateau of broadly equivalent responses was demonstrated between 30 s and 3 min, with a reduction in efficacy seen with 5 min exposure. The effect of cumulative daily exposure to 1 min PBM 11 mW/cm^2 is shown in Figure 3.11 C. Treatments on day 1 post-serum withdrawal (1x) and on days 1-3 (3x) did not reach statistical significance when cultured for five days, only reached by the daily treatment regimen over the full culture period (5x).

The effect of culture with and without suppression of non-neuronal cell proliferation (with addition of 30 mM 5-FDU to the culture media) was assessed (Fig. 3.11 D), and the therapeutic effect occurred independently of proliferative suppression. This explores the hypothesis that an apocrine effect from non-neuronal cell release of unknown factors in response to PBM may mediate or potentiate any direct effect of PBM on neuronal cells. PBM was also delivered in the range of average irradiance values to cells cultured with serum, to assess the effect of PBM on DRGN *in vitro* in a "healthy" or "non-injury" state (Fig. 3.11 E). No discernible detrimental effects on DRGN survival were observed across this range. To confirm the survival effect of PBM on averting apoptosis in DRGN, Annexin-V live culture assay was used to determine the proportion of apoptotic cells after 72 h in culture, showing that PBM significantly reduced this proportion of the remaining cell population (Fig. 3.11 F).

3.3.4 Photobiomodulation increases neurite outgrowth in an *in vitro* model of spinal cord injury

Using the optimum PBM conditions for promoting DRGN survival in a serum withdrawal model *in vitro* (1 min per day, 11 mW/cm^2), the effect of 660 nm PBM on neurite outgrowth was investigated. PBM was demonstrated to increase the length of the longest neurite (Fig. 3.12 A/E) without effects on branching, number of DRGN with neurites, or number of neurites per DRGN (Fig. 3.12 B-D).

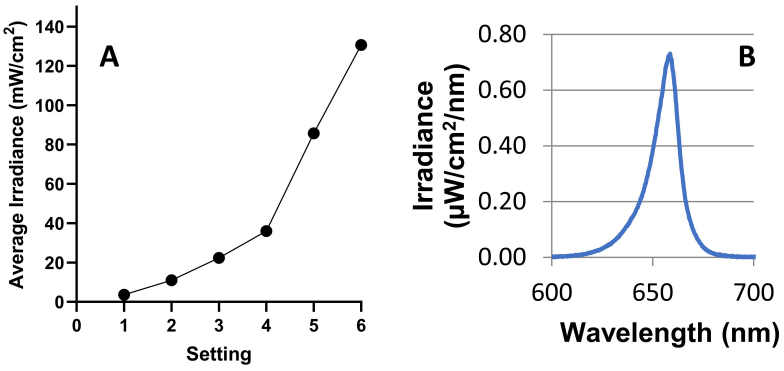
3.3.5 Photobiomodulation can be delivered in effective doses transdermally in an *in vivo* model of spinal cord injury

In order to establish the efficacy of this dosing regimen *in vivo* via implantable and transcutaneous methods, cadaveric modelling was performed to validate the deliverable doses via each method (Fig. 3.13). Three methods were applied:

1. Thor LX2 75 mW 660 nm Laser Therapy System with manufacturer supplied probe.
2. MD-III 660 nm 800 mW laser with integrated diffuser.
3. 200 μm 0.39 numerical aperture (NA) 10 mm diffusion tip catheter (CFDSB10) with implant guide (OGL-5) coupled to MD-III 660 nm 800 mW laser with integrated diffuser.

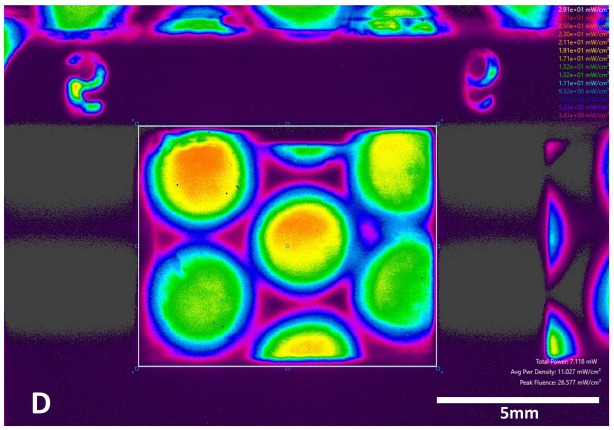
Transcutaneous: Thor LX2

A commercially available handheld probe and laser therapy system was assessed for suitability in a cadaveric rat model. After wound closure, the probe was placed directly on the skin without excessive pressure to model an acceptable level to not cause discomfort in a live subject. Beam profiling was performed from a ventral approach. Figure 3.14 A displays the beam profile, with discernible laminectomy limits visible. Average irradiance delivered is below the therapeutic threshold established in the *in vitro* model (2.96 mW/cm^2) (Fig. 3.14 B). Thermal profiling was performed (Fig. 3.15). Due to the flat surface of the probe tip being in direct circumferential contact with the skin, temporal data did not reveal any tissue heating. After removal of the tip, modest skin heating was revealed (2.9 °C). Whilst this was a suitable product to utilise in an *in vivo* model, the average irradiance value was insufficient at maximum power output. As such, a higher output laboratory laser was assessed for suitability.



C

Setting	Average irradiance (mW/cm²)	λmax	FWHM
1	3.681	658.51 ± 0.22	13.11 ± 0.22
2	11.027	658.58 ± 0.11	13.80 ± 0.11
3	22.341	658.64 ± 0.00	14.93 ± 0.11
4	36.046	660.14 ± 0.65	14.61 ± 0.11
5	85.677	661.58 ± 0.29	16.98 ± 0.11
6	130.636	662.21 ± 0.00	18.48 ± 0.11



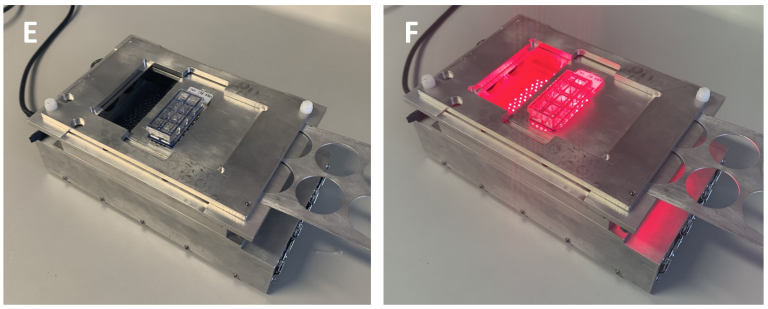


Figure 3.10: Profiling of a device for the metered delivery of PBM to DRGN in culture. A: Average irradiance of the 6 settings used for the variable power 660 nm LED array light source (BioThor device, Thor Photobiomedicine); B: Spectral irradiance for setting 2; C: Average irradiance, λmax and full width at half maximum (FWHM) values for each setting profiled, error show as SD; D: Beam profile through single well of 8 well plate and plate diffuser, scale bar 5mm. E: LED array in OFF mode (sham PBM delivery) and F: in ON mode (PBM delivery).

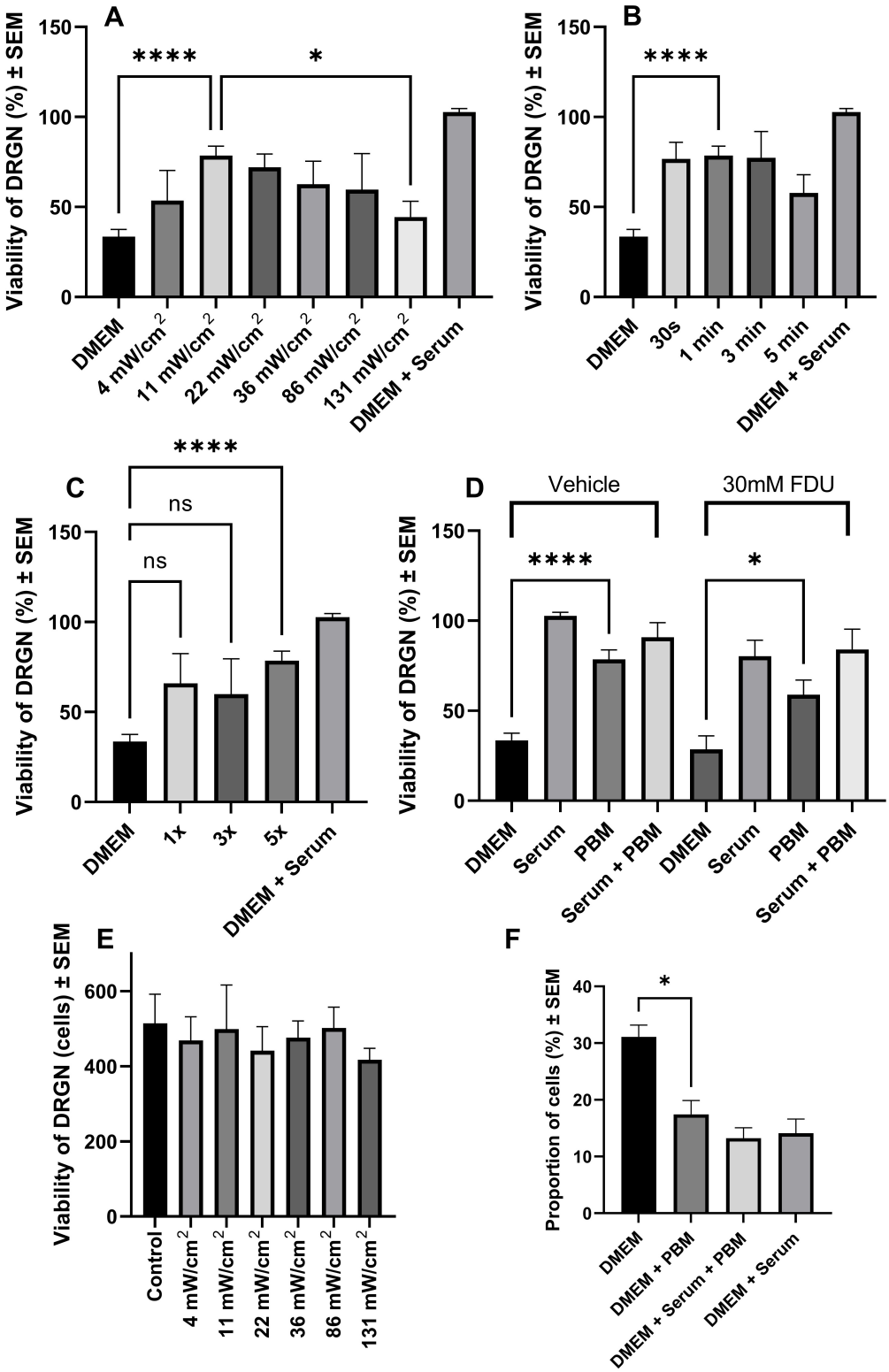


Figure 3.11: Caption on next page

Figure 3.11: 11 mW/cm^2 PBM for 1 min per 24 h improves DRGN viability by 62% at 5 days in a serum withdrawal model of DRGN cell culture. A: viability of DRGN at 120h post serum withdrawal (DMEM alone) was 33.6% ± 3.9 in comparison with continued culture with 10% FBS (100% ± 1.9). Six average irradiance values were utilised for 1 min administered every 20-24 h, with control samples receiving 1 min exposure to ambient light. Optimum viability in serum withdrawal cultures was observed in 11 mW/cm^2 samples, with 78.6% (± 5.3) DRGN viability at 5 days. n = 3, **** = $p < 0.0001$, ns = $p > 0.05$, error bars denote SEM. B: 30 s to 3 min exposure daily achieves increase in DRGN viability at 5 days. All cultures received 15 min exposure out of incubator, DMEM group received 1 min ambient light, treatment groups received 11 mW/cm^2 exposure for given durations. C: 11 mW/cm^2 PBM for 1 min per 24 h on 1, 3 and 5 consecutive days of a 5 day serum withdrawal model DRGN cell culture. Viability of DRGN after 5 days increased with 5 daily PBM treatments vs 1 or 3. All cell cultures removed from incubator for 15 min per day, 1x and 3x groups received ambient light on subsequent days after cessation of PBM. One aberrant result observed in 3x group, and pilot results presented n = 2, error bars denote SEM. D: 11 mW/cm^2 PBM for 1 min per 24 h is not significantly affected by 5-FDU mediated suppression of non-neuronal cell proliferation. E: Samples cultured with DMEM + 10% FBS for 120 h received daily exposure to PBM at six average irradiance values for 1 min per 24 h. No significant difference was observed between PBM exposed samples and ambient light samples (control). n = 3, error bars denote SEM. F: Annexin V + DAPI staining identified reduction in dead cells with PBM treatment at 60h (3x PBM treatments).

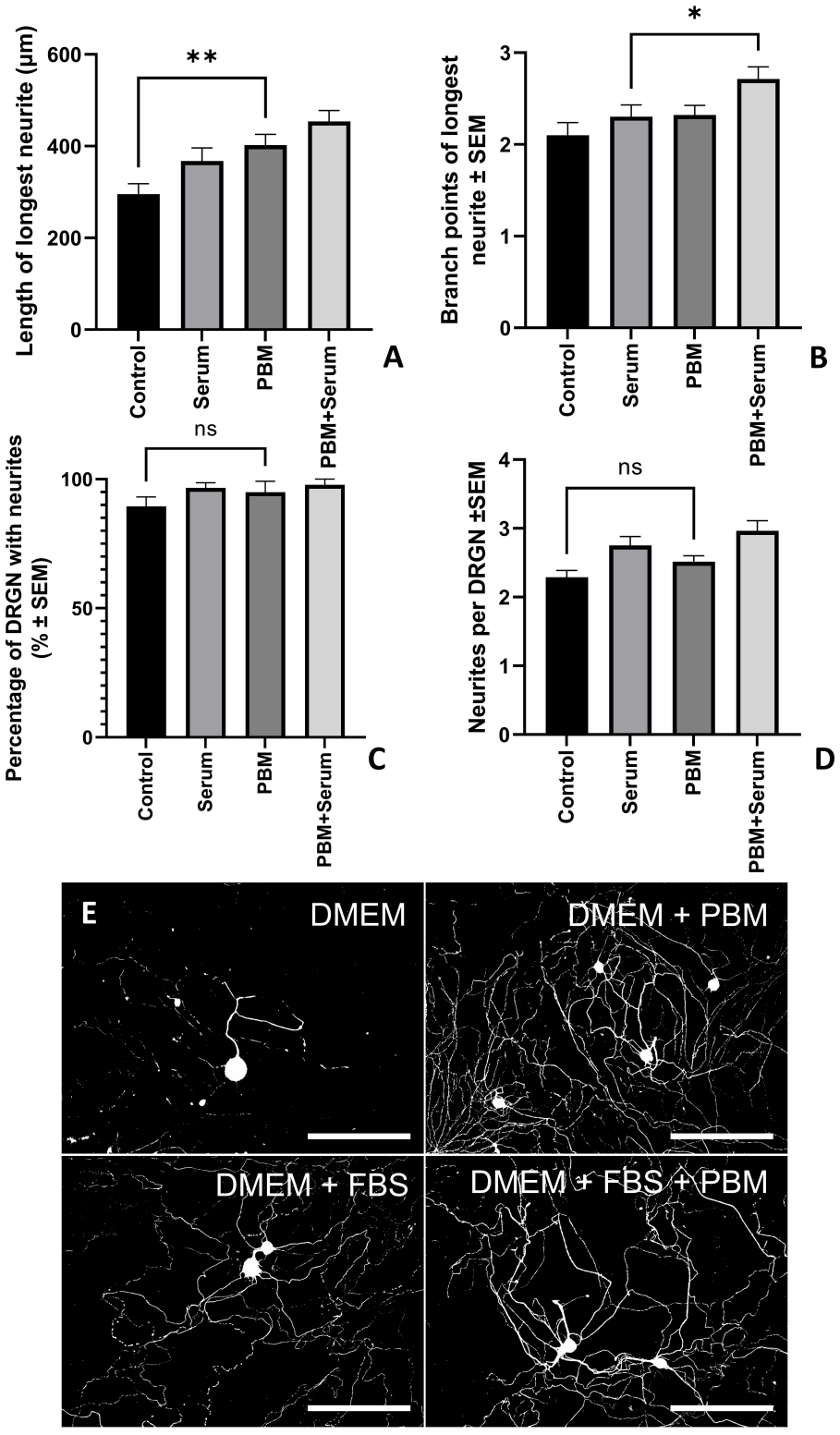


Figure 3.12: Caption on next page

Figure 3.12: 11 mW/cm^2 PBM for 1 min per 24 h increases the length of the longest neurite at 5 days in a serum withdrawal model of DRGN cell culture. A: Length of the longest neurite in control serum withdrawal samples was 295.3μµm (± 22.7) and 367.9 μm (± 28.61) in samples cultured with DRGN + 10% FBS with daily ambient light exposure. With 11 mW/cm^2 1 min daily exposure, length of longest neurite in serum withdrawal samples was 402.0 μm (± 23.9) and with serum was 453.8 μm (± 23.7). n = 3, ** = $p < 0.01$, error bars denote SEM. B: Number of branch points of the longest neurite increased significantly with the application of daily PBM at 11 mW/cm^2 for 1 min per 24 h in samples cultured with DMEM + 10% FBS. n = 3, * = $p < 0.05$, error bars denote SEM C: No significant difference at the level of $p < 0.05$ was identified in the percentage of DRGN with neurites at 5 days. n = 3, error bars denote SEM. D: No significant difference at the level of $p < 0.05$ was identified in the number of neurites per DRGN at 5 days. n = 3, error bars denote SEM. E: βIII tubulin staining (in binary) in each condition. Scale bar = 250 μm.

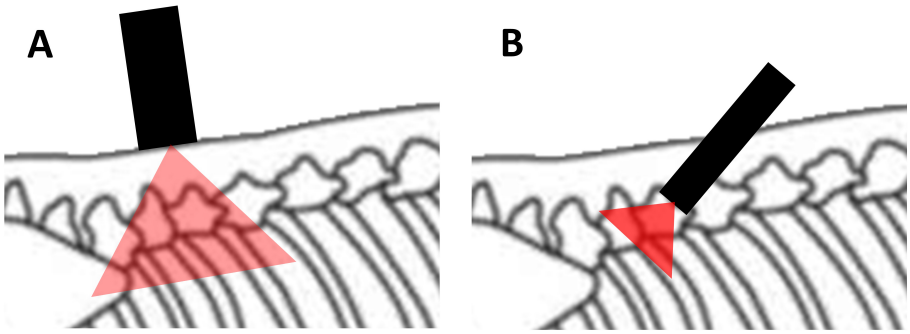
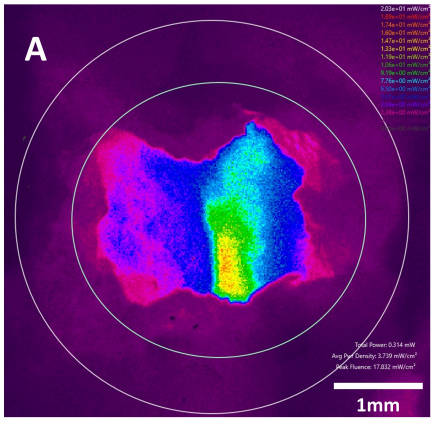
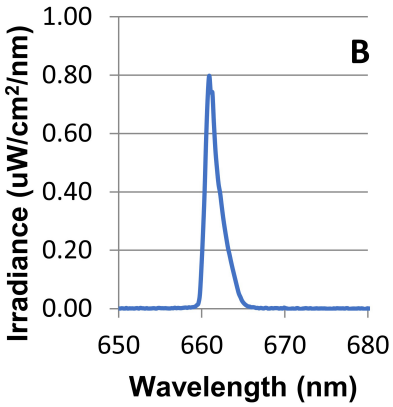


Figure 3.13: Schematic diagrams of transcutaneous PBM (A, tcPBM) and implantable PBM (B, iPBM).





C

Variable	Value
Total power (mW)	0.33 ± 0.11
Average irradiance (mW/cm^2)	2.96 ± 1.05
Peak irradiance (mW/cm^2)	10.96 ± 6.86
D4σ (cm)	0.39 ± 0.06
λmax (nm)	661.02 ± 0.11
FWHM (nm)	1.57 ± 0.11

Figure 3.14: 75 mW Thor LX2 delivers 2.96 mW/cm^2 average irradiance to the dorsal spinal cord via transcutaneous delivery in a cadaveric model. A: beam profile at level of dorsal spinal cord, with PBM via Thor LX2 75 mW administered to dorsal skin over injury site; B: spectral irradiance of Thor LX2 in transcutaneous model; C: table of values for beam profiling and spectral irradiance in Thor LX2 transcutaneous model.

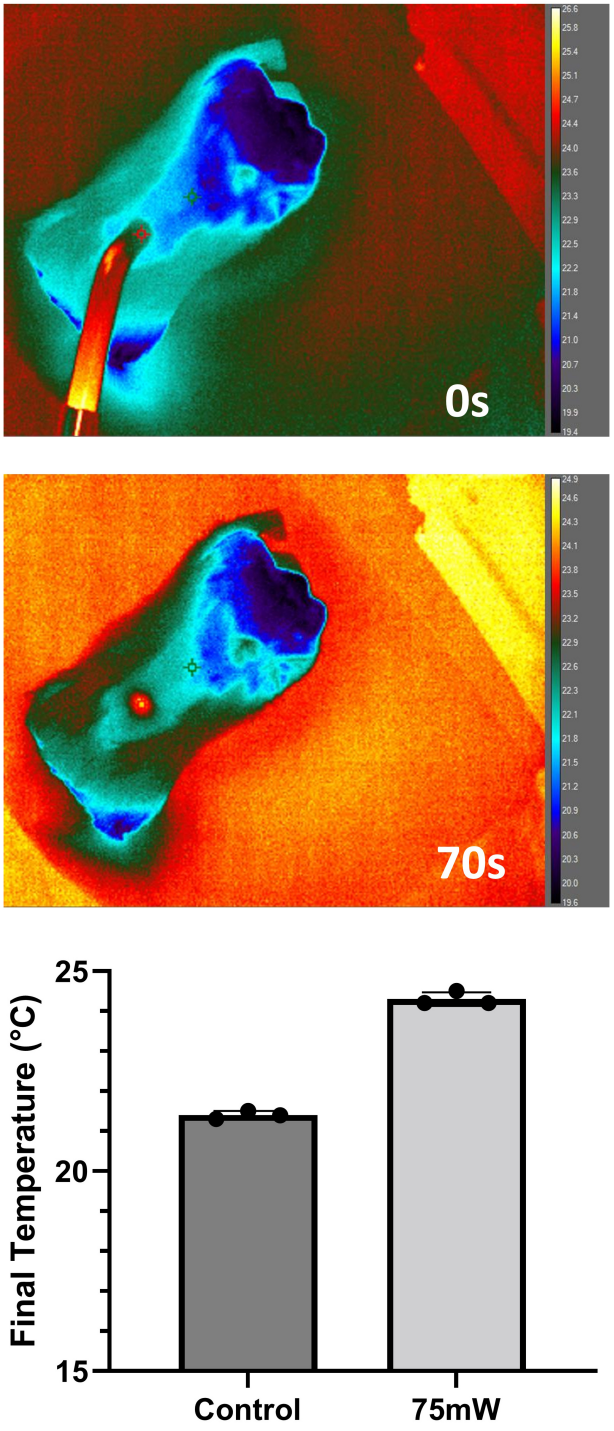


Figure 3.15: 75 mW Thor LX2 application for 1 min results in 3 °C tissue heating in a cadaveric transcutaneous delivery model. 80 second protocol: 10 seconds OFF, 60 seconds ON, 10 seconds OFF AND REMOVED FROM SKIN. n = 3. Discrete results given as dots in bar chart, control temperature taken from non-irradiated skin tissue.

Transcutaneous: MD-III

Transcutaneous PBM was applied to the dorsum of a rat cadaver which had undergone post mortem SCI modelling (DCC), using an MD-III 800 mW laser coupled to a custom fibre. The output of the laser source can be configured to two decimal places on a digital display from 0.00 to 1.40. Calibration of these settings to one decimal place are given in Table 3.3.

Table 3.3: Calibration of device setting with resultant output power (mW)

Setting	Percentage (%)	Power (mW)
0	0.0	0
0.1	7.1	0.08
0.2	14.3	0.24
0.3	21.4	0.48
0.4	28.6	0.83
0.5	35.7	1.76
0.6	42.9	3.89
0.7	50.0	63.1
0.8	57.1	168.7
0.9	64.3	256
1	71.4	380
1.1	78.6	473
1.2	85.7	577
1.3	92.9	689
1.4	100.0	801

Power transmission recordings and beam profilometry were captured at the level of the dorsal column (via anterior approach and corpectomy, with the spinal cord removed) at 50, 75 and 100% power outputs (Fig. 3.16 and Table 3.4).

This demonstrates achievable average irradiance values between 6.74 and 120.43 mW/cm^2. Beam profiles recorded through the laminectomy site are shown in Figure 3.17. This allowed calculation of the required power output of the laser source to achieve 24.42 mW/cm^2, using the linear equation $y = mx + c$. This is a higher value than the optimum *in vitro* value selected to allow for: post-operative bleeding *in vivo* which would attenuate PBM transmission, suboptimal delivery due to animal movement *in vivo*, animal weight gain during a 7 day treatment regimen, and the effect of oxygenated haemoglobin *in vivo*). This was deemed an appropriate

compromise: had the full 24.42 mW/cm^2 transmitted *in vivo*, this dose is still within the effective range determined by the *in vitro* experiments above (Fig. 3.11).

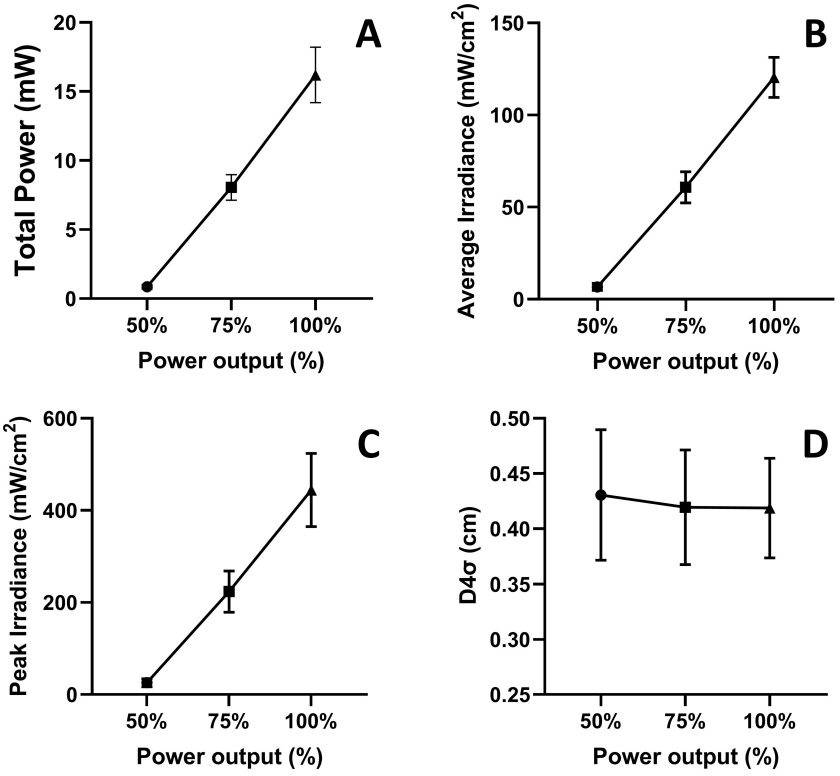


Figure 3.16: Beam profiling values of transcutaneous delivery of 63 mW (50%), 427 mW (75%) and 801 mW (100%) laser power. A: total power; B: average irradiance; C: peak irradiance; D: D4σ. n = 3 error bars represent SD.

Table 3.4: Beam profiling values at three power output settings delivered to the dorsal spinal cord through transcutaneous delivery.

	Total Power (mW)	Average irradiance (mW/cm^2)	Peak irradiance (mW/cm^2)	D4σ (cm)
50%	0.86 ± 0.28	6.74 ± 3.44	25.64 ± 15.03	0.43 ± 0.10
75%	8.05 ± 1.60	60.79 ± 14.65	223.65 ± 77.67	0.42 ± 0.09
100%	16.19 ± 3.48	120.43 ± 18.78	444.12 ± 137.82	0.42 ± 0.08

An output value of 63% of maximum (800 mW) was determined to deliver this average

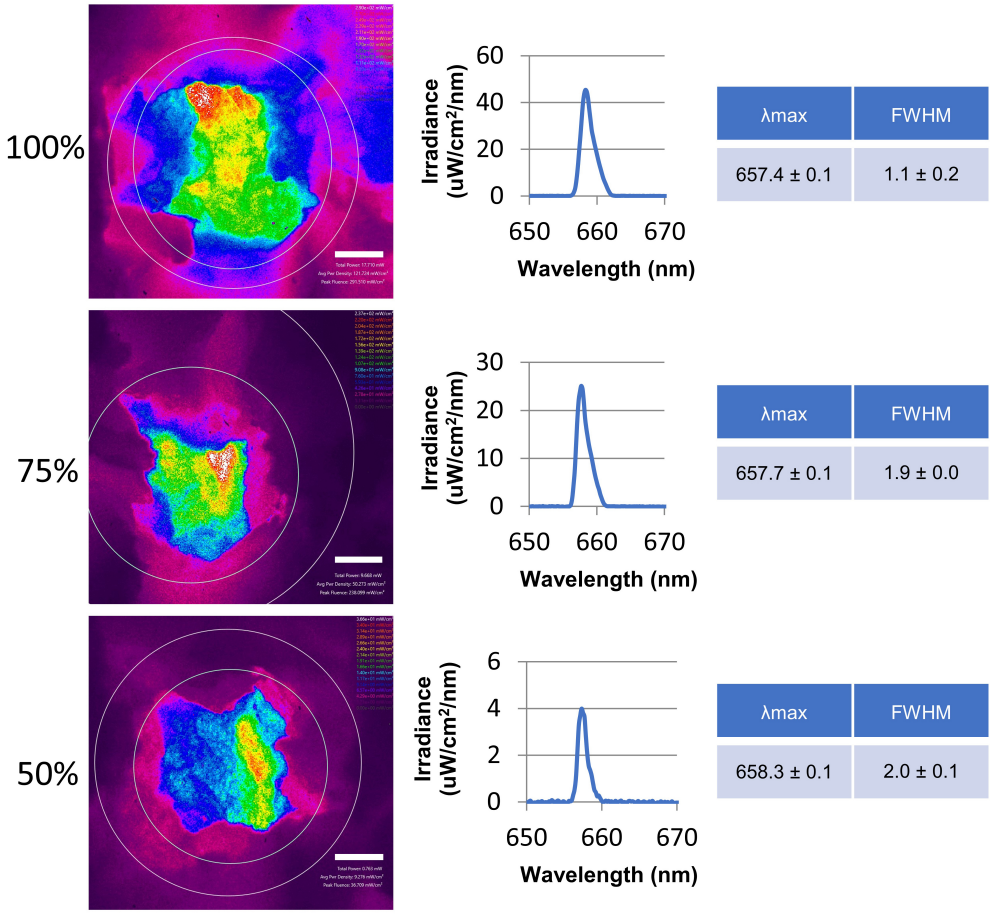


Figure 3.17: Spectral irradiance and beam profiles from transcutaneous administration of MD-III laser to the dorsal spinal cord at three power settings. Left: beam profiles for each given power output setting, scale bar = 1 mm. Middle: spectral irradiance for given power setting. Right: λmax and full width at half maximum (FWHM) values for given power setting.

irradiance to the spinal cord. Thermography of the skin was performed to ensure the safety of applying this output via the skin, with the probe in direct skin contact and thermal readings taken at the end of the 60 s exposure period (Fig. 3.18). This was performed on room temperature cadavers, with a FLIR camera focused on the dorsal skin surface in direct contact with the custom fibre bundle during an 80 s treatment protocol (10 s baseline, 10 s laser activation window, 60 s laser active period, 10 s post-treatment observation). With optimisation of positioning, it was possible to deliver PBM with the probe positioned at a 45 ° angle to allow simultaneous

real-time thermography (Fig. 3.19). The therapeutic level (63%) led to less than 3 °C skin surface heating over the 1 min treatment period. As cadaveric modelling would not replicate heat distribution physiology observed *in vivo* (via local vasodilatation acting as a vascular "heat sink" via local superficial blood flow), this level was deemed safe and compatible with stringent concern for animal welfare during *in vivo* experiments. The highest output powers (and their resultant transmitted average irradiance values) would not be compatible: 100% output resulted in over 20 °C of surface heating which is unacceptable thermal exposure for an *in vivo* model.

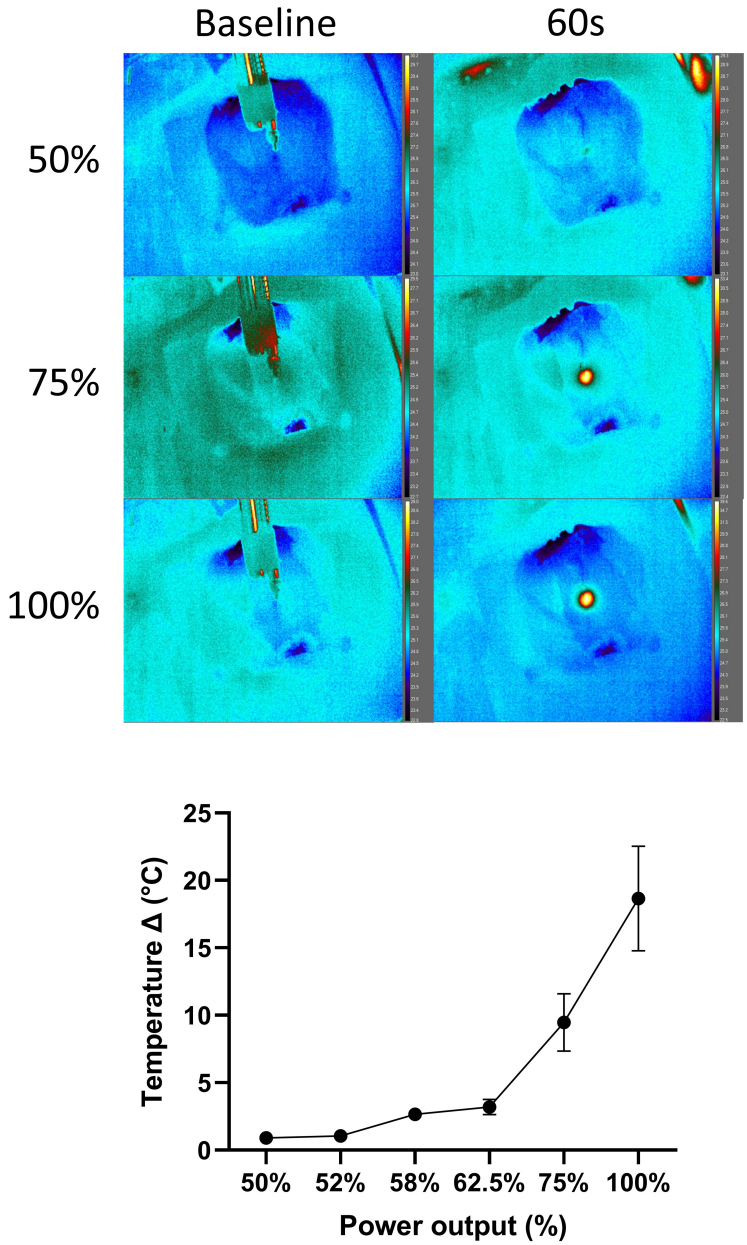


Figure 3.18: FLIR thermography imaging pre- (baseline) and post-60 s exposure of transcutaneous MD-III laser exposure, laser positioned for transcutaneous administration to the skin overlying T8 in the cadaveric SD rat post-DCC injury, at varying power output settings (percentage of maximum (800 mW) power output). 10 s of baseline recording prior to laser ON, followed by 60 s exposure, at which point laser was turned OFF and probe tip removed from contact with skin and field of view of thermography camera. Bottom Panel: Mean FLIR thermography temperature change from baseline (mean of 10 s prior to laser ON) to end of exposure (10 s prior to laser OFF) after 1 min exposure at varying power outputs. All datapoints normalised to ambient temperature by recording change relative to non-exposed cutaneous area. n = 3 (output of 100% n = 6). Error bars denote SD. Emissivity set at 0.95, camera distance 0.2 m, tissue at ambient temperature (22 °C).

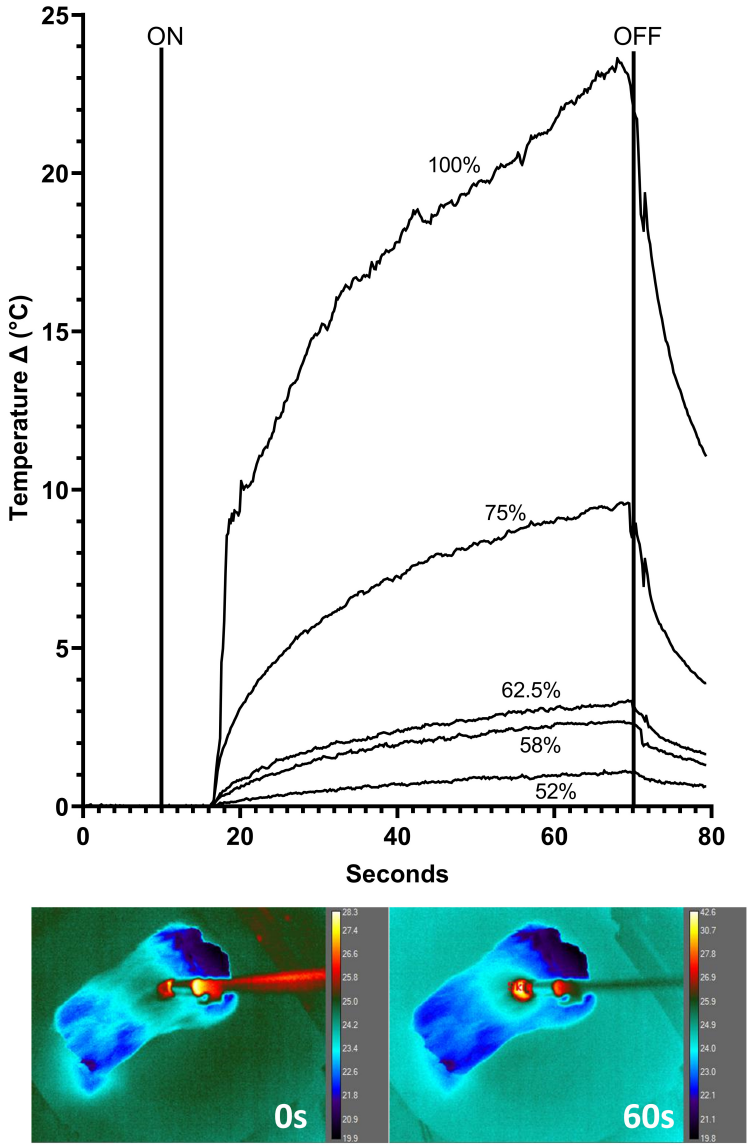


Figure 3.19: FLIR Thermography of MD-III laser positioned for transcutaneous administration to the skin overlying T8 in the cadaveric SD rat post-DCC injury. TOP: Varying power outputs in % of maximum output (800 mW) denoted for each. Mean of n = 3, error bars not shown for clarity, laser ON (10 s) and laser OFF (70 s) time points denoted with labelled lines. Temperature change is relative to a non-irradiated distal cutaneous point, with all data points normalised to baseline of zero. Emissivity set at 0.95, camera distance 0.2 m, tissue at ambient temperature (22 °C). BOTTOM: FLIR images for 100% output power at 0 s and 60 s of 60 s laser exposure protocol (80 second protocol: 10 seconds OFF, 60 seconds ON, 10 seconds OFF and removed from skin.) n = 3. Cord emissivity 0.95; probe emissivity 0.9.

3.3.6 Photobiomodulation can be delivered in effective doses invasively in an *in vivo* model of spinal cord injury

After validation of achievable and safe delivery of 24.42 mW/cm^2 via the transcutaneous route, a method was developed for the delivery of equivalent doses via an implant in a manner which is suitable for an *in vivo* murine model (schematic of concept in Figure 3.13 B). An implantable probe was designed for intermittent dosing at the same average irradiance value at the spinal cord level. A prototype probe was developed using diffusion tip catheter for optogenetics and associated accessories. For the principal fibre, a commercially available 200 μm 0.39 NA 10 mm diffusion tip catheter (CFDSB10), designed for optogenetics applications, was selected. The diffuser tip was deemed favourable in order to permit modest trajectory misalignment with respect to the SCI site, given the diffusivity of the emission from the fibre. A fibre with a ferrule connector system was also favourable, as this allows disconnection between doses. The availability of a compatible implant guide (OGL-5) was also advantageous to permit tethering to the muscle/fascial layers to ensure the implant would remain securely *in situ* for the duration of the experiment. The fibre components could be assembled using cyanoacrylate and were compatible with UV sterilisation. A connector (SMA-FC) system allowed the fibre to be coupled to the MD-III 660 nm 800 mW laser used above, via a phosphor bronze split mating sleeve (ADAL4-5). The initial intention was to use a minimal size of implant, with the mating sleeve to be connected for coupling only (Fig. 3.20 A). However, in pilot trials this configuration proved too short: due to skin mobility in combination with the minimal protrusion of the implant, this version did not remain reliably protruding from the skin to permit intermittent access without interference with the surgical wound. As such, a second design was built, integrating the mating sleeve into the single unit (also fixed with cyanoacrylate), shown in Figure 3.20 B).

After constructing these components and coupling to the laser, initial profiling was performed for the implant. Profiling was performed initially using the implant in isolation. This was performed in 0 ° orientation, perpendicular to profiling spectrometer and profilometry camera using an optomechanics rig to profile at distance in 2.5 mm increments (Fig. 3.21). At 0 mm from probe tip, maximum power output was 145.7 mW at 100% power output (calibrated to 801

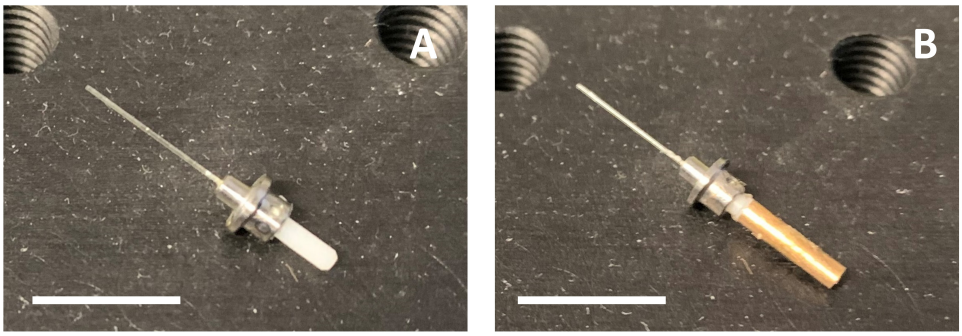


Figure 3.20: Implantable PBM device. A: 200 μm 0.39 NA 10 mm diffusion tip catheter (CFDSB10) with implant guide (OGL-5) (coupled to MD-III 800 mW laser source) Scale bar = 1 cm. B: As in A, with addition of a phosphor bronze split mating sleeve (ADAL4-5).

mW output direct from laser without additional optics) with 3.3 mm spot size (D4σ) with an average irradiance of 1704 mW/cm^2. D4σ increased to 4 mm at 10 mm distance (through room air). Profilometry was then performed *in situ* using cadavers, with the implant secured in the manner proposed *in vivo*. The probe was implanted during a post mortem procedure to replicate the SCI model (DCC) to be used *in vivo*. As described above, profilometry was performed from an anterior approach, resulting in direct visualisation of the probe tip via the corpectomy and laminectomy, and power transmission recordings and beam profilometry were again captured at the level of the dorsal column orientated to capture transmission through the laminectomy site (spinal cord removed). Output settings of 50% (63 mW) to 100% (800 mW) were used in 5% increments to establish a power-output curve for establishing optimum device settings for *in vivo* use, showing the system to be capable of delivering up to 318 mW/cm^2 average irradiance to the target tissue (Fig. 3.22). Lower than anticipated power indices were observed with 100% output, indicating a potential disruption of the fibre or diffuser tip at the highest output settings. Average irradiance values in the region of 24.42 mW/cm^2 were achievable at relatively low laser outputs (55%). Numerical values for beam profiling at these settings are given in with full numerical results for each laser output setting given in Table 3.5. This allowed calculation of the required power output of the laser source to achieve equivalent average irradiance to the transcutaneous

method (24 mW/cm^2), (calculated as above, using the linear equation $y = mx + c$).

Table 3.5: Values for beam characterisation indices for an implantable fibre optic probe coupled to MD-III 800 mW in a cadaveric model of SCI at varying power output values. Profilometry camera focused at level of dorsal spinal cord in a cadaveric model of post-procedure adult Sprague-Dawley rat. All values given ± SD, n = 3.

Power output (%)	Total Power (mW)	Average irradiance (mW/cm^2)	Peak irradiance (mW/cm^2)	D4σ (mm)
50%	0.07 ± 0.03	13.11 ± 3.95	26.26 ± 8.69	0.86 ± 0.09
55%	0.12 ± 0.06	24.42 ± 18.91	49.97 ± 41.36	0.86 ± 0.09
60%	0.24 ± 0.06	45.26 ± 12.68	92.39 ± 30.61	0.86 ± 0.09
65%	0.47 ± 0.11	90.19 ± 45.67	187.52 ± 104.77	0.86 ± 0.09
70%	0.67 ± 0.11	125.83 ± 53.89	262.07 ± 125.29	0.86 ± 0.09
75%	0.84 ± 0.16	154.25 ± 66.38	323.07 ± 152.92	0.86 ± 0.09
80%	1.06 ± 0.24	193.69 ± 85.89	406.95 ± 196.24	0.86 ± 0.09
85%	1.14 ± 0.24	209.82 ± 93.44	440.03 ± 214.10	0.86 ± 0.09
90%	1.56 ± 0.28	278.15 ± 101.21	584.97 ± 235.26	0.86 ± 0.09
95%	1.78 ± 0.33	318.11 ± 118.58	668.95 ± 275.01	0.86 ± 0.09
100%	1.56 ± 0.46	287.94 ± 149.00	606.74 ± 334.61	0.86 ± 0.09

To validate the safety of the implant, with a much lower tolerance for heating the spinal cord than the skin, thermography was performed on cadavers to represent the thermal effects of the intended exposure settings on biological tissue (Fig. 3.23). The implant was positioned with the tip placed directly above the spinal cord (<1 mm distance from cord) with a FLIR camera focused on the spinal cord surface. Regions of interest were recorded from the spinal cord and the implant tip. No discernible heating was recorded at the spinal cord level over a 1 min exposure, up to 75% output. There were transient but negligible probe tip heating at the points of powering on and off the laser source.

3.3.7 *Post mortem* Raman spectroscopy is feasible for injury site spectral analysis in an *in vivo* model of spinal cord injury

In order to establish whether RS can be effectively utilised as a means to monitor the therapeutic effect of PBM, cadaveric modelling was performed prior to embarking upon *in vivo* studies to optimise and validate the methodology. After death, dissection was performed to remove a section of spinal column from T4-T12 *en bloc* including the surrounding musculature and costal

tissue. The laminae were removed, along with any debris or blood, and the dorsal fasciculus exposed. The InVia Raman microscope was focused on the midline of the dorsal fasciculus at the level of T8 to represent the ROI in an *in vivo* model. Two conditions were compared: "dry" specimen (immediately post-dissection, specimen was kept wrapped in aluminium foil for approximately 30 min, on ice); and "PBS" specimen (immediately post-dissection, specimen was submerged in PBS at 4 °C for approximately 30 min) (Fig. 3.24).

Comparison of these two methods demonstrated that the specimens not submerged in PBS permitted greater intensity of the acquired Raman signal compared to the PBS group, with a typical "fingerprint" region identified.

3.3.8 Photobiomodulation increases expression of regeneration associated proteins in an *in vivo* model of spinal cord injury: a pilot study

To confirm efficacy of the parameters of PBM determined *in vitro*, transcutaneous photobiomodulation (tcPBM) was used in n = 2 Sprague-Dawley adult rats after DCC injury. tcPBM was applied to the thoracic injury site for 1 min per day for 6 days. In comparison to controls (sham treatment), tcPBM treated specimens demonstrated clear upregulation of GAP43 expression in axons approaching the lesion site (Fig. 3.25 top panel) and in their respective DRGN (Fig. 3.25 bottom panel). This provided confidence to proceed with the selected dosing parameters for the full investigation.

3.3.9 An implant for delivery of photobiomodulation to the injured spinal cord is feasible *in vivo*

Implantation *in vivo* was trialled (Fig. 3.26). Implantation was successful, as were subsequent administrations of intermittent daily doses of PBM. Implants remained in place, functioning and accessible, reliably for three days. After this point, increasing animal activity and curiosity, coupled with reducing pain in the post-operative recovery phase, led to device damage and displacement, and so experiments using implanted devices were limited to 72 h duration (3x PBM

treatments). All experiments used in the subsequent analysis were confirmed as successful *post mortem* through dissection and confirmation of an intact, correctly positioned and functioning probe after removal at termination of the experiment.

3.3.10 Invasive and transcutaneous photobiomodulation improve early histological outcomes in an *in vivo* model of spinal cord injury

Four groups (n = 4 per group) underwent: (1) DCC with sham treatment; (2) DCC with transcutaneous photobiomodulation (tcPBM) (1 min per day, 24.4 mW/cm^2, 660 nm, delivered by external laser source placed in contact with the skin immediately adjacent to the dorsal wound, in rostro-caudal alignment with T8); (3) invasive photobiomodulation (iPBM) (1 min per day, 24.4 mW/cm^2, 660 nm, delivered by external laser source via implant with tip fixed directly above T8 dorsal column); and (4) laminectomy only (sham injury procedure). For treatment/sham groups, PBM therapy or sham was delivered daily for three days.

Implantable (iPBM) and transcutaneous (tcPBM) were directly compared at 3 dpi after application of 24 mW/cm^2 daily for one minute, commencing 15 min post-injury. As an early marker of initiation of neurorestorative processes, regeneration associated protein (RAP) expression within axons approaching the injury site were evaluated after tcPBM, iPBM and sham therapy (DCC only) (Fig. 3.27). Increased presence of axons 1 mm caudal to the injury site reached statistical significance for both tcPBM ($p < 0.01$) and iPBM ($p < 0.05$) compared with DCC only. This correlated with increased expression within DRGN in L4/5 DRG after both methods of PBM therapy, suggesting RAP activation within the cell body of neurons affected by injury (Fig. 3.28). Analysis of DCC DRG found that 18.0% of cells expressing NF-200 (DRGN) co-expressed GAP43. This increased to 45.8% ± 3.4 and 41.4% ± 10.5 of DRGN after tcPBM and iPBM respectively (both $p < 0.05$).

3.3.11 Photobiomodulation improves neuroregeneration in an *in vivo* model of spinal cord injury

Three groups (n = 4 per group) underwent: (1) DCC with sham treatment; (2) DCC with tcPBM (1 min per day, 24.4 mW/cm^2, 660 nm, delivered by external laser source placed in contact with the skin immediately adjacent to the dorsal wound, in rostro-caudal alignment with T8); and (3) laminectomy only (sham injury procedure). For treatment/sham groups, PBM therapy or sham was delivered daily for 7 days. At 6 weeks, a 1 cm segment of spinal cord at T8 was taken and sliced sagitally. The central two slices through the lesion site were used to assess axonal regeneration and laminin deposition. tcPBM was associated with a significant increase in the number of GAP43$^+$ axons 4 and 6 mm rostral to the injury site (Fig. 3.29) (30.9% ± 5.0 and 29.1% ± 4.8 respectively) with clear visualisation of axons traversing the laminin rich glial scar (Fig. 6A bottom right panel). Intensity of NF-200 immunofluorescence in the dorsal fasciculus in axial sections from T7 (rostral) and T9 (caudal) were also analysed (Fig. 3.30). This demonstrated a statistically significant increase in average integrated density rostral to the lesion site (T7) in specimens exposed to tcPBM. There was a modest and not statistically significant effect of tcPBM within the T9 segment.

3.3.12 Photobiomodulation reduces lesion size in an *in vivo* model of spinal cord injury

Total size of glial scar (based on extent of cavitation and laminin immunofluorescence) and the intensity of immunofluorescence for laminin staining within this region were compared in sham and tcPBM treatment at 6 weeks post-injury (Fig. 3.31). The central two slices through the lesion site were used to assess lesion size. Lesion size after tcPBM treatment reduced in comparison with control (sham treated) specimens from 2.19 mm^2 ± 0.14 (control) to 0.80 mm^2 ± 0.13 (tcPBM). This corresponded to a reduction in immunofluorescent expression of laminin within the glial scar by greater than 50%.

3.3.13 Photobiomodulation improves functional outcomes in an *in vivo* model of spinal cord injury

After tcPBM was applied daily for 7 days, weekly functional assessments of locomotor and sensory recovery for 6 weeks were performed (Fig. 3.32). Functional recovery was demonstrated with a statistically significant improvement in locomotor recovery based on the horizontal ladder crossing test with tcPBM ($p = 0.012$) and in improvement of mean sensing time on the tape removal test ($p = 0.011$).

3.3.14 *Post mortem* Raman spectroscopy detects injury progression in an *in vivo* model of spinal cord injury

Three further groups (n = 4 per group) underwent: (1) DCC with sham treatment; (2) DCC with tcPBM (1 min per day, 24.4 mW/cm^2, 660 nm, delivered by external laser source placed in contact with the skin immediately adjacent to the dorsal wound, in rostro-caudal alignment with T8); and (3) laminectomy only (sham injury procedure). For treatment/sham groups, PBM therapy or sham was delivered daily for three days. 24 h after the third treatment, animals were sacrificed. After confirmation of death, tissues were removed. The T8 section of cord was left *in situ* but exposed via laminectomy from T5-T11, with the entire section wrapped in aluminium foil and kept on ice. 30 min *post mortem*, Raman spectroscopy was performed (Fig. 3.33)[iv]. Clearly discernible and consistent differences were observed between sham and injured groups, with marked reductions in peak intensities at 1440 cm^{-1} and 1660 cm^{-1} regions with injury. A modest and not statistically significant difference was observed between PBM and injury groups at 1660 cm^{-1}, with a trend toward normalisation of the peak with therapy (Fig. 3.34)

[iv]Raman acquisition performed by a collaborator (CS). *In vivo* modelling, tissue dissection and preparation, spectral visualisation and analysis all performed by the author.

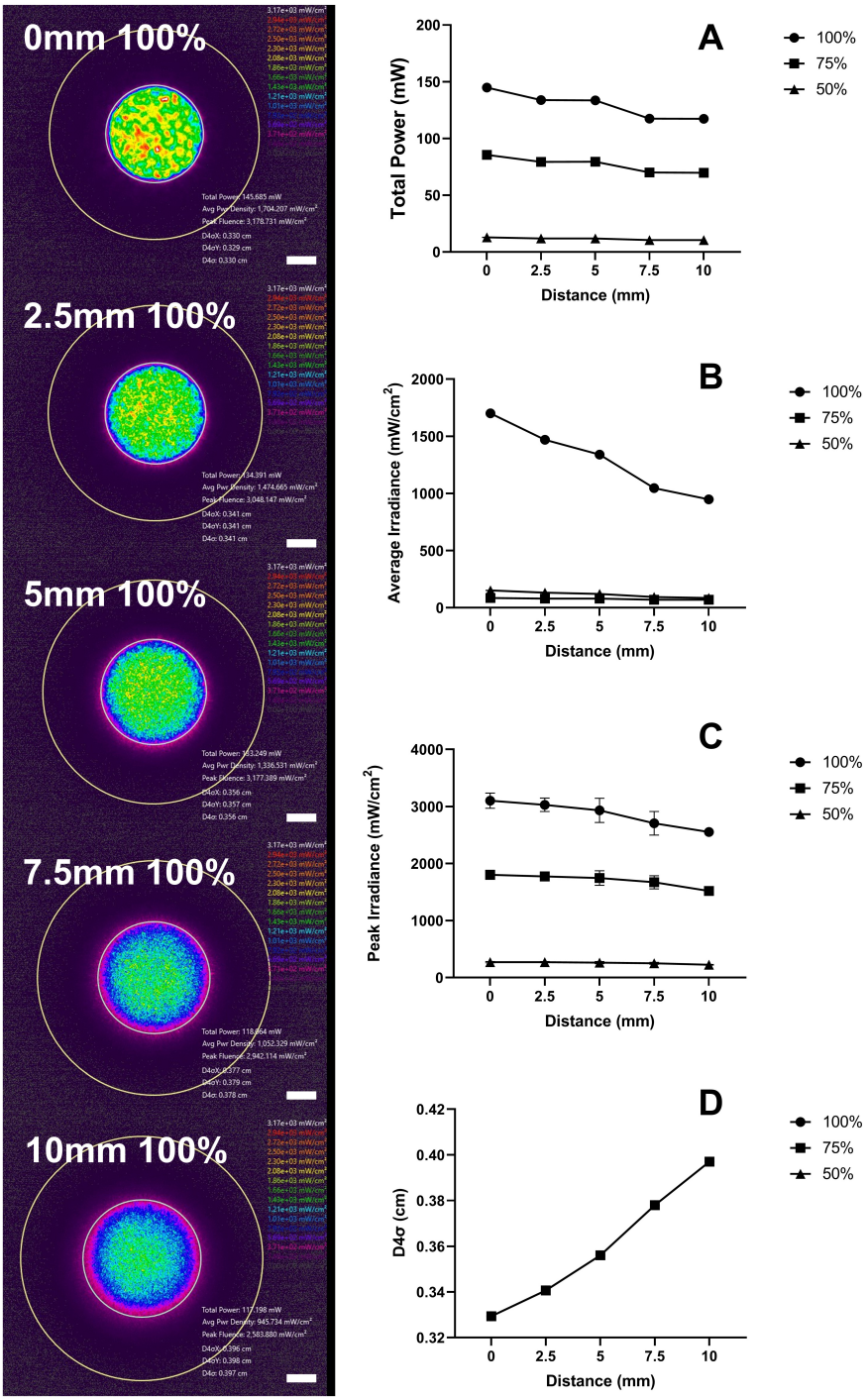


Figure 3.21: Beam profile for Thor CFDSB10 coupled to MD-III 800 mW laser at 100% output setting at given distances from the target screen. A: Total power; B: Average irradiance; C: peak irradiance; D: D4σ. Left panel demonstrates beam profile at interval distances from probe tip, measured with a 0 ° angle (i.e. plane perpendicular to probe orientation). Scale bar 1 mm.

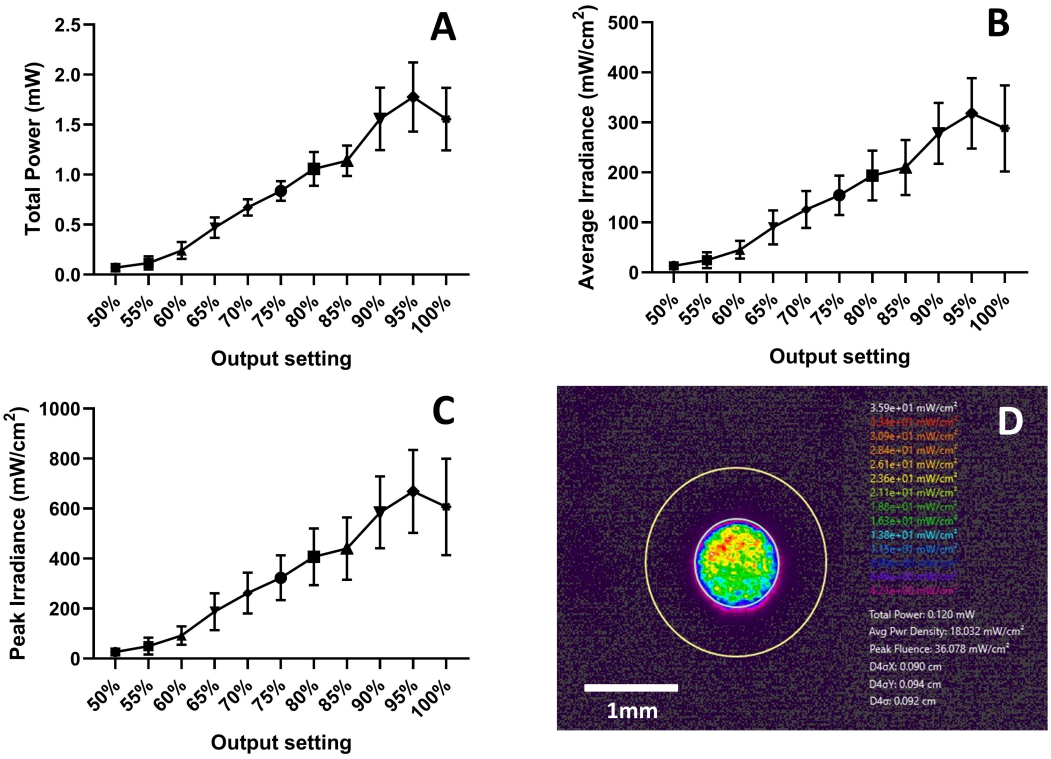


Figure 3.22: An implantable fibre optic probe coupled to MD-III 800 mW is capable of delivering up to 318 mW/cm^2 average irradiance to a target tissue. Beam characterisation outputs of 200 μm 0.39 NA 10 mm diffusion tip catheter (CFDSB10) with implant guide (OGL-5) coupled to MD-III 800 mW laser source. Beam profiler focused at the level of dorsal spinal cord in a cadaveric model of post-procedure adult Sprague-Dawley rat at varying power output values of the MD-III laser (50-100% output); A: total power; B: average irradiance; C: peak irradiance. D: beam profile of implant output at 55% power output setting. Scale bar = 1 mm, error bars represent SD. n = 3.

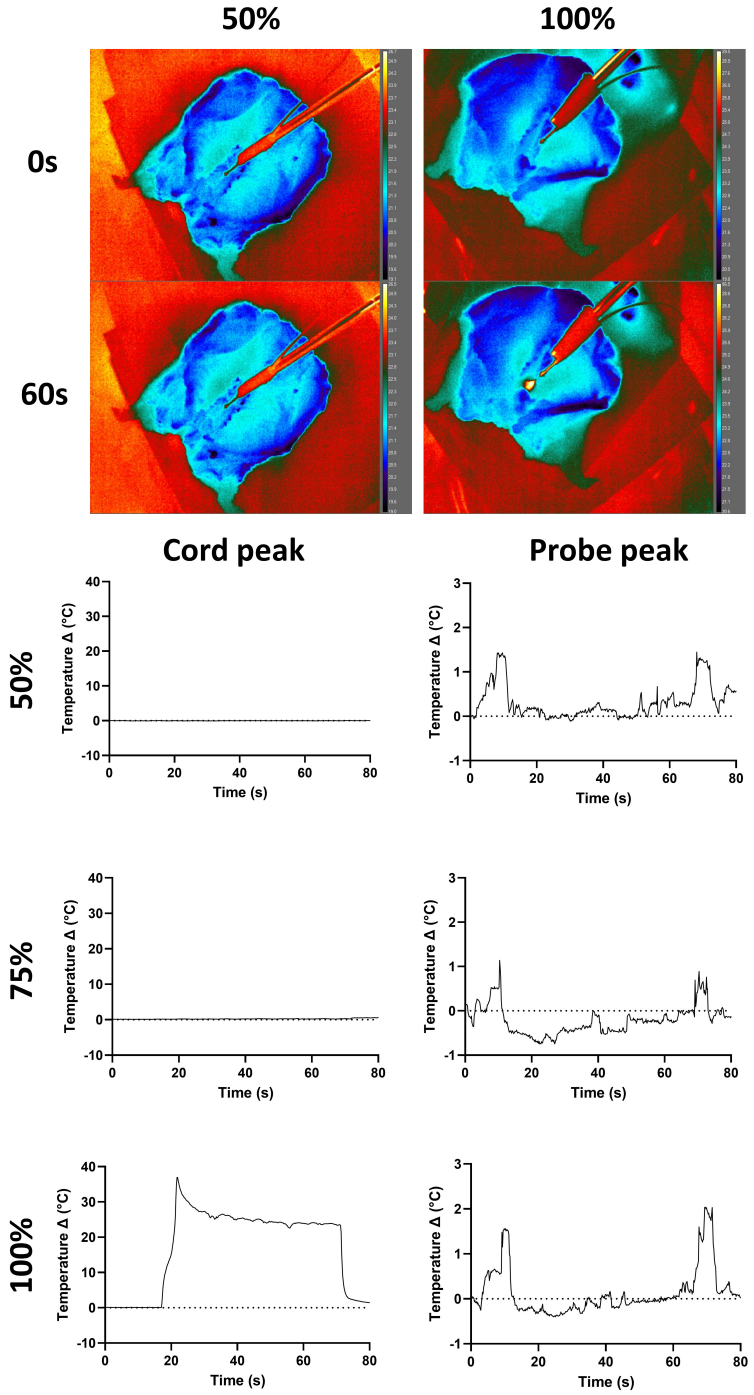


Figure 3.23: Caption on next page

Figure 3.23: Safe levels of tissue heating are demonstrated by thermal imaging at 50-75% power output settings delivered directly to cadaveric spinal cord via implant. 100% power output resulted in unacceptable levels of tissue heating. TOP panel: OFF (0 s) and ON (60 s) temperatures for 50% and 100% power output settings, in an implant placed directly over the ventral aspect of the thoracic spinal cord after anterior dissection and corpectomy. Settings are given in the rows: 50%, 75% and 100%. "Cord peak" demonstrates the peak temperature value in a region of interest (ROI) circumscribed on the spinal cord tissue immediately beneath the probe. The "Probe peak" describes the peak temperature value in an ROI containing the probe length, tip and ferrule. Temperature given as relative change to baseline temperature of non-irradiated animal tissue within the field of view (FOV) of the thermal camera. Results given over time with an 80 second protocol: 10 seconds OFF, 60 seconds ON, 10 seconds OFF. n = 3.

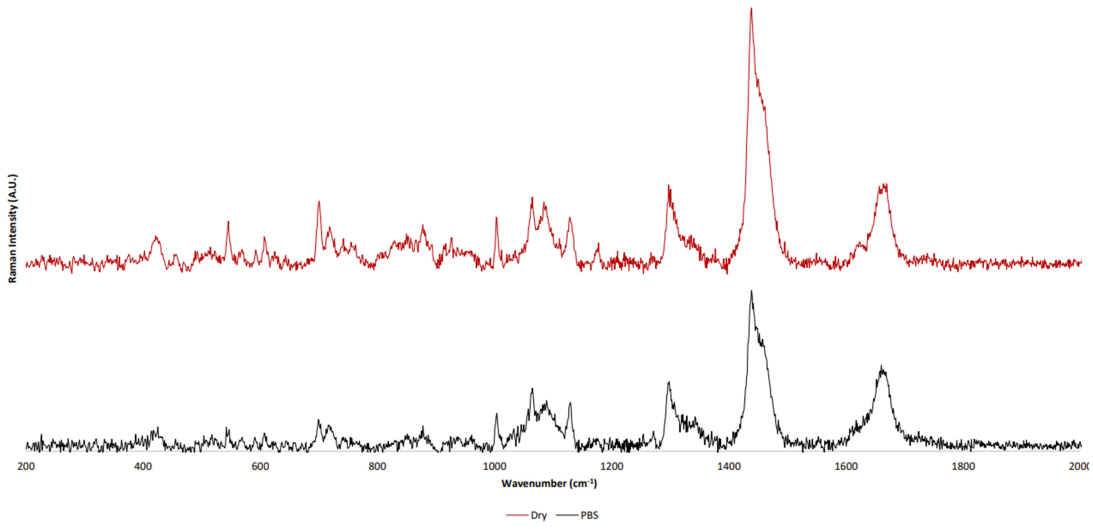


Figure 3.24: Raman spectroscopy of the *ex vivo, post mortem* rat spinal cord. Spectral acquisition settings: 785 nm, x20, static 680 and 1610 centre, 50% (42.55 mW, 1 s exposure time, 10 accumulations. Comparison of "dry" specimen (immediately post-dissection, specimen was kept wrapped in aluminium foil for approximately 30 min, on ice); and "PBS" specimen (immediately post-dissection, specimen was submerged in PBS at 4 °C for approximately 30 min). Dissection and specimen preparation performed by the author; spectral acquisition performed by collaborator.

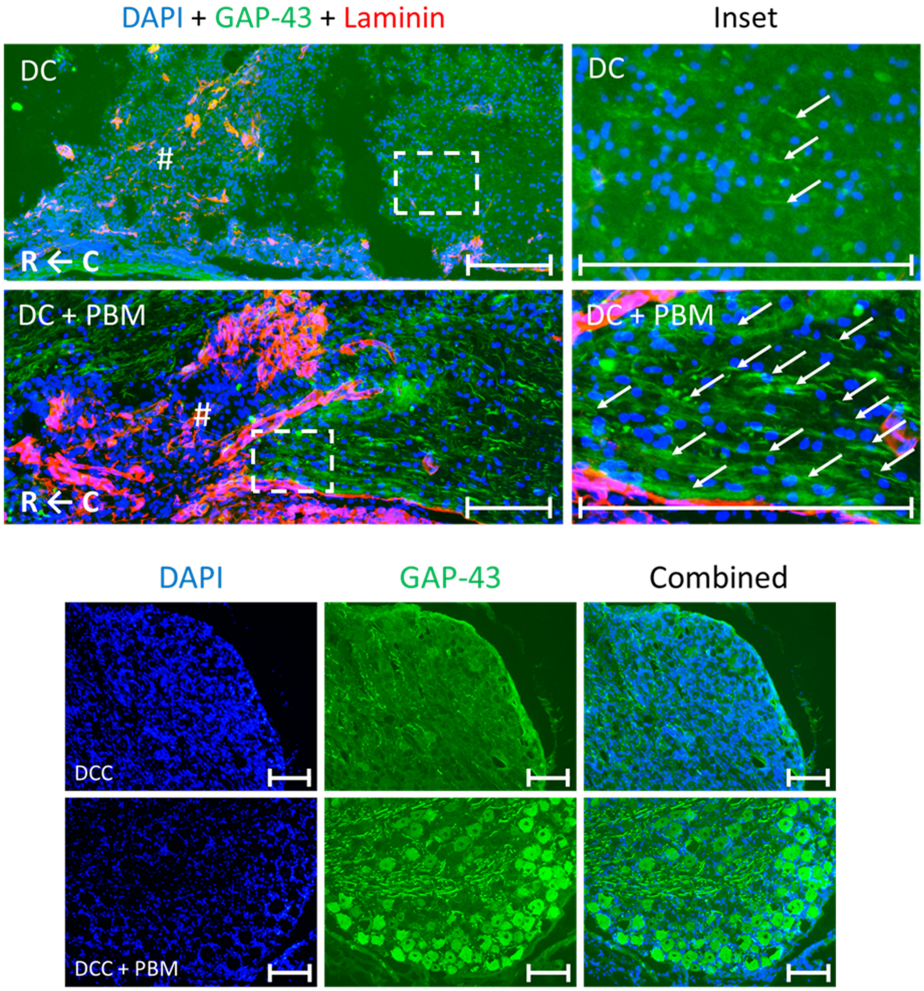


Figure 3.25: Top: Increased expression of GAP43 $^{+ve}$ axons within the dorsal column after exposure to PBM therapy versus vehicle treated control at day 6 post-injury (from previous experiments and exposed to long-term storage). n = 2 per group. DC = dorsal column crush; (transcutaneous 24.4 mW/cm^2 (at lesion site), 1 min per day, 6 day treatment course). R = rostral, C = caudal, # indicates lesion site. Bottom: Increased expression of GAP43 $^+$ DRGN after thoracic exposure to transcutaneous PBM therapy versus untreated control at day 6 post-injury. n = 2 per group. All scale bars = 150 μm.

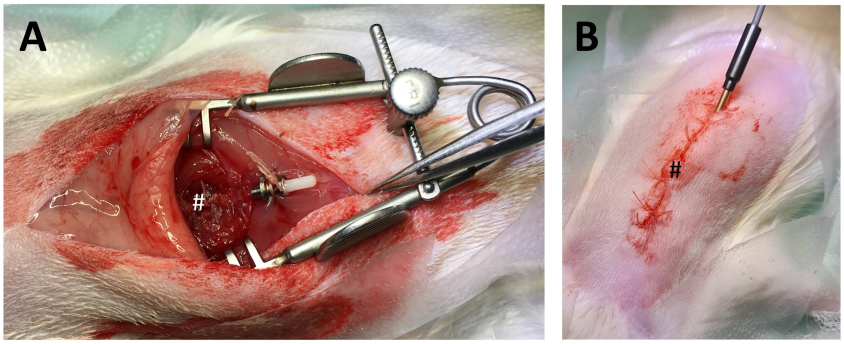


Figure 3.26: A. Photograph of implantation of device, secured to the closed dorsal musculature prior to skin closure. B. Photograph depicting implantable PBM (iPBM) system delivering therapy immediately post-procedure. # = lesion epicentre.

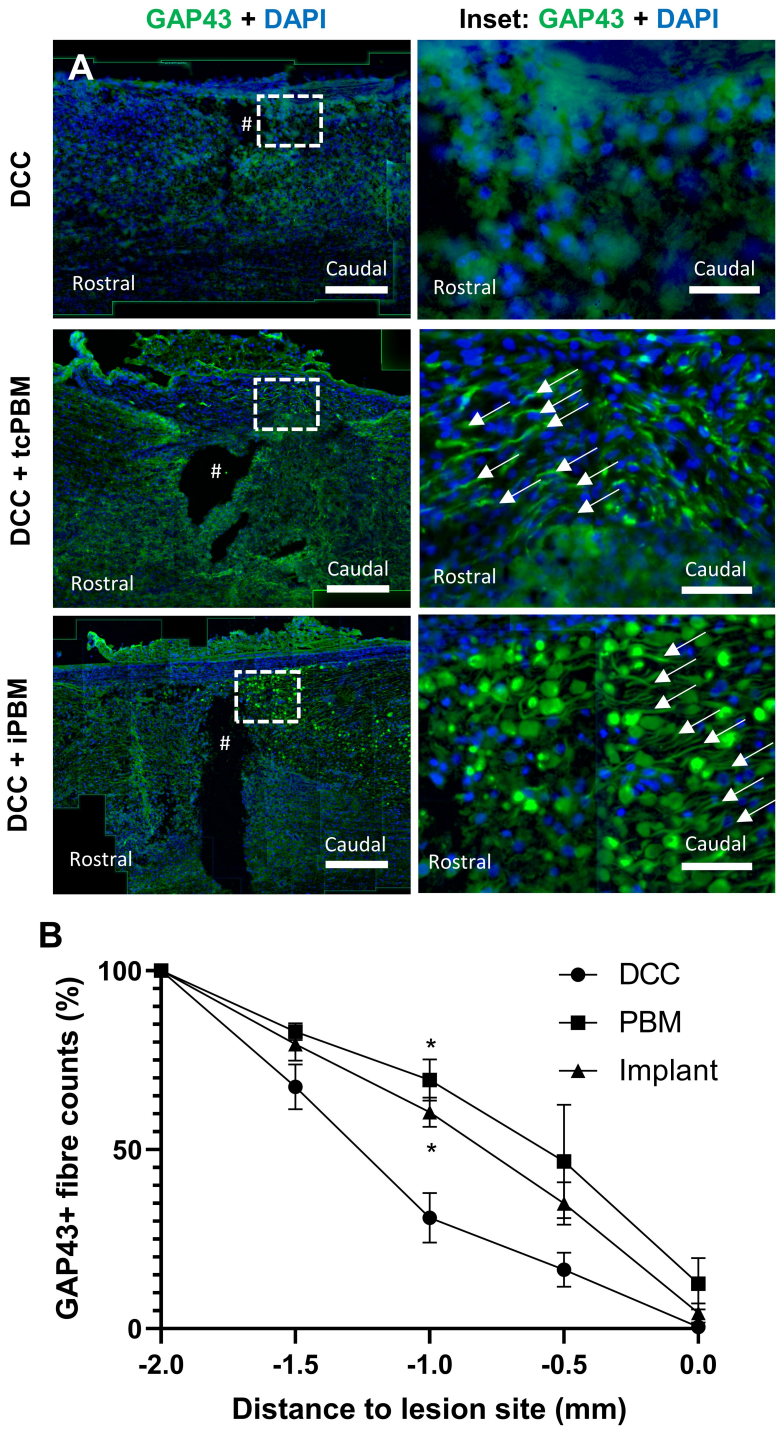


Figure 3.27: PBM delivered by transcutaneous application (tcPBM) and implanted device (iPBM) promote early axonal regeneration. 660 nm tcPBM and iPBM were delivered daily for 1 min at 24.4 mW/cm^2 at the level of the injury site. Injury controls received ambient light transcutaneously for 1 min per day. A: immunohistochemistry of sagittal frozen sections through the injury site (labelled #). n = 4 per group, scale bar = 500 μm, inset scale bar = 100 μm. B. Percentage of GAP43 positive fibre counts approaching the epicentre of the injury site from rostral to caudal. $*$ = $p < 0.05$, error bars denote SEM.

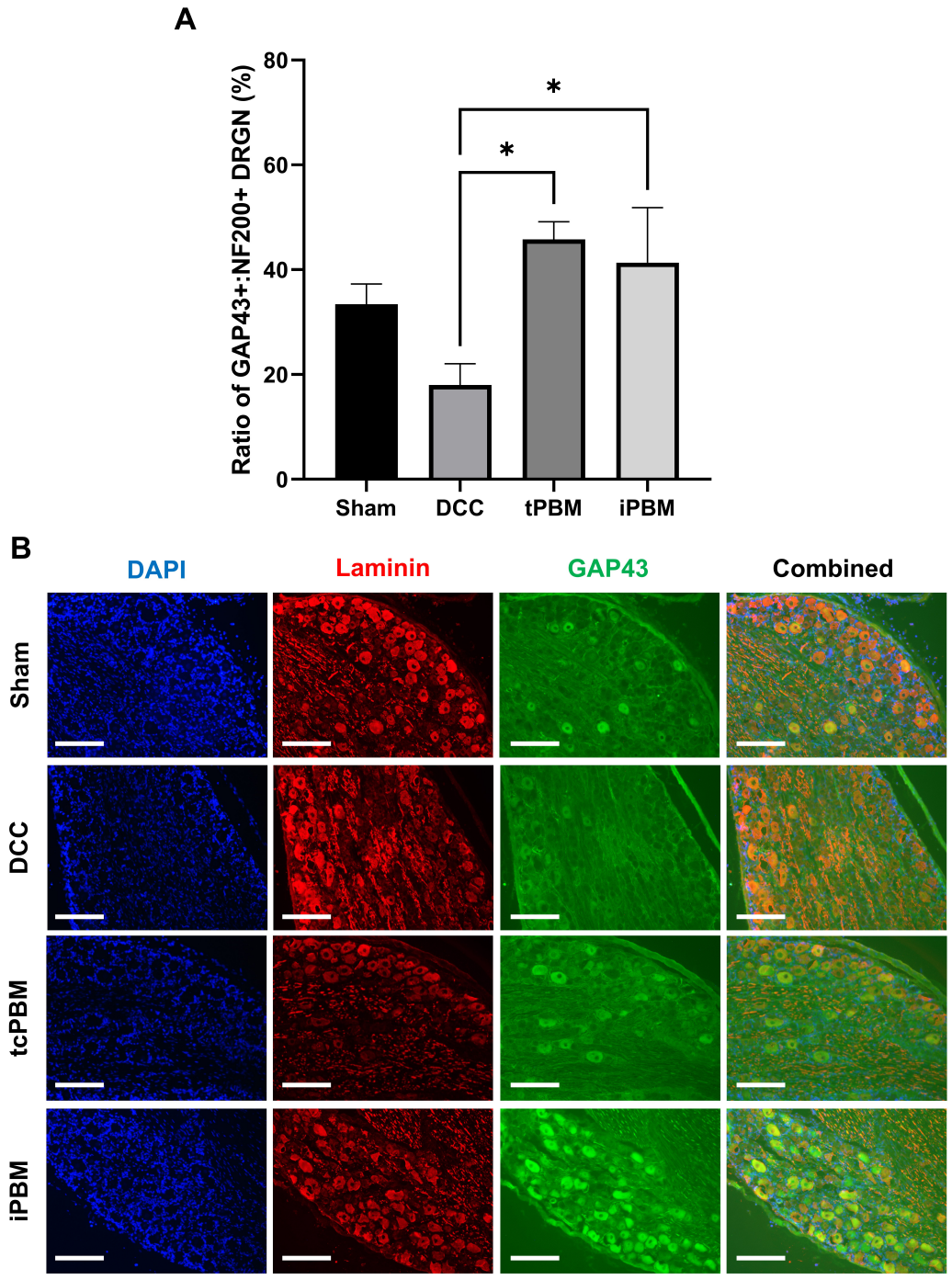


Figure 3.28: PBM delivered by transcutaneous (tcPBM) and implanted device (iPBM) promote early upregulation of GAP43 expression within dorsal root ganglion neurons. 660 nm tcPBM and iPBM were delivered daily for 1 min at 24.4 mW/cm^2 at the level of the injury site. Injury controls received ambient light transcutaneously for 1 min per day, with termination 3 days post-injury. A: Percentage of GAP43 positive DRGN (% of NF-200 positive cells co-expressing GAP43). n = 4 per group, $*$ = $p < 0.05$, error bars denote SEM. B. Representative immunofluorescence images from each group at 10x magnification, from which results in A are taken. n = 4 per group. Scale bar = 200 μm.

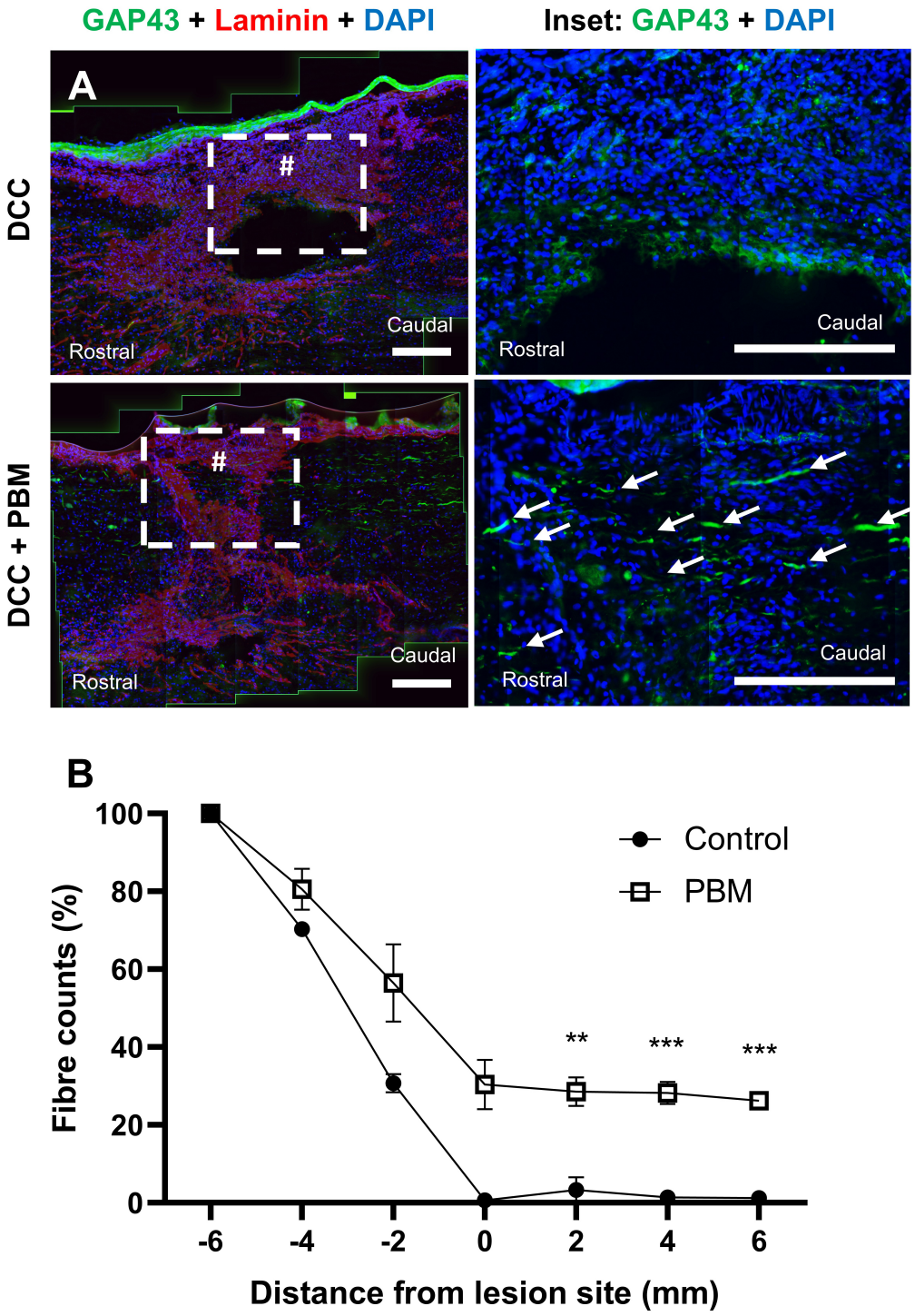


Figure 3.29: GAP43$^+$ axons traverse the glial scar 6 weeks post-SCI with tcPBM therapy. A: Immunofluorescence for GAP43 (green), laminin (red) and DAPI (blue) of T8 lesion site (taken from middle 15 μm parasagittal section) for injured control with sham therapy (DCC) and injury + tcPBM (DCC + PBM). # = lesion site, ↙ = GAP43$^+$ axon, scale bar = 500 μm. B: Fibre counts from 4 mm caudal to 6 mm rostral to centre of SCI lesion site in control (DCC and sham therapy) and injured specimens treated with tcPBM. Error bars denote SEM, n = 4 per group, $**$ = $p < 0.01$; $***$ = $p < 0.001$.

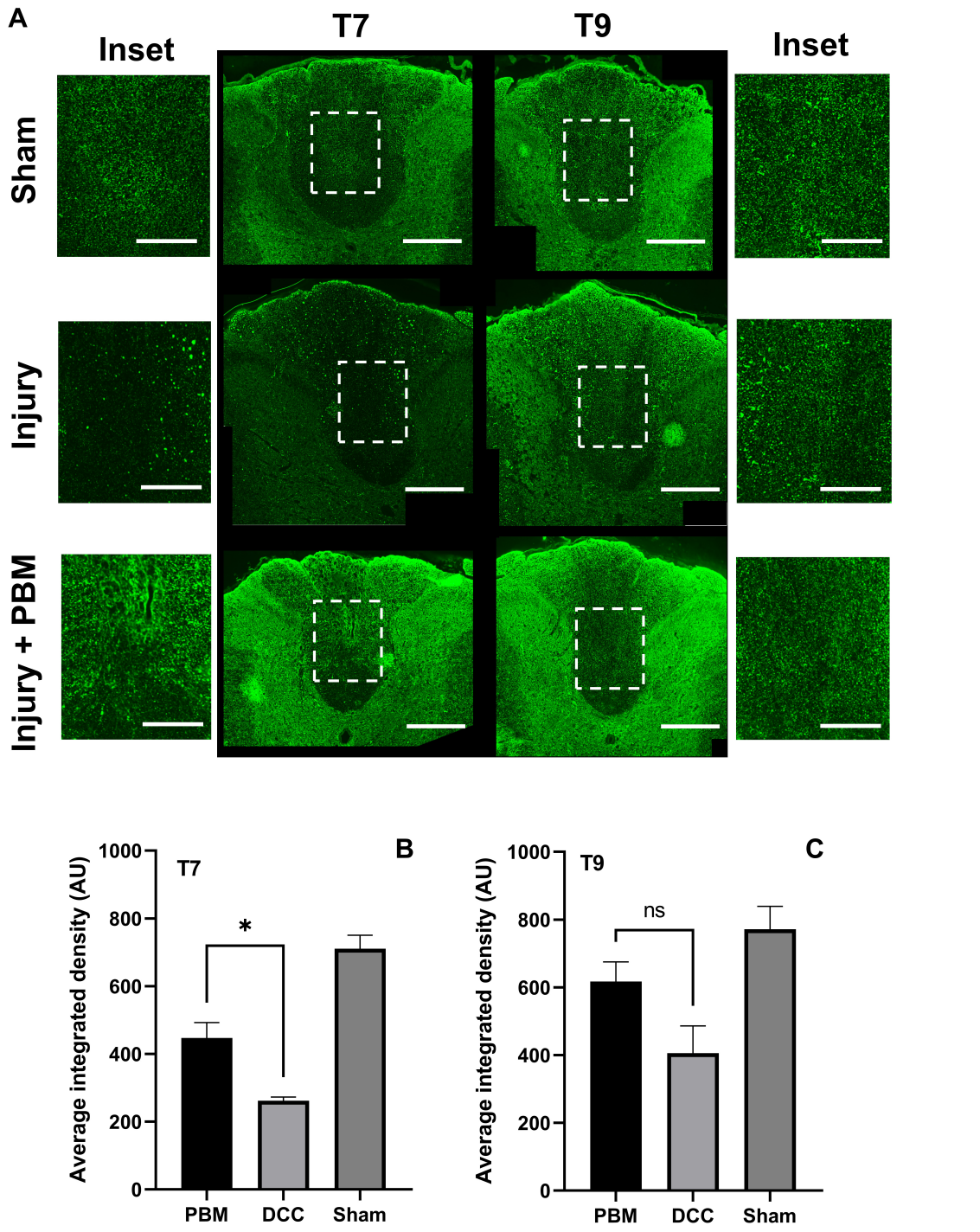


Figure 3.30: tcPBM increases NF-200 immunoreactivity rostral to the lesion site. A: Axial sections through T7 (rostral to lesion site) and T9 (caudal to lesion site) underwent immunostaining for NF-200. B: Intensity of immunofluorescence in the entire dorsal fasciculus at T7 and C: T9 were analysed and compared between the three groups. PBM = transcutaneous photobiomodulation, DCC = injury (sham therapy control). n = 4 per group. Sham = sham surgery (no injury). Scale bar 200 μm, inset scale bar 100 μm, $*$ $p < 0.05$, ns = non-significant ($p > 0.05$). AU = arbitrary units.

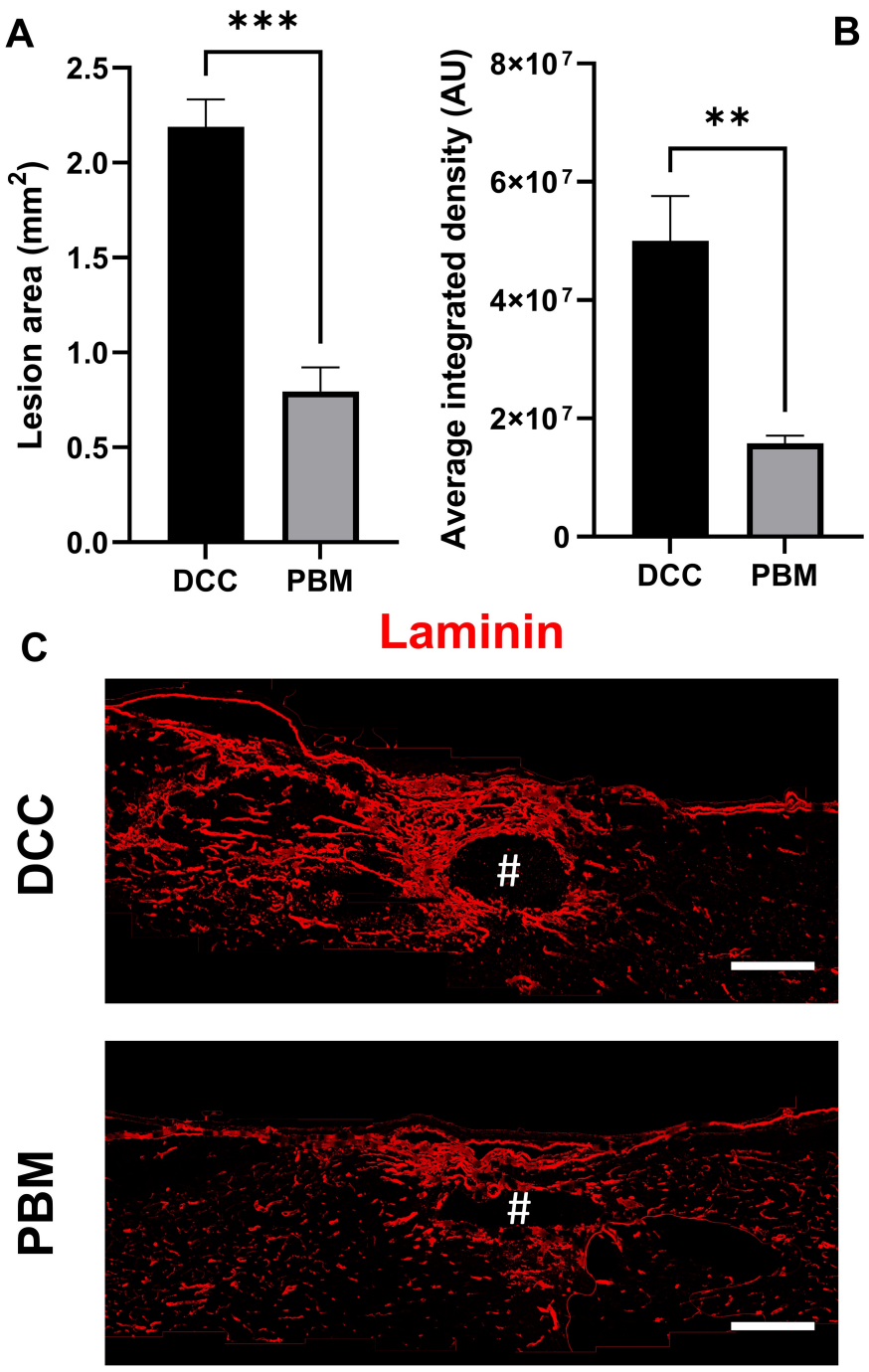


Figure 3.31: tcPBM is associated with reduced glial scar size and reduced laminin immunoreactivity. A: Sagittal lesion area through the middle of the lesion site was significantly reduced in specimens exposed to tcPBM. B: tcPBM was associated with lower immunoreactivity after anti-laminin staining and immunofluorescence. C: representative images from DCC (injury only with sham therapy) and PBM (injury + transcutaneous photobiomodulation) therapy. ** = $p < 0.01$; *** = $p < 0.001$. Scale bars = 500 μm. # = lesion epicentre.

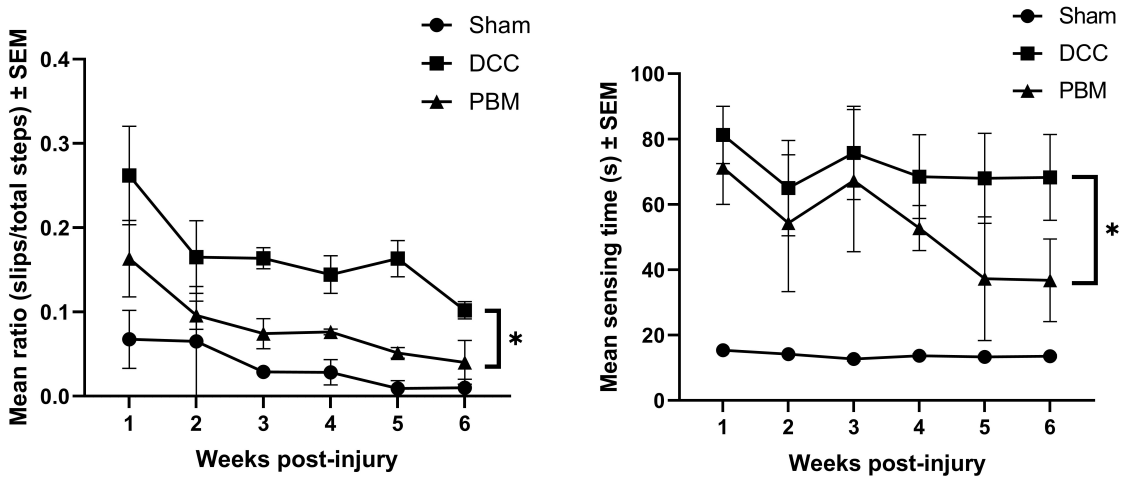


Figure 3.32: Functional recovery at 6 weeks post-injury improved with tcPBM. A: Horizontal ladder crossing test, and B: mean sensing time for the hindpaw tape sensing and removal test. * = $p < 0.05$. Error bars denote SEM. DCC = dorsal column crush injury.

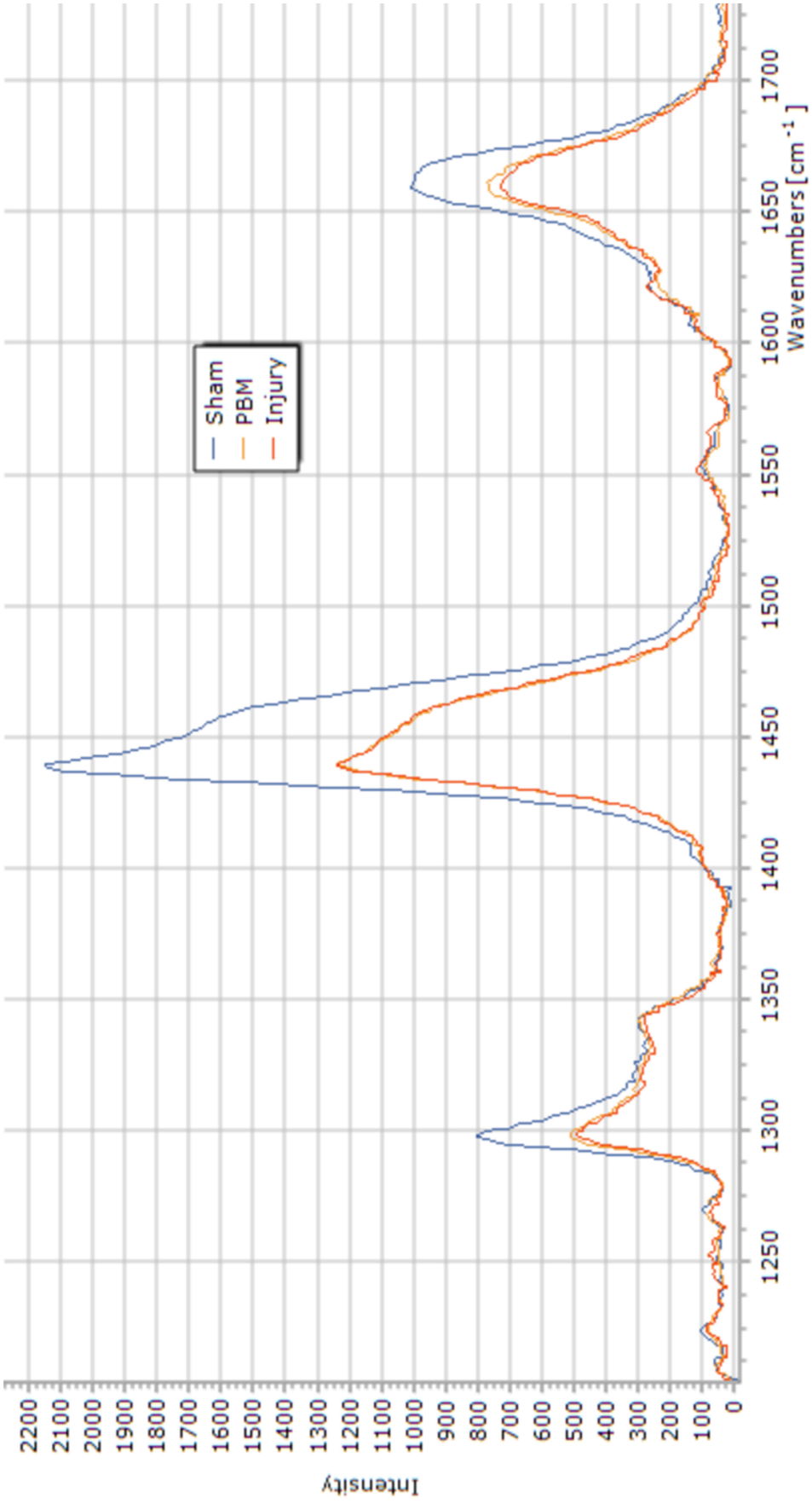


Figure 3.33: *Post mortem* Raman spectra from T8 lesion site demonstrates clear spectral changes associated with injury. Spectral acquisition commenced 30 min after confirmation of death. Spectra from n = 4 per group averaged and presented with baseline correction and without normalisation.

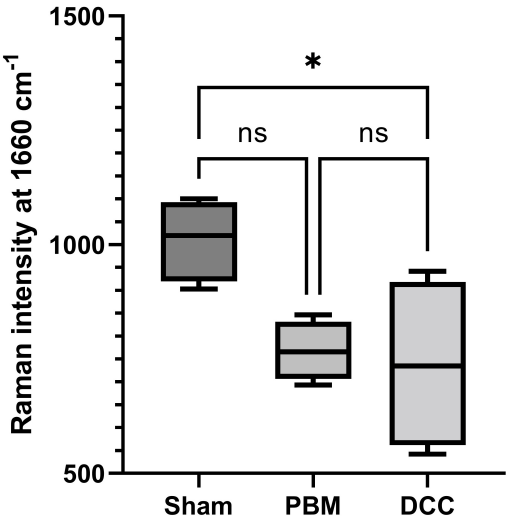


Figure 3.34: Raman spectroscopy of SCI site. *Post mortem* Raman spectra from T8 lesion site demonstrates clear spectral changes associated with injury. Spectral acquisition within 30 min of death. Spectra from n = 4 per group averaged and presented without normalisation. Significant difference in 1660 cm^{-1} peak identified between sham (laminectomy only) group and injury group (DCC only). No significant difference identified between injury group (DCC only) and tcPBM group. $*$ = $p < 0.05$; ns = not significant.

3.4 Discussion

3.4.1 Dosing

This chapter's work has demonstrated that 660 nm PBM significantly improves functional and histological outcomes after SCI, with improvements in sensory and locomotor recovery, correlating with increased axonal regeneration and reduced glial scarring. Furthermore, this chapter demonstrates that early post-injury activation of RAP (GAP43) can be achieved through direct delivery of PBM via a novel implant method for small mammal PBM therapy, with equivalent early beneficial effects to tcPBM. Through rigorous dosimetry in cadaveric studies, this work has validated that these two methods deliver equivalent PBM doses to the SCI site, supporting the hypothesis that iPBM achieves similar therapeutic benefits to tcPBM.

In vivo dose selection considered several factors which were likely to compromise PBM delivery efficacy and constitute a wide variety of possible factors which could not be adequately modelled *ex vivo*, and for which there is no informing literature. For example, during cadaveric modelling, there was considerable variation in transmission dependent on probe positioning or orientation. The above values were measured with the probe optimally placed, which would not be a guarantee post-implantation after animal movement. Furthermore, incomplete coupling at the ferrule connector could also compromise delivery, and this eventuality was deemed more likely when attaching the source in the *in vivo* setting. Also, post-operative bleeding *in vivo* would attenuate PBM transmission due to the high attenuation of 660 nm light caused by haemoglobin.

Further factors were postulated which may also attenuate transcutaneous transmission, such as animal weight gain during a 7-day treatment regimen, and the effect of oxygenated haemoglobin *in vivo*. Of the profiled dose delivery settings (13.11, 24.42 and 45.30 mW/cm^2), 24.42 mW/cm^2 was selected, in order to sufficiently account for these potential losses. Selection of a higher average irradiance value was precluded by rising peak irradiance values. Previous work has shown a biphasic response to PBM[168] and thus it is critical to deliver the correct irradiance at the target site within the effective window, minimising areas of over- or under-exposure. 24.42 mW/cm^2 allows the optimal volume of tissue to be irradiated with irradiances within the therapeutic window and also with minimal localised heating.

In further support of this selection, during *in vitro* modelling, greater consistency and efficacy was observed in dosing at higher (22 and 36 mW/cm^2) than lower (4 mW/cm^2) average irradiance values with respect to the optimum (11 mW/cm^2). Therefore, to account for variability of delivery in cadaveric modelling for both modalities, 24.42 mW/cm^2 was deemed an appropriate compromise to ensure dose delivery within the effective window on each occasion and across individuals. Besides, had the full 24.42 mW/cm^2 been transmitted *in vivo*, this dose is still within the effective range determined by the *in vitro* experiments above.

Whilst delivery of average irradiance values of 24.42 mW/cm^2 at the level of the spinal cord is feasible in rodents, the thickness of overlying tissue in humans renders this impossible without

causing destruction of surface tissue through the use of high transcutaneous power outputs. The implication of this is that iPBM is a more readily translatable method of application of effective doses of PBM to deep anatomical structures, such as the spinal cord. Demonstration of non-inferior efficacy to tcPBM supports onward development of implantable devices to achieve these proven therapeutic levels of PBM at the plane of the target tissue.

This chapter has used an *in vitro* model to explore a broad range of dosing regimens to identify optimal parameters of PBM exposure *in vitro* for survival and neuroregeneration. This was based first on the optimal average irradiance when delivered for 1 min (11 mW/cm^2), which was then optimised based on duration of exposure. It is notable however that, inherent to the irradiance system used, higher average irradiance settings also resulted in a shift in peak wavelength, which may be of importance in selecting a true optimal average irradiance/wavelength though could not be evaluated using this methodology. 1 min was selected initially as this had been previously most successful neuroprotective duration in the *in vitro* model of TBI described in Appendix B.[238] To draw further conclusions on the relative benefits of invasive vs transcutaneous PBM, an exploration on reciprocity of average irradiance/duration is advocated.

This model is not suitable for extensive periods of very low average irradiance exposures (for example 0.11 mW/cm^2) for 100 min, for comparison with the same fluence as 11 mW/cm^2 for 1 min) due to the necessity of limiting exposure time of cultured cells to the normal atmosphere outside the incubator. Development of a system able to irradiate cells during incubation would be valuable for exploring this further. Similarly, exposure to average irradiance values of >131 mW/cm^2 was not achievable using the same LED array, and transcutaneous exposure to such high average irradiance values at spinal cord level produced unacceptable skin heating in the cadaveric modelling. The concept of reciprocity is of translational importance as lower average irradiance values with extended exposure durations are more readily achievable through transcutaneous application modalities. However, given the multitude of known and unknown factors that produce the positive biological effect of PBM, beyond a simple photochemical reaction, it is possible that PBM dosing in *in vivo* models and clinical application would not exhibit a clear reciprocal relationship.

The dose regimen used in the *in vivo* study described here are within the broad range of effective doses described in the previous literature.[303–310] Such broad dosing regimens are problematic for the field of PBM, and development and application of effective technology. Validation of effect is further complicated by variability in transmission through tissue dependent on a broad range of factors, such as superficial tissue thickness and pigmentation. As described previously, accurate measurement and reporting are required.[181] Further to this, implantable devices with better line of sight to the injured tissue provides much greater opportunity for accurate and standardised dose delivery which is proposed to produce greater effects.

Duration of the course of therapy have also varied significantly in previous work, ranging from 3-21 days amongst those demonstrating therapeutic effect. It is notable that Giacci and colleagues found no positive effect when delivering therapy daily for 28 days post-injury.[250] In relation to work in applying PBM after TBI, it has also been noted that longer courses of treatment are less effective.[238] This effect may be attributable to the therapeutic benefit of PBM mitigating neuroinflammation, which is favourable only within the acute and sub-acute phases of injury. This study utilised 1.44 J/cm^2, delivered with an average irradiance of 24 mW/cm^2 for 60 s per day, with a 7 day course commenced 15 min post-injury (3 days only at 3 dpi endpoint).

3.4.2 Mechanism

In vitro experiments described here involve the direct application of PBM to the DRGN cell body, alongside its dendrites and co-cultured non-neuronal cells. The suppression of non-neuronal cell proliferation with 5-FDU mitigated survival of all treatment groups, including those cultured with serum, and the effect size of PBM was comparable with and without 5-FDU. As such, it is not possible to draw conclusions based on this data on the relative contribution of direct neuronal or indirect non-neuronal mechanisms.

In addition to adding confirmatory evidence to the literature of the therapeutic benefit of PBM in promoting neuroregeneration after SCI, this work highlights several important mechanistic insights for PBM. These are: (1) the mechanism of action of PBM is not dependent on systemic activation triggered by PBM's interaction with superficial tissues, based on equivalent expression

of RAP whether delivered directly to the injured spinal cord or through the skin; (2) this activation is independent of temperature change, based on the cadaveric confirmation of zero discernible spinal cord temperature increase with treatment; and (3) PBM dosing is effective within a short range of average irradiances and exposure durations, losing its effect at the extremes.

Through the core understood mechanism of PBM and its interaction with CCO, PBM is able to affect all cell types which are metabolically active with mitochondria. For neurological injury, this includes neurons, glia (microglia, astrocytes, oligodendrocytes) as well as local leucocytes, such as macrophages, present either via migration into the injury site through the damaged blood-spinal cord barrier or present in nearby capillaries. For transcutaneous applications of PBM, this will also include cell types at all transient anatomical tissues (skin, muscle/fascia, remnant lamina, blood cells within overlying/adjacent vasculature). Most notably from *in vivo* experiments described here, by targeting the injury site through both iPBM and tcPBM methods there was no significant irradiance reaching the cell body of the DRGN (located approximately 3 cm caudal in the adult rat), the axons of which undergoing damage in this injury paradigm. Together, it is not possible to draw firm conclusions on whether the predominant mechanism is related to either the effects on axonal mitochondria or non-neuronal cells creating a more permissive environment for regeneration post-injury; or, as the author advocates, both.

In the wider literature, neuroinflammation is increasingly recognised as a key mediator of PBM in neurotrauma. Recent work has identified the effect of PBM on reducing polarisation to the neurotoxic M1 phenotype for macrophages/microglia,[309] (by inhibition of STAT3 expression via increased expression of miR-330-5p; and activity in the Notch1/HIF1A/NFκB pathway) and the A1 phenotype for astrocytes.[307,308] There has also been recent identification of the effect of PBM reducing neuronal mitochondrial fission imbalance after SCI. Together, these further support a mixed effect of PBM on both neuronal and non-neuronal cell populations.

3.4.3 Delivery

This is the first work to demonstrate and validate a methodology for application of PBM via an implantable fibre optic cannula in a rodent model of SCI, with matched doses via transcutaneous

delivery at a tissular level. Few previous works have used direct-to-cord methods of PBM application: Ando and colleagues (2013) applied PBM directly via daily surgery to access the spinal cord for five consecutive days after injury in their rat model, demonstrating improvement in functional outcomes.[295] Two studies from the Wang group have used a direct diffusion fibre orientated over the spinal cord in a piglet model, though the outcome measures used in these studies sought principally to demonstrate the safety of delivering 200-300 mW outputs directly over the cord.[314,338] Implantation of a biocompatible fibre in a murine model has also demonstrated to be effective for promoting repair, though no comparison to transcutaneous administration was explored.[334]

The validation of the comparative efficacy of implantable vs transcutaneous administration is of translational relevance, particularly given the supportive dosimetry cadaveric modelling to demonstrate dosing equivalence. Direct application methods of PBM delivery have been more extensively described in the context of models of Parkinson's disease,[286,312,313] where they have been demonstrated to be safe and effective. Further work in this area has also demonstrated that some efficacy in preventing neurodegeneration in Parkinson's disease can be achieved through remote administration of PBM (to a remote anatomical region to the pathological area, i.e. the femur in CNS degeneration).[204,205,265] Whilst direct application methods have produced most benefit, the efficacy of remote application raises the possibility of a systemic activation of advantageous biological processes which may be involved in the efficacy of transcutaneous application.[204,205,265,286,312,313]

Here, spinal cord level average irradiance was controlled between groups, though the tcPBM arm inevitably received greater overall exposure to PBM due to transmittance through (and absorbance by) superficial tissues (skin, muscle, vasculature, bone). This may explain the marginal (and statistically non-significant) differences in early RAP activation between tcPBM and iPBM, though this could equally be attributed to minor deleterious or pro-inflammatory effects of an indwelling implant. Inclusion of remote application of PBM as a comparative treatment group in future studies may advance the understanding of the contribution of activation of systemic processes in the therapeutic benefits of PBM in SCI.

Whilst some similarities exist between neurodegenerative conditions and the degenerative pathophysiological phenomena of the injured CNS, it is important to validate and understand the relative benefits of differing delivery methods for individual conditions. This is of particular relevance in PBM, where the overall mechanism of the effect is not fully defined, with even further limitations in the understanding of the therapeutic effects of abscopal (indirect/remote) administration.[204,286,312,313]

3.4.4 Raman spectroscopy

Significant differences in 1660 cm^{-1} peak intensity between sham and injury groups after SCI (Fig. 3.34) suggest a dynamic shift of lipid metabolism after SCI, and may represent a method for monitoring such physiological changes post-injury. Whilst these peaks encompass a range of possible candidate lipids, cardiolipin has previously been proposed as a dynamic lipid which is detectable in these regions.[345] The reactivity of cardiolipin in response to neurological trauma, and its role in mitochondrial function, add support to this hypothesis.

On examination of merged spectra, shifts are noted between treatment and injury groups (Fig. 3.33), though these did not reach statistical significance of peak intensities in the 1660 cm^{-1} region. Previous work in SCI has identified a range of changes over several time points following 810 nm PBM delivery to the injured spinal cord using multivariate analysis.[346] Zhang and colleagues identified significant shifts in lipid peaks (1300, 1450, 1660 cm^{-1}) over a 14 day treatment protocol as well as reductions in the 500 cm^{-1} peak which the authors correlate with reduced CSPG deposition. This suggests that an effect is present, and that the single 3 dpi end point and quantitative analysis was insufficient to detect more subtle differences described in this previous work.[v]

[v] Additional work is ongoing by collaborators to utilise machine learning analysis[347] to differentiate spectra between these treatment groups, and has not been duplicated for inclusion in this thesis.

3.4.5 Limitations

Whilst extensive in its scope, the breadth of dosing parameters used in the optimisation phase (*in vitro*) is not comprehensive, and as described above has not explored the concept of reciprocity. Further studies are required to determine the optimum dose regimen from a broader range of tested parameters. Similarly, this study has utilised 660 nm PBM as the only wavelength. Given the recognised efficacy of 810 nm PBM from other studies, the author advocates exploration of the two wavelengths in comparison and in combination in future work. Little is yet known of the differing mechanisms (if any) of effect between these two therapeutic wavelengths, and their comparison may shed light on any relationship which may exist between them and add important evidence to the development of optimal PBM parameters for SCI.

Due to practical limitations of *in vivo* modelling using implants, the duration of studies involving implanted devices were three days. As such the support for the hypothesis that implantable PBM is equivalent in efficacy to transcutaneous PBM is dependent on the inference that equivalence in early RAP activation would result in equivalence in the six week functional recovery observed in the transcutaneous group versus sham therapy. It was not possible to continue therapy or the experiment beyond this 3 dpi stage with an implant without significant compromise to animal welfare (e.g. through single animal housing, Elizabethan collar use, or repeat surgery) which was not deemed ethical or appropriate to instigate based on the strong evidence for equivalence achieved through these shorter duration experiments.

The effect of the implant itself has not been studied directly, and there may have been an immune response to the presence of the indwelling probe. With extended duration, this may result in a localised fibrotic reaction which may mitigate the potential for benefit. Equally, it is possible that the presence of the probe alone accounts for some of the therapeutic benefit of the implant, independently from the PBM treatment, which has not been studied through use of a group receiving an implant without PBM application. This should be the subject of future research. Similarly, concerns about animal welfare precluded a longer duration of study with the implant in situ, and subsequent work should include longer timepoints. Furthermore, utilising *ex vivo* cadaveric models inherently limits the accuracy of dosimetry measurements, as the *in*

vivo setting will differ considerably due to a number of effects including those of blood flow, oxygenated haemoglobin, and progressive fibrosis. *In vivo* measurements are the optimal to ensure accuracy, though this was not technically achievable in this injury model.

Average time to delivery of PBM post-injury was 15 min, though owing to the added step of implantation of a device prior to dose delivery, this resulted in a longer period between injury and first-treatment in the iPBM group. This may therefore have resulted in an underestimation of the beneficial effects of iPBM, as it is well recognised that time-to-first-treatment is an important variable in the efficacy of PBM in CNS injury.[240] The decision to implant and deliver the first PBM dose immediately after wound closure and within minutes post-injury was to optimise efficacy based on the hypothesis that PBM mitigates the early damaging effects of neuroinflammation. It is currently not known whether these parameters for PBM delivery are effective if commenced at a later time point. Discerning a therapeutic window within which therapy must be commenced to achieve efficacy will be the subject of further study to ensure translational relevance, given that timing of surgical intervention in SCI is typically at least 4 h post-injury, and may be up to 24/48 h. Efficacy of PBM in reducing neuropathic pain have proven effective after sciatic nerve injury when commencing therapy one day[348] and one week[349] post-injury, though the mechanisms involved differ considerably. Another possibility for applications in sub-acute/chronic settings is utilizing PBM to augment other therapeutic interventions. A growing area is the use of PBM to promote functional differentiation of stem cells toward neural repair, which has proven successful in pre-clinical testing for SCI and other neural injury models.[350–352]

Despite extensive dosimetry, it is inevitable that to some extent the dose reaching the spinal cord varied. Several factors are likely to have influenced this: mild variations in probe positioning between treatments and animals; variance between device optical coupling (particularly post-implantation), delivery efficiency and diffusion efficacy; progressive degradation of coupling devices over extensive use. These variables are inherent to the use of optical sources *in vivo* and every attempt was made for mitigation, including regular cleaning of optical interfaces, lasers checks and maintenance, and post-experiment quality control of implanted devices.

3.5 Conclusion

This study has developed a method for PBM dose optimisation for the neuroprotection of sensory neurons and a novel approach for the direct application of PBM to the spinal cord, with dosimetry validation of this and transcutaneous PBM in a cadaveric model. Comparison of these two application methods has demonstrated equivalence of PBM-mediated activation of RAP after SCI through invasive or non-invasive delivery paradigms, which correlates with significant improvements in functional recovery, axonal regeneration and lesion size after SCI in a rat model. Administration of PBM via direct application to injured tissue should be further explored as a translational approach to developing future PBM-based treatments for SCI.

Chapter 4

INVESTIGATION OF PHOTOBIOMODULATION AND RAMAN SPECTROSCOPY IN TRAUMATIC BRAIN INJURY

This chapter investigates the efficacy of PBM and the utility of RS feedback using an experimental model of TBI.

4.1 Introduction

To build upon the work described in Chapter 3, this chapter investigates the concept of using PBM with RS monitoring in TBI. Whilst there are significant commonalities in the mechanisms of secondary injury in TBI and SCI, key contrasts in their pathophysiology must be considered for the development of this intervention, with the pathophysiological events following TBI summarised in Figure 4.1. Most pertinent to the development of an implantable therapeutic device is the diffusivity of injury patterns: SCI typically affects a discrete area of spinal cord, whereas it is rare for a purely focal injury to occur in the brain.

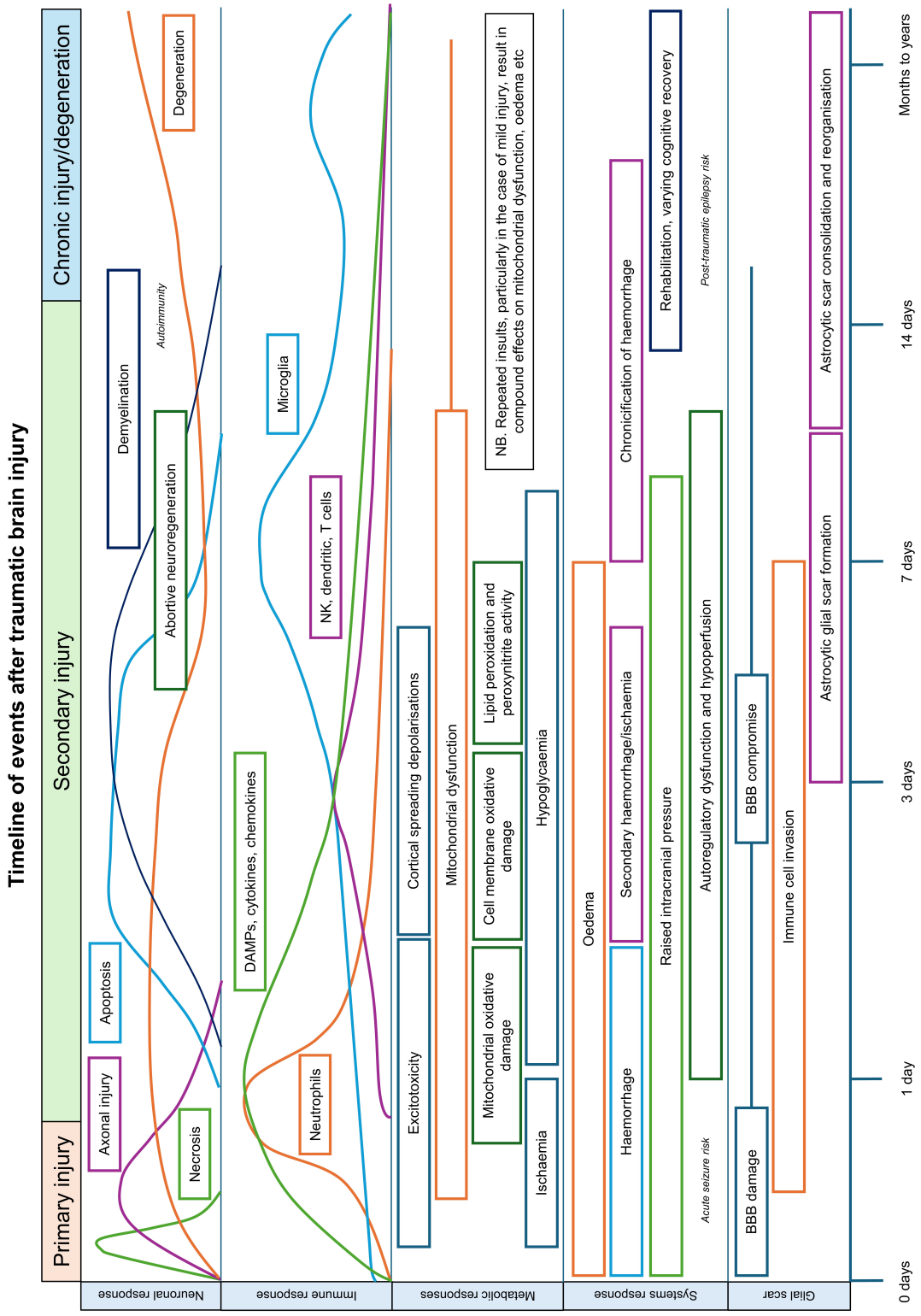


Figure 4.1: Schematic representation of a timeline of pathophysiology in TBI. BBB = blood-brain barrier; NK = natural killer (cells). Combined from multiple sources.[66, 298, 353–355]

As such, there is a need to investigate the efficacy of focal PBM application in diffuse TBI, and to investigate the effectiveness of RS in detecting biomarkers of a beneficial therapeutic response.

4.1.1 Selection of a suitable model of traumatic brain injury

In vitro models

In vitro models are advantageous in some respects to the study of trauma and regeneration, offering high reproducibility and throughput and relatively low cost. Specific cell types may be studied in isolation, or in combination through 2D/3D co-culture/scaffold/organoid models. Use of organotypic tissue slice cultures also offer an *in vitro* model which mimics the composition and cell:cell interactions of their expected state *in vivo*.[356,357] Application of traumatic injury modelling to these culture paradigms allows precise study of the specific effects of mechanical forces (or their ensuing sequelae). Common methodologies to model traumatic injury *in vitro* are given below:

- Compression: direct impact via weight drop or pendular acceleration;[356,357]
- Stretch: distortion of a culture membrane or other substrate, transmitted to the adhering cells or tissue. A multitude of variables are possible (uniaxial stretch; bi-axial stretch; shear etc.);[356,357]
- Transection: scratching or other sharp distortion to cells/tissue, usually perpendicular to the orientation of axons;[356,357]
- Static pressure: high pressure chamber to replicate conditions of raised ICP;[358]
- Chemical: application of adverse biochemical conditions to simulate the post-injury microenvironment, e.g. oxidative stress, oxygen-glucose deprivation, serum withdrawal, excitotoxicity etc.[356,357]

Whilst these methods offer some advantages, observations of cell isolates or co-culture constructs *in vitro* may be markedly different from those observed *in vivo*. As well as the general

differences in behaviour of cells *in vitro* as compared with *in vivo*, this also is attributable to the roles of a broad range of cell-types, and contributions from a diverse array of systems-level adverse conditions (e.g. raised local tissue pressure; regional ischaemia; cortical spreading depolarisation; migrating inflammatory/progenitor cells). As such, whilst *in vitro* investigation has a significant role in the understanding of neuroregeneration, there is an inherent risk of artefactual observations, the possibility of which must always be considered. The concept of PBM with RS has been demonstrated *in vitro* (Chapter 1),[238] therefore furthering the evidence to support this paradigm requires *in vivo* modelling.

In vivo models

A variety of methodologies for administration of traumatic injury to the brain have been employed in the study of the mechanisms and therapeutics of TBI and regeneration.[359–362] These can be considered as diffuse or focal injury models. Diffuse models, weight drop (WD) or blast injury result in damage across the brain, with severity dependent on the magnitude of the exerted force, mainly resulting in diffuse axonal injury (DAI) within white matter tracts such as the corpus callosum (Fig. 4.2).[363] Blast injury modelling, via sound wave propagation and differential impedance at tissue/fluid interfaces, results in a specific injury pattern distinct from WD.[359] These are both closed injury models, where the skull is left intact.

Focal injury methods target a more specific area of brain. A controlled cortical impact (CCI) is induced by a metal or silicone tipped rod driven by a piston into the exposed cortical surface. Cortical stab injury, either through the skull or following craniotomy, is performed with a controlled injury delivered by (typically) a scalpel.[362] A lateral fluid percussion (LFP) injury is delivered by a pendulum device which "percusses" a volume of sterile fluid onto the cortical surface, which somewhat diffuses the injury across a wider area than CCI.[359–362] Penetrating ballistic-like brain injury utilises inflation of a balloon catheter inflated after cannulation of the brain to a subcortical depth. This is designed to mimic the cavitation effect of ballistic injury.[364]

Whilst experimental reproducibility is advantageous, TBI in humans (regardless of military or civilian populations) is often heterogenous and an individual case will usually encompass

features of both diffuse and focal injury. Direct-to-cortex methods (such as LFP or CCI) require a craniotomy to administer, which hold the disadvantage that the injury site has undergone a bony decompression prior to the brain injury. This will inherently alter the local response to injury including oedema, and effectively represents a pre-emptive therapy analogous to a small decompressive craniectomy.

Given the key pathophysiological feature of diffusivity of TBI, a diffuse injury model should be selected. The WD model to represent this is well validated and represents a more relevant model for civilian TBI than a blast injury model. Therefore, use of a WD model for this work was selected. PBM has been demonstrated previously to be beneficial in pre-clinical models of moderate/severe TBI.[168, 172, 174, 244, 246–249, 251, 252, 255] The primary advantage of selection of a mild injury model is to robustly assess the capability of RS to discern injurious states in the brain (and response to therapy) which can be considered more challenging to detect in mild injury in contrast to severe. As such, the capability of RS to detect a therapeutic response after mild injury, from direct tissue monitoring, would provide a strong indication of the capabilities of RS in detecting more subtle changes in brain tissue injury states.

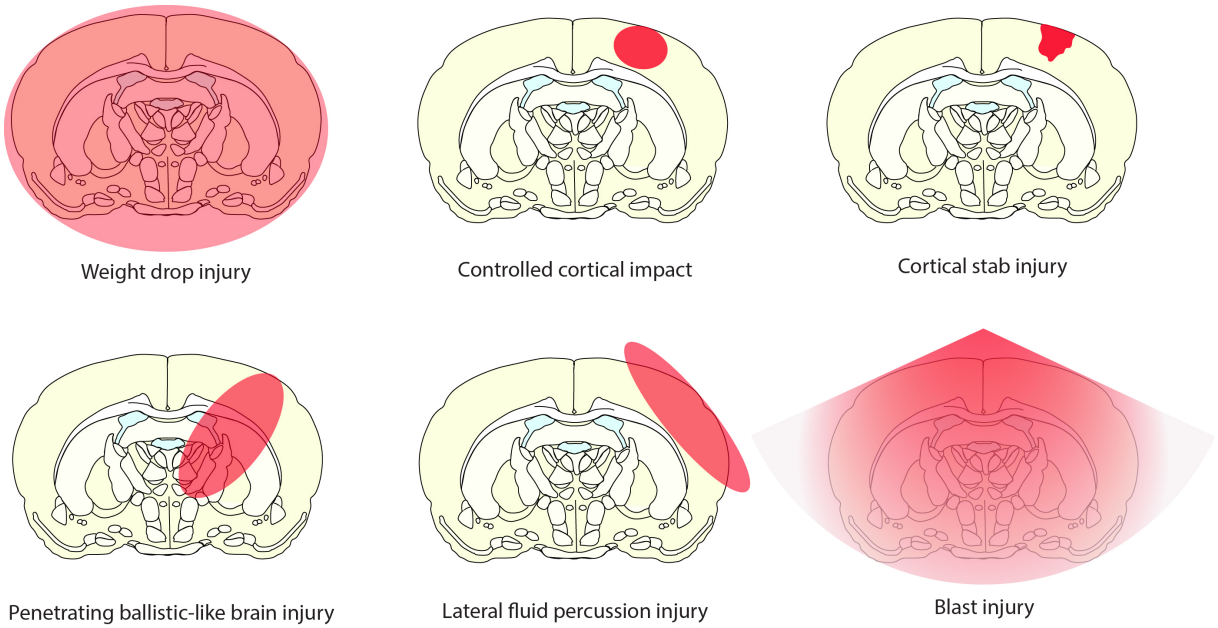


Figure 4.2: Schematic diagram of six pre-clinical TBI models used in the literature to replicate the conditions of traumatic injury.

4.1.2 Selection of photobiomodulation parameters for traumatic brain injury

As described in Chapter 2, meta-analysis for NSS and lesion size were found to favour intervention versus control. Sub-group analysis based on PBM parameter variables for these outcomes showed that favourable parameters were identified as: wavelengths in the region of 665 nm and 810 nm; time to first administration of PBM $\leq$ 4 hours; total number of daily treatments $\leq$ 3. No differences were identified between pulsed and continuous wave modes or energy delivery. As such, key features of the parameters were determined as: use of 660 and/or 810 nm PBM; and first application within 4 h, continuing for up to three days. The relative benefits of 660 vs 810 nm PBM are less clear. 810 nm offers improved penetrance through superficial tissues, though this is of lesser importance as a consideration for an implantable device. Little is known on the difference, if any, in chromophore for these wavelengths, and their use in combination may provide a compound benefit in comparison to a single wavelength alone.

In Chapter 2, the benefits of varying average irradiances were less clear. In Chapter 1, pilot data on the effect of 660 nm PBM in organotypic hippocampal slice cultures were described.[238] This demonstrated optimal efficacy of PBM when delivered at average irradiances of 21-42 mW/cm^2. This serves as important *in vitro* precedence for use of average irradiance values within this range, supported by the efficacy of 24.42 mW/cm^2 in SCI (Chapter 3).

4.1.3 Raman spectroscopy in traumatic brain injury

For a comprehensive background of the application of RS in TBI, see Appendix A.

4.1.4 Objectives

The objectives of this chapter are:

- To validate the delivery of PBM in the region of 20-40 mW/cm^2 to the cortical surface of the rat brain using *ex vivo* modelling;

- Assess the efficacy of PBM for promoting functional and histological recovery after TBI;
- To investigate the efficacy of 660 and 810 nm PBM (alone and in combination) in TBI;
- To investigate the utility of RS to discriminate between injury, treated and normal (uninjured) brain.

4.2 Materials and methods

All animal procedures were licensed by the UK Home Office and approved by the University of Birmingham's Animal and Ethical Review Board. Surgeries were carried out in strict accordance with the guidance of the UK Animals Scientific Procedures Act, 1986. Power calculations using the NC3Rs Experimental Design Assistant was used to determine sample sizes and all animals were randomly assigned to treatment groups, masked to the experimenters until analysis was complete. Pre- and post-operative analgesia was provided as standard and as advised by the named veterinary surgeon.

4.2.1 *Ex vivo* cadaveric modelling and profilometry

Adult (300-350 g) male Wistar rats were sacrificed by exposure to rising concentrations of CO_2. Heads were removed, frozen and stored at -20 °C until use. After shaving of the scalp, heads were cut using a 24 tpi hacksaw parallel along an anatomical plane from the lateral canthus to the external acoustic meatus. The residual brain was removed, and the sample was positioned with the scalp in direct contact with the laser probe surface, with power meter/beam profile focused at the inner skull surface. Lasers used were 660 nm MDL-III-660-FC-800 mW and 810 nm MDL-III-810-FC-800 mW, (both CNI Co., Ltd., China). Profilometry was performed using the methods described in Chapter 3, focused on the inner surface of the skull. Thermography was performed as described in Chapter 3.

4.2.2 Weight drop model of mild traumatic brain injury

Adult (300-350 g) male Wistar rats were anaesthetised using inhalation of 5% isofluorane with 1.8 l/min O_2 after administration of intraperitoneal buprenorphine. For the procedure, anaesthesia was maintained using 2.5% isofluorane. Weight drop injury was performed as described previously.[365–367] A 2 cm incision was made in the scalp, with lateralisation of the periosteum to expose the skull. A cyanoacrylate adhesive was used to temporarily secure a 10 mm diameter 5 mm thickness protective metal disc to the skull surface, centred on the bregma. Animals were then transferred to a foam block and positioned directly under a clear plastic tube containing a 450 g metal weight suspended at 1m height. The weight was released and fell under gravity to impact the metal disc directly. The animal was then returned to the operative field for inspection of the skull to ensure no fracture or haemorrhage had occurred. The wound was closed with 4-0 vicryl (Ethicon, New Jersey, USA) before exposure to either PBM or sham therapy. Control (uninjured) animals received no weight drop injury. n = 4-5 animals were used per group.[i]

4.2.3 Application of photobiomodulation

After injury, animals (in a single animal experimental unit) were randomised to treatment group. PBM was delivered daily (day 0, 1, 2) commencing 10 minutes post-injury, for two minutes per session (one minute per hemisphere) at 20 mW/cm^2 at the level of the cortex (2.4 J). Average irradiance was normalised to the respective wavelength (described below). For each hemisphere, the laser probe was positioned for 10 s each on a map of six adjacent points to avoid accumulation of heating in the skin (Fig. 4.3). For 660/810 nm protocol, 1.2 J of PBM was delivered over one minute (30 s per hemisphere) each for 660 nm and 810 nm (5 s per point shown in Figure 4.3). Subsequent treatments were performed without anaesthesia achieved with gentle manual positioning. For sham treatment, the same process was performed with the source end of the laser probe exposed to ambient room light.

[i] *In vivo* TBI modelling was performed in part by Zubair Ahmed and Valentina Di Pietro, and in part by the thesis author.

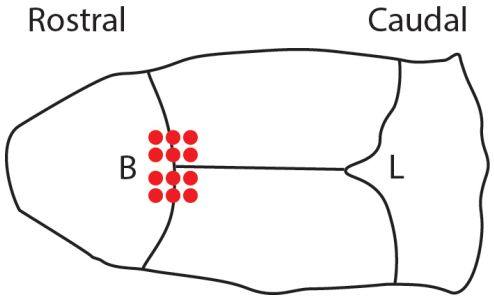


Figure 4.3: Schematic diagram of a rat skull (surface view) with red dots demonstrating the 12 points of PBM administration. B = bregma; L = lambda.

4.2.4 Functional outcome assessments

Beam-walking test For assessment of balance and motor recovery, beam-walking (BW) was performed as described elsewhere.[368–371] Training was performed four to five days prior to administration of injury. For testing, rats were placed on a 1.2 m long 25 mm diameter cylindrical rod traversing two raised platforms. The rod was fixed within mounts and did not rotate. A cage was accessible at one end, with a lamp positioned at the other to encourage walking. Over three trials, interspersed with rest periods of 1 min, two blinded observers independently scored the number of slips/errors and successful steps. Testing was recorded on three occasions over four weeks (every eight days). Beam walk error ratio was calculated by the formula: errors/completed steps.

4.2.5 Tissue processing

After completion of experimental protocols, animals were sacrificed and perfused with 4% formaldehyde, as described in Chapter 3. Whole brains were removed and post-fixed in 4% formaldehyde before cryprotection in graded sucrose solutions. For embedding in OCT mounting media (Avantor, Pennsylvania, United States), 5 mm of the anterior pole of the brain was removed with a single coronal slice, for mounting on the flat coronal edge. Coronal brain sections were taken in 15 μm slices using a cryostat (OTF, Bright Instruments, Huntingdon UK).

4.2.6 Staining of histological samples

Immunofluorescence staining was performed as described in Chapter 3, using antibodies listed in Table C.1. Tissue sections were used from the region of -1.30 mm to the bregma, selected for proximity to the bregma (i.e. the injury epicentre and covered by PBM) and for its broad range of anatomical regions within a single slice.

4.2.7 Image acquisition and analysis

Tissue sections were imaged and analysed by a reviewer blinded to the treatment conditions. Predetermined brain areas (Fig. 4.4) were identified anatomically under a fluorescent microscope with images captured with Axiocam HRc camera (all from Carl Zeiss, Welwyn-Garden City, UK). Sections without primary antibody were used to control for background fluorescence. For analysis, images were transferred to ImageJ (National Institutes of Health, Bethesda, Maryland, USA).[340] Fixed area ROI were applied to images for capture of integrated density. For regions with variable morphology (e.g. choroid plexus), the anatomical region of interest was manually traced and mean gray values acquired for comparison. For cleaved caspase-3 +ve nuclei, counts were taken of cells >100 pixel area and circularity >0.2, after image thresholding.

4.2.8 Raman spectroscopy

For Raman spectroscopy analysis, tissues were collected 3 dpi after TBI, with groups receiving either 810 nm PBM (as described above) or sham treatment. The control (uninjured) group had no surgery. After the treatment protocol, animals were sacrificed as described above. Immediately post-mortem, the head was removed and rapidly frozen by burial in dry ice. Specimens were stored at -20 °C until use. 150 min prior to analysis, rat heads were placed at room temperature to thaw, with dissection and exposure of the cortical surface commenced 15 min prior to analysis. A benchtop InVia system (Renishaw, Gloucester, UK) was used to acquire Raman signal from the centre of the left hemisphere in line with the bregma. All readings were taken using 785 nm, 50% power output. Extended spectra were taken using 10 s exposure,

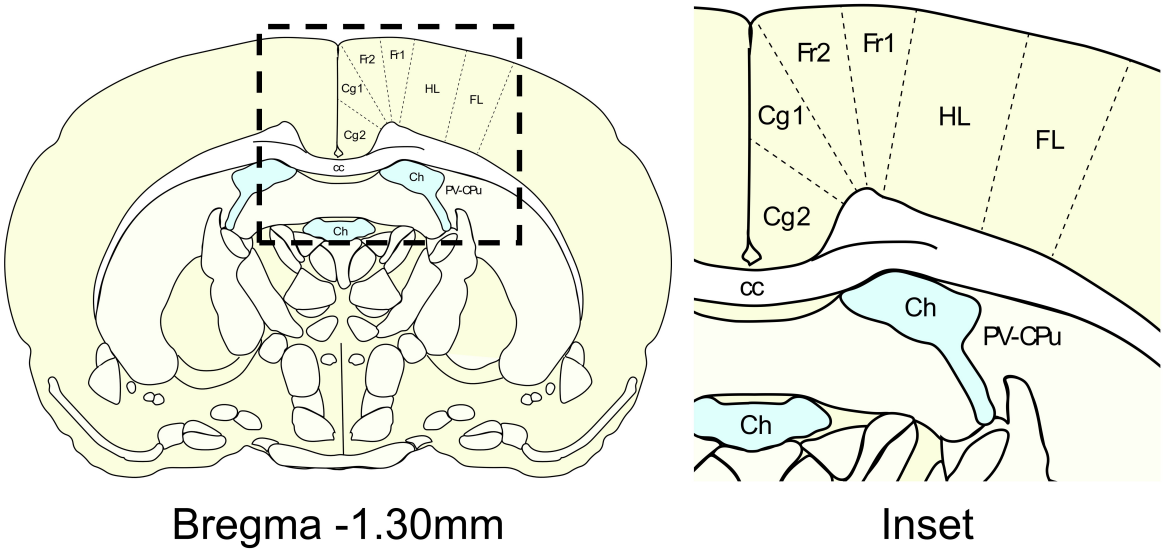


Figure 4.4: Schematic diagram of a coronal section of adult rat brain (bregma - 1.30 mm) with inset demonstrating brain areas (labelled) imaged for assessment of immunofluorescence. cc = corpus callosum; Cg1 = cingulate cortex area 1; Cg2 = cingulate cortex area 2; Ch = choroid plexus (within lateral and third ventricles); FL = forelimb area of cortex; Fr1 = frontal cortex area 1; Fr2 = frontal cortex area 2; HL = hindlimb area of cortex; PV-CPu = periventricular region of caudate putamen.

1 accumulation extended spectral scan centred on 1200 cm^{-1}). Map spectra were acquired using 1 s exposure, 10 accumulations fingerprint spectral scan centred on 1000 cm^{-1}). For initial analysis, spectra were processed using Spectragryph (average across two technical repeats from each specimen; merged across all 6 specimens from each condition; baseline correction; smoothing) and peak intensities and AUC values were extracted using the integrated analytical functions. For principal component analysis (PCA), method is described below.[ii]

4.2.9 Statistical analysis

Analysis of functional outcome data was performed using Prism (V9.2.0 GraphPad, New York, USA) by repeated measures two-way ANOVA with Geisser-Greenhouse correction and post-hoc Dunnett's method for multiple comparisons. Immunostaining outcomes were analysed using one-way ANOVA with post-hoc Dunnett's method. Exploratory data analysis and PCA was

[ii]Raman spectroscopy acquisition was performed in part by Liam Kelleher, and in part by the thesis author.

performed in R[344] (www.R-project.org) using the package ChemoSpec,[372] visualised using ggplot2. Baseline correction (using baselineSpectra function) and normalisation of spectra (using normSpectra function) was performed prior to exploratory data analysis. Spectra were aligned (using clupaSpectra function (MassSpecWavelet package)). Classical PCA was performed, using robust ellipses for graphical representation. Scree plots were used to identify sufficient number of PCs for HCA of PCA.

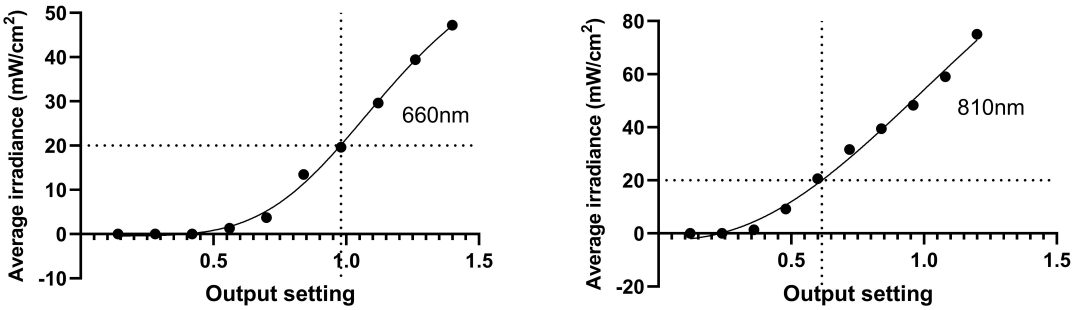
4.3 Results

4.3.1 Effective doses of 660 and 810 nm photobiomodulation to the brain are achievable via transcutaneous administration in an *in vivo* model of traumatic brain injury

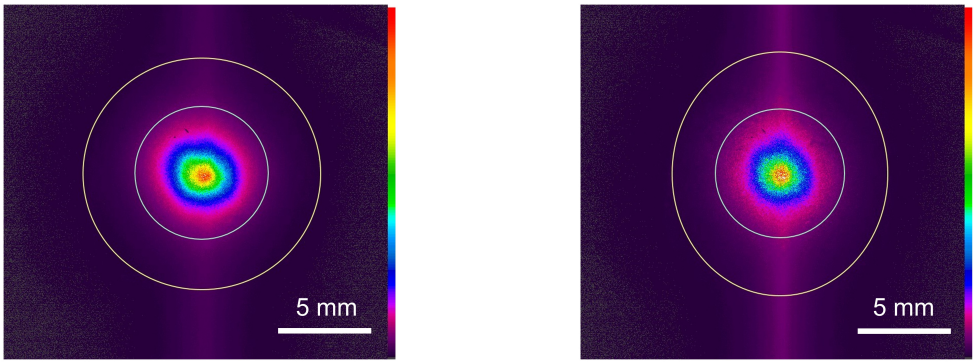
Cadaveric profiling of transcranial transmission from 660 nm and 810 nm was performed using *ex vivo* specimens of male Wistar rat scalp and skull (Fig. 4.5). Probe sources were placed in direct contact with the scalp overlying the bregma, and profilometry was captured from the internal surface of the skull. 810 nm demonstrated improved transmission at lower power outputs compared with 660 nm. Calibration of transmission curves for both sources allowed matching of average irradiance to 20 mW/cm^2 for both (70% output for 660 nm; 63% for 810 nm). D4σ were equivalent for each source. In order to ascertain safe output parameters for avoidance of significant heating, thermography of the internal skull surface during a 60 s treatment was performed (Figs. 4.6/4.7). Maximal heating was less than 2 °C for both treatment output levels, with no focal heating over the first 10 s. *Ex vivo* temperature profiling is likely to considerably overestimate the heating *in vivo*, due to the presence of blood flow and greater tissue volume to act as a heat sink. Nevertheless, these output levels were deemed the highest usable levels to avoid focal skin heating and are well within safe limits to avoid discomfort during short exposures. Movement of the probe across the skin every 10 s was implemented to avoid greater focal skin heating than observed at skull level (Fig. 4.3). Equivalent levels of output did not

result in significant skin heating as described in Chapter 3, section 3.2.2. During *in vivo* trials, no animal discomfort was observed during a 2 min treatment protocol for either wavelength.

A



B



C

Variable	660 nm	810 nm
Total power (mW)	7.0 ± 3.4	6.2 ± 5.4
Average irradiance (mW/cm^2)	20.0 ± 11.4	20.0 ± 14.5
Max irradiance (mW/cm$^{2)}$	132.4 ± 78.4	168.7 ± 137.5
D4σ (cm)	0.72 ± 0.19	0.70 ± 0.34

Figure 4.5: 660 nm and 810 nm PBM are deliverable at a matched average irradiance of 20 mW/cm^2. A: Plot of average irradiance transmitted to inner surface of skull against laser output setting for 660 (left panel) and 810 nm (right panel) lasers. Additional x axis line indicates 20 mW/cm^2 level, with corresponding y axis line at the intersection to plot required output setting. Output settings given in manufacturer determined arbitrary units as a 0-100% output (non-linear) of 1.4 (660 nm) and 1.2 (810 nm). B: beam profiles at inner surface of skull with transcutaneous application of PBM for 660 (left panel) and 810 nm (right panel) lasers. Gaussian distribution of transmitted light with a D4σ of 0.70-0.72 cm. Relative intensity colour bar to right (OSI Rainbow). C: Table showing beam profilometry readings with SD using output settings derived from (A). n = 4 per group.

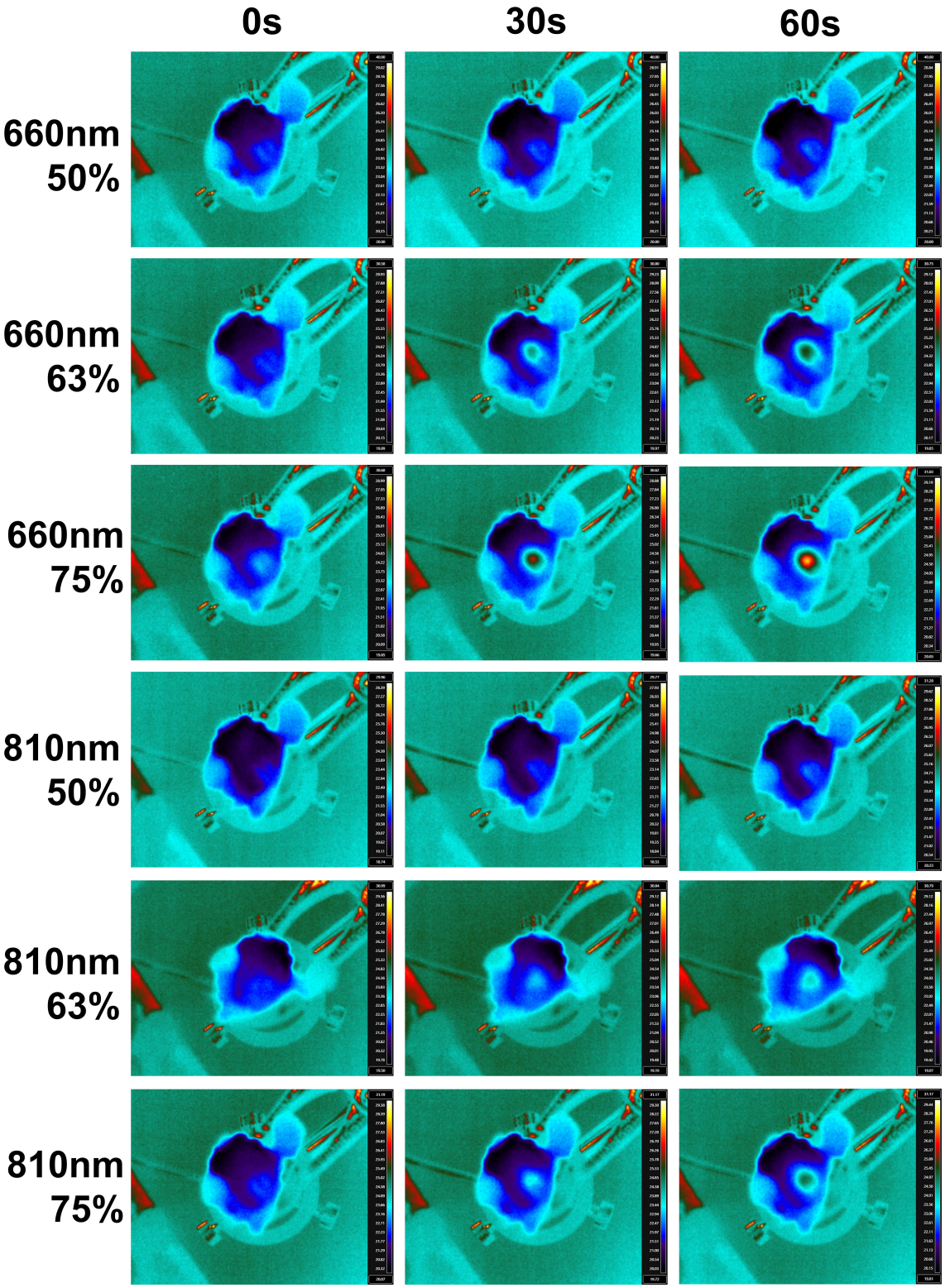


Figure 4.6: Images of FLIR thermal profiling taken from the internal skull surface at 0, 30 and 60 s during 60 s treatment protocol for 660 nm and 810 nm PBM.

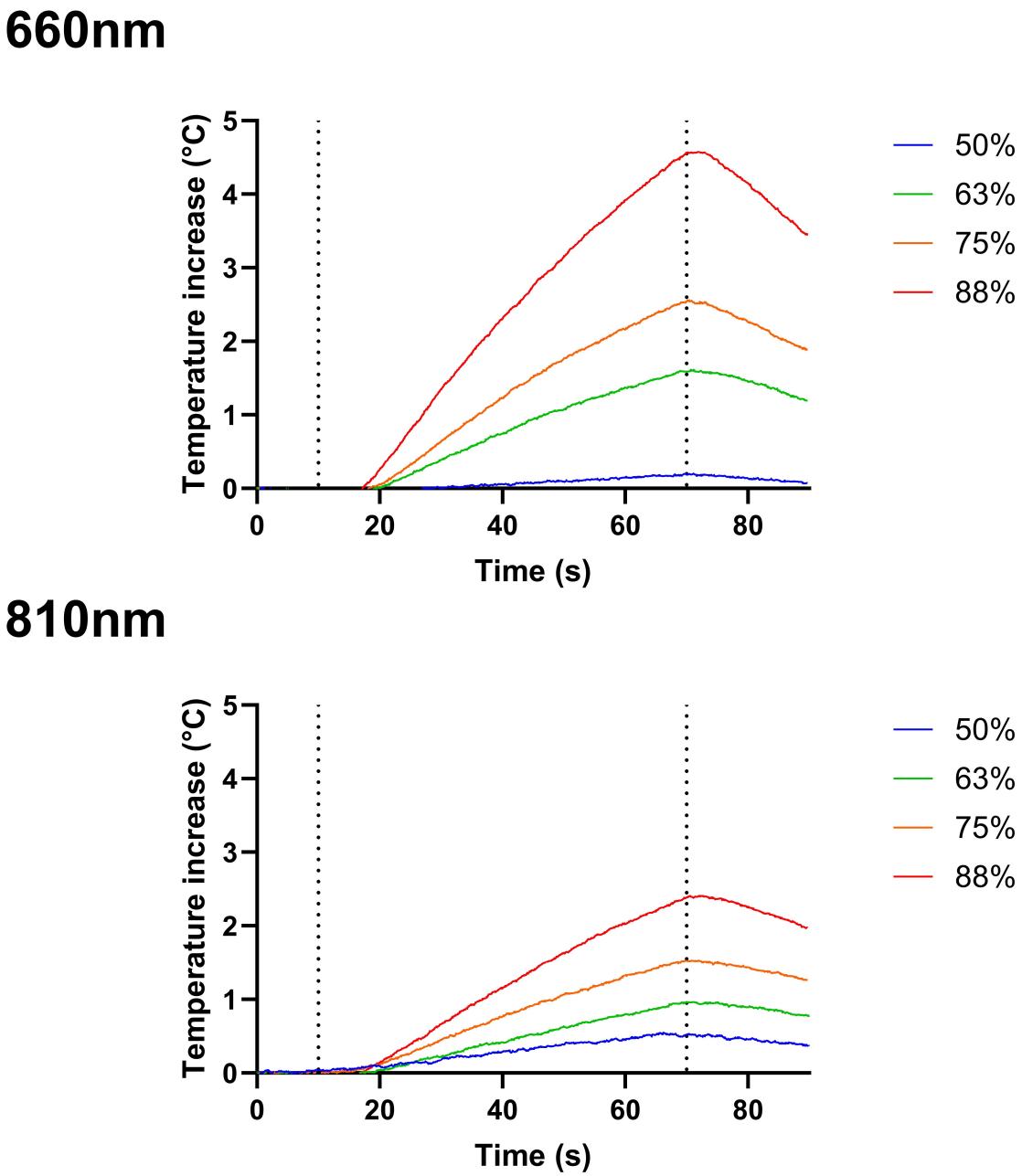


Figure 4.7: Temporal plots of thermal change (maximum temperature) for a region of interest on the internal skull surface during 60 s treatment protocol for 660 nm and 810 nm PBM. x-axis lines denote ON (10 s) and OFF (70 s), with 10 s observation to establish temperature baseline prior to PBM, and 20 s post-administration to observe cooldown. Temperature change given is relative to background temperature recorded within the field of view of the thermal imaging camera, from tissue not exposed to PBM. n = 4 per group. Treatment protocols used for PBM were 70% output for 660 nm and 63% for 810 nm.

4.3.2 Photobiomodulation improves functional recovery after traumatic brain injury

In assessment of balance function, 660 and 810 nm PBM demonstrated significant improvements in function at 16 and 24 dpi (Fig. 4.8). Beam walk performance improved by 65.8% (810 nm, $p < 0.001$), 63.8% (660 nm, $p < 0.05$) and 42.3% (660/810 nm, $p = 0.08$). This suggests that there is no compound benefit from utilisation of both wavelengths versus 660 or 810 nm alone. 810 nm produced improvements with greater consistency in BW tests, and was the selected wavelength in 3 dpi experiments below.

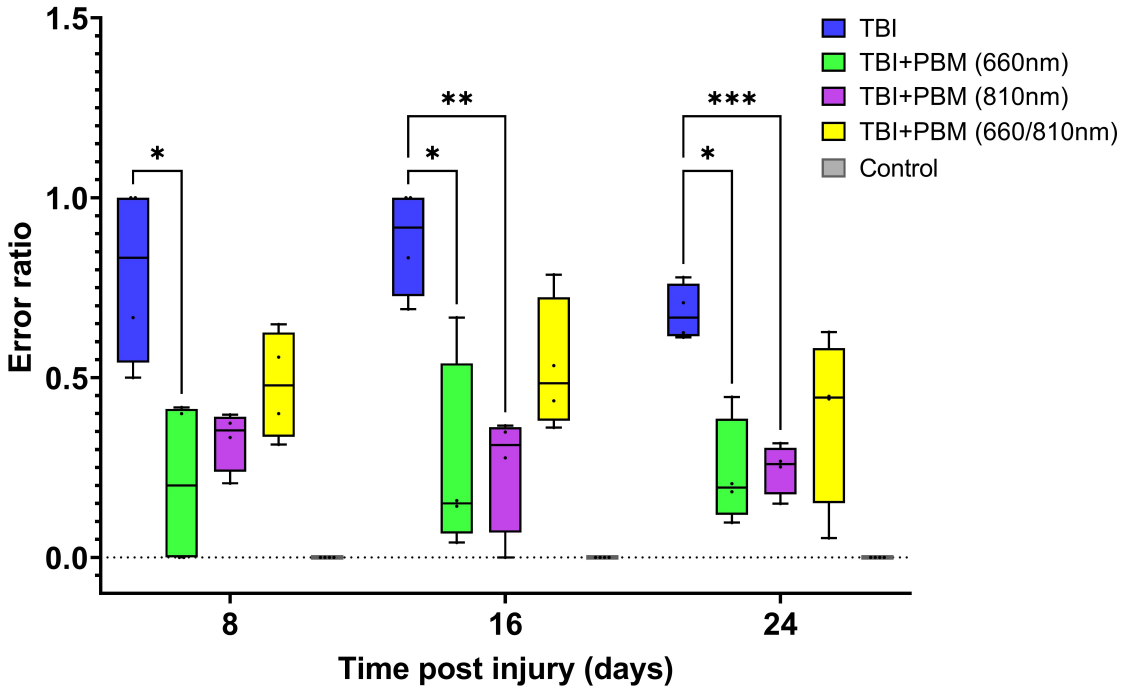


Figure 4.8: PBM promotes functional recovery after mTBI. Adult (300-350 g) male Wistar rats received a calibrated weight drop TBI. PBM was delivered daily (day 0, 1, 2) commencing 10 min post-injury, for 2 min per session (one minute per hemisphere) at 20 mW/cm^2 at the level of the cortex (2.4 J), normalised to the respective wavelength. For 660/810 nm protocol, 1.2 J of PBM was delivered over one minute (30 s per hemisphere) each for 660 nm and 810 nm. Beam walk (error ratio calculated by the formula: errors/completed steps) at three time points. * = $p < 0.05$ ** = $p < 0.01$ *** = $p < 0.001$ **** = $p < 0.0001$. Comparisons for TBI vs control not shown (all $p < 0.0001$). All n = 4 per group. TBI = traumatic brain injury; PBM = photobiomodulation.

4.3.3 Photobiomodulation reduces astrocyte activation in the acute phase after traumatic brain injury

At 3 dpi, 810 nm PBM treatment correlated with significant reductions in immunofluorescence intensity across seven of the eight imaged brain areas (all except FL) (Fig. 4.9). No difference in GFAP staining intensities were observed between any groups at 4 wpi (Fig. 4.10). [iii]

4.3.4 Photobiomodulation reduces microglial activation in the acute phase after traumatic brain injury

Expression of microglial activation marker CD11b was assessed across brain areas, with co-staining for CD68 (Fig. 4.11). CD68 resulted in no increase in staining compared to the background, but was validated as the process successfully stained cells with monocytic morphology within blood vessels. CD11b staining was elevated across all cortical areas, corpus callosum and choroid plexus between control and TBI specimens. In these areas, application of PBM was associated with a significant reduction in fluorescence for CD11b.

4.3.5 Photobiomodulation modestly reduces extracellular matrix deposition after traumatic brain injury

Brain sections were immunostained for presence and distribution of extracellular matrix proteins laminin and fibronectin. No significant differences between control and TBI samples were identified in any brain area, with the exception of modest differences in laminin expression in Cg2 (Fig. 4.12). Variable reductions were identified in treated samples (fibronectin: Ch (**), PV-CPu (*) and HL (**); laminin: Cg2 (**), Cg1 (**), Fr2 (*), FL (*), PV-CPu (**)). At 4 wpi, these observed effects were not identified (Fig. 4.13).

[iii] Immunofluorescence images for all brain areas and all staining protocols are given in Appendix D.

4.3.6 Photobiomodulation reduces expression of cleaved caspase-3 in the acute phase after traumatic brain injury

Cleaved caspase-3 immunostaining was used to assess levels of apoptotic activity in the cortex (areas Cg1, Cg2, Fr1, Fr2, FL). The number of cleaved caspase-3 positive cells was increased after TBI in comparison with control (*) (Fig. 4.14, top left). A non-statistically significant reduction the number of positive cells was observed with 810 nm PBM. Based on intensity analysis using integrated density of fluorescence (Fig. 4.14, top right), there was a strongly significant (****) increase in untreated TBI samples compared to both control and PBM samples.

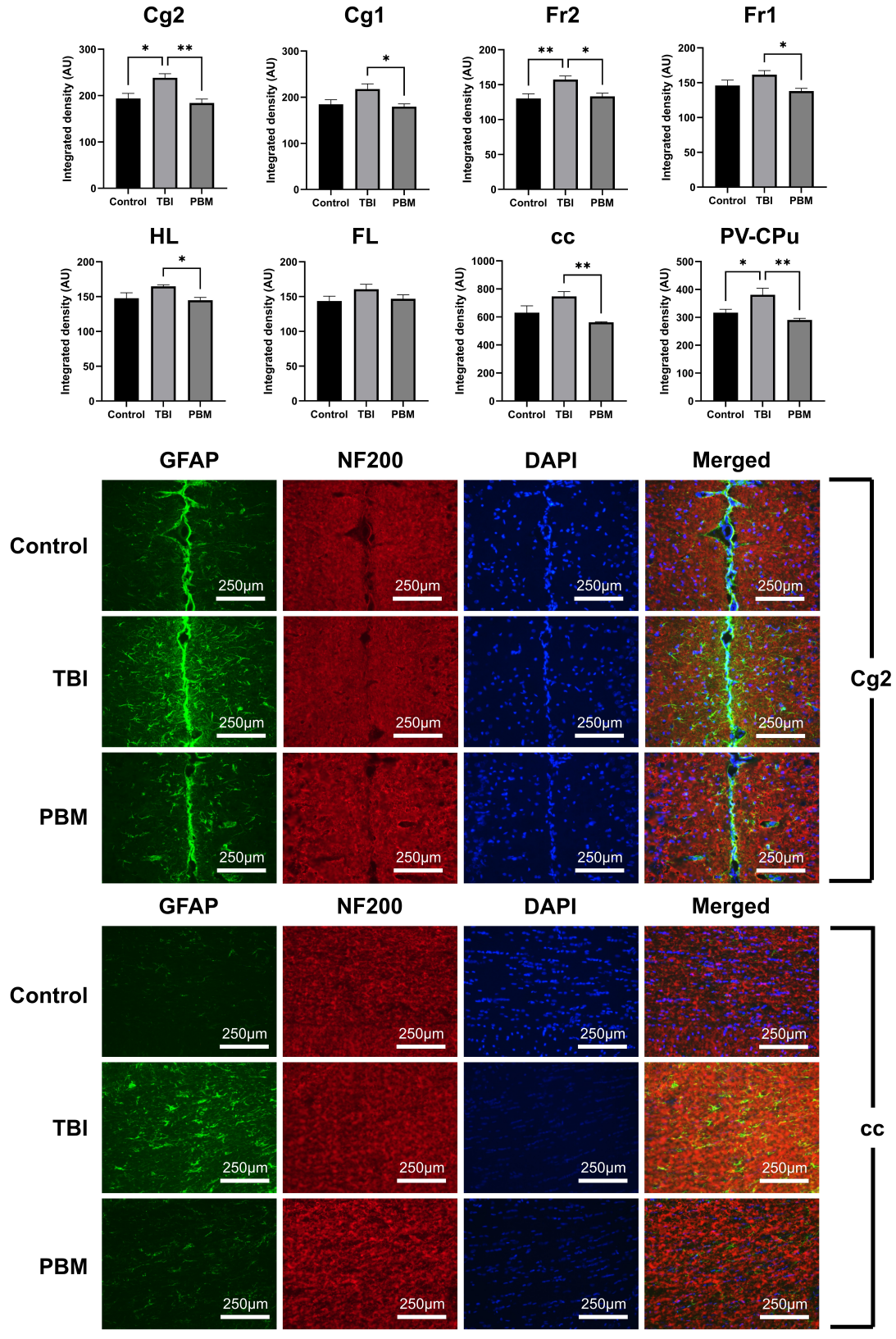


Figure 4.9: Caption on next page.

Figure 4.9: Figure on previous page. PBM reduces GFAP across brain areas at 3 dpi. Top panel: area controlled integrated densities for GFAP in denoted brain areas. Bottom panel: immunofluorescence imaging for Cg2 and cc areas. 810 nm used in PBM group (2 min per day (1 min per hemisphere), 20 mW/cm^2, 2.4J). n = 5 per group (n = 4 for control). * = $p < 0.05$; ** = $p < 0.01$. Non-significant comparisons not shown. cc = corpus callosum; Cg1 = cingulate cortex area 1; Cg2 = cingulate cortex area 2; Ch = choroid plexus (within lateral and third ventricles); FL = forelimb area of cortex; Fr1 = frontal cortex area 1; Fr2 = frontal cortex area 2; HL = hindlimb area of cortex; PV-CPu = periventricular region of caudate putamen; GFAP = glial fibrillary acidic protein; NF200 = neurofilament 200; DAPI = 4,6-diamidino-2-phenylindole; TBI = traumatic brain injury; PBM = photobiomodulation, AU = arbitrary units. Immunofluorescence images for all brain areas are given in Appendix D.

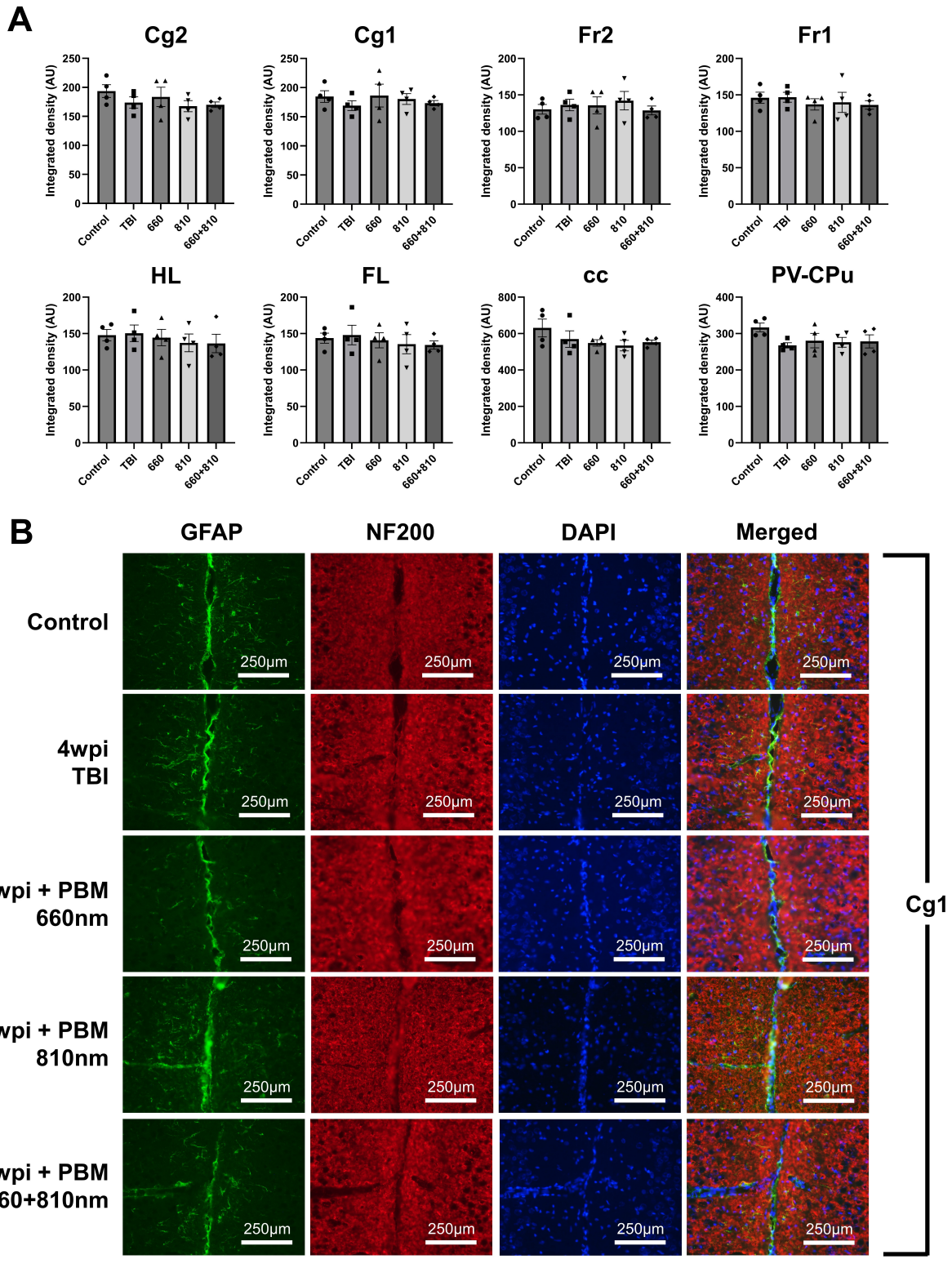


Figure 4.10: Caption on next page.

Figure 4.10: Figure on previous page. There was no discernible difference between injury, control and PBM in GFAP immunofluorescence across brain areas at 4 wpi. Top panel: area controlled integrated densities for GFAP in denoted brain areas. Bottom panel: immunofluorescence imaging for Cg1 areas (3 dpi TBI shown for reference). 660 and/or 810 nm used in PBM group (2 min per day (1 min per hemisphere), 3 day course, 20 mW/cm^2, 2.4J). n = 5 per group (n = 4 for control). Non-significant comparisons not shown. cc = corpus callosum; Cg1 = cingulate cortex area 1; Cg2 = cingulate cortex area 2; Ch = choroid plexus (within lateral and third ventricles); FL = forelimb area of cortex; Fr1 = frontal cortex area 1; Fr2 = frontal cortex area 2; HL = hindlimb area of cortex; PV-CPu = periventricular region of caudate putamen; GFAP = glial fibrillary acidic protein; NF200 = neurofilament 200; DAPI = 4,6-diamidino-2-phenylindole; TBI = traumatic brain injury; PBM = photobiomodulation, AU = arbitrary units. Immunofluorescence images for all brain areas are given in Appendix D.

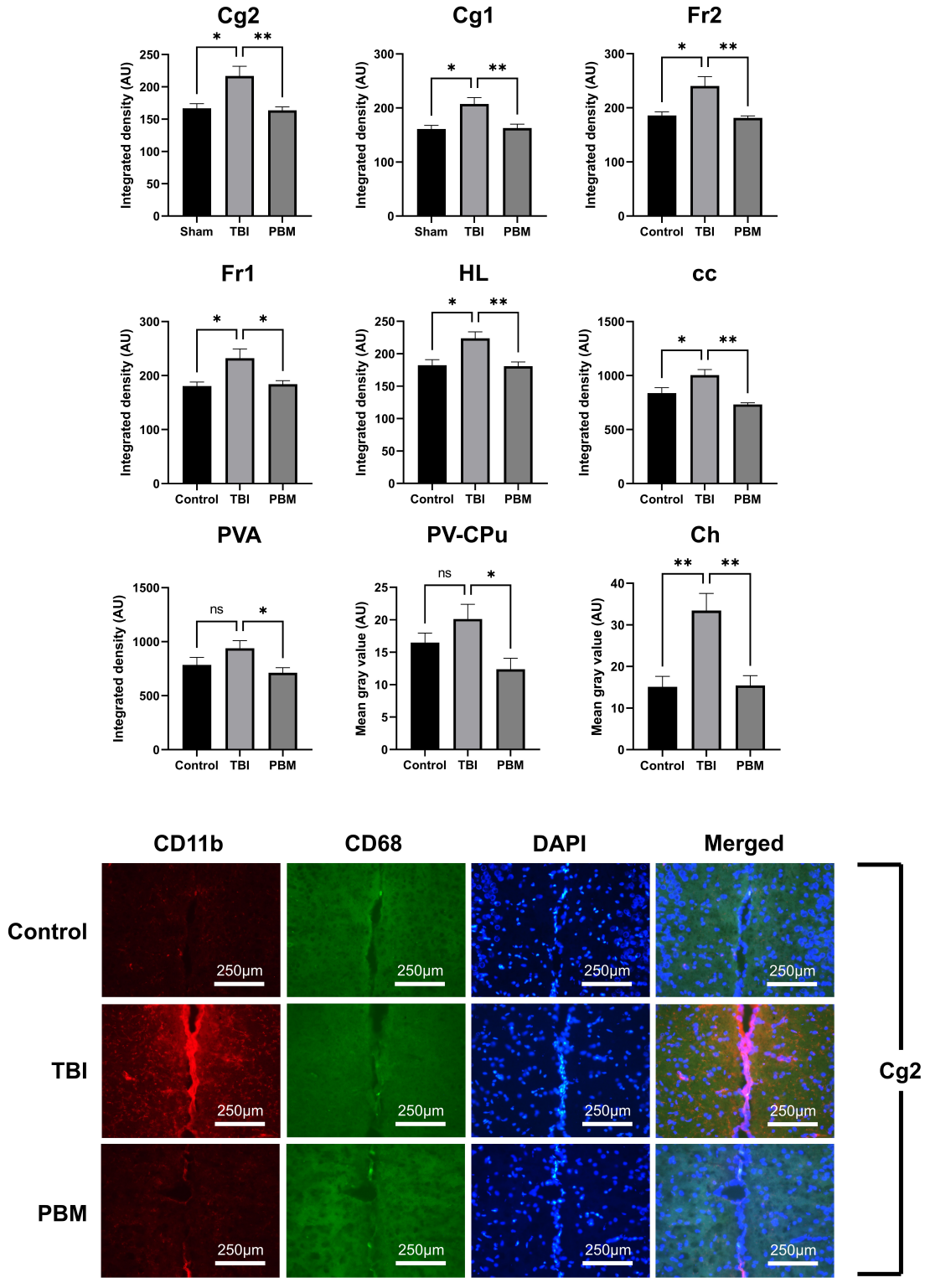


Figure 4.11: Caption on next page.

Figure 4.11: Figure on previous page. PBM reduces CD11b immunofluorescence across brain areas at 3 dpi. Top panel: area controlled integrated densities for CD11b in denoted brain areas. Bottom panel: immunofluorescence imaging for Cg2 areas. 810 nm used in PBM group (2 min per day (1 min per hemisphere), 20 mW/cm^2, 2.4J). n = 5 per group (n = 4 for control). * = $p < 0.05$; ** = $p < 0.01$; ns = not significant. Non-significant comparisons not shown. cc = corpus callosum; Cg1 = cingulate cortex area 1; Cg2 = cingulate cortex area 2; Ch = choroid plexus (within lateral and third ventricles); Fr1 = frontal cortex area 1; Fr2 = frontal cortex area 2; HL = hindlimb area of cortex; PVA = paraventricular thalamic nucleus, area a; PV-CPu = periventricular region of caudate putamen; GFAP = glial fibrillary acidic protein; NF200 = neurofilament 200; DAPI = 4,6-diamidino-2-phenylindole; TBI = traumatic brain injury; PBM = photobiomodulation, AU = arbitrary units. Immunofluorescence images for all brain areas are given in Appendix D.

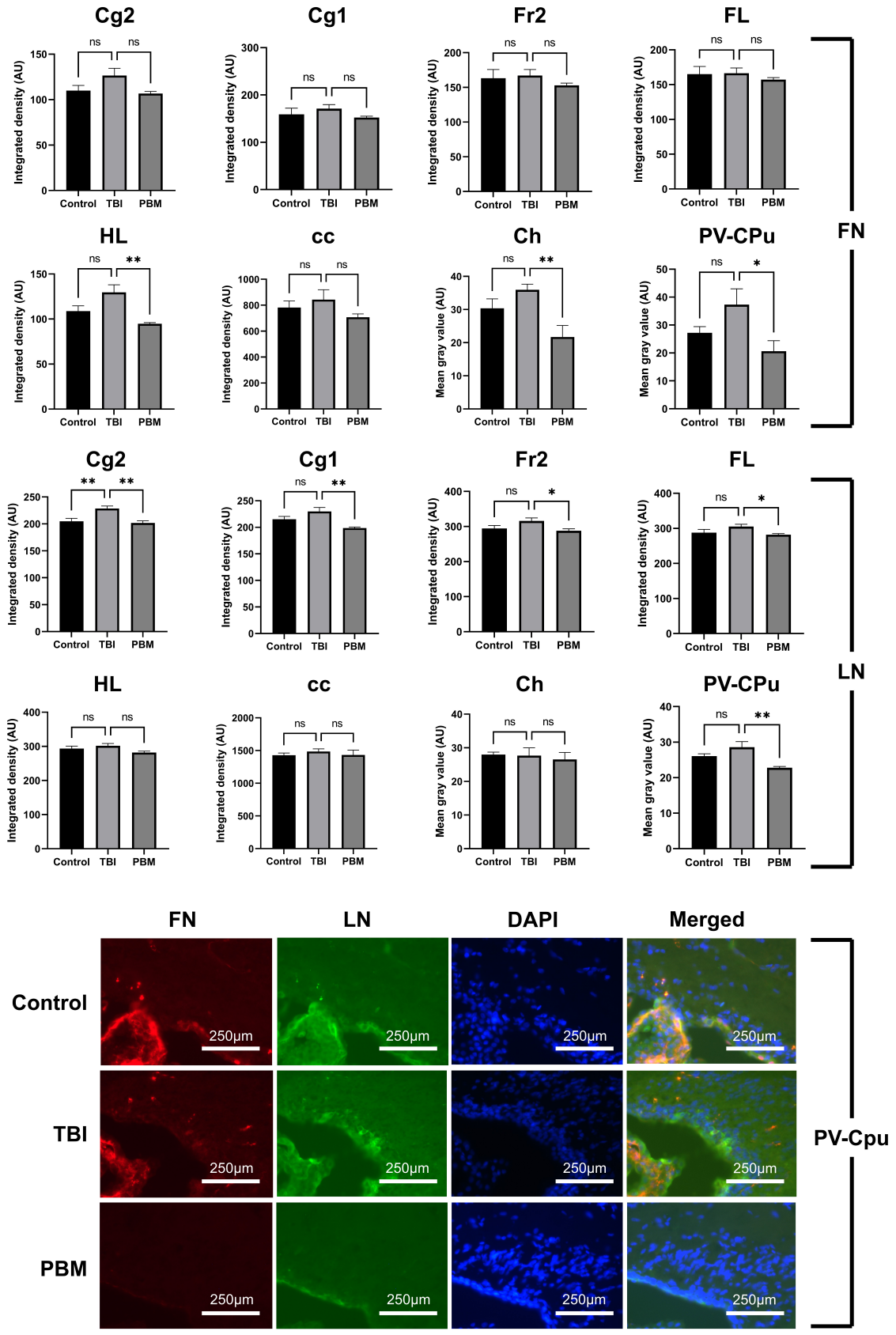


Figure 4.12: Caption on next page.

Figure 4.12: Figure on previous page. PBM results in minimal reductions in fibronectin immunofluorescence across brain areas at 3 dpi. Top panel: area controlled integrated densities for fibronectin (FN) and laminin (LN) in denoted brain areas. Bottom panel: immunofluorescence imaging for PV-CPu areas. 810 nm used in PBM group (2 min per day (1 min per hemisphere), 20 mW/cm^2, 2.4J). n = 5 per group (n = 4 for control). * = $p < 0.05$; ** = $p < 0.01$; ns = not significant. cc = corpus callosum; Cg1 = cingulate cortex area 1; Cg2 = cingulate cortex area 2; Ch = choroid plexus (within lateral and third ventricles); FL = forelimb area of cortex; Fr2 = frontal cortex area 2; HL = hindlimb area of cortex; PVA = paraventricular thalamic nucleus, area a; PV-CPu = periventricular region of caudate putamen; GFAP = glial fibrillary acidic protein; NF200 = neurofilament 200; DAPI = 4,6-diamidino-2-phenylindole; TBI = traumatic brain injury; PBM = photobiomodulation; FN = fibronectin; LN = laminin, AU = arbitrary units. Immunofluorescence images for all brain areas are given in Appendix D.

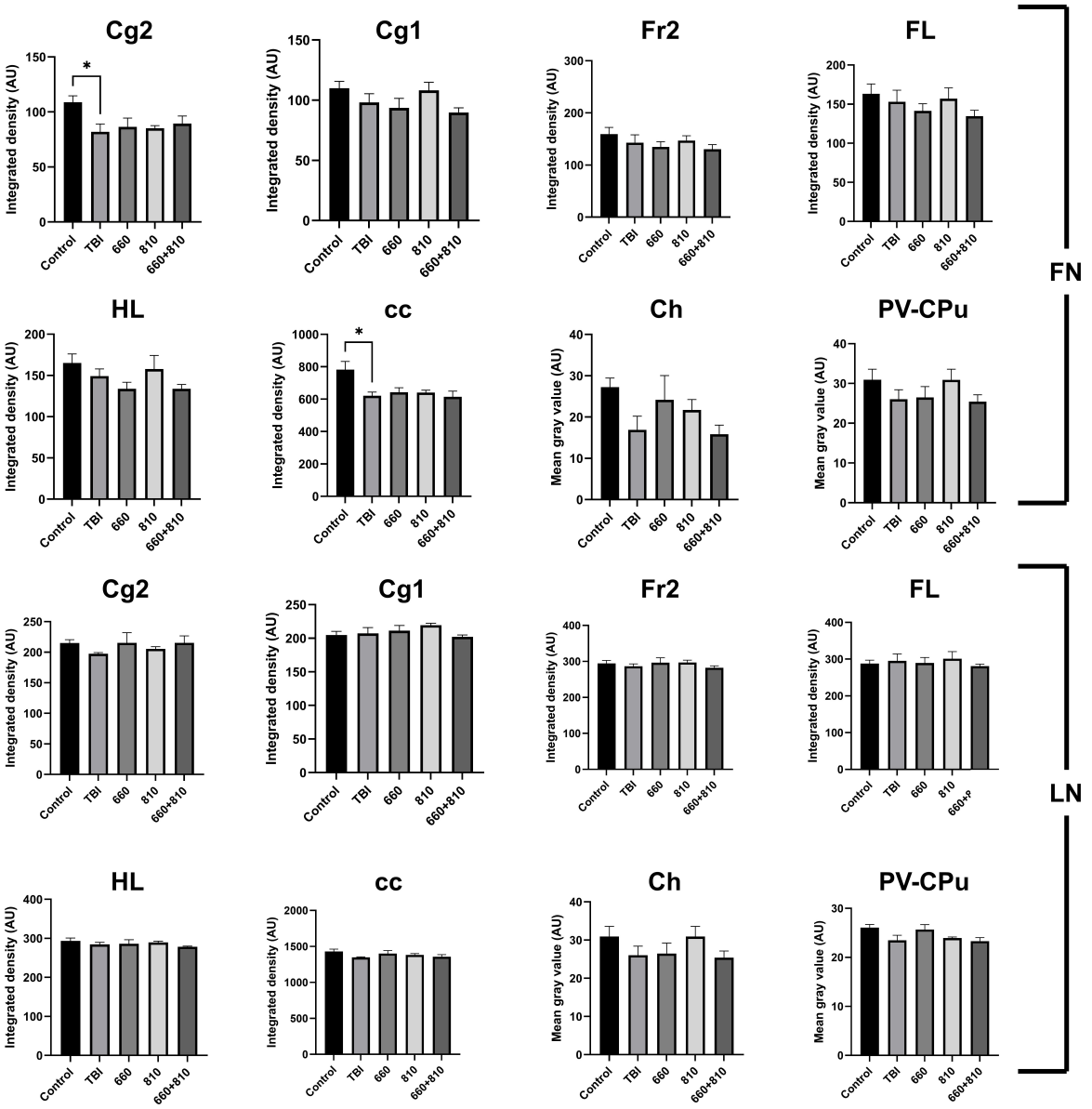


Figure 4.13: No discernible differences in fibronectin or laminin immunofluorescence were present across brain areas at 4 wpi. Top panel: area controlled integrated densities for fibronectin (FN) and laminin (LN) in denoted brain areas. Bottom panel: immunofluorescence imaging for PV-CPu areas. 660 and/or 810 nm used in PBM group (2 min per day (1 min per hemisphere), 20 mW/cm^2, 2.4J). n = 4 per group. * = $p < 0.05$. Non-significant comparisons not shown. cc = corpus callosum; Cg1 = cingulate cortex area 1; Cg2 = cingulate cortex area 2; Ch = choroid plexus (within lateral and third ventricles); FL = forelimb area of cortex; Fr2 = frontal cortex area 2; HL = hindlimb area of cortex; PVA = paraventricular thalamic nucleus, area a; PV-CPu = periventricular region of caudate putamen; GFAP = glial fibrillary acidic protein; NF200 = neurofilament 200; DAPI = 4,6-diamidino-2-phenylindole; TBI = traumatic brain injury; PBM = photobiomodulation; FN = fibronectin; LN = laminin, AU = arbitrary units. Immunofluorescence images for all brain areas are given in Appendix D.

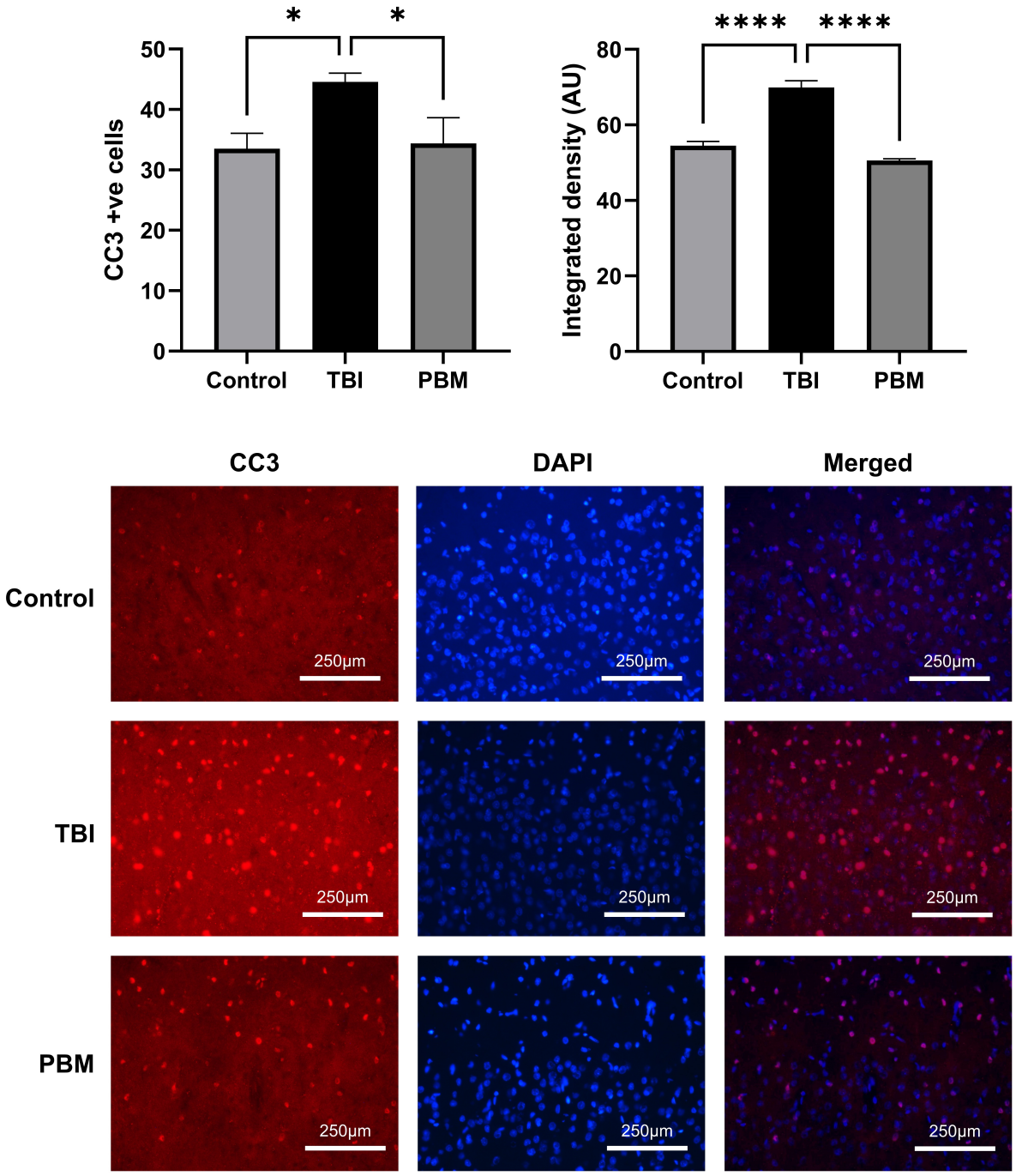


Figure 4.14: PBM reduces expression of cleaved caspase-3 after TBI. Top panel left: comparison of counts of cleaved caspase-3 +ve nuclei across five cortical areas. Top panel right: comparison of fluorescence intensity of cleaved caspase-3 across whole field in five cortical areas. Bottom panel: immunofluorescence imaging in HL area. 660 and/or 810 nm used in PBM group (2 min per day (1 min per hemisphere), 20 mW/cm^2, 2.4J). n = 4 per group. * = $p < 0.05$. ns = not significant. CC3 = cleaved caspase-3; DAPI = 4,6-diamidino-2-phenylindole; TBI = traumatic brain injury; PBM = photobiomodulation; AU = arbitrary units.

4.3.7 Raman spectroscopy discriminates between injury states after traumatic brain injury

Raman spectra were acquired from the cortical surface of *ex vivo* brains after either control (no injury), TBI with sham treatment or TBI with PBM treatment. Using merged spectra from n = 6 samples per group, discernible differences can be observed between the groups (Fig. 4.15). However, quantification of recognised metrics from the fingerprint region (1440cm^{-1}; 1660cm^{-1}; 1440/1660 ratio) did not demonstrate statistically significant differences in any metric used (Fig. 4.16). To further explore the differences between the groups, PCA was performed to assess the differentiation between the groups across multiple spectral components. To identify key contributory regions, the entire spectrum was initially used (10 s exposure, 1 accumulation) (Fig. 4.17). Based on PCA of all three groups (Fig. 4.18), no discernible stratification based on 10 components was shown. Subsequent analysis separated this into two comparisons: of the injured group vs control (uninjured) group (Fig. 4.19); and of the treatment group vs injured (untreated group) (Fig. 4.20). Both of these analyses showed clustering.

Further analysis of the fingerprint region used averaged spectra from 98 points across a cortical map, in the mid-point of each hemisphere in line with the bregma (1 s exposure, 10 accumulations). The spectra are shown in Figure 4.21. Similarly to that shown in analysis of extended scans, clustering was poor when processing three groups together, though spectra from treated specimens clustered well (Fig. 4.22). Clustering of injury vs control groups remained modest when subjecting these groups to PCA without the treatment group (Fig. 4.23). Spectra with greatest variance and correlation (Fig. 4.23 B) were identified in 1620, 1260 and 1430 cm^{-1} regions. Clustering of injury vs treatment groups was strong after PCA without the control group (Fig. 4.24). Spectra with greatest variance and correlation (Fig. 4.23 B) were identified in 1250, 1515, 1580 and 1660 cm^{-1} regions. Additional analysis using individual spectra from these maps is given in Appendix E.

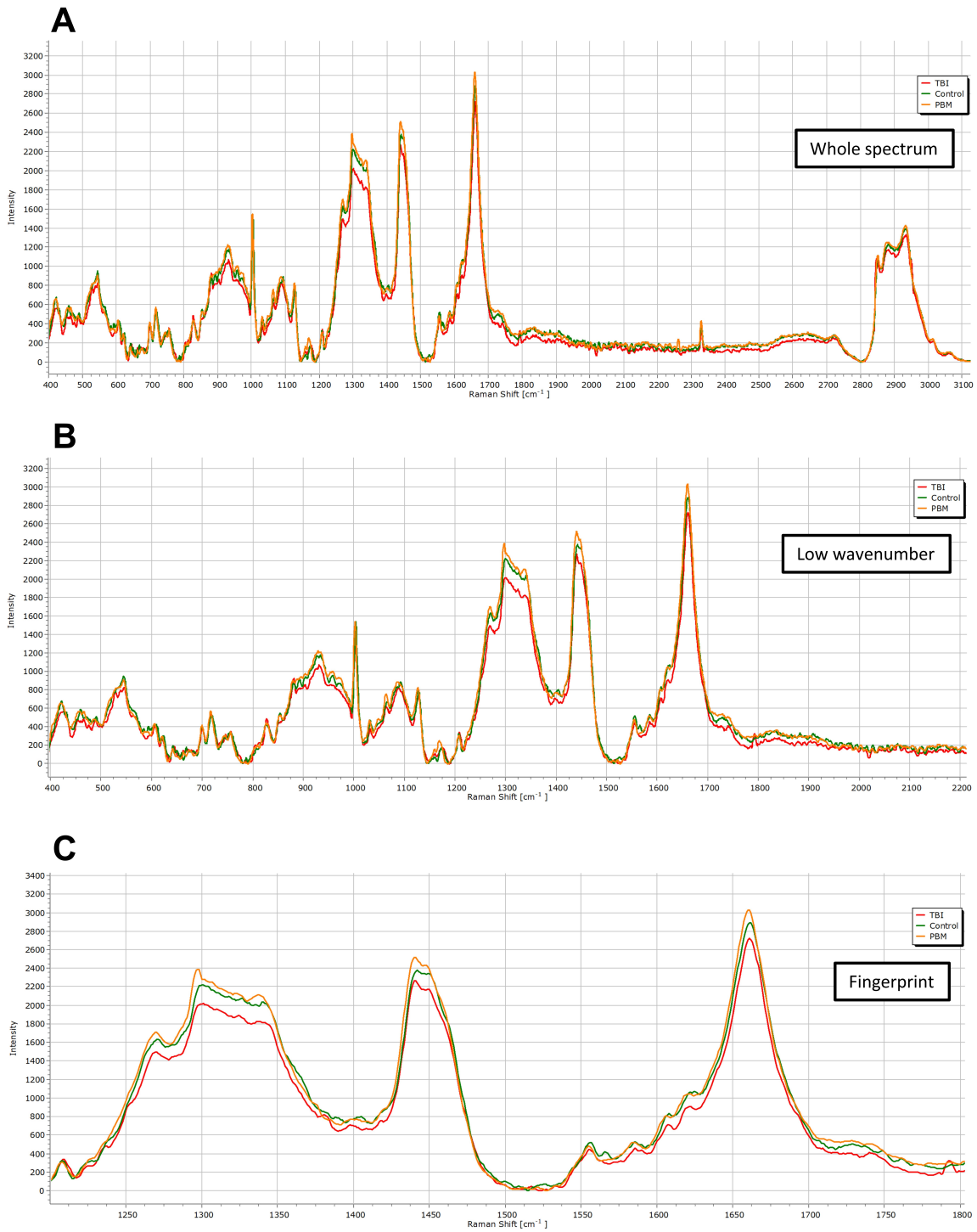


Figure 4.15: Discernible spectral differences between control, TBI and TBI + PBM rat brain cortex from *ex vivo* tissue (3 dpi). 3 dpi, whole rat heads were rapidly frozen from n = 6 rats for each of three conditions: control (no injury); TBI (weight drop injury); and PBM (weight drop injury with 3 days of daily 20 mW/cm^2 810 nm PBM).

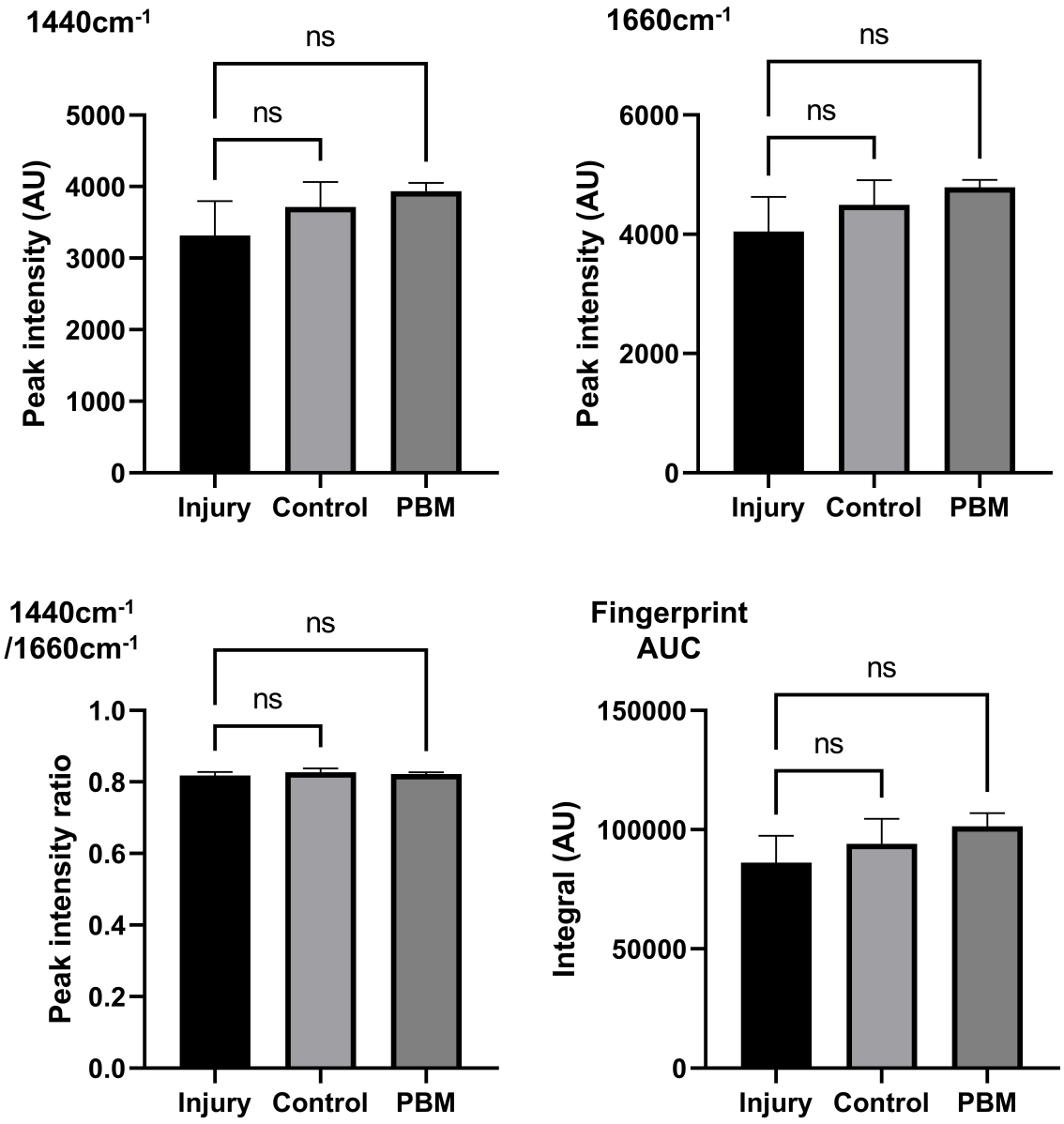


Figure 4.16: Quantitative analysis of peak intensity metrics from Raman spectra. 1440 cm^{-1}: baseline adjusted peak intensity of 1440 cm^{-1}. 1660 cm^{-1}: baseline adjusted peak intensity of 1660 cm^{-1}. 1440 cm^{-1}/1660 cm^{-1}: baseline adjusted peak intensity of 1440 cm^{-1}/1660^{-1} ratio. Fingerprint AUC: baseline adjusted area under the curve (AUC) of fingerprint region (1300-1800 cm^{-1}). n = 6 per group. ns = not significant.

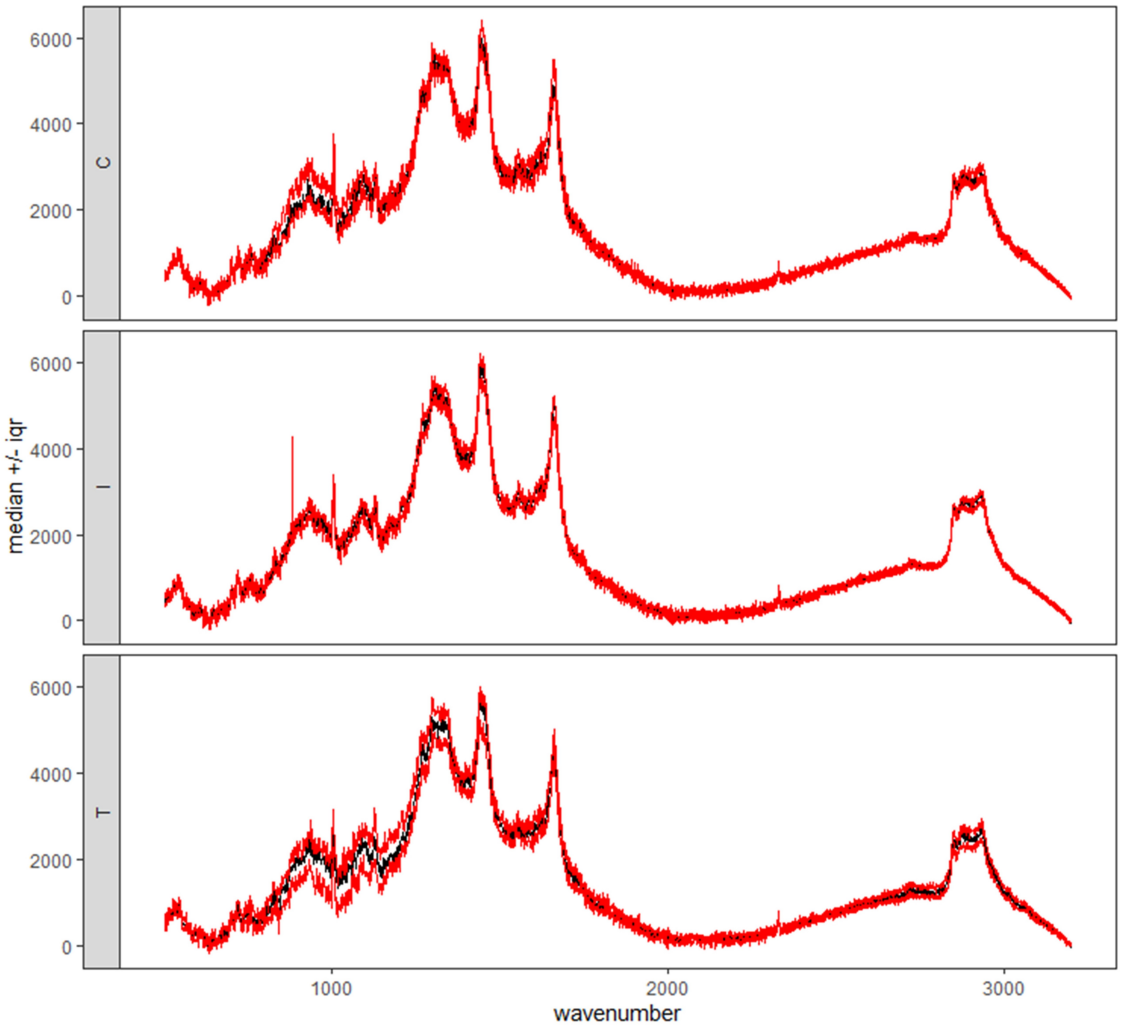


Figure 4.17: Extended spectra of treatment, injury and control groups, black shows median with interquartile range in red. From n = 6 spectra per group, baseline corrected.

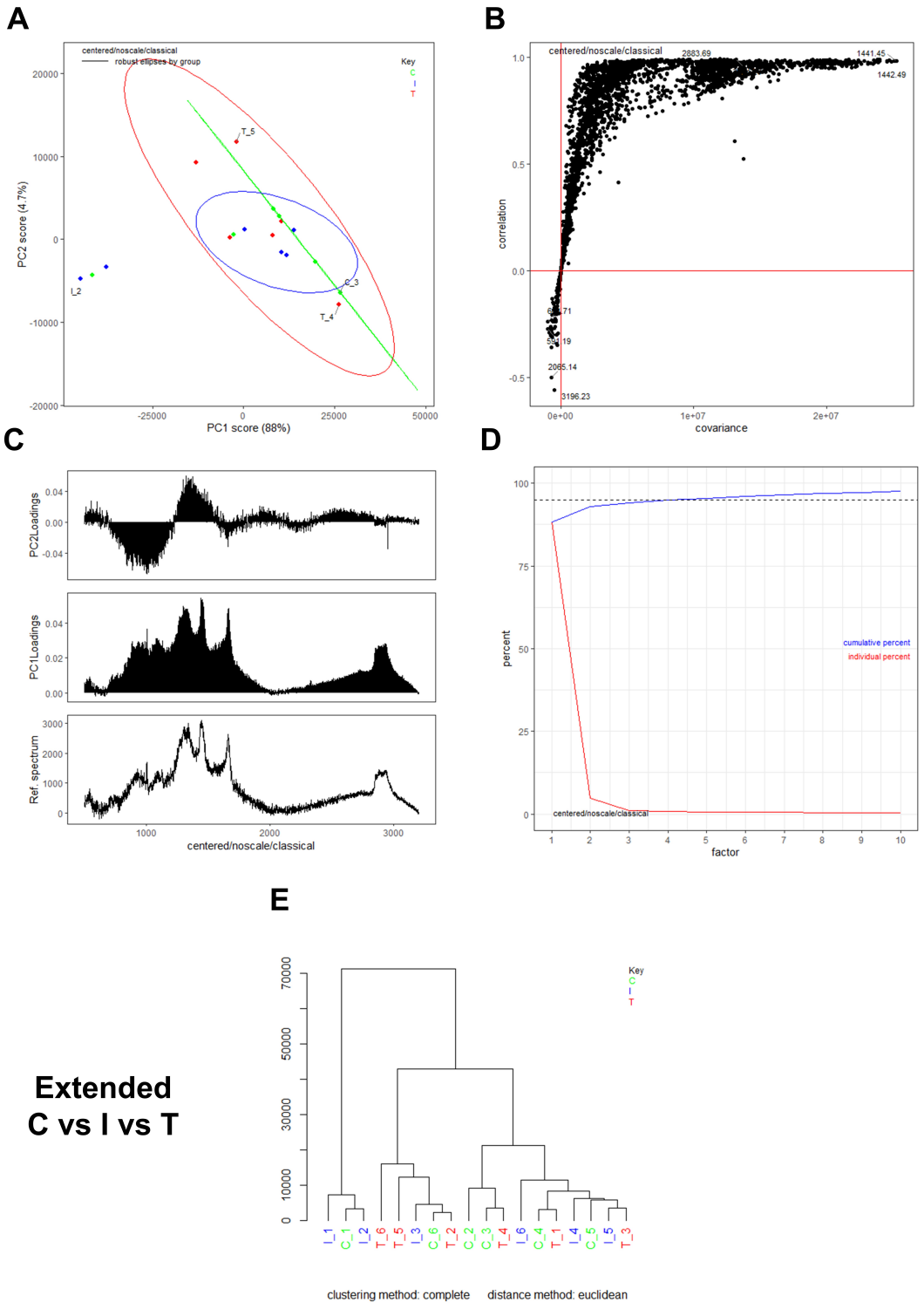


Figure 4.18: Caption on next page.

Figure 4.18: Figure on previous page. Principle component analysis of peak intensities of extended Raman spectra after TBI (treatment vs injury vs control). Exploratory data analysis of all three groups (T = treatment with PBM; I = TBI with sham treatment; C = control (no injury)). A: Classical principal component analysis (PCA) scores B: s-Plot to identify influential frequencies with identification of the most influential frequency variables. C: Loading plot of PC1 and PC2 against reference spectra. D: Scree plot of 10 PC factors. E: hierarchical cluster analysis (HCA) of PCA scores. n = 6 per group.

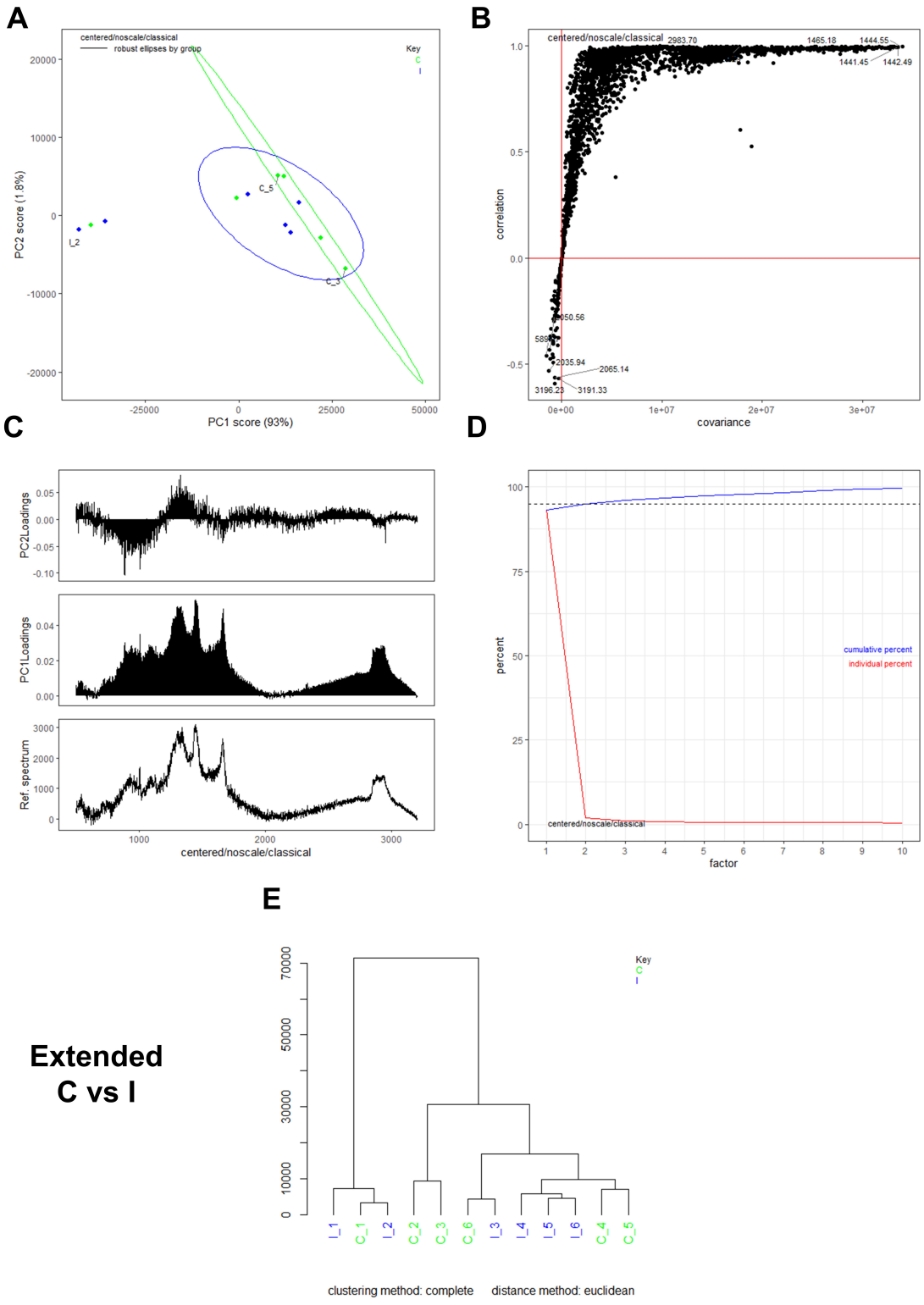


Figure 4.19: Caption on next page.

Figure 4.19: Figure on previous page. PCA of peak intensities of extended Raman spectra after TBI (injury vs control). Exploratory data analysis of injury and control groups (I = TBI with sham treatment; C = control (no injury)). A: Classical principal component analysis (PCA) scores B: s-Plot to identify influential frequencies with identification of the most influential frequency variables. C: Loading plot of PC1 and PC2 against reference spectra. D: Scree plot of 10 PC factors. E: hierarchical cluster analysis (HCA) of PCA scores. n = 6 per group.

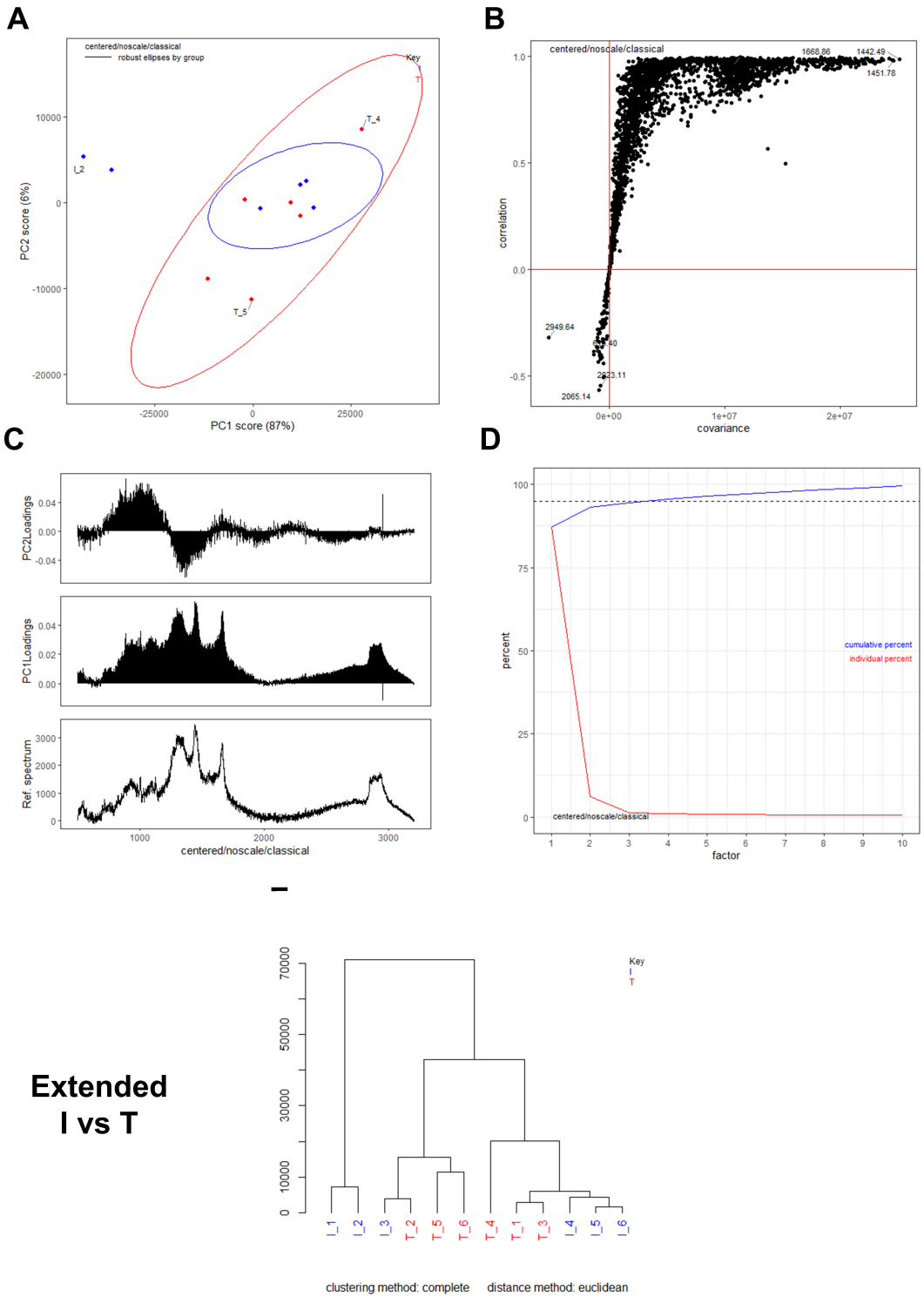


Figure 4.20: Caption on next page

Figure 4.20: Figure on previous page. PCA of peak intensities of Raman spectra after TBI (treatment vs injury). Exploratory data analysis of treatment and injury groups (T = treatment with PBM; I = TBI with sham treatment; C = control (no injury)). A: Classical principal component analysis (PCA) scores B: s-Plot to identify influential frequencies with identification of the most influential frequency variables. C: Loading plot of PC1 and PC2 against reference spectra. D: Scree plot of 10 PC factors. E: hierarchical cluster analysis (HCA) of PCA scores. n = 6 per group.

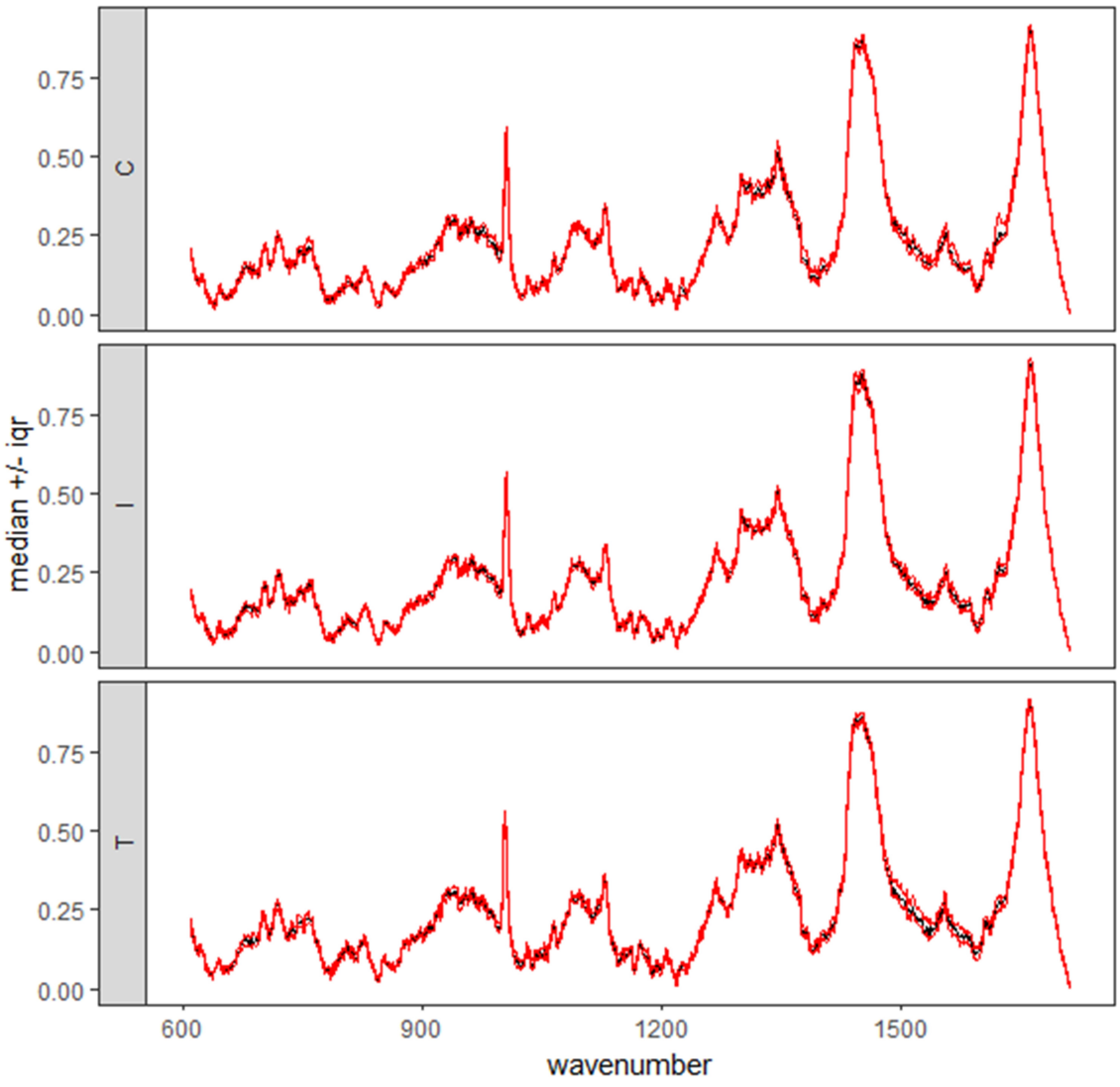


Figure 4.21: Fingerprint region spectra of treatment, injury and control groups, black shows median with interquartile range in red. From n = 6 per group, means of 98x 1 s exposure spectra per specimen, normalised, baseline corrected.

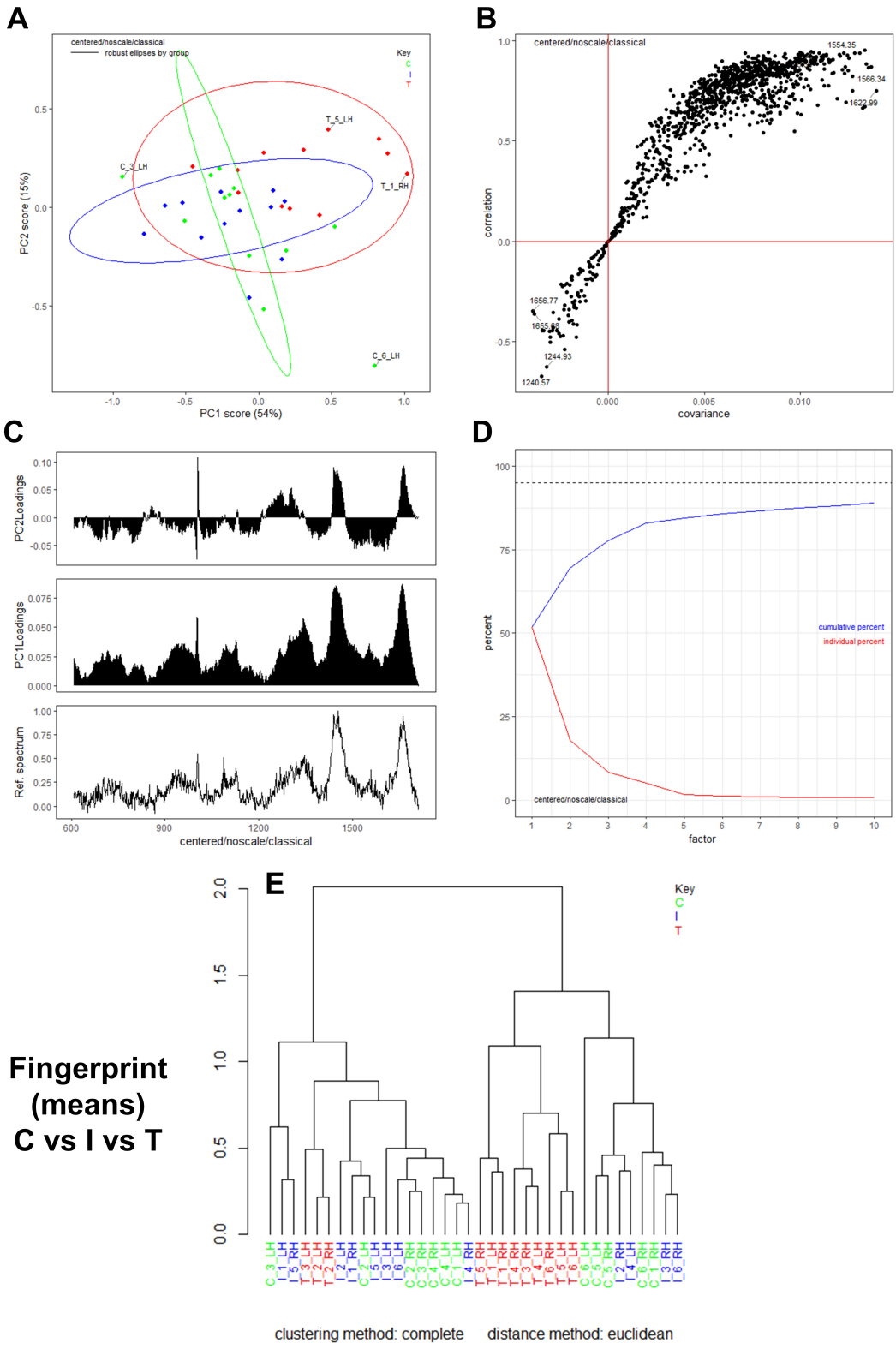


Figure 4.22: Caption on next page.

Figure 4.22: Figure on previous page. PCA of fingerprint region means of mapped Raman spectroscopy after TBI (treatment vs injury vs control). Exploratory data analysis of all three groups (T = treatment with PBM; I = TBI with sham treatment; C = control (no injury)). A: Classical principal component analysis (PCA) scores B: s-Plot to identify influential frequencies with identification of the most influential frequency variables. C: Loading plot of PC1 and PC2 against reference spectra. D: Scree plot of 10 PC factors. E: hierarchical cluster analysis (HCA) of PCA scores. n = 6 per group.

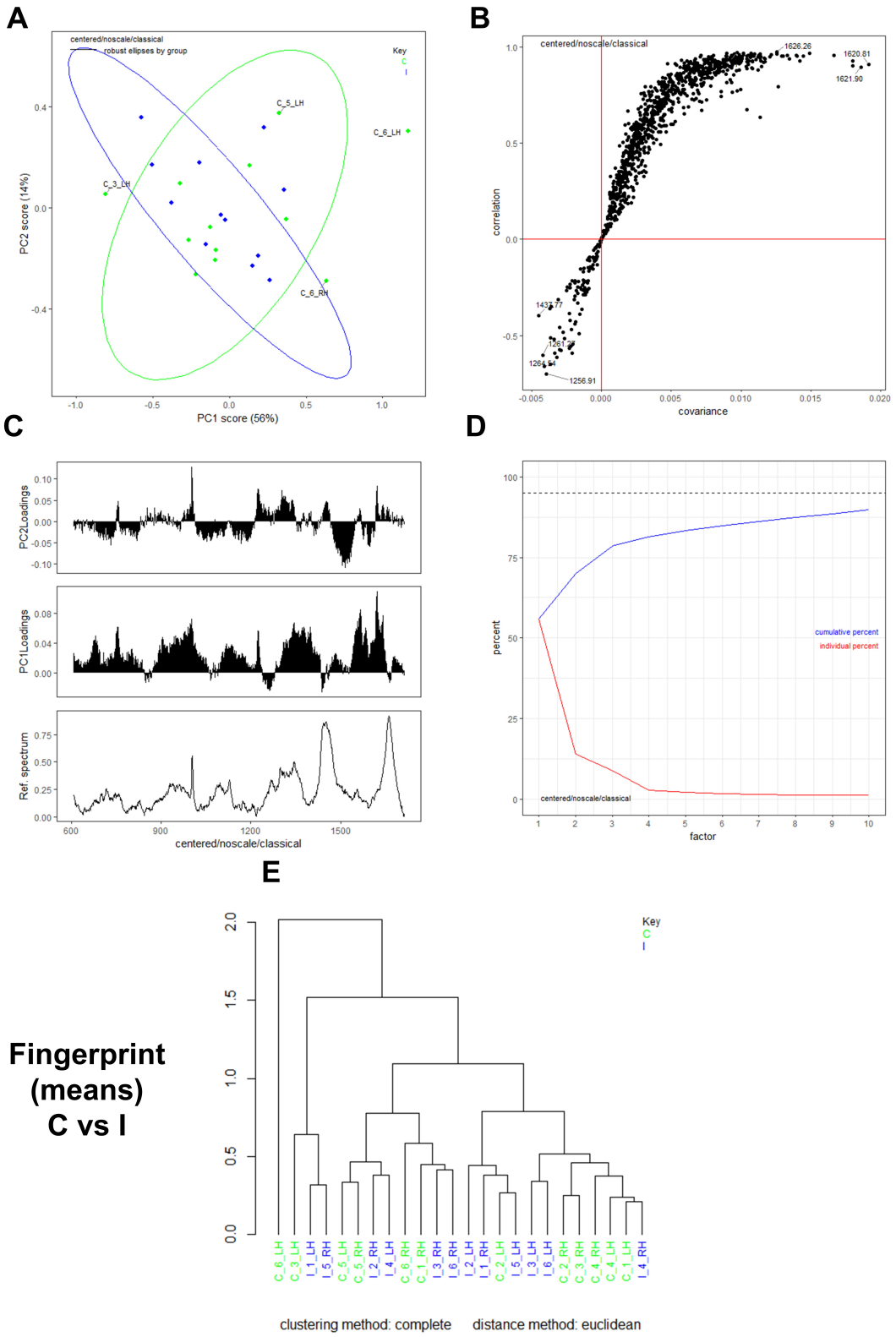


Figure 4.23: Caption on next page.

Figure 4.23: Figure on previous page. PCA of fingerprint region means of mapped Raman spectroscopy after TBI (injury vs control). Exploratory data analysis of injury and control groups (I = TBI with sham treatment; C = control (no injury)). A: Classical principal component analysis (PCA) scores B: s-Plot to identify influential frequencies with identification of the most influential frequency variables. C: Loading plot of PC1 and PC2 against reference spectra. D: Scree plot of 10 PC factors. E: hierarchical cluster analysis (HCA) of PCA scores. n = 6 per group.

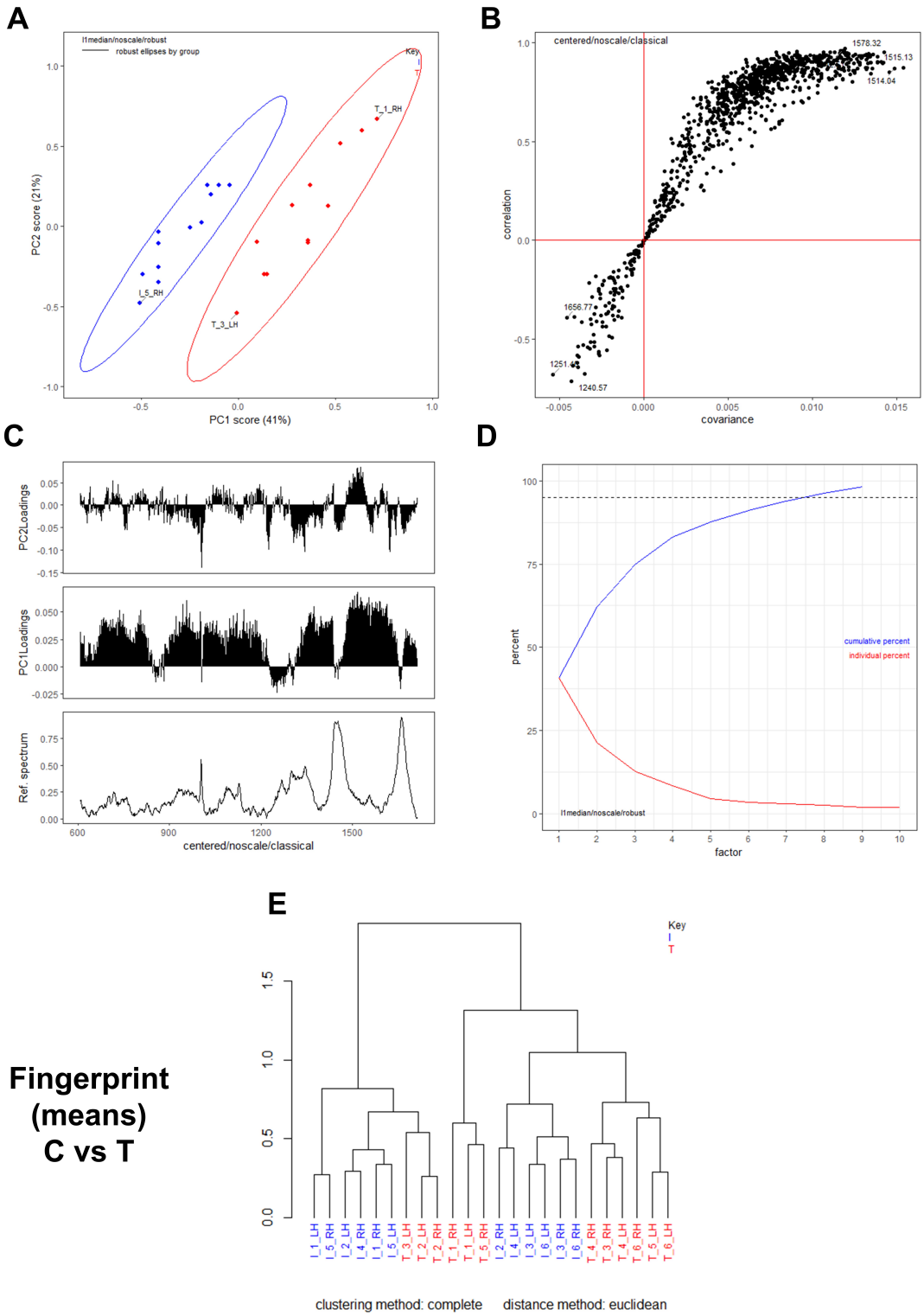


Figure 4.24: Caption on next page

Figure 4.24: Figure on previous page. PCA of fingerprint region means of mapped Raman spectra after TBI (treatment vs injury). Exploratory data analysis of treatment and injury groups (T = treatment with PBM; I = TBI with sham treatment; C = control (no injury)). A: Classical principal component analysis (PCA) scores B: s-Plot to identify influential frequencies with identification of the most influential frequency variables. C: Loading plot of PC1 and PC2 against reference spectra. D: Scree plot of 10 PC factors. E: hierarchical cluster analysis (HCA) of PCA scores. n = 6 per group.

4.4 Discussion

This chapter has demonstrated efficacy of transcranial delivery of 20 mW/cm^2 PBM for the improvement of functional and histological outcomes after mild TBI, reducing astrocyte and microglial activation in the acute phase and is associated with a reduction in expression of pro-apoptotic marker cleaved caspase-3 in the early post-injury phase. Study of Raman spectral signatures of uninjured, injured and treated conditions by direct-to-brain spectral acquisition has shown that these injury states can be differentiated using PCA, and may prove to be of translational benefit for monitoring brain responses to therapeutic intervention.

4.4.1 Wavelength selection

Comparison of 660 nm and 810 nm wavelengths, alone and in combination, demonstrated equivocal efficacy of 660 nm and 810 nm in BW recovery. 660 nm and 810 nm used in combination was ineffective for balance recovery. Combination of 660 nm and 810 nm PBM has been shown to offer differing and advantageous effects in improving brain metabolism compared to use of 810 nm alone, though such an effect was not observed here.[373] The theoretical advantage of combination therapy is that, if complementary wavelengths target differing chromophores, then favourable activity can be stimulated by their use together, eliciting a compound effect over that of activation of a single chromophore via one wavelength. However, it is known that 660 nm and 810 nm both activate a principal PBM target chromophore, CCO.[374] As such, this finding tentatively supports the primary role of CCO as a key mediator in the mechanism of effect after TBI. 810 nm PBM holds a further advantage over 660 nm, due to its increased penetrance through tissue.[375] Whilst an invasive delivery paradigm makes this wavelength property less important for transmission to the cortical surface, longer wavelengths are advantageous in improving transmission to tissue at depth through parenchyma. This too may be an explanation, at least in part, for the greater efficacy observed with 810 nm PBM. Nevertheless, synergistic effects of combined wavelengths have been observed in other pathologies, and the concept warrants further exploration in neurotrauma.[376]

4.4.2 Delivery method

This chapter has used focal transcutaneous delivery of PBM, across 12 adjacent points on the scalp, and as such does this does not provide additional evidence for the efficacy of implantable PBM delivery devices. This has been demonstrated in Chapter 3 for SCI, though the diffuse nature of TBI warrants its separate study. This work however does provide a basis for the future study of invasive intracranial application of PBM through further experiments, using the device principles described in Chapter 3, using this TBI model and the markers of recovery identified in this chapter.

4.4.3 Mechanism

Quantitative immunofluorescence imaging in this chapter has demonstrated that 810 nm PBM reduces expression of astrocyte (GFAP) and microglial (CD11b) activation markers induced in the early phase post-injury after mild TBI. This effect of PBM on microglia and astrocytes has been observed in SCI.[335] Wang and colleagues demonstrated that this effect was mediated by PBM interfering in pro-inflammatory crosstalk between lipocalin-2 (Lcn2) and janus kinases (JAK)/STAT3 pathways to mitigate glial activation after injury.[335] The effect of PBM on microglia/astrocyte activation is highly dose-dependent, in accordance with the biphasic dose-response of PBM. In analgesic contexts, higher energy PBM has been deployed: at these levels (8 J/cm^2 per day) PBM is associated with an increase in microglial activation.[377]

At 3 dpi, it was also shown here that PBM is associated with reduced expression of cleaved caspase-3. Cleaved caspase-3 is a recognised apoptotic mediator in CNS injury,[378,379] and its gross downregulation suggests a reduction in apoptotic activity amongst all cell types in the cortex with PBM. It has been shown previously that mitochondrial damage associated with TBI results in cytochrome c release leading to caspase-3 induction.[380] This may therefore represent a mechanism by which PBM may avert apoptosis specifically in injurious states, by mitigating mitochondrial damage mediated pro-apoptotic pathways.

Minimal changes in ECM proteins, fibronectin and laminin, were observed between unin-

jured and injured brains. The main sites for observed change were in the choroid plexus and periventricular caudate putamen. As the choroid plexus is a site of capillary permeability, as well as an area sensitive to damage after physical force,[381] this is a significant area for entry of immune cells post-injury, which may then subsequently migrate into the periventricular zone.[382] Dampening effects of inflammation in this region after PBM may mediate the reduction observed in the early immunofluorescence of fibronectin/laminin in these areas. The effects of mild TBI and therapeutic interventions specific to these areas, as well as circumventricular organs, should be the subject of further investigation.

4.4.4 Raman spectroscopy

In contrast to the clear metric of the 1440/1660 ratio which was able to differentiate PBM treated hippocampal slices (Appendix B) from untreated slices, this simple metric did not reliably describe injury states in this *in vivo* model. This may be due to differing injury severity: *in vivo* models have previously described similar clear shifts in this ratio after severe injury,[383,384] which are more subtly altered in mild injury.[383] S-plots in Figures 4.18/4.19/4.20 identify the 1660 cm^{-1} region as a key variable area in PCA between groups. Interestingly, PC1 weightings across all extended spectra comparisons loaded the high wavenumber region (2800-3800 cm^{-1}) in addition to the fingerprint region. This is of importance, as work using probe-based RS systems *in vivo* have principally focused on this region as it is technically less challenging to acquire these spectra from *in vivo* brain.[235] Further investigation of the dynamic shifts after injury within this spectral region may identify novel spectral biomarkers which alter with injury/therapy, and may prove more robust for translation to humans. However, the differentiation of the groups using PCA is encouraging for continued work using Raman spectra from direct monitoring as an injury/therapy biomarker. Analysis using advanced machine learning (with greater sample sizes) may describe a more robust differentiation between injury/treated states than that identified here.[347]

4.4.5 Limitations

There are a number of limitations which must be recognised in the interpretation of this work. Whilst there are advantages of the use of a mild TBI model in demonstrating the power of RS in recognition of therapeutic effects of PBM, the pathophysiology of moderate to severe injury significantly differs from that of mild, and limits the scope for extrapolating these findings to more severe injury types. Similarly, as a diffuse injury model, use of a mild weight drop injury does not help to establish the effects of PBM on contusional lesions. However, these have been shown elsewhere,[168,172,174,244,246–249,251,252,255] as well as in the SCI model in Chapter 3. It should also be noted that the control group received no inhalational anaesthesia or scalp incision (i.e. sham injury), and were intact animals which were terminated in the same manner as the experimental groups (injection of anaesthesia). This may introduce some inter-group differences in addition to those elicited by exposure to injury. This chapter has administered PBM in multiple key wavelengths but has not explored other variables. The basis of dose parameter selection was a combination of *in vitro* data (Appendix B); parameters reported in the literature (Chapter 2); and successful doses in SCI (Chapter 3). However, the variables used are clearly not exhaustive, and wider exploration of such variables (including PW, average irradiance, and duration) may yield greater efficacy.

4.5 Conclusion

The work presented in this chapter provides significant evidence on the efficacy of PBM in mild TBI, and importantly the advantage of 810 nm as the most effective wavelength for promoting recovery. This informs the development of the proposed device, with incorporation of 810 nm as the delivered wavelength to become an evidenced design feature. In contrast to Chapter 3, this work has not used invasive delivery of PBM, however this chapter provides a basis upon which implantable PBM for TBI can be explored in subsequent experiments. The ability of RS methods to differentiate injury states, even in mild TBI, supports its continued development as a functional feature of the proposed device. This chapter has also demonstrated insights into the

mechanisms by which PBM can mitigate damage and promote repair after neurotrauma. These mechanisms will be explored further in Chapter 5.

Chapter 5

MECHANISMS OF PHOTOBIOMODULATION IN NEUROTRAUMA

To support the findings of described in Chapters 3 and 4, this chapter investigates the mechanisms of PBM in neurotrauma.

5.1 Introduction

This section introduces the current knowledge of mechanisms of PBM (specifically R/NIR, 600-850 nm) and its interaction with cells of the CNS.

5.1.1 Mechanisms of photobiomodulation

The means by which PBM elicits a biological effect can be understood on four levels:

1. Primary mechanisms: a basis of photobiological interaction where photonic energy is absorbed, and a biological effect initiated;

2. Secondary mechanisms: initiator biological mediators, with their altered activity directly initiated by photon absorption;

3. Tertiary mechanisms: subsequent molecular cascades and cellular level responses which occur as a consequence of secondary mechanisms;

4. Quaternary mechanisms: tissue/organ/system level effects, occurring due to events at a molecular and cellular level.

Primary mechanisms

As observed by the first law of photochemistry (1.5.3), light is absorbed by a compound which allows a chemical event to take place. Within biological systems, it is generally accepted that effective chromophores are predominantly found in mitochondria.

Cytochrome c oxidase Work over several decades from Karu[271,272,374] has firmly established the role of CCO as a core photoacceptor and primary initiator of the mechanism of action of PBM. The metallic components of CCO (two copper and two haem centres) are the specific proposed photoacceptors of wavelengths between 600-850 nm.[82] The location of CCO within the ETC implicates the mitochondria as the main site for the primary action of PBM. Photoexcitation of CCO leads to release of NO, increasing mitochondrial membrane potential (MMP), an increase in ATP and cAMP synthesis, and modulation of calcium signalling.[323]

As specific examples, experiments using 620 and 760 nm PBM showed increased neurite outgrowth, with the effect attenuated by siRNA-induced or ADDA 5 CCO inhibition.[385] However, given the intrinsic necessity of CCO for cell survival, it is not possible to completely eradicate CCO activity whilst maintaining cell viability, and the effect of this suppression alone (in control without PBM) was not shown. Pchelin and colleagues used high resolution respirometry of cerebral cortex isolated mitochondrial samples from hypoxic/control mice. 650 nm light was found to normalise respiration at complex-I of the ETC, but not complex-IV, suggesting the absence of a direct effect of CCO chromophore activity on its own complex, though it may mediate the effects at other complexes. Similar observations have been made in diabetic retinopathy models.[386]

Other photoacceptors Whilst of less relevance to PBM mechanisms using stimulation with wavelengths in the 600-850 nm region, it is worth noting the presence of other chromophores which are photoacceptors for photons from across the UV/Vis/IR spectrum.[154] These include transient receptor potential (channels) (TRP) channels, opsins, flavins, porphyrins, light-gated ion channels, and heat-gated ion channels.[82,154,274,323]

Secondary mechanisms

Reactive oxygen species It is generally considered that PBM stimulates a modest increase in ROS and NO production within the mitochondria in a dose-dependent manner.[323] This emphasises the importance of PBM parameters and energy transmission. Only specific windows of ROS induction appear beneficial in injury states.[385] Kao and colleagues that differing treatment parameters for 620 or 760 nm light (even where wavelength was unchanged) resulted in significant changes in ROS intensity, which in turn correlated with levels of induced neurite outgrowth. Notably, these *in vitro* conditions were not that of a stress model, and so the relative change from baseline ROS levels induced by PBM will differ from those in cells under stressed conditions. For example, ROS concentrations have been shown to be reduced by PBM in cortical neurons under oxidative stress, but increased by cells in a normal state.[270,387] Similarly, in resting state cultured astrocytes, 660 nm PBM has been shown to increase levels of ROS and thereby promotes biological activity such as differentiation and migration.[293]

Nitric oxide Similarly to ROS, PBM induces small increases in the physiological transmitter NO, contributing to its favourable biological effects in a dose-dependent manner.[323] PBM has varying effects on inducible NOS. After cerebral ischaemic injury in pre-clinical models, inducible NOS activity has previously been shown to decrease in response to 660 nm PBM (2.6 J/cm^2 daily) at post-injury day 4.[388] Furthermore inhibition of NOS has been shown to be neuroprotective.[389] However, across a variety of studies on endothelial dysfunction and PBM, NO and NOS have been shown to generally be induced by PBM.[390,391]

Mitochondrial membrane potential Optimal PBM parameters are thought to increase MMP,[323] in a manner which is similarly dose-dependent as previously shown in cortical neurons.[170] PBM has been found to restore the polarisation of the inner mitochondrial membrane in a brain hypoxia model,[392] which correlates with findings from *in vitro* studies.[387,393,394] For example, JC-1 dye derived measurements of MMP were significantly improved by PBM using 810 nm exposure in OGD injured cortical neurons.[394] Mitochondrial activity has been shown to be improved by PBM *in vitro* by using 3-(4, 5-dimethylthiazolyl-2)-2, 5-diphenyltetrazolium bromide (MTT) reduction assays[394]

Adenosine triphosphate Impaired ATP production in an OGD model has been shown to improve toward normal levels with 810 nm PBM.[394] Additionally, the role of ATP as a signalling molecule has been recognised as a mediator of the effects of PBM.[271] ATP receptors P2Y2 and P2Y11 have been shown to be expressed by neural progenitor cells (NPrC).[395] NPrCs increase neurite outgrowth *in vitro* in response to 810 nm light treatment in the absence of growth factors, by stimulating production of BDNF, FGF2 and NGF. This effect can be inhibited by suramin, a non-specific P2 receptor antagonist, suggesting that PBM induced ATP signalling at these receptors acts as an initiator mechanism. In neurotrauma states, it is more difficult to perceive that increased P2 receptor signalling activity would be beneficial. For example, P2 (subtype P2X7) signalling has been demonstrated to have a key role in promoting neuroinflammation after TBI and SCI,[396–398] and antagonists have been shown to attenuate inflammation and improve outcomes *in vivo*.[397] Mechanistically this is comprehended on the basis that ATP binding at P2X receptors results in a transmembrane channel to form, which permits intracellular entry of Na^+ and Ca^{2+} cations, which potentiates excitotoxicity and metabolic/mitochondrial distress. However, some work has shown that PBM reduces intracellular Ca^{2+} concentrations in excitotoxicity models.[393] Further work is required on understanding the effects of PBM on ATP signalling, calcium homeostasis and neuroinflammation to harmonise these currently conflicting concepts, and like other mechanisms is likely to be dependent on the baseline state of the cell as to its response to stimulation by PBM.

Calcium homeostasis PBM activity in the increase of ATP production has been proposed as a key mechanism in increasing intracellular calcium via activity at P2Y receptors,[399] leading to influx and release from endoplasmic reticulum (ER) endoplasmic reticulum via NMDA receptors.[400] PBM has been shown to improve intracellular calcium homeostasis and reduce intracellular calcium levels in cultured cortical neurons.[170,393] It is thought that at low levels of irradiance, this does not breach cytotoxic levels via PBM activity mitigating ER stress.[400,401] This again suggests a mechanism which is dependent on the pathophysiological stress state of the cell: glutamate, NMDA or kainate induced excitotoxicity in a primary cell culture model of mouse cortical neurons showed a modest reduction in apoptosis with PBM. This was accompanited by significant increases in ATP concentration and MMP, with reductions in NO concentrations, oxidative stress levels and intracellular Ca^{2+}.[393] As such, calcium homeostasis effects of PBM can be understood as a context-dependent modulation rather than an absolute up- or down-regulation in activity. For example, it has been shown that PBM normalises mouse brain cortical respiration in hypoxic conditions, whilst in normal conditions respiration is suppressed with PBM exposure.[392] Similarly for oxidative stress, ROS concentration changes in response to PBM are entirely dependent on the baseline level.[387]

Tertiary mechanisms

Cellular and molecular signalling mechanisms, and the subsequent cellular effects on biological activity, can be considered as tertiary mechanisms which follow the triggers of the above described primary and secondary mechanisms.

Pathways A number of intracellular signalling pathways have been implicated in mediating the beneficial effects of PBM. Upregulation of cAMP production (via increased ATP availability) has been recognised as a central mediator for activation of PKA and Ras signalling.[402] Calcium dependent activation of the Raf/ERK and ERK/CREB pathway has been proposed as a mechanism by which growth factor (BDNF) transcription is upregulated after PBM in DRGN.[322] Downregulation of mitogen-activated protein kinases (MAPK), and consequently

reduced activation of NFκB, has been identified as an effect of PBM in attenuation of microglial and astrocytic activation in brain ischaemia.[403] cAMP mediated reduction in NFκB activity has been shown to attenuate inflammation.[404] Similarly, reductions in astrocyte activation with PBM has been demonstrated in SCI, mediated via reduced crosstalk between Lcn2 and JAK/STAT3 pathways.[43] PBM has also been shown to mediate beneficial effects by promotion of PI3K/Akt pathway,[405] associated with improved recovery in neurotrauma.[6] This effect has been proposed as a further effect of increased intracellular calcium, via calmodulin activity.[402]

Effects The anti-inflammatory effects of PBM, particularly in neuroinflammation, are well recognised.[294] PBM has a dose-dependent action on the polarisation of macrophages and microglia, and in the range of 1-10 J/cm^2 has anti-inflammatory (pro-M2) effects.[406] Further cellular effects of tertiary mechanisms of PBM, such as on apoptosis, synaptogenesis and inflammation, specific to neurotrauma are discussed in Chapter 2.

Quaternary mechanisms

Systemic or regional mechanisms have been described as a result of PBM therapy. These include increases in cerebral blood flow,[323] improved glymphatic drainage,[407] modulation of encephalographic oscillations[408] and improvements in synaptic plasticity.[409] These are also discussed further in Chapter 2.

5.1.2 Objectives

The mechanisms of PBM are not currently well elucidated, and are highly dependent on context and PBM parameters. Understanding of the mechanisms of PBM for improving outcomes in neurotrauma are vital for clinical acceptability, as well as to make well-reasoned hypothesis for the optimum parameters given the many variables involved. To this end, the objectives of this chapter are:

- To determine the effects of PBM on microglia to establish the role of neuroinflammation in the mechanism of PBM.

- To use DRGN cell culture and microglial cultures to evaluate the effects of PBM in resting state cultures CNS cells (via preconditioning).
- To use DRGN cell cultures (conditioned media model) to evaluate the role of paracrine signalling (e.g. through growth factor release) in neuroprotection.
- To investigate the effects of PBM *in vivo* on: apoptosis; ECM protein deposition; and glial cell activation.
- To further investigate the mechanisms of PBM in neurotrauma using transcriptomics.

5.2 Materials and methods

All experiments using human blood were approved by the University of Birmingham's Ethical Review Board and conducted in accordance with Human Tissue Act legislation. All animal procedures were licensed by the UK Home Office and approved by the University of Birmingham's Animal and Ethical Review Board. Surgeries were carried out in strict accordance with the guidance of the UK Animals Scientific Procedures Act, 1986. Power calculations using the National Centre for the Replacement Refinement and Reduction of Animals in Research (NC3Rs) Experimental Design Assistant was used to determine sample sizes and all animals were randomly assigned to treatment groups and masked to the experimenters until analysis was complete.

5.2.1 Induced monocyte-derived microglia cell culture

Human peripheral blood mononuclear cells (PBMC) were purified from blood cones (National Health Service Blood and Transplant Service, Birmingham, UK) from five healthy donors through density centrifugation with Ficoll-Paque PLUS (GE Healthcare, Illinois, USA). Monocytes were then enriched by negative selection (EasySep Human Monocyte Enrichment Kits; STEMCELL Technologies, Vancouver, Canada) and purity confirmed using anti-CD14 labelling (Biolegend, San Diego, California) to identify CD14+ monocytes. For differentiation

into induced monocyte-derived microglia (iMDM), monocytes were cultured in black-walled imaging plates (Greiner, Kremsmunster, Austria) at 1.0 x10^5 cells/well in RPMI-1640 with Penicillin/Streptomycin (penicillin 100 U, streptomycin 0.1 mg/mL; both Sigma, Missouri, USA), containing CNS-relevant human cytokines; M-CSF, GM-CSF and IL-34 (all Biolegend) for 6 days at 5.0% CO_2 at 37 °C. [i]

5.2.2 Application of photobiomodulation to iMDM

A bespoke device for PBM delivery was used (Fig. 5.1), composed of LEDs of varying wavelengths arranged in columns. An LED driver with variable resistors permitted fine adjustment of power output for each column. Calibration of output was performed using spectrometry (as described in Section 6.2.1). The fibre was positioned at the bottom of wells in 96 well plate placed directly on top of the device. Resistors were manually adjusted, guided by spectrometer outputs, targeting 24 mW/cm^2 aiming to minimise variability within and between wavelengths. The final average irradiance values recorded at the bottom of each well are given in the plate map (Fig. 5.2). For treatments, cell culture plates were removed from the incubator and placed on the PBM device (as in Figure 5.1), with a black cover positioned over the plate before activating the device for 2 or 5 min.

[i] Preparation of iMDM was performed by a collaborator, Jamie Cowley.

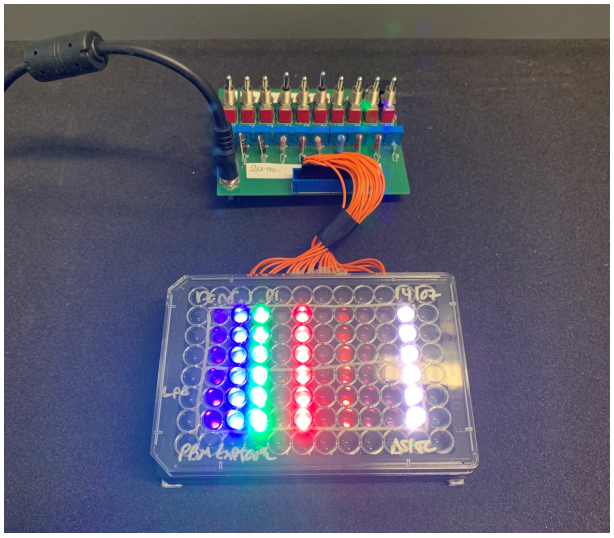


Figure 5.1: Bespoke 96 well plate illumination device

	1	2	3	4	5	6	7	8	9	10	11	12
λ (nm)	Empty	400 nm	450 nm	525 nm	Control	660 nm	Control	740 nm	810 nm	830 nm	White	Empty
A	Empty	Empty	Empty	Empty	Empty	Empty	Empty	Empty	Empty	Empty	Empty	Empty
B	Empty	23	23	26	0	23	0	20	23	24	24	Empty
C	Empty	23	23	27	0	26	0	22	23	27	31	Empty
D	Empty	24	24	13	0	25	0	29	27	25	26	Empty
E	Empty	25	25	14	0	20	0	27	18	22	23	Empty
F	Empty	25	25	12	0	24	0	29	23	24	20	Empty
G	Empty	24	24	30	0	22	0	23	25	23	20	Empty
H	Empty	Empty	Empty	Empty	Empty	Empty	Empty	Empty	Empty	Empty	Empty	Empty

B-D mean ± SEM	23.3 ± 1.2	23.0 ± 0.3	22.0 ± 4.5	0	24.7 ± 0.9	0	23.7 ± 2.7	24.3 ± 1.3	25.3 ± 0.8	27.0 ± 2.1
E-G mean ± SEM	23.3 ± 1.5	24.6 ± 0.3	18.7 ± 5.7	0	22.0 ± 1.1	0	25.3 ± 1.8	22.0 ± 2.1	23.0 ± 0.6	22.0 ± 1.0
B-G mean ± SEM	23.3 ± 0.7	24.0 ± 0.4	20.3 ± 3.3	0	23.3 ± 0.9	0	25.0 ± 1.6	23.2 ± 1.2	24.2 ± 1.2	24.0 ± 1.7

Figure 5.2: Calibration of bespoke 96 well plate illumination device. Values B2-G11 in mW/cm^2 recorded for the given well, values in bottom table averages for given zones. Colouration for 810/830 nm given for illustrative purposes.

5.2.3 Cytokine release quantification

Quantification of TNFα was performed on cell culture supernatants using a human TNFα DuoSet enzyme-linked immunosorbent assay (ELISA) kit, as per the manufacturer's instructions (R+D Systems, Minnesota, USA; catalogue number DY210). Supernatants were harvested from each well at the end of the culture period and stored at -20 °C until use. 96 well flat-bottomed high binding plates (Greiner, Austria) were coated with 100 μl capture antibody diluted in PBS (4 μg/ml) and incubated overnight at room temperature. Plates were washed 3x in PBS containing 0.05% Tween-20 (Sigma), followed by blocking with 300 μl reagent diluent (PBS containing 1% BSA) for 1 h. Plates were washed and samples were transferred from a prepared dilution plate (100 μl at 1:5-1:20), including 2-fold serial dilutions of standard up to a top standard of 1000 pg/ml. Plates were incubated for 2 h, washed, and then incubated for a further 2 h with 100 μl detection antibody (50 ng/ml). After further 3x washes, plates were protected from light and incubated for 20 min with 100 μl horseradish peroxidase conjugated streptavidin (strep-HRP), washed, and incubated with 100 μl colour substrate solution for 20 min before addition of 50 μl of stop solution. Plates were read on a colorimetric microplate reader (Infinite 200 Pro, TECAN, Mannedorf, Switzerland), measuring optical density at 450 nm after 10 s orbital shaking. Values were interpolated from the standard curve after plotting a 4-parameter logistic curve using Prism (GraphPad). Triplicate samples per condition were evaluated against a standard curve (performed in duplicate).

5.2.4 iMDM immunofluorescence

After harvesting the supernatant, cells were fixed using 4% formaldehyde for 10 min. Cells were washed 3x with PBS, and permeabilised in PBS containing 0.1% Triton-X-100 for 10 min. After washing, wells were blocked for 30 min using PBS containing 1% goat serum and 0.1% Tween-20. Primary antibodies were added and incubated for 1 h, before washing followed by addition of secondary antibodies (all antibody clones shown in Table C.1). Hoescht solution was added at a concentration of 1:1000 with secondary antibodies. Finally, wells were washed

3x, with cells left in 200 μl PBS prior to imaging.

5.2.5 iMDM imaging and image analysis

Imaging was performed using EVOS M5000 with integrated software (Invitrogen, Massachusetts, USA). Per well, 5 fields were taken at 20x magnification and analysed using ImageJ (imagej.net). For cell counts, Hoescht-stained images were processed by thresholding and automated cell count after watershed adjustment. For corrected total cell fluorescence (CTCF), for each condition 25 cells were selected (5 cells per image, chosen for highest fluorescent intensity) and individually traced. A representative background area was also traced. Measurements were taken for area, mean gray value and integrated density. CTCF was calculated using the formula:[410]

$$CTCF = id - (area \times background)$$

Where: CTCF = corrected total cell fluorescence; id = integrated density; area = area of selected cell; background = mean fluorescence of background.

5.2.6 DRGN serum transfer model

To investigate the effect of PBM on the release of factors into the media by cells in DRGN culture, as a possible mediator of neuroprotective effects, a serum transfer of conditioned media model was used. Concentration of the media was performed using Pierce Protein Concentrators (3kDa cut-off, 5-20 ml, 88525 Thermo Fisher Scientific, Massachusetts, USA). Protein Concentrators were sterilised using a 70% ethanol solution. The filter chamber was filled with ethanol and the concentrator was centrifuged at 300 g for 10 minutes. After discarding the ethanol, this process was repeated with sterile PBS. A further wash-centrifuge cycle was repeated with ethanol, and two further cycles with PBS. Concentrators were then allowed to air dry in a laminar hood for 45 min.

DRGN primary cell culture preparation was performed as above, with treatment with PBM or ambient light control performed every 20-24 h for 4 days post-serum withdrawal. 1 h after

the final treatment, the media was withdrawn and centrifuged at 1600 rpm for 5 min to remove any remnant cellular debris. After centrifugation, the supernatant was transferred to protein concentrators, and subjected to further centrifugation at 1000 g for 10 min cycles at 4 °C, repeated *pro re nata* to achieve 4x concentration.[411] P/S solution was then added at a v/v 0.5% to the concentrated media, and the solution was warmed to 37 °C. Fresh DRGN cell cultures were prepared as above. After 24 h, the media was withdrawn and cells gently washed with PBS at 37 °C 1X. Media was then replaced with media from PBM treated or control treated plates, at varying concentrations (100, 50 and 20%, diluted with DMEM (0 g/dL glucose, Gibco) containing 1% P/S) and cultured for a further 5 days.

5.2.7 DRGN preconditioning model

To assess the effects of PBM on neuronal survival by administration only prior to serum withdrawal injury (preconditioning), DRGN primary cell cultures were prepared as described above, initially plated with DMEM + PBS. 3x PBM treatments were administered over the first 16-24 h. 30 min after the third treatment, the media was removed and cells washed gently with warmed PBS, before replacing with either DMEM + PBS or DMEM alone (both with 1% P/S).

5.2.8 Cell lysis and protein extraction

After treatment or controlled conditions, cells were lysed for protein extraction and subsequent analysis. After removal of media, wells were washed with two changes of room temperature PBS. 150 μL of ice cold cell lysis buffer (Cell Lysis Buffer II, FN0021 Invitrogen) (supplemented with protease inhibitor cocktail (P1860, Sigma) at a concentration of 5 μL/ml) was then added to each well. 8 well plates were then agitated at 30 rpm on an orbital shaker at 4 °C for 30 min. Lysate was then removed and centrifuged for 10 min at 13,000 rpm at 4 °C. The supernatant was then homogenised and aliquoted for subsequent analysis, after storage at -20 °C until use.

5.2.9 BDNF ELISA

A rat BDNF ELISA kit (ab213899, Abcam, Cambridge, UK) was used according to the manufacturer's instructions, using the technique described above for cytokine quantification.

5.2.10 *In vivo* model

In vivo SCI modelling, and associated tissue preparation and immunofluorescence techniques, were performed here as described in Chapter 3. Antibody clones used are given in Table C.1. For cleaved caspase-3 cell counts, after thresholding in ImageJ, Neuronal nuclei with positive fluorescence were counted and expressed as a ratio of number of NF-200 $^{+ve}$ DRGN. For quantitative immunofluorescence of glial activation markers and ECM proteins, fixed area ROI were used between images and conditions to capture integrated density of fluorescence from the injury site.

5.2.11 Transcriptomics

In vivo SCI modelling was performed as described in 3.2.4. Animals were randomised to receive either DCC injury alone, or DCC injury plus 3 days' treatment with daily PBM (24.42 mW/cm^2, transcutaneous, 1 min per day), as described in 3.2.2. n = 4 animals were used per group.

5.2.12 Tissue extraction and RNA purification

Instruments and surfaces were prepared with copious RNase Zap solution (Invitrogen, Massachusetts, USA). Animals were sacrificed 3 days post-injury by intraperitoneal injection of pentobarbital, and immediately *post mortem* a 0.5 cm section of T8 spinal cord (centred on the injury site) was isolated and immediately frozen in liquid nitrogen until use. RNA extraction and purification was performed using an RNeasy lipid tissue Mini Kit (Qiagen, Germany), according to the manufacturer's instructions. The tissue was removed from liquid nitrogen storage homogenised in 1 ml QIAzol lysis reagent (Qiagen) using an IKA T10 Ultra-Turbax (IKA-Werke, Staufen, Germany) for 40 s per sample. The homogenate was kept at room temperature for 5

min. 200 μl chloroform was added and the sample was vigorously agitated before a further period of 3 min at room temperature. Samples were centrifuged at 12,000 g for 15 min at 4 °C and the aqueous phase transferred to a fresh tube. 600 μl 70% ethanol was added and the sample vortexed before duplicate centrifugation through the RNeasy mini spin column for 15 s at 8,000 g. The spin column membrane was washed with buffer RW1 by centrifugation for 15 s at 8,000 g. Two centrifugation steps were performed at 8,000 g with RPE buffer, first for 15 s, then 2 min with fresh RPE buffer. To eliminate carryover, the spin column was centrifuged dry in a fresh collection tube at full speed for 1 min. The RNA was captured by adding RNase-free water to the spin column and collecting the elute. This step was repeated, resulting in a high and low concentration sample. Concentration of RNA was determined using a nanophotometer (N60, IMPLEN, Germany) to derive A260/A280 ratio.

5.2.13 WT-seq and analysis

Further quality control measures and library preparation for whole transcriptome analysis were outsourced to Qiagen (Germany). Detail is given in the appendix (F). Trimmed raw read counts were analysed using iDEP96.[412] Genes were pre-processed to limit genes to 0.5 counts per million and appearing in at least one library. Samples were grouped into T (treatment: DCC+PBM) and C (control: DCC and sham therapy) for comparative analysis. Count data was transformed for clustering and principle component analysis using EdgeR: log2(CPM+c). Differentially expressed genes were identified using DESeq2 with a FDR adjusted p value of 0.05, with a minimum fold change of 2. Volcano plots were rendered using Prism (GraphPad). k-means analysis was performed in iDEP96 using the top 1000 variable genes (with FDR<0.05) limiting clusters to 3. Heatmaps were plotted in R[344] (www.R-project.org) using ggplot2[413] (for top 1000 variable genes) and using the ComplexHeatMap package[414] (for top 10/20 up/downregulated genes and specific gene families).

Pathway analysis using generally applicable gene-set enrichment (GAGE) method was performed with a pathway significance cut off of 0.05 (FDR). Gene set size range used was 5-2000. The top 20 pathways for gene ontology (GO) and Kyoto encyclopedia of genes and genomes

(KEGG) terms were identified. For KEGG pathway analysis, absolute fold changes were used. For cross-validation of GO/KEGG hits, supplementary functional enrichment analysis was performed in g:profiler,[415] selecting the top 20 relevant hits across all databases. For exploratory network analysis of GO terms and KEGG pathways, pathway networks were retrieved from STRING Database (V10[416]) and imported into Cytoscape (v3.10.1, Washington, USA). For large pathways, central nodes were selected from the top ten hits (by fold change, filtered by FDR < 0.05) and first neighbours of selected nodes were integrated into a new pathway (undirected neighbours). Fold changes were mapped to network components using integrated functionality of Cytoscape, and Z-scores were generated to display fold change of nodes.

5.2.14 Statistical analysis

Statistical analysis was performed using Prism (Version 9.2.0, GraphPad). For comparisons of TNFα concentrations, repeated measures one-way ANOVA with Sidak's multiple comparisons test was performed (for paired data). Due to inter-donor variability in response to LPS stimulation, TNFα concentrations were standardised as relative concentrations to LPS with control conditions (no PBM). For comparison of BDNF concentrations, unpaired t-test was used. For immunofluorescence analysis, one-way ANOVA was performed with post-hoc Dunnett's method for multiple comparisons.

5.3 Results

5.3.1 Induced monocyte-derived microglia model

To investigate the specific response of microglia to PBM at varying wavelengths, iMDM from human donors were used. After differentiation, iMDM expressed phenotypic markers of adult human microglia, and reacted when challenged with 100 ng/ml LPS, showing increased activation states (determined by Iba1 expression) and anticipated features of activation (adapting amoeboid morphology, cellular clumping/aggregation) (Fig. 5.3).

iMDM were exposed to vehicle or LPS, with columnar plate irradiation using the PBM device in Figures 5.1 and 5.2. PBM was administered at 23 mW/cm^2 for 2 and 5 minutes. For cells in resting state (vehicle), modest responses to PBM were elicited below the threshold for statistical significance (Fig. 5.4 A/C). With 120 s PBM of wavelengths 525, 660, 740 and 810 nm, TNFα concentrations in the supernatant were below control levels. TNFα release was significantly above control levels for LPS exposed iMDM also exposed to 400 nm PBM, and significantly (though modestly) below control levels after exposure to 660 nm (Fig. 5.4 B). After 5 min exposure, 400 nm PBM correlated with a similar increase in TNFα release, though this did not reach statistical significance. Reductions in TNFα release after 5 min exposure to 660 nm were more modest, and did not reach statistical significance (Fig. 5.4 D).

Immunofluorescence staining was performed on cultures exposed to 2 min PBM conditions (Fig. 5.5). Quantification of Iba1 as a marker of microglial activation was performed, which demonstrated a reduction in Iba1 expression in microglia after 660 nm exposure, in correlation with findings of reduced TNFα release (Fig. 5.6 A). Increase in Iba1 activation was not demonstrated in iMDM exposed to 400 nm PBM, though cell counts were significantly reduced suggestive of significant cell loss over the culture period (Fig. 5.6 B). Exposure to other wavelengths did not result in differing cell survival. The effect of preconditioning with PBM on TNFα release was investigated by application of PBM daily for three days prior to addition of LPS (Fig. 5.7). This resulted in a variable (and not statistically significant) reduction in TNFα concentrations in cultures preconditioned with 400 nm PBM. Given the findings of cell loss after 400 nm exposure in Figure 5.6 B, this is likely attributable to reduced cell viability – whereby a smaller population of iMDM survived to release TNFα in response to PBM, though cell survival was not quantified after these culture conditions.

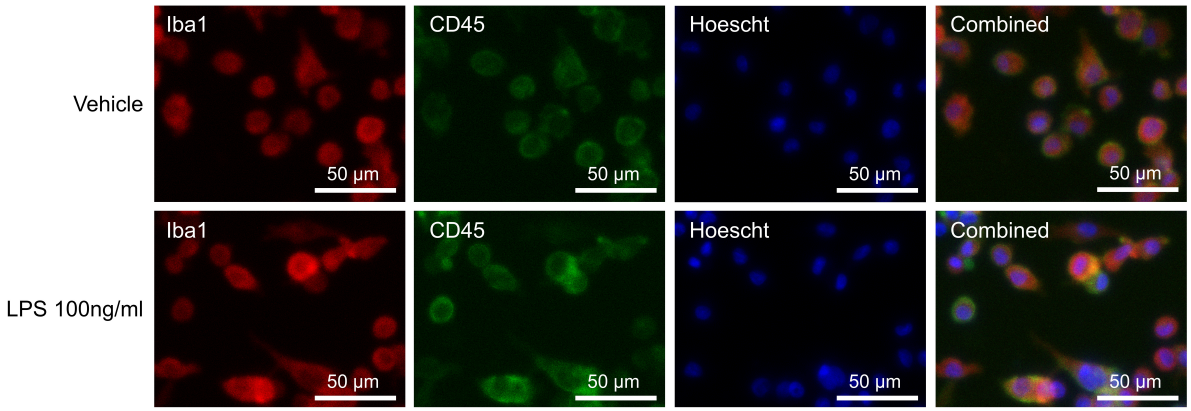


Figure 5.3: Immunofluorescence images of iMDM cultured for 6 days with either vehicle or LPS (100 ng/ml) (added at 0 h at the beginning of differentiation). LPS = lipopolysaccharide.

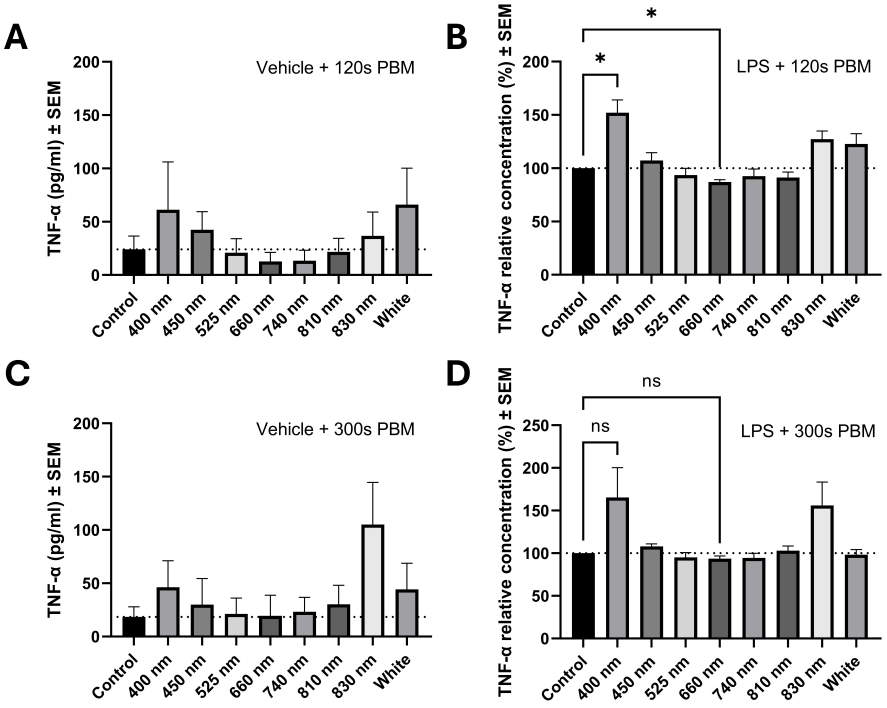


Figure 5.4: Supernatant concentrations of TNFα following 6 day culture with vehicle/LPS (100 ng/ml) (LPS added at 0 h at the beginning of differentiation). PBM at stated wavelength values were delivered at 23 mW/cm^2 for 2 or 5 min daily (2.76 or 6.9 J) at 20-24 h intervals. Control wells received no light. A: Vehicle ± daily PBM for 120 s, n = 4; B: LPS ± daily PBM for 120 s (values normalised to control (LPS) TNFα concentration for each donor), n = 4; C: Vehicle ± daily PBM for 300 s, n = 3. D: LPS ± daily PBM for 300 s (bars normalised to control (LPS) no light treatment for each donor), n = 3. ns = not significant ($p > 0.05$); * = $p < 0.05$. All values given ± SEM.

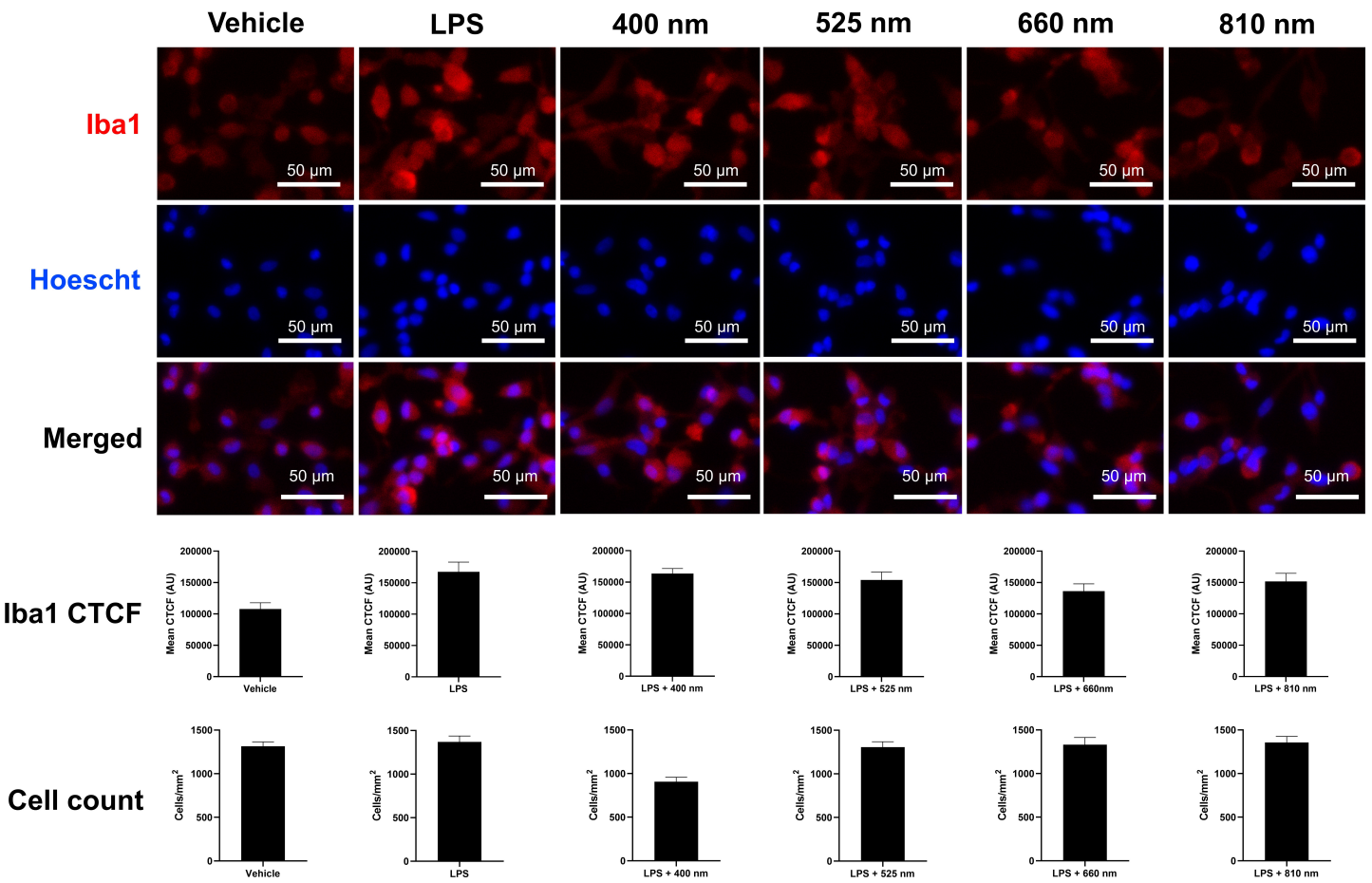


Figure 5.5: Immunofluorescence images of iMDM cultured for 6 days with either vehicle or LPS (100 ng/ml) ± PBM at varying wavelengths (LPS added at 0 h at the beginning of differentiation). CTCF = corrected total cell fluorescence; cell counts derived from Hoescht. Error bars denote SEM. LPS = lipopolysaccharide.

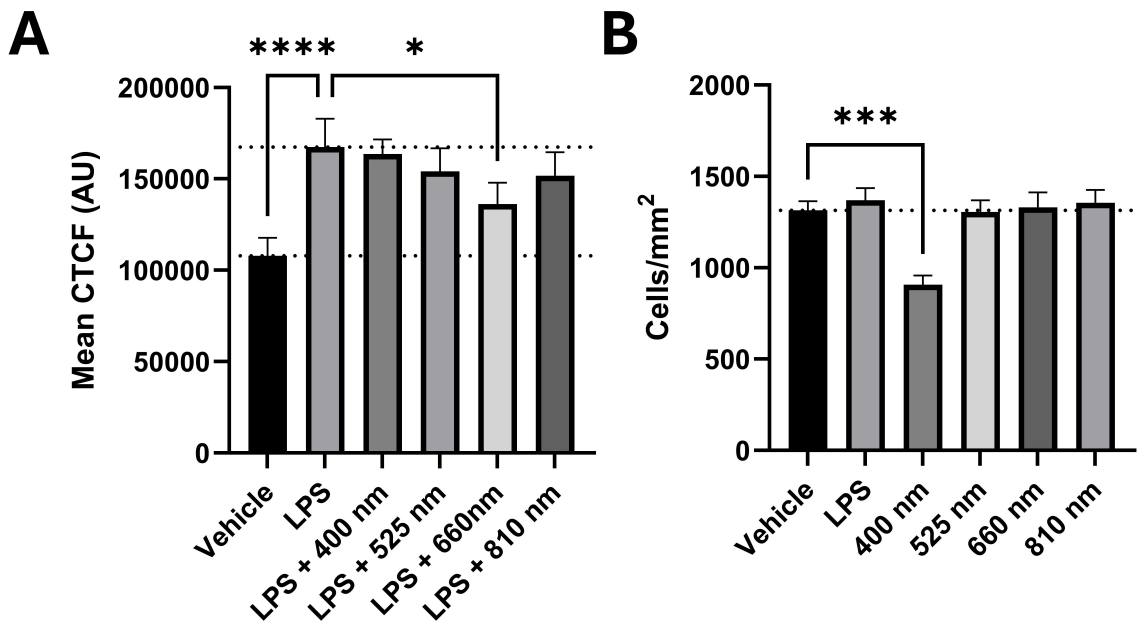


Figure 5.6: Corrected total cell fluorescence and cell counts after 6 day culture of iMDM with vehicle or LPS (100 ng/ml) ± PBM at varying wavelengths (23 mW/cm^2 for 2 min per day, 2.76 J), (LPS added at 0 h at the beginning of differentiation). A: Mean CTCF (averaged from 75 cells per replicate, n = 4: 300 cells per condition). Dotted lines represent CTCF for vehicle and LPS. B: Number of (Hoescht^{+ve}) cells per mm^2. Dotted line represents cell count for vehicle. * = p < 0.05; *** = p < 0.001; **** = p < 0.0001. All values given ± SEM.

5.3.2 DRGN cell culture model

In addition to the results described in Chapter 3, further modelling using serum withdrawal of cultured DRGN was performed to further understand the effects of PBM in stress or injury state neurons. In the first experiment (Fig. 5.8 A), concentrated serum from DRGN cultures, with or without treatment with PBM for 3 days was transferred to freshly prepared DRGN plates. The only significant difference in cell survival after 5 days incubated with the conditioned media was between 20% control media and DMEM (*). In a second experiment, prior to serum withdrawal, cells were cultured with DMEM+FBS for three days with or without daily PBM exposure (1 min per day, 660 nm, 11 mW/cm^2). Media was then exchanged for fresh DMEM without FBS. Cell survival was assessed three days after serum withdrawal, with or without preconditioning, with no discernible effect of PBM identified (Fig. 5.8 B).

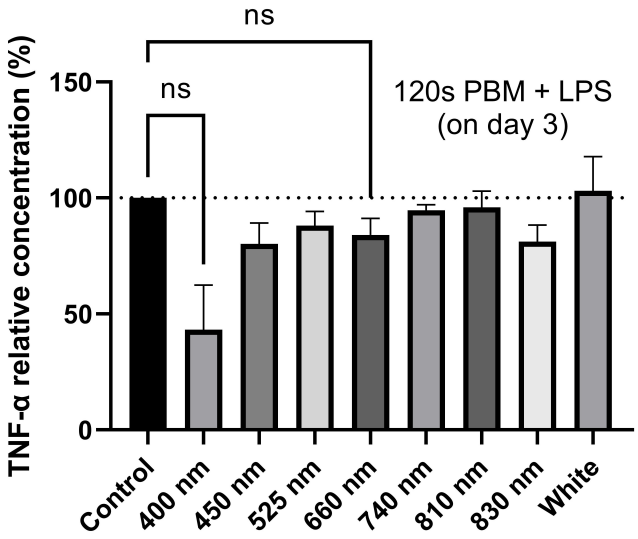


Figure 5.7: Supernatant concentrations of TNFα following 6 day culture with LPS (100 ng/ml). LPS added at 72 h after the beginning of differentiation, with PBM daily from day 0 (pre- and post-conditioning). PBM at stated wavelength values were delivered at 23 mW/cm^2 for 2 min daily (2.76 J) at 20-24 h intervals. Control wells received no light. Values normalised to control (LPS) TNFα concentration for each donor, n = 4; ns = not significant ($p > 0.05$).

To investigate the release of paracrine signalling to support neurite outgrowth in the DRGN model, assay of BDNF release into supernatant, and assay of BDNF concentrations in cell lysates were performed. Insufficient levels of BDNF concentration were detectable in supernatant (1:2 dilution) suggestive of a concentration in both PBM and control treated cultures of less than 62.5 pg/ml (not shown). No significant difference was found in cell lysates from DRGN treated with either 5 days' PBM or control (ambient) light (Fig. 5.9).

5.3.3 *In vivo* spinal cord injury model

Using sections of spinal cord and DRG generated in Chapter 3, additional staining was performed to further elucidate the early effects of PBM on the acute injury state 3 dpi. To assess neuroprotective effects, activation of cleaved caspase-3 was assessed through immunofluorescence staining of DRG (Fig. 5.10). This demonstrated significantly increased expression of cleaved caspase-3 in DRGN nuclei after SCI, which was reduced with daily transcutaneous

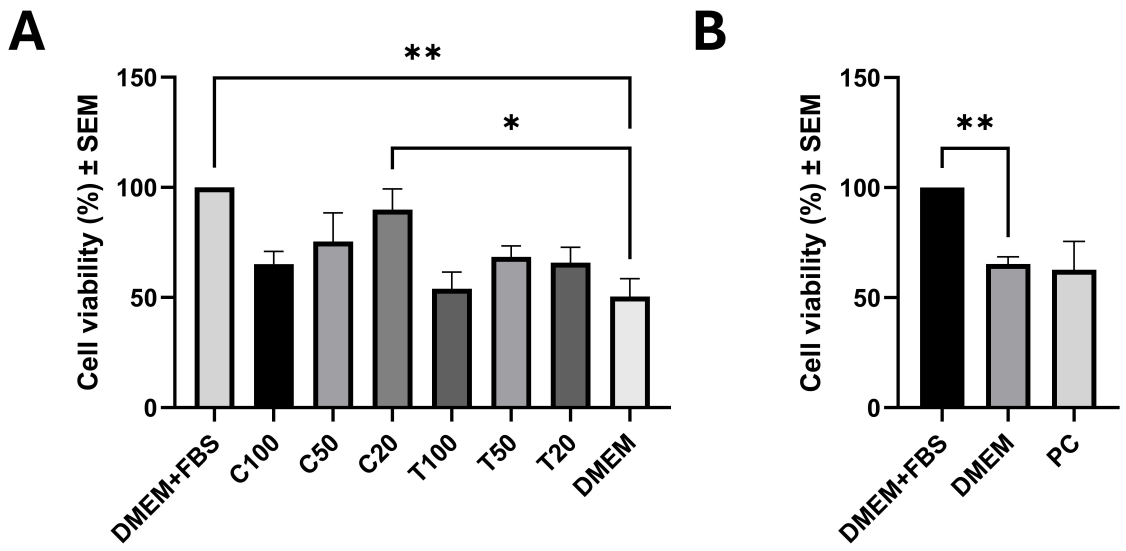


Figure 5.8: A: Cell viability of DRGN after 5 day culture with conditioned media. C = control conditioned media; T = treated conditioned media (100%, 50% or 20% conditioned media (diluted in fresh DMEM). B: Cell viability after 3 day culture, with or without 3 day PBM preconditioning. n = 4 per group, error bars denote SEM; * $p < 0.05$, ** $p < 0.01$; where no comparator is shown, no statistically significant difference was identified.

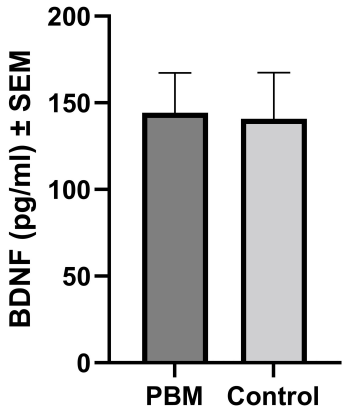


Figure 5.9: BDNF concentrations of DRGN cell lysates from PBM and control treated DRGN cultures. No significant difference was identified between groups. n = 4 per group, error bars denote SEM; where no comparator is shown no statistically significant difference was identified.

PBM treatment. Non-neuronal cleaved caspase-3 activity was preserved between groups which represents normal glial cell turnover. To further understand the early effect of PBM on the

injury site, additional staining was performed on T8 sections to assess quantitative fluorescence of key ECM and glial activation markers (Fig. 5.11). Injury resulted in significant increase in fluorescence of laminin, fibronectin, GFAP and Iba1. No statistically significant reductions in any of these markers was observed in the group treated with PBM.

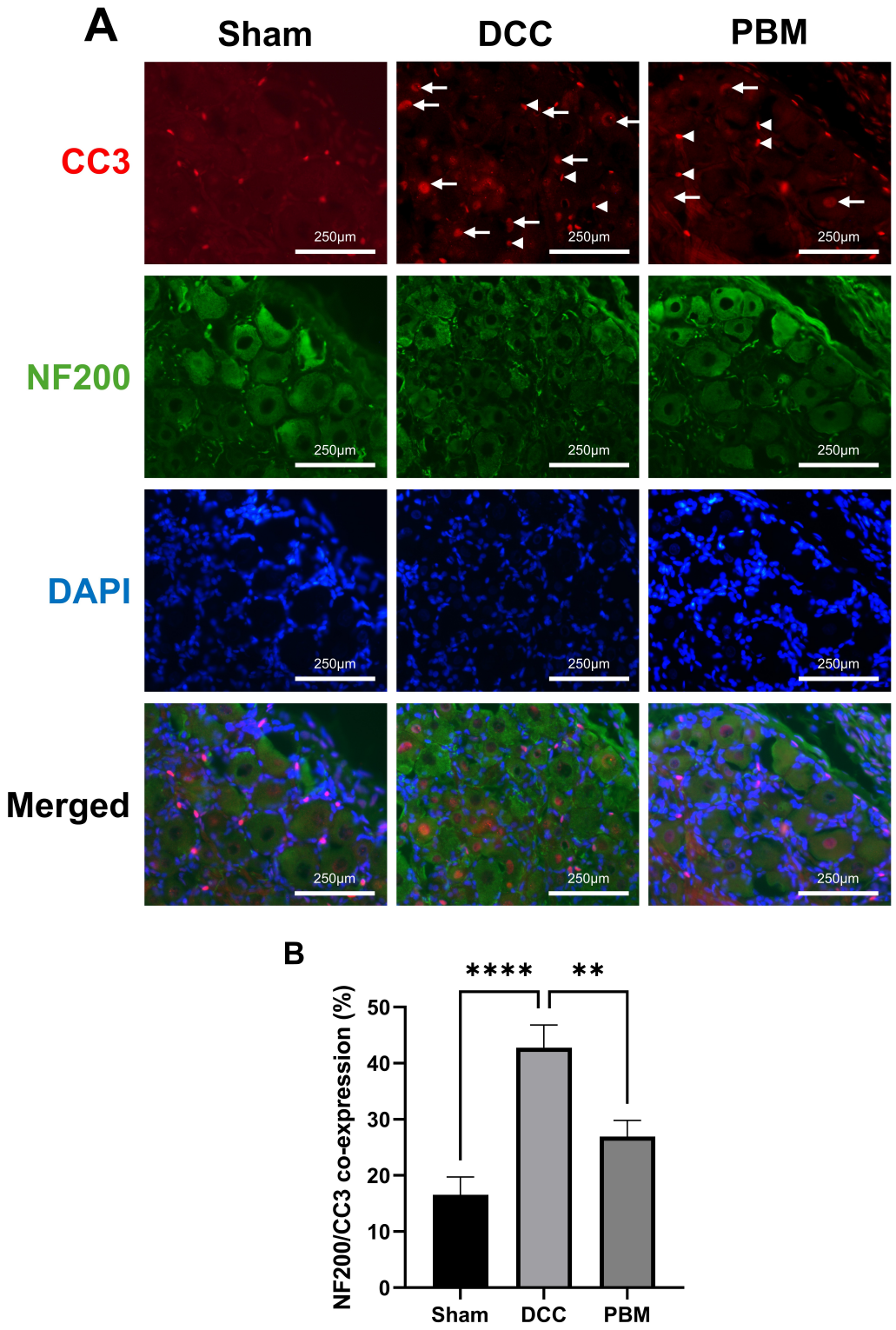


Figure 5.10: A: Immunofluorescence of cleaved caspase-3 in DRG taken 3 dpi following either sham (laminectomy alone); DCC (laminectomy + dorsal column crush) or PBM (laminectomy + dorsal column crush + PBM). Arrows denote CC3 $^{+ve}$ DRGN nuclei. B: Ratio of DRGN co-expressing both NF-200 and CC3. CC3 = cleaved caspase-3. **** $p < 0.0001$, ** $p < 0.01$, error bars denote SEM).

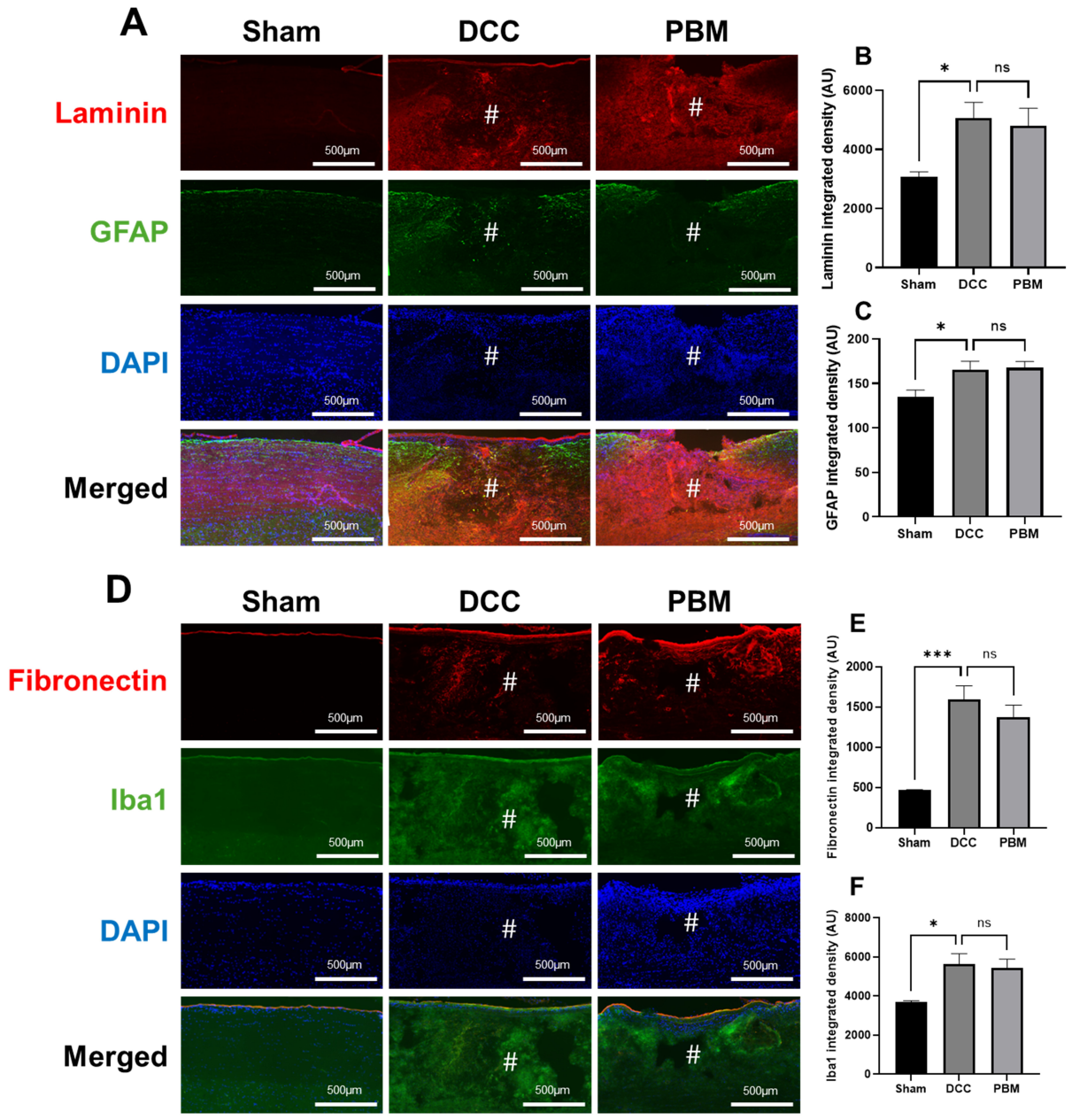


Figure 5.11: A: Immunofluorescence of laminin/GFAP across conditions 3 dpi. B: Quantitative immunofluorescence of laminin from lesion site epicentre. C: Quantitative immunofluorescence of GFAP from lesion site margins. D: Immunofluorescence of fibronectin/Iba1 across conditions 3 dpi. B: Quantitative immunofluorescence of fibronectin from lesion site epicentre. C: Quantitative immunofluorescence of Iba1 from lesion site margins. All 3 dpi following either sham (laminectomy alone); DCC (laminectomy + dorsal column crush) or PBM (laminectomy + dorsal column crush + PBM). # denotes injury site epicentre; * $p < 0.05$; ** $p < 0.01$; *** $p < 0.001$; error bars denote SEM).

5.3.4 Transcriptomics

Analysis and visualisation of DEGs was performed, identifying 1275 genes with an adjusted p value (FDR) <0.05 and a fold change greater than two (397 up- and 878 down-regulated) (Fig. 5.12). k-means analysis allowed clustering of the top 1000 DEGs for initial GAGE method pathway enrichment across GO and KEGG libraries (Fig. 5.13). Across all libraries, clear divisions of pathway type were identifiable in each cluster. (A) cluster identifies pathways associated with neuroregeneration, neurite outgrowth, cytoskeleton development and synaptic transmissions. (B) cluster, featuring a smaller gene population than A and C, features actin and calcium signalling-related pathways, highlighting pathways typically associated with muscle development and maintenance. (C) cluster is predominantly metabolic, with features identified across libraries associated with mitochondrial function and the electron transport chain.

These pathway types were cross-validated by similar results generated using the same gene set (without clustering) in g:profiler (Fig. 5.14). Further unclustered analysis was performed (limited to GO and KEGG libraries) using iDEP.96. In this analysis, inclusion of fold enrichment of DEGs generated insights on the direction of pathway enrichment (Fig. 5.15). These pathways were used to inform network visualisation exploratory analysis.

The GO:BP term "Neuron projection morphogenesis" was identified as a key mechanism in correlation with previous results. Genes from the top ten upregulated DEGs within this pathway were used to visualise interconnected components of this large pathway, based on Notch3, Robo2 and Sema3g (Fig. 5.16). Neuron projection and associated pathways were the predominant theme across much of the pathways identified as enriched.

Key downregulated pathways were also identified. "Ribosome" (and associated pathways e.g. translation and peptide biosynthetic processes) demonstrated negative fold enrichments. The ribosome pathway is shown as a network in Figure 5.17, demonstrating exclusively downregulated transcription of genes contributing to ribosomal function in the PBM treated specimens. Similarly NADH (ubiquinone) pathways showed predominant downregulation across the pathway (Fig. 5.18), formed principally of components of the electron transport chain. Visualisation of the effects on KEGG pathway of calcium signalling demonstrated a variety of effects of

PBM, including upregulation of nitric oxide synthases (Nos1/Nos3), NMDA receptor subunits (Grin1/Grin2c), P2 ATP receptors and substance P receptor (Tacr1) (Fig. 5.19).

The top 20 upregulated genes and top 20 downregulated genes are shown in Figures 5.20 and 5.21 respectively. The top 20 genes associated with GO:BP term "Neuron projection morphogenesis" are shown in Figure 5.22; and the top 20 genes associated with GO:BP term "Apoptotic process" are shown in Figure 5.23. Figure 5.24 demonstrates a heat map of key transcriptional changes observed with PBM treatment (but poorly represented in pathway analysis elsewhere), with two groups of genes also shown which were consistently downregulated: the S100 and COX families. Gene terms with full names and summary of function are given in Table 5.1.

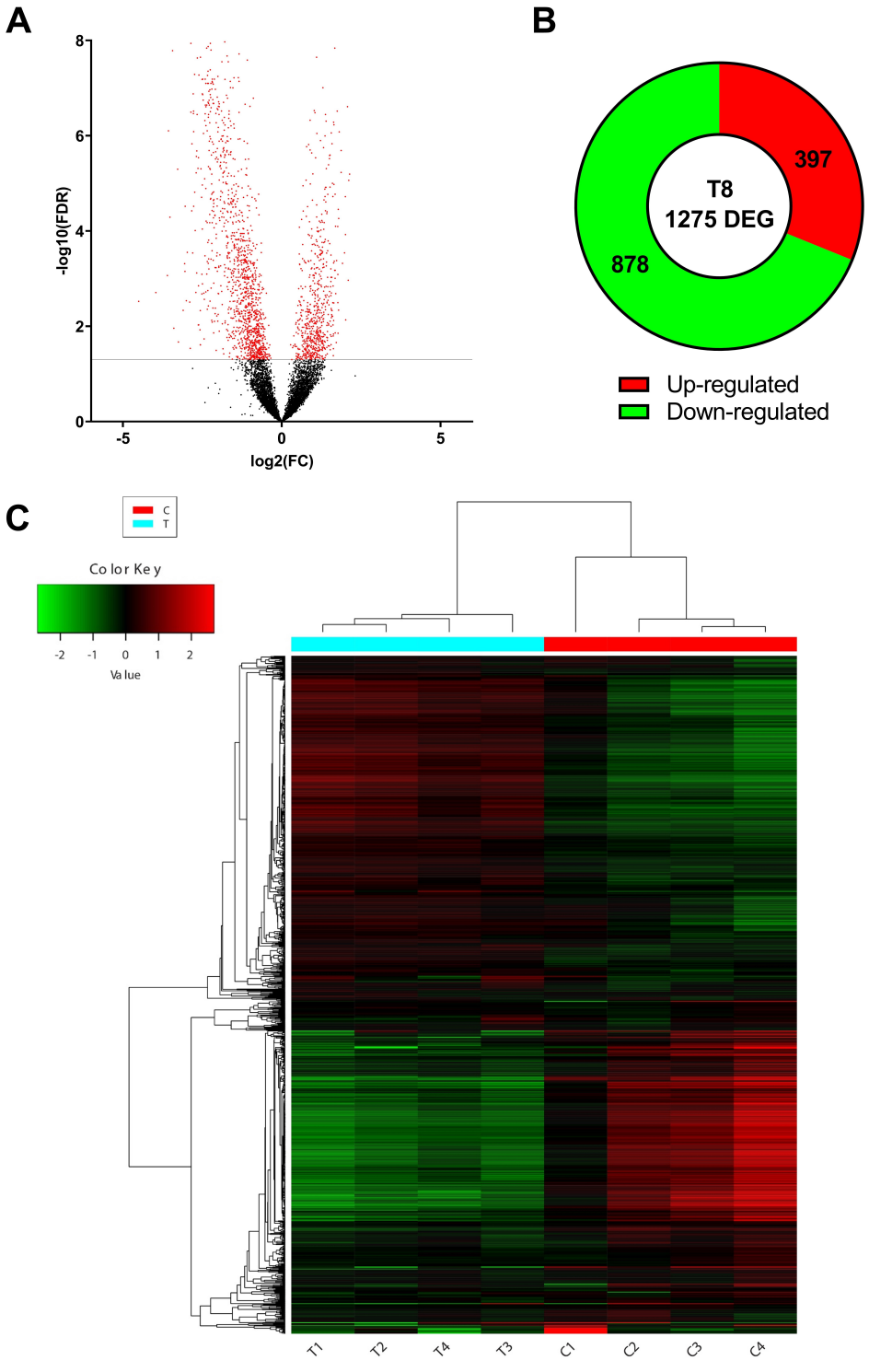
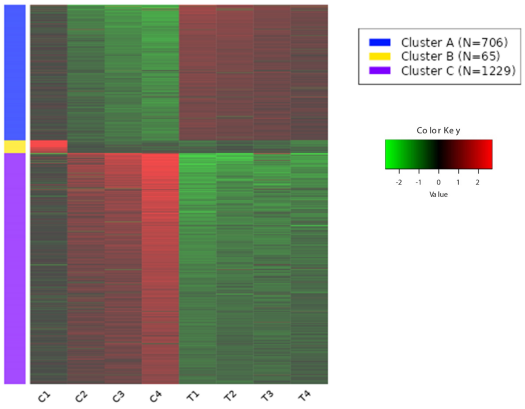


Figure 5.12: A: Volcano plot with identification (in red) of DEGs defined by FDR<0.05. B: number of DEGs up or downregulated after PBM in SCI. C: Heatmap of top 2000 DEGs in T (treatment (PBM) and C (control (DCC and sham therapy)) groups (n = 4 per group). DEGs = differentially expressed genes; FDR = false discovery rate.

A



B

GO:BP			
Cluster	adj.Pval	nGenes	Pathways
A	4.60e-31	190	Nervous system development
	8.00e-21	137	Neurogenesis
	1.30e-17	58	Synapse organization
	9.90e-17	92	Neuron projection development
	8.20e-16	110	Neuron differentiation
B	3.20e-15	11	Myofibril assembly
	3.20e-15	11	Striated muscle cell development
C	1.80e-51	161	Translation
	1.30e-19	41	Electron transport chain
	4.80e-19	40	Oxidative phosphorylation
	9.20e-17	33	Mitochondrial respiratory chain complex assembly
	9.10e-15	27	ATP synthesis coupled electron transport chain

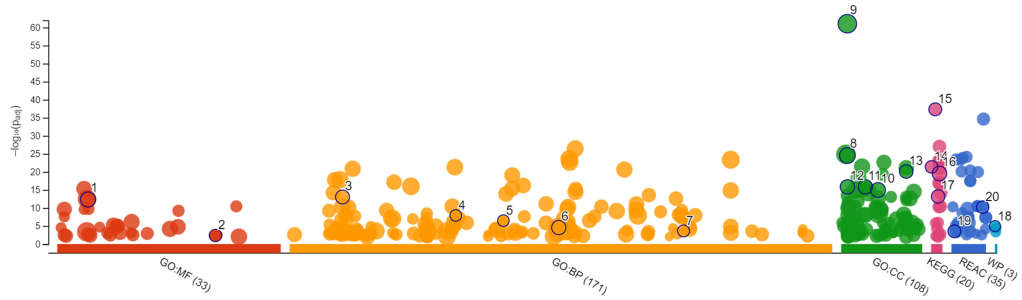
GO:CC			
Cluster	adj.Pval	nGenes	Pathways
A	3.2e-28	153	Cell junction
	5.6e-22	110	Synapse
	8.1e-21	104	Neuron projection
	1.8e-19	239	Plasma membrane
	3.3e-16	72	Somatodendritic compartment
	6.9e-15	60	Axon
	2.9e-13	57	Postsynapse
	1.4e-11	46	Neuronal cell body
B	6.5e-40	28	Myofibril
	6.7e-38	26	Sarcomere
	2.6e-13	17	Actin cytoskeleton
C	9.2e-94	159	Ribosome
	7.9e-45	88	Mitochondrial protein-containing complex
	3.4e-32	54	Inner mitochondrial membrane protein complex
	5.3e-28	76	Mitochondrial inner membrane
	7.1e-27	99	Mitochondrial envelope
	1.0e-25	38	Mitochondrial respirasome

GO:MF			
Cluster	adj.Pval	nGenes	Pathways
A	9.6e-09	74	Cytoskeletal protein binding
	1.4e-05	35	Metal ion transmembrane transporter
	2.0e-05	46	Cation transmembrane transporter
	1.2e-04	11	Extracellular matrix binding
	1.4e-04	46	Calcium ion binding
B	8.8e-21	29	Cytoskeletal protein binding
	2.4e-15	18	Actin binding
	2.1e-10	11	Actin filament binding
	1.6e-07	14	Calcium ion binding
	5.9e-04	21	Cation binding
C	4.0e-92	144	Structural constituent of ribosome
	1.5e-17	32	Electron transfer activity
	8.5e-17	27	Oxidoreduction-driven active transmembrane transporter activity
	1.9e-08	12	Cytochrome-c oxidase activity
	1.8e-07	12	NADH dehydrogenase (ubiquinone)
	4.2e-07	12	NAD(P)H dehydrogenase (quinone)

KEGG			
Cluster	adj.Pval	nGenes	Pathways
A	1.2e-06	17	ECM-receptor interaction
	1.4e-05	25	Focal adhesion
	1.4e-05	14	Synaptic vesicle cycle
	2.8e-03	12	GABAergic synapse
	3.7e-03	19	CAMP signaling pathway
B	3.6e-10	9	Cardiac muscle contraction
	9.4e-04	6	Calcium signaling pathway
C	1.7e-94	105	Ribosome
	6.0e-30	53	Oxidative phosphorylation
	1.3e-19	56	Thermogenesis
	2.3e-15	38	Neutrophil extracellular trap formation
	9.10E-15	27	ATP synthesis coupled electron transport

Figure 5.13: A: k-means clusters across C and T groups with relative expression per specimen B: GO and KEGG enrichments per cluster. adj.Pval = false discovery rate p value; nGenes = number of genes in pathway; GO = gene ontology; KEGG = Kyoto encyclopaedia of genes and genomes; GO:BP = GO biological processes; GO:MF = GO molecular function; GO:CC = GO cellular component.

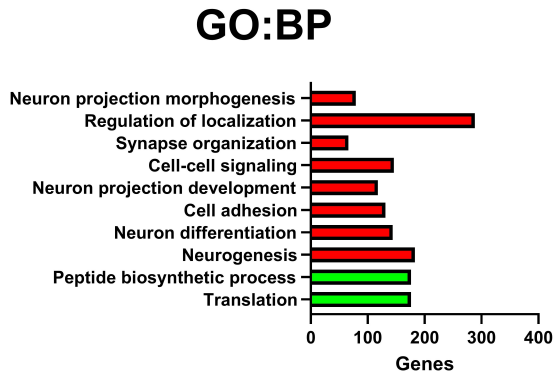
A



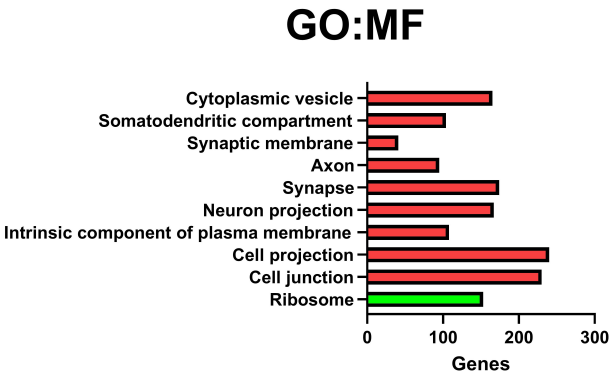
B

ID	Source	Term ID	Term name	p_{adj}
1	GO:MF	GO:008092	Cytoskeletal protein binding	4.5×10^{-13}
2	GO:MF	GO:0051015	Actin filament binding	4.2×10^{-3}
3	GO:BP	GO:0007005	Mitochondrial organization	9.1×10^{-14}
4	GO:BP	GO:0033108	Mitochondrial respiratory chain complex assembly	1.2×10^{-8}
5	GO:BP	GO:0042775	Mitochondrial ATP synthesis coupled electron transport	3.2×10^{-7}
6	GO:BP	GO:0048812	Neuron projection morphogenesis	2.6×10^{-5}
7	GO:BP	GO:0099643	Signal release from synapse	2.3×10^{-4}
8	GO:CC	GO:0005739	Mitochondrion	2.9×10^{-25}
9	GO:CC	GO:0005737	Cytoplasm	8.9×10^{-62}
10	GO:CC	GO:0043005	Neuron projection	1.1×10^{-15}
11	GO:CC	GO:0031966	Mitochondrial membrane	1.4×10^{-16}
12	GO:CC	GO:0005740	Mitochondrial envelope	1.5×10^{-16}
13	GO:CC	GO:0098798	Mitochondrial protein-containing complex	7.9×10^{-21}
14	KEGG	KEGG:00190	Oxidative phosphorylation	4.1×10^{-22}
15	KEGG	KEGG:03010	Ribosome	4.7×10^{-38}
16	KEGG	KEGG:05022	Pathways of neurodegeneration – multiple diseases	2.8×10^{-20}
17	KEGG	KEGG:04714	Thermogenesis	6.6×10^{-14}
18	WP	WP:WP1283	Oxidative phosphorylation	1.0×10^{-5}
19	REAC	REAC:R-RNO-422475	Axon guidance	2.9×10^{-4}
20	REAC	REAC:R-RNO-1428517	The citric acid (TCA) cycle and respiratory electron transport	6.0×10^{-11}

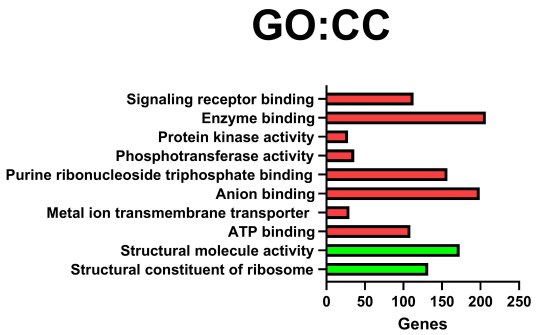
Figure 5.14: A: g:profiler interface output with top 20 relevant hits highlighted. B: listed top 20 pathway hits across all libraries (GO and KEGG. Padj = false discovery rate p value; GO = gene ontology; KEGG = Kyoto encyclopaedia of genes and genomes; GO:BP = GO biological processes; GO:MF = GO molecular function; GO:CC = GO cellular component; WP = wikipathways; REAC = reactome pathways.



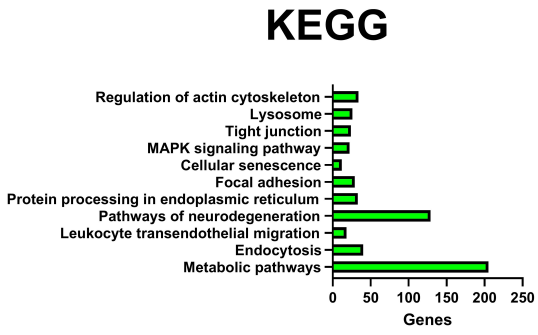
GO:BP Term	Fold enrichment	p(adj)
Translation	-8.1935	3.20E-12
Peptide biosynthetic process	-8.1935	3.20E-12
Neurogenesis	9.6558	4.70E-17
Neuron differentiation	9.1299	3.80E-15
Cell adhesion	8.8058	2.70E-14
Neuron projection development	8.6661	9.10E-14
Cell-cell signaling	7.8186	6.20E-12
Synapse organization	7.7524	2.40E-10
Regulation of localization	7.6783	4.50E-12
Neuron projection morphogenesis	7.4844	3.50E-10



GO:MF Term	Fold enrichment	p(adj)
Ribosome	-10.6543	3.70E-19
Cell junction	9.7219	3.20E-18
Cell projection	9.0757	1.90E-16
Int. comp. of plasma membrane	8.8366	9.90E-15
Neuron projection	8.7793	3.80E-15
Synapse	8.4663	1.40E-14
Axon	7.438	7.20E-11
Synaptic membrane	7.3028	9.00E-09
Somatodendritic compartment	6.9482	7.30E-10
Cytoplasmic vesicle	6.2352	1.30E-08



GO:CC Term	Fold enrichment	p(adj)
Structural constituent of ribosome	-10.8419	6.00E-19
Structural molecule activity	-5.7173	1.40E-06
ATP binding	8.1096	2.80E-12
Metal ion transmembrane transporter activity	7.7327	4.30E-08
Anion binding	7.0712	1.40E-10
Purine ribonucleoside triphosphate binding	6.9397	2.90E-10
Phosphotransferase activity, alcohol group as acceptor	5.9756	1.50E-06
Protein kinase activity	5.7325	8.30E-06
Enzyme binding	5.7264	1.70E-07
Signaling receptor binding	5.0436	6.50E-06



KEGG Pathway	Fold enrichment	p(adj)
Metabolic pathways	-4.4767	7.60E-04
Endocytosis	-3.6407	2.20E-02
Leukocyte transendothelial migration	-3.527	2.80E-02
Pathways of neurodegeneration	-3.1703	2.80E-02
Protein processing in ER	-3.152	2.80E-02
Focal adhesion	-3.1124	2.80E-02
Cellular senescence	-3.1117	3.10E-02
MAPK signaling pathway	-3.0551	2.80E-02
Tight junction	-3.021	2.80E-02
Lysosome	-2.8655	3.10E-02
Regulation of actin cytoskeleton	-2.784	3.10E-02

Figure 5.15: Bar plots with tables demonstrating the top ten relevant hits for each library, with fold enrichment of the pathway. Upregulated pathways shown in red, downregulated pathways shown in green. P(adj) = false discovery rate p value; GO = gene ontology; KEGG = Kyoto encyclopaedia of genes and genomes; GO:BP = GO biological processes; GO:MF = GO molecular function; GO:CC = GO cellular component.

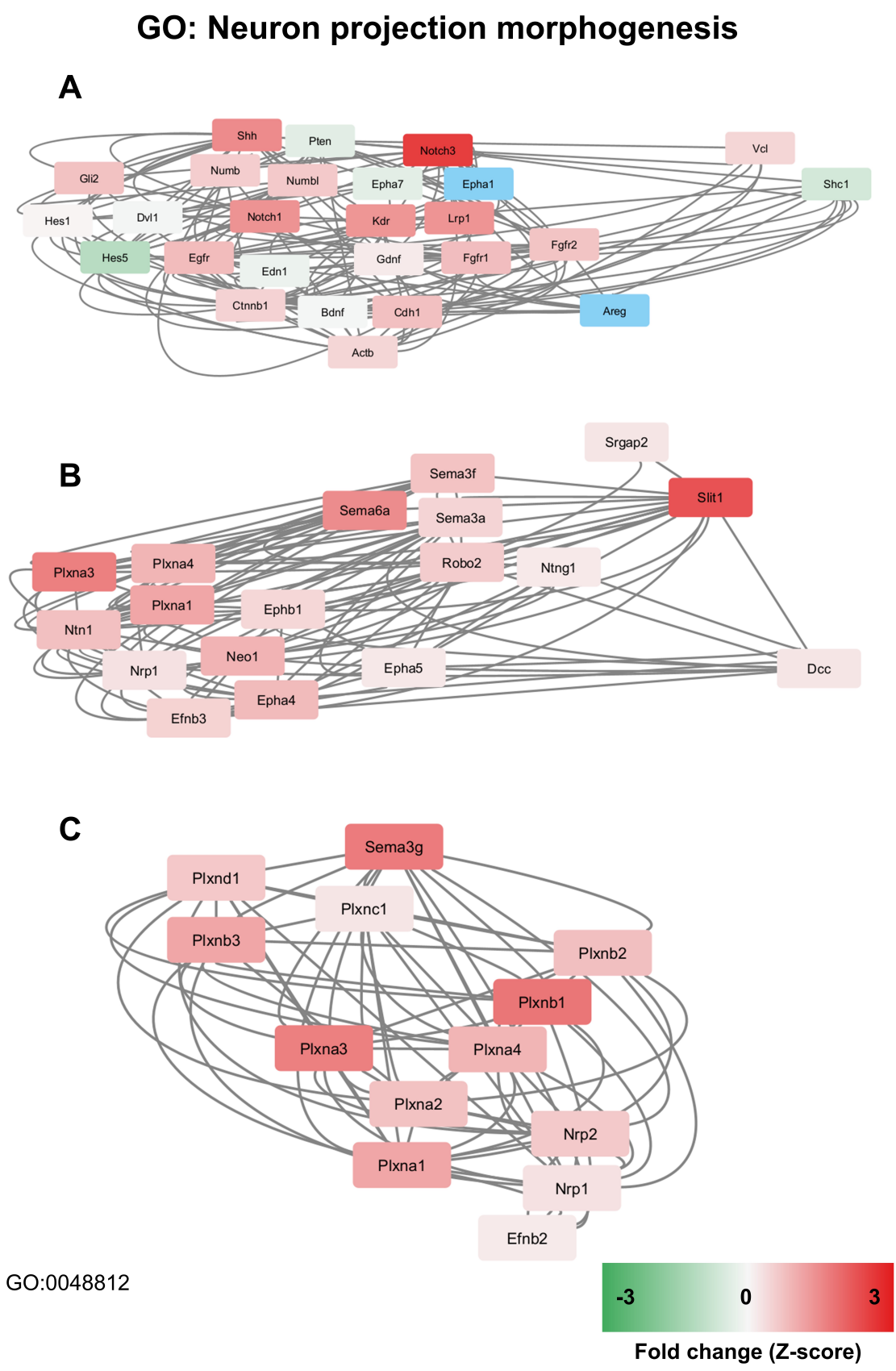


Figure 5.16: Figure caption on next page.

Figure 5.16: (Figure on previous page) Networks based on top DEGs within neuron projection morphogenesis (GO term - GO:0006915), with their immediate neighbours (undirected). A: based on Notch3. B: Based on Robo2 (receptor for Slit1). C: Based on Sema3g. GO = gene ontology. Genes shown in blue were filtered from the pathway analysis due to inadequate read counts

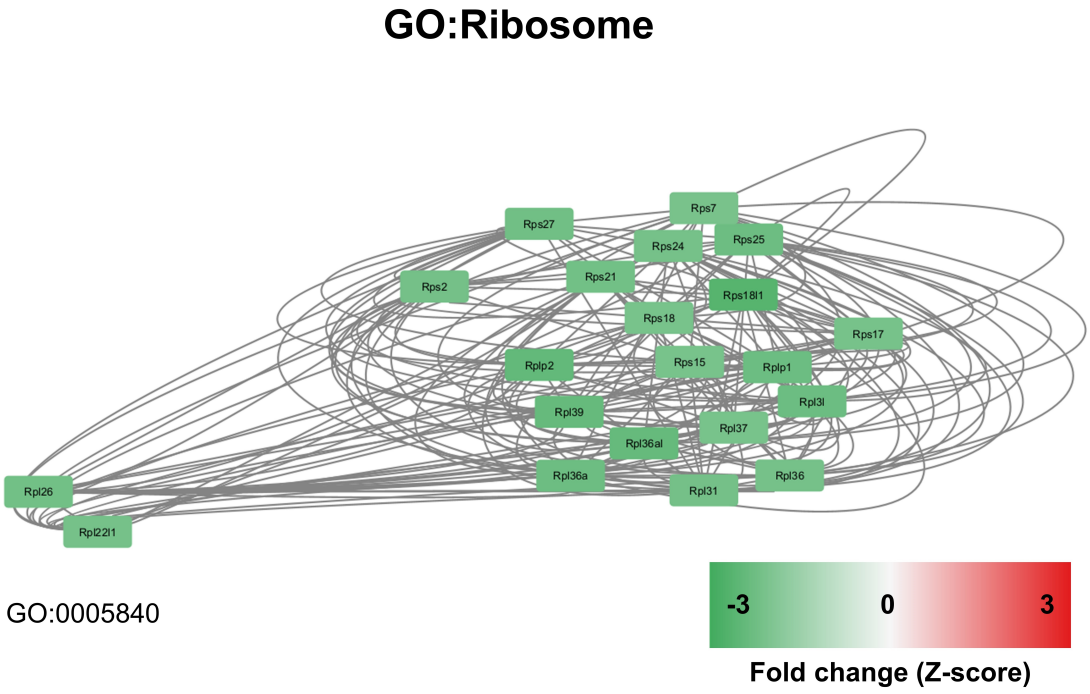


Figure 5.17: Networks based on top 20 DEGs within GO:ribosome (GO term - GO:0006915). GO = gene ontology. Genes shown in blue were filtered from the pathway analysis due to inadequate read counts.

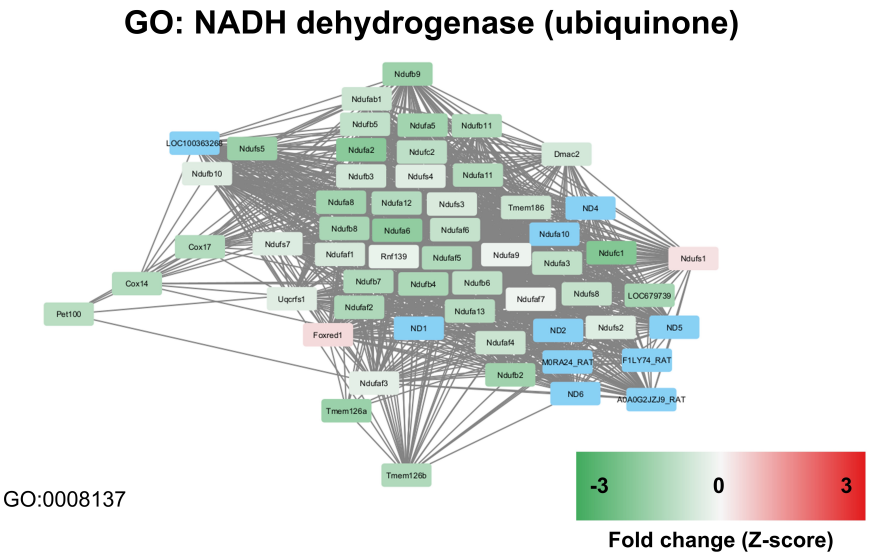


Figure 5.18: Networks based on top 3 DEGs within NADH dehydrogenase (ubiquinone) GO term (GO term - GO:0006915), with their immediate neighbours (undirected). GO = gene ontology. Genes shown in blue were filtered from the pathway analysis due to inadequate read counts.

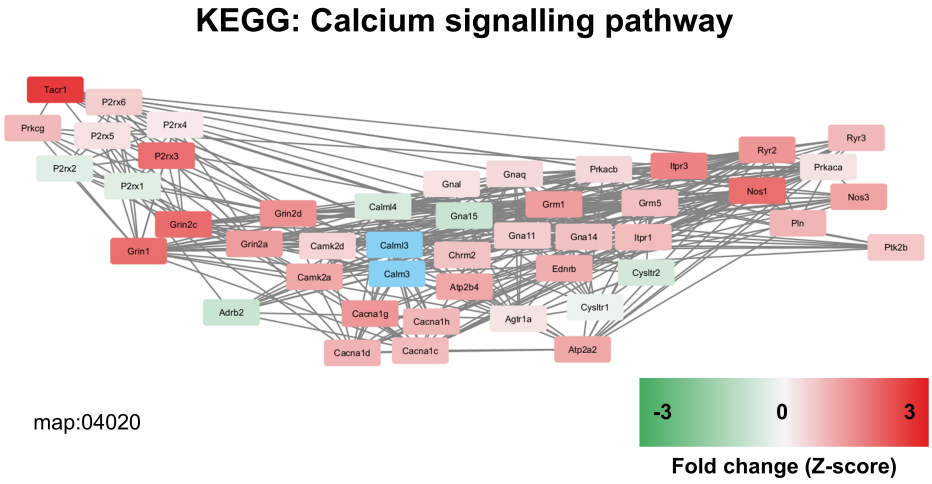


Figure 5.19: Networks based on top 3 DEGs within calcium signalling pathway (KEGG pathway - map 04020), with their immediate neighbours (undirected). Genes shown in blue were filtered from the pathway analysis due to inadequate read counts.

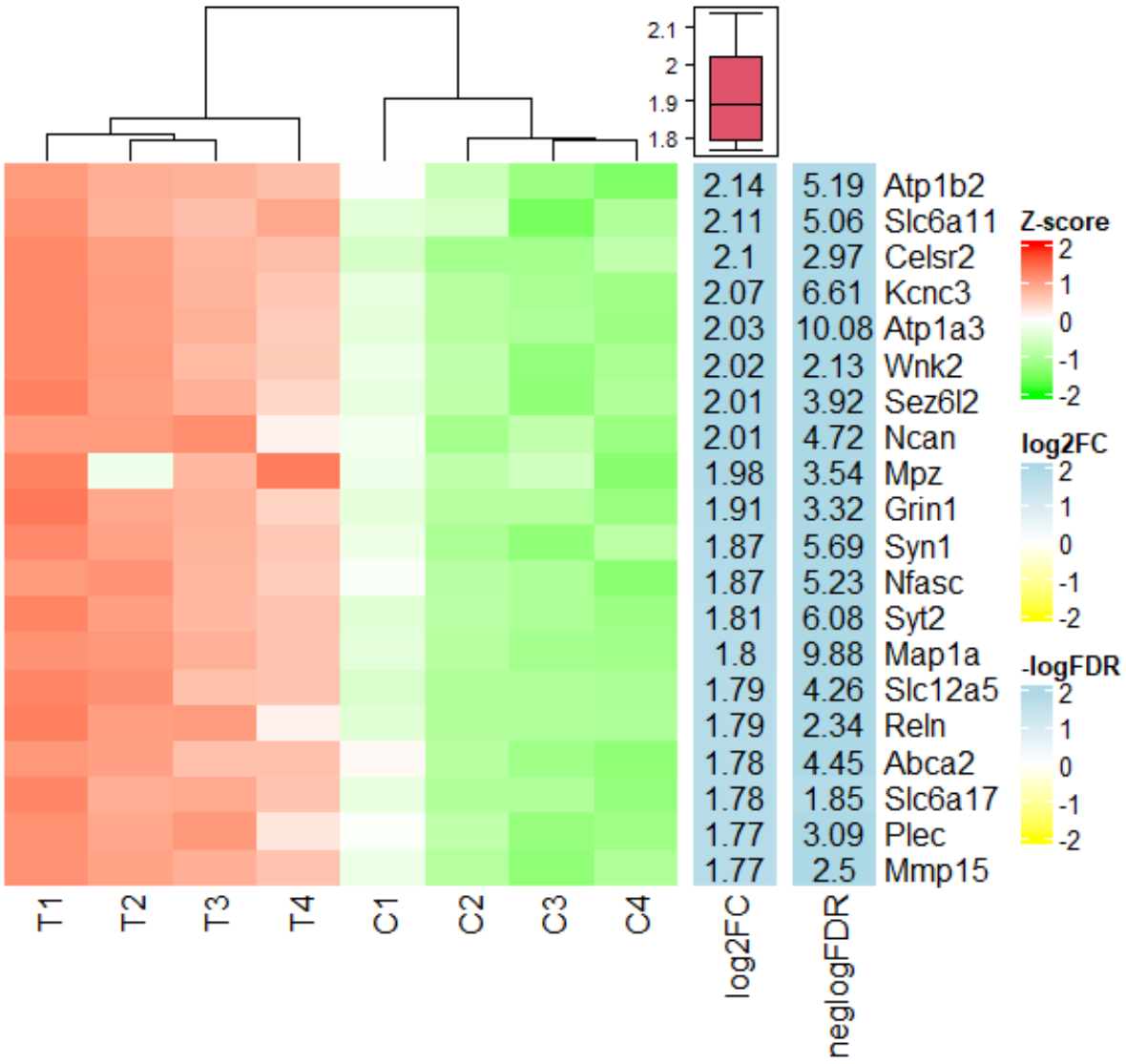


Figure 5.20: Heat map demonstrating top 20 upregulated genes. FDR = false discovery rate; log2FC = log2 fold change; C = control specimens (DCC and sham treatment); T = treatment specimens (DCC+PBM).

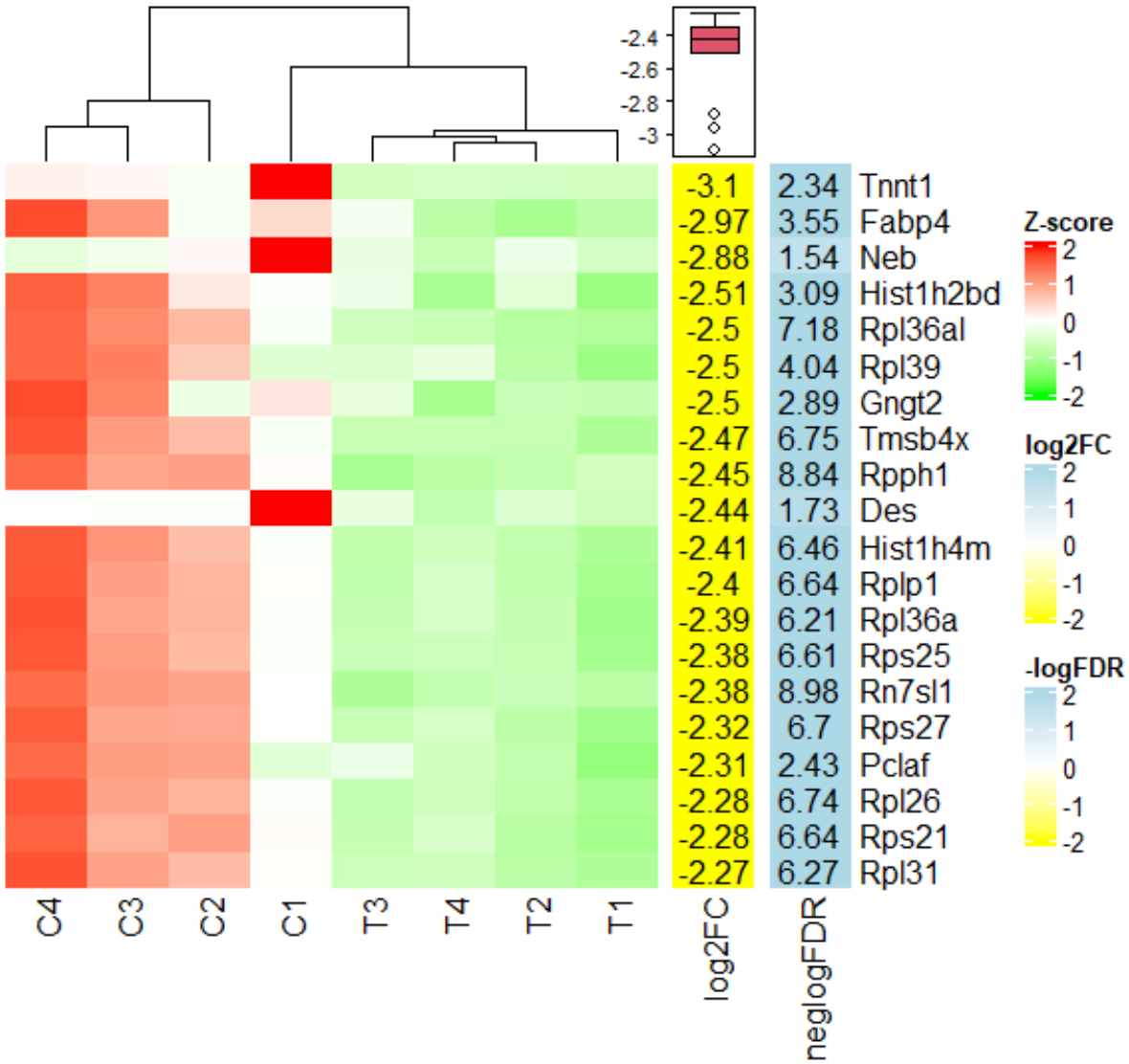


Figure 5.21: Heat map demonstrating top 20 downregulated genes. FDR = false discovery rate; log2FC = log2 fold change; C = control specimens (DCC and sham treatment); T = treatment specimens (DCC+PBM).

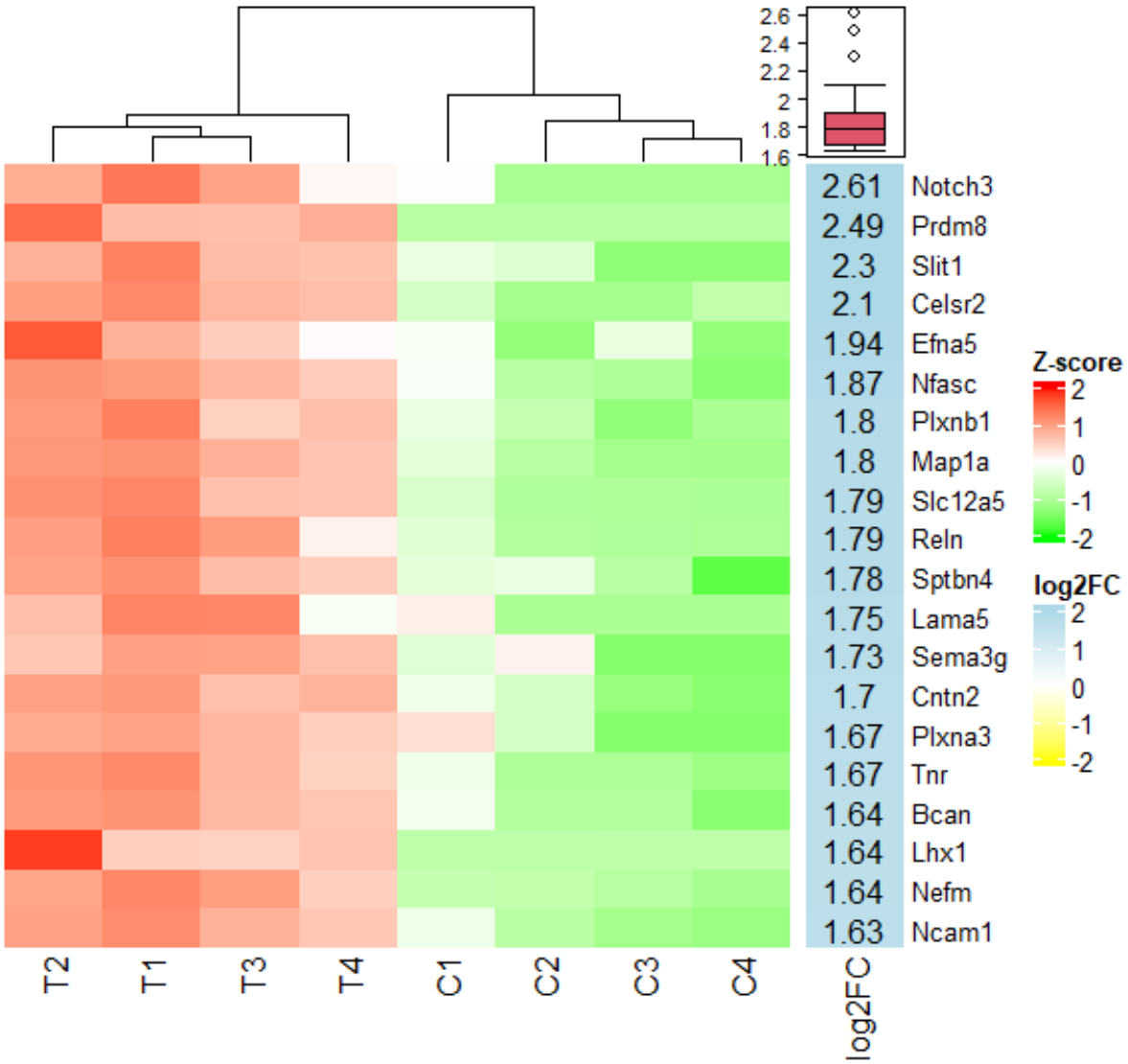


Figure 5.22: Heat map demonstrating top 20 regeneration associated genes. FDR = false discovery rate; log2FC = log2 fold change; C = control specimens (DCC and sham treatment); T = treatment specimens (DCC+PBM).

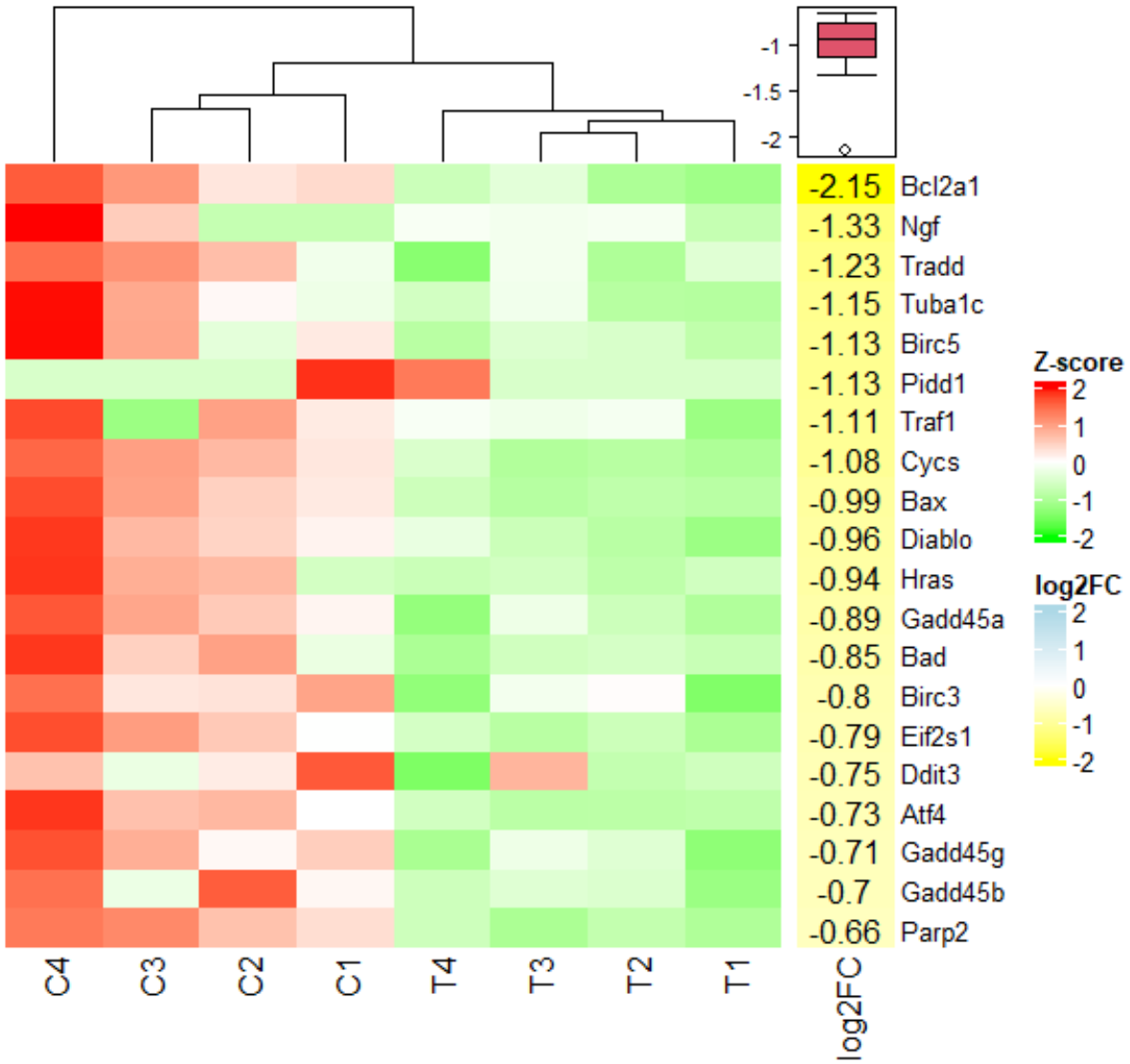


Figure 5.23: Heat map demonstrating top 20 apoptosis associated genes. FDR = false discovery rate; log2FC = log2 fold change; C = control specimens (DCC and sham treatment); T = treatment specimens (DCC+PBM).

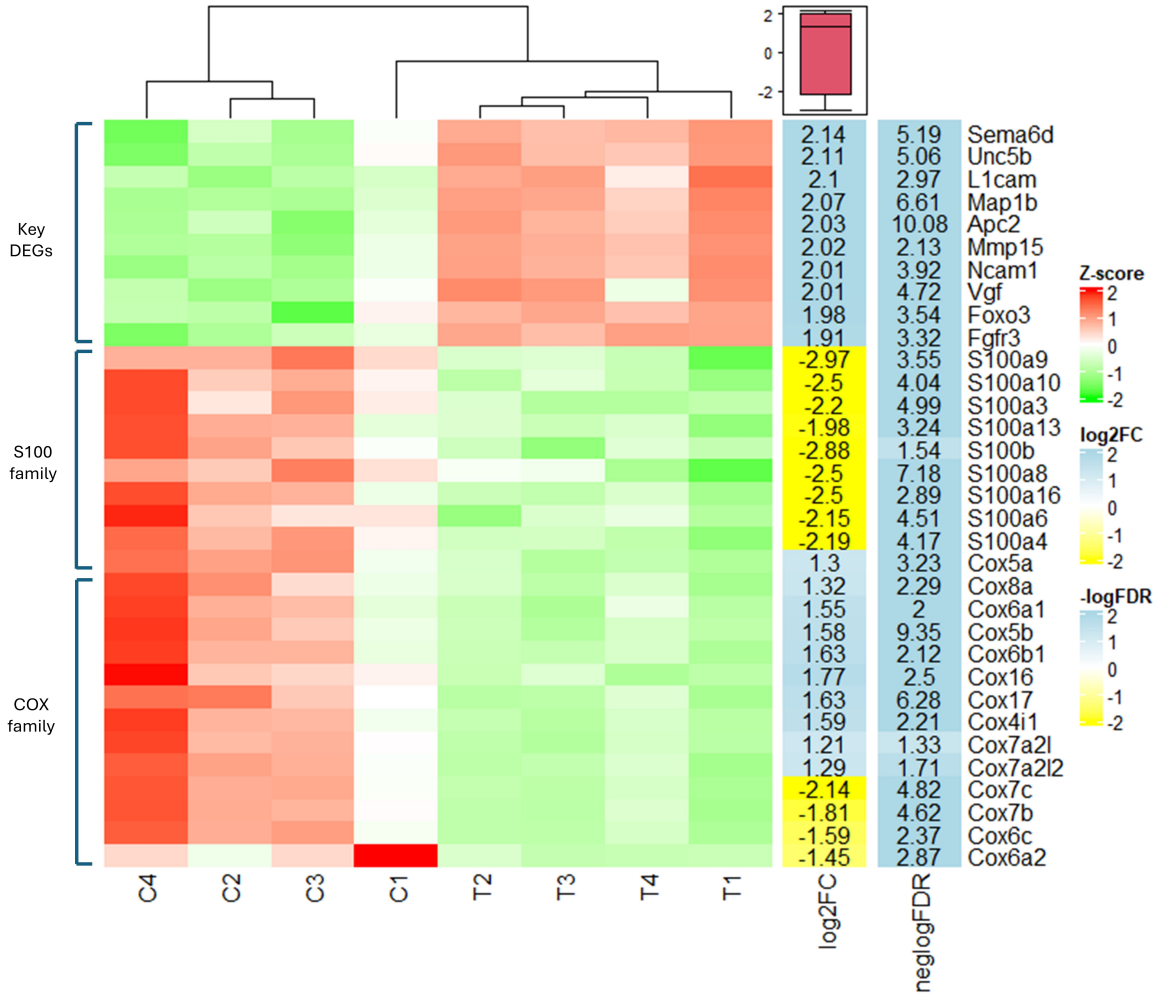


Figure 5.24: Heat map demonstrating families as shown. DEGs = differentially expressed genes; FDR = false discovery rate; log2FC = log2 fold change; C = control specimens (DCC and sham treatment); T = treatment specimens (DCC+PBM).

Table 5.1: Summary table of discussed gene terms with full names and functions (taken from genecards.org).

Gene	**Definition**	**Function**
Bax	Bcl-2 associated X, apoptosis regulator	Anti-apoptotic
Casp3	Caspase 3	Pro-apoptotic
Casp8	Caspase 8	Pro-apoptotic
Cox	Cytochrome c oxidase assembly factors	Electron transport chain
Cycs	Cytochrome c, somatic	Electron transport chain, apoptotic mediator
Diablo	Diablo, inhibitors of apoptosis-binding mitochondrial protein	Cytochrome c-mediated apoptotic pathway
Fabp4	Fatty acid binding protein 4	Fatty acid uptake, transport and metabolism
Grin1/2c	Glutamate ionotropic receptor N-methyl-D-aspartate type subunit 1/2c	Critical subunit of N-methyl-D-aspartate receptors
Mpz	Myelin protein zero	Specifically expressed in Schwann cells of the peripheral nervous system in mammals
Nos1/3	Nitric oxide synthase 1/3	Synthesise nitric oxide from L-arginine
Notch3	Notch receptor 3	Involved in Notch signaling pathway and neurogenesis
P2	Purinergic adenosine triphosphate receptors	Ligand gated ion channels involved in neuron-glial interactions, apoptosis and macrophage activation
Robo2	Roundabout guidance receptor 2	Function in axon guidance
S100	S100 calcium binding protein A	Generally mediate responses to intracellular calcium levels. B proteins are primarily astrocytic, with involvement in a variety of neuronal functions
S100A8/9	Complex of S100A8 and 9	Role both in intracellular calcium sensing but is also released in pro-inflammatory states whereupon it stimulates leucocyte migration and inflammatory cytokine release
Sema3g	Semaphorin 3G	Function in axon guidance
Syn1	Synapsin 1	Implicated in modulation of neurotransmitter release, as well as axonogenesis and synaptogenesis
Tacr1	Tachykinin receptor 1	Substance P (neurokinin 1) receptor

5.4 Discussion

This chapter has demonstrated a variety of important findings in establishing a mechanism for PBM in neurotrauma. Experiments here have shown that:

- Reducing microglial activation is a key mechanism of PBM;
- The beneficial effects of PBM are dependent on adverse biological conditions;
- PBM reduces neuronal apoptosis in SCI via reduction in cleavage of caspase-3;
- PBM induces a variety of pro-regenerative pathways and calcium signalling, with downregulation of transcriptional and ribosomal activity, downregulation of key apoptotic mediators, S100 class proteins, and reduced transcription of mitochondrial components.

5.4.1 Neuroinflammation and glial activation

This chapter has demonstrated that 660 nm PBM attenuates the activation of microglia, as shown by reductions in Iba1 expression and functionally through reduced TNFα release. These observations have been made previously in a variety of models,[307,311,417] but the use of matched average irradiance PBM across the vis/NIR spectrum in a single model to investigate microglial responses is novel. Mechanisms within the microglia that lead to this phenomenon are not established here, but work elsewhere has suggested this may be attributable to increased mitophagy.[311] Attenuation of monocyte activation has also been linked to reduction in A1-like astrocytic activation, by using conditioned media from PBM treated M1-like macrophages, leading to reduced expression of GFAP in astrocytes.

Clearly there are further mechanisms involved in attenuating microglial activation. This work does demonstrate a relationship between wavelength and pro/anti-inflammatory effects, as 400 nm blue light appeared pro-inflammatory in the LPS treated group, and was associated with a reduced number of iMDM at the end of the culture period, either due to inhibition of proliferation, induction of apoptosis/necrosis, or both. In the preconditioning model, this may have led to the appearance that preconditioning with 400 nm light attenuated inflammation, whereas this

observation is more likely attributable to the loss of cells during the pre-treatment phase leading to lower levels of TNFα release from the reduced population of viable cells. This is in contrast to 660 nm treatment *in vitro* which appeared to reduce inflammatory activity when applied after LPS, with no observed reductions in cell populations when applied as preconditioning treatment or post-LPS treatment in either model.

The evidence given in Chapter 3 for functional and histological improvement with PBM in SCI suggest that PBM elicits differences in glial responses in the acute phase post-injury. However, no significant differences were observed with PBM treatment in immunofluorescence staining of GFAP or Iba1 using injury site SCI samples (Fig. 5.11). Differences were detected between sham and control for both of these markers, though they were more subtle than expected. This is possibly attributable to technical factors. The method for assay of these proteins may be insufficient compared with other methods such as liquid chromatography-mass spectrometry.[418] Alternatively, this single time point (3 days post-injury) may be too soon to discern differences.

Notably however, significant differences were observed in CD11b and GFAP in the brain in Chapter 4 (Fig. 4.11 and 4.9) using the same methodology, at the same time point. This suggests that the assay methodology and timing is suitable to detect shifts in expression of these markers (though it is noteworthy that this is a comparison between a mild diffuse injury model in the brain and a moderate focal crush model in the spinal cord). The difference in findings may therefore be attributable other unknown factors. One such possibility is the complexity of glial function in the acute post-injury phase: whereby the alteration in glial function with PBM treatment of the injured spinal cord does result in functional and molecular changes in microglia and astrocytes, but does not significantly affect GFAP/Iba1 expression. However, assessment across the broad range of microglial and astrocytic phenotype is not possible from the methodology described in this chapter, and should be prioritised in future work.

Differing functional phenotypes of microglia and astrocytes have been shown to contribute significantly to the formation and quality of the glial scar, with shifting behaviours over the period post-injury.[419] This is further support for the predominant role of glial phenotype as a variable of greater significance than proliferation alone. Whilst such differences in glial phenotype in

response to PBM may not be detected by the methods described here, they may be reflected in transcriptional changes, discussed below. To further elucidate the complex mechanisms involved in PBM, understanding the response of individual cell types to PBM in neurotrauma is an important area for future research.

5.4.2 Glial activation and the glial scar

Glial activation, particularly astrocyte activation, is closely associated with the formation of the glial scar.[419–422] As was demonstrated in Chapter 3, PBM appears to modulate scar morphology and reduces the volume of the lesion site after SCI. Beyond this, in Figure 3.29, regenerating axons are shown within the scar itself. This suggests that PBM results in modulation of the microenvironment of the scar, as well as its morphology. This reflects the dual role of the glial scar as both a positive and negative influence on neuroregeneration. For example, differing phenotypes of scar-forming astrocytes have been described in association with beneficial sequelae of scar formation, such as acting as a bridge for axonal regeneration.[420] The molecular features in "pro-regeneration" scar-forming astrocytes are yet to be fully elucidated, but nevertheless such features would not be captured through quantification of GFAP expression alone. Furthermore, whilst fibronectin and laminin are prominent components of the glial scar, CSPGs (produced by astrocytes and, more so, by a variety of $GFAP^-$ cell types) also form both a physical and chemical component of the scar which is thought to influence regeneration of neurons,[420] though CSPGs were not evaluated here.

The 3 dpi end-point described in this chapter is early in the astrogliotic process of scar formation, and consolidation of the scar begins from 10-14 dpi as reactive astrocytes become scar-forming, and subsequently mature scar-forming, astrocytes. Similarly in TBI, between 1-10 dpi, there is migration and proliferation of microglia and OPCs toward the lesion site(s), followed later by astrocytes, leading to a maturation phase between days 7-21[421] and eventual remodelling of peri-lesional tissue. Reactive glia during the acute and sub-acute phases have been recognised to influence the quality of the glial scar and, accordingly, the regenerative microenvironment for local neuronal populations, through a complex interplay of molecular

phenotype, functional behaviour, and cross-talk between cell types.[72,335,421,422] The dynamic response of glial cells continues well beyond this consolidation phase in TBI, and differs between mild and severe injury, which may explain the observed differences in GFAP expression between 4 wpi and control specimens described in mild TBI in Chapter 4. Future work which examines the influence of PBM on both morphology and microenvironment of the glial scar at multiple time points in SCI and TBI may elucidate further detail on how PBM may influence astrogliosis and glial scar formation after neurotrauma.

5.4.3 Preconditioning

Preconditioning with PBM in advance of an injurious state has enjoyed increasing interest, and has been demonstrated to be effective in reducing post-injury apoptosis in a variety of neurological models.[423] No discernible effect was noted here using DRGN. This may be attributable to the use of low level PBM in the same parameters successful in post-injury treatment (11 mW/cm^2, 60 s, 660 nm, 0.66 J/cm^2). Significantly different preconditioning parameters have been used *in vitro* previously, utilising much higher radiant energies. For example, 30 J/cm^2 of 670 nm PBM was used to reduce potassium cyanide induced apoptosis in cultured visual cortical neurons;[424] and 18 J/cm^2 of 635 nm PBM was shown to reduce mitochondrial dependent apoptosis with administration of sodium nitroprusside to SH-SY5Y cells.[425] This negative result then offers further tentative support to the notion that PBM mechanisms are highly dependent on the context of cell stress state, and that the suitable parameters for eliciting effect are also dependent on this state.

5.4.4 Paracrine signalling

No significant differences were observed with the transfer of PBM conditioned media compared with control serum withdrawal treated DRGN. A trend is observed that greater dilution across both treated and control conditioned media results in improved survival, with the only significant difference observed in greater survival amongst the 20% control conditioned media group (Fig. 5.8). This may be related to a beneficial effect of low levels of paracrine signalling molecules

released from distressed (untreated) cells subjected to serum withdrawal. Such molecules may have been at lower (ineffective) levels in treated conditioned media, and this may account for the observation. Calcium dependent activation of the ERK/CREB has been proposed as a mechanism by which growth factor transcription is upregulated after PBM in DRGN,[322] though no evidence for increased BDNF release with PBM treatment was identified here.

5.4.5 Extracellular matrix deposition

No significant differences in laminin or fibronectin deposition were observed with PBM treatment in the early post-injury phase (Fig. 5.11), though this assay method using quantitative immunofluorescence may be insufficient to detect more subtle changes in this group size. A significant increase between sham and injured groups was noted for fibronectin, which was anticipated as a more acute-phase ECM protein. The role of PBM in reducing lesion size and morphology after SCI, as observed in Chapter 3, is predictably more complex than the quantity of fibronectin and laminin deposition during the early treatment phase. Given the necessity of ECM proteins, particularly fibronectin, in establishing an extracellular scaffold to support axonal regeneration, the quality of glial scarring and its milieu and composition are likely much more influential than the quantity of material deposited.[426] For example, interaction with ECM proteins by cell adhesion molecules (CAM) are important in use of ECM as a scaffold. PBM has previously been shown to increase transcription of CAM genes[427] (notably, significant increases in NCAM1 and L1CAM were identified with PBM in this chapter's transcriptomics data).

5.4.6 Transcriptomics

The enrichment of pathways associated with neurite outgrowth is an encouraging finding to support the phenomenology observed in Chapters 3 and 4. This correlates further with evidence from broader works demonstrating the synaptogenic activity of PBM after TBI *in vivo*.[172–174] The effects on metabolic processes are suggestive of reduced necessity for mitochondrial subunit composition, potentially due to the supportive activity of PBM in mitochondrial function. Transcription of genes associated with cytochrome c mediated apoptosis were consistently

reduced (Diablo, cycs, Bax, caspase-3/8), and provide a link between mitochondrial primary mechanisms and tertiary anti-apoptotic mechanisms.[428]

GO:CC terms enriched include ATP binding and metal ion transmembrane transporter activity, which support described mechanisms of ATP mediated calcium signalling pathway activation, and activation of calcium homeostatic processes in the ER. This is further supported by activation of calcium signalling pathways (Fig. 5.19) including P2 receptors. Here there are also marked upregulation of NMDA receptor subunits (e.g. Grin1, Grin2c), which may be a mechanism by which ATP dependent processes activate neurite outgrowth: it has been previously shown that inhibition of activation of NMDA receptors impairs dendritic spine outgrowth, with ER implicated in maintenance of neurite outgrowth.[429] Increases in calcium and cAMP activity have been associated with growth cone morphogenesis[430] and are recognised effects of PBM.[399] Upregulation of inducible NOS seen in this calcium signalling pathway also correlate with previous findings.[390,391]

Linking recognised pathways from transcriptomics to observations such as reduced inflammation, has generated several further hypotheses. For example, S100A8/9 complex has a role both in intracellular calcium sensing but is also released in pro-inflammatory states whereupon it stimulates leucocyte migration and inflammatory cytokine release.[431] Syn1, amongst several other of the upregulated genes described here with PBM treatment, is implicated in modulation of neurotransmitter release, as well as axonogenesis and synaptogenesis. Modulation of neuronal excitation through a primary mitochondrial mechanism may therefore be involved in the favourable effects of PBM. Mpz was shown here to be upregulated in the spinal cord after PBM, though it is known to be specifically expressed in Schwann cells of the peripheral nervous system in mammals. Notably however, Mpz has been implicated in regeneration of the spinal cord in zebrafish, and presents a potential novel mechanism for PBM's neurorestorative effects which warrants further investigation.[432] Fabp4 was strongly downregulated with PBM treatment, and inhibition of this protein has been shown to improve locomotor function in rats after SCI by modulating macrophage and microglial activity.[433]

5.4.7 Limitations

The transcriptomics analysis has generated supportive evidence for existing hypotheses, as well as generating some novel hypotheses for future research. However, the used of a single set of PBM parameters with a single timepoint post-injury somewhat limits the insights that can be derived from this work. Similarly, no sham control group was used to demonstrate a relative baseline, which would be of particular interest for comparison of metabolic activity-related transcription with that of the injured-treated condition. Furthermore, the tissue used here was a homogenate of the entire injury site, and as such contains the transcriptome of all cell types within the tissue. As such, resolution of any particular mechanism to within certain cell types (particularly distinguishing between non-neuronal cells) is not possible for intracellular pathways which are well preserved between cell types.

The phenotype of iMDM holds strong similarities to that of primary microglia,[434] however phenotypic differences are inevitable. Such differences are likely to be compounded by the culture of iMDM in isolation, and behaviour more representative of *in vivo* conditions would be anticipated in co-culture modelling. As described above, preconditioning is a markedly different context to post-injury treatment, and successful parameters for PBM in such conditions are accordingly in contrast.[424,425] Successful model development using preconditioning is likely to require more extensive dose trials than performed in this chapter, and should be addressed through future work.

5.4.8 Future directions

An -omics approach to delineating the complex mechanism of PBM in neurotrauma has showed initial success here for generating novel insights and new hypotheses. Validation of these observations through polymerase chain reaction (PCR) and further mechanistic studies using *in vitro* models would add valuable support to the findings. Further -omics approaches, particularly metabolomics, are likely to provide further important insights on the mechanism of PBM. The use of variable wavelengths and parameters through these approaches would provide vital advances,

not only to the knowledge of PBM mechanisms, but also importantly toward generating optimal protocols for PBM treatment based on improved scientific reasoning to design future work to compare treatment parameters. Combining methodologies described in this chapter, such as through the use of single-cell transcriptomics, or -omic analysis of single cell-type culture experiments, would likely provide valuable insights into the cell-type-specific mechanisms of PBM. Use of mitochondrial imaging/dyes (e.g. JC-1) and functional assays of mitochondria (Seahorse assay) would also provide useful information on the temporal response of mitochondria to PBM.

5.4.9 Conclusions

This chapter has generated important and novel insights into the mechanisms of action of PBM in neurotrauma. PBM has been shown to attenuate microglial activation in a translational human *in vitro* model. The effects of PBM have also been elucidated using transcriptomics from an *in vivo* model, which support a hypothesis that primary effects within the mitochondria enhance intracellular calcium signalling, reduce necessity for mitochondrial component transcription, reduce apoptosis and promote neuronal projection development. Such insights are important to support the translation of medical devices using PBM to clinical contexts, by providing a more well-defined rationale for use. The next phase in translation of this concept toward patients is the development of feasible prototypes which are capable of delivery of invasive PBM, which will be explored in the next chapter.

Chapter 6

DEVELOPMENT OF CLINICALLY RELEVANT TRANSLATIONAL PHOTOBIOMODULATION DEVICES FOR APPLICATION IN NEUROTRAUMA

The concept described in this thesis, using invasive delivery of PBM with monitoring using RS, requires development of a novel medical device to establish an optical interface with the brain/spinal cord. In Chapter 3, it was demonstrated that invasive application of PBM directly to an injured area of the CNS promotes neuroregeneration. Delivery of the doses of PBM described throughout this thesis are not achievable in humans through transcutaneous administration. Therefore, development of an implantable device which can safely delivery PBM directly is required as a translational step in progressing this concept toward application in humans. This chapter describes the development of such a device as a prototype for the invasive delivery of PBM in TBI and SCI.

6.1 Introduction

6.1.1 Delivery methods of photobiomodulation

Previous work using transcranial applications of PBM in TBI has resulted in limited transmission of photons to neuronal tissue (Fig. 6.1). Whilst this approach can reach effective dose parameters in small mammals, as shown in Chapters 3 and 4, in humans this approach would severely limit the opportunity to deliver the optimal energy dose to the injurious target site. Direct application can achieve 20 fold greater light delivery:[239] as such development of method of direct light delivery to overcome this challenge may confer much greater efficacy in translation to humans. In Chapter 3, *in vivo* work demonstrated support for equivalent efficacy of invasive PBM delivery in SCI in comparison with transcutaneous administration. Previous work has also demonstrated similar support for efficacy of intracranial delivery using models of Parkinson's disease.[312,313]

The concept of invasive neuromonitoring is well established in severe TBI given the prevalence of invasive intraparenchymal ICP monitoring, and growing implementation of PbtO2 monitoring. The concept of this invasive device is that such intracranial access to permit the standard of care (twist drill craniostomy) can be readily adapted to permit the application of the system, without additional risk burden to patients: patients suitable for this invasive therapeutic system would inherently require invasive monitoring. Similarly, in SCI, the advent of intrathecal monitoring may provide a similar justification for invasive therapeutic/monitoring devices. Regardless, the use of wound drains after spinal decompression surgery provides further precedence for the short term deployment of invasive paraspinal medical devices.

PBM has hitherto most commonly been deployed as a therapeutic for topical or superficial conditions, such as oral mucositis, where PBM can be delivered directly to the affected area. Similarly, many application of PBM to the CNS to date have been via a transcutaneous or transcranial route. Some previous reports have utilised the concept of an implantable device to enhance capability for PBM dose delivery. In cranial applications, a flexible LED array for implantation over the brain cortex has been described for use in pre-clinical models of stroke.[435] Probe based implants for delivery of PBM to deep brain structures have also been developed for

use in pre-clinical models of Parkinson's disease.[312] For the spinal cord, a modified fibre which can be inserted parallel to the spinal cord and diffuse light along its length has been developed and demonstrated in a large mammal model.[314,338] Implantation of fibres to transmit PBM have also been used in a murine model[334] and demonstrated a beneficial effect.

Given the biphasic effect of PBM therapy,[166] precision dose delivery is key to translational success. Furthermore, success of real-time monitoring and dose adjustment feedback would permit personalisation of doses based on biochemical cellular responses which are proposed to vary based on numerous patient factors including injury severity and biochemical injury response. Work in Chapters 3 and 4 has demonstrated in the concept that Raman spectroscopy could provide this feedback to inform a closed-loop stimulation-monitoring system. From these findings, the purpose of this chapter is to develop a medical device which can deliver direct-to-CNS PBM stimulation and monitor its effect via closed-loop feedback, monitor wider brain biochemistry, and integrate into current "standard-of-care" minimally invasive neuromonitoring modalities.

6.1.2 Objectives

Non-invasive delivery of PBM significantly limits the transmittance of effective doses of photons to injured tissue. In the neurotrauma patient, accessing the cranium and spinal column for monitoring or therapy is commonplace after severe injury. This lends an opportunity to integrate implantable PBM devices into these procedures to offer further therapeutic potential, based upon the concept of the established temporary implant of the ICP bolt in the brain (Fig. 1.1); and the implantation opportunity of posterior approaches to the spine for post-traumatic fixation.

Therefore, the objectives of this chapter are to:

- Develop an implantable cranial device as a brain-optical interface
- Develop an implantable spinal device as a spinal-optical interface

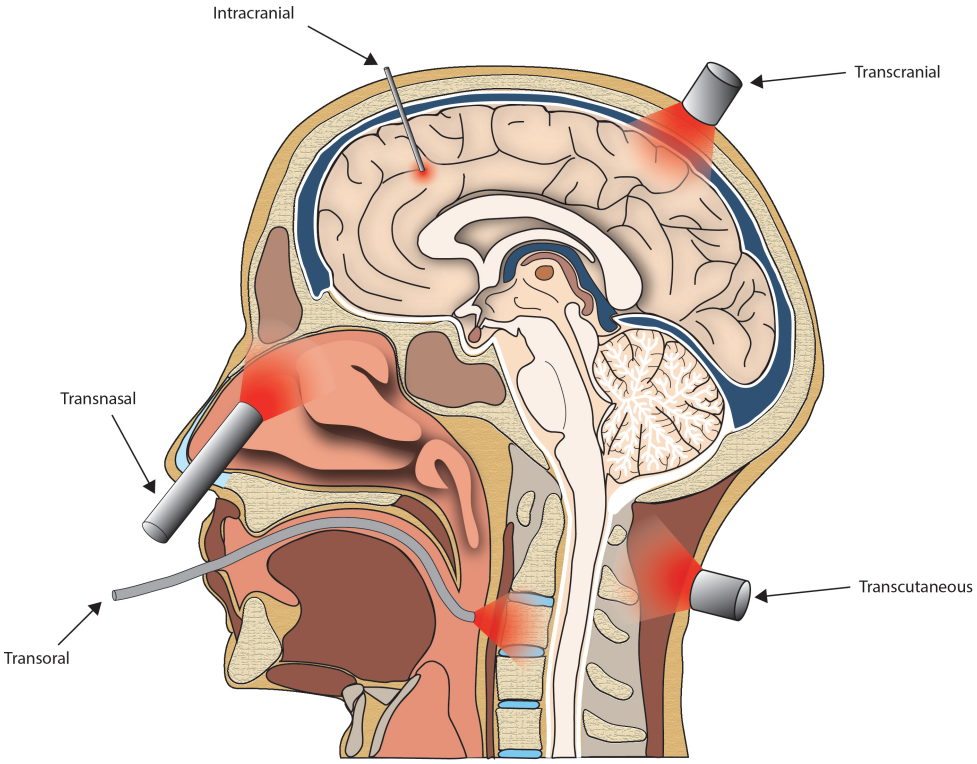


Figure 6.1: Schematic diagram of mid-sagittal section through the head and neck, with devices represented to deliver PBM via currently utilised routes: transcranial, intracranial, transnasal, transoral, and transcutaneous.

6.2 Materials and methods

6.2.1 Beam characterisation

Methodology for beam characterisation is described in Section 6.2.1. The set up used is shown in Figure 3.5.

6.2.2 Prototype design and rendering

Prototypes were created through computer-aided design (CAD) and computer-aided design (CAD) software. Designs were created in Fusion 360 2.0 (Autodesk, CA, USA). Slicing for CAM was performed with Ultimaker Cura software 4.12.1 (Zaltbommel, Netherlands). Prototypes were rendered in polylactic acid (PLA) filament (RS Components, UK), using a 3D printer

(CR-10 S5, Creality, Shenzhen, China).

6.2.3 Optical phantom

A lipid/protein emulsion turbid optical media was produced to a standardised recipe used within our research group. This formulation has been developed based on previously described formulae using intralipid to represent an analogous R/NIR scatter and absorption profile to normal brain parenchyma.[436–438] Whole milk is used in place of intralipid, and this phantom media has been validated against brain tissue in Appendix G. Whole milk with 5% w/w gelatin from porcine skin (Sigma, USA) and black ink (Parker, USA) (19.79 μl per 100 g milk) were mixed and heated to 50 °C until the gelatin dissolved. The media were cast into 3D printed white PLA moulds lined with acetate to contain a standardized thickness of set media: 2.5 mm, 5 mm, 10 mm, 15 mm and 20 mm (Fig. 6.2). Media was transferred with 3 ml Pasteur pipette to avoid inclusion of air bubbles within set phantom. Media was allowed to set at 20 °C and was stored at 4 °C for up to six hours, but returned to room temperature prior to use. Once set, room temperature phantoms were positioned within calibrated profilometry equipment to measure transmission of light (Fig. 6.3). Validation of the transmission of the phantom material in comparison to brain tissue is shown in Appendix G.

6.2.4 Porcine tissue modelling

Porcine tissue was obtained from a local butcher (Brown's of Harborne, Birmingham, UK). For head specimens, hemisection along mid-sagittal plane was performed by the vendor using an industrial standard bandsaw. Cranial access was achieved through use of a standard 14 mm cranial perforator (Codman, Integra LifeSciences, NJ, USA). For isolated brain specimens, hemispheres were removed from cranial cavity after sagittal hemisection as described above. Tissue was stored at 4 °C until use.

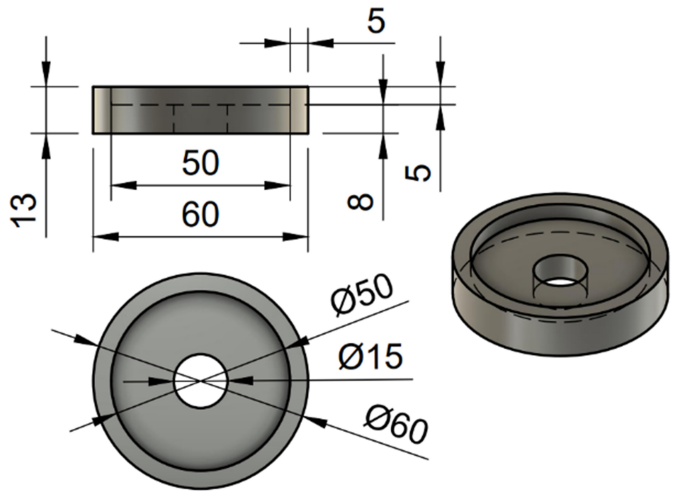


Figure 6.2: 5 mm thickness phantom mould design, for the casting of optical phantom as an optically similar media to brain. Dimensions shown in mm.

6.2.5 Optical sources and fibres

Four 660 nm coherent laser sources (MDL-III-660-FC-800 mW, CNI Co., Ltd., China) were used individually or in combination, with manufacturer supplied system-integrated fibre/diffuser. Where coupling to a subsequent fibre, coupling was achieved by SMA-SMA mating sleeve ADASMAB3 (Thor Labs, USA). Multimodal optical fibres were used: M107L01 single core fibres and FG55UEC bundled custom fibres (single fibre splitting to seven terminal cores. Ends were cleaved flat and polished with successive grades of silicon carbide abrasive paper (P1000, 1200, 2000, Struers, Copenhagen, Denmark).

6.2.6 Thermal imaging

For thermal imaging of the temperature changes associated with light administration, an AX5 (Teledyne FLIR LLC, Oregon, USA) camera was focused onto the tissue in contact with the highest irradiance from a given source. Image capture and thermal profiling was performed using FLIR ResearchIR (Teledyne FLIR). Animal tissue was assigned an emissivity of 0.95, probes were assigned an emissivity of 0.90.

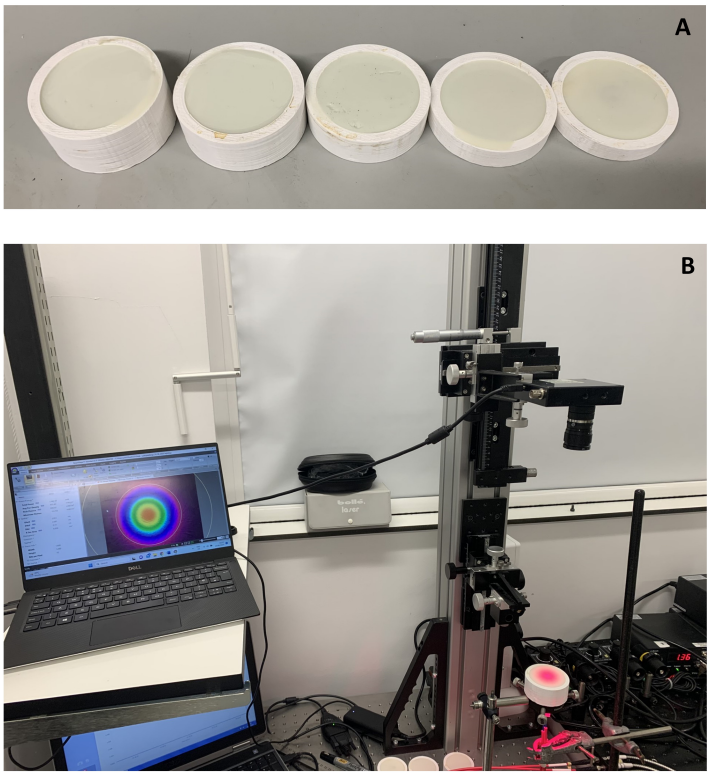


Figure 6.3: A: phantom moulds filled with set lipid emulsion gel at thicknesses (from left to right) of 20 mm, 15 mm, 10 mm, 5 mm and 2.5 mm; B: profilometry of optical transmission using 660 nm light via a custom-made interface.

For calculation of phantom emissivity, a standard emissivity material (Scotch Super 88, 3M, Minnesota, USA, emissivity 0.95) was used to cover half of the phantom and allowed to equilibrate to phantom temperature. Two thermocouple probes were used, secured to the surface: (1) on the surface of the Super 88 tape; and (2) on the surface of the uncovered phantom. 10 s simultaneous FLIR and thermocouple readings were recorded (n = 5).

Emissivity 0.95 was used for Super 88 ROI and thermocouple temperatures were used to calibrate the FLIR camera temperature measurements. For each replicate across the ambient temperature range (18-22 °C), emissivity was adjusted for the mean temperature for the ROI focused on bare phantom to achieve the readings given by the respective thermocouple. The mean value of optimal emissivity across the n = 5 replicates was 0.92. This emissivity value was then used in each replicate for correlation data analysis (Fig. 6.4), which demonstrated good correlation (r = 0.97 [0.95 to 0.98 95% CI], p < 0.0001).

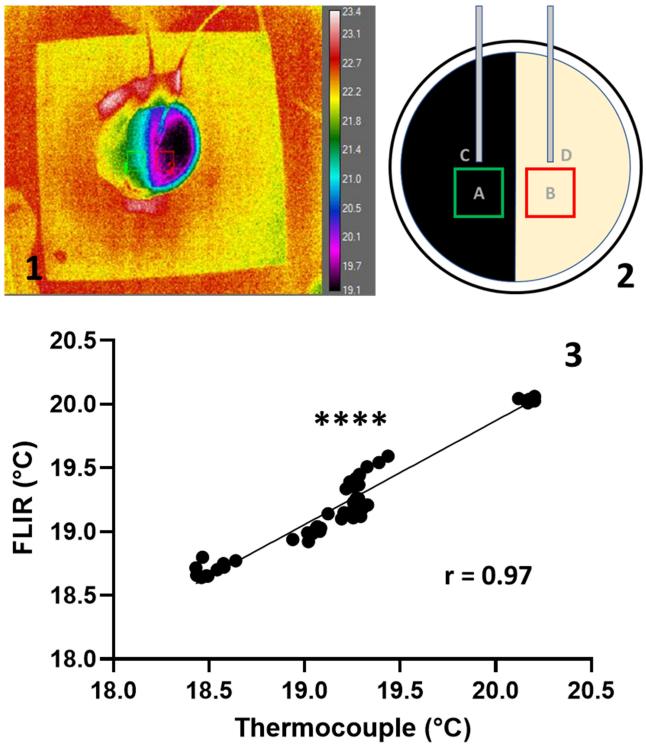


Figure 6.4: Calculating emissivity. Top left: FLIR Research IR view of calibration/emissivity method, with ROI and thermal colour bar; top right: schematic view of calibration/emissivity method: A = ROI for Super 88; B = ROI for phantom; C = thermocouple probe for Super 88; D = thermocouple probe for phantom; bottom: correlation of FLIR and thermocouple readings for phantom ROI, with emissivity set at 0.92. (r = 0.97 [0.95 to 0.98 95% CI], $p < 0.0001$ (= ****), n = 5, 62 xy pairs for Pearson correlation, line of best fit calculated by simple linear regression).

6.2.7 Statistical analysis

Statistical analysis was performed using Prism 9.2.0 (GraphPad, California, USA). Shapiro-Wilk analysis was performed to test for normal distribution. For non-parametric data: Wilcoxon signed rank test was used for two group comparison; for comparison between more than two groups, Friedman test was used. For parametric data: paired t-test was used for comparison between two groups; for comparison between more than two groups, one-way row-matching ANOVA was used with Geisser-Greenhouse correction.

6.3 Results: Brain interface

To maintain fixed-orientation of optical fibers for light delivery (to a phantom media or cadaveric tissue), a housing was designed and rendered. Due to the translational intention of the concept, design constraints were imposed on the anatomical and practical considerations required for a translational cranial access device, listed below:

1. The device must be of dimensions which could be externally accessed, with an internal component traversing the skull. Based on craniometric/cephalometric data at Kocher's point (International 10-20 system point F4) the average required depth from external surface to cortical surface is 7.9 mm (2.3 mm for skull, 5.5 mm for scalp, with 0.1 mm between).

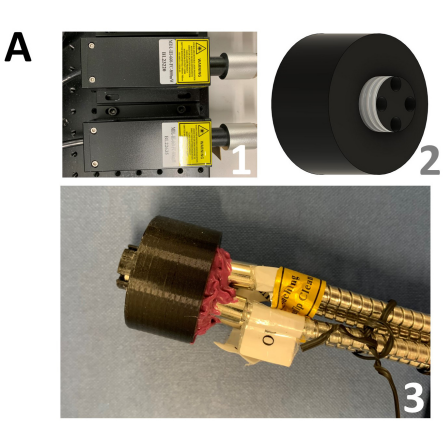
2. The component for access through skull should be compatible for use with a standard neurosurgical cranial access device (9, 11, or 14 mm).

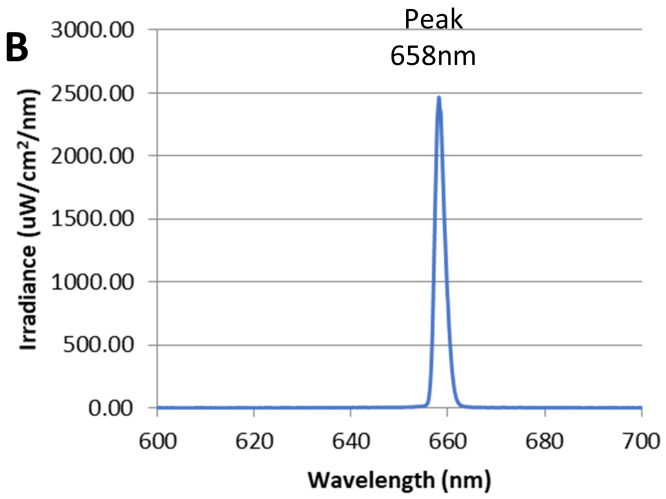
Conceptually, the design of the system is based on the skull "bolt", a hollow-lumen plastic tube with external self-tapping thread for securing the transcranial interface, which self-secures to prevent inadvertent advancement into parenchyma.

6.3.1 Original prototype

The original prototype was profiled as a baseline reference[i]. 660 nm laser sources were used (MDL-III-660-FC-800 mW, (CNI Co., Ltd., China), Fig. 6.5 A1). A bolt housing was rendered in black PLA (Fig. 6.5 A2), designed to house four FG550UEC Custom Fibre Bundle (Thor Labs, USA) (metal housing) (Fig. 6.5 A3) which were coupled directly to four laser sources. Spectral irradiance for the system demonstrated a peak at 658 nm (Fig. 6.5 B). The beam profiling results (Fig. 6.5 C) shows the values of key beam characteristics when directed at a target screen (0 mm) and at optical phantom at 5 thicknesses. Total power, and average/peak irradiance fell exponentially at increasing depth, and D4σ and cross-sectional area increased at increasing depth.

[i]Developed by David Davies in unpublished material.





C

Phantom depth (mm)	Total Power (mW)	Average irradiance (mW/cm²)	Peak irradiance (mW/cm²)	D4σ (cm)	Cross-sectional area (cm²)
0	1487.78	89842.85	216966.54	1.22	0.16
2.5	352.04	402.07	13509.37	1.39	0.73
5	135.62	51.90	202.31	1.86	2.65
10	38.99	9.22	23.73	2.24	4.14
15	13.21	2.08	4.92	2.80	6.27
20	5.33	0.75	1.63	3.05	7.09

Figure 6.5: Original cranial bolt profiling. A1: MD-III 800 mW laser sources (two of four shown); A2: CAD design of prototype fibre housing "bolt"; A3: photograph of housing with fibres in situ; B: spectral irradiance values with peak irradiance at 658 nm; C: table of mean beam characterisation results at target screen (0 mm) and through five thicknesses of phantom cast in standardised thickness moulds. n = 3 technical replicates per n = 3 independent experiments.

These initial pilot results present a number of issues which would be problematic for clinical translation: (1) average irradiance values would represent overdosing (and consequent heating) at surface and insufficient dose at depth; (2) very high peak irradiance values at the surface; (3) beam area values would represent low volumes of irradiance of target tissue. Therefore, the key aims are to: increase beam diameter, particularly at the surface, and homogenise power distribution.

With the original prototype, significant heating was noted, of the optical phantom (Fig. 6.6) and of the bolt housing itself (Fig. 6.7). This demonstrated unacceptable levels of heating within

predominantly the superficial 2.5 mm. In a cadaveric model, using a porcine head cut in half in the sagittal plane, a 14 mm burr hole was drilled, into which the bolt was inserted. Due to the relative thickness of the porcine skull, this was not in contact with the cortical surface, and led to heating predominantly within the skull. To ascertain the effect on brain parenchyma, the bolt was positioned directly over the cortical surface of a cadaveric brain after removal from the skull. Significant heating to unacceptable levels was observed within brain parenchyma and the bolt housing itself. Whilst this observation is likely, at least in part, direct heating caused by high power output of the 660 nm laser (radiation heating), considerable heating within the bolt housing was observed which may have contributed via conduction. Given the high intrinsic absorbance of black rendering material across the visible spectrum, alternative bolt rendering materials were explored. A further key to development of this device is to achieve diffusion of the light prior to contact with the cortical surface, to avoid the hot spots shown in Figure 6.6 which correspond to the distribution of the four laser probes.

6.3.2 Rendering material

The rendering material of 3D printed prototypes was considered and compared. Identical CAD designs were rendered in: black PLA; white PLA; and resin (Fig. 6.8). White PLA demonstrated greatest power and area performance across all groups, with statistically significant difference between groups for total power, D4σ and beam area. Accordingly, subsequent prototypes were manufactured in white PLA unless otherwise stated.

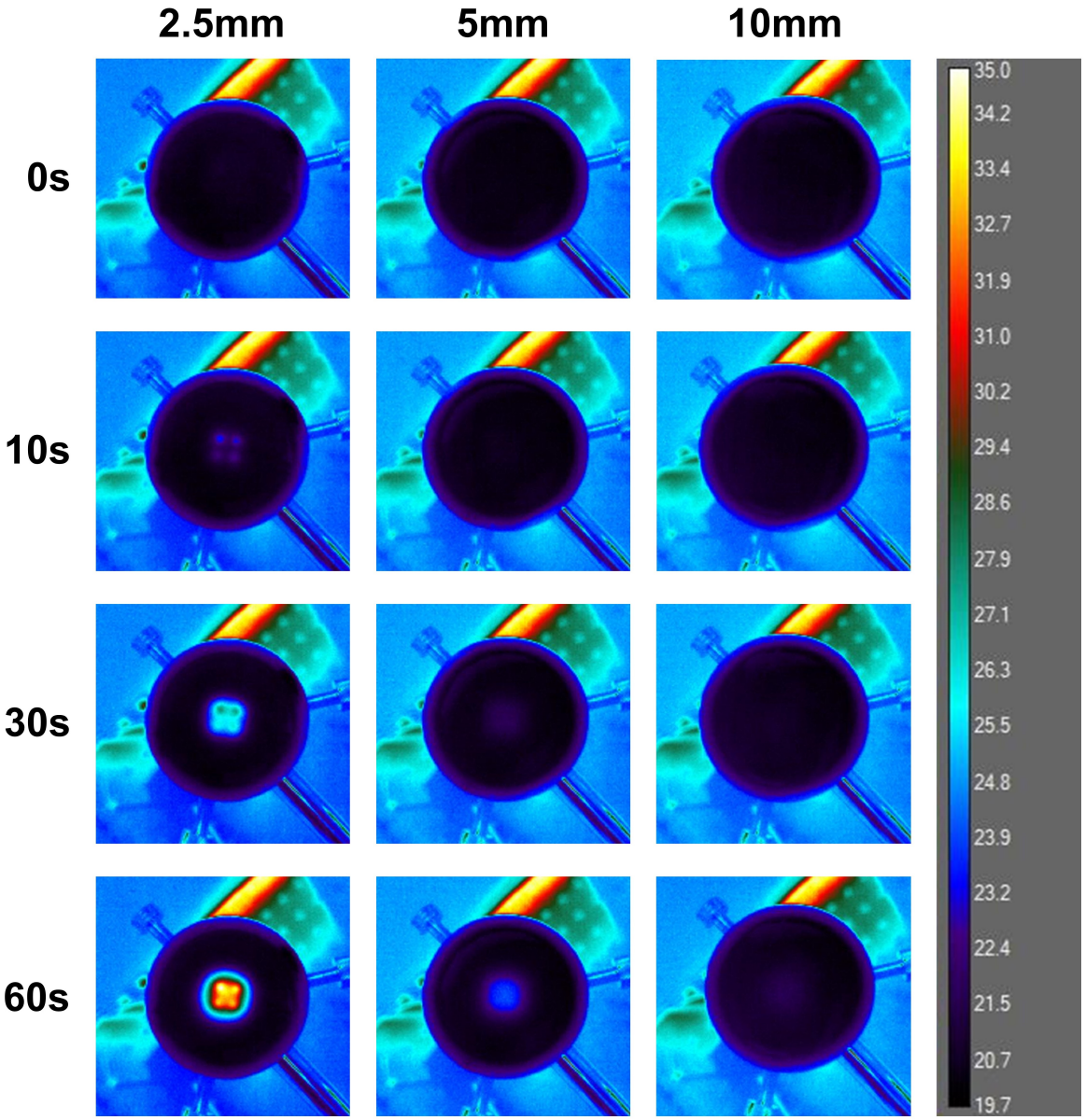


Figure 6.6: Thermography of 60 s exposure to PBM delivered by original bolt (at maximum power output) in 2.5 mm, 5 mm and 10 mm optical phantom moulds. Scale bar colour denotes temperature in Celsius.

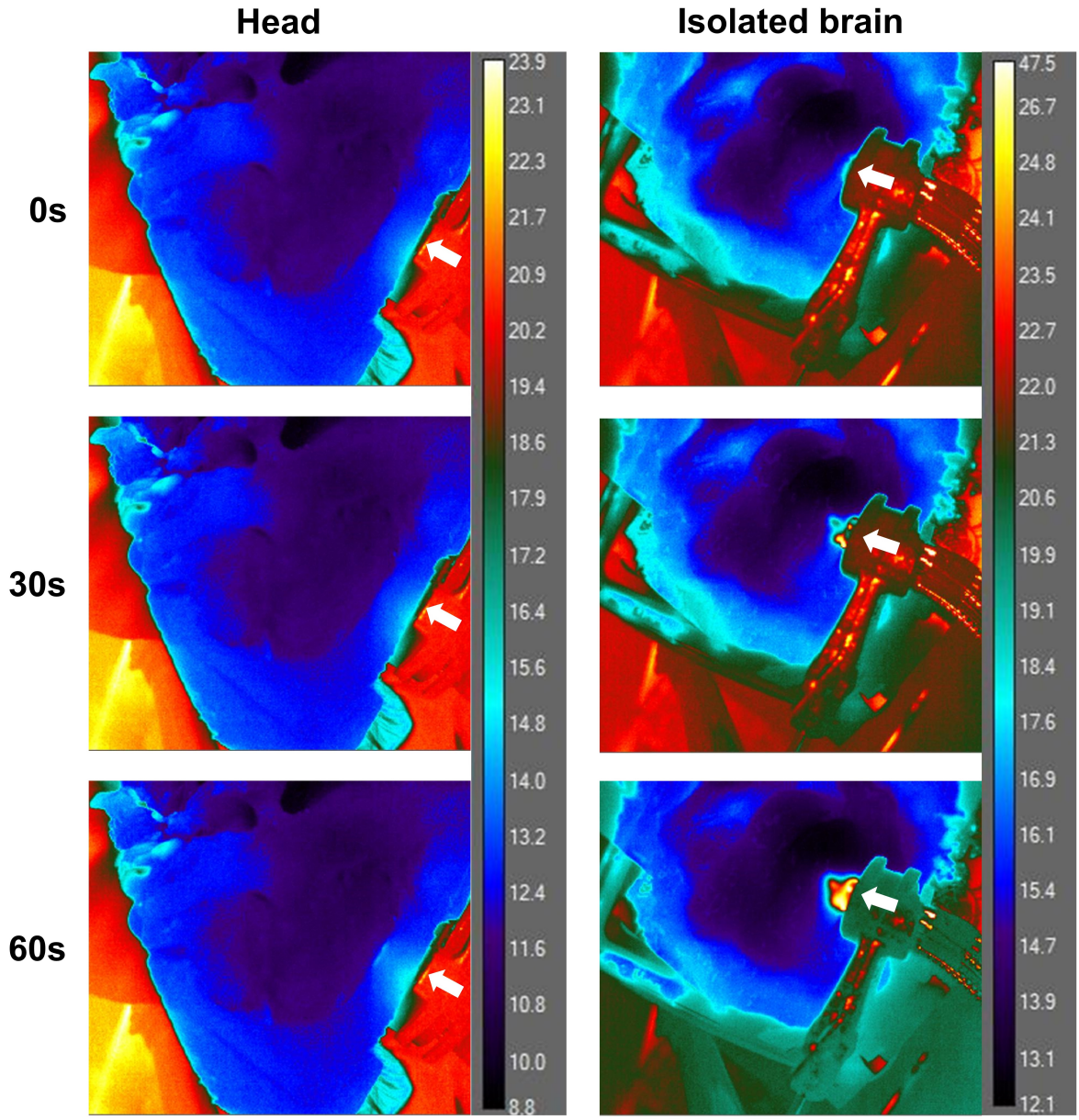


Figure 6.7: Thermography of 60 s exposure to PBM delivered by original bolt (at maximum power output). Head = *in situ* within a pig skull (cut in half in sagittal plane, shown from medial view with brain *in situ*); isolated brain = bolt placed directly over cortical brain surface after removal from skull. Scale bar colour denotes temperature in Celsius. Arrows denote position of bolt housing.

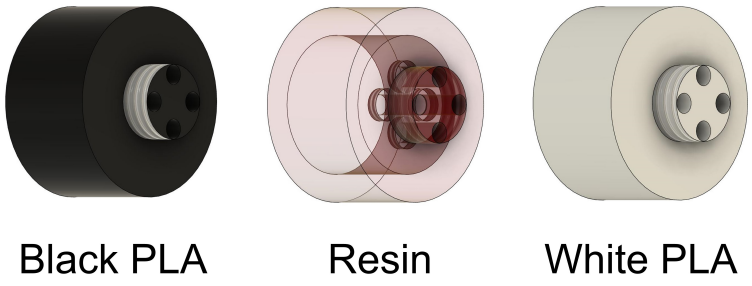


Figure 6.8: Identical CAD design images, rendered to represent manufacture in (left to right): black PLA; resin; and white PLA.

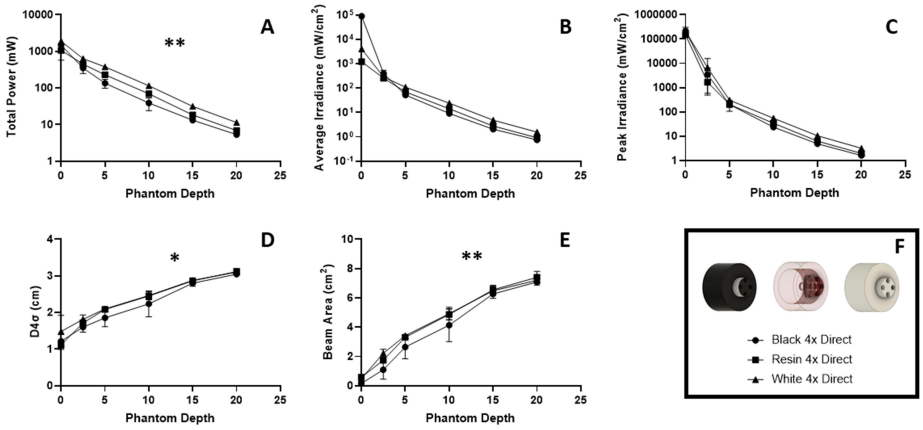


Figure 6.9: Bolt rendering material significantly affects 660 nm light transfer to an optical phantom. CAD design images were manufactured in black PLA; resin; and white PLA, and underwent profilometry through five thicknesses of phantom cast in standardised thickness moulds. A: total power (y axis on log10 scale); B: average irradiance (y axis on log10 scale); C: peak irradiance (y axis on log10 scale); D: D4σ; E: beam area; F: key with Fusion 360 rendered representations of respective bolt housing for (left to right): black, resin, white. For each prototype, four MD-III lasers at 100% power output were coupled to integrated, manufacturer supplied fibre directly from output, and fitted into each bolt housing. Beam characterisation results at target screen (0 mm) and through five thicknesses of phantom cast in standardised thickness moulds. n = 3 technical replicates per n = 3 independent experiments. * = $p < 0.05$, ** = $p < 0.01$ (Friedman test). Error bars represent SD; not visible in all instances due to logarithmic scale and/or symbol size.

6.3.3 Fibre coupling

As depicted in Figure 6.5 the diameter and rigidity of the termination of manufactured supplied integrated fibre output severely restricted fibre housing design opportunities. Within a 14 mm aperture, there is just sufficient space to accommodate four of these housed fibre terminations immediately adjacent and parallel to each other, with no tolerance for any angular adjustments. To explore the efficiency and possibilities of alternative fibres, two fibre types were used and coupled to integrated fibre via SMA/SMA. A multicore fibre (each splitting each MD-III laser output into seven discrete fibres (7 x 4 = 28 terminal fibres)), and single core fibre (each coupling MD-III laser output to a single core fibre (1 x 4 = 4 terminal fibres)). These were compared with the direct output model described in Figure 6.9 (white PLA as optimal rendering material). The results demonstrate statistically significant losses in power and irradiance values where coupled to multicore fibres. No difference was observed between direct and single core coupled models.

As illustrated in Figure 6.10, heterogeneity of discrete beam fibres for multicore fibre modelling was more apparent than in four single core fibre coupling. The narrow incident beam into the SMA/SMA connector is proposed to result in unequal distribution of the beam between the discrete seven terminal fibres. Despite attempts at minor adjustments to optimise coupling efficiency, no significant improvements in distribution across the seven termination fibres were achievable. Demonstration of satisfactory coupling efficiency with single core fibres permits further design freedom: spatial orientation of fibres; altered exit geometry from fibre housing; alterations of fibre terminus quality; lensing of terminal fibre output; and recessing of the fibre from the interface to permit diffusion.

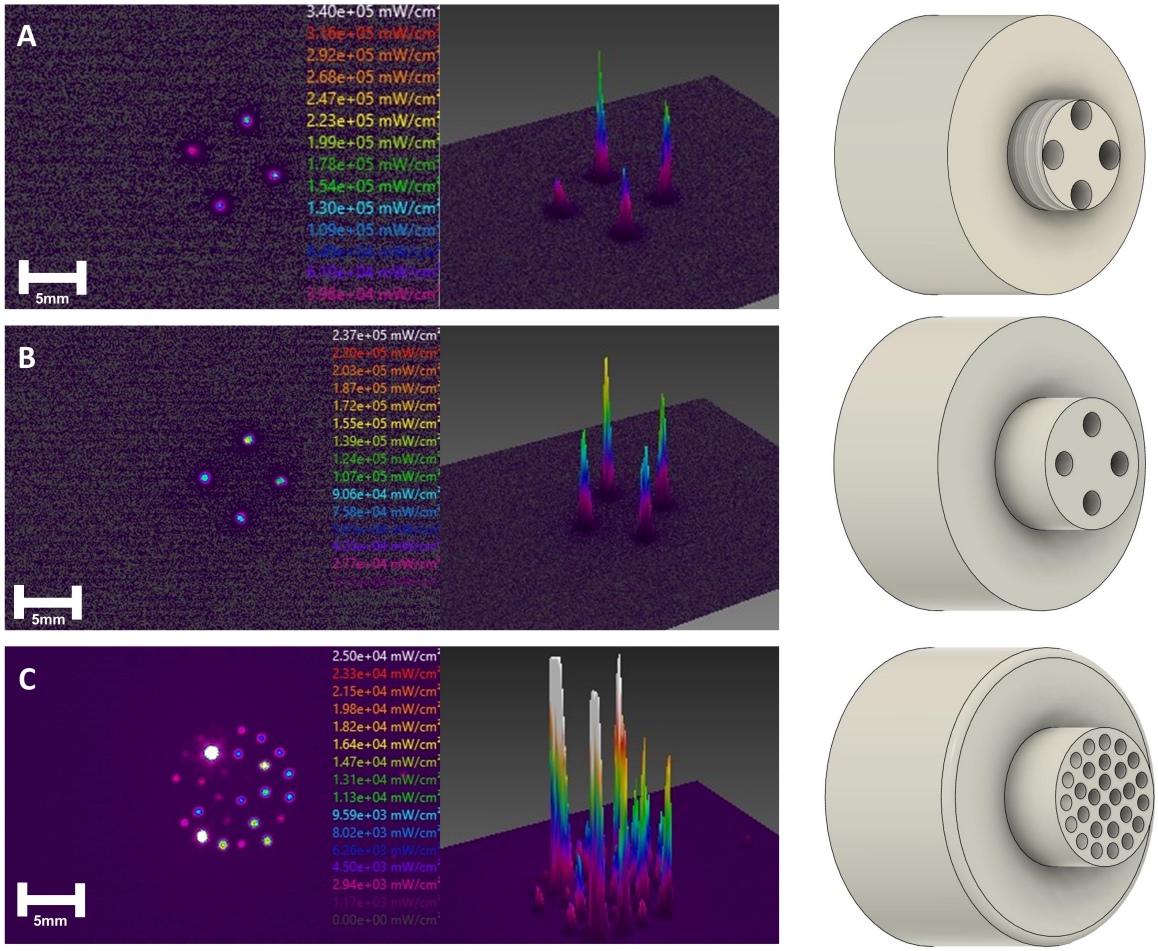


Figure 6.10: Beam profiles for fibre coupling prototypes, shown with CAD representation of the bolt design. Four MDL-III lasers used with (A) native direct fibre from manufacturer, 100% power output; (B) SMA/SMA connector (Thor Labs) to couple each to a 1000 μm single core fibre; (C) SMA/SMA connector (Thor Labs) to couple each to a 1000 μm multi core fibre (splitting to seven fibres 650 μm per fibre). Beam profiles taken from target screen positioned directly on surface of bolt.

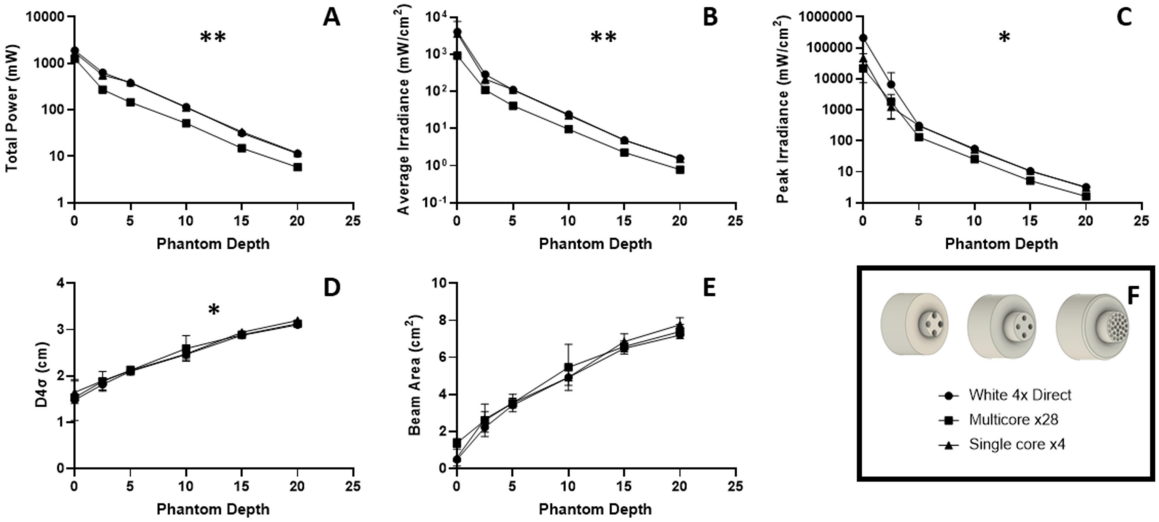


Figure 6.11: Multi-fibre coupling attenuates light transmission to an optical phantom. A: total power (y axis on log10 scale); B: average irradiance (y axis on log10 scale); C: peak irradiance (y axis on log10 scale); D: D4σ; E: beam area; F: key with Fusion 360 rendered representations of respective bolt housing for (left to right): white 4x direct, white multicore x28, white single core x4. For white 4x direct, four MD-III lasers at 100% power output were coupled to integrated, manufacturer supplied fibre directly from output, and fitted into bolt housing. For multicore x28 , four MD-III lasers at 100% power output were coupled to an FG550UEC custom fibre bundle (SMA to SMA, ThorLabs) and subsequently coupled each to a respective custom fibre splitting each into seven fibres, For single core x4 , four MD-III lasers at 100% power output were coupled via to an FG550UEC custom fibre bundle (SMA to SMA, ThorLabs) and subsequently coupled via SMA/SMA each to a respective single core 1000 μm 0.39 NA fibre. Beam characterisation results at target screen (0 mm) and through five thicknesses of phantom cast in standardised thickness moulds. n = 3 technical replicates per n = 3 independent experiments. * = $p < 0.05$, ** = $p < 0.01$. Error bars represent SD; not visible in all instances due to logarithmic scale and/or symbol size.

6.3.4 Exit geometry

An optical design feature proposed to influence beam-phantom interaction was the exit geometry, i.e. the physical architecture of the beam housing at the bolt-brain interface (Fig. 6.12). This was proposed due to the significant influence of the colour of bolt rendering material and possible role of reflectance/absorption by white/black PLA respectively with resulting effect on energy transmission and distribution. Varying geometries were therefore considered to have theoretical potential for maximising beam transmission or distribution via reflectance. To explore this, varying exit geometries were rendered as single fibre bolt designs to rigorously assess the efficacy of these features at improving transmission and distribution in this application (Fig. 6.12).

Conical exit geometry Initially, a flat and conical geometry housing were used for comparison. Cone architecture corresponded with marginal but statistically significant increase in total power (Fig. 6.13, and an observable but not statistically significant trend of increased beam diameter/area both in phantom and directed at target screen.

Punch and concave exit geometries Alternative architecture options were explored. The cone design was compared with a concave exit geometry and "punched out" uniform margin around the fibre (punch) geometry. These are shown in Figure 6.12 (concave in Figure 6.12 C; punch in Figure 6.12 D). There were no statistically significant differences between groups in any measured beam characteristic (Fig. 6.14). A marginal but not statistically significant difference at the beam surface is suggestive of a potential benefit of cone over other architectures.

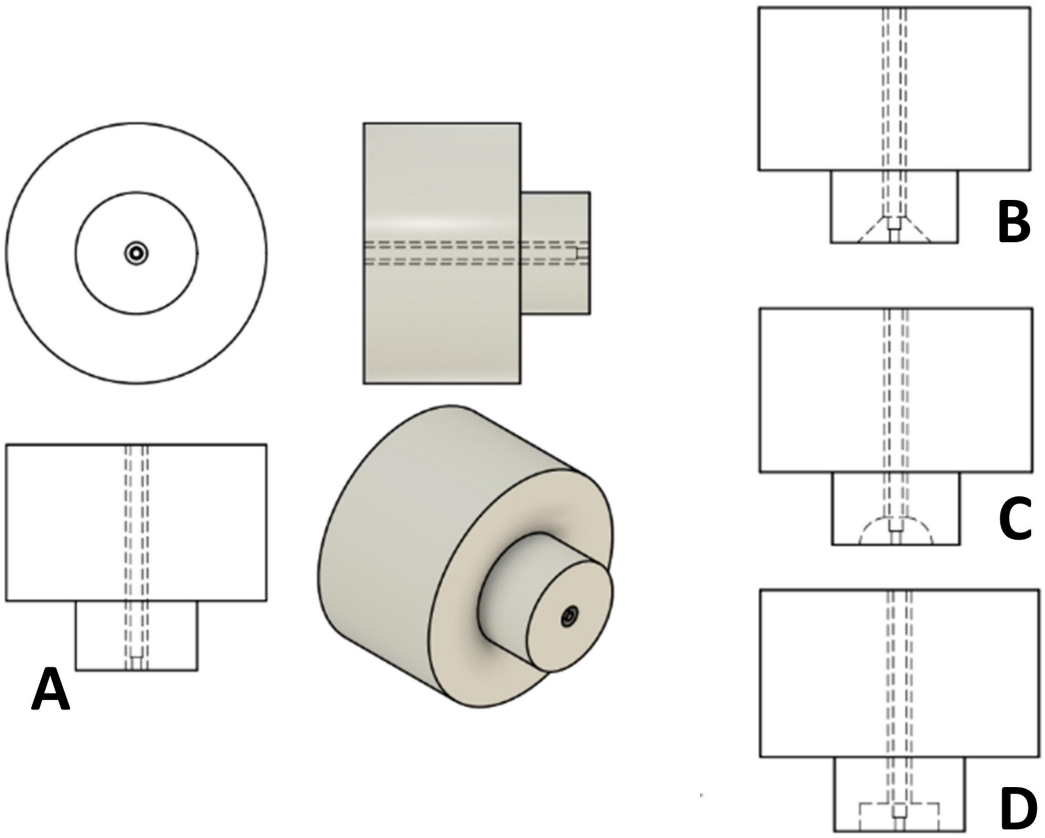


Figure 6.12: Single fibre bolt designs for specific exit geometry profiling, with optical fibre position included in design. A: Flat interface architecture, aperture for fibre/beam exit only, four profiles shown; B: Cross section of cone interface; C: Cross section of concave interface; D: Cross section of punch interface. All designs rendered in white PLA.

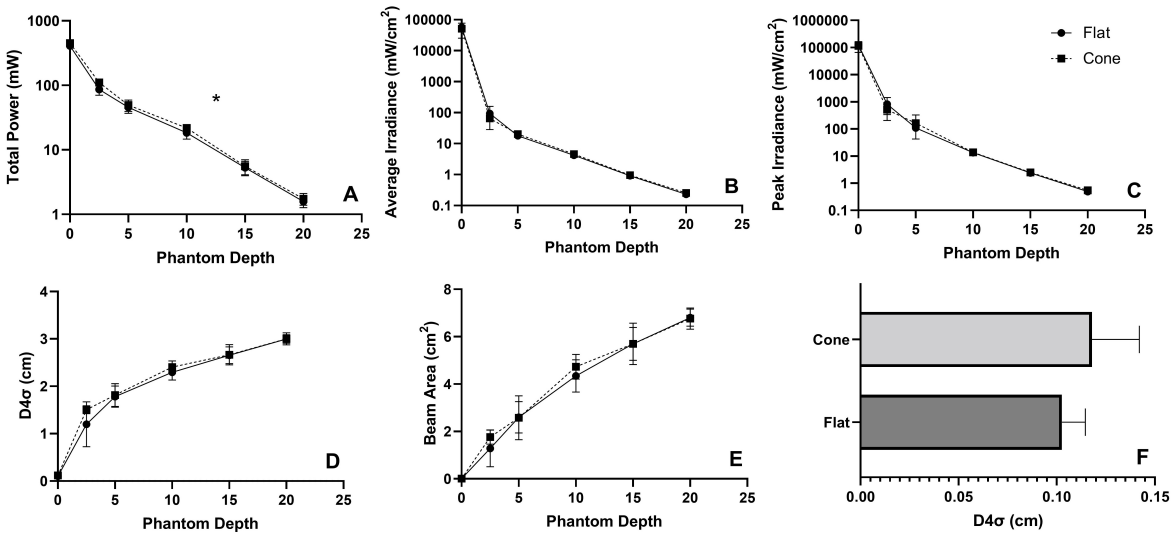


Figure 6.13: Comparison of conical and flat exit geometries. A: total power (y axis on log10 scale); B: average irradiance (y axis on log10 scale); C: peak irradiance (y axis on log10 scale); D: D4σ; E: beam area; F: surface D4σ (cm) at target screen. Cone design refers to design presented in Figure 6.12 B; flat design refers to design shown in Figure 6.12 A. For both models, a single MD-III laser at 100% power output was coupled to an FG550UEC custom fibre bundle (SMA to SMA, ThorLabs) and subsequently coupled via SMA:SMA to a single core 1000 μm 0.39 NA fibre. Fibres were positioned level with the phantom-facing surface of the bolt as shown in Figure 6.12. Beam characterisation results at target screen (0 mm) and through five thicknesses of phantom cast in standardised thickness moulds. n = 3 technical replicates per n = 3 independent experiments. * = $p < 0.05$. Error bars represent SD; not visible in all instances due to logarithmic scale and/or symbol size.

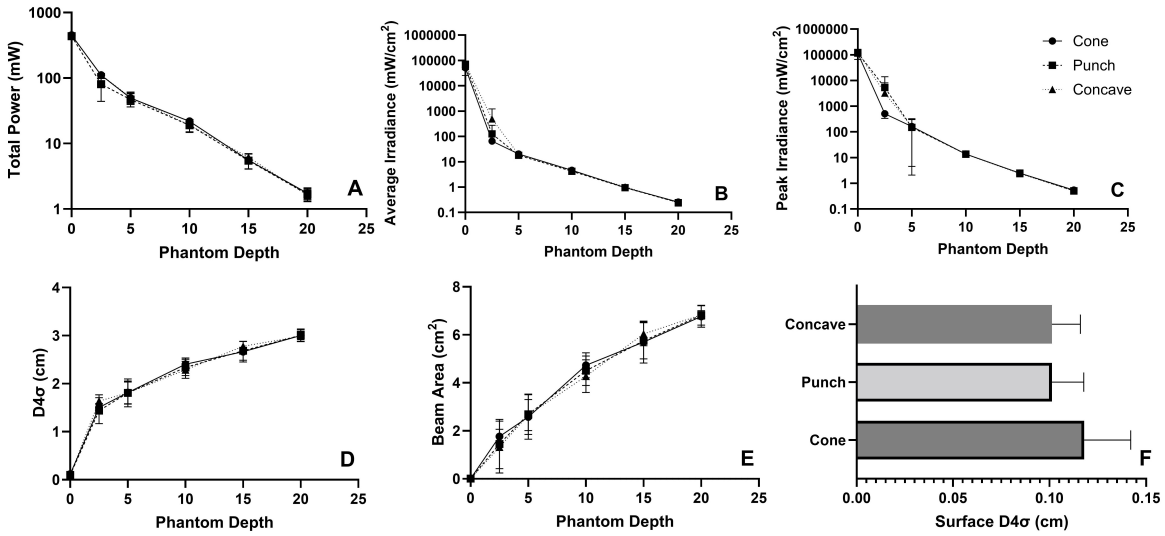


Figure 6.14: Comparison of punch, concave and conical exit geometries. A: total power (y axis on log10 scale); B: average irradiance (y axis on log10 scale); C: peak irradiance (y axis on log10 scale); D: D4σ; E: beam area; F: surface D4σ (cm) at target screen. Cone design refers to design presented in Figure 6.12 B; concave design refers to design shown in Figure 6.12 C; punch design refers to design shown in Figure 6.12 D. For all models, a single MD-III laser at 100% power output was coupled to an FG550UEC custom fibre bundle (SMA to SMA, ThorLabs) and subsequently coupled via SMA:SMA to a single core 1000 μm 0.39 NA fibre. Fibres were positioned level with the phantom-facing surface of the bolt as shown in Figure 6.12. Beam characterisation results at target screen (0 mm) and through five thicknesses of phantom cast in standardised thickness moulds. n = 3 technical replicates per n = 3 independent experiments. * = $p < 0.05$. Error bars represent SD; not visible in all instances due to logarithmic scale and/or symbol size.

6.3.5 Fibre modifications

Fibre tip modifications were investigated as a potential feature to increasing surface distribution and attenuate the focus of surface incident power, by increasing the surface area of beam exit from the fibre. This can be achieved to an extent by modifying an intact fibre: by scoring the fibre surface along its distal length, a proportion of photons will exit the fibre before the tip, with the intended effect of increasing photon distribution and reducing photon density. This was initially explored in a single fibre model with a closed bolt interface architecture (flat, 6.12 A). Normal (intact, unscored) fibres were used (NF). After NF profilometry, the distal 3 mm of the fibre cladding was stripped and the fibre was scored with a razor blade at 0.5 mm intervals (circumferentially and perpendicular to fibre direction) throughout the outer circumference of the fibre and assessed as "LF". Fibre scoring correlated with a statistically significant increase in D4σ with no statistically significant changes in other variables.

In Figure 6.15, the scored portion of the distal fibre tip is concealed within the PLA housing. As such, a decrease in total power would be expected if a significant proportion of the emitted photons are through the scored aspects. As power values are unchanged, there is likely a minimal effect from this factor. To explore this further, a closed (flat) architecture was compared with an open (cone) architecture (Fig. 6.12), both with leaky fibres (Fig. 6.15). In this case, a statistically significant marginal increase in total power is observed in the Cone LF model compared with the Flat LF model (Fig. 6.16). The surface beam diameter is significantly increased in the presence of a cone architecture, which is suggestive of some benefit of opening the interface to expose the scored areas to increase beam diameter, though these low levels of photons released from scored areas may be readily attenuated by scatter and absorption resulting in minimal effect at any depth.

Combination of fibre modification with a conical exit geometry result in significantly increased surface beam diameter compared with conical exit geometry and normal fibre tip (Fig. 6.17). There was no statistically significant attenuation in the overall peak or average irradiance values across all depths by increasing the beam distribution in this way.

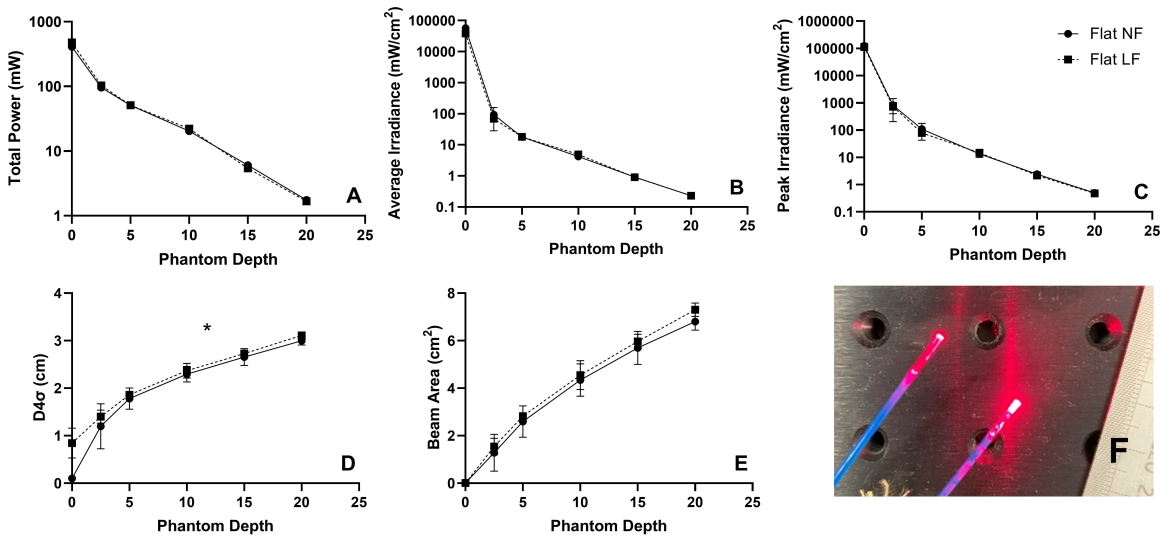


Figure 6.15: Comparison of intact (normal [NF]) and scored ("leaky" [LF]) fibre tip modification using a flat bolt exit geometry. A: total power (y axis on log10 scale); B: average irradiance (y axis on log10 scale); C: peak irradiance (y axis on log10 scale); D: D4σ; E: beam area; F: photograph of intact NF (left) and leaky LF (right) fibre. For both models, a single MD-III laser at 100% power output was coupled to an FG550UEC custom fibre bundle (SMA to SMA, ThorLabs) and subsequently coupled via SMA:SMA to a single core 1000 μm 0.39 NA fibre, placed in single fibre bolt housing with flat interface (Fig. 6.12 A). Fibres were positioned level with the phantom-facing surface of the bolt as shown in Figure 6.12. For leaky (LF) fibres, the distal 3 mm of the fibre was stripped and scored with a razor blade at 0.5 mm intervals throughout the outer circumference of the fibre. Beam characterisation results at target screen (0 mm) and through five thicknesses of phantom cast in standardised thickness moulds. n = 3 technical replicates per n = 3 independent experiments. * = $p < 0.05$. Error bars represent SD; not visible in all instances due to logarithmic scale and/or symbol size.

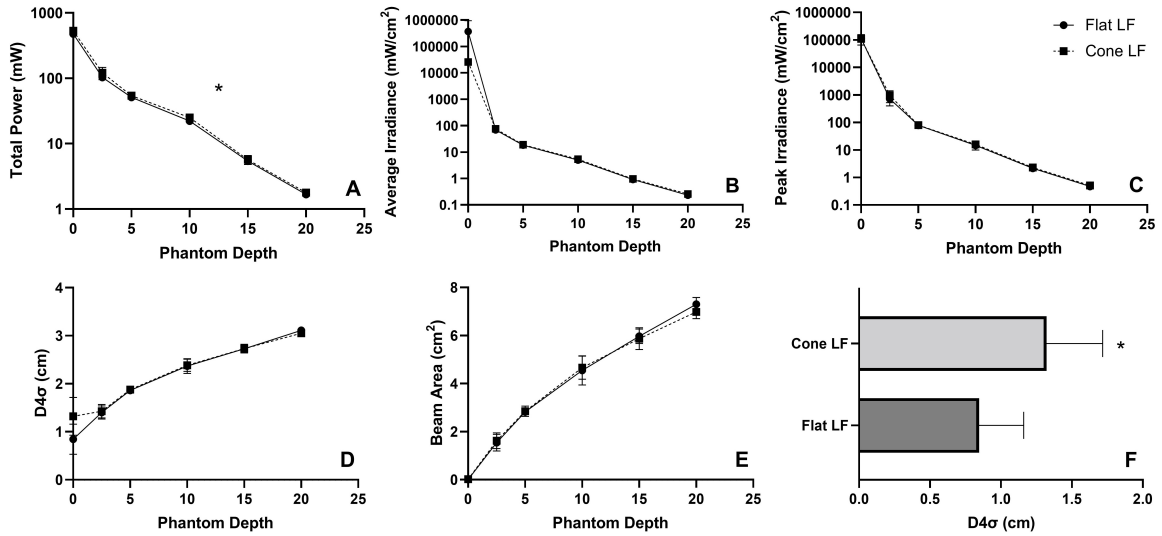


Figure 6.16: Conical exit geometry increases surface beam diameter with fibre modification. A: total power (y axis on log10 scale); B: average irradiance (y axis on log10 scale); C: peak irradiance (y axis on log10 scale); D: D4σ; E: beam area; F: surface D4σ (cm) at target screen. For both models, a single MD-III laser at 100% power output was coupled to an FG550UEC custom fibre bundle (SMA to SMA, ThorLabs) and subsequently coupled via SMA:SMA to a single core 1000 μm 0.39 NA fibre, placed in single fibre bolt housing with flat or conical interface (Fig. 6.12 A). Fibres were positioned level with the phantom-facing surface of the bolt as shown in Figure 6.12. For leaky fibres, the distal 3 mm of the fibre was stripped and scored with a razor blade at 0.5 mm intervals throughout the outer circumference of the fibre. Beam characterisation results at target screen (0 mm) and through five thicknesses of phantom cast in standardised thickness moulds. n = 3 technical replicates per n = 3 independent experiments. * = $p < 0.05$. Error bars represent SD; not visible in all instances due to logarithmic scale and/or symbol size.

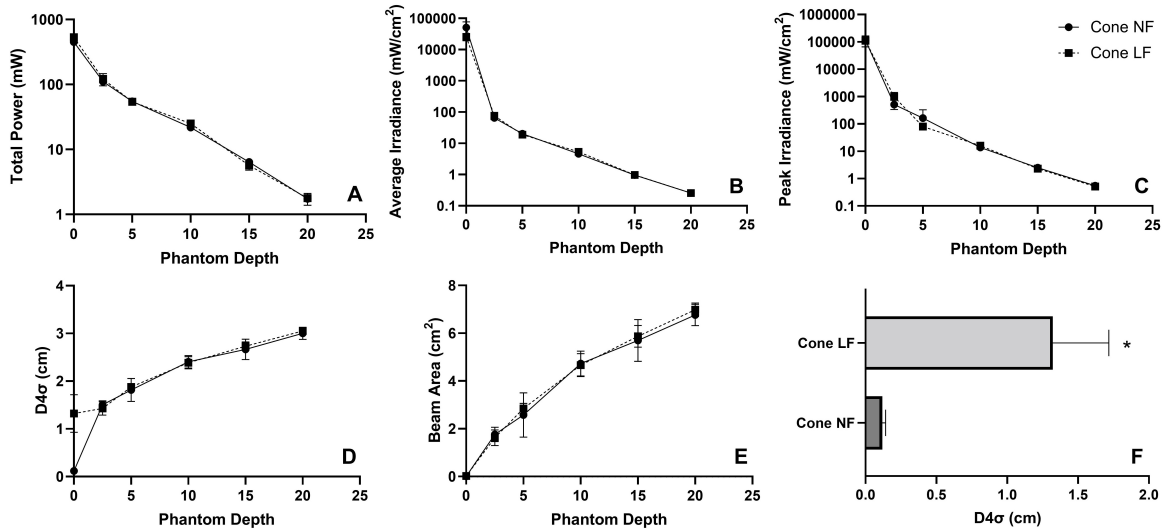


Figure 6.17: Conical exit geometry combined with fibre modification increases surface beam diameter. A: total power (y axis on log10 scale); B: average irradiance (y axis on log10 scale); C: peak irradiance (y axis on log10 scale); D: D4σ; E: beam area; F: surface D4σ (cm) at target screen. For both models, a single MD-III laser at 100% power output was coupled to an FG550UEC custom fibre bundle (SMA to SMA, ThorLabs) and subsequently coupled via SMA:SMA to a single core 1000 μm 0.39 NA fibre, placed in single fibre bolt housing with conical interface (Fig. 6.12 A). Fibres were positioned level with the phantom-facing surface of the bolt as shown in Figure 6.12. For leaky fibres, the distal 3 mm of the fibre was stripped and scored with a razor blade at 0.5 mm intervals throughout the outer circumference of the fibre. Beam characterisation results at target screen (0 mm) and through five thicknesses of phantom cast in standardised thickness moulds. n = 3 technical replicates per n = 3 independent experiments. * = $p < 0.05$. Error bars represent SD; not visible in all instances due to logarithmic scale and/or symbol size.

6.3.6 Lensing

To attenuate the Gaussian distribution, a polymethyl methacrylate (PMMA) plano-convex collimating lens was investigated. A single fibre bolt design was rendered in white PLA to house a fibre and 7.5 mm PMMA lens with fibre adjustable to working distance of lens (5 mm) with a suitable intervening aperture (Fig. 6.18). This was directly compared with the same fibre and bolt housing with the lens removed (Fig. 6.19). The presence of the lens marginally attenuated power and irradiance, with a statistically significant reduction in average irradiance. The lens significantly increased surface beam diameter from 0.25 ± 0.04 to 0.91 ± 0.08 cm ($p < 0.01$).

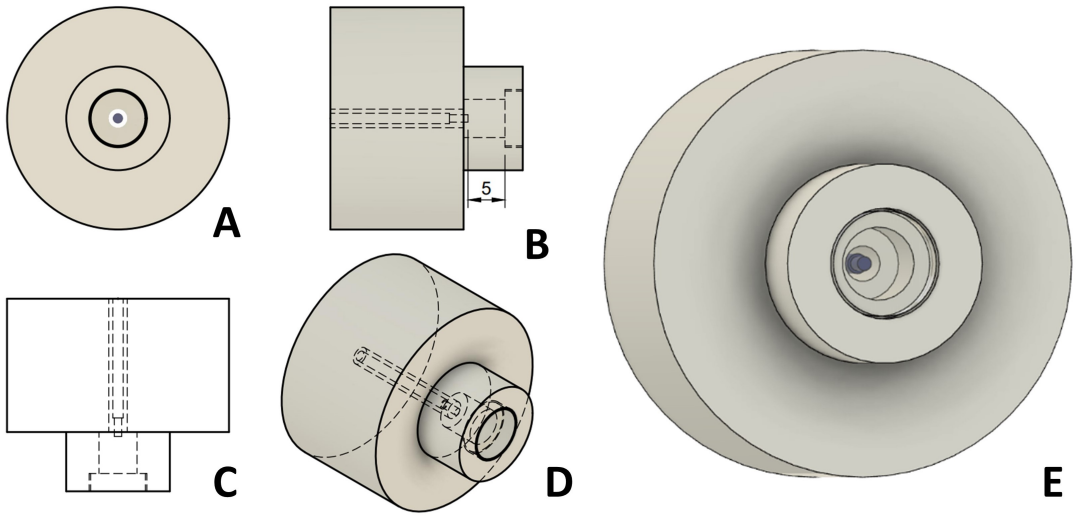


Figure 6.18: PMMA lens-fibre coupled bolt housing. A: phantom/brain-surface; B: side view, rendered in matte white plastic, fibre to internal lens distance given in mm (5 mm) ; C: side view with visible and hidden edges; D: projected isometric view with visible and hidden edges; E: lens and fibre in situ rendering in isometric view

6.3.7 Fibre recess

In addition to the presence of the lens, the model introduced in Figure 6.18 also carries an additional feature: recession of the fibre within the bolt housing to be at working distance of the lens. As such, it is integral to determine the relative contributions of (a) the fibre recess;

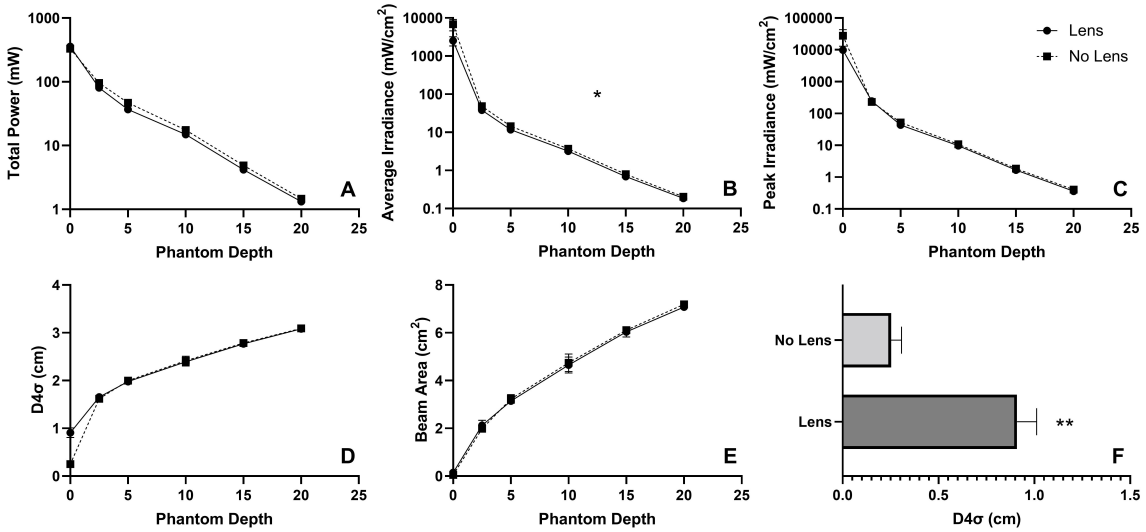


Figure 6.19: Surface beam distribution increases plano-convex PMMA lens in situ, using lens bolt housing (Fig. 6.18). A: total power (y axis on log10 scale); B: average irradiance (y axis on log10 scale); C: peak irradiance (y axis on log10 scale); D: D4σ; E: beam area; F: surface D4σ (cm) at target screen. For both models, a single MD-III laser at 100% power output was coupled to an FG550UEC custom fibre bundle (SMA to SMA, ThorLabs) and subsequently coupled via SMA:SMA to a single core 1000 μm 0.39 NA fibre, placed in single fibre bolt housing with PMMA plano-convex lens (with or without lens in situ). Beam characterisation results at target screen (0 mm) and through five thicknesses of phantom cast in standardised thickness moulds. n = 3 technical replicates per n = 3 independent experiments. * = $p < 0.05$, ** = $p < 0.01$. Error bars represent SD; not visible in all instances due to logarithmic scale and/or symbol size.

and (b) the presence of the lens. First, the same fibre housing was compared with the fibre recessed as in Figure 6.18, and also level with the fibre housing phantom interface (Fig. 6.20). This demonstrated that lens recession produces modest but statistically significant reductions in power and average/peak irradiance values, accompanied by an increase in D4σ. The recess of the fibre increased the D4σ at surface from 0.11 ± 0.4 to 0.25 ± 0.02 ($p < 0.05$).

To compare the relative contributions of the fibre recess and the lens, beam characterisation images are given in Figure 6.21. Incomplete collimation is observed in Figure 6.21 from the lens, though effective collimation was observed at greater distance visually. The principle however does demonstrate that lensing holds some potential for achieving a broader surface irradiance and should be further explored.

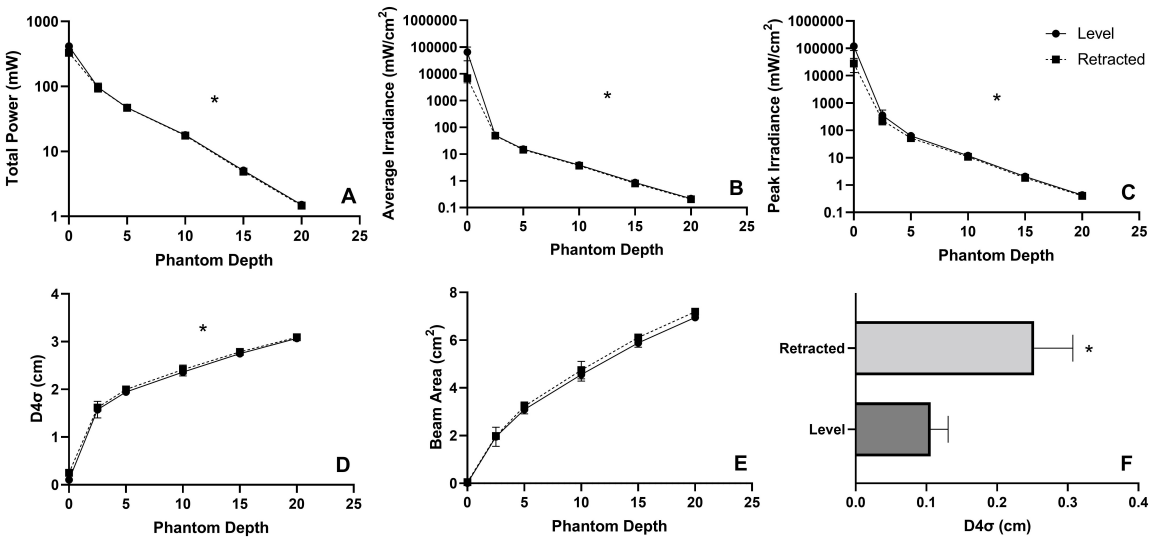


Figure 6.20: Fibre recess/retraction increases incident beam diameter. A: total power (y axis on log10 scale); B: average irradiance (y axis on log10 scale); C: peak irradiance (y axis on log10 scale); D: D4σ; E: beam area; F: surface D4σ (cm) at target screen. For both models, a single MD-III laser at 100% power output was coupled to an FG550UEC custom fibre bundle (SMA to SMA, ThorLabs) and subsequently coupled via SMA:SMA to a single core 1000 μm 0.39 NA fibre, placed in single fibre bolt housing without PMMA plano-convex lens (Fig. 6.18). Retracted fibre model placed the fibre tip as in Figure 6.18, Level fibre model placed the fibre tip level with the phantom surface of the bolt. Beam characterisation results at target screen (0 mm) and through five thicknesses of phantom cast in standardised thickness moulds. n = 3 technical replicates per n = 3 independent experiments. * = $p < 0.05$. Error bars represent SD; not visible in all instances due to logarithmic scale and/or symbol size.

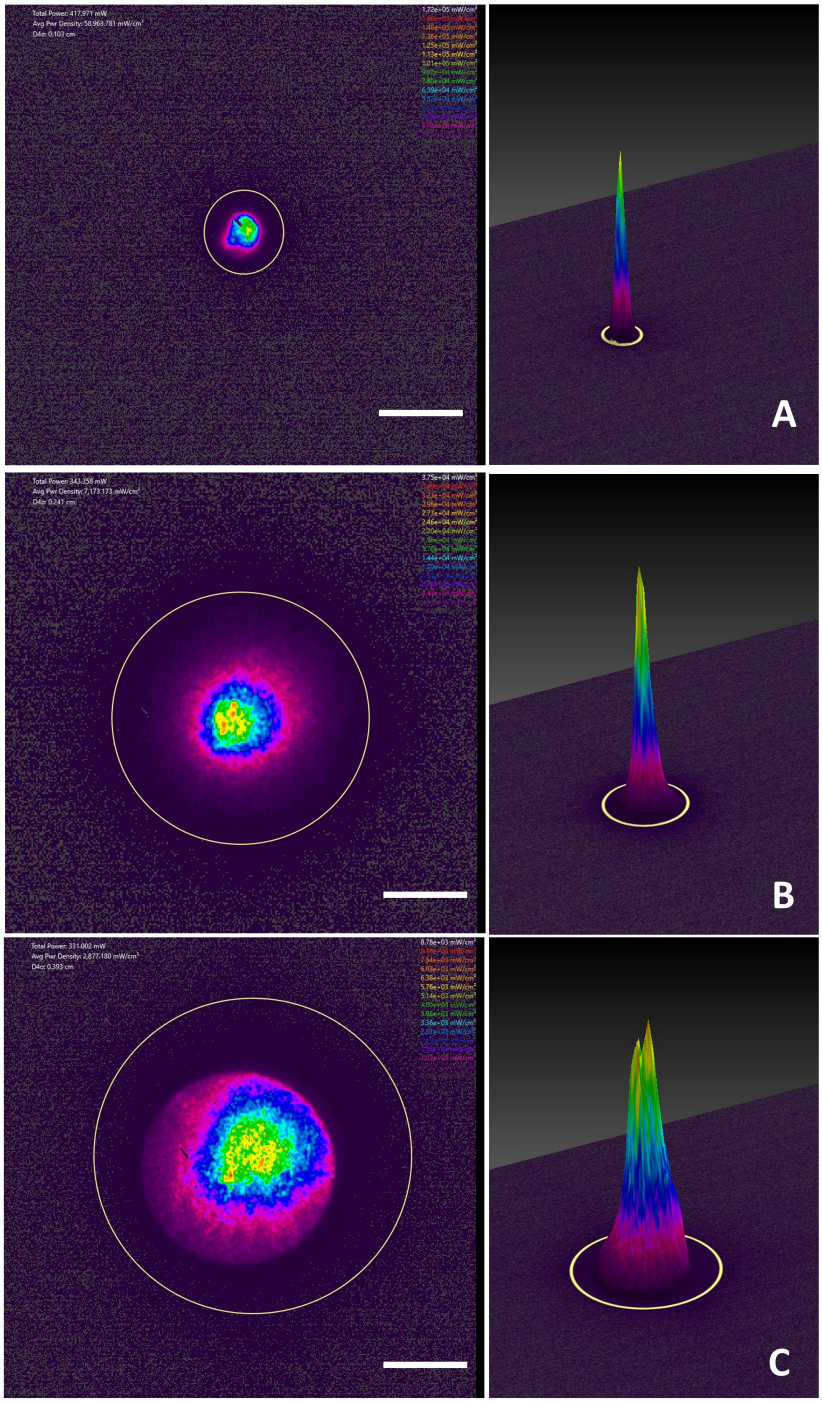


Figure 6.21: Beam distribution with plano-convex lens. A: Level fibre (D4σ = 0.11 ± 0.4 cm) with no PMMA [plano-convex lens]; B: retracted fibre (5 mm retraction) without PMMA plano-convex lens (D4σ = 0.25 ± 0.02 cm); C: retracted fibre (5 mm retraction) with PMMA plano-convex lens (D4σ = 0.91 ± 0.08 cm).

6.3.8 Fibre diameter and numerical aperture

To investigate the effects of fibre diameter and NA on distribution and propagation through the phantom media, two fibres were compared: a single core 1000 μm 0.39 NA multimodal fibre (FP1500URT, ThorLabs) and a single core 1500 μm 0.50 NA multimodal fibre (FG550UEC, ThorLabs) (Fig. 6.22). Qualitatively, the beam profile at the target screen (Fig. 6.22 E-F) demonstrates a larger diameter profile of the 1500 μm fibre, as expected, with a corresponding reduction in peak average irradiance and average irradiance overall. The reduction in peak likely owes to the greater homogeneity of the intensity across the beam profile, which is a favourable feature. However, Gaussian distributions returned after propagation through the phantom (Fig. 6.23), and across all thicknesses, there were no significant differences in beam profile parameters. Furthermore, it was observed that the flexibility of the 1500 μm core fibre was considerably less than that of the 1000 μm core fibre.

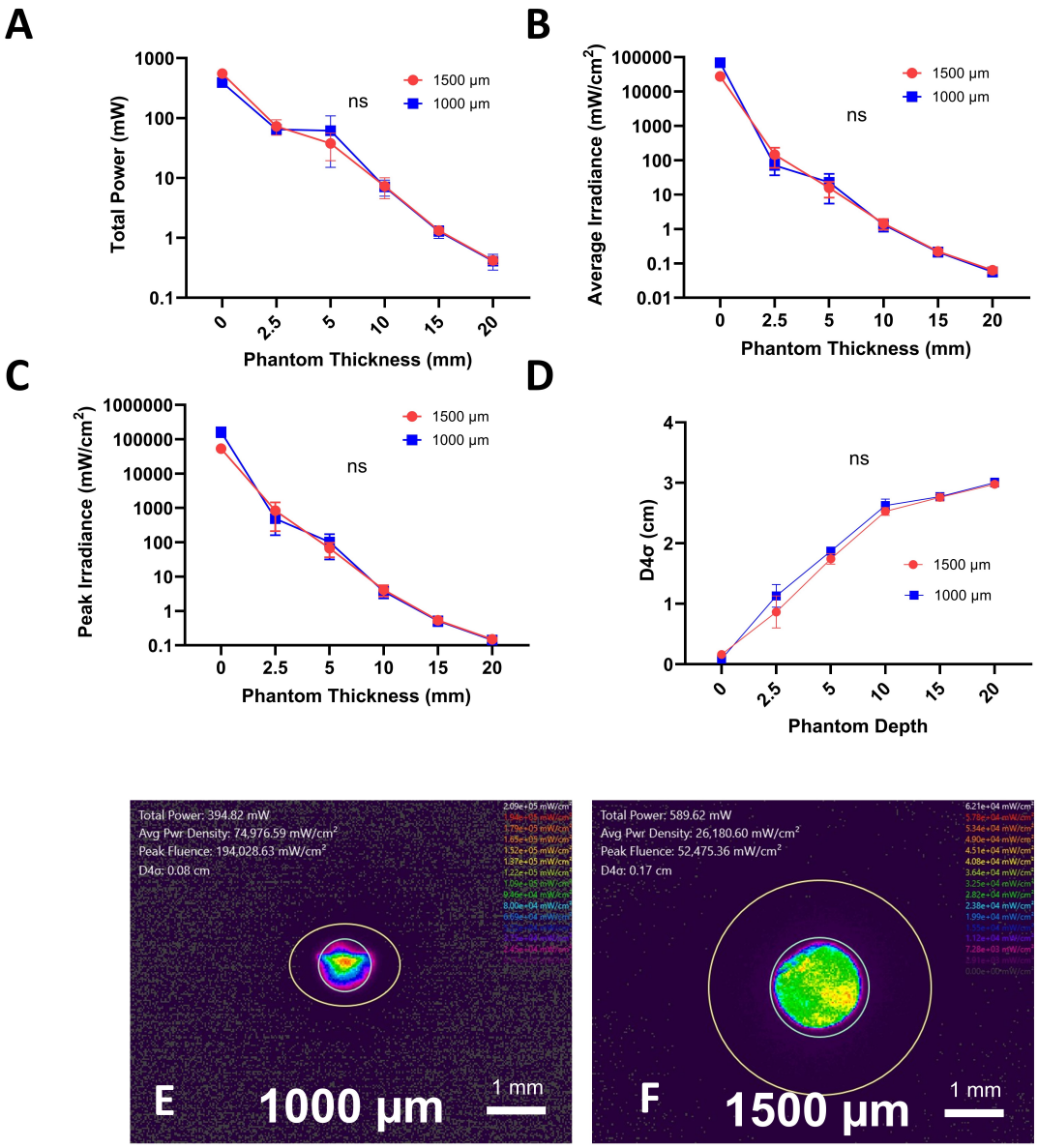


Figure 6.22: Comparison of a single core 1000 μm 0.39 NA multimodal fibre and a single core 1500 μm 0.50 NA multimodal fibre. A: total power (y axis on log10 scale); B: average irradiance (y axis on log10 scale); C: peak irradiance (y axis on log10 scale); D: D4σ; E: beam profile of 1000 μm fibre at target screen; F: beam profile of 1500 μm fibre at target screen. For both fibres, a single MD-III laser at 100% power output was coupled to an FG550UEC custom fibre bundle (SMA to SMA, ThorLabs) and subsequently coupled via SMA:SMA to the fibre which was secured in single fibre bolt housing. Beam characterisation results at target screen (0 mm) and through five thicknesses of phantom cast in standardised thickness moulds. n = 3 technical replicates per n = 3 independent experiments. ns = not significant. Error bars represent SD; not visible in all instances due to logarithmic scale and/or symbol size.

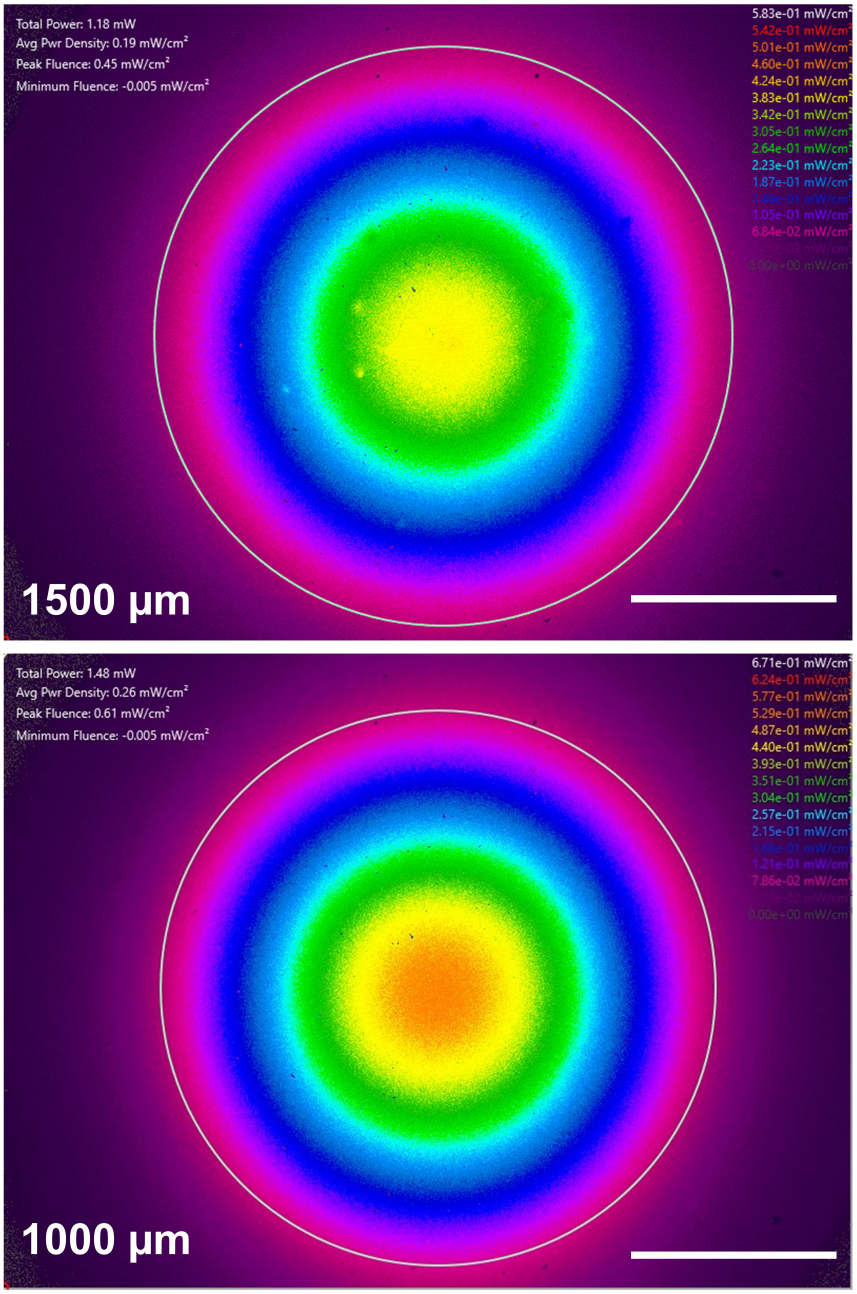


Figure 6.23: Comparison of a single core 1000 μm 0.39 NA multimodal fibre and a single core 1500 μm 0.50 NA multimodal fibre beam profiles at 15 mm depth. Scale bar = 1 cm.

6.3.9 Diffuser

A 12.7 mm ground glass diffuser (DG05120, ThorLabs) was used over a bare 1500 μm fibre (Fig. 6.24). This marginally increased beam diameter with statistical significance, with a corresponding marginal but statistically significant attenuation of power, average irradiance, and peak irradiance values.

A 9 mm biconcave lens (LD2568-A, ThorLabs) was used over a bare 1500 μm fibre (Fig. 6.25). This also marginally increased beam diameter with statistical significance, with a corresponding marginal but statistically significant attenuation of power, average irradiance, and peak irradiance values. The lens also reformed a Gaussian distribution at the target screen (Fig. 6.25 F) when compared to the bare fibre. The effect was similar for the planoconvex lens seen in Figure 6.19, though different fibres were used which prevents their direct comparison.

6.3.10 Light source

Comparisons were made between a laser source (MDL-III-660-FC-800 mW) and an LED source (M660L4 mounted 660 nm 940 mW LED (ThorLabs) coupled to LEDD1B driver) (Fig. 6.26). The same coupled fibre was used for both sources. Similar beam distributions in a Gaussian pattern were observed for both sources. Power, average irradiance and peak irradiance were significantly lower using the LED source. The distribution at all depths measured by beam diameter did not differ between sources.

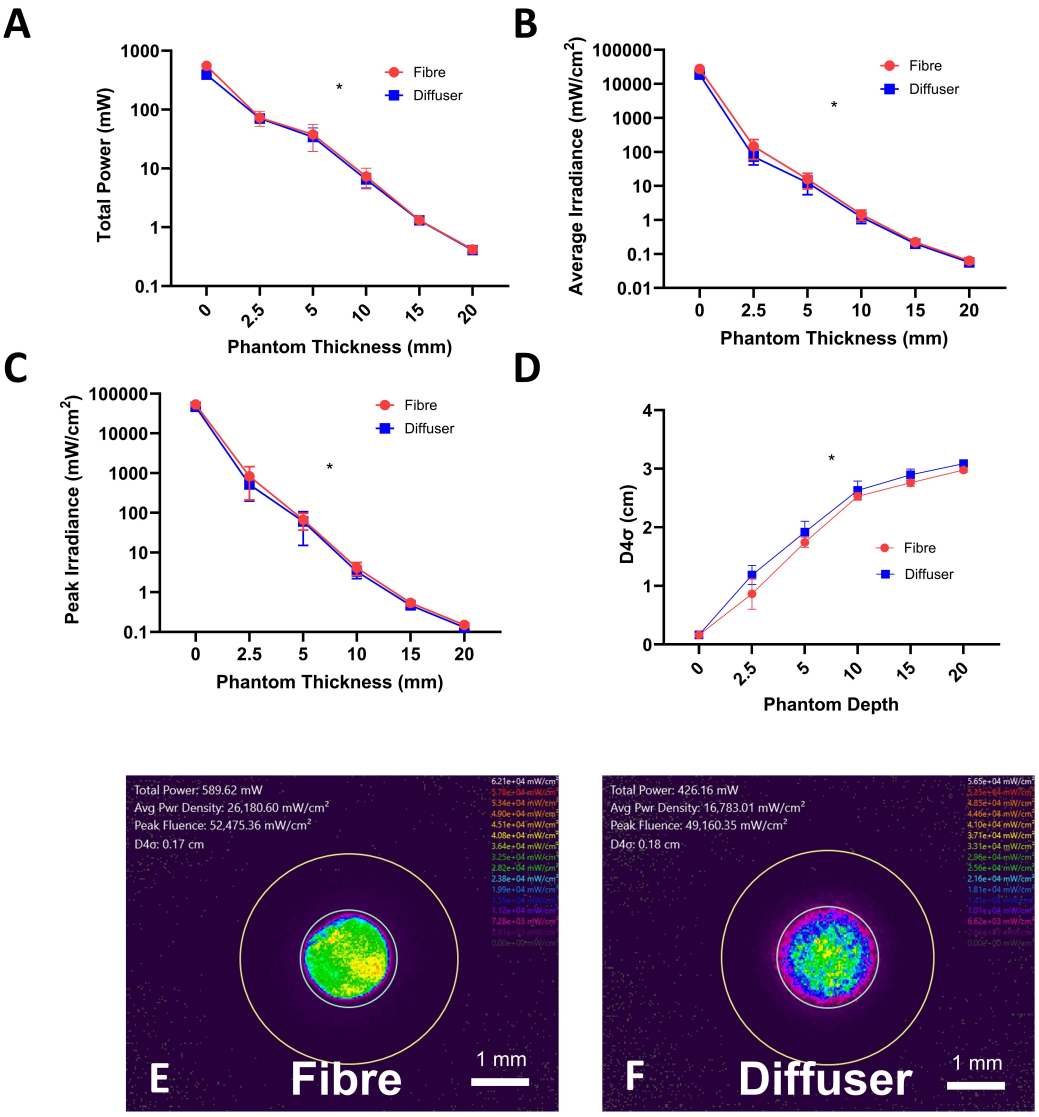


Figure 6.24: Comparison of a single core 1500 μm 0.39 NA with and without a ground glass diffuser (DG05120). A: total power (y axis on log10 scale); B: average irradiance (y axis on log10 scale); C: peak irradiance (y axis on log10 scale); D: D4σ; E: beam profile of 1500 μm fibre at target screen; F: beam profile of 1500 μm fibre with ground glass diffuser at target screen. For both conditions, a single MD-III laser at 100% power output was coupled to an FG550UEC custom fibre bundle (SMA to SMA, ThorLabs) and subsequently coupled via SMA:SMA to the fibre which was secured in single fibre bolt housing, with or without a diffuser. Beam characterisation results at target screen (0 mm) and through five thicknesses of phantom cast in standardised thickness moulds. n = 3 technical replicates per n = 3 independent experiments. ns = not significant, * = $p < 0.05$. Error bars represent SD; not visible in all instances due to logarithmic scale and/or symbol size.

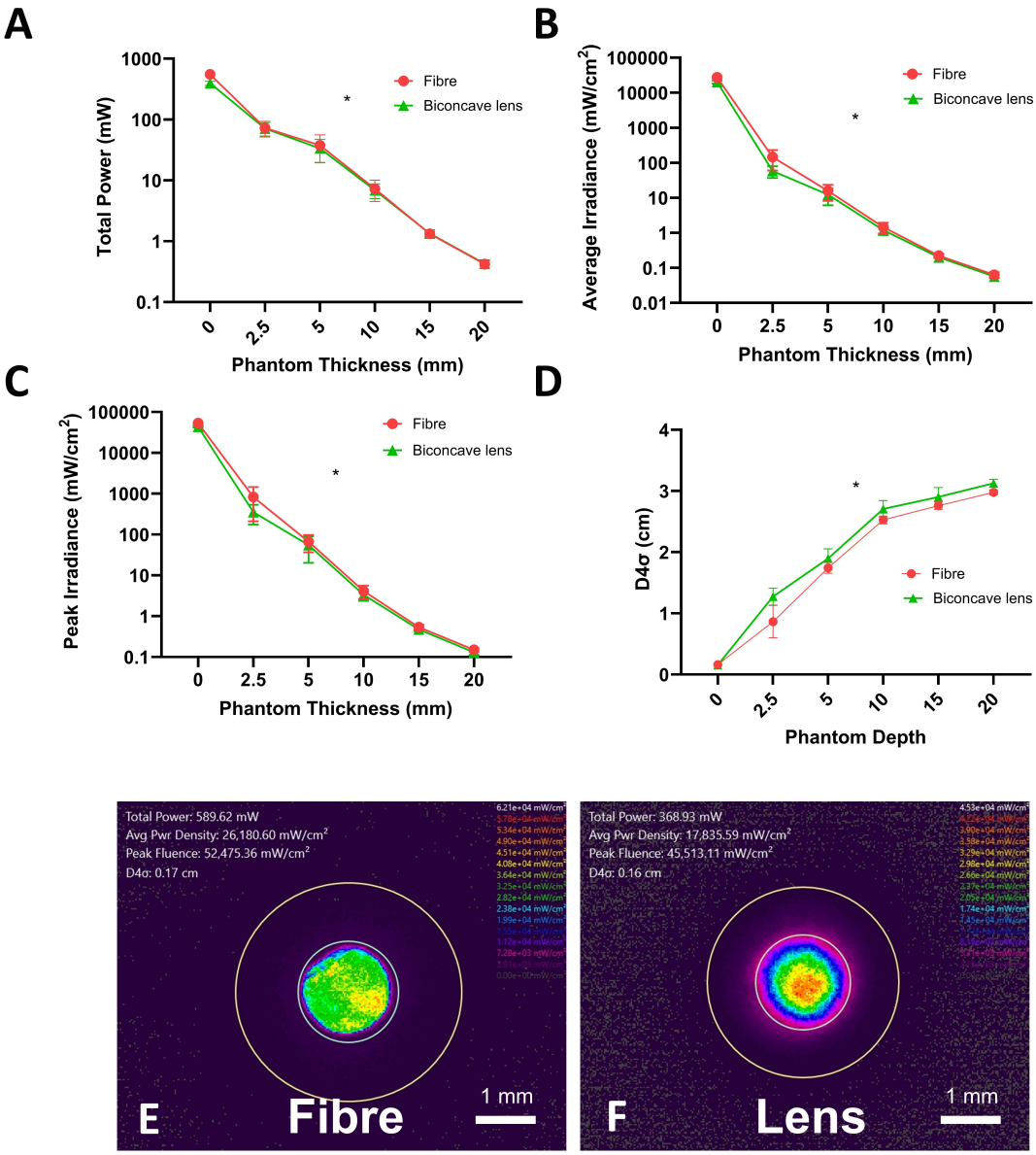


Figure 6.25: Comparison of a single core 1500 μm 0.39 NA with and without a 9 mm biconcave lens (LD2568-A). A: total power (y axis on log10 scale); B: average irradiance (y axis on log10 scale); C: peak irradiance (y axis on log10 scale); D: D4σ; E: beam profile of 1500 μm fibre at target screen; F: beam profile of 1500 μm fibre with lens at target screen. For both conditions, a single MD-III laser at 100% power output was coupled to an FG550UEC custom fibre bundle (SMA to SMA, ThorLabs) and subsequently coupled via SMA:SMA to the fibre which was secured in single fibre bolt housing, with or without lens. Beam characterisation results at target screen (0 mm) and through five thicknesses of phantom cast in standardised thickness moulds. n = 3 technical replicates per n = 3 independent experiments. ns = not significant, * = $p < 0.05$. Error bars represent SD; not visible in all instances due to logarithmic scale and/or symbol size.

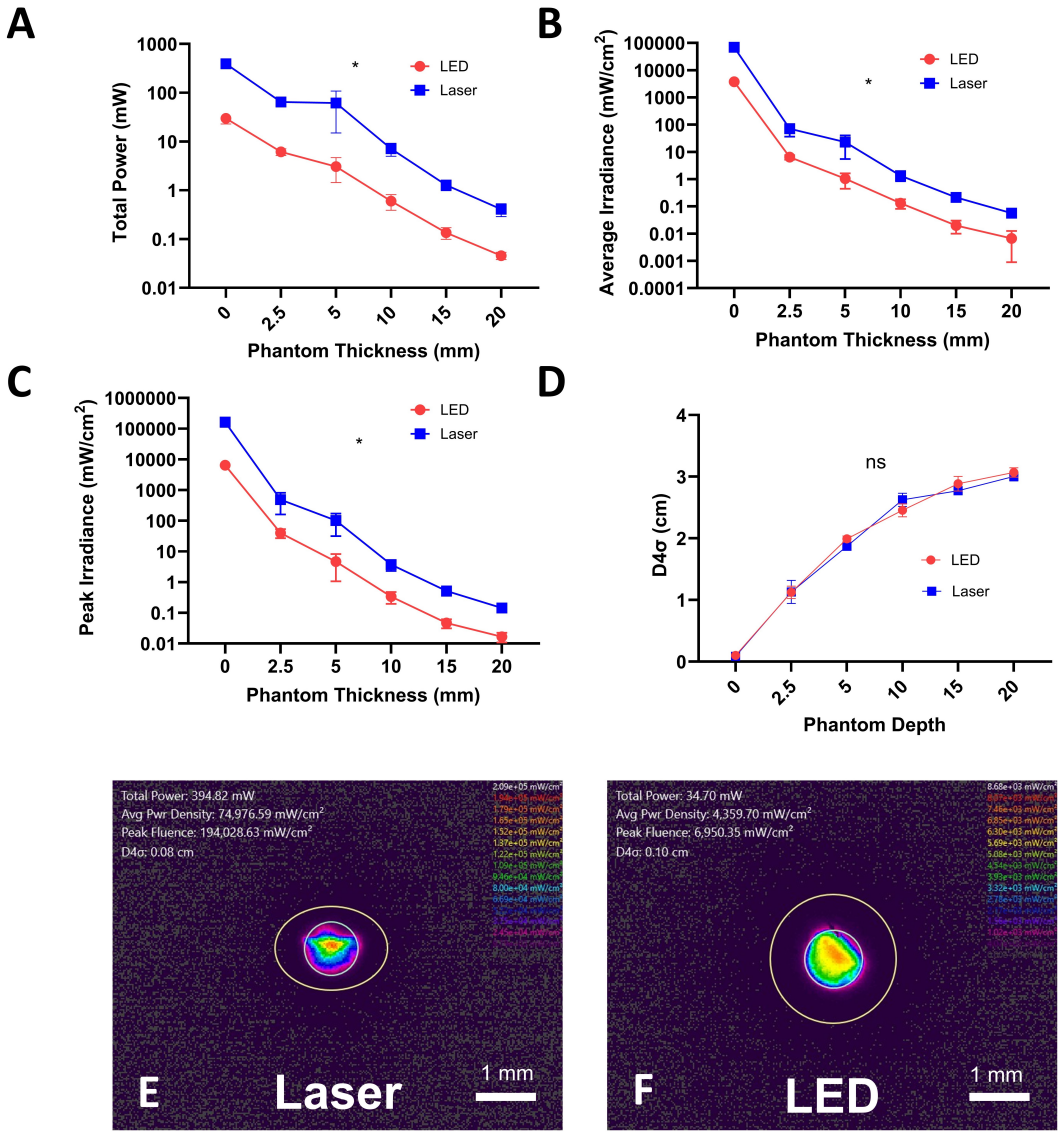


Figure 6.26: Comparison of a MDL-III-660-FC-800 mW laser with M660L4 mounted 660 nm 940 mW LED (ThorLabs) coupled to LEDD1B driver. A: total power (y axis on log10 scale); B: average irradiance (y axis on log10 scale); C: peak irradiance (y axis on log10 scale); D: D4σ; E: beam profile of 1000 μm fibre with MDL-III-660-FC-800 mW at target screen; F: beam profile of 1000 μm fibre with M660L4 mounted 660 nm 940 mW LED at target screen. For both conditions, the optical source at 100% power output was coupled to an FG550UEC custom fibre bundle (SMA to SMA, ThorLabs) and subsequently coupled via SMA:SMA to the fibre which was secured in single fibre bolt housing, with or without lens. Beam characterisation results at target screen (0 mm) and through five thicknesses of phantom cast in standardised thickness moulds. n = 3 technical replicates per n = 3 independent experiments. ns = not significant, * = $p < 0.05$. Error bars represent SD; not visible in all instances due to logarithmic scale and/or symbol size.

6.3.11 Spatial fibre orientation

To mitigate cumulative regions of exposure from multiple incident beams (i.e. beam crossover), and to increase surface beam diameter, a radial distribution of terminal fibre orientation was designed. To avoid fibre crossover within the bolt housing in transit from external to internal interfaces, a radial rotational distribution was used.

Lampshade (V01) The “Lampshade” model was developed as prototype to allow radial outward distribution of individual fibres (Fig. 6.27). This prototype demonstrated significantly greater surface beam diameter compared with the "straight" four coupled fibre bolt (seen in Figure 6.10), but there were no other statistically significant differences between the models in all measured indices of beam characteristics (Fig. 6.28).

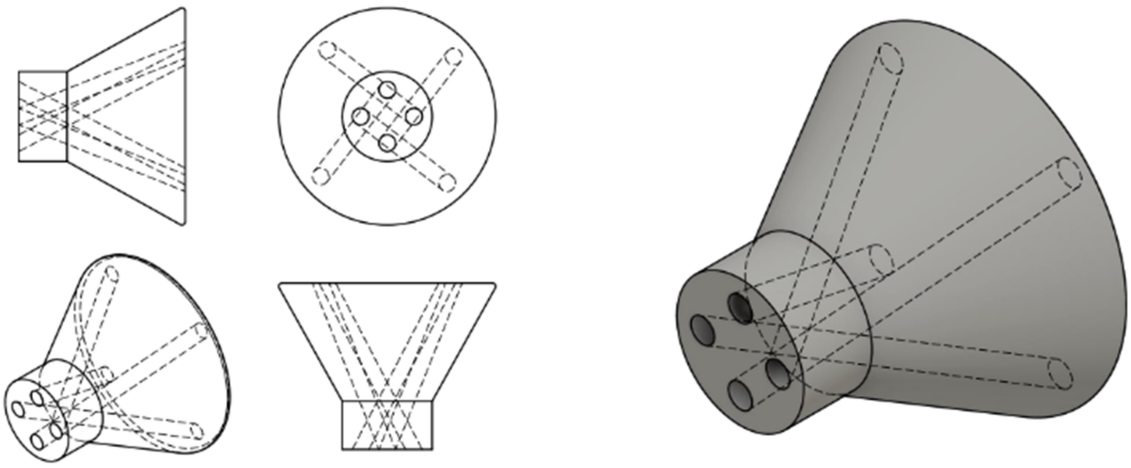


Figure 6.27: CAD drawing of Lampshade V01

Lampshade (V02) To further explore spatial orientation, the “Lampshade” model was adapted to increase the radial angle between fibre exit interfaces. Given the limitations of the 14 mm cranial access standard, this was most easily achieved by reducing the number of input fibres. This design also incorporated a recessed fibre within a conical exit geometry at each of the

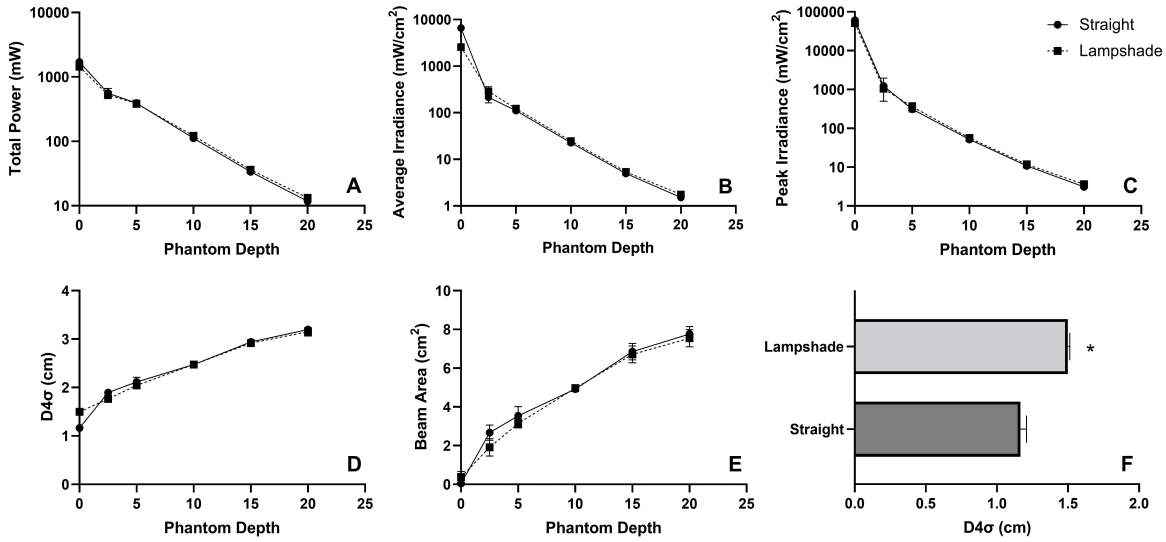


Figure 6.28: Lampshade V01 model improves distribution in comparison to straight fibre orientation. Beam distribution with straight or "Lampshade V01" fibre distribution. A: total power (y axis on log10 scale); B: average irradiance (y axis on log10 scale); C: peak irradiance (y axis on log10 scale); D: D4σ; E: beam area; F: surface D4σ (cm) at target screen. For both models, four MD-III laser sources at 100% power output were coupled to integrated, manufacturer supplied fibres directly from output and subsequently coupled via SMA:SMA to a single core 1000 μm 0.39 NA fibre, placed in fibre bolt housing either in a radial or straight orientation. Beam characterisation results at target screen (0 mm) and through five thicknesses of phantom cast in standardised thickness moulds. n = 3 technical replicates per n = 3 independent experiments. * = $p < 0.05$. Error bars represent SD; not visible in all instances due to logarithmic scale and/or symbol size.

three exit points. This was named the “Lampshade V02” (Fig. 6.29), though the conical outer bolt shape was altered to a cylindrical shape for improved compatibility with optomechanical clamps. A chamfered tip aspect was incorporated with the intention of minimizing central beam summation at the surface.

The “Lampshade V02” model had a statistically increased surface beam diameter in comparison to the “straight” model (Fig. 6.30). In concordance with the 25% reduction in incident power output (due to reduction of fibres, and therefore lasers, from four to three), power and average irradiance values of the “Lampshade V02” were significantly reduced in comparison with four flatly orientated fibres.

Lampshade V02 was compared to Lampshade V01, and demonstrated significantly greater

surface beam diameter, but there was no other statistically significant differences between the models in all measured indices of beam characteristics (Fig. 6.31. For comparison between Lampshade V01 (Fig. 6.27) and Lampshade V02 (Fig. 6.29), D4σ and beam area were compared, including surface D4σ (Fig. 6.32). Increased beam diameter is recognised in the V02 model compared to V01 when compared at all depths (Fig. 6.31 A) including at the surface (Fig. 6.31 C). Beam area was not significantly different though there is an evident corresponding increase in V02 areas in comparison with V01. Qualitative beam characteristics between "Straight", "Lampshade V01" and "Lampshade V02" models are compared in Figure 6.32, with an observable beam distribution shift between the models, particularly at 2.5 mm and 5 mm, supporting a conferred advantage by spatial orientation in this manner.

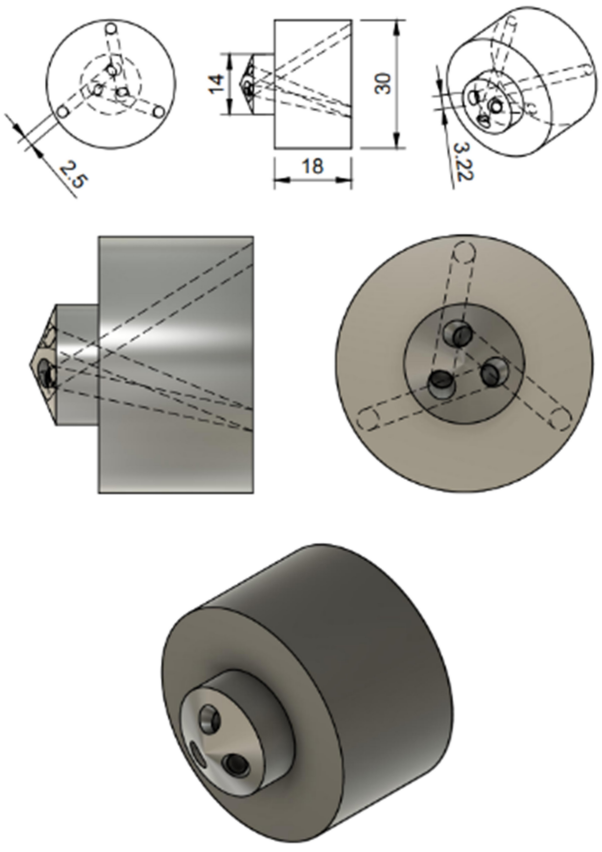


Figure 6.29: CAD drawing of Lampshade V02. Dimensions in mm.

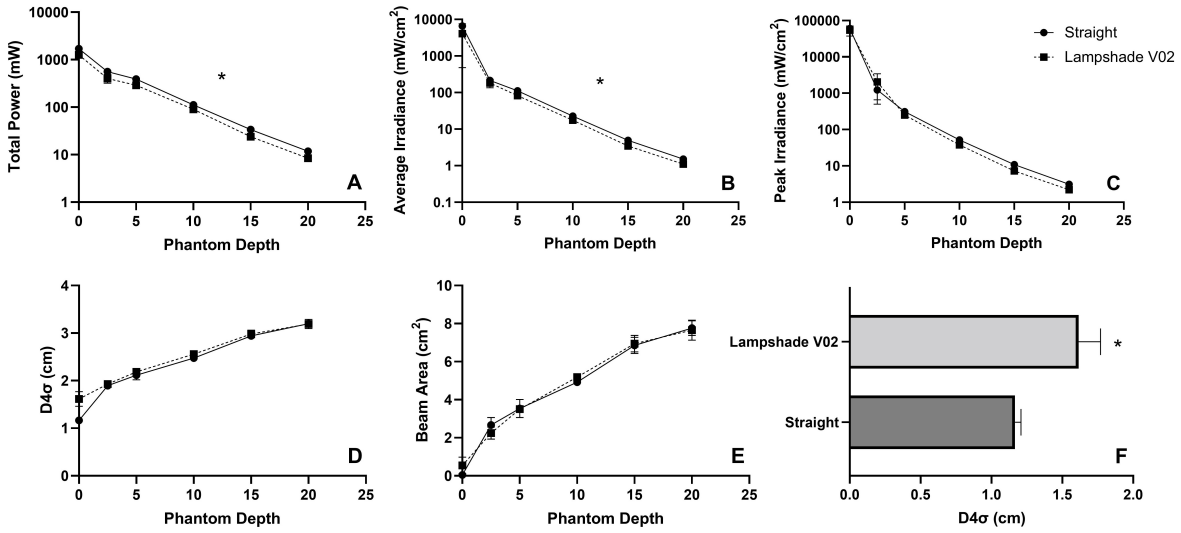


Figure 6.30: Lampshade V02 model improves distribution in comparison to straight fibre orientation. Beam distribution with straight or "Lampshade V02" fibre distribution. A: total power (y axis on log10 scale); B: average irradiance (y axis on log10 scale); C: peak irradiance (y axis on log10 scale); D: D4σ; E: beam area; F: surface D4σ (cm) at target screen. For both models, three/four MD-III laser sources at 100% power output were coupled to integrated, manufacturer supplied fibres directly from output and subsequently coupled via SMA:SMA to a single core 1000 μm 0.39 NA fibre, placed in fibre bolt housing either in a radial or straight orientation. Beam characterisation results at target screen (0 mm) and through five thicknesses of phantom cast in standardised thickness moulds. n = 3 technical replicates per n = 3 independent experiments. * = $p < 0.05$. Error bars represent SD; not visible in all instances due to logarithmic scale and/or symbol size.

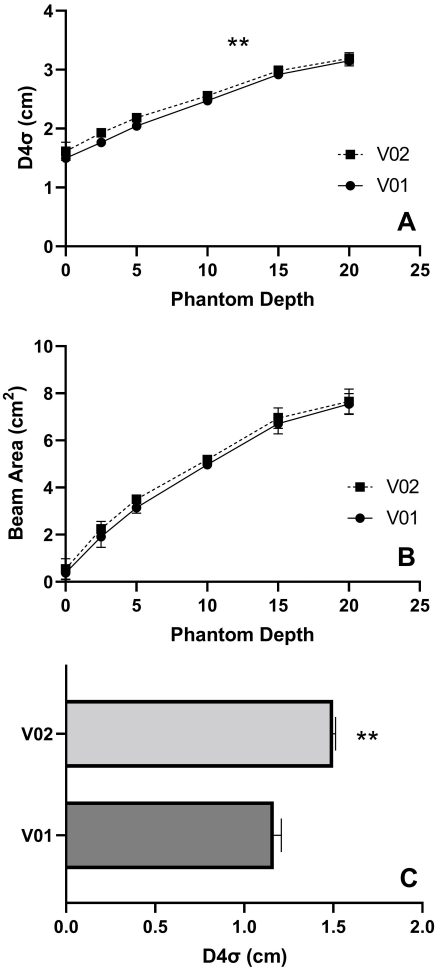


Figure 6.31: Lampshade V02 model improves distribution in comparison to Lampshade V01. Beam distribution with "Lampshade V01" or "Lampshade V02" fibre distribution. A: total power (y axis on log10 scale); B: average irradiance (y axis on log10 scale); C: peak irradiance (y axis on log10 scale); D: D4σ; E: beam area; F: surface D4σ (cm) at target screen. For both models, four MD-III laser sources at 100% power output were coupled to integrated, manufacturer supplied fibres directly from output and subsequently coupled via SMA:SMA to a single core 1000 μm 0.39 NA fibre, placed in fibre bolt housing either in a radial or straight orientation. Beam characterisation results at target screen (0 mm) and through five thicknesses of phantom cast in standardised thickness moulds. n = 3 technical replicates per n = 3 independent experiments. ** = $p < 0.01$. Error bars represent SD; not visible in all instances due to logarithmic scale and/or symbol size.

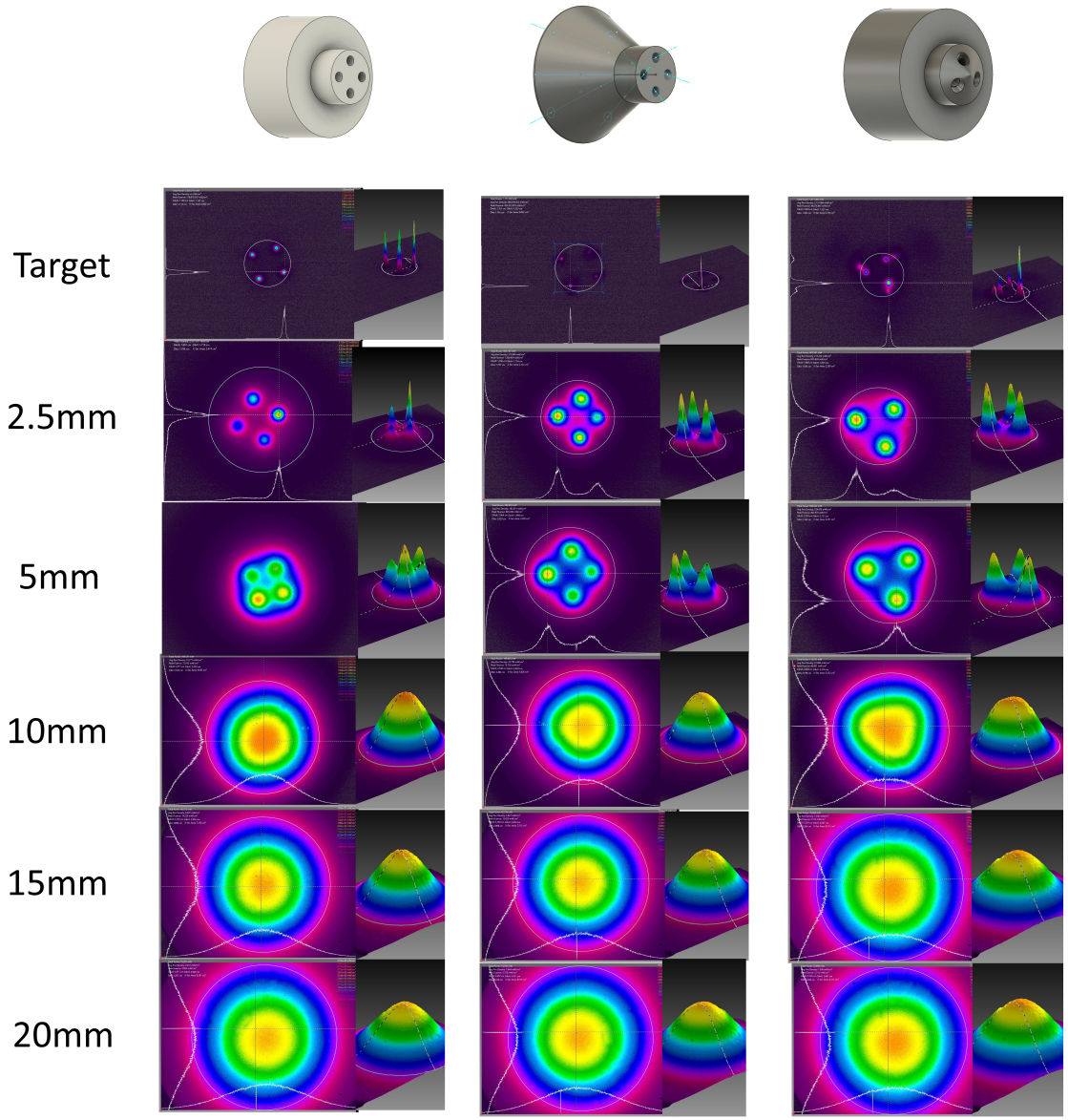


Figure 6.32: Beam profilometry of Lampshade V01, V02 and straight fibre orientations. 2D and 3D beam distributions of 0 mm (target) to 20 mm phantom depth, using three bolt designs.

6.3.12 Optimal design features

As identified by the above work, optimal design features can be considered as:

- White fibre housing;
- Three fibres which are spatially distributed, both in their exit position and exit orientation (facilitated through use of radial orientation);
- Fibre retraction to maximise distance from brain surface;
- Bolt housing exit geometry with a conical shape;
- Use of ground glass diffuser and/or lens;
- Fibre diameter core largest feasible (limited by poor flexibility of fibres with larger core diameters);
- Fibre NA of 0.50;
- Laser or LED sources can be used, dependent on power output or modulation needs.

These features are most closely demonstrated in the Lampshade V02 model. This is shown *in situ* in a model of the human skull in Figure 6.33.

6.3.13 Summary

Whilst these design features have optimised the distribution of light using the bolt paradigm, the volume of effective dose delivery remains extremely limited. Specific positioning over a specific discrete lesion may offer device utility but is not able to directly effect the considerable volumes of tissue affected by diffuse TBI. Increasing the diameter of the access site for the bolt would increase the opportunity to include further design features (such as cortical LED arrays), though expansion beyond the standard 14 mm cranial access paradigm adds issues for compatibility and acceptability. Therefore, alternative approaches should be explored (presented in the discussion section) for diffuse TBI. However, the nature of traumatic SCI is typically of a discrete nature, and relevant volumes of spinal cord tissue can be targeted using a localised fibre-based paradigm.

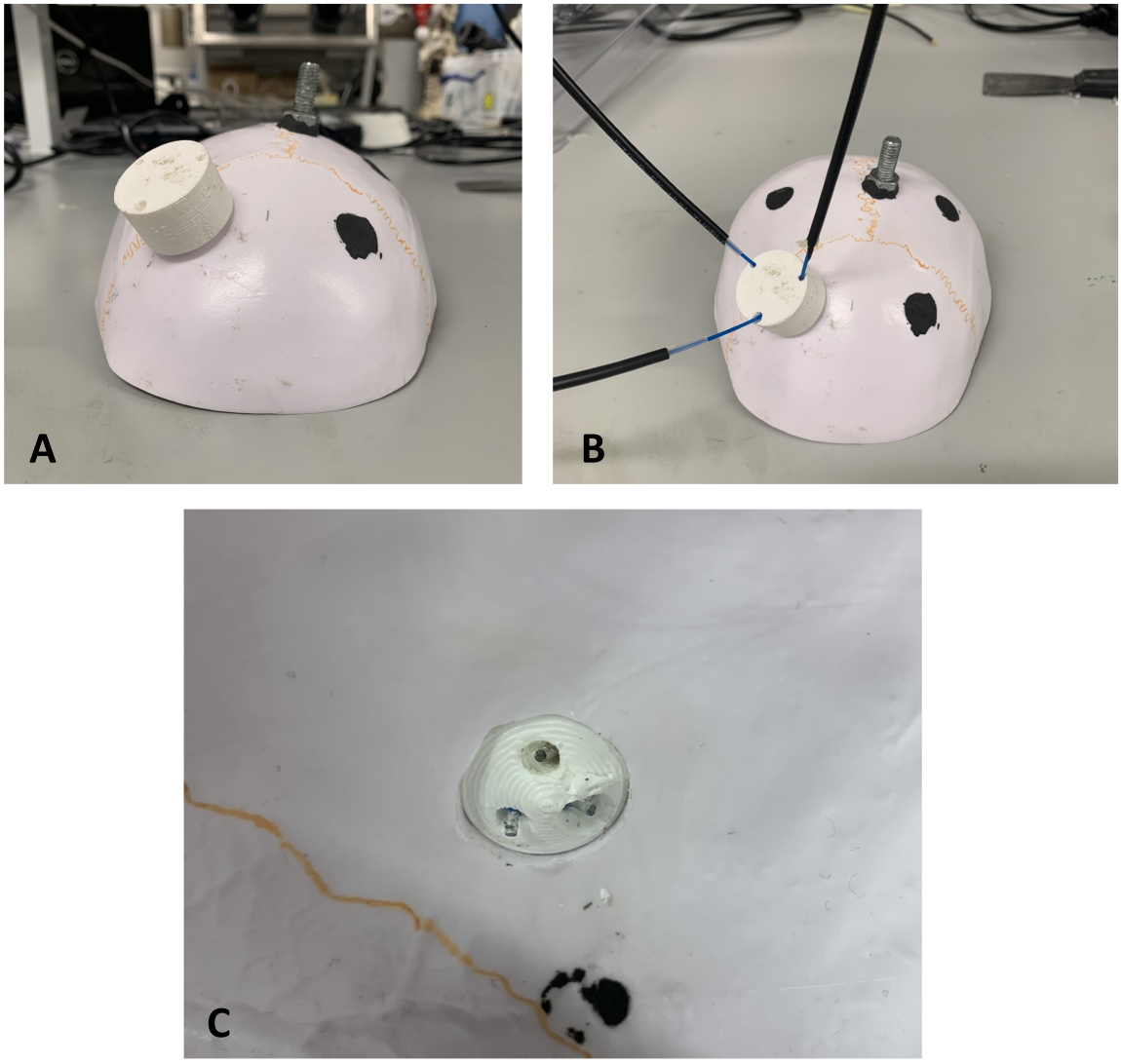


Figure 6.33: Lampshade V02 bolt in situ in a model of the human skull, shown A: with bolt alone; B: with bolt and accompanying fibres; and C: bolt viewed from cranial cavity, with three fibres in situ.

6.4 Results: Spinal cord interface

Several design constraints, differing to those for a cranial device, apply to the indwelling spinal device:

1. The device must implantable during a posterior approach to the spine for decompressive laminectomy and fixation of the spinal column;
2. The device must be externally accessible, with required depths varying due to traversing dorsal fascia and muscle, subcutaneous fat and skin;
3. The device must be securable to avoid inadvertent advancement or other displacement;
4. The device must interface with the skin in a manner to avoid development of pressure damage when supine;
5. The device should ideally be accessible without the need to manoeuvre the patient from a supine position.

According to these proposed principles, a fibre-based device is described below. This allows externalisation via a traditional wound drain kit, using a trocar to tunnel a hollow lumen housing from internal to external. This then permits the introduction of a fibre-based device from external to internal, which can then be secured. Similarly, for intermittent administration, the concept of a lumbar puncture can be used to similarly introduce a fibre-based device to the proximity of the injury site. In order to be introduced and withdrawn in such a manner, the device should not exceed 7.5 mm diameter.

Based upon the findings from the development of a cranial device, favourable design features for improving beam distribution can be presumed to be similar. The use of lenses or diffusers at a fibre termination would improve distribution for example, though this may increase the diameter of the overall device. The expense of miniature lenses or diffusers precludes their investigation at this stage of development, as these would require custom bespoke production. As such, the following design features are explored below: fibre diameter; number of fibres; and fibre orientation. These are shown in Figure 6.34.

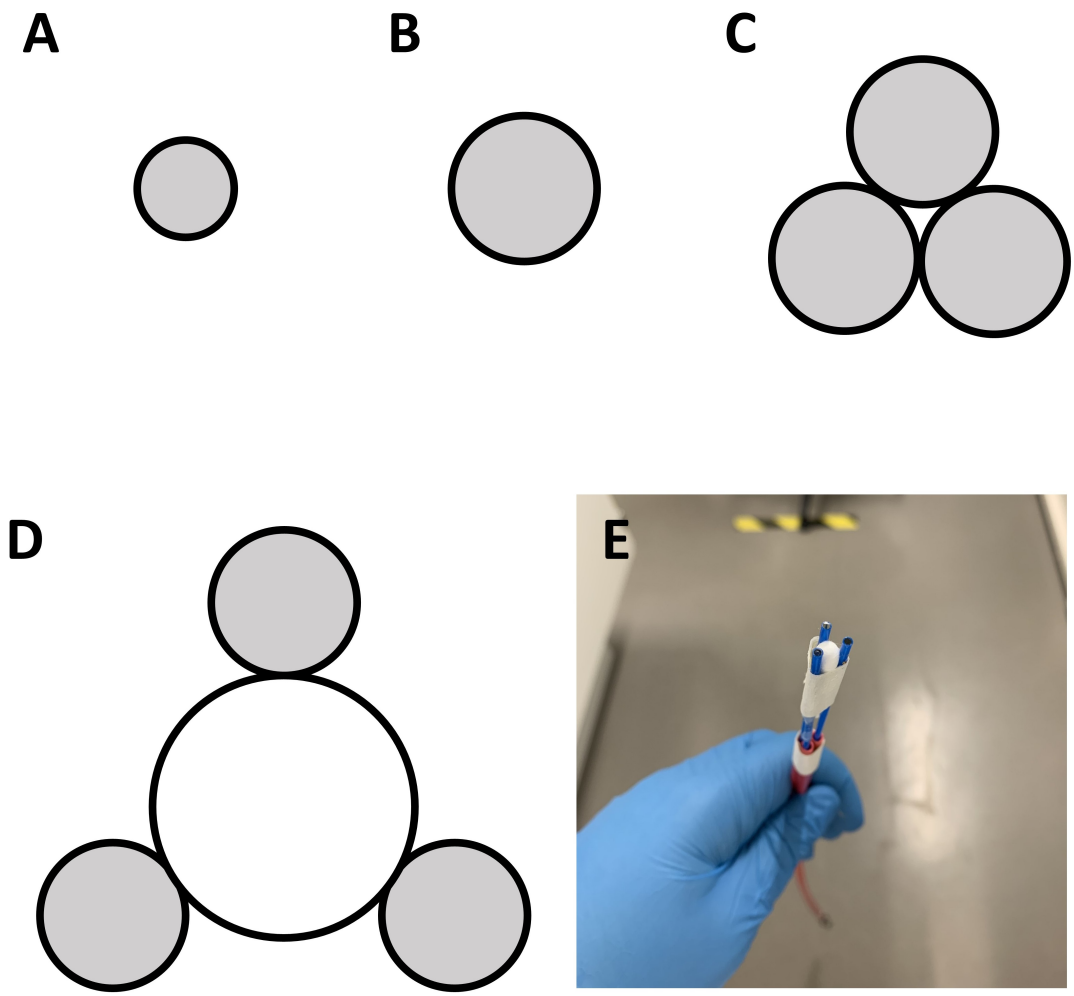


Figure 6.34: Schematic diagram of fibre orientations for a spinal-optical interface, using A: a single core 1000 μm 0.39 NA multimodal fibre; B: a single core 1500 μm 0.50 NA multimodal fibre; C: a triple core 1500 μm 0.50 NA multimodal fibre, bound together; C: a triple core 1500 μm 0.50 NA multimodal fibre, split using a 2.7 mm conical soft-tipped splitter, shown in photograph E.

6.4.1 Fibre diameter

Comparison of a single core 1000 μm 0.39 NA multimodal fibre and a single core 1500 μm 0.50 NA multimodal fibre was performed, with orientation at 90 ^{o} to the phantom media[ii]. Fibres were housed within a standard surgical drain. Though power was marginally increased with the

[ii]Use of the same optical phantom is based on an assumption that optical properties of spinal cord are similar to that of brain

large diameter fibre, but no other effects were identified. It was again noted that the large fibre had considerably reduced flexibility. Despite use of the same sources and fibres as in the cranial device development, there were considerable power losses. This is attributable to the retrograde reflectance back toward the device. Using a cranial "bolt", this reflected light will be reflected again toward the phantom from the bolt surface (particularly so with the white PLA rendered bolt).

6.4.2 Multiple fibres

Use of three fibres resulted in an expected increase in power due to the tripling of output power through use of three sources. Irradiance and beam diameter parameters were increased but not reaching statistical significance.

6.4.3 Fibre orientation

Multiple splayed fibres increased beam diameter significantly, with an expected increase in power due to the tripling of output power through use of three sources. This design, though increasing distribution, is limited for translational potential due to the large bore at the fibre array terminus: the diameter at the tip exceeds that of the surgical tract through which it would be removed. Whilst this could be adjusted to create a homogenous diameter for the length of the cable, the overall diameter and flexibility of the device would make it difficult to use.

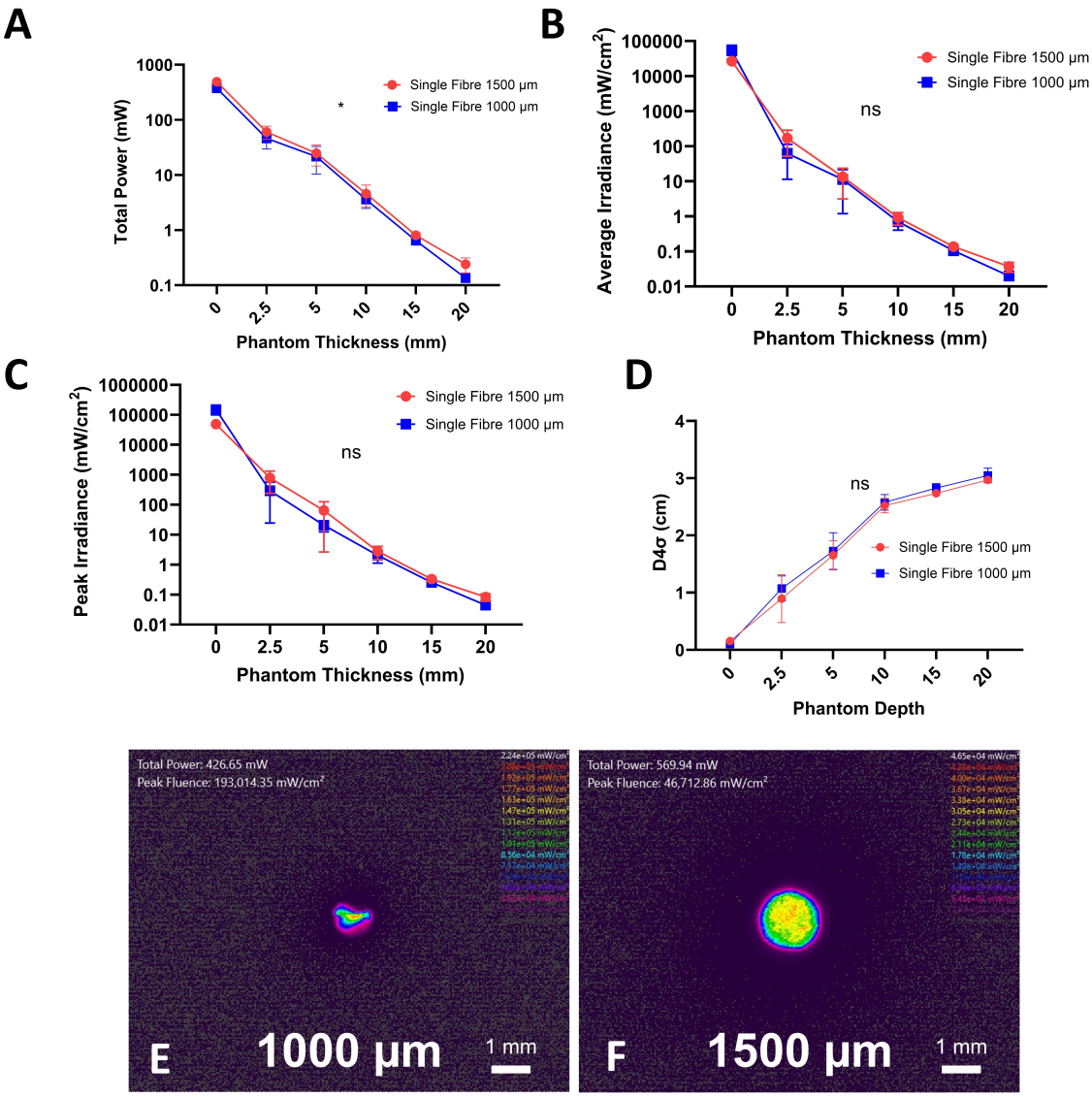


Figure 6.35: Comparison of a single core 1000 μm 0.39 NA multimodal fibre and a single core 1500 μm 0.50 NA multimodal fibre. The fibres were housed in a standard surgical drain. A: total power (y axis on log10 scale); B: average irradiance (y axis on log10 scale); C: peak irradiance (y axis on log10 scale); D: D4σ; E: beam profile of 1000 μm fibre at target screen; F: beam profile of 1500 μm fibre at target screen. For both fibres, a single MD-III laser at 100% power output was coupled to an FG550UEC custom fibre bundle (SMA to SMA, ThorLabs) and subsequently coupled via SMA:SMA to the fibre which was secured using optomechanics accessories. Beam characterisation results at target screen (0 mm) and through five thicknesses of phantom cast in standardised thickness moulds. n = 3 technical replicates per n = 3 independent experiments. ns = not significant, * = $p < 0.05$. Error bars represent SD; not visible in all instances due to logarithmic scale and/or symbol size.

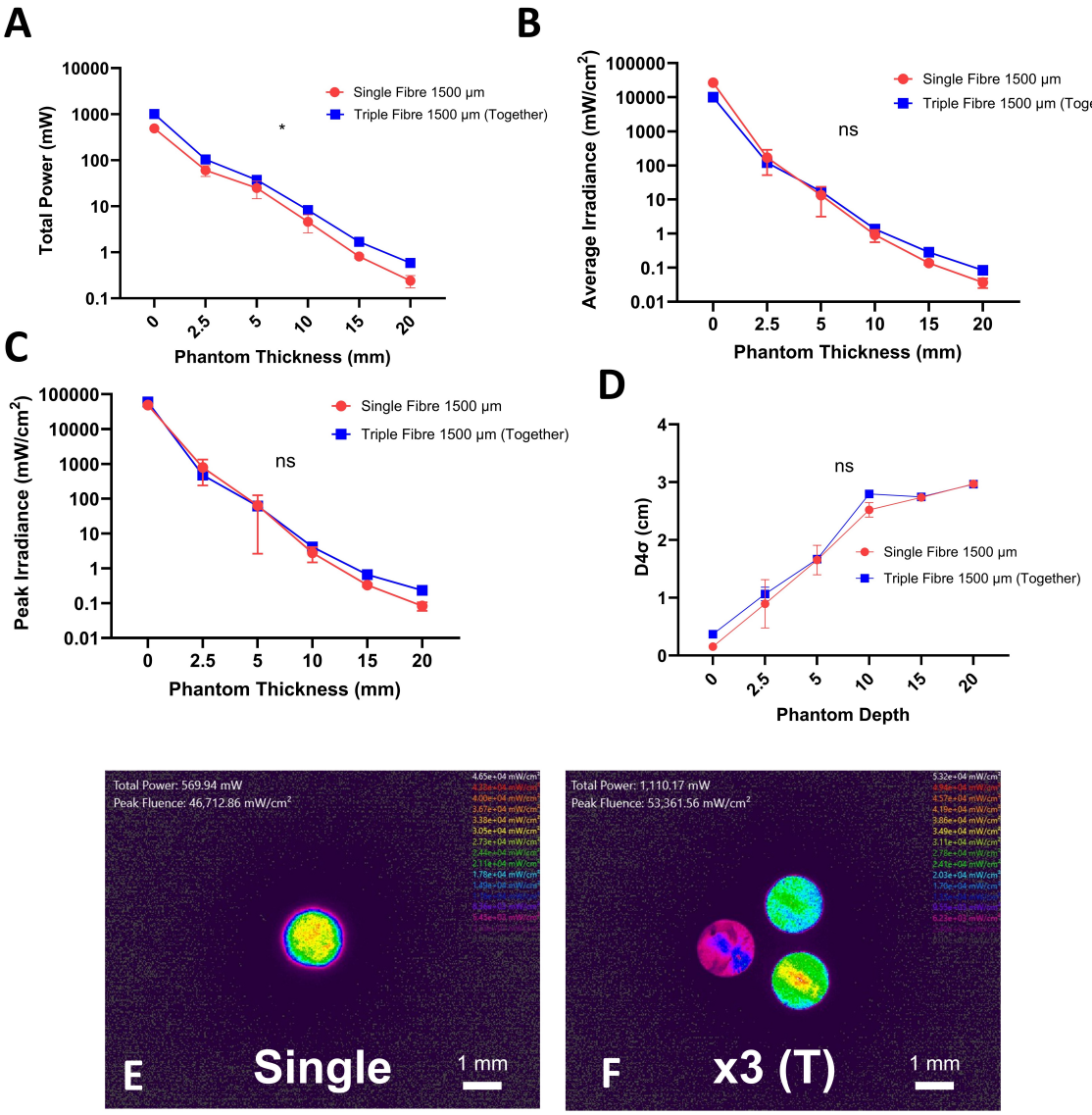


Figure 6.36: Comparison of a single core 1500 μm core 0.50 NA multimodal fibre, with three bound single core 1500 μm core 0.50 NA multimodal fibres. A: total power (y axis on log10 scale); B: average irradiance (y axis on log10 scale); C: peak irradiance (y axis on log10 scale); D: D4σ; E: beam profile of 1000 μm fibre at target screen; F: beam profile of 1500 μm fibre at target screen. For both configurations, one or three MD-III lasers at 100% power output was/were coupled to an FG550UEC custom fibre bundle (SMA to SMA, ThorLabs) and subsequently coupled via SMA:SMA to the fibre which was secured using optomechanics accessories. Beam characterisation results at target screen (0 mm) and through five thicknesses of phantom cast in standardised thickness moulds. n = 3 technical replicates per n = 3 independent experiments. ns = not significant, * = $p < 0.05$. Error bars represent SD; not visible in all instances due to logarithmic scale and/or symbol size. (T) denotes "together" fibres.

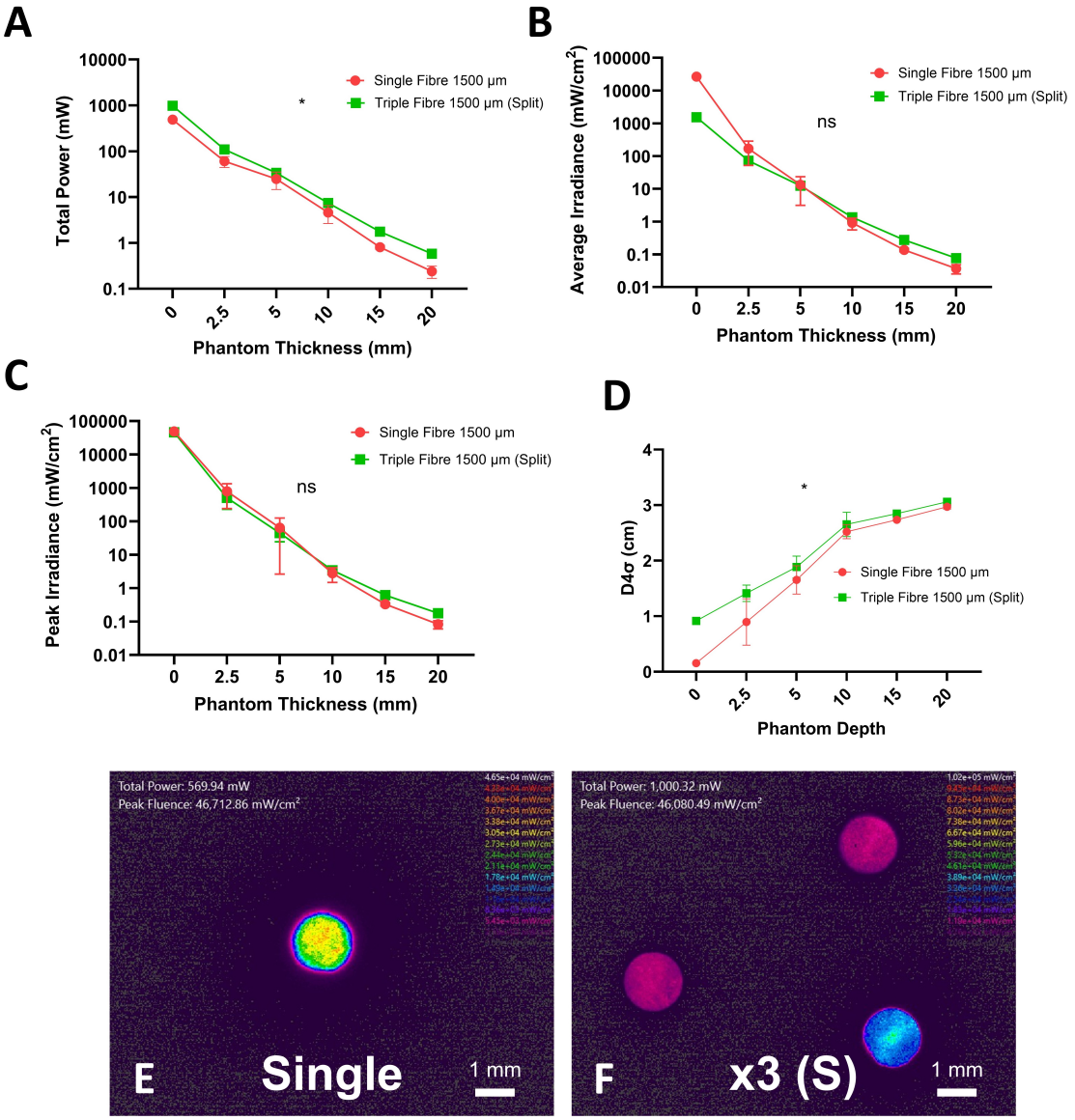


Figure 6.37: Comparison of a single core 1500 μm core 0.50 NA multimodal fibre, with three bound single core 1500 μm core 0.50 NA multimodal fibres, splayed using a 2.7 mm diameter conical splitter (Fig. 6.34 D-E). A: total power (y axis on log10 scale); B: average irradiance (y axis on log10 scale); C: peak irradiance (y axis on log10 scale); D: D4σ; E: beam profile of 1000 μm fibre at target screen; F: beam profile of 1500 μm fibre at target screen. For both configurations, one or three MD-III lasers at 100% power output was/were coupled to an FG550UEC custom fibre bundle (SMA to SMA, ThorLabs) and subsequently coupled via SMA:SMA to the fibre which was secured using optomechanics accessories. Beam characterisation results at target screen (0 mm) and through five thicknesses of phantom cast in standardised thickness moulds. n = 3 technical replicates per n = 3 independent experiments. ns = not significant, * = $p < 0.05$. Error bars represent SD; not visible in all instances due to logarithmic scale and/or symbol size. (S) denotes "split" fibres.

6.4.4 Summary

Increased numbers of fibres, with maximised spatial distribution, similarly appears to be the key design features. These could be further enhanced through use of lensing or diffusers, as explored in the cranial section of this chapter. Furthermore, this method ascertains the propagation of 660 nm light through a media analogous to spinal cord but does not factor in the diffusive effect of the overlying dura. Since there is no necessity for positioning probes intra-durally, this is likely to increase light distribution with only modest beam attenuation.

Whilst increasing the number of fibres improves distribution, this inherently reduces device flexibility and usability. An alternative is to use multiple independent single fibres. Positioning the fibre tips in multiple positions over the injury site is feasible during open surgery, with multiple tunnelled drains serving as an insertion method, and as a fibre housing which can be secured through standard surgical strategies to prevent movement of the drain and fibre during the post-operative period;[439] as well as allowing closed removal without surgical access. This allows flexibility in the positioning of the fibre(s), as shown in Figure 6.38.

An alternative introduction method would be intermittent insertion of a spinal needle to the extradural space, with the trocar removed and the lumen used for the introduction of a spinal optical fibre. PBM therapy could then be administered, and then the whole system withdrawn. As treatment appears effective with a short duration daily exposure, this may be suitable. This approach to the spinal canal/thecal sac is very common using a needle by neurosurgical clinicians, and other than familiarity with the fibre system, no additional skills would be required.

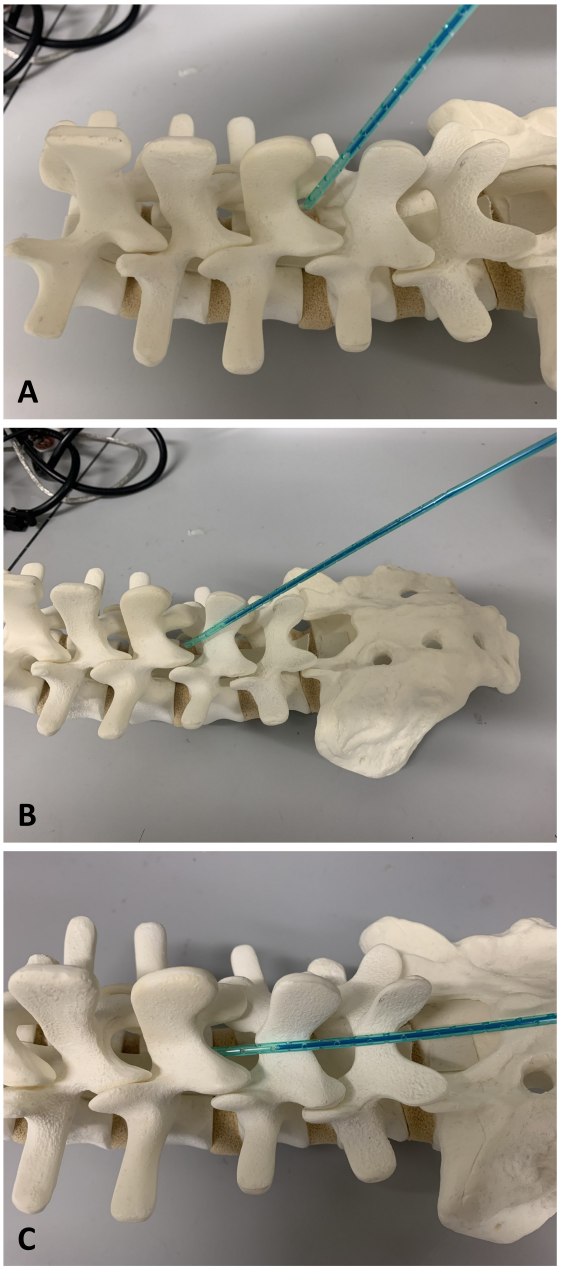


Figure 6.38: Using a model of the lumbosacral spine, differing positions of a spinal drain (containing an optical fibre) are shown, approximated to 45, 20 and 5 ^{o} angles to the rostro-caudal orientation of the spinal cord (A-c respectively). Similarly, these could be externalised along the midline as shown, or preferably lateral to the midline via a trocar method, in order to preserve the integrity of a tight fascial closure, as with a spinal wound drain.

6.5 Discussion

Further to those seen in Figure 6.1, this work establishes two additional paradigms of PBM delivery to the CNS (Fig. 6.39).

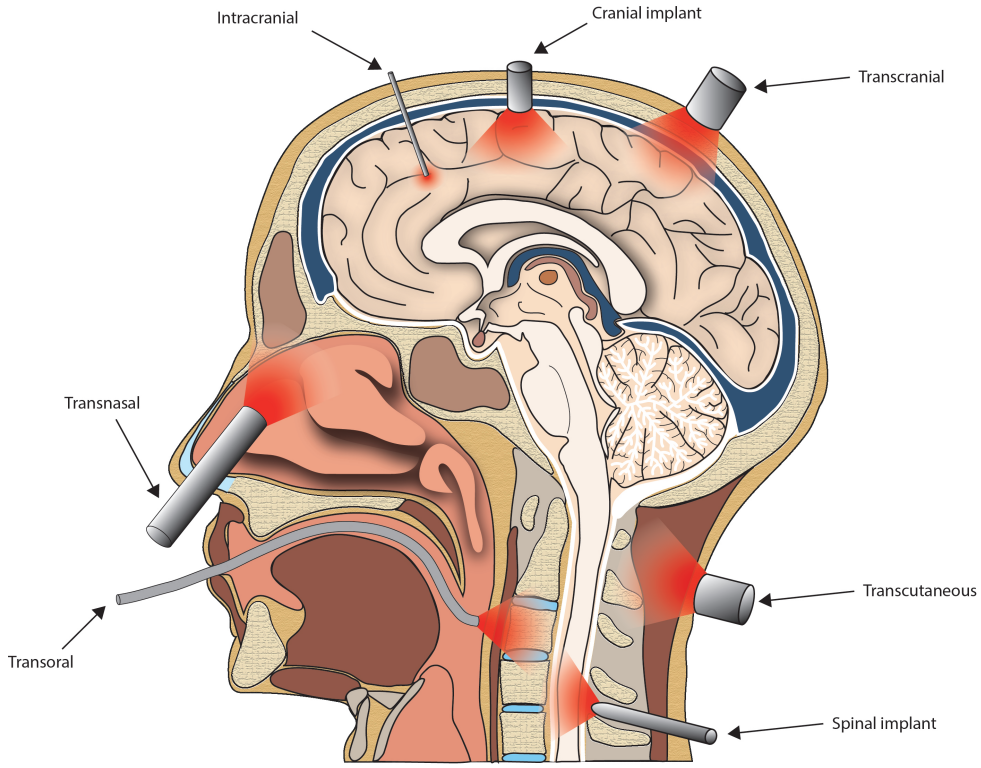


Figure 6.39: Schematic diagram of mid-sagittal section through the head and neck, with devices represented to deliver PBM via currently utilised routes: transcranial, intracranial, transnasal, transoral, and transcutaneous; and via the novel methods described in this chapter: cranial and spinal implants.

Significant improvements in design and light delivery have been made in this phase of prototyping. Clearly however, further work needs to be accomplished for these devices to be compatible for implantation into humans. Several significant findings have been made to inform ongoing device design and optimisation:

- Rendering material significantly affects light delivery and reflective surface coatings are likely to further improve delivery and diffusivity of incident light to cortical surface.
- Bolt-brain interface geometry significantly affects power delivery and distribution and in

combination with reflective surface coatings is an avenue for optimisation.

- Lensing and diffusion are important optical methods to improve illumination variables for this application and are feasible within this device.
- NA, fibre diameter and source-fibre interface factors are a current limitation.
- Heating and high average irradiance appear to correlate, so thermal and over-irradiance barriers are likely to have a shared solution.
- Phase modulated illumination, whereby adjacent light sources have offset phases which result in separated (rather than merged) beams.
- Pulsed wave administration,[173] where pulses of applied light mitigate heating compared to continuous wave beams.
- Ultrasound modulation,[288] where ultrasound waves are used to alter the optical properties of tissue, thereby altering beam distribution.

This work has also confirmed that delivery of PBM via a single point of cranial access is inherently limited. As such, diffuse delivery across much of the damaged tissue after a typical TBI would require multiple points of such access, likely too many to be viable. This is less problematic in SCI, due to the typically more focal nature of the injury site. To improve delivery capabilities in TBI, alternative implantable or intraoperative delivery devices may be more successful. These concepts may include flexible cortical arrays, intraoperative treatment arrays (for a single therapeutic dose during craniotomy/craniectomy) or invasive devices combined with high-powered transcranial administration. This would allow greater proportions of the cortical surface/brain volume to be exposed to effective doses of PBM during treatment. Other additional measures may yield further improvements in distribution of PBM from a limited access space. Arrays of micro-LED could offer a more diffuse light source, which may also offer more flexibility in spatial orientation.

During this phase, important features of a prospective final device have not yet been fully considered during the development. Interface with the skin, particularly with a spinal probe,

and safety features to prevent inadvertent advancement of the probes to a deeper level, would both need to be considered in future work. Furthermore, as there is ongoing optimisation of the device itself and novel components (such as a Raman probe) yet to be included, these prototypes have not sought to involve standard-of-care neuromonitoring, which the final device would incorporate[iii].

Future development work should also consider factors of acceptability of the device by end users: principally patients and clinicians. Feedback on the device concept and important considerations from patients and the public have been sought for both cranial and spinal devices (see Appendix H). Once a functioning prototype is has been developed, usability studies using anatomical models or cadavers in a simulated clinical environment would provide valuable feedback to optimise the ergonomics of the design, as well as fulfilling regulatory requirements for medical devices. Once further optimisation work has been completed, repeat profilometry will be required to ensure that maximal light delivery is within safe parameters to avoid any significant heating to neuronal tissues, as well as peak irradiances which are within the effective window of dosing to promote neuroprotection (as higher average irradiance values are associated with inhibitory effects[166]).

In conclusion, this chapter presents strategies to optimise PBM distribution to the brain and spinal cord, using an implantable device based on clinically feasible paradigms. For the spinal cord, effective levels of PBM delivery using a multi-fibre implant are achievable to a focal SCI site. As such, this is closest to a complete prototype. The cranial implant, based on the diffuse nature of TBI, is unlikely to be able to deliver relevant doses to all injured tissue without significant design alterations beyond what has been achieved in the work reported above.

[iii] The development of the Raman probe itself is ongoing with collaborators, and as such has not been included in this thesis.

Chapter 7

GENERAL DISCUSSION

7.1 Key findings

Several key findings of the work described in this thesis represent significant advances to the knowledge on the use of PBM and RS in neurotrauma:

- Evidence-based effective parameters for PBM in TBI are: 660 nm/810 nm wavelength; treatment duration of up to three days; and minimising time to first treatment;
- 660 nm PBM improves functional and histological recovery after SCI;
- Implantable PBM improves early expression of RAP after SCI;
- 810 nm PBM alone is the optimal wavelength to improve functional and histological recovery after mild TBI;
- 810 nm PBM reduces microglial and astrocytic activation after mild TBI;
- RS can identify therapy-associated biomarkers of PBM treatment after TBI;
- 660 nm PBM reduces microglial Iba1 expression and TNFα release in an *in vitro* model;
- 660 nm PBM activates regeneration-associated pathways in the injury site after SCI; with reductions in transcription of mitochondrial components and ribosomal transcriptional pathways;

- Doses of PBM within effective windows for neuroprotection can feasibly be delivered to the human brain and spinal cord by use of a temporarily implantable fibre-optic device.

7.2 Interpretations

7.2.1 Efficacy of photobiomodulation

This thesis has demonstrated evidence for the favourable effects of PBM administration to the injured CNS. Through optimisation of dose parameters *in vitro*, rationalised dosing strategies with daily administration of energies within the range of 1-3 J/cm^2 have been demonstrated to be effective, in correlation with previous work using 660/810 nm wavelengths within this energy window.[213,240] This work has advanced the evidence base, with particular relevance to direct delivery in neurotrauma. By direct comparison of PBM administration via implant and transcutaneous routes, using matched average irradiance values, the equivalence of efficacy in regeneration associated outcomes is supportive of implantable PBM as a viable translational strategy. Whilst previous studies have used invasive administration, no prior studies have directly compared the two strategies in neurotrauma.[314,334,338,435] This effect is further supported by previous studies in models of Parkinson's disease, which have also demonstrated equivocal neuroprotective effects via invasive and non-invasive administration in pre-clinical models.[204] Demonstration of efficacy across both SCI and TBI serves to increase confidence in the ability of PBM to beneficially impact common pathophysiological processes across both types of neurotrauma. Through use of both functional and histological outcomes in each model, impact on clinically relevant outcomes has been shown which is supported by demonstration of biological measures of recovery.

7.2.2 Mechanisms of photobiomodulation

The transcriptomics results have offered some valuable insights into the action of PBM in neurotrauma. Most notably, there are marked similarities between the PBM treated state and

a hypometabolic state previously described in more mild TBI in comparison to moderate and severe injuries.[440,441] In this work, Di Pietro and colleagues used a stretch injury model of organotypic hippocampal slice cultures subjected to mild, moderate and severe stretch injury. This was associated with a downregulation in NADH subunits, COX subunits, ATP synthases and histone clusters, in a remarkably similar pattern to that shown in Chapter 5. The authors describe this as a "hibernational state" or "energy conservation programme", only achievable in mild injury, which mitigates mitochondrial dysfunction and the ensuing oxidative stress patterns and apoptosis. Administration of PBM then may achieve a similar state, whereby the supportive action of PBM on mitochondrial function acts to allow energy conservation. This may be involved in a reduction in activation of ribosomal stress responses.[442] In combination with averted activation of cytochrome c apoptotic pathways, this state may not only minimise apoptotic processes, but permit energy use toward growth cone activation (supported by augmented calcium homeostasis and signalling pathways). These processes may also relate to wider mitochondrial processes: regulation of mitochondrial fission is an emerging mechanism by which PBM is neuroprotective in SCI, with abnormal fission leading to Bax-mediated cellular apoptosis after injury.[443] Increased mitochondrial fission is associated with more severe injury in TBI,[444] and regulation of this process may support transition of the severely injured brain and spinal cord into a more "mild" phenotype injurious state.

7.2.3 Raman spectroscopy

RS has been demonstrated in this thesis to identify spectral differences between injury/treatment groups after TBI (Fig. 4.22). Significant differences in 1660 cm^{-1} peak intensity were identified between sham and injury groups after SCI (Fig. 3.34), and discernible spectral shifts were noted between treatment and injury groups (Fig. 3.33). In correlation with previous work demonstrating the spectral biomarkers to discern injury severity in TBI,[345,383] and in PBM treatment after SCI,[346] this provides further evidence toward the development of RS as a method for providing real-time feedback on injury states and treatment responses in neurotrauma.

Understanding spectral data from RS in neurotrauma is integral to identifying translatable

value for clinical applications. Principle peaks of interest across a number of studies have been 1440 and 1660 cm^{-1} regions. The 1440 cm^{-1} region has been associated with CH_2 twisting and bending, lipid, cholesterol, phospholipid, mixed amide I protein and tyrosine.[445–447] The 1660 cm^{-1} region is associated with lipids, C=C stretching, amide I vibration, tyrosine, mixed lipids and proteins, alpha-helix/random coil and cardiolipin.[345,445–451] Often the ratio of these peaks is used, as 1660 cm^{-1} is dynamic after injury with reference to the more static 1440 cm^{-1}. Statistically significant differences between the contralateral and pericontusional/contusional regions from experimental models of TBI have been shown in the 1440/1660 ratio at 2, 3 and 7 days after injury.[345,383,445]

The dynamic shifts in lipid peaks may represent dysfunctional mitochondrial lipid metabolism, which plays a role in both acute and chronic sequelae of neurotrauma.[292] Tissue levels of free fatty acids are dynamic following TBI in rat models and may play a role in secondary tissue damage.[452] Differences between lipid concentrations between injured and uninjured brain tissue are also present after injury,[453] and lipid composition changes can be identified with RS to discern such changes.[445] Oxidative states of cardiolipin and its interaction with cytochrome c is altered after injury and may be a mechanism for production of reactive oxygen species.[292] Cardiolipin has been identified as a potential source for band shift after injury[345] and presents a potential for spectral shifts identified in the 1660 cm^{-1} region. Similarly, injury-associated molecules ganglioside and glutathione also have peaks within these regions and correlation with these emerging spectral biomarkers may provide further explanation for the observed shifts between injury groups.[454]

Whilst no gross shift in 1440/1660 ratio was detected between groups, differences in 1660 cm^{-1} region were identified in PCA of spectra between injury/treatment groups in Figure 4.24. Of interest, peaks in the 1560 cm^{-1} region have also been identified as dynamic between groups through PCA (Fig. 4.22), and this region has been shown to correlate with mitochondrial activity.[450] Further work to identify robust spectral changes with injury severity and therapy is required to elucidate both the biological processes represented by spectral shifts, and the clinical relevance of monitoring such processes to better inform treatment. Nevertheless, the

work described in this thesis provides some support for the ongoing investigation of the concept of RS as a novel means of neuromonitoring in CNS trauma. Beyond this, bands in the high wavenumber 2600-3800 cm^{-1} region were identified in PCA of extended spectra as key variable components (Fig. 4.20). Shifts in this region are able to identify the water fraction of brain tissue in the region of 0.75-0.95 to an accuracy of 0.01,[455] and may explain the observed shifts between injury/treatment states. Real-time assessment of progression of brain oedema has clear clinical applications for guiding medical and surgical therapy for acute neurotrauma in the intensive care unit setting.

7.2.4 Devices

The development of clinically feasible prototypes in this thesis serves to demonstrate the translational potential of invasive application of PBM to the injured brain and spinal cord. The precedence for the implantation of such devices is provided by the widespread uptake of invasive neuromonitoring (particularly in the brain after moderate/severe injury) and positioning of surgical wound drains (in the spinal cord). Basing design features on these existing surgical devices (intraparenchymal bolt or surgical wound drain) has assisted in the demonstration of clinical suitability and would aid potential future uptake given that insertion techniques would be familiar to clinicians.

Due to the focal nature of typical SCI, the demonstration of relevant doses of PBM to an injury site in the spinal cord was achievable using spatial distribution of optical fibres, and it was shown that this can be further enhanced using lenses or diffusers. As shown using an *in vivo* model of SCI, this focal administration directly over the injury site is sufficient to achieve favourable biological effects, and in this respect the spinal cord device is not distant in its features from a final device suitable for translation.

For the brain implant prototype, optical measures of spatial distribution and lensing were also effective for improving distribution of PBM, though clearly the paradigm of a 14mm cranial access port is inherently insufficient for whole brain coverage. Despite this drawback, focal application of PBM through a single small burr hole has been shown to be effective *in*

vivo.[240] Similarly, the administration of transcranial PBM described in Chapter 4 did not result in coverage of the whole brain. It may be that application of direct PBM to even a small area within the brain, through influence on microglial and astrocyte populations, may have a wider effect on parenchyma which is not directly irradiated, i.e. microglial or astrocytic phenotypic switching in a discrete area may have a more generalised effect. Nevertheless, prototyping work has demonstrated that, even with further optimisation of PBM distribution, whole brain irradiation via a single device is not possible. Further design features, or methods for clinical use of the device (such as use of multiple access sites) may resolve the issue somewhat, and are described later in this chapter.

7.3 Limitations

Whilst extensive *in vitro* dose optimisation work was performed in this thesis, the many and various possibilities of PBM parameters were not possible to comprehensively trial and explore. Even if such extensive study were possible *in vitro*, differences in cellular responses *in vivo* would also warrant investigation of a broad variety using experimental animal models. As such, whilst described as "optimal", further investigation may identify strategies which hold greater efficacy beyond those described in this thesis.

This thesis describes the equivalence of implanted and transcutaneous administration of PBM. This observation is limited, as due to increasing animal mobility and curiosity, as well as decreasing pain, removal of the implant by the animals became increasingly likely. As such, the viability of the implant was not examined beyond 3 dpi, and so the biological effects of longer duration of invasive treatment could not be studied. Furthermore, the effects of the implant itself, independent from PBM treatment, were not studied here. This is important as the presence of the implant itself may have elicited a positive or negative biological effect. Future study should include a control group which receives an implant, but without activation of PBM through it. The effects of implantable PBM were not studied using the TBI model, and is a focus for future work.

The *in vivo* experiments described in this thesis utilised a short interval (15 min) between injury and first PBM treatment. This is not a clinically achievable time frame, and this interval was selected to provide optimal conditions for PBM to be effective. Further investigation using later time points would be useful in determining a "cut-off" time for instigating PBM.

Both biological outcomes and RS analysis used limited numbers of end points (3 dpi and either 4 wpi or 6 wpi for biological outcomes; 3 dpi alone for RS). Whilst acute and chronic mechanisms are the key outcomes of interest for biological responses, observation of temporal trends in RS biomarkers would be an important factor for improving understanding of how these change in response to injury and treatment. Using a single acute time point post-injury limits the scope for such temporal interpretation of the spectral data. A further improvement would be the use of repeated *in vivo* measures, allowing for inter-animal variability to be accounted for. This would allow comparison of pre-injury, post-injury and post-treatment spectra all paired to a single animal. However, a Raman probe capable of acquiring high-resolution data in the *in vivo* setting is not yet available.

The use of a single point of comparison, and single PBM dosing method, also limits the scope of the transcriptomic data. The insights likely achievable through comparison of multiple wavelengths, energy delivery protocols and time points would offer more data on the mechanism of PBM. This dataset is also limited by the exclusion of a baseline (sham injury) group, which would serve as a useful comparator, particularly for the transcription of metabolic proteins such as mitochondrial subunits. Furthermore, the use of whole injury site tissue homogenates for RNA extraction results in combined transcriptional data from all cell types present in the injured area. This methodology does not therefore allow for resolution of transcriptional activity to specific cell types (i.e. neuronal, microglial, astrocytic). As such, heterogenous changes in the transcriptional regulation with PBM between these group are likely lost. This could be addressed through future use of single cell RNA-seq using techniques such as laser capture microdissection.

Use of *ex vivo* tissue for profilometry will inevitably result in differing transmission of PBM compared to *in vivo*. Due to the size of profilometry equipment relative to the rodent models

used, it was not possible to perform any profiling in the living animal model. The use of the *ex vivo* setting for acquisition of Raman spectra was also necessary for this reason, and spectra acquired *post mortem* will differ from that which would have been observed *in vivo*. Use of an optical phantom for profiling transmission of PBM from developed prototype is a further limitation. This has been shown in Appendix G to be somewhat representative of *ex vivo* brain parenchyma, though the transmission is significantly different between the materials (Fig. G.5). The optical phantom impedes transmission less than brain parenchyma (higher average irradiances in phantom) but results in lower diffusion (lower D4σ values than brain parenchyma). This model was used for reproducibility and production of plates with uniform thickness, though it must be recognised the transmission through brain does differ.

7.4 Recommendations

7.4.1 Photobiomodulation

The SCI investigation in this thesis utilised 660 nm PBM as the only wavelength. Given the recognised efficacy of 810 nm in the TBI investigation, similar comparison of wavelengths in SCI may identify parameters for additional benefit to that shown here. Little is yet known of the differing mechanisms (if any) of effect between these two therapeutic wavelengths, and their comparison may shed light on any relationship which may exist between them and add important evidence to the development of optimal PBM parameters for SCI. Whilst no synergistic effect was identified in TBI in the work described in this thesis, further work may elucidate parameters for combination of these (or other) wavelengths to enhance the efficacy of PBM in neurotrauma.

There are further parameters of PBM (beyond metrics of power and time) which warrant further exploration in both TBI and SCI. Comparative use of pulsed wave, continuous wave, and nano-pulsed laser therapy have yielded tangible differences in studies in TBI[173] but are yet to be explored thoroughly in SCI studies. Polarisation may too offer a variable which should be optimized through future study: Ando and colleagues (2014) have demonstrated that treating SCI with linear polarisation of PBM parallel to the spinal cord, in comparison to perpendicular

to the cord, resulted in improved functional outcomes, attributable to deeper PBM penetrance and improved anisotropic scattering.[295] Further work comparing delivery methods of PBM is encouraged to inform the mechanism and the translational potential of the respective approaches (transcutaneous, remote, invasive). Inclusion of remote application groups may be beneficial for comparison of the efficacy of abscopal effects to those directed at the injurious tissue.[265]

The failure of the NEST-3 trial to show significant benefit to patients of PBM after ischaemic stroke has highlighted the necessity for rigorous pre-clinical optimisation of PBM therapeutic protocols prior to clinical trials.[214] Given the breadth of possible parameters for PBM treatment, more extensive optimisation is required than in comparable studies using pharmaceutical treatments. Delivery modalities should be considered alongside wavelength and dosimetry variables as a key feature of PBM which can considerably affect its efficacy in treating the injured CNS.

Further work on elucidating the mechanisms of PBM would also be advantageous in advancing this treatment toward the clinical setting. PBM is a NICE recommended treatment for oral mucositis,[188,189] yet uptake has been poor. This has been attributed, in part, to the lack of understanding of its mechanism of action.[456] As described above, "-omic" approaches across multiple time points and using multiple PBM protocols would be highly beneficial to advancing our understanding of the mechanisms and how PBM therapies can be best designed for optimal effects.

7.4.2 Raman spectroscopy

A key feature of the proposed device which has not been explored in this thesis is the development of a suitable Raman probe, capable of providing *in situ* Raman monitoring *in vivo*. This component is being developed with collaborators and was deemed beyond the scope of this thesis to include. Development of such a probe however should be technically feasible, given the success of similar probes developed previously for neurosurgical applications, demonstrated in the clinical setting during brain biopsy procedures.[235] Based on the precedence of intraparenchymal monitoring in TBI, for the brain it is foreseeable that a Raman probe could be placed within, or directly adjacent to, brain parenchyma. This minimises possible feedback from blood vessels

and dura, which may obfuscate signals which indicate brain states. In the spinal cord, there is less precedence for intradural probe placement, and the possibility of probe movement (for example during patient turns) may result in iatrogenic injury. The *ex vivo* spectra acquired in Chapter 3 were taken with the dura intact, yet spectra were that expected for neurological tissue. The thickness of human dura may result in greater interference with the return of Raman signal, an inherently weak phenomenon. As such, further investigation using post mortem tissue from large mammals or humans should be performed with the developed probe in order to identify the plane in which the probe must be situated (i.e. extradural vs subdural) in order to acquire usable neurological spectra.

Further work using advanced analytical methods to identify spectral differences between groups is ongoing, using a self-optimising Kohonen index network (SKiNET) based analysis by collaborators based at the University of Birmingham.[345,347,383] It is anticipated that this will further elucidate spectral shifts between groups, and may identify novel insights into the mechanisms of both injury and PBM, as well as providing more robust support for the ongoing translation of RS based neuromonitoring for inclusion in the proposed device. It is also hoped that identification of specific dynamic peaks or peak clusters through this method may identify specific chemical structures for further investigation. These may then be correlated with results from techniques such as lipid/proteomics of injured/uninjured/treated tissue in order to correlate spectral shifts with biological changes.

7.4.3 Device development

The work in development of an initial prototype in this thesis is considered successful in the demonstration of proof-of-concept. However, toward translation to clinical settings, a fully functioning optimised prototype is required, featuring the inclusion of standard-of-care neuromonitoring and a functioning Raman probe. Further work to improve the distribution of PBM would permit more homogenous (i.e. less Gaussian) PBM delivery and mitigate any potential for focal tissue heating. This has a secondary effect of minimising any tissue heating during treatment. This could be explored further through the use of microlenses, or alternative

light sources such as arrays of micro-LED.[435,457] Whilst transcranial application is limited in humans, supplementary arrays of non-invasive scalp sources may augment the effects of an invasive delivery device and offer greater cortical coverage at lower doses. It could also be considered necessary to use multiple sites for implantation of PBM delivery devices, in order to maximise delivery to affected brain tissue. However, this should be minimised as this would increase costs in clinical settings, as well as potentially compromise acceptability. Consideration of alternative device paradigms may prove fruitful. For more severe cases, craniotomy/craniectomy surgery provides a window of great exposure of brain cortex, which could be an opportunity for administration of a single therapeutic dose applied using a different type of (yet to be developed) device.

Once optimised, fully functioning devices have been established, a rigorous battery of additional testing will be required. This will include validation of device safety. Given the use of laser sources, this will involve ensuring that all optical outputs are internal and fail-safe components would need to be incorporated to prevent inadvertent exposure of operators, bystanders, or unintended administration sites of the patient. Devices will also require safety testing to ensure minimal and safe levels of heating (both for tissue and device components). Previous work using PBM devices in a piglet model has demonstrated that heating only occurs *in vivo* with average irradiance levels far beyond those identified as effective in this thesis.[314] It is also anticipated that validation of the device in a large mammal model, as well as clinical simulation testing for clinical feasibility and usability, will be required in order to progress the device toward first-in-human trials.

Chapter 8

CONCLUSIONS

This thesis has explored the development of an optical device for promoting recovery after traumatic brain and spinal cord injury, specifically employing PBM as a neuroprotective and neurorestorative therapy, with RS as a monitoring technique to identify injury progression and therapeutic responses. This was approached through demonstrating this concept in SCI (Chapter 3) and TBI (Chapter 4); by investigating the mechanisms of PBM (Chapter 5); and by demonstrating translational feasibility through development of a device prototype (Chapter 6).

It has been demonstrated that PBM is neuroprotective and neurorestorative in SCI, and results in reduction in lesion size. It was also demonstrated that an implantable device for delivery of PBM offers similar efficacy to transcutaneous application in promoting early activation of RAP. This suggests that an implantable PBM device is a suitable translational approach for delivering effective doses to elicit favourable effects post-injury in humans. PBM is also effective in improving functional recovery in TBI, and is associated with reduction in astrocyte and microglial activation. Spectral analysis of injury/treatment states using an *ex vivo* model showed that RS can be used to validate responses to treatment, and with further development, may be a useful adjunct in identification of treatment efficacy and permit dose optimisation.

Further elucidating the mechanisms of PBM is important to improve clinical acceptability of this device as a novel therapy, as well as allowing well-reasoned dose parameters to be studied and implemented. This thesis has demonstrated that PBM may activate a favourable metabolic

"hibernation" state in the injured CNS, by supporting mitochondrial function. It is hypothesised that this mitigates oxidative stress and cytochrome c/calcium-induced apoptotic pathways; dampens ribosomal stress responses and microglial/astrocytic activation; thereby producing a more favourable micro-environment and metabolic state to facilitate neuronal survival and repair.

Through identification of effective PBM dose parameters in this thesis, a device prototype was developed which has demonstrated that these doses can be delivered by implantable fibre arrays. Further work is required to improve the distribution of PBM over larger areas of affected neuronal tissue, and to integrate standard-of-care neuromonitoring, as well as a RS probe. However, the prototypes described in this thesis demonstrate proof-of-concept for feasibility of this device as a promising therapy to promote restoration of function after neurotrauma.

In conclusion, the use of PBM with RS neuromonitoring holds significant promise as a therapeutic approach to mitigate the secondary injury of neurotrauma, and to facilitate CNS repair. Future work should be conducted to robustly delineate: the optimum dose parameters of PBM; and the relationship between therapeutic effect and Raman spectral biomarkers. Further development of a device toward large mammal and first-in-human studies are key next steps in the translation of this device as a therapy which may be effective to improve recovery after traumatic brain and spinal cord injury.

Bibliography

[1] Zheng B, Tuszynski MH. Regulation of axonal regeneration after mammalian spinal cord injury. Nature Reviews Molecular Cell Biology. 2023 Jan. Available from: https://doi.org/10.1038/s41580-022-00562-y.

[2] Langlois JA, Rutland-Brown W, Wald MM. The epidemiology and impact of traumatic brain injury: a brief overview. The Journal of Head Trauma Rehabilitation. 2006;21(5):375-8. Available from: 10.1097/00001199-200609000-00001.

[3] Jazayeri SB, Beygi S, Shokraneh F, Hagen EM, Rahimi-Movaghar V. Incidence of traumatic spinal cord injury worldwide: a systematic review. European Spine Journal. 2015;24(5):905-18. Available from: https://doi.org/10.1007/s00586-014-3424-6.

[4] Maas AIR, Menon DK, David Adelson PD, Andelic N, Bell MJ, Belli A, et al. Traumatic brain injury: integrated approaches to improve prevention, clinical care, and research. The Lancet Neurology. 2017 Dec;16(12):987-1048. Available from: https://doi.org/10.1016/S1474-4422(17)30371-X.

[5] Allen BC, Cummer E, Sarma AK. Traumatic Brain Injury in Select Low- and Middle-Income Countries: A Narrative Review of the Literature. Journal of Neurotrauma. 2023 Mar. Available from: https://doi.org/10.1089/neu.2022.0068.

[6] Li LM, Dilley MD, Carson A, Twelftree J, Hutchinson PJ, Belli A, et al. Management of traumatic brain injury (TBI): a clinical neuroscience-led pathway for the NHS. Clinical Medicine. 2021 Mar;21(2):e198-205. Available from: https://doi.org/10.7861/clinmed.2020-0336.

[7] Cassidy JD, Cancelliere C, Carroll LJ, Côté P, Hincapié CA, Holm LW, et al. Systematic Review of Self-Reported Prognosis in Adults After Mild Traumatic Brain Injury: Results of the International Collaboration on Mild Traumatic Brain Injury Prognosis. Archives of Physical Medicine and Rehabilitation. 2014 Mar;95(3):S132-51. Available from: https://doi.org/10.1016/j.apmr.2013.08.299.

[8] Temkin NR, Corrigan JD, Dikmen SS, Machamer J. Social Functioning After Traumatic Brain Injury. Journal of Head Trauma Rehabilitation. 2009 Nov;24(6):460-7. Available from: https://doi.org/10.1097/htr.0b013e3181c13413.

[9] Sercy E, Orlando A, Carrick M, Lieser M, Madayag R, Vasquez D, et al. Long-term mortality and causes of death among patients with mild traumatic brain injury: a 5-year multicenter study. Brain Injury. 2020 Feb;34(4):556-66. Available from: https://doi.org/10.1080/02699052.2020.1725981.

[10] Madsen T, Erlangsen A, Orlovska S, Mofaddy R, Nordentoft M, Benros ME. Association Between Traumatic Brain Injury and Risk of Suicide. JAMA. 2018 Aug;320(6):580. Available from: https://doi.org/10.1001/jama.2018.10211.

[11] Bullock MR, Chesnut R, Ghajar J, Gordon D, Hartl R, Newell DW, et al. Surgical management of traumatic brain injury. Neurosurgery. 2006;58(3):16-24.

[12] Teasdale G, Jennett B. Assessment of coma and impaired consciousness. The Lancet. 1974 Jul;304(7872):81-4. Available from: https://doi.org/10.1016/s0140-6736(74)91639-0.

[13] Mena JH, Sanchez AI, Rubiano AM, Peitzman AB, Sperry JL, Gutierrez MI, et al. Effect of the Modified Glasgow Coma Scale Score Criteria for Mild Traumatic Brain Injury on Mortality Prediction: Comparing Classic and Modified Glasgow Coma Scale Score Model Scores of 13. Journal of Trauma: Injury, Infection & Critical Care. 2011 Nov;71(5):1185-93. Available from: https://doi.org/10.1097/ta.0b013e31823321f8.

[14] Management of Concussion/mTBI Working Group. VA/DoD clinical practice guideline for management of concussion/mild traumatic brain injury. Journal of Rehabilitation Research and Development. 2009;46(6):CP1-68.

[15] Maas AIR, Hukkelhoven CWPM, Marshall LF, Steyerberg EW. Prediction of Outcome in Traumatic Brain Injury with Computed Tomographic Characteristics: A Comparison between the Computed Tomographic Classification and Combinations of Computed Tomographic Predictors. Neurosurgery. 2005 Dec;57(6):1173-82. Available from: https://doi.org/10.1227/01.neu.0000186013.63046.6b.

[16] Marshall LF, Marshall SB, Klauber MR, Clark MVB, Eisenberg H, Jane JA, et al. The diagnosis of head injury requires a classification based on computed axial tomography. J Neurotrauma. 1992;9(Suppl 1):S287-92. Available from: https://pubmed.ncbi.nlm.nih.gov/1588618/.

[17] Yip PK, Hasan S, Liu ZH, Uff CEG. Characterisation of Severe Traumatic Brain Injury Severity from Fresh Cerebral Biopsy of Living Patients: An Immunohistochemical Study. Biomedicines. 2022 Feb;10(3):518. Available from: https://doi.org/10.3390/biomedicines10030518.

[18] Ng SY, Lee AYW. Traumatic Brain Injuries: Pathophysiology and Potential Therapeutic Targets. Frontiers in Cellular Neuroscience. 2019 Nov;27(13):528. Available from: https://doi.org/10.3389/fncel.2019.00528.

[19] Stocchetti N, Carbonara M, Citerio G, Ercole A, Skrifvars MB, Smielewski P, et al. Severe traumatic brain injury: targeted management in the intensive care unit. The Lancet Neurology. 2017 Jun;16(6):452–464. Available from: http://dx.doi.org/10.1016/S1474-4422(17)30118-7.

[20] Ahluwalia M, Kumar M, Ahluwalia P, Rahimi S, Vender JR, Raju RP, et al. Rescuing mitochondria in traumatic brain injury and intracerebral hemorrhages - A potential ther-

apeutic approach. Neurochemistry International. 2021 Nov;150:105192. Available from: https://doi.org/10.1016/j.neuint.2021.105192.

[21] Khatri N, Thakur M, Pareek V, Kumar S, Sharma S, Datusalia AK. Oxidative Stress: Major Threat in Traumatic Brain Injury. CNS & Neurological Disorders - Drug Targets. 2018 Nov;17(9):689-95. Available from: https://doi.org/10.2174/1871527317666180627120501.

[22] Vespa P, Bergsneider M, Hattori N, Wu HM, Huang SC, Martin NA, et al. Metabolic Crisis without Brain Ischemia is Common after Traumatic Brain Injury: A Combined Microdialysis and Positron Emission Tomography Study. Journal of Cerebral Blood Flow & Metabolism. 2005 Feb;25(6):763-74. Available from: https://doi.org/10.1038/sj.jcbfm.9600073.

[23] Chamoun R, Suki D, Gopinath SP, Goodman JC, Robertson C. Role of extracellular glutamate measured by cerebral microdialysis in severe traumatic brain injury. Journal of Neurosurgery. 2010 Sep;113(3):564-70. Available from: https://doi.org/10.3171/2009.12.jns09689.

[24] Hinzman JM, Wilson JA, Mazzeo AT, Bullock MR, Hartings JA. Excitotoxicity and Metabolic Crisis Are Associated with Spreading Depolarizations in Severe Traumatic Brain Injury Patients. Journal of Neurotrauma. 2016 Oct;33(19):1775-83. Available from: https://doi.org/10.1089/neu.2015.4226.

[25] Stevens AR, Ng IHX, Helmy A, Hutchinson PJA, Menon DK, Ercole A. Glucose Dynamics of Cortical Spreading Depolarization in Acute Brain Injury: A Systematic Review. Journal of Neurotrauma. 2019 Jul;36(14):2153-66. Available from: https://doi.org/10.1089/neu.2018.6175.

[26] Mokri B. The Monro-Kellie hypothesis: Applications in CSF volume depletion. Neurology. 2001 Jun;56(12):1746-8. Available from: https://doi.org/10.1212/wnl.56.12.1746.

[27] Davalos D, Grutzendler J, Yang G, Kim JV, Zuo Y, Jung S, et al. ATP mediates rapid microglial response to local brain injury in vivo. Nature Neuroscience. 2005 May;8(6):752–758. Available from: http://dx.doi.org/10.1038/nn1472.

[28] Carney N, Totten AM, O'Reilly C, Ullman JS, Hawryluk GWJ, Bell MJ, et al. Guidelines for the Management of Severe Traumatic Brain Injury, Fourth Edition. Neurosurgery. 2016 Sep;80(1):6-15. Available from: https://doi.org/10.1227/neu.0000000000001432.

[29] Okonkwo DO, Shutter LA, Moore C, Temkin NR, Puccio AM, Madden CJ, et al. Brain Oxygen Optimization in Severe Traumatic Brain Injury Phase-II. Critical Care Medicine. 2017 Nov;45(11):1907-14. Available from: https://doi.org/10.1097/ccm.0000000000002619.

[30] Robba C, Taccone FS, Citerio G. Monitoring cerebral oxygenation in acute brain-injured patients. Intensive Care Medicine. 2022 Jul;48(10):1463-6. Available from: https://doi.org/10.1007/s00134-022-06788-w.

[31] Stovell MG, Helmy A, Thelin EP, Jalloh I, Hutchinson PJ, Carpenter KLH. An overview of clinical cerebral microdialysis in acute brain injury. Frontiers in Neurology. 2023 Feb;14. Available from: https://doi.org/10.3389/fneur.2023.1085540.

[32] Hachem LD, Ahuja CS, Fehlings MG. Assessment and management of acute spinal cord injury: From point of injury to rehabilitation. The Journal of Spinal Cord Medicine. 2017 Jun;40(6):665-75. Available from: https://doi.org/10.1080/10790268.2017.1329076.

[33] van den Berg MEL, Castellote JM, Mahillo-Fernandez I, de Pedro-Cuesta J. Incidence of Spinal Cord Injury Worldwide: A Systematic Review. Neuroepidemiology. 2010;34(3):184-92. Available from: https://doi.org/10.1159/000279335.

[34] Spinal Injuries Association. Spinal cord injury paralyses someone every four hours, new estimates reveal;. Available from: https://www.spinal.co.uk/news/spinal-cord-injury-paralyses-someone-every-four-hours-new-estimates-reveal/.

[35] McDaid D, Park AL, Gall A, Purcell M, Bacon M. Understanding and modelling the economic impact of spinal cord injuries in the United Kingdom. Spinal Cord. 2019 May;57(9):778-88. Available from: https://doi.org/10.1038/s41393-019-0285-1.

[36] Clifford T, Finkel Z, Rodriguez B, Joseph A, Cai L. Current Advancements in Spinal Cord Injury Research—Glial Scar Formation and Neural Regeneration. Cells. 2023 Mar;12(6):853. Available from: https://doi.org/10.3390/cells12060853.

[37] American Spinal Injury Association. International standards for neurological classification of spinal cord injury. Richmond, VA. 2019.

[38] Alizadeh A, Dyck SM, Karimi-Abdolrezaee S. Traumatic Spinal Cord Injury: An Overview of Pathophysiology, Models and Acute Injury Mechanisms. Frontiers in Neurology. 2019 Mar;10. Available from: https://doi.org/10.3389/fneur.2019.00282.

[39] van Middendorp JJ, Goss B, Urquhart S, Atresh S, Williams RP, Schuetz M. Diagnosis and Prognosis of Traumatic Spinal Cord Injury. Global Spine Journal. 2011 Dec;1(1):001-7. Available from: https://doi.org/10.1055/s-0031-1296049.

[40] van Middendorp JJ, Hosman AJ, Donders ART, Pouw MH, Ditunno JF, Curt A, et al. A clinical prediction rule for ambulation outcomes after traumatic spinal cord injury: a longitudinal cohort study. The Lancet. 2011 Mar;377(9770):1004-10. Available from: https://doi.org/10.1016/s0140-6736(10)62276-3.

[41] Diaz E, Morales H. Spinal Cord Anatomy and Clinical Syndromes. Seminars in Ultrasound, CT and MRI. 2016 Oct;37(5):360-71. Available from: https://doi.org/10.1053/j.sult.2016.05.002.

[42] McKinley W, Santos K, Meade M, Brooke K. Incidence and Outcomes of Spinal Cord Injury Clinical Syndromes. The Journal of Spinal Cord Medicine. 2007 Jan;30(3):215-24. Available from: https://doi.org/10.1080/10790268.2007.11753929.

[43] Wang TY, Park C, Zhang H, Rahimpour S, Murphy KR, Goodwin CR, et al. Management of Acute Traumatic Spinal Cord Injury: A Review of the Literature. Frontiers in Surgery. 2021 Dec;8. Available from: https://doi.org/10.3389/fsurg.2021.698736.

[44] Park E, Velumian AA, Fehlings MG. The Role of Excitotoxicity in Secondary Mechanisms of Spinal Cord Injury: A Review with an Emphasis on the Implications for White Matter Degeneration. Journal of Neurotrauma. 2004 Jun;21(6):754-74. Available from: https://doi.org/10.1089/0897715041269641.

[45] Shi Z, Yuan S, Shi L, Li J, Ning G, Kong X, et al. Programmed cell death in spinal cord injury pathogenesis and therapy. Cell Proliferation. 2021 Jan;54(3). Available from: https://doi.org/10.1111/cpr.12992.

[46] Jia Z, Zhu H, Li J, Wang X, Misra H, Li Y. Oxidative stress in spinal cord injury and antioxidant-based intervention. Spinal Cord. 2011 Oct;50(4):264-74. Available from: https://doi.org/10.1038/sc.2011.111.

[47] Cheng L, Cai B, Lu D, Zeng H. The role of mitochondrial energy metabolism in neuroprotection and axonal regeneration after spinal cord injury. Mitochondrion. 2023 Mar;69:57-63. Available from: https://doi.org/10.1016/j.mito.2023.01.009.

[48] Jin LY, Li J, Wang KF, Xia WW, Zhu ZQ, Wang CR, et al. Blood–Spinal Cord Barrier in Spinal Cord Injury: A Review. Journal of Neurotrauma. 2021 May;38(9):1203-24. Available from: https://doi.org/10.1089/neu.2020.7413.

[49] Chen J, Shen Y, Shao X, Wu W. An emerging role of inflammasomes in spinal cord injury and spinal cord tumor. Frontiers in Immunology. 2023 Mar;14:1119591. Available from: https://doi.org./10.3389/fimmu.2023.1119591.

[50] Beattie MS, Farooqui AA, Bresnahan JC. Review of Current Evidence for Apoptosis After Spinal Cord Injury. Journal of Neurotrauma. 2000 Oct;17(10):915-25. Available from: https://doi.org/10.1089/neu.2000.17.915.

[51] Mizuno Y, Mochizuki H, Sugita Y, Goto K. Apoptosis in Neurodegenerative Disorders. Internal Medicine. 1998;37(2):192-3. Available from: https://doi.org/10.2169/internalmedicine.37.192.

[52] Fitch MT, Silver J. CNS injury, glial scars, and inflammation: Inhibitory extracellular matrices and regeneration failure. Experimental Neurology. 2008 Feb;209(2):294-301. Available from: https://doi.org/10.1016/j.expneurol.2007.05.014.

[53] Committee on Trauma. Advanced Trauma Life Support. American College of Surgeons; 2018.

[54] National Institute for Health and Care Excellence (NICE). Spinal injury: assessment and initial management NG41;. Accessed: 2024-04-21. https://www.nice.org.uk/guidance/ng41.

[55] Theodore N, Hadley MN, Aarabi B, Dhall SS, Gelb DE, Hurlbert RJ, et al. Prehospital Cervical Spinal Immobilization After Trauma. Neurosurgery. 2013 Mar;72(supplement 2):22-34. Available from: https://doi.org/10.1227/neu.0b013e318276edb1.

[56] Hsieh YL, Tay J, Hsu SH, Chen WT, Fang YD, Liew CQ, et al. Early versus Late Surgical Decompression for Traumatic Spinal Cord Injury on Neurological Recovery: A Systematic Review and Meta-Analysis. Journal of Neurotrauma. 2021 Nov;38(21):2927-36. Available from: https://doi.org/10.1089/neu.2021.0102.

[57] Fehlings MG, Vaccaro A, Wilson JR, Singh A, Cadotte DW, Harrop JS, et al. Early versus Delayed Decompression for Traumatic Cervical Spinal Cord Injury: Results of the Surgical Timing in Acute Spinal Cord Injury Study (STASCIS). PLoS ONE. 2012 Feb;7(2):e32037. Available from: https://doi.org/10.1371/journal.pone.0032037.

[58] Maas AIR, Peul W, Thomé C. Surgical decompression in acute spinal cord injury: earlier is better. The Lancet Neurology. 2021 Feb;20(2):84-6. Available from: https://doi.org/10.1016/s1474-4422(20)30478-6.

[59] Bagnall AM, Jones L, Duffy S, Riemsma RP. Spinal fixation surgery for acute traumatic spinal cord injury. Cochrane Database of Systematic Reviews. 2008 Jan. Available from: https://doi.org/10.1002/14651858.cd004725.pub2.

[60] Squair JW, Bélanger LM, Tsang A, Ritchie L, Mac-Thiong JM, Parent S, et al. Spinal cord perfusion pressure predicts neurologic recovery in acute spinal cord injury. Neurology. 2017 Sep;89(16):1660-7. Available from: https://doi.org/10.1212/wnl.0000000000004519.

[61] Saadeh YS, Smith BW, Joseph JR, Jaffer SY, Buckingham MJ, Oppenlander ME, et al. The impact of blood pressure management after spinal cord injury: a systematic review of the literature. Neurosurgical Focus. 2017 Nov;43(5):E20. Available from: https://doi.org/10.3171/2017.8.focus17428.

[62] Hu X, Xu W, Ren Y, Wang Z, He X, Huang R, et al. Spinal cord injury: molecular mechanisms and therapeutic interventions. Signal Transduction and Targeted Therapy. 2023 Jun;8(1). Available from: https://doi.org/10.1038/s41392-023-01477-6.

[63] Assoian RK, Sporn MB. Type beta transforming growth factor in human platelets: release during platelet degranulation and action on vascular smooth muscle cells. The Journal of Cell Biology. 1986 Apr;102(4):1217-23. Available from: https://doi.org/10.1083/jcb.102.4.1217.

[64] Anjum A, Yazid MD, Daud MF, Idris J, Ng AMH, Naicker AS, et al. Spinal Cord Injury: Pathophysiology, Multimolecular Interactions, and Underlying Recovery Mechanisms. International Journal of Molecular Sciences. 2020 Oct;21(20):7533. Available from: https://doi.org/10.3390/ijms21207533.

[65] Nguyen HX, Beck KD, Anderson AJ. Quantitative Assessment of Immune Cells in the Injured Spinal Cord Tissue by Flow Cytometry: a Novel Use for a Cell Purification Method. Journal of Visualized Experiments. 2011 Apr;(50). Available from: https://doi.org/10.3791/2698.

[66] Simon DW, McGeachy MJ, Bayır H, Clark RSB, Loane DJ, Kochanek PM. The far-reaching scope of neuroinflammation after traumatic brain injury. Nature Reviews Neurology. 2017 Feb;13(3):171-91. Available from: https://doi.org/10.1038/nrneurol.2017.13.

[67] Tang Y, Le W. Differential Roles of M1 and M2 Microglia in Neurodegenerative Diseases. Molecular Neurobiology. 2015 Jan;53(2):1181-94. Available from: https://doi.org/10.1007/s12035-014-9070-5.

[68] Jurga AM, Paleczna M, Kuter KZ. Overview of General and Discriminating Markers of Differential Microglia Phenotypes. Frontiers in Cellular Neuroscience. 2020 Aug;14. Available from: https://doi.org/10.3389/fncel.2020.00198.

[69] Zhou T, Huang Z, Sun X, Zhu X, Zhou L, Li M, et al. Microglia Polarization with M1/M2 Phenotype Changes in rd1 Mouse Model of Retinal Degeneration. Frontiers in Neuroanatomy. 2017 Sep;11. Available from: https://doi.org/10.3389/fnana.2017.00077.

[70] Healy LM, Zia S, Plemel JR. Towards a definition of microglia heterogeneity. Communications Biology. 2022 Oct;5(1). Available from: http://dx.doi.org/10.1038/s42003-022-04081-6.

[71] Wang J, He W, Zhang J. A richer and more diverse future for microglia phenotypes. Heliyon. 2023 Apr;9(4):e14713. Available from: http://dx.doi.org/10.1016/j.heliyon.2023.e14713.

[72] Shaito A, Kobeissy F, Haidar MA, Ibeh S, Shakkour Z, Reslan MA, et al. Crosstalk between Microglia and Neurons in Neurotrauma: An Overview of the Underlying Mechanisms. Current Neuropharmacology. 2022 Nov;20(11):2050-65. Available from: https://doi.org/10.2174/1570159x19666211202123322.

[73] Wang X, Cao K, Sun X, Chen Y, Duan Z, Sun L, et al. Macrophages in spinal cord injury: Phenotypic and functional change from exposure to myelin debris. Glia. 2014 Nov;63(4):635-51. Available from: https://doi.org/10.1002/glia.22774.

[74] Sun G, Yang S, Cao G, Wang Q, Hao J, Wen Q, et al. $\gamma\delta$ T cells provide the early source of IFN-γ to aggravate lesions in spinal cord injury. Journal of Experimental Medicine. 2017 Dec;215(2):521-35. Available from: https://doi.org/10.1084/jem.20170686.

[75] Liu Z, Yang Y, He L, Pang M, Luo C, Liu B, et al. High-dose methylprednisolone for acute traumatic spinal cord injury. Neurology. 2019 Jul;93(9):e841-50. Available from: https://doi.org/10.1212/wnl.0000000000007998.

[76] Hu JG, Shi LL, Chen YJ, Xie XM, Zhang N, Zhu AY, et al. Differential effects of myelin basic protein-activated Th1 and Th2 cells on the local immune microenvironment of injured spinal cord. Experimental Neurology. 2016 Mar;277:190-201. Available from: https://doi.org/10.1016/j.expneurol.2016.01.002.

[77] Landeghem FKHV, Weiss T, Oehmichen M, Deimling AV. Decreased Expression of Glutamate Transporters in Astrocytes after Human Traumatic Brain Injury. Journal of Neurotrauma. 2006 Oct;23(10):1518-28. Available from: https://doi.org/10.1089/neu.2006.23.1518.

[78] Halsey A, Conner A, Bill R, Logan A, Ahmed Z. Aquaporins and Their Regulation after Spinal Cord Injury. Cells. 2018 Oct;7(10):174. Available from: https://doi.org/10.3390/cells7100174.

[79] Papadopoulos MC, Verkman AS. Aquaporin-4 and brain edema. Pediatric Nephrology. 2007 Jun;22(6):778-84. Available from: https://doi.org/10.1007/s00467-006-0411-0.

[80] Hamblin MR. Shining light on the head: Photobiomodulation for brain disorders. BBA Clinical. 2016 Dec;6:113-24. Available from: https://doi.org/10.1016/j.bbacli.2016.09.002.

[81] Hamblin MR. Photobiomodulation for Traumatic Brain Injury and Stroke. Journal of Neuroscience Research. 2019 Jan;97(3):373-3. Available from: https://doi.org/10.1002/jnr.24376.

[82] de Freitas LF, Hamblin MR. Proposed Mechanisms of Photobiomodulation or Low-Level Light Therapy. IEEE Journal of Selected Topics in Quantum Electronics. 2016 May;22(3):348-64. Available from: https://doi.org/10.1109/jstqe.2016.2561201.

[83] Hamblin MR. Photobiomodulation for traumatic brain injury and stroke. Journal of Neuroscience Research. 2017 Nov;96(4):731-43. Available from: https://doi.org/10.1002/jnr.24190.

[84] Liu C, Liu Y, Ma B, Zhou M, Zhao X, Fu X, et al. Mitochondrial regulatory mechanisms in spinal cord injury: A narrative review. Medicine. 2022 Nov;101(46):e31930. Available from: https://doi.org/10.1097/md.0000000000031930.

[85] Cheng G, hua Kong R, ming Zhang L, ning Zhang J. Mitochondria in traumatic brain injury and mitochondrial-targeted multipotential therapeutic strategies. British Journal of Pharmacology. 2012 Sep;167(4):699-719. Available from: https://doi.org/10.1111/j.1476-5381.2012.02025.x.

[86] Slater PG, Domínguez-Romero ME, Villarreal M, Eisner V, Larraín J. Mitochondrial function in spinal cord injury and regeneration. Cellular and Molecular Life Sciences. 2022 Apr;79(5). Available from: https://doi.org/10.1007/s00018-022-04261-x.

[87] Venturini S, Bhatti F, Timofeev I, Carpenter KLH, Hutchinson PJ, Guilfoyle MR, et al. Microdialysis-Based Classifications of Abnormal Metabolic States after Traumatic Brain Injury: A Systematic Review of the Literature. Journal of Neurotrauma. 2023 Feb;40(3–4):195–209. Available from: http://dx.doi.org/10.1089/neu.2021.0502.

[88] Brooks GA, Martin NA. Cerebral metabolism following traumatic brain injury: new discoveries with implications for treatment. Frontiers in Neuroscience. 2015 Feb;8. Available from: http://dx.doi.org/10.3389/fnins.2014.00408.

[89] Ryan AK, Rich W, Reilly MA. Oxidative stress in the brain and retina after traumatic injury. Frontiers in Neuroscience. 2023 Feb;17. Available from: http://dx.doi.org/10.3389/fnins.2023.1021152.

[90] Hakiminia B, Alikiaii B, Khorvash F, Mousavi S. Oxidative stress and mitochondrial dysfunction following traumatic brain injury: From mechanistic view to targeted therapeutic opportunities. Fundamental amp; Clinical Pharmacology. 2022 Feb;36(4):612–662. Available from: http://dx.doi.org/10.1111/fcp.12767.

[91] Guilfoyle MR, Helmy A, Donnelly J, Stovell MG, Timofeev I, Pickard JD, et al. Characterising the dynamics of cerebral metabolic dysfunction following traumatic brain injury:

A microdialysis study in 619 patients. PLOS ONE. 2021 Dec;16(12):e0260291. Available from: http://dx.doi.org/10.1371/journal.pone.0260291.

[92] Forman HJ, Zhang H. Targeting oxidative stress in disease: promise and limitations of antioxidant therapy. Nature Reviews Drug Discovery. 2021 Jun;20(9):689–709. Available from: http://dx.doi.org/10.1038/s41573-021-00233-1.

[93] Olas B, Wachowicz B. Role of reactive nitrogen species in blood platelet functions. Platelets. 2007 Jan;18(8):555–565. Available from: http://dx.doi.org/10.1080/09537100701504087.

[94] Nguyen A, Patel AB, Kioutchoukova IP, Diaz MJ, Lucke-Wold B. Mechanisms of Mitochondrial Oxidative Stress in Brain Injury: From Pathophysiology to Therapeutics. Oxygen. 2023 Apr;3(2):163–178. Available from: http://dx.doi.org/10.3390/oxygen3020012.

[95] van Niekerk EA, Tuszynski MH, Lu P, Dulin JN. Molecular and Cellular Mechanisms of Axonal Regeneration After Spinal Cord Injury. Molecular & Cellular Proteomics. 2016 Feb;15(2):394-408. Available from: https://doi.org/10.1074/mcp.r115.053751.

[96] Gordon T. The role of neurotrophic factors in nerve regeneration. Neurosurgical Focus. 2009 Feb;26(2):E3. Available from: https://doi.org/10.3171%2Ffoc.2009.26.2.e3.

[97] Silver J, Miller JH. Regeneration beyond the glial scar. Nature Reviews Neuroscience. 2004 Feb;5(2):146-56. Available from: https://doi.org/10.1038/nrn1326.

[98] Sofroniew MV, Vinters HV. Astrocytes: biology and pathology. Acta Neuropathologica. 2009 Dec;119(1):7–35. Available from: http://dx.doi.org/10.1007/s00401-009-0619-8.

[99] Cunningham C, Dunne A, Lopez-Rodriguez AB. Astrocytes: Heterogeneous and Dynamic Phenotypes in Neurodegeneration and Innate Immunity. The Neuroscientist. 2018 Nov;25(5):455–474. Available from: http://dx.doi.org/10.1177/1073858418809941.

[100] Zamanian JL, Xu L, Foo LC, Nouri N, Zhou L, Giffard RG, et al. Genomic Analysis of Reactive Astrogliosis. The Journal of Neuroscience. 2012 May;32(18):6391-410. Available from: https://doi.org/10.1523/jneurosci.6221-11.2012.

[101] Liddelow SA, Guttenplan KA, Clarke LE, Bennett FC, Bohlen CJ, Schirmer L, et al. Neurotoxic reactive astrocytes are induced by activated microglia. Nature. 2017 Jan;541(7638):481-7. Available from: https://doi.org/10.1038/nature21029.

[102] Liddelow SA, Barres BA. Reactive astrocytes: production, function, and therapeutic potential. Immunity. 2017;46(6):957-67. Available from: https://doi.org/10.1016/j.immuni.2017.06.006.

[103] Hyvärinen T, Hagman S, Ristola M, Sukki L, Veijula K, Kreutzer J, et al. Co-stimulation with IL-1β and TNF-α induces an inflammatory reactive astrocyte phenotype with neurosupportive characteristics in a human pluripotent stem cell model system. Scientific Reports. 2019 Nov;9(1). Available from: https://doi.org/10.1038/s41598-019-53414-9.

[104] Herrmann JE, Imura T, Song B, Qi J, Ao Y, Nguyen TK, et al. STAT3 is a Critical Regulator of Astrogliosis and Scar Formation after Spinal Cord Injury. The Journal of Neuroscience. 2008 Jul;28(28):7231-43. Available from: https://doi.org/10.1523/jneurosci.1709-08.2008.

[105] Anderson MA, Burda JE, Ren Y, Ao Y, O'Shea TM, Kawaguchi R, et al. Astrocyte scar formation aids central nervous system axon regeneration. Nature. 2016 Mar;532(7598):195-200. Available from: https://doi.org/10.1038/nature17623.

[106] Huber RE, Babbitt C, Peyton SR. Heterogeneity of brain extracellular matrix and astrocyte activation. Journal of Neuroscience Research. 2024 May;102(5). Available from: http://dx.doi.org/10.1002/jnr.25356.

[107] Winkler EA, Bell RD, Zlokovic BV. Central nervous system pericytes in health and disease. Nature Neuroscience. 2011 Oct;14(11):1398-405. Available from: https://doi.org/10.1038/nn.2946.

[108] Huntemer-Silveira A, Patil N, Brickner MA, Parr AM. Strategies for Oligodendrocyte and Myelin Repair in Traumatic CNS Injury. Frontiers in Cellular Neuroscience. 2021 Jan;14. Available from: https://doi.org/10.3389/fncel.2020.619707.

[109] Cox AL, Coles AJ, Nortje J, Bradley PG, Chatfield DA, Thompson SJ, et al. An investigation of auto-reactivity after head injury. Journal of Neuroimmunology. 2006 May;174(1-2):180-6. Available from: https://doi.org/10.1016/j.jneuroim.2006.01.007.

[110] Aghili-Mehrizi S, Williams E, Yan S, Willman M, Willman J, Lucke-Wold B. Secondary Mechanisms of Neurotrauma: A Closer Look at the Evidence. Diseases. 2022 May;10(2):30. Available from: https://doi.org/10.3390/diseases10020030.

[111] Raghupathi R, Graham DI, McIntosh TK. Apoptosis After Traumatic Brain Injury. Journal of Neurotrauma. 2000 Oct;17(10):927-38. Available from: https://doi.org/10.1089/neu.2000.17.927.

[112] Bredesen DE. Apoptosis: Overview and Signal Transduction Pathways. Journal of Neurotrauma. 2000 Oct;17(10):801-10. Available from: https://doi.org/10.1089/neu.2000.17.801.

[113] McIlwain DR, Berger T, Mak TW. Caspase Functions in Cell Death and Disease. Cold Spring Harbor Perspectives in Biology. 2013 Apr;5(4):a008656-6. Available from: https://doi.org/10.1101/cshperspect.a008656.

[114] Surey S, Berry M, Logan A, Bicknell R, Ahmed Z. Differential cavitation, angiogenesis and wound-healing responses in injured mouse and rat spinal cords. Neuroscience. 2014 Sep;275:62-80. Available from: https://doi.org/10.1016/j.neuroscience.2014.06.003.

[115] Coulthard MG, Morgan M, Woodruff TM, Arumugam TV, Taylor SM, Carpenter TC, et al. Eph/Ephrin Signaling in Injury and Inflammation. The American Journal of Pathology. 2012 Nov;181(5):1493-503. Available from: https://doi.org/10.1016/j.ajpath.2012.06.043.

[116] Winter FD, Oudega M, Lankhorst AJ, Hamers FP, Blits B, Ruitenberg MJ, et al. Injury-Induced Class 3 Semaphorin Expression in the Rat Spinal Cord. Experimental Neurology. 2002 May;175(1):61-75. Available from: https://doi.org/10.1006/exnr.2002.7884.

[117] Frendo ME, da Silva A, Phan KD, Riche S, Butler SJ. The Cofilin/Limk1 Pathway Controls the Growth Rate of Both Developing and Regenerating Motor Axons. The Journal of

Neuroscience. 2019 Oct;39(47):9316-27. Available from: https://doi.org/10.1523/jneurosci.0648-19.2019.

[118] Meeker R, Williams K. The p75 neurotrophin receptor: at the crossroad of neural repair and death. Neural Regeneration Research. 2015;10(5):721. Available from: https://doi.org/10.4103/1673-5374.156967.

[119] Amatu A, Sartore-Bianchi A, Siena S. NTRK gene fusions as novel targets of cancer therapy across multiple tumour types. ESMO Open. 2016;1(2):e000023. Available from: https://doi.org/10.1136/esmoopen-2015-000023.

[120] Haddad Y, Adam V, Heger Z. Trk Receptors and Neurotrophin Cross-Interactions: New Perspectives Toward Manipulating Therapeutic Side-Effects. Frontiers in Molecular Neuroscience. 2017 May;10. Available from: https://doi.org/10.3389/fnmol.2017.00130.

[121] Bracken MB, Shepard MJ, Collins WF, Holford TR, Young W, Baskin DS, et al. A Randomized, Controlled Trial of Methylprednisolone or Naloxone in the Treatment of Acute Spinal-Cord Injury. New England Journal of Medicine. 1990 May;322(20):1405-11. Available from: https://doi.org/10.1056/nejm199005173222001.

[122] Geisler FH, Moghaddamjou A, Wilson JRF, Fehlings MG. Methylprednisolone in acute traumatic spinal cord injury: case-matched outcomes from the NASCIS2 and Sygen historical spinal cord injury studies with contemporary statistical analysis. Journal of Neurosurgery: Spine. 2023 Jan:1-12. Available from: https://doi.org/10.3171/2022.12.spine22713.

[123] Evaniew N, Belley-Côté EP, Fallah N, Noonan VK, Rivers CS, Dvorak MF. Methylprednisolone for the Treatment of Patients with Acute Spinal Cord Injuries: A Systematic Review and Meta-Analysis. Journal of Neurotrauma. 2016 Mar;33(5):468-81. Available from: https://doi.org/10.1089/neu.2015.4192.

[124] Roberts I, Yates D, Sandercock P, Farrell B, Wasserberg J, Lomas G, et al. Effect of intravenous corticosteroids on death within 14 days in 10 008 adults with clinically significant

head injury (MRC CRASH trial): randomised placebo-controlled trial. The Lancet. 2004 Oct;364(9442):1321-8. Available from: https://doi.org/10.1016/s0140-6736(04)17188-2.

[125] Wilson JR, Doty S, Petitt JC, El-Abtah M, Francis JJ, Sharpe MG, et al. Feasibility of gabapentin as an intervention for neurorecovery after an acute spinal cord injury: Protocol. Frontiers in Neurology. 2022 Nov;13. Available from: https://doi.org/10.3389/fneur.2022.1033386.

[126] Wilson JR, Forgione N, Fehlings MG. Emerging therapies for acute traumatic spinal cord injury. Canadian Medical Association Journal. 2012 Dec;185(6):485-92. Available from: https://doi.org/10.1503/cmaj.121206.

[127] Cragg JJ, Haefeli J, Jutzeler CR, Röhrich F, Weidner N, Saur M, et al. Effects of Pain and Pain Management on Motor Recovery of Spinal Cord–Injured Patients. Neurorehabilitation and Neural Repair. 2016 Jul;30(8):753-61. Available from: https://doi.org/10.1177/1545968315624777.

[128] Warner FM, Cragg JJ, Jutzeler CR, Röhrich F, Weidner N, Saur M, et al. Early Administration of Gabapentinoids Improves Motor Recovery after Human Spinal Cord Injury. Cell Reports. 2017 Feb;18(7):1614-8. Available from: https://doi.org/10.1016/j.celrep.2017.01.048.

[129] van Hedel HJA, Curt A. Fighting for Each Segment: Estimating the Clinical Value of Cervical and Thoracic Segments in SCI. Journal of Neurotrauma. 2006 Nov;23(11):1621-31. Available from: https://doi.org/10.1089/neu.2006.23.1621.

[130] Warner FM, Jutzeler CR, Cragg JJ, Tong B, Grassner L, Bradke F, et al. The Effect of Non-Gabapentinoid Anticonvulsants on Sensorimotor Recovery After Human Spinal Cord Injury. CNS Drugs. 2019 Apr;33(5):503-11. Available from: https://doi.org/10.1007/s40263-019-00622-6.

[131] Saadoun S, Papadopoulos MC. Spinal cord injury: is monitoring from the injury site the future? Critical Care. 2016 Oct;20(1). Available from: https://doi.org/10.1186/s13054-016-1490-3.

[132] Saadoun S, Papadopoulos MC. Targeted Perfusion Therapy in Spinal Cord Trauma. Neurotherapeutics. 2020 Jan;17(2):511-21. Available from: https://doi.org/10.1007/s13311-019-00820-6.

[133] Saadoun S, Papadopoulos MC. Acute, Severe Traumatic Spinal Cord Injury. Neurosurgery Clinics of North America. 2021 Jul;32(3):365-76. Available from: https://doi.org/10.1016/j.nec.2021.03.008.

[134] Papadopoulos M, Saadoun S, Sinai P. Does duroplasty improve outcomes after spinal cord injury?. Springer Science and Business Media LLC; 2021. Available from: https://doi.org/10.1186/isrctn25573423.

[135] Kwon BK, Curt A, Belanger LM, Bernardo A, Chan D, Markez JA, et al. Intrathecal pressure monitoring and cerebrospinal fluid drainage in acute spinal cord injury: a prospective randomized trial. Journal of Neurosurgery: Spine. 2009 Mar;10(3):181-93. Available from: https://doi.org/10.3171/2008.10.spine08217.

[136] Kim HN, McCrea MR, Li S. Advances in molecular therapies for targeting pathophysiology in spinal cord injury. Expert Opinion on Therapeutic Targets. 2023 Apr:1-17. Available from: https://doi.org/10.1080/14728222.2023.2194532.

[137] Hutchinson PJ, Kolias AG, Timofeev IS, Corteen EA, Czosnyka M, Timothy J, et al. Trial of Decompressive Craniectomy for Traumatic Intracranial Hypertension. New England Journal of Medicine. 2016 Sep;375(12):1119–1130. Available from: http://dx.doi.org/10.1056/NEJMoa1605215.

[138] Andrews PJD, Sinclair HL, Rodriguez A, Harris BA, Battison CG, Rhodes JKJ, et al. Hypothermia for Intracranial Hypertension after Traumatic Brain Injury. New England Journal of Medicine. 2015 Dec;373(25):2403–2412. Available from: http://dx.doi.org/10.1056/NEJMoa1507581.

[139] Zafonte RD, Bagiella E, Ansel BM, Novack TA, Friedewald WT, Hesdorffer DC, et al. Effect of Citicoline on Functional and Cognitive Status Among Patients With Traumatic Brain

Injury: Citicoline Brain Injury Treatment Trial (COBRIT). JAMA. 2012 Nov;308(19):1993. Available from: http://dx.doi.org/10.1001/jama.2012.13256.

[140] Maas AI, Murray G, Henney H, Kassem N, Legrand V, Mangelus M, et al. Efficacy and safety of dexanabinol in severe traumatic brain injury: results of a phase III randomised, placebo-controlled, clinical trial. The Lancet Neurology. 2006 Jan;5(1):38–45. Available from: http://dx.doi.org/10.1016/S1474-4422(05)70253-2.

[141] Nichol A, French C, Little L, Haddad S, Presneill J, Arabi Y, et al. Erythropoietin in traumatic brain injury (EPO-TBI): a double-blind randomised controlled trial. The Lancet. 2015 Dec;386(10012):2499–2506. Available from: http://dx.doi.org/10.1016/S0140-6736(15)00386-4.

[142] Temkin NR, Anderson GD, Winn HR, Ellenbogen RG, Britz GW, Schuster J, et al. Magnesium sulfate for neuroprotection after traumatic brain injury: a randomised controlled trial. The Lancet Neurology. 2007 Jan;6(1):29–38. Available from: http://dx.doi.org/10.1016/S1474-4422(06)70630-5.

[143] Edwards, P, Arango, M, Balica, L, Cottingham, R, El-Sayed, H, Farrell, B, et al. Final results of MRC CRASH, a randomised placebo-controlled trial of intravenous corticosteroid in adults with head injury-outcomes at 6 months. The Lancet. 2005. Available from: https://www.zora.uzh.ch/id/eprint/19833.

[144] Skolnick BE, Maas AI, Narayan RK, van der Hoop RG, MacAllister T, Ward JD, et al. A Clinical Trial of Progesterone for Severe Traumatic Brain Injury. New England Journal of Medicine. 2014 Dec;371(26):2467–2476. Available from: http://dx.doi.org/10.1056/NEJMoa1411090.

[145] Tadie M, Gaviria M, Mathe JF, Menthonnex P, Loubert G, Lagarrigue J, et al. Early care and treatment with a neuroprotective drug, gacyclidine, in patients with acute spinal cord injury. Rachis. 2003;15:363-76.

[146] Bracken MB. Administration of Methylprednisolone for 24 or 48 Hours or Tirilazad Mesylate for 48 Hours in the Treatment of Acute Spinal Cord Injury: Results of the Third National Acute Spinal Cord Injury Randomized Controlled Trial. JAMA. 1997 May;277(20):1597. Available from: http://dx.doi.org/10.1001/jama.1997.03540440031029.

[147] Tani J, Wen YT, Hu CJ, Sung JY. Current and potential pharmacologic therapies for traumatic brain injury. Pharmaceuticals (Basel). 2022 Jul;15(7):838.

[148] Ahmed Z. Current Clinical Trials in Traumatic Brain Injury. Brain Sciences. 2022 Apr;12(5):527. Available from: https://doi.org/10.3390/brainsci12050527.

[149] Chung H, Dai T, Sharma SK, Huang YY, Carroll JD, Hamblin MR. The Nuts and Bolts of Low-level Laser (Light) Therapy. Annals of Biomedical Engineering. 2011 Nov;40(2):516-33. Available from: https://doi.org/10.1007/s10439-011-0454-7.

[150] Bigio IJ, Fantini S. Quantitative Biomedical Optics. Cambridge University Press; 2016. Available from: https://doi.org/10.1017/cbo9781139029797.

[151] Jacques SL. Optical properties of biological tissues: a review. Physics in Medicine and Biology. 2013 May;58(11):R37-61. Available from: https://doi.org/10.1088/0031-9155/58/11/r37.

[152] Baskar R, Dai J, Wenlong N, Yeo R, Yeoh KW. Biological response of cancer cells to radiation treatment. Frontiers in Molecular Biosciences. 2014 Nov;1. Available from: https://doi.org/10.3389/fmolb.2014.00024.

[153] Cohen–Jonathan E, Bernhard EJ, McKenna WG. How does radiation kill cells? Current Opinion in Chemical Biology. 1999 Feb;3(1):77-83. Available from: https://doi.org/10.1016/s1367-5931(99)80014-3.

[154] Serrage H, Heiskanen V, Palin WM, Cooper PR, Milward MR, Hadis M, et al. Under the spotlight: mechanisms of photobiomodulation concentrating on blue and green light.

Photochemical & Photobiological Sciences. 2019 Aug;18(8):1877-909. Available from: https://doi.org/10.1039/c9pp00089e.

[155] Tsai SR, Hamblin MR. Biological effects and medical applications of infrared radiation. Journal of Photochemistry and Photobiology B: Biology. 2017 May;170:197-207. Available from: https://doi.org/10.1016/j.jphotobiol.2017.04.014.

[156] Mumtaz S, Rana JN, Choi EH, Han I. Microwave Radiation and the Brain: Mechanisms, Current Status, and Future Prospects. International Journal of Molecular Sciences. 2022 Aug;23(16):9288. Available from: https://doi.org/10.3390/ijms23169288.

[157] Kesari KK, Jamal QMS, Sharma A, Chauhan P, Dhasmana A, Siddiqui MH, et al. LPO and ROS Production in Rat Brain Exposed to Microwaves: Computational Elucidation of Melatonin in Repair System. In: Perspectives in Environmental Toxicology. Springer International Publishing; 2017. p. 31-46. Available from: https://doi.org/10.1007/978-3-319-46248-6_2.

[158] Stokowski LA. Fundamentals of phototherapy for neonatal jaundice. Advances in Neonatal Care. 2006 Dec;6(6):303-12. Available from: https://doi.org/10.1016/j.adnc.2006.08.004.

[159] McDonagh AF. Light Effects on Transport and Excretion of Bilirubin in Newbornsa. Annals of the New York Academy of Sciences. 1985 Sep;453(1):65-72. Available from: https://doi.org/10.1111/j.1749-6632.1985.tb11798.x.

[160] Smith AM, Mancini MC, Nie S. Second window for in vivo imaging. Nature Nanotechnology. 2009 Nov;4(11):710-1. Available from: https://doi.org/10.1038/nnano.2009.326.

[161] Hale GM, Querry MR. Optical constants of water in the 200nm to 200 micron wavelength region. Appl Opt. 1973;12:555-63. Available from: https://omlc.org/spectra/water/data/hale73.txt.

[162] Prahl S. Tabulated Molar Extinction Coefficient for Hemoglobin in Water;. https://omlc.org/spectra/hemoglobin/summary.html.

[163] Davies DJ, Su Z, Clancy MT, Lucas SJE, Dehghani H, Logan A, et al. Near-Infrared Spectroscopy in the Monitoring of Adult Traumatic Brain Injury: A Review. Journal of Neurotrauma. 2015 Jul;32(13):933-41. Available from: https://doi.org/10.1089/neu.2014.3748.

[164] Stepp H, Stummer W. 5-ALA in the management of malignant glioma. Lasers in Surgery and Medicine. 2018 May;50(5):399-419. Available from: https://doi.org/10.1002/lsm.22933.

[165] Calabrese EJ. Hormesis and medicine. British Journal of Clinical Pharmacology. 2008 Aug:94–617. Available from: https://doi.org/10.1111/j.1365-2125.2008.03243.x.

[166] Huang YY, Chen ACH, Carroll JD, Hamblin MR. Biphasic Dose Response in Low Level Light Therapy. Dose-Response. 2009 Sep;7(4):358–383. Available from: https://doi.org/10.2203/dose-response.09-027.hamblin.

[167] Huang YY, Sharma SK, Carroll J, Hamblin MR. Biphasic Dose Response in Low Level Light Therapy – an Update. Dose-Response. 2011 Sep;9(4):dose-response.1. Available from: https://doi.org/10.2203/dose-response.11-009.hamblin.

[168] Xuan W, Huang L, Hamblin MR. Repeated transcranial low-level laser therapy for traumatic brain injury in mice: biphasic dose response and long-term treatment outcome. Journal of Biophotonics. 2016 Mar;9(11-12):1263-72. Available from: https://doi.org/10.1002/jbio.201500336.

[169] Luna GLF, de Andrade ALM, Brassolatti P, Bossini PS, de Freitas Anibal F, Parizotto NA, et al. Biphasic Dose/Response of Photobiomodulation Therapy on Culture of Human Fibroblasts. Photobiomodulation, Photomedicine, and Laser Surgery. 2020 Jul;38(7):413-8. Available from: https://doi.org/10.1089/photob.2019.4729.

[170] Sharma SK, Kharkwal GB, Sajo M, Huang YY, Taboada LD, McCarthy T, et al. Dose response effects of 810 nm laser light on mouse primary cortical neurons. Lasers in Surgery and Medicine. 2011 Sep;43(8):851-9. Available from: https://doi.org/10.1002/lsm.21100.

[171] Suski JM, Lebiedzinska M, Bonora M, Pinton P, Duszynski J, Wieckowski MR. Relation Between Mitochondrial Membrane Potential and ROS Formation. In: Mitochondrial Bioenergetics. Humana Press; 2011. p. 183-205. Available from: https://doi.org/10.1007/978-1-61779-382-0_12.

[172] Yang B, Xu J, Li Y, Dong Y, Li Y, Tucker L, et al. Photobiomodulation therapy for repeated closed head injury in rats. Journal of Biophotonics. 2019 Nov;13(2). Available from: https://doi.org/10.1002/jbio.201960117.

[173] Esenaliev RO, Petrov IY, Petrov Y, Guptarak J, Boone DR, Mocciaro E, et al. Nano-Pulsed Laser Therapy Is Neuroprotective in a Rat Model of Blast-Induced Neurotrauma. Journal of Neurotrauma. 2018 Jul;35(13):1510-22. Available from: https://doi.org/10.1089/neu.2017.5249.

[174] Xuan W, Vatansever F, Huang L, Hamblin MR. Transcranial low-level laser therapy enhances learning, memory, and neuroprogenitor cells after traumatic brain injury in mice. Journal of Biomedical Optics. 2014 Oct;19(10):108003. Available from: https://doi.org/10.1117/1.jbo.19.10.108003.

[175] Vatansever F, Xuan W, Huang YY, Hamblin MR. Transcranial low-level light therapy produces neuroprotection, neurogenesis and BDNF after TBI in mice. In: Hamblin MR, Carroll JD, Arany PR, editors. SPIE Proceedings. SPIE; 2013. Available from: https://doi.org/10.1117/12.2001900.

[176] Khuman J, Zhang J, Park J, Carroll JD, Donahue C, Whalen MJ. Low-Level Laser Light Therapy Improves Cognitive Deficits and Inhibits Microglial Activation after Controlled Cortical Impact in Mice. Journal of Neurotrauma. 2012 Jan;29(2):408-17. Available from: https://doi.org/10.1089/neu.2010.1745.

[177] Longo MGF, Tan CO, tak Chan S, Welt J, Avesta A, Ratai E, et al. Effect of Transcranial Low-Level Light Therapy vs Sham Therapy Among Patients With Moderate Traumatic

Brain Injury. JAMA Network Open. 2020 Sep;3(9):e2017337. Available from: https://doi.org/10.1001/jamanetworkopen.2020.17337.

[178] Schawlow AL, Townes CH. Infrared and Optical Masers. Physical Review. 1958 Dec;112(6):1940-9. Available from: https://doi.org/10.1103/physrev.112.1940.

[179] Maiman TH. Stimulated Optical Radiation in Ruby. Nature. 1960 Aug;187(4736):493-4. Available from: https://doi.org/10.1038/187493a0.

[180] Mester E, Szende B, Gärtner P. The effect of laser beams on the growth of hair in mice. Radiobiology and Radiotherapy (Berl). 1968;9(5):621-6.

[181] Hadis MA, Zainal SA, Holder MJ, Carroll JD, Cooper PR, Milward MR, et al. The dark art of light measurement: accurate radiometry for low-level light therapy. Lasers in Medical Science. 2016 Mar;31(4):789-809. Available from: https://doi.org/10.1007/s10103-016-1914-y.

[182] Dompe C, Moncrieff L, Matys J, Grzech-Leśniak K, Kocherova I, Bryja A, et al. Photobiomodulation—Underlying Mechanism and Clinical Applications. Journal of Clinical Medicine. 2020 Jun;9(6):1724. Available from: https://doi.org/10.3390/jcm9061724.

[183] Zhang P, Wu MX. A clinical review of phototherapy for psoriasis. Lasers in Medical Science. 2017 Oct;33(1):173-80. Available from: https://doi.org/10.1007/s10103-017-2360-1.

[184] Li Y, Cao Z, Guo J, Li Q, Zhu W, Kuang Y, et al. Assessment of efficacy and safety of UV-based therapy for psoriasis: a network meta-analysis of randomized controlled trials. Annals of Medicine. 2022 Jan;54(1):159–169. Available from: http://dx.doi.org/10.1080/07853890.2021.2022187.

[185] Yadav A, Gupta A. Noninvasive red and near-infrared wavelength-induced photobiomodulation: promoting impaired cutaneous wound healing. Photodermatology, Photoimmunology & Photomedicine. 2017 Jan;33(1):4-13. Available from: https://doi.org/10.1111/phpp.12282.

[186] Dhlamini T, Houreld NN. Clinical Effect of Photobiomodulation on Wound Healing of Diabetic Foot Ulcers: Does Skin Color Needs to Be Considered? Journal of Diabetes Research. 2022 Dec;2022:1–12. Available from: http://dx.doi.org/10.1155/2022/3312840.

[187] Baxter GD, Liu L, Petrich S, Gisselman AS, Chapple C, Anders JJ, et al. Low level laser therapy (Photobiomodulation therapy) for breast cancer-related lymphedema: a systematic review. BMC Cancer. 2017 Dec;17(1). Available from: https://doi.org/10.1186/s12885-017-3852-x.

[188] Cronshaw M, Parker S, Anagnostaki E, Mylona V, Lynch E, Grootveld M. Photobiomodulation and Oral Mucositis: A Systematic Review. Dentistry Journal. 2020 Aug;8(3):87. Available from: https://doi.org/10.3390/dj8030087.

[189] National Institute for Health and Care Excellence (NICE). Low-level laser therapy for preventing or treating oral mucositis caused by radiotherapy or chemotherapy IPG615;. Accessed: 2023-07-21. https://www.nice.org.uk/guidance/ipg615.

[190] Ocon CA, dos Santos SA, Caires JR, de Oliveira MFD, Serra AJ, Leal-Junior EC, et al. Effects and parameters of the photobiomodulation in experimental models of third-degree burn: systematic review. Lasers in Medical Science. 2018 Sep;34(3):637-48. Available from: https://doi.org/10.1007/s10103-018-2633-3.

[191] Brassolatti P, de Andrade ALM, Bossini PS, Otterço AN, Parizotto NA. Evaluation of the low-level laser therapy application parameters for skin burn treatment in experimental model: a systematic review. Lasers in Medical Science. 2018 May;33(5):1159–1169. Available from: http://dx.doi.org/10.1007/s10103-018-2526-5.

[192] Lu YS, Chen YJ, Lee CL, Kuo FY, Tseng YH, Chen CH. Effects of photobiomodulation as an adjunctive treatment in chronic obstructive pulmonary disease: a narrative review. Lasers in Medical Science. 2023 Jan;38(1). Available from: https://doi.org/10.1007/s10103-022-03661-6.

[193] da Silva Tonetto L, da Silva CCF, Gonzatti N, Guex CG, Hartmann DD, Boschi ES, et al. Effects of photobiomodulation on oxidative stress in rats with type 2 diabetes mellitus. Lasers in Medical Science. 2023 Mar;38(1). Available from: https://doi.org/10.1007/s10103-023-03745-x.

[194] Bian J, Liebert A, Bicknell B, Chen XM, Huang C, Pollock CA. Therapeutic Potential of Photobiomodulation for Chronic Kidney Disease. International Journal of Molecular Sciences. 2022 Jul;23(14):8043. Available from: https://doi.org/10.3390/ijms23148043.

[195] Hossein-Khannazer N, Arki MK, Keramatinia A, Rezaei-Tavirani M. Low-Level Laser Therapy for Rheumatoid Arthritis: A Review of Experimental Approaches. Journal of Lasers in Medical Sciences. 2022 Dec;13:e62. Available from: https://doi.org/10.34172/jlms.2022.62.

[196] Soheilifar S, Fathi H, Naghdi N. Photobiomodulation therapy as a high potential treatment modality for COVID-19. Lasers in Medical Science. 2020 Nov;36(5):935-8. Available from: https://doi.org/10.1007/s10103-020-03206-9.

[197] Cheng W, Yao M, Sun K, Li W. Progress in Photobiomodulation for Bone Fractures: A Narrative Review. Photobiomodulation, Photomedicine, and Laser Surgery. 2020 May;38(5):260-71. Available from: https://doi.org/10.1089/photob.2019.4732.

[198] de Oliveira Rosso MP, Buchaim DV, Pomini KT, Coletta BBD, Reis CHB, Pilon JPG, et al. Photobiomodulation Therapy (PBMT) Applied in Bone Reconstructive Surgery Using Bovine Bone Grafts: A Systematic Review. Materials. 2019 Dec;12(24):4051. Available from: https://doi.org/10.3390/ma12244051.

[199] Alzyoud JAM, Omoush SA, Al-Qtaitat A. Photobiomodulation for Tendinopathy: A Review of Preclinical Studies. Photobiomodulation, Photomedicine, and Laser Surgery. 2022 Jun;40(6):370-7. Available from: https://doi.org/10.1089/photob.2021.0192.

[200] Hossein-khannazer N, Arki MK, Keramatinia A, Rezaei-Tavirani M. The Role of Low-Level Laser Therapy in the Treatment of Multiple Sclerosis: A Review Study. Journal of Lasers

in Medical Sciences. 2021 Dec;12(1):e88-8. Available from: https://doi.org/10.34172/jlms.2021.88.

[201] Enengl J, Hamblin MR, Dungel P. Photobiomodulation for Alzheimer's Disease: Translating Basic Research to Clinical Application. Journal of Alzheimer's Disease. 2020 Jun;75(4):1073-82. Available from: https://doi.org/10.3233/jad-191210.

[202] Liebert A, Bicknell B, Laakso EL, Heller G, Jalilitabaei P, Tilley S, et al. Improvements in clinical signs of Parkinson's disease using photobiomodulation: a prospective proof-of-concept study. BMC Neurology. 2021 Jul;21(1). Available from: https://doi.org/10.1186/s12883-021-02248-y.

[203] Liebert A, Bicknell B, Laakso EL, Jalilitabaei P, Tilley S, Kiat H, et al. Remote Photobiomodulation Treatment for the Clinical Signs of Parkinson's Disease: A Case Series Conducted During COVID-19. Photobiomodulation, Photomedicine, and Laser Surgery. 2022 Feb;40(2):112-22. Available from: https://doi.org/10.1089/photob.2021.0056.

[204] Johnstone DM, Hamilton C, Gordon LC, Moro C, Torres N, Nicklason F, et al. Exploring the Use of Intracranial and Extracranial (Remote) Photobiomodulation Devices in Parkinson's Disease: A Comparison of Direct and Indirect Systemic Stimulations. Journal of Alzheimer's Disease. 2021 Oct;83(4):1399-413. Available from: https://doi.org/10.3233/jad-210052.

[205] Johnstone DM, el Massri N, Moro C, Spana S, Wang XS, Torres N, et al. Indirect application of near infrared light induces neuroprotection in a mouse model of Parkinsonism – An abscopal neuroprotective effect. Neuroscience. 2014 Aug;274:93-101. Available from: https://doi.org/10.1016/j.neuroscience.2014.05.023.

[206] Vieira WF, Iosifescu DV, McEachern KM, Gersten M, Cassano P. Photobiomodulation. Psychiatric Clinics of North America. 2023 Jun;46(2):331-48. Available from: https://doi.org/10.1016/j.psc.2023.02.013.

[207] Gutiérrez-Menéndez A, Marcos-Nistal M, Méndez M, Arias JL. Photobiomodulation as a promising new tool in the management of psychological disorders: A systematic review.

Neuroscience & Biobehavioral Reviews. 2020 Dec;119:242-54. Available from: https://doi.org/10.1016/j.neubiorev.2020.10.002.

[208] Mansouri V, Razzaghi M, Rostami-Nejad M, Rezaei-Tavirani M, Heidari MH, Safari S, et al. Neuroprotective Properties of Photobiomodulation in Retinal Regeneration in Rats: Perspectives From Interaction Levels. Journal of Lasers in Medical Sciences. 2020 Jun;11(3):280-6. Available from: https://doi.org/10.34172/jlms.2020.47.

[209] Geneva I. Photobiomodulation for the treatment of retinal diseases: a review. International Journal of Ophthalmology. 2016 Jan;9(1). Available from: https://doi.org/10.18240/ijo.2016.01.24.

[210] Hacke W, Schellinger PD, Albers GW, Bornstein NM, Dahlof BL, Fulton R, et al. Transcranial Laser Therapy in Acute Stroke Treatment. Stroke. 2014 Nov;45(11):3187-93. Available from: https://doi.org/10.1161/strokeaha.114.005795.

[211] Ibarra AMC, Biasotto-Gonzalez DA, Kohatsu EYI, de Oliveira SSI, Bussadori SK, Tanganeli JPC. Photobiomodulation on trigeminal neuralgia: systematic review. Lasers in Medical Science. 2020 Nov. Available from: https://doi.org/10.1007/s10103-020-03198-6.

[212] Lodewijckx J, Robijns J, Bensadoun RJ, Mebis J. Photobiomodulation Therapy for the Management of Chemotherapy-Induced Peripheral Neuropathy: An Overview. Photobiomodulation, Photomedicine, and Laser Surgery. 2020 Jun;38(6):348-54. Available from: https://doi.org/10.1089/photob.2019.4771.

[213] Ramezani F, Razmgir M, Tanha K, Nasirinezhad F, Neshastehriz A, Bahrami-Ahmadi A, et al. Photobiomodulation for spinal cord injury: A systematic review and meta-analysis. Physiology & Behavior. 2020 Oct;224:112977. Available from: https://doi.org/10.1016/j.physbeh.2020.112977.

[214] Lapchak PA, Boitano PD. Transcranial Near-Infrared Laser Therapy for Stroke: How to Recover from Futility in the NEST-3 Clinical Trial. In: Acta Neurochirurgica Supplement.

Springer International Publishing; 2016. p. 7-12. Available from: https://doi.org/10.1007/978-3-319-18497-5_2.

[215] Cassano P, Tran AP, Katnani H, Bleier BS, Hamblin MR, Yuan Y, et al. Selective photobiomodulation for emotion regulation: model-based dosimetry study. Neurophotonics. 2019 Feb;6(01):1. Available from: https://doi.org/10.1117/1.nph.6.1.015004.

[216] Ercole A, Magnoni S, Vegliante G, Pastorelli R, Surmacki J, Bohndiek SE, et al. Current and Emerging Technologies for Probing Molecular Signatures of Traumatic Brain Injury. Frontiers in Neurology. 2017 Aug;8. Available from: http://dx.doi.org/10.3389/FNEUR.2017.00450.

[217] Cordero E. In-vivo Raman spectroscopy: from basics to applications. Journal of Biomedical Optics. 2018 Jun;23(07):1. Available from: http://dx.doi.org/10.1117/1.JBO.23.7.071210.

[218] Hanlon EB, Manoharan R, Koo TW, Shafer KE, Motz JT, Fitzmaurice M, et al. Prospects forin vivoRaman spectroscopy. Physics in Medicine and Biology. 2000 Jan;45(2):R1–R59. Available from: http://dx.doi.org/10.1088/0031-9155/45/2/201.

[219] Bik E, Mateuszuk L, Stojak M, Chlopicki S, Baranska M, Majzner K. Menadione-induced endothelial inflammation detected by Raman spectroscopy. Biochimica et Biophysica Acta (BBA) - Molecular Cell Research. 2021 Feb;1868(2):118911. Available from: http://dx.doi.org/10.1016/J.BBAMCR.2020.118911.

[220] Zhang W, Rhodes JS, Garg A, Takemoto JY, Qi X, Harihar S, et al. Label-free discrimination and quantitative analysis of oxidative stress induced cytotoxicity and potential protection of antioxidants using Raman micro-spectroscopy and machine learning. Analytica Chimica Acta. 2020 Sep;1128:221–230. Available from: http://dx.doi.org/10.1016/J.ACA.2020.06.074.

[221] Lalonde JW, O'Connor SP, Noojin GD, Gonzales CC, Yakovlev VV, Denton ML. Measuring cytochrome c redox state using resonance Raman spectroscopy to determine metabolic rates

in electron transport chain when exposed to light. In: Hamblin MR, Carroll JD, Arany P, editors. Mechanisms of Photobiomodulation Therapy XIV. SPIE; 2019. Available from: http://dx.doi.org/10.1117/12.2508684.

[222] Jung GB, Kang SW, Lee GJ, Kim D. Biochemical Characterization of the Brain Hippocampal Areas after Cerebral Ischemia-Reperfusion Using Raman Spectroscopy. Applied Spectroscopy. 2018 Jun;72(10):1479–1486. Available from: http://dx.doi.org/10.1177/0003702818776627.

[223] Chaichi A, Hasan SMA, Mehta N, Donnarumma F, Ebenezer P, Murray KK, et al. Label-free lipidome study of paraventricular thalamic nucleus (PVT) of rat brain with post-traumatic stress injury by Raman imaging. The Analyst. 2021;146(1):170–183. Available from: http://dx.doi.org/10.1039/D0AN01615B.

[224] Lakshmi RJ, Kartha VB, Murali Krishna C, R Solomon JG, Ullas G, Uma Devi P. Tissue Raman Spectroscopy for the Study of Radiation Damage: Brain Irradiation of Mice. Radiation Research. 2002 Feb;157(2):175–182. Available from: http://dx.doi.org/10.1667/0033-7587(2002)157[0175:trsfts]2.0.co;2.

[225] Devitt G, Howard K, Mudher A, Mahajan S. Raman Spectroscopy: An Emerging Tool in Neurodegenerative Disease Research and Diagnosis. ACS Chemical Neuroscience. 2018 Jan;9(3):404–420. Available from: http://dx.doi.org/10.1021/ACSCHEMNEURO.7B00413.

[226] Aguiar RP, Silveira L, Falcão ET, Pacheco MTT, Zângaro RA, Pasqualucci CA. Discriminating Neoplastic and Normal Brain Tissuesin VitroThrough Raman Spectroscopy: A Principal Components Analysis Classification Model. Photomedicine and Laser Surgery. 2013 Dec;31(12):595–604. Available from: http://dx.doi.org/10.1089/PHO.2012.3460.

[227] Desroches J, Jermyn M, Mok K, Lemieux-Leduc C, Mercier J, St-Arnaud K, et al. Characterization of a Raman spectroscopy probe system for intraoperative brain tissue classification. Biomedical Optics Express. 2015 Jun;6(7):2380. Available from: http://dx.doi.org/10.1364/BOE.6.002380.

[228] Livermore LJ, Isabelle M, Bell IM, Edgar O, Voets NL, Stacey R, et al. Raman spectroscopy to differentiate between fresh tissue samples of glioma and normal brain: a comparison with 5-ALA–induced fluorescence-guided surgery. Journal of Neurosurgery. 2021 Aug;135(2):469–479. Available from: http://dx.doi.org/10.3171/2020.5.JNS20376.

[229] Koljenović S, Schut TB, Vincent A, Kros JM, Puppels GJ. Detection of Meningioma in Dura Mater by Raman Spectroscopy. Analytical Chemistry. 2005 Nov;77(24):7958–7965. Available from: http://dx.doi.org/10.1021/AC0512599.

[230] Hollon T, Lewis S, Freudiger CW, Sunney Xie X, Orringer DA. Improving the accuracy of brain tumor surgery via Raman-based technology. Neurosurgical Focus. 2016 Mar;40(3):E9. Available from: http://dx.doi.org/10.3171/2015.12.FOCUS15557.

[231] Depciuch J, Tołpa B, Witek P, Szmuc K, Kaznowska E, Osuchowski M, et al. Raman and FTIR spectroscopy in determining the chemical changes in healthy brain tissues and glioblastoma tumor tissues. Spectrochimica Acta Part A: Molecular and Biomolecular Spectroscopy. 2020 Jan;225:117526. Available from: http://dx.doi.org/10.1016/J.SAA.2019.117526.

[232] Kalkanis SN, Kast RE, Rosenblum ML, Mikkelsen T, Yurgelevic SM, Nelson KM, et al. Raman spectroscopy to distinguish grey matter, necrosis, and glioblastoma multiforme in frozen tissue sections. Journal of Neuro-Oncology. 2014 Jan;116(3):477–485. Available from: http://dx.doi.org/10.1007/S11060-013-1326-9.

[233] Jermyn M, Mok K, Mercier J, Desroches J, Pichette J, Saint-Arnaud K, et al. Intraoperative brain cancer detection with Raman spectroscopy in humans. Science Translational Medicine. 2015 Feb;7(274). Available from: http://dx.doi.org/10.1126/SCITRANSLMED.AAA2384.

[234] Jermyn M, Desroches J, Mercier J, St-Arnaud K, Guiot MC, Leblond F, et al. Raman spectroscopy detects distant invasive brain cancer cells centimeters beyond MRI capability in humans. Biomedical Optics Express. 2016 Nov;7(12):5129. Available from: http://dx.doi.org/10.1364/BOE.7.005129.

[235] Desroches J, Jermyn M, Pinto M, Picot F, Tremblay MA, Obaid S, et al. A new method using Raman spectroscopy for in vivo targeted brain cancer tissue biopsy. Scientific Reports. 2018 Jan;8(1). Available from: http://dx.doi.org/10.1038/s41598-018-20233-3.

[236] Galli R, Meinhardt M, Koch E, Schackert G, Steiner G, Kirsch M, et al. Rapid Label-Free Analysis of Brain Tumor Biopsies by Near Infrared Raman and Fluorescence Spectroscopy—A Study of 209 Patients. Frontiers in Oncology. 2019 Nov;9. Available from: http://dx.doi.org/10.3389/fonc.2019.01165.

[237] Hollon TC, Pandian B, Adapa AR, Urias E, Save AV, Khalsa SSS, et al. Near real-time intraoperative brain tumor diagnosis using stimulated Raman histology and deep neural networks. Nature Medicine. 2020 Jan;26(1):52–58. Available from: http://dx.doi.org/10.1038/S41591-019-0715-9.

[238] Davies DJ, Hadis M, Pietro VD, Lazzarino G, Forcione M, Harris G, et al. Photobiomodulation reduces hippocampal apoptotic cell death and produces a Raman spectroscopic "signature". PLOS ONE. 2022 Mar;17(3):e0264533. Available from: https://doi.org/10.1371/journal.pone.0264533.

[239] Pitzschke A, Lovisa B, Seydoux O, Zellweger M, Pfleiderer M, Tardy Y, et al. Red and NIR light dosimetry in the human deep brain. Physics in Medicine and Biology. 2015 Mar;60(7):2921-37. Available from: https://doi.org/10.1088/0031-9155/60/7/2921.

[240] Stevens AR, Hadis M, Milward M, Ahmed Z, Belli A, Palin W, et al. Photobiomodulation in Acute Traumatic Brain Injury: A Systematic Review and Meta-Analysis. Journal of Neurotrauma. 2023 Feb;40(3-4):210-27. Available from: https://doi.org/10.1089/neu.2022.0140.

[241] Moher D, Liberati A, Tetzlaff J, and DGA. Preferred reporting items for systematic reviews and meta-analyses: the PRISMA statement. BMJ. 2009 Jul;339(jul21 1):b2535-5. Available from: https://doi.org/10.1136/bmj.b2535.

[242] Hooijmans CR, Rovers MM, de Vries RB, Leenaars M, Ritskes-Hoitinga M, Langendam MW. SYRCLE's risk of bias tool for animal studies. BMC Medical Research Methodology. 2014 Mar;14(1). Available from: https://doi.org/10.1186/1471-2288-14-43.

[243] Cochrane Collaboration. Risk of Bias (RoB2) tool;. Accessed: 2023-04-05. https://methods.cochrane.org/risk-bias-2.

[244] Ando T, Xuan W, Xu T, Dai T, Sharma SK, Kharkwal GB, et al. Comparison of Therapeutic Effects between Pulsed and Continuous Wave 810-nm Wavelength Laser Irradiation for Traumatic Brain Injury in Mice. PLoS ONE. 2011 Oct;6(10):e26212. Available from: https://doi.org/10.1371/journal.pone.0026212.

[245] Dong T, Zhang Q, Hamblin MR, Wu MX. Low-Level Light in Combination with Metabolic Modulators for Effective Therapy of Injured Brain. Journal of Cerebral Blood Flow and Metabolism. 2015 May;35(9):1435-44. Available from: https://doi.org/10.1038/jcbfm.2015.87.

[246] Wu Q, Xuan W, Ando T, Xu T, Huang L, Huang YY, et al. Low-Level Laser Therapy for Closed-Head Traumatic Brain Injury in Mice: Effect of Different Wavelengths. Lasers in Surgery and Medicine. 2012 Jan;44(3):218-26. Available from: https://doi.org/10.1002/lsm.22003.

[247] Xuan W, Vatansever F, Huang L, Wu Q, Xuan Y, Dai T, et al. Transcranial Low-Level Laser Therapy Improves Neurological Performance in Traumatic Brain Injury in Mice: Effect of Treatment Repetition Regimen. PLoS ONE. 2013 Jan;8(1):e53454. Available from: https://doi.org/10.1371/journal.pone.0053454.

[248] Xuan W, Agrawal T, Huang L, Gupta GK, Hamblin MR. Low-level laser therapy for traumatic brain injury in mice increases brain derived neurotrophic factor (BDNF) and synaptogenesis. Journal of Biophotonics. 2014 Sep;8(6):502-11. Available from: https://doi.org/10.1002/jbio.201400069.

[249] Zhang Q, Zhou C, Hamblin MR, Wu MX. Low-Level Laser Therapy Effectively Prevents Secondary Brain Injury Induced by Immediate Early Responsive Gene X-1 Deficiency. Journal of Cerebral Blood Flow & Metabolism. 2014 May;34(8):1391-401. Available from: https://doi.org/10.1038/jcbfm.2014.95.

[250] Giacci MK, Wheeler L, Lovett S, Dishington E, Majda B, Bartlett CA, et al. Differential Effects of 670 and 830 nm Red near Infrared Irradiation Therapy: A Comparative Study of Optic Nerve Injury, Retinal Degeneration, Traumatic Brain and Spinal Cord Injury. PLoS ONE. 2014 Aug;9(8):e104565. Available from: https://doi.org/10.1371/journal.pone.0104565.

[251] Oron A, Oron U, Streeter J, Taboada LD, Alexandrovich A, Trembovler V, et al. Low-Level Laser Therapy Applied Transcranially to Mice following Traumatic Brain Injury Significantly Reduces Long-term Neurological Deficits. Journal of Neurotrauma. 2007 Apr;24(4):651-6. Available from: https://doi.org/10.1089/neu.2006.0198.

[252] Oron A, Oron U, Streeter J, Taboada LD, Alexandrovich A, Trembovler V, et al. Near Infrared Transcranial Laser Therapy Applied at Various Modes to Mice following Traumatic Brain Injury Significantly Reduces Long-Term Neurological Deficits. Journal of Neurotrauma. 2012 Jan;29(2):401-7. Available from: https://doi.org/10.1089/neu.2011.2062.

[253] Quirk BJ, Torbey M, Buchmann E, Verma S, Whelan HT. Near-Infrared Photobiomodulation in an Animal Model of Traumatic Brain Injury: Improvements at the Behavioral and Biochemical Levels. Photomedicine and Laser Surgery. 2012 Sep;30(9):523-9. Available from: https://doi.org/10.1089/pho.2012.3261.

[254] Shemesh D, Aburus O, Turgeman G, Abookasis D. Quantification of the effectivity of laser therapy shortly following brain injury via dual-wavelength laser imaging. Optics & Laser Technology. 2022 Jan;145:107506. Available from: https://doi.org/10.1016/j.optlastec.2021.107506.

[255] Wu Q, Huang YY, Dhital S, Sharma SK, Chen ACH, Whalen MJ, et al. Low level laser therapy for traumatic brain injury. In: Hamblin MR, Waynant RW, Anders J, editors. SPIE Proceedings. SPIE; 2010. Available from: https://doi.org/10.1117/12.841014.

[256] Bunce SC, Izzetoglu M, Izzetoglu K, Onaral B, Pourrezaei K. Functional near-infrared spectroscopy. IEEE Engineering in Medicine and Biology Magazine. 2006 Jul;25(4):54-62. Available from: https://doi.org/10.1109/memb.2006.1657788.

[257] Zein R, Selting W, Hamblin MR. Review of light parameters and photobiomodulation efficacy: dive into complexity. Journal of Biomedical Optics. 2018 Dec;23(12):1. Available from: https://doi.org/10.1117/1.jbo.23.12.120901.

[258] Salehpour F, Cassano P, Rouhi N, Hamblin MR, Taboada LD, Farajdokht F, et al. Penetration Profiles of Visible and Near-Infrared Lasers and Light-Emitting Diode Light Through the Head Tissues in Animal and Human Species: A Review of Literature. Photobiomodulation, Photomedicine, and Laser Surgery. 2019 Oct;37(10):581-95. Available from: https://doi.org/10.1089/photob.2019.4676.

[259] Salehpour F, Mahmoudi J, Kamari F, Sadigh-Eteghad S, Rasta SH, Hamblin MR. Brain Photobiomodulation Therapy: a Narrative Review. Molecular Neurobiology. 2018 Jan;55(8):6601-36. Available from: https://doi.org/10.1007/s12035-017-0852-4.

[260] Hamblin MR. Mechanisms and Mitochondrial Redox Signaling in Photobiomodulation. Photochemistry and Photobiology. 2018 Jan;94(2):199–212. Available from: http://dx.doi.org/10.1111/php.12864.

[261] Farfara D, Tuby H, Trudler D, Doron-Mandel E, Maltz L, Vassar RJ, et al. Low-Level Laser Therapy Ameliorates Disease Progression in a Mouse Model of Alzheimer's Disease. Journal of Molecular Neuroscience. 2014 Jul;55(2):430-6. Available from: https://doi.org/10.1007/s12031-014-0354-z.

[262] Mazzitelli JA, Smyth LCD, Cross KA, Dykstra T, Sun J, Du S, et al. Cerebrospinal fluid regulates skull bone marrow niches via direct access through dural channels. Nature Neuroscience. 2022 Mar;25(5):555-60. Available from: https://doi.org/10.1038/s41593-022-01029-1.

[263] Yilmaz MT, Elmali A, Yazici G. Abscopal Effect, From Myth to Reality: From Radiation Oncologists' Perspective. Cureus. 2019 Jan. Available from: https://doi.org/10.7759/cureus.3860.

[264] Craig DJ, Nanavaty NS, Devanaboyina M, Stanbery L, Hamouda D, Edelman G, et al. The abscopal effect of radiation therapy. Future Oncology. 2021 May;17(13):1683-94. Available from: https://doi.org/10.2217/fon-2020-0994.

[265] Johnstone DM, Mitrofanis J, Stone J. Targeting the body to protect the brain: inducing neuroprotection with remotely-applied near infrared light. Neural Regeneration Research. 2015;10(3):349. Available from: https://doi.org/10.4103/1673-5374.153673.

[266] Meng C, He Z, Xing D. Low-Level Laser Therapy Rescues Dendrite Atrophy via Upregulating BDNF Expression: Implications for Alzheimer's Disease. The Journal of Neuroscience. 2013 Aug;33(33):13505-17. Available from: https://doi.org/10.1523/jneurosci.0918-13.2013.

[267] Yang L, Tucker D, Dong Y, Wu C, Lu Y, Li Y, et al. Photobiomodulation therapy promotes neurogenesis by improving post-stroke local microenvironment and stimulating neuroprogenitor cells. Experimental Neurology. 2018 Jan;299:86-96. Available from: https://doi.org/10.1016/j.expneurol.2017.10.013.

[268] Oron A, Oron U, Chen J, Eilam A, Zhang C, Sadeh M, et al. Low-Level Laser Therapy Applied Transcranially to Rats After Induction of Stroke Significantly Reduces Long-Term Neurological Deficits. Stroke. 2006 Oct;37(10):2620-4. Available from: https://doi.org/10.1161/01.str.0000242775.14642.b8.

[269] Ghanbari A, Ghareghani M, Zibara K, Delaviz H, Ebadi E, Jahantab MH. Light-Emitting Diode (LED) therapy improves occipital cortex damage by decreasing apoptosis and increas-

ing BDNF-expressing cells in methanol-induced toxicity in rats. Biomedicine & Pharmacotherapy. 2017 May;89:1320-30. Available from: https://doi.org/10.1016/j.biopha.2017.03.024.

[270] Heo JC, Park JA, Kim DK, Lee JH. Photobiomodulation (660 nm) therapy reduces oxidative stress and induces BDNF expression in the hippocampus. Scientific Reports. 2019 Jul;9(1). Available from: https://doi.org/10.1038/s41598-019-46490-4.

[271] Karu TI. Multiple roles of cytochrome c oxidase in mammalian cells under action of red and IR-A radiation. IUBMB Life. 2010 Jul;62(8):607-10. Available from: https://doi.org/10.1002/iub.359.

[272] Karu TI. Molecular Mechanism of the Therapeutic Effect of Low-Intensity Laser Radiation. Lasers Life Sci. 1988;2(1):53-74.

[273] Hamblin MR. The role of nitric oxide in low level light therapy. In: Hamblin MR, Waynant RW, Anders J, editors. SPIE Proceedings. SPIE; 2008. Available from: https://doi.org/10.1117/12.764918.

[274] Wang Y, Huang YY, Wang Y, Lyu P, Hamblin MR. Photobiomodulation of human adipose-derived stem cells using 810 nm and 980 nm lasers operates via different mechanisms of action. Biochimica et Biophysica Acta (BBA) - General Subjects. 2017 Feb;1861(2):441-9. Available from: https://doi.org/10.1016/j.bbagen.2016.10.008.

[275] Naeser MA, Saltmarche A, Krengel MH, Hamblin MR, Knight JA. Improved Cognitive Function After Transcranial, Light-Emitting Diode Treatments in Chronic, Traumatic Brain Injury: Two Case Reports. Photomedicine and Laser Surgery. 2011 May;29(5):351-8. Available from: https://doi.org/10.1089/pho.2010.2814.

[276] Bogdanova Y, Ho V, Martin P, Ho M, Yee M, Hamblin M, et al. Transcranial LED Treatment for Cognitive Dysfunction and Sleep in Chronic TBI: Randomized Controlled Pilot Trial. Archives of Physical Medicine and Rehabilitation. 2017 Oct;98(10):e122-3. Available from: https://doi.org/10.1016/j.apmr.2017.08.398.

[277] Henderson TA, Morries LD. SPECT Perfusion Imaging Demonstrates Improvement of Traumatic Brain Injury With Transcranial Near-Infrared Laser Phototherapy. Advances in Mind Body Medicine. 2015;29(4):27-33.

[278] Nawashiro H, Wada K, Nakai K, Sato S. Focal Increase in Cerebral Blood Flow After Treatment with Near-Infrared Light to the Forehead in a Patient in a Persistent Vegetative State. Photomedicine and Laser Surgery. 2012 Apr;30(4):231-3. Available from: https://doi.org/10.1089/pho.2011.3044.

[279] Naeser MA, Zafonte R, Krengel MH, Martin PI, Frazier J, Hamblin MR, et al. Significant Improvements in Cognitive Performance Post-Transcranial, Red/Near-Infrared Light-Emitting Diode Treatments in Chronic, Mild Traumatic Brain Injury: Open-Protocol Study. Journal of Neurotrauma. 2014 Jun;31(11):1008-17. Available from: https://doi.org/10.1089/neu.2013.3244.

[280] Naeser MA, Martin PI, Ho MD, Krengel MH, Bogdanova Y, Knight JA, et al. Transcranial, Red/Near-Infrared Light-Emitting Diode Therapy to Improve Cognition in Chronic Traumatic Brain Injury. Photomedicine and Laser Surgery. 2016 Dec;34(12):610-26. Available from: https://doi.org/10.1089/pho.2015.4037.

[281] Henderson TA, Morries L, Cassano P. Treatments for traumatic brain injury with emphasis on transcranial near-infrared laser phototherapy. Neuropsychiatric Disease and Treatment. 2015 Aug:2159. Available from: https://doi.org/10.2147/ndt.s65809.

[282] da Cruz Ribeiro Poiani G, Zaninotto AL, Carneiro AMC, Zangaro RA, Salgado ASI, Parreira RB, et al. Photobiomodulation using low-level laser therapy (LLLT) for patients with chronic traumatic brain injury: a randomized controlled trial study protocol. Trials. 2018 Jan;19(1). Available from: https://doi.org/10.1186/s13063-017-2414-5.

[283] Lampl Y, Zivin JA, Fisher M, Lew R, Welin L, Dahlof B, et al. Infrared Laser Therapy for Ischemic Stroke: A New Treatment Strategy. Stroke. 2007 Jun;38(6):1843-9. Available from: https://doi.org/10.1161/strokeaha.106.478230.

[284] Huisa BN, Stemer AB, Walker MG, Rapp K, Meyer BC, and JAZ. Transcranial Laser Therapy for Acute Ischemic Stroke: A Pooled Analysis of NEST-1 and NEST-2. International Journal of Stroke. 2012 Feb;8(5):315-20. Available from: https://doi.org/10.1111/j.1747-4949.2011.00754.x.

[285] Naeser MA, Ho MD, Martin PI, Hamblin MR, Koo BB. Increased Functional Connectivity Within Intrinsic Neural Networks in Chronic Stroke Following Treatment with Red/Near-Infrared Transcranial Photobiomodulation: Case Series with Improved Naming in Aphasia. Photobiomodulation, Photomedicine, and Laser Surgery. 2020 Feb;38(2):115-31. Available from: https://doi.org/10.1089/photob.2019.4630.

[286] Darlot F, Moro C, Massri NE, Chabrol C, Johnstone DM, Reinhart F, et al. Near-infrared light is neuroprotective in a monkey model of Parkinson disease. Annals of Neurology. 2015 Dec;79(1):59-75. Available from: https://doi.org/10.1002/ana.24542.

[287] Liu Y, Lai P, Ma C, Xu X, Grabar AA, Wang LV. Optical focusing deep inside dynamic scattering media with near-infrared time-reversed ultrasonically encoded (TRUE) light. Nature Communications. 2015 Jan;6(1). Available from: https://doi.org/10.1038/ncomms6904.

[288] Scopelliti MG, Chamanzar M. Ultrasonically sculpted virtual relay lens for in situ microimaging. Light: Science & Applications. 2019 Jul;8(1). Available from: https://doi.org/10.1038/s41377-019-0173-7.

[289] Sagar V, Atluri VSR, Tomitaka A, Shah P, Nagasetti A, Pilakka-Kanthikeel S, et al. Coupling of transient near infrared photonic with magnetic nanoparticle for potential dissipation-free biomedical application in brain. Scientific Reports. 2016 Jul;6(1). Available from: https://doi.org/10.1038/srep29792.

[290] Hart NS, Fitzgerald M. A new perspective on delivery of red-near-infrared light therapy for disorders of the brain. Discovery Medicine. 2016;22(120):147-56.

[291] Hamblin MR. Mechanisms and applications of the anti-inflammatory effects of photobiomodulation. AIMS Biophysics. 2017;4(3):337–361. Available from: http://dx.doi.org/10.3934/biophy.2017.3.337.

[292] Lamade AM, Anthonymuthu TS, Hier ZE, Gao Y, Kagan VE, Bayır H. Mitochondrial damage & lipid signaling in traumatic brain injury. Experimental Neurology. 2020 Jul;329:113307. Available from: http://dx.doi.org/10.1016/j.expneurol.2020.113307.

[293] Yoon SR, Hong N, Lee MY, Ahn JC. Photobiomodulation with a 660-Nanometer Light-Emitting Diode Promotes Cell Proliferation in Astrocyte Culture. Cells. 2021 Jul;10(7):1664. Available from: http://dx.doi.org/10.3390/cells10071664.

[294] Cardoso FS, Salehpour F, Coimbra NC, Gonzalez-Lima F, Gomes da Silva S. Photobiomodulation for the treatment of neuroinflammation: A systematic review of controlled laboratory animal studies. Frontiers in Neuroscience. 2022 Sep;16. Available from: http://dx.doi.org/10.3389/fnins.2022.1006031.

[295] Ando T, Sato S, Kobayashi H, Nawashiro H, Ashida H, Hamblin MR, et al. Low-level laser therapy for spinal cord injury in rats: effects of polarization. Journal of Biomedical Optics. 2013 Sep;18(9):098002. Available from: https://doi.org/10.1117/1.jbo.18.9.098002.

[296] Li C, Xiong W, Wan B, Kong G, Wang S, Wang Y, et al. Role of peripheral immune cells in spinal cord injury. Cellular and Molecular Life Sciences. 2022 Dec;80(1). Available from: http://dx.doi.org/10.1007/s00018-022-04644-0.

[297] Yamazaki K, Kawabori M, Seki T, Houkin K. Clinical Trials of Stem Cell Treatment for Spinal Cord Injury. International Journal of Molecular Sciences. 2020 Jun;21(11):3994. Available from: http://dx.doi.org/10.3390/ijms21113994.

[298] Putatunda R, Bethea JR, Hu WH. Potential immunotherapies for traumatic brain and spinal cord injury. Chinese Journal of Traumatology. 2018 Jun;21(3):125–136. Available from: http://dx.doi.org/10.1016/j.cjtee.2018.02.002.

[299] Ahuja CS, Martin AR, Fehlings MG. Recent advances in managing a spinal cord injury secondary to trauma. F1000Research. 2016 May;5:1017. Available from: http://dx.doi.org/10.12688/f1000research.7586.1.

[300] Bodart OH, Glaser EP, MacLean SM, Chen MA, Gensel JC. The Role of Neuroinflammation in the Response to Spinal Cord Injury. Oxford University Press; 2021. Available from: http://dx.doi.org/10.1093/acrefore/9780190264086.013.349.

[301] Hellenbrand DJ, Quinn CM, Piper ZJ, Morehouse CN, Fixel JA, Hanna AS. Inflammation after spinal cord injury: a review of the critical timeline of signaling cues and cellular infiltration. Journal of Neuroinflammation. 2021 Dec;18(1). Available from: http://dx.doi.org/10.1186/s12974-021-02337-2.

[302] Chaudhari LR, Kawale AA, Desai SS, Kashte SB, Joshi MG. In: Pathophysiology of Spinal Cord Injury and Tissue Engineering Approach for Its Neuronal Regeneration: Current Status and Future Prospects. Springer Nature Switzerland; 2022. p. 51–81. Available from: http://dx.doi.org/10.1007/5584_2022_731.

[303] Sotoudeh A, Jahanshahi A, Zareiy S, Darvishi M, Roodbari N, Bazzazan A. The influence of low-level laser irradiation on spinal cord injuries following ischemia- reperfusion in rats. Acta Cirurgica Brasileira. 2015 Sep;30(9):611–616. Available from: http://dx.doi.org/10.1590/S0102-865020150090000005.

[304] Song JW, Li K, Liang ZW, Dai C, Shen XF, Gong YZ, et al. Low-level laser facilitates alternatively activated macrophage/microglia polarization and promotes functional recovery after crush spinal cord injury in rats. Scientific Reports. 2017 Apr;7(1). Available from: http://dx.doi.org/10.1038/s41598-017-00553-6.

[305] Mojarad N, Janzadeh A, Yousefifard M, Nasirinezhad F. The role of low level laser therapy on neuropathic pain relief and interleukin-6 expression following spinal cord injury: An experimental study. Journal of Chemical Neuroanatomy. 2018 Jan;87:60–70. Available from: http://dx.doi.org/10.1016/j.jchemneu.2017.04.005.

[306] Veronez S, Assis L, Del Campo P, de Oliveira F, de Castro G, Renno ACM, et al. Effects of different fluences of low-level laser therapy in an experimental model of spinal cord injury in rats. Lasers in Medical Science. 2016 Dec;32(2):343–349. Available from: http://dx.doi.org/10.1007/s10103-016-2120-7.

[307] Sun J, Zhang J, Li K, Zheng Q, Song J, Liang Z, et al. Photobiomodulation Therapy Inhibit the Activation and Secretory of Astrocytes by Altering Macrophage Polarization. Cellular and Molecular Neurobiology. 2019 Aug;40(1):141–152. Available from: http://dx.doi.org/10.1007/s10571-019-00728-x.

[308] Ma Y, Li P, Ju C, Zuo X, Li X, Ding T, et al. Photobiomodulation Attenuates Neurotoxic Polarization of Macrophages by Inhibiting the Notch1-HIF-1α/NF-B Signalling Pathway in Mice With Spinal Cord Injury. Frontiers in Immunology. 2022 Mar;13. Available from: http://dx.doi.org/10.3389/fimmu.2022.816952.

[309] Ju C, Ma Y, Zuo X, Wang X, Song Z, Zhang Z, et al. Photobiomodulation promotes spinal cord injury repair by inhibiting macrophage polarization through lncRNA TUG1-miR-1192/TLR3 axis. Cellular & Molecular Biology Letters. 2023 Jan;28(1). Available from: http://dx.doi.org/10.1186/s11658-023-00417-0.

[310] Zheng Q, Zhang J, Zuo X, Sun J, Liang Z, Hu X, et al. Photobiomodulation Promotes Neuronal Axon Regeneration After Oxidative Stress and Induces a Change in Polarization from M1 to M2 in Macrophages via Stimulation of CCL2 in Neurons: Relevance to Spinal Cord Injury. Journal of Molecular Neuroscience. 2021 Jan;71(6):1290-300. Available from: https://doi.org/10.1007/s12031-020-01756-9.

[311] Li W, Gu X, Yue F, Zhou F. Photobiomodulation attenuates microglial activation by enhancing mitophagy. In: Carroll JD, Liebert A, Lyons JA, editors. Mechanisms of Photobiomodulation Therapy XVII. SPIE; 2023. Available from: http://dx.doi.org/10.1117/12.2647097.

[312] Moro C, Massri NE, Torres N, Ratel D, Jaeger XD, Chabrol C, et al. Photobiomodulation inside the brain: a novel method of applying near-infrared light intracranially and its im-

pact on dopaminergic cell survival in MPTP-treated mice. Journal of Neurosurgery. 2014 Mar;120(3):670-83. Available from: https://doi.org/10.3171/2013.9.jns13423.

[313] Reinhart F, Massri NE, Chabrol C, Cretallaz C, Johnstone DM, Torres N, et al. Intracranial application of near-infrared light in a hemi-Parkinsonian rat model: the impact on behavior and cell survival. Journal of Neurosurgery. 2016 Jun;124(6):1829-41. Available from: https://doi.org/10.3171/2015.5.jns15735.

[314] Liang Z, Lei T, Wang S, Zuo X, Li K, Song J, et al. Photobiomodulation by diffusing optical fiber on spinal cord: A feasibility study in piglet model. Journal of Biophotonics. 2020 Jan;13(4). Available from: https://doi.org/10.1002/jbio.201960022.

[315] Zuo X, Liang Z, Zhang J, Wang S, Zheng Q, Ma Y, et al. Photobiomodulation and diffusing optical fiber on spinal cord's impact on nerve cells from normal spinal cord tissue in piglets. Lasers in Medical Science. 2021 Jan;37(1):259–267. Available from: http://dx.doi.org/10.1007/s10103-020-03231-8.

[316] Stevens AR, Ahmed U, Vigneswara V, Ahmed Z. Pigment Epithelium-Derived Factor Promotes Axon Regeneration and Functional Recovery After Spinal Cord Injury. Molecular Neurobiology. 2019 May;56(11):7490-507. Available from: https://doi.org/10.1007/s12035-019-1614-2.

[317] Ahmed Z, Dent RG, Suggate EL, Barrett LB, Seabright RJ, Berry M, et al. Disinhibition of neurotrophin-induced dorsal root ganglion cell neurite outgrowth on CNS myelin by siRNA-mediated knockdown of NgR, p75NTR and Rho-A. Molecular and Cellular Neuroscience. 2005 Mar;28(3):509-23. Available from: https://doi.org/10.1016/j.mcn.2004.11.002.

[318] Vigneswara V, Berry M, Logan A, Ahmed Z. Caspase-2 Is Upregulated after Sciatic Nerve Transection and Its Inhibition Protects Dorsal Root Ganglion Neurons from Apoptosis after Serum Withdrawal. PLoS ONE. 2013 Feb;8(2):e57861. Available from: https://doi.org/10.1371/journal.pone.0057861.

[319] Burland M, Paris L, Quintana P, Bec JM, Diouloufet L, Sar C, et al. Neurite growth acceleration of adult Dorsal Root Ganglion neurons illuminated by low-level Light Emitting Diode light at 645 nm. Journal of Biophotonics. 2014 Jul;8(6):480-8. Available from: https://doi.org/10.1002/jbio.201400052.

[320] Zheng L, Wang Y, He Y, Zhou J, Yang H, Zhang Y, et al. Modulating nitric oxide levels in dorsal root ganglion neurons of rat with low-level laser therapy. Optoelectronics Letters. 2015 May;11(3):233-6. Available from: https://doi.org/10.1007/s11801-015-5032-z.

[321] Wang L, Hu L, Grygorczyk R, Shen X, Schwarz W. Modulation of Extracellular ATP Content of Mast Cells and DRG Neurons by Irradiation: Studies on Underlying Mechanism of Low-Level-Laser Therapy. Mediators of Inflammation. 2015;2015:1-9. Available from: https://doi.org/10.1155/2015/630361.

[322] Yan X, Liu J, Zhang Z, Li W, Sun S, Zhao J, et al. Low-level laser irradiation modulates brain-derived neurotrophic factor mRNA transcription through calcium-dependent activation of the ERK/CREB pathway. Lasers in Medical Science. 2016 Nov;32(1):169-80. Available from: https://doi.org/10.1007/s10103-016-2099-0.

[323] Salehpour F, Sadigh-Eteghad S, Mahmoudi J, Kamari F, Cassano P, Hamblin MR. Photobiomodulation for the Brain. Springer Nature Switzerland; 2023. Available from: https://doi.org/10.1007/978-3-031-36231-6.

[324] Cheriyan T, Ryan DJ, Weinreb JH, Cheriyan J, Paul JC, Lafage V, et al. Spinal cord injury models: a review. Spinal Cord. 2014 Jun;52(8):588–595. Available from: http://dx.doi.org/10.1038/sc.2014.91.

[325] Poon PC, Gupta D, Shoichet MS, Tator CH. Clip Compression Model Is Useful for Thoracic Spinal Cord Injuries: Histologic and Functional Correlates. Spine. 2007 Dec;32(25):2853–2859. Available from: http://dx.doi.org/10.1097/BRS.0B013E31815B7E6B.

[326] Vanický I, Urdzíková L, Saganová K, Čízková D, Gálik J. A Simple and Reproducible Model of Spinal Cord Injury Induced by Epidural Balloon Inflation in the Rat. Journal of Neurotrauma. 2001 Dec;18(12):1399–1407. Available from: http://dx.doi.org/10.1089/08977150152725687.

[327] Alilain WJ, Horn KP, Hu H, Dick TE, Silver J. Functional regeneration of respiratory pathways after spinal cord injury. Nature. 2011 Jul;475(7355):196–200. Available from: http://dx.doi.org/10.1038/nature10199.

[328] Barbeau H, Chau C, Rossignol S. Noradrenergic agonists and locomotor training affect locomotor recovery after cord transection in adult cats. Brain Research Bulletin. 1993 Jan;30(3–4):387–393. Available from: http://dx.doi.org/10.1016/0361-9230(93)90270-L.

[329] Tuxworth RI, Taylor MJ, Anduaga AM, Hussien-Ali A, Chatzimatthaiou S, Longland J, et al. Attenuating the DNA damage response to double-strand breaks restores function in models of CNS neurodegeneration. Brain Communications. 2019 Jan;1(1). Available from: https://doi.org/10.1093/braincomms/fcz005.

[330] Ahmed Z, Bansal D, Tizzard K, Surey S, Esmaeili M, Gonzalez AM, et al. Decorin blocks scarring and cystic cavitation in acute and induces scar dissolution in chronic spinal cord wounds. Neurobiology of Disease. 2014 Apr;64:163-76. Available from: https://doi.org/10.1016/j.nbd.2013.12.008.

[331] Matthews J, Surey S, Grover LM, Logan A, Ahmed Z. Thermosensitive collagen/fibrinogen gels loaded with decorin suppress lesion site cavitation and promote functional recovery after spinal cord injury. Scientific Reports. 2021 Sep;11(1). Available from: https://doi.org/10.1038/s41598-021-97604-w.

[332] Byrnes KR, Waynant RW, Ilev IK, Wu X, Barna L, Smith K, et al. Light promotes regeneration and functional recovery and alters the immune response after spinal cord injury. Lasers in Surgery and Medicine. 2005;36(3):171–185. Available from: http://dx.doi.org/10.1002/lsm.20143.

[333] Svobodova B, Kloudova A, Ruzicka J, Kajtmanova L, Navratil L, Sedlacek R, et al. The effect of 808nm and 905nm wavelength light on recovery after spinal cord injury. Scientific Reports. 2019;9(7660). Available from: https://doi.org/10.1038/s41598-019-44141-2.

[334] Wang X, Zhang Z, Zhu Z, Liang Z, Zuo X, Ju C, et al. Photobiomodulation Promotes Repair Following Spinal Cord Injury by Regulating the Transformation of A1/A2 Reactive Astrocytes. Frontiers in Neuroscience. 2021 Nov;15. Available from: http://dx.doi.org/10.3389/fnins.2021.768262.

[335] Wang X, Li X, Zuo X, Liang Z, Ding T, Li K, et al. Photobiomodulation inhibits the activation of neurotoxic microglia and astrocytes by inhibiting Lcn2/JAK2-STAT3 crosstalk after spinal cord injury in male rats. Journal of Neuroinflammation. 2021 Nov;18(1). Available from: http://dx.doi.org/10.1186/s12974-021-02312-x.

[336] Zhu Z, Wang X, Song Z, Zuo X, Ma Y, Zhang Z, et al. Photobiomodulation promotes repair following spinal cord injury by restoring neuronal mitochondrial bioenergetics via AMPK/PGC-1/TFAM pathway. Frontiers in Pharmacology. 2022 Sep;13. Available from: http://dx.doi.org/10.3389/fphar.2022.991421.

[337] Zhang Z, Zhu Z, Zuo X, Wang X, Ju C, Liang Z, et al. Photobiomodulation reduces neuropathic pain after spinal cord injury by downregulating <scp>CXCL10</scp> expression. CNS Neuroscience amp; Therapeutics. 2023 Jul;29(12):3995–4017. Available from: http://dx.doi.org/10.1111/cns.14325.

[338] Liang Z, Lei T, Wang S, Li P, Chen B, Pan D, et al. Clinical safety study of photobiomodulation in acute spinal cord injury by scattering fiber. Lasers in Medical Science. 2022 Jul;37(9):3433-42. Available from: https://doi.org/10.1007/s10103-022-03601-4.

[339] Ahmed Z, Mazibrada G, Seabright RJ, Dent RG, Berry M, Logan A, et al. TACE-induced cleavage of NgR and p75NTR in dorsal root ganglion cultures disinhibits outgrowth and promotes branching of neurites in the presence of inhibitory CNS myelin. The FASEB Journal. 2006 Jul;20(11):1939-41. Available from: https://doi.org/10.1096/fj.05-5339fje.

[340] Schneider CA, Rasband WS, Eliceiri KW. NIH Image to ImageJ: 25 years of image analysis. Nature Methods. 2012 Jun;9(7):671-5. Available from: https://doi.org/10.1038/nmeth.2089.

[341] Ahmed Z. Schwann cell-derived factor-induced modulation of the NgR/p75NTR/EGFR axis disinhibits axon growth through CNS myelin in vivo and in vitro. Brain. 2006 Apr;129(6):1517-33. Available from: https://doi.org/10.1093/brain/awl080.

[342] Kitchen P, Salman MM, Halsey AM, Clarke-Bland C, MacDonald JA, Ishida H, et al. Targeting Aquaporin-4 Subcellular Localization to Treat Central Nervous System Edema. Cell. 2020 May;181(4):784-99.e19. Available from: https://doi.org/10.1016/j.cell.2020.03.037.

[343] Ahmed Z, Bansal D, Tizzard K, Surey S, Esmaeili M, Gonzalez AM, et al. Decorin blocks scarring and cystic cavitation in acute and induces scar dissolution in chronic spinal cord wounds. Neurobiology of Disease. 2014 Apr;64:163-76. Available from: https://doi.org/10.1016/j.nbd.2013.12.008.

[344] R Core Team. R: A Language and Environment for Statistical Computing. Vienna, Austria; 2021. Available from: https://www.R-project.org/.

[345] Banbury C, Styles I, Eisenstein N, Zanier ER, Vegliante G, Belli A, et al. Spectroscopic detection of traumatic brain injury severity and biochemistry from the retina. Biomedical Optics Express. 2020 Oct;11(11):6249. Available from: http://dx.doi.org/10.1364/BOE.399473.

[346] Zhang F, Liang Z, Song D, Wang Z, Wang K, Wang S. Raman spectroscopic investigation on the biomedical evolution of spinal cord injury and the therapeutic outcomes of its low-level laser therapy. Vibrational Spectroscopy. 2022 Jan;118:103337. Available from: http://dx.doi.org/10.1016/j.vibspec.2022.103337.

[347] Banbury C, Mason R, Styles I, Eisenstein N, Clancy M, Belli A, et al. Development of the Self Optimising Kohonen Index Network (SKiNET) for Raman Spectroscopy Based

Detection of Anatomical Eye Tissue. Scientific Reports. 2019 Jul;9(1). Available from: http://dx.doi.org/10.1038/s41598-019-47205-5.

[348] Janzadeh A, Nasirinezhad F, Masoumipoor M, Jameie SB, hayat P. Photobiomodulation therapy reduces apoptotic factors and increases glutathione levels in a neuropathic pain model. Lasers in Medical Science. 2016 Sep;31(9):1863–1869. Available from: http://dx.doi.org/10.1007/s10103-016-2062-0.

[349] Micheli L, Cialdai F, Pacini A, Branca JJV, Morbidelli L, Ciccone V, et al. Effect of NIR laser therapy by MLS-MiS source against neuropathic pain in rats: in vivo and ex vivo analysis. Scientific Reports. 2019 Jun;9(1). Available from: http://dx.doi.org/10.1038/s41598-019-45469-5.

[350] Chen H, Wang Y, Tu W, Wang H, Yin H, Sha H, et al. Effects of photobiomodulation combined with MSCs transplantation on the repair of spinal cord injury in rat. Journal of Cellular Physiology. 2020 Jun;236(2):921–930. Available from: http://dx.doi.org/10.1002/jcp.29902.

[351] Chang SY, Lee MY. Photobiomodulation with a wavelength >800 nm induces morphological changes in stem cells within otic organoids and scala media of the cochlea. Lasers in Medical Science. 2021 Feb;36(9):1917–1925. Available from: http://dx.doi.org/10.1007/s10103-021-03268-3.

[352] Chang SY, Lee MY. Photobiomodulation of Neurogenesis through the Enhancement of Stem Cell and Neural Progenitor Differentiation in the Central and Peripheral Nervous Systems. International Journal of Molecular Sciences. 2023 Oct;24(20):15427. Available from: http://dx.doi.org/10.3390/ijms242015427.

[353] Alam A, Thelin EP, Tajsic T, Khan DZ, Khellaf A, Patani R, et al. Cellular infiltration in traumatic brain injury. Journal of Neuroinflammation. 2020 Nov;17(1). Available from: http://dx.doi.org/10.1186/s12974-020-02005-x.

[354] Pop V, Badaut J. A Neurovascular Perspective for Long-Term Changes After Brain Trauma. Translational Stroke Research. 2011 Nov;2(4):533–545. Available from: http://dx.doi.org/10.1007/s12975-011-0126-9.

[355] Jarrahi A, Braun M, Ahluwalia M, Gupta RV, Wilson M, Munie S, et al. Revisiting Traumatic Brain Injury: From Molecular Mechanisms to Therapeutic Interventions. Biomedicines. 2020 Sep;8(10):389. Available from: http://dx.doi.org/10.3390/biomedicines8100389.

[356] Omelchenko A, Singh NK, Firestein BL. Current advances in in vitro models of central nervous system trauma. Current Opinion in Biomedical Engineering. 2020 Jun;14:34–41. Available from: http://dx.doi.org/10.1016/j.cobme.2020.05.002.

[357] Dwyer MKR, Morrison B. Recent advancements in in vitro models of traumatic brain injury. Current Opinion in Biomedical Engineering. 2022 Sep;23:100396. Available from: http://dx.doi.org/10.1016/J.COBME.2022.100396.

[358] Hanna ME, Pfister BJ. Advancements in in vitro models of traumatic brain injury. Current Opinion in Biomedical Engineering. 2023 Mar;25:100430. Available from: http://dx.doi.org/10.1016/J.COBME.2022.100430.

[359] Petersen A, Soderstrom M, Saha B, Sharma P. Animal models of traumatic brain injury: a review of pathophysiology to biomarkers and treatments. Experimental Brain Research. 2021 Jul;239(10):2939–2950. Available from: http://dx.doi.org/10.1007/S00221-021-06178-6.

[360] Zhao Q, Zhang J, Li H, Li H, Xie F. Models of traumatic brain injury-highlights and drawbacks. Frontiers in Neurology. 2023 Jun;14. Available from: http://dx.doi.org/10.3389/fneur.2023.1151660.

[361] Dixon CE, Clifton GL, Lighthall JW, Yaghmai AA, Hayes RL. A controlled cortical impact model of traumatic brain injury in the rat. Journal of Neuroscience Methods. 1991 Oct;39(3):253–262. Available from: http://dx.doi.org/10.1016/0165-0270(91)90104-8.

[362] Xia Y, Kong L, Yao Y, Jiao Y, Song J, Tao Z, et al. Osthole confers neuroprotection against cortical stab wound injury and attenuates secondary brain injury. Journal of Neuroinflammation. 2015 Sep;12(1). Available from: http://dx.doi.org/10.1186/S12974-015-0373-X.

[363] Kalish BT, Whalen MJ. In: Weight Drop Models in Traumatic Brain Injury. Springer New York; 2016. p. 193–209. Available from: http://dx.doi.org/10.1007/978-1-4939-3816-2_12.

[364] Cartagena CM, Mountney A, Hwang H, Swiercz A, Rammelkamp Z, Boutte AM, et al. Subacute Changes in Cleavage Processing of Amyloid Precursor Protein and Tau following Penetrating Traumatic Brain Injury. PLoS ONE. 2016 Jul;11(7):e0158576. Available from: http://dx.doi.org/10.1371/JOURNAL.PONE.0158576.

[365] Marmarou A, Foda M, Abd Elfattah A, van den Brink W, Campbell J, Kita H, et al. A new model of diffuse brain injury in rats: Part I: Pathophysiology and biomechanics. Journal of Neurosurgery. 1994 Feb;80(2):291–300. Available from: http://dx.doi.org/10.3171/jns.1994.80.2.0291.

[366] Lazzarino G, Mangione R, Saab MW, Tavazzi B, Pittalà A, Signoretti S, et al. Traumatic Brain Injury Alters Cerebral Concentrations and Redox States of Coenzymes Q9 and Q10 in the Rat. Antioxidants. 2023 Apr;12(5):985. Available from: http://dx.doi.org/10.3390/antiox12050985.

[367] Amorini AM, Lazzarino G, Di Pietro V, Signoretti S, Lazzarino G, Belli A, et al. Severity of experimental traumatic brain injury modulates changes in concentrations of cerebral free amino acids. Journal of Cellular and Molecular Medicine. 2016 Oct;21(3):530–542. Available from: http://dx.doi.org/10.1111/jcmm.12998.

[368] Zhao Z, Loane DJ, Murray MG, Stoica BA, Faden AI. Comparing the Predictive Value of Multiple Cognitive, Affective, and Motor Tasks after Rodent Traumatic Brain Injury. Journal of Neurotrauma. 2012 Oct;29(15):2475–2489. Available from: http://dx.doi.org/10.1089/neu.2012.2511.

[369] Goldstein LB, Davis JN. Beam-walking in rats: studies towards developing an animal model of functional recovery after brain injury. Journal of Neuroscience Methods. 1990 Feb;31(2):101–107. Available from: http://dx.doi.org/10.1016/0165-0270(90)90154-8.

[370] Hausser N, Johnson K, Parsley MA, Guptarak J, Spratt H, Sell SL. Detecting Behavioral Deficits in Rats After Traumatic Brain Injury. Journal of Visualized Experiments. 2018 Jan;(131). Available from: http://dx.doi.org/10.3791/56044.

[371] Sweis BM, Bachour SP, Brekke JA, Gewirtz JC, Sadeghi-Bazargani H, Hevesi M, et al. A modified beam-walking apparatus for assessment of anxiety in a rodent model of blast traumatic brain injury. Behavioural Brain Research. 2016 Jan;296:149–156. Available from: http://dx.doi.org/10.1016/j.bbr.2015.09.015.

[372] Hanson BA. ChemoSpec: Exploratory Chemometrics for Spectroscopy; 2024. R package version 6.1.10. Available from: https://bryanhanson.github.io/ChemoSpec/.

[373] Zorzo C, Rodríguez-Fernández L, Martínez JA, Arias JL. Photobiomodulation increases brain metabolic activity through a combination of 810 and 660 wavelengths: a comparative study in male and female rats. Lasers in Medical Science. 2024 Jan;39(1). Available from: http://dx.doi.org/10.1007/s10103-023-03966-0.

[374] Karu TI, Kolyakov SF. Exact Action Spectra for Cellular Responses Relevant to Phototherapy. Photomedicine and Laser Surgery. 2005 Aug;23(4):355–361. Available from: http://dx.doi.org/10.1089/pho.2005.23.355.

[375] Stolik S, Delgado JA, Pérez A, Anasagasti L. Measurement of the penetration depths of red and near infrared light in human "ex vivo" tissues. Journal of Photochemistry and Photobiology B: Biology. 2000 Sep;57(2–3):90–93. Available from: http://dx.doi.org/10.1016/S1011-1344(00)00082-8.

[376] Zhang R, Zhou T, Samanta S, Luo Z, Li S, Xu H, et al. Synergistic photobiomodulation with 808-nm and 1064-nm lasers to reduce the β-amyloid neurotoxicity in the in vitro

Alzheimer's disease models. Frontiers in Neuroimaging. 2022 Jul;1. Available from: http://dx.doi.org/10.3389/fnimg.2022.903531.

[377] Daigo E, Daigo Y, Idogaki J, Fukuoka H, Fukuoka N, Ishikawa M, et al. Photobiomodulation Activates Microglia/Astrocytes and Relieves Neuropathic Pain in Inferior Alveolar Nerve Injury. Photobiomodulation, Photomedicine, and Laser Surgery. 2023 Dec;41(12):694–702. Available from: http://dx.doi.org/10.1089/photob.2023.0078.

[378] Springer JE, Azbill RD, Knapp PE. Activation of the caspase-3 apoptotic cascade in traumatic spinal cord injury. Nature Medicine. 1999 Aug;5(8):943–946. Available from: http://dx.doi.org/10.1038/11387.

[379] Namura S, Zhu J, Fink K, Endres M, Srinivasan A, Tomaselli KJ, et al. Activation and Cleavage of Caspase-3 in Apoptosis Induced by Experimental Cerebral Ischemia. The Journal of Neuroscience. 1998 May;18(10):3659–3668. Available from: http://dx.doi.org/10.1523/jneurosci.18-10-03659.1998.

[380] Büki A, Okonkwo DO, Wang KKW, Povlishock JT. Cytochrome c Release and Caspase Activation in Traumatic Axonal Injury. The Journal of Neuroscience. 2000 Apr;20(8):2825–2834. Available from: http://dx.doi.org/10.1523/JNEUROSCI.20-08-02825.2000.

[381] Podvin S, Gonzalez AM, Miller MC, Dang X, Botfield H, Donahue JE, et al. Esophageal Cancer Related Gene-4 Is a Choroid Plexus-Derived Injury Response Gene: Evidence for a Biphasic Response in Early and Late Brain Injury. PLoS ONE. 2011 Sep;6(9):e24609. Available from: http://dx.doi.org/10.1371/journal.pone.0024609.

[382] Szmydynger-Chodobska J, Strazielle N, Zink BJ, Ghersi-Egea JF, Chodobski A. The Role of the Choroid Plexus in Neutrophil Invasion after Traumatic Brain Injury. Journal of Cerebral Blood Flow & Metabolism. 2009 May;29(9):1503–1516. Available from: http://dx.doi.org/10.1038/jcbfm.2009.71.

[383] Mowbray M, Banbury C, Rickard JJS, Davies DJ, Goldberg Oppenheimer P. Development and Characterization of a Probe Device toward Intracranial Spectroscopy of Traumatic Brain

Injury. ACS Biomaterials Science & Engineering. 2021 Feb;7(3):1252–1262. Available from: http://dx.doi.org/10.1021/acsbiomaterials.0c01156.

[384] Kawon K, Setkowicz Z, Drozdz A, Janeczko K, Chwiej J. The methods of vibrational microspectroscopy reveals long-term biochemical anomalies within the region of mechanical injury within the rat brain. Spectrochimica Acta Part A: Molecular and Biomolecular Spectroscopy. 2021 Dec;263:120214. Available from: http://dx.doi.org/10.1016/j.saa.2021.120214.

[385] Kao YC, Lin GY, Cheng JY, Lee CH. Neurite growth induced by red light-caused intracellular reactive oxygen species production through cytochrome c oxidase activation. Journal of Photochemistry and Photobiology B: Biology. 2023 Apr;241:112681. Available from: https://doi.org/10.1016/j.jphotobiol.2023.112681.

[386] Tang J, Du Y, Lee CA, Talahalli R, Eells JT, Kern TS. Low-Intensity Far-Red Light Inhibits Early Lesions That Contribute to Diabetic Retinopathy: In Vivo and In Vitro. Investigative Opthalmology & Visual Science. 2013 May;54(5):3681. Available from: https://doi.org/10.1167/iovs.12-11018.

[387] Huang YY, Nagata K, Tedford CE, McCarthy T, Hamblin MR. Low-level laser therapy (LLLT) reduces oxidative stress in primary cortical neurons in vitro. Journal of Biophotonics. 2012 Dec:829-38. Available from: https://doi.org/10.1002/jbio.201200157.

[388] Leung MCP, Lo SCL, Siu FKW, So KF. Treatment of experimentally induced transient cerebral ischemia with low energy laser inhibits nitric oxide synthase activity and up-regulates the expression of transforming growth factor-beta 1. Lasers in Surgery and Medicine. 2002 Sep;31(4):283–288. Available from: http://dx.doi.org/10.1002/lsm.10096.

[389] Louin G, Marchand-Verrecchia C, Palmier B, Plotkine M, Jafarian-Tehrani M. Selective inhibition of inducible nitric oxide synthase reduces neurological deficit but not cerebral edema following traumatic brain injury. Neuropharmacology. 2006 Feb;50(2):182–190. Available from: http://dx.doi.org/10.1016/j.neuropharm.2005.08.020.

[390] Kashiwagi S, Morita A, Yokomizo S, Ogawa E, Komai E, Huang PL, et al. Photobiomodulation and nitric oxide signaling. Nitric Oxide. 2023 Jan;130:58–68. Available from: http://dx.doi.org/10.1016/j.niox.2022.11.005.

[391] Yokomizo S, Roessing M, Morita A, Kopp T, Ogawa E, Katagiri W, et al. Near-infrared photobiomodulation augments nitric oxide bioavailability via phosphorylation of endothelial nitric oxide synthase. The FASEB Journal. 2022 Aug;36(9). Available from: http://dx.doi.org/10.1096/fj.202101890R.

[392] Pchelin P, Shkarupa D, Smetanina N, Grigorieva T, Lapshin R, Schelchkova N, et al. Red light photobiomodulation rescues murine brain mitochondrial respiration after acute hypobaric hypoxia. Journal of Photochemistry and Photobiology B: Biology. 2023 Feb;239:112643. Available from: https://doi.org/10.1016/j.jphotobiol.2022.112643.

[393] Huang YY, Nagata K, Tedford CE, Hamblin MR. Low-level laser therapy (810 nm) protects primary cortical neurons against excitotoxicity in vitro. Journal of Biophotonics. 2013 Oct;7(8):656-64. Available from: https://doi.org/10.1002/jbio.201300125.

[394] Yu Z, Liu N, Zhao J, Li Y, McCarthy TJ, Tedford CE, et al. Near infrared radiation rescues mitochondrial dysfunction in cortical neurons after oxygen-glucose deprivation. Metabolic Brain Disease. 2014 Mar;30(2):491-6. Available from: https://doi.org/10.1007/s11011-014-9515-6.

[395] Anders JJ, Romanczyk TB, Ilev IK, Moges H, Longo L, Wu X, et al. Light Supports Neurite Outgrowth of Human Neural Progenitor Cells In Vitro: The Role of P2Y Receptors. IEEE Journal of Selected Topics in Quantum Electronics. 2008;14(1):118-25. Available from: https://doi.org/10.1109/jstqe.2008.916181.

[396] Territo PR, Zarrinmayeh H. P2X7 Receptors in Neurodegeneration: Potential Therapeutic Applications From Basic to Clinical Approaches. Frontiers in Cellular Neuroscience. 2021 Apr;15. Available from: https://doi.org/10.3389/fncel.2021.617036.

[397] Fan X, Ma W, Zhang Y, Zhang L. P2X7 Receptor (P2X7R) of Microglia Mediates Neuroinflammation by Regulating (NOD)-Like Receptor Protein 3 (NLRP3) Inflammasome-Dependent Inflammation After Spinal Cord Injury. Medical Science Monitor. 2020 Jul;26. Available from: https://doi.org/10.12659/msm.925491.

[398] Liu X, Zhao Z, Ji R, Zhu J, Sui QQ, Knight GE, et al. Inhibition of P2X7 receptors improves outcomes after traumatic brain injury in rats. Purinergic Signalling. 2017 Aug;13(4):529-44. Available from: https://doi.org/10.1007/s11302-017-9579-y.

[399] Choi JE. Proposed Mechanisms of Photobiomodulation (PBM) Mediated via the Stimulation of Mitochondrial Activity in Peripheral Nerve Injuries. Medical Lasers. 2021 Dec;10(4):195–200. Available from: http://dx.doi.org/10.25289/ML.2021.10.4.195.

[400] Pan W, Liu P, Ma D, Yang J. Advances in photobiomodulation for cognitive improvement by near-infrared derived multiple strategies. Journal of Translational Medicine. 2023 Feb;21(1). Available from: http://dx.doi.org/10.1186/s12967-023-03988-w.

[401] Biswas R, Ahn JC, Moon JH, Kim J, Choi YH, Park SY, et al. Low-level laser therapy with 850nm recovers salivary function via membrane redistribution of aquaporin 5 by reducing intracellular Ca2+ overload and ER stress during hyperglycemia. Biochimica et Biophysica Acta (BBA) - General Subjects. 2018 Aug;1862(8):1770–1780. Available from: http://dx.doi.org/10.1016/j.bbagen.2018.05.008.

[402] Bathini M, Raghushaker CR, Mahato KK. The Molecular Mechanisms of Action of Photobiomodulation Against Neurodegenerative Diseases: A Systematic Review. Cellular and Molecular Neurobiology. 2020 Dec;42(4):955–971. Available from: http://dx.doi.org/10.1007/s10571-020-01016-9.

[403] Lee HI, Lee S, Kim NG, Park K, Choi BT, Shin Y, et al. Low-level light emitting diode (LED) therapy suppresses inflammasome-mediated brain damage in experimental ischemic stroke. Journal of Biophotonics. 2017 Feb;10(11):1502–1513. Available from: http://dx.doi.org/10.1002/jbio.201600244.

[404] Chen ACH, Huang YY, Sharma SK, Hamblin MR. Effects of 810-nm Laser on Murine Bone-Marrow-Derived Dendritic Cells. Photomedicine and Laser Surgery. 2011 Jun;29(6):383–389. Available from: http://dx.doi.org/10.1089/pho.2010.2837.

[405] Jere SW, Houreld NN, Abrahamse H. Photobiomodulation activates the PI3K/AKT pathway in diabetic fibroblast cells in vitro. Journal of Photochemistry and Photobiology B: Biology. 2022 Dec;237:112590. Available from: http://dx.doi.org/10.1016/j.jphotobiol.2022.112590.

[406] Tian T, Wang Z, Chen L, Xu W, Wu B. Photobiomodulation activates undifferentiated macrophages and promotes M1/M2 macrophage polarization via PI3K/AKT/mTOR signaling pathway. Lasers in Medical Science. 2023 Mar;38(1). Available from: http://dx.doi.org/10.1007/s10103-023-03753-x.

[407] Salehpour F, Khademi M, Bragin DE, DiDuro JO. Photobiomodulation Therapy and the Glymphatic System: Promising Applications for Augmenting the Brain Lymphatic Drainage System. International Journal of Molecular Sciences. 2022 Mar;23(6):2975. Available from: http://dx.doi.org/10.3390/ijms23062975.

[408] Zomorrodi R, Loheswaran G, Pushparaj A, Lim L. Modulation of Neural Oscillation Power Spectral Density with Transcranial Photobiomodulation. Brain Stimulation. 2019 Mar;12(2):457–458. Available from: http://dx.doi.org/10.1016/j.brs.2018.12.486.

[409] Buendía D, Guncay T, Oyanedel M, Lemus M, Weinstein A, Ardiles AO, et al. The Transcranial Light Therapy Improves Synaptic Plasticity in the Alzheimer's Disease Mouse Model. Brain Sciences. 2022 Sep;12(10):1272. Available from: http://dx.doi.org/10.3390/brainsci12101272.

[410] McCloy RA, Rogers S, Caldon CE, Lorca T, Castro A, Burgess A. Partial inhibition of Cdk1 in G2 phase overrides the SAC and decouples mitotic events. Cell Cycle. 2014 Mar;13(9):1400–1412. Available from: http://dx.doi.org/10.4161/CC.28401.

[411] Alvites RD, Branquinho MV, Sousa AC, Lopes B, Sousa P, Prada J, et al. Effects of Olfactory Mucosa Stem/Stromal Cell and Olfactory Ensheating Cells Secretome on Peripheral Nerve

Regeneration. Biomolecules. 2022 Jun;12(6):818. Available from: https://doi.org/10.3390/biom12060818.

[412] Ge SX, Son EW, Yao R. iDEP: an integrated web application for differential expression and pathway analysis of RNA-Seq data. BMC Bioinformatics. 2018 Dec;19(1). Available from: http://dx.doi.org/10.1186/s12859-018-2486-6.

[413] Wickham H. ggplot2: Elegant Graphics for Data Analysis. Springer-Verlag New York; 2016. Available from: https://ggplot2.tidyverse.org.

[414] Gu Z, Eils R, Schlesner M. Complex heatmaps reveal patterns and correlations in multidimensional genomic data. Bioinformatics. 2016 May;32(18):2847–2849. Available from: http://dx.doi.org/10.1093/bioinformatics/btw313.

[415] Reimand J, Kull M, Peterson H, Hansen J, Vilo J. g:Profiler—a web-based toolset for functional profiling of gene lists from large-scale experiments. Nucleic Acids Research. 2007 Jul;35(suppl2):W193–W200. Available from: http://dx.doi.org/10.1093/nar/gkm226.

[416] Szklarczyk D, Franceschini A, Wyder S, Forslund K, Heller D, Huerta-Cepas J, et al. STRING v10: protein–protein interaction networks, integrated over the tree of life. Nucleic Acids Research. 2014 Oct;43(D1):D447–D452. Available from: http://dx.doi.org/10.1093/nar/gku1003.

[417] Kobiela Ketz A, Byrnes KR, Grunberg NE, Kasper CE, Osborne L, Pryor B, et al. Characterization of Macrophage/Microglial Activation and Effect of Photobiomodulation in the Spared Nerve Injury Model of Neuropathic Pain. Pain Medicine. 2016 Aug:pnw144. Available from: http://dx.doi.org/10.1093/pm/pnw144.

[418] Havlikova J, Randall EC, Griffiths RL, Swales JG, Goodwin RJA, Bunch J, et al. Quantitative Imaging of Proteins in Tissue by Stable Isotope Labeled Mimetic Liquid Extraction Surface Analysis Mass Spectrometry. Analytical Chemistry. 2019 Oct;91(22):14198–14202. Available from: http://dx.doi.org/10.1021/acs.analchem.9b04148.

[419] Yang T, Dai Y, Chen G, Cui S. Dissecting the Dual Role of the Glial Scar and Scar-Forming Astrocytes in Spinal Cord Injury. Frontiers in Cellular Neuroscience. 2020 Apr;14. Available from: http://dx.doi.org/10.3389/fncel.2020.00078.

[420] Wang H, Song G, Chuang H, Chiu C, Abdelmaksoud A, Ye Y, et al. Portrait of glial scar in neurological diseases. International Journal of Immunopathology and Pharmacology. 2018 Jan;31:205873841880140. Available from: http://dx.doi.org/10.1177/2058738418801406.

[421] Amlerova Z, Chmelova M, Anderova M, Vargova L. Reactive gliosis in traumatic brain injury: a comprehensive review. Frontiers in Cellular Neuroscience. 2024 Feb;18. Available from: http://dx.doi.org/10.3389/fncel.2024.1335849.

[422] Nespoli E, Hakani M, Hein TM, May SN, Danzer K, Wirth T, et al. Glial cells react to closed head injury in a distinct and spatiotemporally orchestrated manner. Scientific Reports. 2024 Jan;14(1). Available from: http://dx.doi.org/10.1038/s41598-024-52337-4.

[423] Salehpour F, Sadigh-Eteghad S, Mahmoudi J, Kamari F, Cassano P, Hamblin MR. In: Preconditioning with Photobiomodulation in Neuronal Cells and the Brain. Springer Nature Switzerland; 2023. p. 137–142. Available from: http://dx.doi.org/10.1007/978-3-031-36231-6_7.

[424] Liang HL, Whelan HT, Eells JT, Meng H, Buchmann E, Lerch-Gaggl A, et al. Photobiomodulation partially rescues visual cortical neurons from cyanide-induced apoptosis. Neuroscience. 2006 Jan;139(2):639–649. Available from: http://dx.doi.org/10.1016/j.neuroscience.2005.12.047.

[425] Lim W, Kim JH, Gook E, Kim J, Ko Y, Kim I, et al. Inhibition of mitochondria-dependent apoptosis by 635-nm irradiation in sodium nitroprusside-treated SH-SY5Y cells. Free Radical Biology and Medicine. 2009 Sep;47(6):850–857. Available from: http://dx.doi.org/10.1016/j.freeradbiomed.2009.06.023.

[426] Tonge DA, de Burgh HT, Docherty R, Humphries MJ, Craig SE, Pizzey J. Fibronectin supports neurite outgrowth and axonal regeneration of adult brain neurons in vitro. Brain

Research. 2012 May;1453:8–16. Available from: http://dx.doi.org/10.1016/j.brainres.2012.03.024.

[427] Houreld N, Ayuk S, Abrahamse H. Cell Adhesion Molecules are Mediated by Photobiomodulation at 660 nm in Diabetic Wounded Fibroblast Cells. Cells. 2018 Apr;7(4):30. Available from: http://dx.doi.org/10.3390/cells7040030.

[428] Di Giorgio E, Ferino A, Huang W, Simonetti S, Xodo L, De Marco R. Dual-targeting peptides@PMO, a mimetic to the pro-apoptotic protein Smac/DIABLO for selective activation of apoptosis in cancer cells. Frontiers in Pharmacology. 2023 Aug;14. Available from: http://dx.doi.org/10.3389/fphar.2023.1237478.

[429] Ng AN, Doherty AJ, Lombroso PJ, Emptage NJ, Collingridge GL. Rapid regulation of endoplasmic reticulum dynamics in dendritic spines by NMDA receptor activation. Molecular Brain. 2014 Aug;7(1). Available from: http://dx.doi.org/10.1186/s13041-014-0060-3.

[430] Ghosh-Roy A, Wu Z, Goncharov A, Jin Y, Chisholm AD. Calcium and Cyclic AMP Promote Axonal Regeneration in Caenorhabditis elegans and Require DLK-1 Kinase. The Journal of Neuroscience. 2010 Mar;30(9):3175–3183. Available from: http://dx.doi.org/10.1523/JNEUROSCI.5464-09.2010.

[431] Wang S, Song R, Wang Z, Jing Z, Wang S, Ma J. S100A8/A9 in Inflammation. Frontiers in Immunology. 2018 Jun;9. Available from: http://dx.doi.org/10.3389/fimmu.2018.01298.

[432] Bai Q, Sun M, Stolz DB, Burton EA. Major isoform of zebrafish P0 is a 23.5 kDa myelin glycoprotein expressed in selected white matter tracts of the central nervous system. Journal of Comparative Neurology. 2011 Apr;519(8):1580–1596. Available from: http://dx.doi.org/10.1002/CNE.22587.

[433] Licero Campbell J, Serrano-Illàn M, Descorbeth M, Cordero K, Figueroa JD, De León M. Fatty Acid-Binding Protein 4 Inhibition Promotes Locomotor and Autonomic Recovery in Rats following Spinal Cord Injury. Journal of Neurotrauma. 2022 Aug;39(15–16):1099–1112. Available from: http://dx.doi.org/10.1089/NEU.2021.0346.

[434] Abud EM, Ramirez RN, Martinez ES, Healy LM, Nguyen CHH, Newman SA, et al. iPSC-Derived Human Microglia-like Cells to Study Neurological Diseases. Neuron. 2017 Apr;94(2):278-93.e9. Available from: http://dx.doi.org/10.1016/j.neuron.2017.03.042.

[435] Kim H, Kim MJ, Kwon YW, Jeon S, Lee S, Kim C, et al. Benefits of a Skull-Interfaced Flexible and Implantable Multilight Emitting Diode Array for Photobiomodulation in Ischemic Stroke. Advanced Science. 2022 Jan;9(11). Available from: http://dx.doi.org/10.1002/advs.202104629.

[436] Flock ST, Jacques SL, Wilson BC, Star WM, van Gemert MJC. Optical properties of intralipid: A phantom medium for light propagation studies. Lasers in Surgery and Medicine. 1992 Jan;12(5):510–519. Available from: http://dx.doi.org/10.1002/lsm.1900120510.

[437] Spinelli L, Botwicz M, Zolek N, Kacprzak M, Milej D, Sawosz P, et al. Determination of reference values for optical properties of liquid phantoms based on Intralipid and India ink. Biomedical Optics Express. 2014 Jun;5(7):2037. Available from: http://dx.doi.org/10.1364/BOE.5.002037.

[438] Di Ninni P, Martelli F, Zaccanti G. The use of India ink in tissue-simulating phantoms. Optics Express. 2010 Dec;18(26):26854. Available from: http://dx.doi.org/10.1364/OE.18.026854.

[439] Heskin L, Cahill V, Filobbos G, Regan P, O'Sullivan S, Bryan K. A new adaptation for a secure surgical drain placement and a comparison with four common drain fixation methods. The Annals of The Royal College of Surgeons of England. 2019 Jan;101(1):60-8. Available from: https://doi.org/10.1308/rcsann.2018.0177.

[440] Di Pietro V, Amorini AM, Tavazzi B, Hovda DA, Signoretti S, Giza CC, et al. Potentially neuroprotective gene modulation in an in vitro model of mild traumatic brain injury. Molecular and Cellular Biochemistry. 2012 Dec;375(1–2):185–198. Available from: http://dx.doi.org/10.1007/s11010-012-1541-2.

[441] Di Pietro V, Amin D, Pernagallo S, Lazzarino G, Tavazzi B, Vagnozzi R, et al. Transcriptomics of Traumatic Brain Injury: Gene Expression and Molecular Pathways of Different Grades

of Insult in a Rat Organotypic Hippocampal Culture Model. Journal of Neurotrauma. 2010 Feb;27(2):349–359. Available from: http://dx.doi.org/10.1089/neu.2009.1095.

[442] Kilanczyk E, Andres KR, Hallgren J, Ohri SS, Laiho M, Whittemore SR, et al. Pharmacological inhibition of spinal cord injury-stimulated ribosomal biogenesis does not affect locomotor outcome. Neuroscience Letters. 2017 Mar;642:153–157. Available from: http://dx.doi.org/10.1016/j.neulet.2017.02.011.

[443] Wang Z, Hu XY, Li X, Wang XK, Zhu ZJ, Liang ZW, et al. Photobiomodulation provides neuroprotection through regulating mitochondrial fission imbalance in the subacute phase of spinal cord injury. Neural Regeneration Research. 2023;18(9):2005-10. Available from: http://dx.doi.org/10.4103/1673-5374.366491.

[444] Di Pietro V, Lazzarino G, Amorini AM, Signoretti S, Hill LJ, Porto E, et al. Fusion or Fission: The Destiny of Mitochondria In Traumatic Brain Injury of Different Severities. Scientific Reports. 2017 Aug;7(1). Available from: http://dx.doi.org/10.1038/s41598-017-09587-2.

[445] Surmacki JM, Ansel-Bollepalli L, Pischiutta F, Zanier ER, Ercole A, Bohndiek SE. Label-free monitoring of tissue biochemistry following traumatic brain injury using Raman spectroscopy. The Analyst. 2017;142(1):132–139. Available from: http://dx.doi.org/10.1039/C6AN02238C.

[446] Sacharz J, Wesełucha-Birczyńska A, Zięba-Palus J, Lewandowski MH, Kowalski R, Palus K, et al. Epileptic rat brain tissue analyzed by 2D correlation Raman spectroscopy. Spectrochimica Acta Part A: Molecular and Biomolecular Spectroscopy. 2018 Jan;188:581–588. Available from: http://dx.doi.org/10.1016/j.saa.2017.07.046.

[447] Staniszewska-Slezak E, Malek K, Baranska M. Complementary analysis of tissue homogenates composition obtained by Vis and NIR laser excitations and Raman spectroscopy. Spectrochimica Acta Part A: Molecular and Biomolecular Spectroscopy. 2015 Aug;147:245–256. Available from: http://dx.doi.org/10.1016/j.saa.2015.03.086.

[448] Dutta A, Gautam R, Chatterjee S, Ariese F, Sikdar SK, Umapathy S. Ascorbate Protects Neurons against Oxidative Stress: A Raman Microspectroscopic Study. ACS Chemical Neuroscience. 2015 Aug;6(11):1794–1801. Available from: http://dx.doi.org/10.1021/ACSCHEMNEURO.5B00106.

[449] Lemler P, Premasiri WR, DelMonaco A, Ziegler LD. NIR Raman spectra of whole human blood: effects of laser-induced and in vitro hemoglobin denaturation. Analytical and Bioanalytical Chemistry. 2013 Oct;406(1):193–200. Available from: http://dx.doi.org/10.1007/S00216-013-7427-7.

[450] Tay LL, Tremblay RG, Hulse J, Zurakowski B, Thompson M, Bani-Yaghoub M. Detection of acute brain injury by Raman spectral signature. The Analyst. 2011;136(8):1620. Available from: http://dx.doi.org/10.1039/C0AN00897D.

[451] Talari ACS, Movasaghi Z, Rehman S, Rehman Iu. Raman Spectroscopy of Biological Tissues. Applied Spectroscopy Reviews. 2014 Aug;50(1):46–111. Available from: http://dx.doi.org/10.1080/05704928.2014.923902.

[452] Demediuk P, Fadan AI, Romhanyi R, Vink R, McIntosh TK. Traumatic Brain Injury in the Rat: Effects on Lipid Metabolism, Tissue Magnesium, and Water Content. Journal of Neurotrauma. 1988 Jan;5(2):105–119. Available from: http://dx.doi.org/10.1089/neu.1988.5.105.

[453] Mallah K, Quanico J, Trede D, Kobeissy F, Zibara K, Salzet M, et al. Lipid Changes Associated with Traumatic Brain Injury Revealed by 3D MALDI-MSI. Analytical Chemistry. 2018 Aug;90(17):10568–10576. Available from: http://dx.doi.org/10.1021/ACS.ANALCHEM.8B02682.

[454] Harris G, Stickland CA, Lim M, Goldberg Oppenheimer P. Raman Spectroscopy Spectral Fingerprints of Biomarkers of Traumatic Brain Injury. Cells. 2023 Nov;12(22):2589. Available from: http://dx.doi.org/10.3390/cells12222589.

[455] Wolthuis R, van Aken M, Fountas K, Robinson, Bruining HA, Puppels GJ. Determination of water concentration in brain tissue by Raman spectroscopy. Analytical Chemistry. 2001 Jul;73(16):3915–3920. Available from: https://doi.org/10.1021/ac0101306.

[456] Heggie C, Gray-Burrows KA, Day PF, Phillips B. An exploration of the use of photobiomodulation for management of oral mucositis in children and young people undergoing cancer treatment in the UK. Supportive Care in Cancer. 2022 Nov;30(12):10179–10190. Available from: http://dx.doi.org/10.1007/s00520-022-07450-3.

[457] Serrage HJ, Eling CJ, Alves PU, Mcbain AJ, O'neill C, Laurand N. Spectral Characterization of a Blue Light-Emitting Micro-LED Platform and Microbial Chromophores for Therapeutic Applications in Skin Conditions. bioRxiv pre-print. 2024 Mar. Available from: http://dx.doi.org/10.1101/2024.03.05.582921.

Appendix A

RAMAN SPECTROSCOPY IN TRAUMATIC BRAIN INJURY

This appendix has been published in a peer-reviewed journal:

A.R. Stevens, C. Stickland, G. Harris, Z. Ahmed, P. Goldberg Oppenheimer, A. Belli, D.J. Davies. Raman Spectroscopy as a Neuromonitoring Tool in Traumatic Brain Injury: A Systematic Review and Clinical Perspectives. *Cells* 2022 Apr 5;11(7):1227. doi: 10.3390/cells11071227.

cells

MDPI

Systematic Review

Raman Spectroscopy as a Neuromonitoring Tool in Traumatic Brain Injury: A Systematic Review and Clinical Perspectives

Andrew R. Stevens [1,2,*], Clarissa A. Stickland [3], Georgia Harris [3], Zubair Ahmed [1,2,4], Pola Goldberg Oppenheimer [3], Antonio Belli [1,2,4] and David J. Davies [1,2,4]

1 Neuroscience, Trauma and Ophthalmology, Institute of Inflammation and Ageing, University of Birmingham, Birmingham B15 2TT, UK; z.ahmed.1@bham.ac.uk (Z.A.); a.belli@bham.ac.uk (A.B.); daviesdj@doctors.org.uk (D.J.D.)
2 NIHR Surgical Reconstruction and Microbiology Research Centre, University Hospitals Birmingham, Birmingham B15 2TH, UK
3 School of Chemical Engineering, University of Birmingham, Birmingham B15 2TT, UK; cas784@student.bham.ac.uk (C.A.S.); gxh975@student.bham.ac.uk (G.H.); p.goldbergoppenheimer@bham.ac.uk (P.G.O.)
4 Centre for Trauma Science Research, University of Birmingham, Birmingham B15 2TT, UK
* Correspondence: a.stevens@bham.ac.uk

Abstract: Traumatic brain injury (TBI) is a significant global health problem, for which no disease-modifying therapeutics are currently available to improve survival and outcomes. Current neuromonitoring modalities are unable to reflect the complex and changing pathophysiological processes of the acute changes that occur after TBI. Raman spectroscopy (RS) is a powerful, label-free, optical tool which can provide detailed biochemical data in vivo. A systematic review of the literature is presented of available evidence for the use of RS in TBI. Seven research studies met the inclusion/exclusion criteria with all studies being performed in pre-clinical models. None of the studies reported the in vivo application of RS, with spectral acquisition performed ex vivo and one performed in vitro. Four further studies were included that related to the use of RS in analogous brain injury models, and a further five utilised RS in ex vivo biofluid studies for diagnosis or monitoring of TBI. RS is identified as a potential means to identify injury severity and metabolic dysfunction which may hold translational value. In relation to the available evidence, the translational potentials and barriers are discussed. This systematic review supports the further translational development of RS in TBI to fully ascertain its potential for enhancing patient care.

Keywords: traumatic brain injury; neuromonitoring; Raman spectroscopy; point-of-care diagnostics; neuroinflammation; oxidative stress; metabolic dysfunction

check for updates

Citation: Stevens, A.R.; Stickland, C.A.; Harris, G.; Ahmed, Z.; Goldberg Oppenheimer, P.; Belli, A.; Davies, D.J. Raman Spectroscopy as a Neuromonitoring Tool in Traumatic Brain Injury: A Systematic Review and Clinical Perspectives. *Cells* **2022**, *11*, 1227. https://doi.org/10.3390/cells11071227

Academic Editors: Andrew Chih Wei Huang, Seong Soo A. An, Bai Chuang Shyu, Muh-Shi Lin and Anna Kozłowska

Received: 17 March 2022
Accepted: 4 April 2022
Published: 5 April 2022

Publisher's Note: MDPI stays neutral with regard to jurisdictional claims in published maps and institutional affiliations.

Copyright: © 2022 by the authors. Licensee MDPI, Basel, Switzerland. This article is an open access article distributed under the terms and conditions of the Creative Commons Attribution (CC BY) license (https://creativecommons.org/licenses/by/4.0/).

1. Introduction

Traumatic brain injury (TBI) is a significant global health problem [1,2]. The incidence of TBI in Europe is estimated at 1012 cases per 100,000 people per year, and 939 per 100,000 globally [3]. The total annual cost globally is estimated in the region of EUR 55 billion [4]. At present, there are no disease-modifying treatments shown to improve outcomes [5], and it remains a leading cause of death and disability across age groups [6]. After an injury, survivors may develop a range of physical, cognitive, and behavioural symptoms which can have a significant and permanent impact on quality of life [7,8], and TBI is associated with an increased risk of neurodegeneration and dementia [9].

'Primary brain injury' is sustained from the trauma itself, whilst 'secondary brain injury' occurs after injury due to adverse sequelae resulting in further cell death and dysfunction [10]. In the early stage after injury, the development of cerebral oedema and expansion of surgical mass lesions result in increased intracranial pressure (ICP) and compromise of cerebral blood flow and oxygenation [11]. Contemporary therapeutic paradigms

are based on the correction and normalisation of these indices as supportive measures [5,11]. However, TBI has a complex pathophysiology, with a number of mechanisms contributing to the development of secondary injury [12]. Mitochondrial dysfunction [13], metabolic failure [14], excitotoxicity [15], oxidative stress [16], and neuroinflammation [17] are established mediators of ongoing neural injury burden after primary trauma and contribute to poor outcomes to an as-yet unquantified extent.

Current neuromonitoring strategies principally centre on ICP through the introduction of an invasive fibre optic probe into the parenchyma [5,11]. Growing evidence for partial brain tissue oxygen monitoring has increased its implementation in clinical practice [18,19]. Microdialysis of parenchymal tissue is implemented in some centres which provide some metabolic indices [20]. Beyond these modalities, few established means of interrogating the state of neural tissue exist in clinical practice. With the growing complexities of known pathophysiological mechanisms in TBI, there is an increasing need for neuromonitoring to increase in breadth, fidelity, and detail, particularly in monitoring tissue biochemistry.

Raman spectroscopy (RS) is a molecular monitoring technique, dependent on the inelastic scattering of photons detectable after excitation from a monochromatic light source. RS has gained interest in medical applications as a sensitive, label-free optical monitoring modality, capable of detecting molecular changes in real time [21–23]. The key to the suitability of RS is its non-destructive nature: it permits accurate tissue interrogation at a molecular level without compromising tissue integrity. RS has in recent years developed a growing interest in a number of potential medical diagnostic applications [22]. These include the diagnosis of atherosclerotic plaques during endovascular cardiac interventions, diagnosis of inflammatory bowel disease during endoscopy, and cancer diagnosis in a number of organs and tissue types.

RS is the technique in which the inelastically scattered light detectable from an excited molecule is exploited for information on the molecule's structure. Upon excitation by a monochromatic light source (e.g., a laser), electrons in a molecule are excited, inducing a dipole. The dipole interacts with the light and can hereafter be distinctly categorised as follows: elastic Rayleigh scattering and inelastic Stokes and anti-Stokes scattering. The Raman effect is observed through the latter two, in which the scattered light has either a higher or lower frequency than that of the laser. For the light to have a higher frequency, as in anti-Stokes scattering, the molecule will have been in an excited state prior to being exposed to light. As the molecule relaxes to its ground state, the emitted photon has more energy in comparison to the photon emitted from the laser. Most molecules, however, are found in their ground state at room temperature, making this event unlikely. For this reason, usually, only Stokes scattering is considered. Stokes scattering consists of a ground state molecule being raised to a higher energy state as a result of exposure to the laser. The molecule returns to an energy state above the ground state: as such, the photon has a lower energy value than that of the laser. RS data acquired are expressed as a function of the Raman wavenumber, the shift being the difference in frequency between the induced light and the scattered light. Each Raman shift is distinct due to the specific molecular vibration each molecule will have, dependent on the number of atoms present, bond lengths, atoms present, etc. The differences recorded provide each molecule a unique, label-free fingerprint, regardless of the concentration of sample present, and is non-destructive, making RS a powerful tool [24] and compatible with use in vivo.

The downfall of RS lies in its inherently weak nature. The number of photons inelastically scattered is comparatively small, compared with the elastically scattered light. This means the signal is easily overwhelmed by fluorescence, especially from organic molecules. To counter this, the lasers used tend to lie in the near-infrared range, the industrial standard being 785 nm, which allows for the least fluorescence without compromising on the resolution. Other approaches to improve outputs have been to take advantage of nanoscale features of surfaces such as gold or copper to chemically and electromagnetically enhance the sample. This is known as surface-enhanced Raman scattering (SERS) and is considered

the most effective way to increase the Raman signal. The need to place the sample on a specialised surface for the SERS procedure, however, limits its use to ex vivo applications.

RS has been the subject of growing interest in pre-clinical studies for the identification and study of a number of pathophysiological mechanisms. For example, RS has been used to detect oxidative stress-induced inflammation in human endothelial cells [25], excitotoxicity in epithelial cells [26], and tracking mitochondrial function [27]. Raman techniques have been utilised in alternative brain injury models, demonstrating consistent RS spectral changes in response to injury, including rat ischaemia–reperfusion injury [28], biochemical change in post-traumatic stress disorder rat models [29], and radiation damage to the brain in mice [30]. RS has been used in the identification of pathognomonic biochemical alterations in a number of neurodegenerative disorders in pre-clinical studies [31] and the identification of neoplasia in cerebral tissue [32]. RS has found applications and interest in neuro-oncological surgery in recent years [33–43]. For rapid intraoperative diagnosis of excised tissue, interest has grown in Raman histology, that is, the use of Raman microscopy with deep convolutional neural networks for rapid and accurate prediction of tissue diagnosis for use in the operating theatre [44]. The application of RS for intraoperative differentiation of normal brain tissue and glioma tissue demonstrates a proof of concept for monitoring applications in the human brain [33], but the exploration of this in the context of TBI has been limited.

The aim of this systematic review was to perform a literature search to identify the purpose of RS in TBI. We discuss the current literature on the utilisation of RS methods in pre-clinical and clinical development for monitoring in TBI and explore the translational challenges and the potential future clinical applications.

2. Materials and Methods

A systematic review of the literature was performed to identify relevant articles employing RS analysis in the setting of TBI. A comprehensive search was performed on 29 September 2021 following the methodology of the Cochrane Handbook for Systematic Reviewers and presented in accordance with the Preferred Reporting Items for Systematic Reviews and Meta-Analyses (PRISMA) [45].

Two authors (A.S. and Z.A.) systematically searched the following databases, from their respective inception to 29 September 2021: MEDLINE, EMBASE, Cochrane Central, Scopus, Google Scholar, and Web of Science. Reference lists of pertinent articles on the topic were hand-searched for suitable articles. Reference lists of identified articles for inclusion were also hand-searched for suitable articles. An example search strategy for Medline is given below:

1. Exp Traumatic brain injury;
2. Exp craniocerebral trauma;
3. Keywords 1 or 2;
4. Raman spectroscopy;
5. Exp spectrum analysis, Raman;
6. Keywords 4 or 5;
7. Keywords 3 and 6.

2.1. Study Selection

Studies were independently screened for inclusion by two reviewers (A.S. and Z.A.). Initial screening based on title and abstract was performed, followed by full-text screening. Inclusion criteria were defined as utilisation of RS methods (alone or in combination with other methods) for analysis of cerebral tissue from either in vitro or in vivo models of TBI, or clinical use in patients with TBI. Exclusion criteria were articles in which no RS methods were used, or no TBI tissue was utilised.

2.2. Data Extraction

Data were extracted from included reports using a piloted form. Data extracted included animal model used, number of replicates, Raman techniques used, the wavelength of the excitatory laser, any tissue fixing prior to analysis, reported outcome, analytical methods, spectral signatures identified, and author conclusions.

2.3. Risk of Bias

Risk of bias in individual studies was assessed using SYRCLE's tool for assessing the risk of bias [46], and the overall risk of bias was determined as low, moderate, or high for each included article.

2.4. Synthesis of Results

The heterogeneous nature of data collection and analysis methods precludes our ability to combine and synthesise results into a meta-analysis, and therefore, what follows is a qualitative summary of the results.

3. Results

3.1. Animal Models of TBI

The search identified 131 articles and after the removal of duplicates, 62 remained. Fifteen articles met our inclusion/exclusion criteria and, after full-text reading, seven studies were included in our final analysis (flow diagram in Figure 1). The included study characteristics are summarised in Table 1. Five additional studies utilised RS techniques for ex vivo biofluid assessment in the context of TBI, and four additional studies investigated RS in mechanistic models relevant to TBI. These are discussed separately in this review. Due to the heterogeneity in the data presented, a meta-analysis was not possible; hence, we performed a qualitative analysis of each study (Figure 1).

Table 1. Characteristics of the included studies. CCI = controlled cortical impact; FTIR = Fourier transform infrared spectroscopy; mTBI = mild traumatic brain injury; RS = Raman spectroscopy; sTBI = severe traumatic brain injury.

Author	Year	Type	Animal	Model Used	Raman Technique (Wavelength)	Overall Risk of Bias
Banbury et al.	2020	Article	Mouse	In vivo CCI mTBI/sTBI	Confocal RS (785 nm)	Moderate
Ercole et al.	2017	Abstract	Mouse	In vivo CCI sTBI	Confocal RS imaging (785 nm)	Moderate
Hu et al.	2016	Article	Rat	Stretch organotypic hippocampal slice cultures	Stimulated Raman scattering (720–990 nm pump beam, 1064 nm Stokes laser)	Moderate
Mowbray et al.	2021	Article	Rat	In vivo CCI sTBI	Confocal RS (785 nm)	Moderate
Surmacki et al.	2016	Article	Mouse	In vivo CCI	Confocal RS (785 nm)	Moderate
Tay et al.	2011	Article	Mouse	In vivo CCI	Confocal RS (785 nm)	Moderate
Kawon et al.	2021	Article	Rat	In vivo drill focal injury	Confocal RS (532 nm)—Additionally, FTIR-only Raman findings reported in this article	Moderate

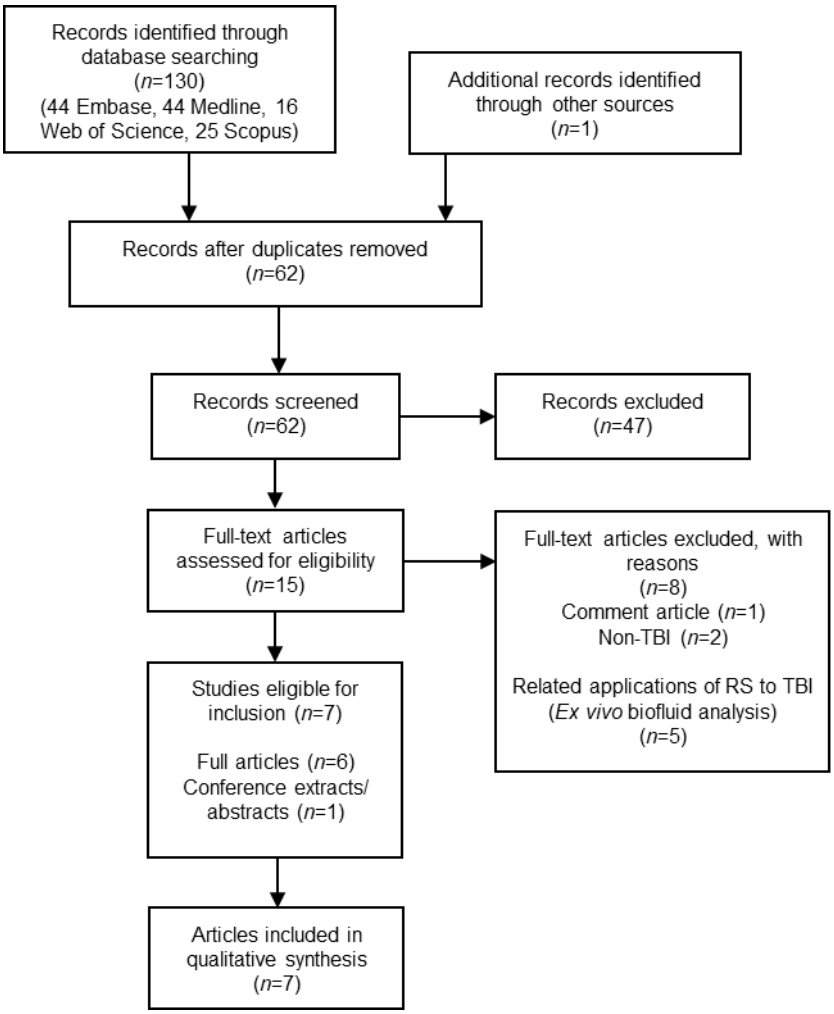


Figure 1. PRISMA flowchart of the systematic review process.

Banbury et al. [47] utilised a murine model of controlled cortical impact (CCI) to administer either a mild TBI, severe TBI, or no injury (sham). Three days post-injury, the animal was sacrificed. Brain and retina samples were prepared for confocal RS after paraformaldehyde fixation and air drying. 80% of spectral readings were used as input for a 'self-optimising Kohonen index network' (SKiNET [48]), a machine learning technique. The remaining 20% were utilised as 'test' spectra. With this, RS of the retina was able to 'predict' sTBI in 82% of cases and mild TBI in 75.1%. Brain tissue samples demonstrated a number of spectral changes between injury groups. Severe TBI resulted in a modest relative increase at 1447 cm^{-1}, accompanied by a significant decrease at 1660 cm^{-1}. Mild TBI demonstrated the same decrease at 1660 cm^{-1} but remained unchanged at 1447 cm^{-1} in comparison to sham. Both injury severities demonstrated a decrease in the band at 1266 cm^{-1}. Spectra retrieved were compared with a spectral library to ascertain possible biochemical candidates responsible for the spectral shift observed in injury. Cardiolipin and cytochrome c spectra from a library were identified to fit well and as potential candidates for the spectral effect.

Ercole et al. [49] utilised false colour imaging with a Raman microscope in fresh frozen sections of mouse brain tissue 2 and 7 days after severe TBI. Injured specimens demonstrated strong signals at 1003 and 1560 cm^{-1} persisting at 7 days. They also imaged ipsilateral corpus callosum and internal capsule sections from a site distant from the lesion. These demonstrated reductions in peaks at 1301 and 1440 cm^{-1}, partially recovering at 7 days. In a similar study by this group, reported by Surmacki et al. [50], they used these time points of 2 and 7 days in a CCI mouse model of TBI. In this study, they took spectroscopic readings from whole-brain specimens from the contralateral brain, ipsilateral

brain distant from contusion core, pericontusional tissue, and contusion core tissue, as well as comparison to sham injury. Their results demonstrated changes in the 1440/1660 cm^{-1} ratio both early (2 days) in the contusion core and late (7 days) in contralateral tissue, suggestive of both local and global biochemical changes in lipid/protein ratio content in response to TBI. The further principal component analysis identified changes in the 701/718 cm^{-1} ratio, corresponding with cholesterol/phospholipid. They hypothesised that the relative increase in cholesterol signal in the contusion core may relate to increasing amyloid-β formation. The group also noted striking features of haem protein in the Raman spectra in early samples from contusion core which resolved by day 7, demonstrating the potential of RS for identifying haemorrhagic conversion/resolution.

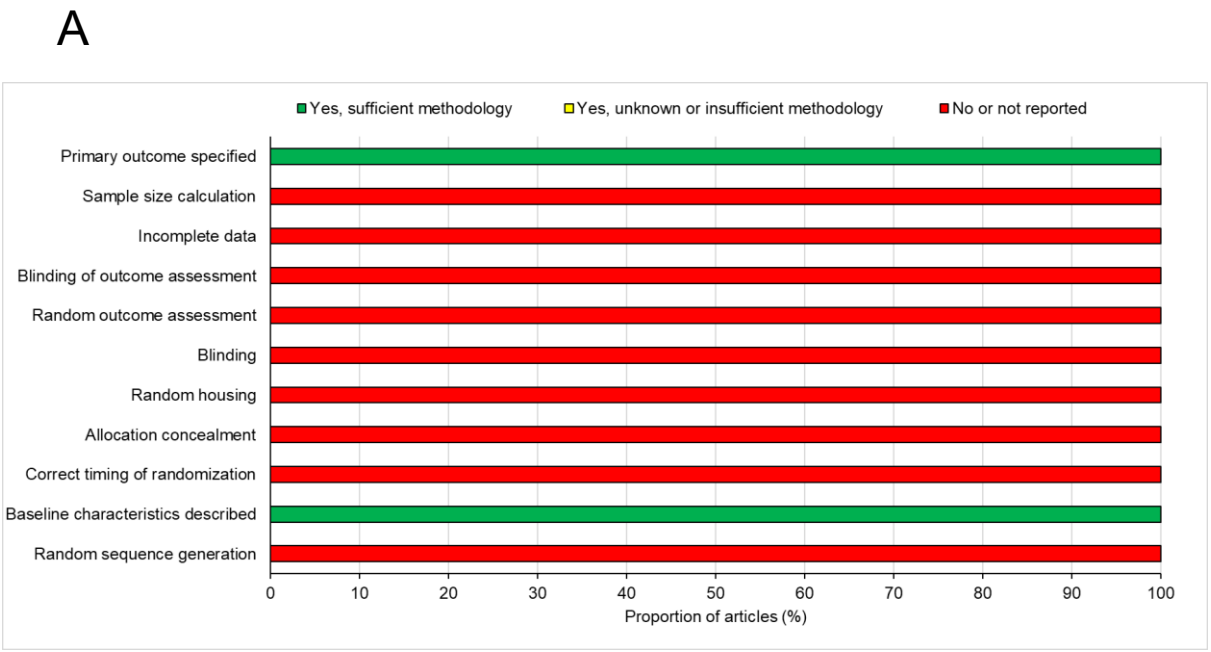
Mowbray et al. [51] utilised a controlled cortical impact model of TBI from Sprague Dawley rats. The group observed a fall in 1266 and 1660 cm^{-1} peaks in injured specimens when compared with control. Control specimens also had a relatively smaller 1447 cm^{-1} peak in comparison to TBI. The group utilised a handheld probe device (InPhotonics Raman Probe II, Norwood, MA, USA) with a novel transcranial bolt device fitted with a quartz 'window' to permit optical access to the parenchyma. The results of spectra gained from ex vivo animal tissue were obtained using this probe system, which demonstrates proof of concept for the translational ability of RS for in vivo human monitoring of brain issue biochemistry. Research by Tay et al. also identified spectral shifts associated with immunohistochemical findings of caspase-3 expression, adding further observations to support a role for RS as a monitoring modality for levels of cell death or survival after injury.

Kawon et al. [52] principally studied the use of Fourier transform infrared microspectroscopy, supplemented by RS to analyse rat brain samples 30 days after focal injury. They too noted RS changes at 1658 cm^{-1}, increasing in intensity associated with glial scarring which they postulated to correspond to matricellular protein release by astrocytes. They also observed reductions at 30 days in 2955 cm^{-1} bands which they hypothesised to be linked to reduced levels of lipids from the destruction of healthy tissue.

Hu et al. [53] utilised rat organotypic hippocampal slice cultures for 'live' qualitative imaging by stimulated Raman scattering. Slices after cultured were subjected to stretch mechanical injury and cultured with deuterated amino acids and lipids, which were then visualised with stimulated Raman scattering after 24 h. This was able to demonstrate that increased protein and lipid synthesis occurred in injured hippocampal slices in comparison with uninjured tissue. Due to the necessity of deuterated substrates added to culture media, this technique involves labelling. The 'label-free' potential of Raman spectroscopic methods is an attractive feature when considering the translational potential to in vivo settings and is not the case with the methods used here. However, this study demonstrates in principle the potential for Raman spectroscopic methods to be able to interrogate the biochemistry of living injured tissue.

3.2. Risk of Bias

All of the included studies stated their primary outcomes and described baseline characteristics (Figure 2). However, none of the studies reported whether they performed a sample size calculation, how incomplete data were dealt with, whether outcomes were randomly assessed, blinding of investigators, random housing of animals, whether the allocation of animals to groups was concealed, correct timing of randomisation, and whether a random sequence was generated in terms of study design. Therefore, there is potentially high risk of bias in all of these animal studies. However, future studies may avoid the apparent high risk of bias by following a set of standardised techniques in animal experiments based on the ARRIVE guidelines [54].



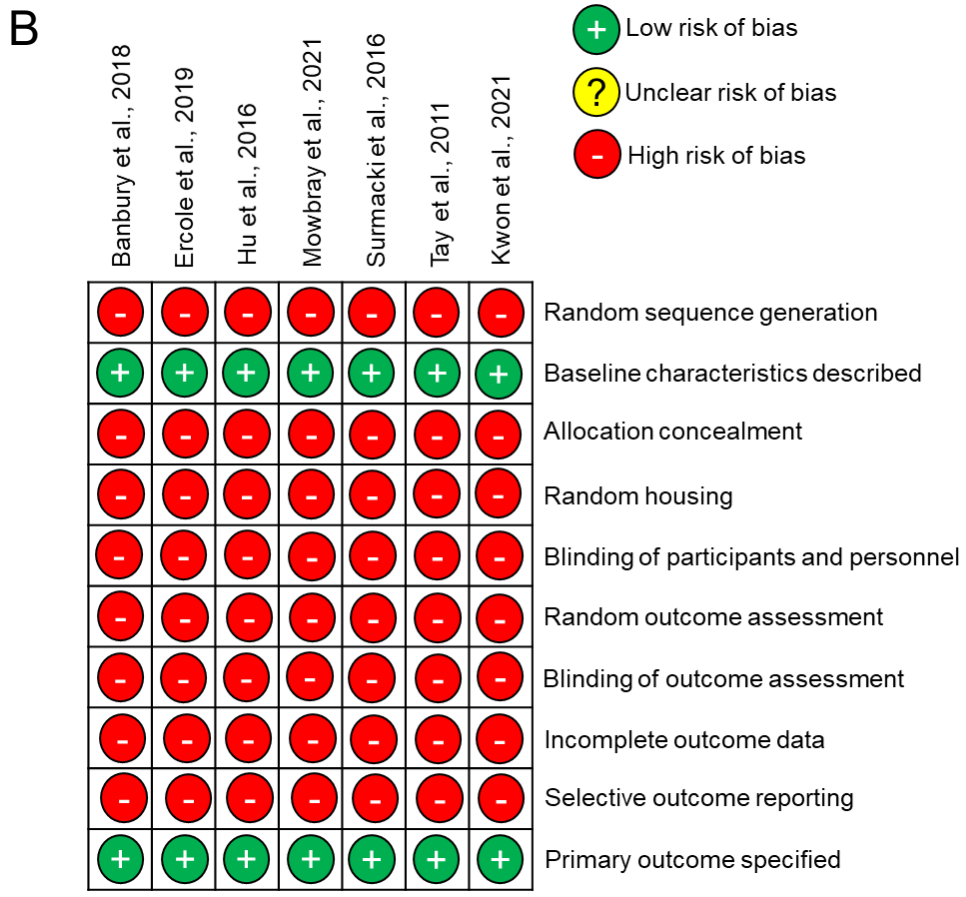


Figure 2. Risk of bias analysis for the included studies using the SYRCLE tool: (**A**) risk of bias summary in all studies; (**B**) risk of bias in individual studies.

3.3. Analogous Animal Studies with Applicable Adverse Tissue Conditions

Hackett et al. [55] utilised resonance RS for selective imaging of haem components in the lesion site and perilesional tissue in a collagenase model of intracerebral haemor-

rhage (ICH) in the rat. Whilst a model of primary haemorrhagic stroke, ICH models can be considered translatable to the TBI pathophysiology given the frequent incidence of contusion, an analogous pathology, in the traumatically injured cohort. This group was able to utilise haem signal intensity to quantitatively identify the haemorrhagic boundary, peri-haemorrhagic tissue, and normal tissue. This was utilised in a multimodal array, with RR, Fourier transform infrared imaging, and X-ray fluorescence imaging, to improve accuracy and quantitative assessment, and was further used to assess haematoma volume response to rehabilitative therapy [56].

Jung et al. [28] investigated RS in ischaemia–reperfusion injury in a rat model. Though an established model, their study had very small sample sizes, with one specimen in each arm. The group was able to gain spectral data from hippocampal (cornu ammonis area 1) tissue post-mortem ex vivo. In ischaemic versus control models, 1276 and 1658 cm^{-1} bands increased in injury, whereas 1300 and 1438 cm^{-1} bands decreased.

Dutta et al. [57] modelled oxidative stress in hippocampal primary network neuronal culture with the addition of hydrogen peroxide in the presence of Fe^{2+}. Oxidative stress is an established mechanism of secondary injury after TBI [58]. Based on their results, 725 cm^{-1} and 1320/40 cm^{-1} bands decreased progressively at the measured 20 min intervals over the 80 min post-exposure. This effect of oxidative stress was ameliorated by the addition of ascorbate, which correlated with live–dead cell counts. As such, the group further demonstrated the ability of RS to identify this therapeutic response.

Lakshmi et al. [30] conducted RS studies on radiation damage to the brain tissue in mice. After exposure to 10 Gy irradiation or control (anaesthesia alone), Raman spectra were obtained from both white and grey matter. These demonstrated early shifts in 1440 and 1660 cm^{-1} regions which were sustained over one-week post-exposure.

3.4. Biofluid Diagnostics

Detecting biochemical changes via TBI biomarkers using accessible samples such as blood, saliva and urine can provide early information in the vital acute phase (<24 h) of injury incidence [59] for triaging, monitoring, and diagnostics. Highly investigated TBI biomarkers include S100B, glial fibrillary acidic protein (GFAP), neuron-specific enolase (NSE), and ubiquitin C-terminal hydrolase-L1 (UCHL1) [60]. In 2007, the Scandinavian healthcare system introduced S100B into clinical practice guidelines to predict negative CT scans, thus reducing the number of unnecessary scans [61].

A popular modified RS technique is surface-enhanced Raman spectroscopy (SERS) which links the optimum excitation wavelength to the size, shape, composition, and dielectric environment of nanoparticles [62]. This method requires a rough, metal SERS active substrate to absorb the analyte or for the SERS substrate to be coated in nanostructures [63], via metal colloids in a thin film layer. Rickard et al. [64] developed an optofluidic device using SERS capable of detecting picomolar concentrations of *N*-acetylaspartate (NAA) [64]. NAA is an abundant molecule in the central nervous system (CNS) which is released following TBI and is believed to correlate with injury severity and poor prognosis [65]. The device was also able to detect and discriminate concentrations of S100B and GFAP, (glial fibrillary acidic protein) also recognised biomarkers of neurological injury burden [66]. Whilst this device is developed as an ex vivo tool for monitoring the presence of markers in biofluids, its ability to detect such biomarkers in minute concentrations represents the significant potential of RS for diagnostic resolution for biomarker monitoring.

Gao et al. [67,68] utilised SERS with a paper-based lateral flow assay system with a SERS labelled detection antibody to identify S100B in human blood samples. Using blood samples from patients with TBI, they demonstrated a good correlation with laboratory ELISA measured values of S100B concentration in the samples. Their system was developed to offer a reduced cost and time for the identification of biomarkers of TBI. Li et al. [69] similarly implemented SERS for the assessment of neuron-specific enolase (NSE), a biomarker of TBI, in diluted plasma samples from patients with TBI. With a 'lateral-flow glass-hemostix'-based SERS assay, the group identified a lower limit of detection of 0.74 ng/mL. These

studies demonstrate sufficient fidelity and performance of SERS-based assay in clinically relevant biomarker assay to suggest potential translatability to point-of-care testing.

O'Neal et al. [70,71] demonstrated the utility of SERS for the identification of excitatory amino acids in dialysate from a rat model of ischaemic brain injury after middle cerebral artery occlusion. Glutamate and aspartate in microdialysate were found to be distinguishable using SERS. A comparison of a SERS-based assay with high-performance liquid chromatography was able to identify concentrations of glutamate between 0.4 and 5 μmol/L.

3.5. Spectral Evidence from Animal Models

Understanding spectral data from RS in TBI is integral to identifying translatable value for clinical applications. Table 2 offers a summary of the literature on observed spectral changes in animal models of TBI and analogous mechanistic animal studies. Clear and reproducible shifts in peaks are identified across multiple studies and models. A notable contradiction is the 1660 cm^{-1} peak: TBI models have identified a consistent reduction in 1660 cm^{-1} intensity in comparison with control [48,51,52,72]. In contrast, an ischaemia–reperfusion model of brain injury identified an increase in the 1660 cm^{-1} intensity. The shift may alter between these pathologies; however, the validity of these results is highly questionable given the use of $n = 1$ specimen in control and test groups.

Table 2. Consolidation of Raman spectral data for noted wavenumbers which have demonstrated changes in TBI models or analogous mechanistic models. Assignment data are taken from corresponding references or alternative sources [43,47,50,57,72–97]. Peak assignments based on spectra from excitation with 785 nm laser unless otherwise stated. DNA = deoxyribonucleic acid; Hb = haemoglobin; A = adenine; C = cytosine; G = guanine; mTBI = mild traumatic brain injury; sTBI = severe traumatic brain injury; T = thymine.

Peak Wavenumber (cm^{-1})	Appropriation	TBI
426	Hb [50] Cholesterol [50]	Increasing in contusion core between 2 and 7 days [50]
491-2	Combination modes of the uracil ring plus ribose vibrations [92]	Increasing in contusion core between 2 and 7 days [50]
605	Cholesterol [50]	Increased in contusion core vs. contralateral hemisphere [50]
675	Hb [50], glycerol [93]	Decreasing in contusion core between 2 and 7 days [50]
701-2	Lipids (701 cm^{-1}) [50], cholesterol, cholesterol ester	Increasing in contusion core between 2 and 7 days [50]
718	Symmetric and anti-symmetric stretch vibrations of the choline group $N+(CH_3)_3$ in phospholipid, lipids [50]	Decreased in contusion core vs. contralateral hemisphere (2 and 7 days) [50]
725	nucleic acid (A) [57,94]	Reduced oxidative stress [57]
754	Hb [50]	Increased in contusion core vs. contralateral hemisphere (2 and 7 days) [50], decreasing in contusion core between 2 and 7 days [50]
782	DNA peak, cytosine (C), uracil (U), thymine (T), C, T, U-ring breathing [57,95]	Reduced oxidative stress [57]
801	Cyclohexane [74,75,98] (532 nm [96], 575 nm [73] and 785 nm [97] excitation)	Increased in contusion core vs. contralateral hemisphere [50]
850-2	C-H wagging [72] (850 cm^{-1}), C−C stretch in proline (collagen) [94]; ring breathing (tyrosine) [94]; C−O−C stretching (glycogen, polysaccharides) [57,94], albumin (852 cm^{-1}) [50]	Increased in mTBI and sTBI (3 days) [47]

Table 2. *Cont.*

Peak Wavenumber (cm^{-1})	Appropriation	TBI
970	Intralipid [50] haem aggregation marker bands, fibrin components [74]; C-C stretching mixed with C-H rocking, biliverdin, protoporphyrin IX [75]	Decreasing in contusion core between 2 and 7 days [50]
1002	Ring breathing mode of phenylalanine (1002 cm^{-1}) [50] and (1005 cm^{-1}) [57]	Decreasing in contusion core between 2 and 7 days [50], decreased in sTBI (3 days) [47,51], decreasing in contusion core between 2 and 7 days [50], weak or absent in injured samples [77]
1003	C-C skeletal [72], phenylalanine [76,94], Hb, albumin [50]	Decreasing in contusion core between 2 and 7 days [50], strong signal in pericontusional tissue (days 2 and 7) [49]
1079	Intralipid [50]	Decreasing in contusion core between 2 and 7 days [50]
1090	PO_2 stretch, phospholipids and nucleic acid [77]	Stable in oxidative stress [57]
1096-8	Phosphodioxy PO_2 [78], nucleic acid (1097 cm^{-1}) [94]	Increased in mTBI and sTBI (3 days) [47]
1154	Phenylalanine, tryptophan, hypro, tyr, phe, m(CC/CN) proteins (1155 cm^{-1}) [94] and (1156 cm^{-1}) [57]	Decreasing in contusion core between 2 and 7 days [50]
1175	Amide III vibration, cholesterol [77]	Band appears after injury [77]
1224	Hb [50]	Increased in contusion core vs. contralateral hemisphere (2 days) [50], decreasing in contusion core between 2 and 7 days [50]
1227-8	Amide III vibration, phospholipid [77] (1227 cm^{-1}); C-H methine bending vibration with changing methaemaglobin content (1228 cm^{-1}) [79]	Increased in contusion core vs. contralateral hemisphere [50], band after injury [77]
1266	CH bending modes [72]: amide groups in lipids and proteins [76], cardiolipin [47]	Decreased in mTBI and sTBI (3 days) [47,51], decreased in contusion core vs. contralateral hemisphere (2 and 7 days) [50]
1301	CH_2 twist/wag/deformation: phospholipid, mixed fatty acid chains, mixed amide III protein vibration [77], lipids [50]	Increasing in contusion core between 2 and 7 days [50], reduction in peak in ipsilateral corpus callosum and internal capsule (distant from lesion) at 2 days, partially recovering by 7 days [49]
1320	CH_2 CH_3 twisting; Proteins/lipids nucleic acid [57]	Reduced oxidative stress [57]
1337-1340	Nucleic acid (A,G) [57]; b protein CH_2 deformation [72], amide III [76] (1337 cm^{-1}); collagen (1338 cm^{-1}) [94]; albumin(1339 cm^{-1}) [50]; CH_2 scissors, C-OH bending [80]	Reduced in oxidative stress [57], increased in sTBI (3 days) [47,51]
1420	DNA peak, nucleic acid (A, G) [57]; -CH_2 bending mode for proteins and lipids, indicates change in cytochrome c, intracellular environment, and mitochondrial membrane structures [81]	Reduced oxidative stress [57]
1440	CH_2 twisting and bending [51,82,96], Lipid, cholesterol, phospholipid, mixed amide I protein, tyrosine [80,94]	Initially decreased in contusion core vs. contralateral hemisphere (2 and 7 days), increasing progressively in contralateral hemisphere and contusion core between 2 and 7 days, to above control levels [50], reduced after ischaemic injury
1447-50	CH_2 bending [72], mixed proteins and lipids [76] (1447 cm^{-1}) [94], albumin, CH_2 deformation from lipids and proteins (1450 cm^{-1}) [77]	Increased in sTBI (3 days) [47,51]
1462	Lipids [50]	Increasing in contralateral hemisphere between 2 and 7 days [50]

Table 2. *Cont.*

Peak Wavenumber (cm^{-1})	Appropriation	TBI
1547	Hb [50]	Decreased in contusion core vs. contralateral hemisphere (2 and 7 days), decreasing progressively over time [50]
1560	Associated with mitochondrial activity of cells [77]	Strong signal in pericontusional tissue (days 2 and 7) [49]
1562	Hb [50]	Increased in contusion core vs. contralateral hemisphere (2 days resolving by 7 days) [50]
1576	DNA peak, nucleic acid (A, G) [57]; Hb in red blood cells [82] (though not identified by dedicated erythrocyte RS at 785 nm [83]; N = N stretching vibration [84]	Reduced oxidative stress [57]
1586	Albumin [50]	Sharp band after injury [77]
1618-1620	Predominantly C = O stretch in protein, Hb, Amide I (1618 cm^{-1}) [77], tyrosine/tryptophan [94]	Sharp band after injury [77]
1620	Hb [50]	Increased in contusion core vs. contralateral hemisphere (2 days, resolving by 7 days) [50]
1648	Predominantly C = O stretch in protein, Amide I [57]	Decreased in contusion core vs. contralateral hemisphere (2 and 7 days), increasing progressively in contralateral hemisphere over time [50]
1660	Lipids [50], C = C stretching [72,76,82], amide I vibration [57,77], Tyrosine [80,94], mixed lipids and proteins [76], alpha-helix/random coil [94], cardiolipin [47]	Decreased in mTBI and sTBI (3 days) [47,51], decreased in contusion core vs. contralateral hemisphere (2 and 7 days) increasing progressively in contralateral hemisphere and contusion core between 2 and 7 days [50,77]. Increased after ischaemic injury.
1670	Cholesterol, C = C stretching [50]	Marginal increase in contusion core vs. contralateral to lesion [50]

Metrics offer a means of rationalising an otherwise arbitrary intensity measurement obtained from spectra. Table 3 offers a summary of the literature on ratio-based metrics from TBI animal studies. Identification of a consistent, unchanged 'reference' peak which is minimally altered in the context of injury, allows an internal comparator for a dynamic peak of interest. Based on the data, 1440 cm^{-1} is an example of a 'reference' peak, with minimal shift in TBI models; 1660 cm^{-1} operates as a 'dynamic' peak which alters in injury.

Table 3. Metrics utilised in the literature for ratio-based comparative analysis of spectral data [48,51,52]. TBI = traumatic brain injury.

Metrics cm^{-1}/cm^{-1}	Remark	Changes in Animal Models
701/718	Cholesterol/phospholipid	Statistically significant difference between the contralateral and pericontusional/contusional regions at 7 days after TBI [50]
1301/1250	Mixed fatty acid chains/amide III protein	Statistically significant difference between the contralateral and pericontusional/contusional regions at 7 days after TBI [50]
1440/1660	CH deformation/mixed amide I protein and C=C stretching of lipids	Statistically significant difference between the contralateral and pericontusional/contusional regions at 2, 3, and 7 days after TBI [48,51,52]
1301/1620	Mixed amide III protein and fatty acid chains/haemoglobin	Statistically significant difference between the contralateral and pericontusional/contusional regions at 7 days after TBI [50]

Resolution of early strong band signals from haem occurs between 2 and 7 days [50]. Whilst initial haem signal may obfuscate underlying metabolic tissue signal, identification of alterations in haem signal may be clinically advantageous to identify and monitor the temporal evolution of contusion. Utilisation of RS amongst other methods to delineate haematoma boundaries further suggests the potential for this application [55].

Dysfunctional mitochondrial lipid metabolism plays a role in both acute and chronic sequelae of TBI [99]. Tissue levels of free fatty acids are dynamic following TBI in rat models and may play a role in secondary tissue damage [98]. Differences between lipid concentrations between injured and uninjured brain tissue are also present after injury [100], and lipid composition changes can be identified with RS to discern such changes [50]. Oxidative states of cardiolipin and its interaction with cytochrome c are altered after injury and may be a mechanism for the production of reactive oxygen species [99]. Cardiolipin has been identified as a potential source for band shift after injury [47] and presents a potential for monitoring by RS, though there are consistent strong Raman bands from numerous brain lipids in the 1440 cm^{-1} region [91]. Whilst there is some overlap of lipid and protein signals, increased acquisition of data and utilisation of neural network analysis may provide means to differentiate and utilise such data.

Beyond this, bands in the 2600–3800 cm^{-1} region are able to identify the water content of the brain in the region of 0.75–0.95 to an accuracy of 0.01 [101–103]. Real-time assessment of the progression of brain oedema has clear clinical applications for guiding medical and surgical therapy for acute TBI in the intensive care unit setting.

4. Discussion

4.1. Translational Considerations

RS is a powerful, label-free, non-destructive modality for biochemical analysis. As demonstrated by early studies using ex vivo analysis of injured and normal brain tissue, it can produce relevant biochemical data relatable to tissue integrity, injury burden, and progression or resolution. Similarly, ex vivo techniques have found clinical utility in neuro-oncology settings for 'operating table-side' histological diagnostics. Clearly, in contrast to this application, the clinical setting of TBI is directed at maximal tissue salvage, rather than identifying tissue for excision. As such, in vivo RS would be necessary for providing clinically useful data in TBI. Whilst a number of the studies identified to use in vivo modelling of traumatic brain injury, the RS measurements have been taken ex vivo. In vivo applications of RS in TBI are yet to arise, though the technique has found applications in patients in neuro-oncological surgery [33,34,36–43]. Particularly, Jermyn and colleagues report the development of an intraoperative probe used for the detection of brain cancer tissue, compared with healthy brain tissue, and have demonstrated its safe and effective use in humans [34,41,43]. This concept has been further demonstrated with the development of a fibre optic probe for inclusion within a brain biopsy probe, which has been validated in human pilot studies [104]. The success of 'live-tissue' RS in vitro amongst included studies, though not in vivo, does further support the concept of gaining biochemical data from living brain tissue using RS.

There are a number of translational barriers to the effective application of RS for the benefit of patients. One consideration is the access to brain parenchyma: unlike near-infrared spectroscopy, the Raman scattering return signal does not display skull penetrance rendering a transcranial approach vulnerable to excessive 'noise' from extracranial tissue scatter, to the extent of rendering it impractical. Subsequently, there are three options: (1) intraoperative cortical access; (2) a probe device which allows optical passage across the skull via a 'window' [51]; (3) a temporarily implanted fibre optic probe array capable of excitation and detection, either as an intraparenchymal or cortical monitoring device.

4.2. Cranial Access

Proof of principle of utilising RS as an intraoperative means of brain tissue interrogation has been established in the field of neuro-oncology [34,41,43]. As described above,

numerous publications have described the developments required for the translation of an intraoperative application of RS—specifically, the localised differentiation between tumour tissue and normal parenchyma as a means to optimise maximal safe resection in glioma surgery. This demonstrates in vivo brain RS as a workable concept.

Whilst the intraoperative period provides cortical access opportunity, readings during surgery will be unable to avoid a degree of ambient light. Whilst the highly fluorescent direct lighting could be averted for readings, it is neither practical nor safe to be able to take cortical readings in circumstances at or nearing darkness. RS is a highly sensitive method but vulnerable to such background optical 'noise'. Adjustments to laser power and background reference measurements can be applied to overcome this potential [40].

Though the intraoperative period provides cortical access for RS monitoring in patients with traumatic brain injury, the majority of the acute phase of severe TBI is spent in the intensive care unit rather than the operating theatre. Single-time-point (intraoperative) biochemical interrogation with RS could provide clinically relevant data which may correlate with the burden of injury and thus prognosis. However, to permit longitudinal data throughout the acute phase, alternative means of access are required.

Our group has explored a quartz lens as a 'window' technique as a means for gaining optical access to the intracranial compartment [51]. Mowbray et al. [51] designed and engineered a novel device which functions as a means of eliminating extra- and cranial tissue, with a polished quartz disc as a transparent window to facilitate spectral interrogation of brain tissue intermittently. This carries a relative advantage that the RS is external and has, therefore, no requirement for sterilisation between patients and is reusable within the lifespan of the equipment, with the comparatively simple cranial access device as a single-patient 'consumable'.

Standard cranial access techniques to facilitate intracranial monitoring devices are well integrated into modern neurosurgical practice. Up to a fifth of patients with traumatic brain injury who require admission to secondary care facilities need such invasive placement of monitoring probes, principally for the monitoring of ICP as a key paradigm in the supportive management after severe injury. In recent years, additional modalities have become integrated, including brain tissue oxygen monitoring and the insertion of microdialysis probes for the sampling of small molecules of metabolic interest (such as glucose, lactate, pyruvate, etc). The standard of care, therefore, involves the invasive component required, and additional monitoring requires only adaptation of the systems already established, with minimal additional risk burden to patients. An example of this principle is the integration of a near-infrared spectroscopy probe with ICP monitoring [105]. This device has utilised existing intracranial access to introduce an optical monitoring modality for the assessment of cerebral haemodynamics, successfully implemented in a small pilot group without safety concerns.

4.3. Probe Development

Whilst a cranial window has been demonstrated as a technically feasible means to facilitate cortical RS, it holds a number of potential limitations. The device is too bulky and cumbersome for continual monitoring in clinical practice. Furthermore, obfuscation of the window with blood, inflammatory tissue, serous fluid, or other tissue may render the implanted device unusable for monitoring at depths beyond this layer which would inherently carry its own Raman signal.

An alternative means of facilitating RS monitoring in parenchyma is through the temporary implantation of a probe. This would require a fibre optic system for delivery of excitation wavelengths, and a further fibre optic system for collection and transmission of detected photons to a charge-coupled device (CCD) for spectroscopic analysis. The system at its most basic could comprise two optical fibres, one dedicated to each of these purposes. Filtering and focussing optics, too large for integration at a probe tip, are external to the probe tip and patient. More complex arrays, typically increasing the number of detection fibres or introducing lens tips, have been developed for endoscopic and probe-

based monitoring systems [34,41,43]. One difficulty with fibre optic RS is the inherent Raman signal of silica-based fibre optic surrounds, though this can be accounted for with computational methods. Data resolution may be compromised with a reductionist system, but similarly, computational methods have been demonstrated to achieve optimal data interpretation from such data [48].

Implanted cerebral devices are typically for single use. Cost effectiveness of disposable devices should be considered: minimising production costs of consumables and materials required would both increase the likelihood of cost-effective uptake, as well as achieve favourable sustainability in implementation.

4.4. Wavelength Selection

Raman signal is weak and is inversely proportional to the fourth power of the excitation wavelength: longer wavelengths result in reduced scatter and, therefore, reduced sensitivity [106]. Conversely, lower wavelengths (particularly in biological tissues) induce autofluorescence: this signal creates significant 'noise' alongside the Raman scatter, making achieving usable resolution more challenging. As such, 785 nm is a typically used wavelength as a 'middle ground' [22].

4.5. Potential Clinical Applications

4.5.1. In Vivo Monitoring: Detailed Biochemical Assessment

Current therapeutic paradigms in acute TBI are aimed at restoring physiological intracranial haemostasis to minimise secondary injury [5]. Most commonly, this involves measurement of ICP via an implanted probe and therapeutic intervention based on avoiding high ICP [11]. However, numerous further known and unknown mechanisms contribute to poor functional outcomes in secondary brain injury after trauma. These include neural apoptosis, glial scarring, axonal degeneration, excitotoxicity, metabolic failure, mitochondrial dysfunction, neuroinflammatory responses, and oxidative stress [12].

Detection of optical biomarkers in the injured brain could have prognostic value and guide further therapy in the acute phase. RS has demonstrated a pre-clinical aptitude for the assessment of aspects of these pathophysiological pathways, as outlined above. For example, metabolic failure from mitochondrial dysfunction is a key factor in poor outcomes from TBI, but the real-time assessment of this is minimally addressed with current standard neuromonitoring and therapeutic methods [107–110]. In vivo RS monitoring in the gastrocnemius muscle of the rat has been demonstrated to be able to detect early changes in mitochondrial redox states in response to sepsis, prior to any change detected in lactate levels. Translation of this concept to brain tissue as a single example would provide great potential for clinical applications; an illustration of a potential application and a general summary are given in Figure 3.

As described above, there are a number of possible methods of accessing brain tissue for optical interrogation. The standard of care in moderate-to-severe TBI routinely involves the invasive placement of probes into the brain parenchyma and would add a minimal excess risk burden to utilise such access for RS. This would permit 'online' or 'real-time' detailed biochemical assessment and response to therapy.

Further considerations are required for the utility of Raman spectra in clinical decision making. Given the currently sparse available data, it is not possible a priori to determine the exact influence RS may in the future have on the clinical care of patients with TBI. To consider ICP monitoring in comparison, since first-in-human measurements in 1951, and its integration into standard practice in the 1970s [111], further study and optimisation of the interpretation and clinical applications of the indices and derivatives of ICP are ongoing to this day [112]. However, it can be reasonably argued that a technique such as RS has the potential to offer molecular insights into the function and dysfunction of the human brain far beyond that of intraparenchymal pressure. In discerning the potential utility and clinical relevance of RS in acute traumatic brain injury, clinical studies to gain spectral data from humans with traumatic brain injury would be of tremendous benefit in the exploration of

future applications. A summary of commercially available probes which have been applied in neurosurgical settings is available in a review article from DePaoli et al. [113].

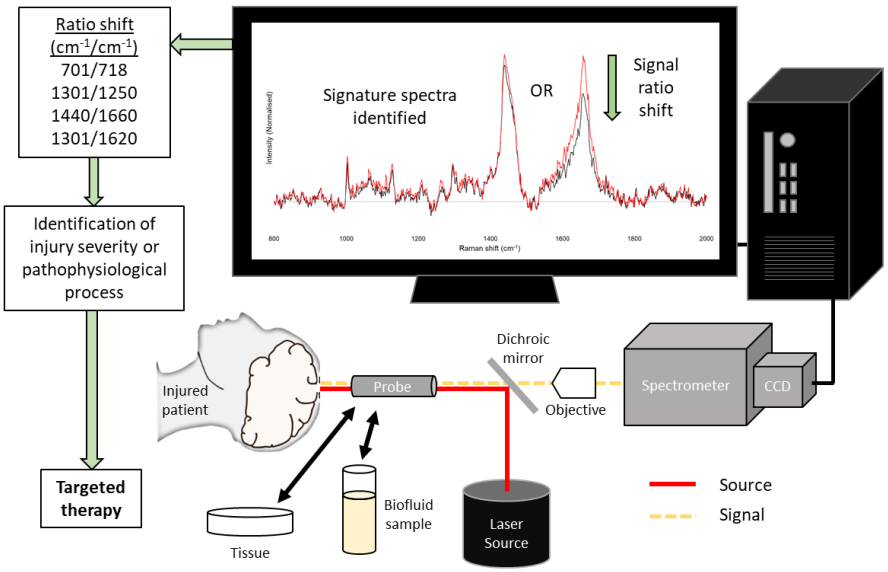


Figure 3. Illustration of a simplified Raman spectroscopy system and its potential application in clinical environments. CCD = charge-coupled device.

The spectral data from implanted fibre optics may be technically problematic. RS is sensitive to a number of factors which may adversely affect data quality and consequently, utility. Implanted fibre optic probes inherently are affected by 'background' spectra from silica fibre covering, and using small numerical aperture optics (as is preferable for minimising invasiveness) may further compromise the data. Previously, our research group has used machine learning tools to overcome such difficulties (SKiNET [47,51]). As demonstrated by SKiNET, it is possible to train such a system to accurately discern subtle modalities of biochemical derangement which correspond with differing adverse tissue conditions.

RS is able to identify a spectral 'signature' of normalisation of biochemical derangement. This effect has been observed in an oxidative stress model, with normalisation of deranged Raman signal with the addition of ascorbate [57]. Applied in vivo, this permits an immediate optical monitoring mechanism for oxidative stress states. Given the wide-ranging capabilities of RS to resolve spectral fingerprints of biochemical change at the molecular level, there is significant potential for such a concept to be applicable to other pathophysiological mechanisms in TBI. At present, outcome measures in TBI require at least three months of follow-up. Even with extensive longitudinal outcome assessments, the heterogeneity of injury necessitates vast numbers required in clinical trials to demonstrate clinical efficacy. Immediate biochemical feedback of normalisation of such mechanisms which may correspond to neural survival could provide such a proxy measure for early indication of effect.

4.5.2. Microdialysis Online Analysis

A microdialysis is a tool for neuromonitoring of cerebral metabolic function, used in limited centres in clinical practice [20]. Presently, samples of effluent dialysate are collected over intervals (one hour is typical) and intermittently analysed. This creates limitations in both clinical and research practice: changes in metabolite composition of the dialysate are not immediately recognisable, and any change is 'binned' into a mean sample for each hour. As such, establishing a true temporal relationship between patient or therapeutic variables and the metabolic observed effect is not possible [114]. RS-based methods have been established as effective in identifying clinically relevant quantitative information on metabolites [70,71]. Given the high sampling rate and accuracy of RS-based methods,

there is the potential for continuous analysis of passing dialysate: a bedside system for microdialysis with continuous 'online' analysis.

4.5.3. Pitchside/Bedside Concussion Assessment

A number of studies have utilised RS (or a variation thereof) in developing point-of-care applicable diagnostic devices for the recognition of biomarkers of TBI [64–69]. Point-of-care detection for TBI has the most relevance in mild TBI and particularly concussion. In severe TBI, the clinical condition of the patient (typified by impaired consciousness or seizure) or the severity of the injury mechanism necessitates urgent radiological diagnosis. However, clinical diagnosis of concussion can be more challenging, both for sportspeople and patients.

Currently, TBI point-of-care diagnostic and monitoring techniques routinely used by healthcare professionals are those of clinical examination and assessment. For moderate-to-severe injury with markedly altered levels of consciousness, the Glasgow Coma Scale (GCS) is the standard examination tool, alongside the assessment of pupillary responses to light. GCS is a fast and simple assessment method that can be performed by a healthcare professional of any level, by assessing the patient's motor, verbal, and eye responses [115]. Clinical assessment of suspected concussion and mild TBI can rely upon a more nuanced and detailed neurocognitive and symptomatology in addition to an assessment of consciousness, as in the Sports Concussion Assessment Tool, currently in its fifth version (SCAT5) [116].

Clinical examination methods are subjective, with moderate interrater reliability. There are inconsistencies between scores when undertaken by different healthcare workers and at varied timeframes [117]. GCS may also be affected by the presence of intoxicants, medication, sedation, and pre-morbid disability. SCAT5 assessments particularly require patient compliance and participation in both baseline and incident examinations. Attempts to develop objective bedside/pitchside diagnostics in recent years include pupillometry devices to improve interrater reliability of such clinical assessment [118], but as yet, a true point-of-care diagnostic device is not available to clinicians.

The available assessment methods have numerous limitations which highlight the need for an alternative point-of-care method that may be fulfilled by an RS diagnostic device. For maximal clinical utility, prospective diagnostic advice should be relatively portable and rapid for 'point-of-care' testing, in both geographical and temporal senses. As with any diagnostic test, the accuracy of the device (specificity and sensitivity) should also be appropriate to the cohort. For a pitch-side application, the ideal device would be user-friendly, such that a monitored first-aid provider would be able to take readings. In this context, the patient would also be outside of a hospital setting, so a pitch-side device would be capable of non-invasive measurements without incisions. RS has also been applied to non-invasive identification of traumatic brain injury diagnosis and severity stratification via examination of the retina [47] and may hold future potential with further development.

5. Conclusions

RS is a powerful diagnostic tool with the potential to provide detailed biochemical diagnostic information on the injured brain. This review highlights the success of RS in identifying biochemical changes after injury in tissue from in vivo models and holds significant potential for applications in in vivo or clinical settings for TBI diagnostics and monitoring. Potential applications in TBI are broad and include direct brain monitoring and biofluid diagnostics, with the opportunity to obtain detailed and temporally resolved detail of metabolic and biochemical shifts in response to injury which could increase understanding and inform clinical decision making. Novel spectral biomarkers of injury severity observed from in vivo models represent a significant opportunity for monitoring and treating the complex pathophysiological processes as yet uncaptured by neuromonitoring modalities. Further pre-clinical and clinical studies are required to fully recognise the potential for RS

in TBI. Whilst there are translational challenges, discussed examples from neuro-oncology and related optical monitoring modalities set a proof of concept for further investigation and application of RS in TBI.

Author Contributions: A.R.S. was responsible for conceptualisation and manuscript preparation. A.R.S. and Z.A. performed the searches and risk of bias assessments, extracted the data from the included articles, and performed the analysis. All authors contributed to the development of the ideas/writing/final review of the submitted article. All authors have read and agreed to the published version of the manuscript.

Funding: This article presents independent research funded by the National Institute for Health Research (NIHR) Surgical Reconstruction and Microbiology Research Centre (a partnership between University Hospitals Birmingham NHS Foundation Trust, the University of Birmingham, and the Royal Centre for Defence Medicine). The views expressed are those of the author(s) and not necessarily those of the NHS, the NIHR, or the Department of Health.

Institutional Review Board Statement: Ethical review and approval were waived for this study as per advice from the NHS Health Research Authority (UK) decision tool since it is a systematic review of published literature.

Informed Consent Statement: Patient consent was waived because no patients or members of the public were involved in the design, conduct of this study, or reporting of this research.

Data Availability Statement: All data generated as part of this study are included in the article.

Conflicts of Interest: The authors declare no conflict of interest. The funders had no role in the design of the study; in the collection, analyses, or interpretation of data; in the writing of the manuscript; in the decision to publish the results.

Abbreviations

CCI	Controlled cortical impact
FTIR	Fourier transform infrared spectroscopy
GCS	Glasgow coma scale
GFAP	Glial fibrillary acidic protein
ICP	Intracranial pressure
mTBI	Mild TBI
NAA	n-Acetyle aspartate
NSE	Neuron-specific enolase
RS	Raman spectroscopy
SCAT5	Sports concussion assessment tool 5
SERS	Surface-enhanced Raman scattering
SKiNET	Self-optimising Kohonen index network
sTBI	Severe traumatic brain injury
TBI	Traumatic brain injury
UCHL1	Ubiquitin C-terminal hydrolase-L1

References

1. Langlois, J.A.; Rutland-Brown, W.; Wald, M.M. The epidemiology and impact of traumatic brain injury: A brief overview. *J. Head Trauma Rehabil.* **2006**, *21*, 375–378. [CrossRef] [PubMed]
2. Jazayeri, S.B.; Beygi, S.; Shokraneh, F.; Hagen, E.M.; Rahimi-Movaghar, V. Incidence of traumatic spinal cord injury worldwide: A systematic review. *Eur. Spine J.* **2015**, *24*, 905–918. [CrossRef] [PubMed]
3. Dewan, M.; Rattani, A.; Gupta, S.; Baticulon, R.; Hung, Y.; Punchak, M.; Agrawal, A.; Adeleye, A.; Shrime, M.; Rubiano, A.; et al. Estimating the global incidence of traumatic brain injury. *J. Neurosurg.* **2018**, *130*, 1080–1097. [CrossRef] [PubMed]
4. Xiong, Y.; Mahmood, A.; Chopp, M. Emerging treatments for traumatic brain injury. *Expert Opin. Emerg. Drugs* **2009**, *14*, 67–84. [CrossRef]
5. Bullock, M.R.; Chesnut, R.; Ghajar, J.; Gordon, D.; Hartl, R.; Newell, D.W.; Servadei, F.; Walters, B.C.; Wilberger, J. Surgical management of traumatic brain injury. *Neurosurgery* **2006**, *58*, 16–24.
6. Faul, M.; Coronado, V. Epidemiology of traumatic brain injury. *Handb. Clin. Neurol.* **2015**, *127*, 3–13. [CrossRef]

7. Polinder, S.; Haagsma, J.A.; van Klaveren, D.; Steyerberg, E.W.; van Beeck, E.F. Health-related quality of life after TBI: A systematic review of study design, instruments, measurement properties, and outcome. *Popul. Health Metr.* **2015**, *13*, 4. [CrossRef]
8. Pavlovic, D.; Pekic, S.; Stojanovic, M.; Popovic, V. Traumatic brain injury: Neuropathological, neurocognitive and neurobehavioral sequelae. *Pituitary* **2019**, *22*, 270–282. [CrossRef]
9. Graham, N.S.N.; Sharp, D.J. Understanding neurodegeneration after traumatic brain injury: From mechanisms to clinical trials in dementia. *J. Neurol. Neurosurg. Psychiatry* **2019**, *90*, 1221–1233. [CrossRef]
10. Chesnut, R.M.; Chesnut, R.M.; Marshall, L.F.; Klauber, M.R.; Blunt, B.A.; Baldwin, N.; Eisenberg, H.M.; Jane, J.A.; Marmarou, A.; Foulkes, M.A. The role of secondary brain injury in determining outcome from severe head injury. *J. Trauma* **1993**, *34*, 216. [CrossRef]
11. Brain Trauma Foundation Guidelines for the Management of Severe TBI, 4th Ed. Available online: https://braintrauma.org/guidelines/guidelines-for-the-management-of-severe-tbi-4th-ed#/ (accessed on 26 August 2021).
12. Ng, S.Y.; Lee, A.Y.W. Traumatic Brain Injuries: Pathophysiology and Potential Therapeutic Targets. *Front. Cell. Neurosci.* **2019**, *13*, 528. [CrossRef] [PubMed]
13. Cheng, G.; Kong, R.H.; Zhang, L.M.; Zhang, J.N. Mitochondria in traumatic brain injury and mitochondrial-targeted multipotential therapeutic strategies. *Br. J. Pharmacol.* **2012**, *167*, 699–719. [CrossRef] [PubMed]
14. Belli, A.; Sen, J.; Petzold, A.; Russo, S.; Kitchen, N.; Smith, M. Clinical Article Metabolic failure precedes intracranial pressure rises in traumatic brain injury: A microdialysis study. *Acta Neurochir.* **2008**, *150*, 461–470. [CrossRef] [PubMed]
15. Chamoun, R.; Suki, D.; Gopinath, S.P.; Goodman, J.C.; Robertson, C. Role of extracellular glutamate measured by cerebral microdialysis in severe traumatic brain injury: Clinical article. *J. Neurosurg.* **2010**, *113*, 564–570. [CrossRef] [PubMed]
16. Deng, Y.; Thompson, B.M.; Gao, X.; Hall, E.D. Temporal relationship of peroxynitrite-induced oxidative damage, calpain-mediated cytoskeletal degradation and neurodegeneration after traumatic brain injury. *Exp. Neurol.* **2007**, *205*, 154–165. [CrossRef] [PubMed]
17. Semple, B.D.; Bye, N.; Rancan, M.; Ziebell, J.M.; Morganti-Kossmann, M.C. Role of CCL2 (MCP-1) in traumatic brain injury (TBI): Evidence from severe TBI patients and CCL2−/− mice. *J. Cereb. Blood Flow Metab.* **2010**, *30*, 769–782. [CrossRef]
18. Okonkwo, D.O.; Shutter, L.A.; Moore, C.; Temkin, N.R.; Puccio, A.M.; Madden, C.J.; Andaluz, N.; Chesnut, R.M.; Bullock, M.R.; Grant, G.A.; et al. Brain tissue oxygen monitoring and management in severe traumatic brain injury (BOOST-II): A phase II randomized trial. *Crit. Care Med.* **2017**, *45*, 1907. [CrossRef]
19. Chesnut, R.; Aguilera, S.; Buki, A.; Bulger, E.; Citerio, G.; Cooper, D.; Arrastia, R.; Diringer, M.; Figaji, A.; Gao, G.; et al. A management algorithm for adult patients with both brain oxygen and intracranial pressure monitoring: The Seattle International Severe Traumatic Brain Injury Consensus Conference (SIBICC). *Intensive Care Med.* **2020**, *46*, 919–929. [CrossRef]
20. Carpenter, K.; Young, A.; Hutchinson, P. Advanced monitoring in traumatic brain injury: Microdialysis. *Curr. Opin. Crit. Care* **2017**, *23*, 103–109. [CrossRef]
21. Ercole, A.; Magnoni, S.; Vegliante, G.; Pastorelli, R.; Surmacki, J.; Bohndiek, S.; Zanier, E. Current and Emerging Technologies for Probing Molecular Signatures of Traumatic Brain Injury. *Front. Neurol.* **2017**, *8*, 450. [CrossRef]
22. Cordero, E.; Latka, I.; Matthäus, C.; Schie, I.; Popp, J. In-vivo Raman spectroscopy: From basics to applications. *J. Biomed. Opt.* **2018**, *23*, 071210. [CrossRef] [PubMed]
23. Hanlon, E.B.; Manoharan, R.; Koo, T.W.; Shafer, K.E.; Motz, J.T.; Fitzmaurice, M.; Kramer, J.R.; Itzkan, I.; Dasari, R.R.; Feld, M.S. Prospects for in vivo Raman spectroscopy. *Phys. Med. Biol.* **2000**, *45*, R1. [CrossRef] [PubMed]
24. Demtröder, W. Laser Raman Spectroscopy. In *Laser Spectroscopy2*; Springer: Berlin/Heidelberg, Germany, 2015; pp. 149–181. [CrossRef]
25. Bik, E.; Mateuszuk, L.; Stojak, M.; Chlopicki, S.; Baranska, M.; Majzner, K. Menadione-induced endothelial inflammation detected by Raman spectroscopy. *Biochim. Biophys. Acta Mol. Cell Res.* **2021**, *1868*, 118911. [CrossRef] [PubMed]
26. Zhang, W.; Rhodes, J.S.; Garg, A.; Takemoto, J.Y.; Qi, X.; Harihar, S.; Tom Chang, C.W.; Moon, K.R.; Zhou, A. Label-free discrimination and quantitative analysis of oxidative stress induced cytotoxicity and potential protection of antioxidants using Raman micro-spectroscopy and machine learning. *Anal. Chim. Acta* **2020**, *1128*, 221–230. [CrossRef]
27. Lalonde, J.W.; O'Connor, S.P.; Noojin, G.D.; Gonzales, C.C.; Yakovlev, V.V.; Denton, M.L. Measuring cytochrome c redox state using resonance Raman spectroscopy to determine metabolic rates in electron transport chain when exposed to light. In *Mechanisms of Photobiomodulation Therapy XIV*; Hamblin, M.R., Carroll, J.D., Arany, P., Eds.; SPIE: Bellingham, WA, USA, 2019; Volume 10861, p. 18. [CrossRef]
28. Jung, G.; Kang, S.; Lee, G.; Kim, D. Biochemical Characterization of the Brain Hippocampal Areas after Cerebral Ischemia-Reperfusion Using Raman Spectroscopy. *Appl. Spectrosc.* **2018**, *72*, 1479–1486. [CrossRef]
29. Chaichi, A.; Hasan, S.; Mehta, N.; Donnarumma, F.; Ebenezer, P.; Murray, K.; Francis, J.; Gartia, M. Label-free lipidome study of paraventricular thalamic nucleus (PVT) of rat brain with post-traumatic stress injury by Raman imaging. *Analyst* **2021**, *146*, 170–183. [CrossRef]
30. Lakshmi, R.; Kartha, V.; Krishna Murali, C.; Solomon, J.; Uma Devi, P. Tissue Raman Spectroscopy for the Study of Radiation Damage: Brain Irradiation of Mice. *Radiat. Res.* **2002**, *157*, 175–182. [CrossRef]
31. Devitt, G.; Howard, K.; Mudher, A.; Mahajan, S. Raman Spectroscopy: An Emerging Tool in Neurodegenerative Disease Research and Diagnosis. *ACS Chem. Neurosci.* **2018**, *9*, 404–420. [CrossRef]

32. Aguiar, R.P.; Silveira, L.; Falcão, E.T.; Pacheco, M.T.T.; Zângaro, R.A.; Pasqualucci, C.A. Discriminating Neoplastic and Normal Brain Tissues in Vitro Through Raman Spectroscopy: A Principal Components Analysis Classification Model. *Photomed. Laser Surg.* **2013**, *31*, 595–604. [CrossRef]
33. Desroches, J.; Jermyn, M.; Pinto, M.; Picot, F.; Tremblay, M.; Obaid, S.; Marple, E.; Urmey, K.; Trudel, D.; Soulez, G.; et al. A new method using Raman spectroscopy for in vivo targeted brain cancer tissue biopsy. *Sci. Rep.* **2018**, *8*, 1792. [CrossRef]
34. Livermore, L.; Isabelle, M.; Bell, I.; Edgar, O.; Voets, N.; Stacey, R.; Ansorge, O.; Vallance, C.; Plaha, P. Raman spectroscopy to differentiate between fresh tissue samples of glioma and normal brain: A comparison with 5-ALA-induced fluorescence-guided surgery. *J. Neurosurg.* **2020**, *135*, 469–479. [CrossRef] [PubMed]
35. Koljenović, S.; Schut, T.; Vincent, A.; Kros, J.; Puppels, G. Detection of meningioma in dura mater by Raman spectroscopy. *Anal. Chem.* **2005**, *77*, 7958–7965. [CrossRef] [PubMed]
36. Zhang, J.; Fan, Y.; He, M.; Ma, X.; Song, Y.; Liu, M.; Xu, J. Accuracy of Raman spectroscopy in differentiating brain tumor from normal brain tissue. *Oncotarget* **2017**, *8*, 36824–36831. [CrossRef] [PubMed]
37. Hollon, T.; Lewis, S.; Freudiger, C.; Sunney Xie, X.; Orringer, D. Improving the accuracy of brain tumor surgery via Raman-based technology. *Neurosurg. Focus* **2016**, *40*, E9. [CrossRef] [PubMed]
38. Depciuch, J.; Tołpa, B.; Witek, P.; Szmuc, K.; Kaznowska, E.; Osuchowski, M.; Król, P.; Cebulski, J. Raman and FTIR spectroscopy in determining the chemical changes in healthy brain tissues and glioblastoma tumor tissues. *Spectrochim. Acta. A. Mol. Biomol. Spectrosc.* **2020**, *225*, 117526. [CrossRef]
39. Kalkanis, S.; Kast, R.; Rosenblum, M.; Mikkelsen, T.; Yurgelevic, S.; Nelson, K.; Raghunathan, A.; Poisson, L.; Auner, G. Raman spectroscopy to distinguish grey matter, necrosis, and glioblastoma multiforme in frozen tissue sections. *J. Neurooncol.* **2014**, *116*, 477–485. [CrossRef]
40. Jermyn, M.; Mok, K.; Mercier, J.; Desroches, J.; Pichette, J.; Saint-Arnaud, K.; Bernstein, L.; Guiot, M.; Petrecca, K.; Leblond, F. Intraoperative brain cancer detection with Raman spectroscopy in humans. *Sci. Transl. Med.* **2015**, *7*, 274ra19. [CrossRef]
41. Jermyn, M.; Desroches, J.; Mercier, J.; St-Arnaud, K.; Guiot, M.; Leblond, F.; Petrecca, K. Raman spectroscopy detects distant invasive brain cancer cells centimeters beyond MRI capability in humans. *Biomed. Opt. Express* **2016**, *7*, 5129. [CrossRef]
42. Desroches, J.; Jermyn, M.; Mok, K.; Lemieux-Leduc, C.; Mercier, J.; St-Arnaud, K.; Urmey, K.; Guiot, M.; Marple, E.; Petrecca, K.; et al. Characterization of a Raman spectroscopy probe system for intraoperative brain tissue classification. *Biomed. Opt. Express* **2015**, *6*, 2380. [CrossRef]
43. Galli, R.; Meinhardt, M.; Koch, E.; Schackert, G.; Steiner, G.; Kirsch, M.; Uckermann, O. Rapid Label-Free Analysis of Brain Tumor Biopsies by Near Infrared Raman and Fluorescence Spectroscopy—A Study of 209 Patients. *Front. Oncol.* **2019**, *9*, 1165. [CrossRef]
44. Hollon, T.; Pandian, B.; Adapa, A.; Urias, E.; Save, A.; Khalsa, S.; Eichberg, D.; D'Amico, R.; Farooq, Z.; Lewis, S.; et al. Near real-time intraoperative brain tumor diagnosis using stimulated Raman histology and deep neural networks. *Nat. Med.* **2020**, *26*, 52–58. [CrossRef] [PubMed]
45. Moher, D.; Liberati, A.; Tetzlaff, J.; Altman, D.G. Preferred reporting items for systematic reviews and meta-analyses: The PRISMA statement. *BMJ* **2009**, *339*, 332–336. [CrossRef] [PubMed]
46. Hooijmans, C.R.; Rovers, M.M.; De Vries, R.B.M.; Leenaars, M.; Ritskes-Hoitinga, M.; Langendam, M.W. SYRCLE's risk of bias tool for animal studies. *BMC Med. Res. Methodol.* **2014**, *14*, 43. [CrossRef] [PubMed]
47. Banbury, C.; Styles, I.; Eisenstein, N.; Zanier, E.R.; Vegliante, G.; Belli, A.; Logan, A.; Oppenheimer, P.G. Spectroscopic detection of traumatic brain injury severity and biochemistry from the retina. *Biomed. Opt. Express* **2020**, *11*, 6249–6261. [CrossRef] [PubMed]
48. Banbury, C.; Mason, R.; Styles, I.; Eisenstein, N.; Clancy, M.; Belli, A.; Logan, A.; Goldberg Oppenheimer, P. Development of the Self Optimising Kohonen Index Network (SKiNET) for Raman Spectroscopy Based Detection of Anatomical Eye Tissue. *Sci. Rep.* **2019**, *9*, 10812. [CrossRef]
49. Ercole, A.; Surmaki, J.; Ansel-Bollepalli, L.; Pischiutta, F.; Bohndiek, S.; Zanier, E. Mapping spatial biochemical changes in a mouse model of traumatic brain injury with Raman imaging. *Intensive Care Med. Exp.* **2017**, *5*.
50. Surmacki, J.M.; Ansel-Bollepalli, L.; Pischiutta, F.; Zanier, E.R.; Ercole, A.; Bohndiek, S.E. Label-free monitoring of tissue biochemistry following traumatic brain injury using Raman spectroscopy. *Analyst* **2017**, *142*, 132. [CrossRef]
51. Mowbray, M.; Banbury, C.; Rickard, J.J.S.; Davies, D.J.; Goldberg Oppenheimer, P. Development and Characterization of a Probe Device toward Intracranial Spectroscopy of Traumatic Brain Injury. *ACS Biomater. Sci. Eng.* **2021**, *7*, 1252–1262. [CrossRef]
52. Kawon, K.; Setkowicz, Z.; Drozdz, A.; Janeczko, K.; Chwiej, J. The methods of vibrational microspectroscopy reveals long-term biochemical anomalies within the region of mechanical injury within the rat brain. *Spectrochim. Acta A Mol. Biomol. Spectrosc.* **2021**, *263*, 120214. [CrossRef]
53. Hu, F.; Lamprecht, M.; Wei, L.; Morrison, B.; Min, W. Bioorthogonal chemical imaging of metabolic activities in live mammalian hippocampal tissues with stimulated Raman scattering. *Sci. Rep.* **2016**, *6*, 39660. [CrossRef]
54. Du Sert, N.P.; Ahluwalia, A.; Alam, S.; Avey, M.T.; Baker, M.; Browne, W.J.; Clark, A.; Cuthill, I.C.; Dirnagl, U.; Emerson, M.; et al. Reporting animal research: Explanation and elaboration for the ARRIVE guidelines 2.0. *PLoS Biol.* **2020**, *18*, e3000411. [CrossRef]
55. Hackett, M.J.; Desouza, M.; Caine, S.; Bewer, B.; Nichol, H.; Paterson, P.G.; Colbourne, F. A New Method To Image Heme-Fe, Total Fe, and Aggregated Protein Levels after Intracerebral Hemorrhage. *ACS Chem. Neurosci.* **2015**, *6*, 761–770. [CrossRef] [PubMed]
56. Williamson, M.R.; Dietrich, K.; Hackett, M.J.; Caine, S.; Nadeau, C.A.; Aziz, J.R.; Nichol, H.; Paterson, P.G.; Colbourne, F. Rehabilitation Augments Hematoma Clearance and Attenuates Oxidative Injury and Ion Dyshomeostasis After Brain Hemorrhage. *Stroke* **2017**, *48*, 195–203. [CrossRef] [PubMed]

57. Dutta, A.; Gautam, R.; Chatterjee, S.; Ariese, F.; Sikdar, S.K.; Umapathy, S. Ascorbate Protects Neurons against Oxidative Stress: A Raman Microspectroscopic Study. *ACS Chem. Neurosci.* **2015**, *6*, 1794–1801. [CrossRef]
58. Khatri, N.; Thakur, M.; Pareek, V.; Kumar, S.; Sharma, S.; Datusalia, A.K. Oxidative Stress: Major Threat in Traumatic Brain Injury. *CNS Neurol. Disord. Drug Targets* **2018**, *17*, 689–695. [CrossRef]
59. Mehta, T.; Fayyaz, M.; Giler, G.E.; Kaur, H.; Raikwar, S.P.; Kempuraj, D.; Selvakumar, G.P.; Ahmed, M.E.; Thangavel, R.; Zaheer, S.; et al. Current Trends in Biomarkers for Traumatic Brain Injury. *Open access J. Neurol. Neurosurg.* **2020**, *12*, 86.
60. Wang, K.K.; Yang, Z.H.; Zhu, T.; Shi, Y.; Rubenstein, R.; Tyndall, J.A.; Manley, G.T. An update on diagnostic and prognostic biomarkers for traumatic brain injury. *Expert Rev. Mol. Diagn.* **2018**, *18*, 165–180. [CrossRef]
61. Calcagnile, O.; Anell, A.; Undén, J. The addition of S100B to guidelines for management of mild head injury is potentially cost saving. *BMC Neurol.* **2016**, *16*, 200. [CrossRef]
62. Granger, J.H.; Schlotter, N.E.; Crawford, A.C.; Porter, M.D. Prospects for point-of-care pathogen diagnostics using surface-enhanced Raman scattering (SERS). *Chem. Soc. Rev.* **2016**, *45*, 3865–3882. [CrossRef]
63. McNay, G.; Eustace, D.; Smith, W.E.; Faulds, K.; Graham, D. Surface-enhanced Raman scattering (SERS) and surface-enhanced resonance raman scattering (SERRS): A review of applications. *Appl. Spectrosc.* **2011**, *65*, 825–837. [CrossRef]
64. Rickard, J.J.; Di-Pietro, V.; Smith, D.; Davies, D.; Belli, A.; Goldberg Oppenheimer, P. Rapid optofluidic detection of biomarkers for traumatic brain injury via surface-enhanced Raman spectroscopy. *Nat. Biomed. Eng.* **2020**, *4*, 610–623. [CrossRef] [PubMed]
65. Osier, N.; Ziari, M.; Puccio, A.; Poloyac, S.; Okonkwo, D.; Minnigh, M.; Beers, S.; Conley, Y. Elevated cerebrospinal fluid concentrations of N-acetylaspartate correlate with poor outcome in a pilot study of severe brain trauma. *Brain Inj.* **2019**, *33*, 1364–1371. [CrossRef] [PubMed]
66. Toman, E.; Harrisson, S.; Belli, T. Biomarkers in traumatic brain injury: A review. *J.R. Army Med. Corps* **2016**, *162*, 103–108. [CrossRef] [PubMed]
67. Gao, X.; Zheng, P.; Kasani, S.; Wu, S.; Yang, F.; Lewis, S.; Nayeem, S.; Engler-Chiurazzi, E.; Wigginton, J.; Simpkins, J.; et al. Paper-Based Surface-Enhanced Raman Scattering Lateral Flow Strip for Detection of Neuron-Specific Enolase in Blood Plasma. *Anal. Chem.* **2017**, *89*, 10104–10110. [CrossRef]
68. Gao, X.; Boryczka, J.; Zheng, P.; Kasani, S.; Yang, F.; Engler-Chiurazzi, E.; Simpkins, J.; Wigginton, J.; Wu, N. A "hot Spot"-Enhanced paper lateral flow assay for ultrasensitive detection of traumatic brain injury biomarker S-100β in blood plasma. *Biosens. Bioelectron.* **2021**, *177*, 112967. [CrossRef]
69. Li, D.; Yang, M.; Li, H.; Mao, L.; Wang, Y.; Sun, B. SERS based protocol using flow glass-hemostix for detection of neuron-specific enolase in blood plasma. *New J. Chem.* **2019**, *43*, 5925–5931. [CrossRef]
70. O'Neal, P.; Motamedi, M.; Lin, W.; Chen, J.; Coté, G. Feasibility study using surface-enhanced Raman spectroscopy for the quantitative detection of excitatory amino acids. *J. Biomed. Opt.* **2003**, *8*, 33. [CrossRef]
71. O'Neal, D.P.; Motamedi, M.; Chen, J.; Cote, G.L. Surface-enhanced Raman spectroscopy for the in-vitro and ex-vivo detection of excitatory amino acids. In *Biomedical Applications of Raman Spectroscopy*; SPIE: Bellingham, WA, USA, 1999; Volume 3608, pp. 211–216. [CrossRef]
72. Larkin, P. IR and Raman Spectra-Structure Correlations. In *Infrared Raman Spectrosc*; Elsevier: Amsterdam, The Netherlands, 2011; pp. 73–115. [CrossRef]
73. Kang, D.G.; Woo, K.C.; Kang, D.H.; Park, C.; Kim, S.K. Improved spectral resolution of the femtosecond stimulated Raman spectroscopy achieved by the use of the 2nd-order diffraction method. *Sci. Rep.* **2021**, *11*, 3361. [CrossRef]
74. Lemler, P.; Premasiri, W.R.; DelMonaco, A.; Ziegler, L.D. NIR Raman spectra of whole human blood: Effects of laser-induced and in vitro hemoglobin denaturation. *Anal. Bioanal. Chem.* **2014**, *406*, 193–200. [CrossRef]
75. Thomas, D.B.; Hauber, M.E.; Hanley, D.; Waterhouse, G.I.N.; Fraser, S.; Gordon, K.C. Analysing avian eggshell pigments with Raman spectroscopy. *J. Exp. Biol.* **2015**, *218*, 2670–2674. [CrossRef]
76. Talari, A.C.S.; Movasaghi, Z.; Rehman, S.; Rehman, I.U. Raman Spectroscopy of Biological Tissues. *Appl. Spectrosc. Rev.* **2014**, *50*, 46–111. [CrossRef]
77. Tay, L.; Tremblay, R.; Hulse, J.; Zurakowski, B.; Thompson, M.; Bani-Yaghoub, M. Detection of acute brain injury by Raman spectral signature. *Analyst* **2011**, *136*, 1620–1626. [CrossRef] [PubMed]
78. Girard, A.; Cooper, A.; Mabbott, S.; Bradley, B.; Asiala, S.; Jamieson, L.; Clucas, C.; Capewell, P.; Marchesi, F.; Gibbins, M.P.; et al. Raman spectroscopic analysis of skin as a diagnostic tool for Human African Trypanosomiasis. *PLoS Pathog.* **2021**, *17*, e1010060. [CrossRef]
79. Journal, A.I.; Lu, M.; Zhao, L.; Wang, Y.; You, G.; Kan, X.; Zhang, Y.; Zhang, N.; Wang, B.; Guo, Y.-J.; et al. Measurement of the methemoglobin concentration using Raman spectroscopy, Artificial Cells. *Nanomed. Biotechnol.* **2014**, *42*, 63–69. [CrossRef]
80. Sacharz, J.; Wesełucha-Birczyńska, A.; Zięba-Palus, J.; Lewandowski, M.H.; Kowalski, R.; Palus, K.; Chrobok, Ł.; Moskal, P.; Birczyńska, M.; Sozańska, A. Epileptic rat brain tissue analyzed by 2D correlation Raman spectroscopy. *Spectrochim. Acta-Part A Mol. Biomol. Spectrosc.* **2018**, *188*, 581–588. [CrossRef]
81. Shin, H.J.; Lee, J.H.; Kim, Y.D.; Shin, I.; Sim, T.; Lim, D.K. Raman-Based in Situ Monitoring of Changes in Molecular Signatures during Mitochondrially Mediated Apoptosis. *ACS Omega* **2019**, *4*, 8188–8195. [CrossRef] [PubMed]
82. Codrich, D. Applications and Limits of Raman Spectroscopy in the Study of Colonic and Pulmonary Malformations. Ph.D. Thesis, Universita' Degli Studi di Trieste, Trieste, Italy, 2006.

83. Wood, B.R.; Caspers, P.; Puppels, G.J.; Pandiancherri, S.; McNaughton, D. Resonance Raman spectroscopy of red blood cells using near-infrared laser excitation. *Anal. Bioanal. Chem.* **2007**, *387*, 1691–1703. [CrossRef] [PubMed]
84. Castro, M.A.; Pereira, F.J.; Aller, A.J.; Littlejohn, D. Raman spectrometry as a screening tool for solvent-extracted azo dyes from polyester-based textile fibres. *Polym. Test.* **2020**, *91*, 106765. [CrossRef]
85. Bankapur, A.; Krishnamurthy, R.S.; Zachariah, E.; Santhosh, C.; Chougule, B.; Praveen, B.; Valiathan, M.; Mathur, D. Micro-Raman Spectroscopy of Silver Nanoparticle Induced Stress on Optically-Trapped Stem Cells. *PLoS ONE* **2012**, *7*, e35075. [CrossRef]
86. Yao, H.; Tao, Z.; Ai, M.; Peng, L.; Wang, G.; He, B.; Li, Y.-Q. Raman spectroscopic analysis of apoptosis of single human gastric cancer cells. *Vib. Spect.* **2009**, *50*, 193–197. [CrossRef]
87. Notingher, I.; Green, C.; Dyer, C.; Perkins, E.; Hopkins, N.; Lindsay, C.; Hench, L. Discrimination between ricin and sulphur mustard toxicity in vitro using Raman spectroscopy. *J.R. Soc. Interface* **2004**, *1*, 79–90. [CrossRef] [PubMed]
88. Krafft, C.; Knetschke, T.; Funk, R.; Salzer, R. Studies on stress-induced changes at the subcellular level by Raman microspectroscopic mapping. *Anal. Chem.* **2006**, *78*, 4424–4429. [CrossRef] [PubMed]
89. Muthuselvi, C.; Pandiaraja, S.S.; Ravikumar, B.; Athimoolam, S.; Srinivasan, N.; Krishnakum, R.V. FT-IR and FT-Raman Spectroscopic Analyzes of Indeno Quinoxaline Derivative Crystal. *Asian J. Appl. Sci.* **2018**, *11*, 83–91. [CrossRef]
90. Kumar, V.; Panikar, Y.; Palafox, M.A.; Vats, J.; Kostova, I.; Lang, K.; Rastogi, V. Ab-initio calculations, FT-IR and FT-Raman spectra of 2-chloro-6-methyl benzonitrile. *Indian J. Pure Appl. Phys.* **2010**, *48*, 85–94.
91. Krafft, C.; Neudert, L.; Simat, T.; Salzer, R. Near infrared Raman spectra of human brain lipids. *Spectrochim. Acta-Part A Mol. Biomol. Spectrosc.* **2005**, *61*, 1529–1535. [CrossRef] [PubMed]
92. Farquharson, S.; Gift, A.; Shende, C.; Inscore, F.; Ordway, B.; Farquharson, C.; Murren, J. Surface-enhanced Raman Spectral Measurements of 5-Fluorouracil in Saliva. *Molecules* **2008**, *13*, 2608. [CrossRef] [PubMed]
93. De Gelder, J.; De Gussem, K.; Vandenabeele, P.; Moens, L. Reference database of Raman spectra of biological molecules. *J. Raman Spectrosc.* **2007**, *38*, 1133–1147. [CrossRef]
94. Staniszewska-Slezak, E.; Malek, K.; Baranska, M. Complementary analysis of tissue homogenates composition obtained by Vis and NIR laser excitations and Raman spectroscopy. *Spectrochim. Acta-Part A Mol. Biomol. Spectrosc.* **2015**, *147*, 245–256. [CrossRef]
95. Clemens, G.; Butler, H.J.; Ashton, K.M.; Brodbelt, A.; Dawson, T.P.; Fullwood, L.M.; Jenkinson, M.D.; Stables, R.; Baker, M.J.; North, L.; et al. Feature Driven Classification of Raman Spectra for Real-Time Spectral Brain Tumour Diagnosis Using Sound. *Analyst* **2017**, *142*, 98–109.
96. Acosta-Maeda, T.E. Raman Spectroscopy for Planetary Exploration and Characterization of Extraterrestrial Materials. Ph.D. Thesis, University of Hawai'i at Manoa, Honolulu, HI, USA, 2016.
97. Mccreery, R.L.; Chalmers, J.M.; Griffiths, P.R. Photometric Standards for Raman Spectroscopy. In *Handbook of Vibrational Spectroscopy Photometric Standards for Raman Spectroscopy*; John Wiley & Sons Ltd: Chichester, UK, 2002.
98. Demediuk, P.; Faden, A.I.; Romhanyi, R.; Vink, R.; Mcintosh, T.K. Traumatic Brain Injury in the Rat: Effects on Lipid Metabolism, Tissue Magnesium, and Water Content. *J. Neurotrauma* **1988**, *5*, 105–119. [CrossRef]
99. Lamade, A.M.; Anthonymuthu, T.S.; Hier, Z.E.; Gao, Y.; Kagan, V.E.; Bayır, H. Mitochondrial Damage & Lipid Signaling in Traumatic Brain Injury HHS Public Access. *Exp. Neurol.* **2020**, *329*, 113307. [CrossRef] [PubMed]
100. Mallah, K.; Quanico, J.; Trede, D.; Kobeissy, F.; Zibara, K.; Salzet, M.; Fournier, I. Lipid Changes Associated with Traumatic Brain Injury Revealed by 3D MALDI-MSI. *Anal. Chem.* **2018**, *90*, 10568–10576. [CrossRef] [PubMed]
101. Tashibu, K. Analysis of water content in rat brain using Raman spectroscopy. *Brain Nerve* **1990**, *42*, 999–1004.
102. Kitajima, T.; Tashibu, K.; Tani, S.; Mizuno, A.; Nakamura, N. Analysis of water content in young rats brain edema by Raman spectroscopy. *No Shinkei* **1993**, *45*, 519–524.
103. Wolthuis, R.; van Aken, M.; Fountas, K.; Robinson, J.S.; Bruining, H.A.; Puppels, G.J. Determination of water concentration in brain tissue by Raman spectroscopy. *Anal. Chem.* **2001**, *73*, 3915–3920. [CrossRef] [PubMed]
104. Desroches, J.; Lemoine, É.; Pinto, M.; Marple, E.; Urmey, K.; Diaz, R.; Guiot, M.; Wilson, B.; Petrecca, K.; Leblond, F. Development and first in-human use of a Raman spectroscopy guidance system integrated with a brain biopsy needle. *J. Biophotonics* **2019**, *12*, e201800396. [CrossRef]
105. Seule, M.; Sikorski, C.; Sakowitz, O.; von Campe, G.; Santos, E.; Orakcioglu, B.; Unterberg, A.; Keller, E. Evaluation of a New Brain Tissue Probe for Intracranial Pressure, Temperature, and Cerebral Blood Flow Monitoring in Patients with Aneurysmal Subarachnoid Hemorrhage. *Neurocrit. Care* **2016**, *25*, 193–200. [CrossRef]
106. Tuschel, D. Selecting an Excitation Wavelength for Raman Spectroscopy. *Spectroscopy* **2016**, *31*, 14–23.
107. Signoretti, S.; Marmarou, A.; Aygok, G.; Fatouros, P.; Portella, G.; Bullock, R. Assessment of mitochondrial impairment in traumatic brain injury using high-resolution proton magnetic resonance spectroscopy. *J. Neurosurg.* **2008**, *108*, 42–52. [CrossRef]
108. Adjunctive therapies in lifethreatening CNS infections. *Eur. J. Neurol.* **2015**, *22*, 19. [CrossRef]
109. Nordström, C.; Nielsen, T.; Schalén, W.; Reinstrup, P.; Ungerstedt, U. Biochemical indications of cerebral ischaemia and mitochondrial dysfunction in severe brain trauma analysed with regard to type of lesion. *Acta Neurochir.* **2016**, *158*, 1231–1240. [CrossRef] [PubMed]
110. Stovell, M.; Mada, M.; Helmy, A.; Carpenter, T.; Thelin, E.; Yan, J.; Guilfoyle, M.; Jalloh, I.; Howe, D.; Grice, P.; et al. The effect of succinate on brain NADH/NAD + redox state and high energy phosphate metabolism in acute traumatic brain injury. *Sci. Rep.* **2018**, *8*, 11140. [CrossRef] [PubMed]

111. Sonig, A.; Jumah, F.; Raju, B.; Patel, N.V.; Gupta, G.; Nanda, A. The Historical Evolution of Intracranial Pressure Monitoring. *World Neurosurg.* **2020**, *138*, 491–497. [CrossRef] [PubMed]
112. Tas, J.; Beqiri, E.; van Kaam, C.; Ercole, A.; Bellen, G.; Bruyninckx, D.; Cabeleira, M.; Czosnyka, M.; Depreitere, B.; Donnelly, J.; et al. An Update on the COGiTATE Phase II Study: Feasibility and Safety of Targeting an Optimal Cerebral Perfusion Pressure as a Patient-Tailored Therapy in Severe Traumatic Brain Injury. *Acta Neurochir. Suppl.* **2021**, *131*, 143–147. [CrossRef] [PubMed]
113. DePaoli, D.; Lemoine, E.; Ember, K.; Parent, M.; Prud'homme, M.; Cantin, L.; Petrecca, K.; Leblond, F.; Côté, D. Rise of Raman spectroscopy in neurosurgery: A review. *J. Biomed. Opt.* **2020**, *25*, 050901. [CrossRef] [PubMed]
114. Stevens, A.R.; Ng, I.H.X.; Helmy, A.; Hutchinson, P.J.A.; Menon, D.K.; Ercole, A. Glucose Dynamics of Cortical Spreading Depolarization in Acute Brain Injury: A Systematic Review. *J. Neurotrauma* **2019**, *36*, 2153–2166. [CrossRef]
115. Teasdale, G.; Maas, A.; Lecky, F.; Manley, G.; Stocchetti, N.; Murray, G. The Glasgow Coma Scale at 40 years: Standing the test of time. *Lancet Neurol.* **2014**, *13*, 844–854. [CrossRef]
116. Echemendia, R.J.; Meeuwisse, W.; McCrory, P.; Davis, G.A.; Putukian, M.; Leddy, J.; Makdissi, M.; Sullivan, S.J.; Broglio, S.P.; Raftery, M.; et al. The sport concussion assessment tool 5th edition (SCAT5): Background and rationale. *Br. J. Sports Med.* **2017**, *51*, 851–858. [CrossRef]
117. Gill, M.R.; Reiley, D.G.; Green, S.M. Interrater reliability of Glasgow Coma Scale scores in the emergency department. *Ann. Emerg. Med.* **2004**, *43*, 215–223. [CrossRef]
118. Stevens, A.R.; Su, Z.; Toman, E.; Belli, A.; Davies, D. Optical pupillometry in traumatic brain injury: Neurological pupil index and its relationship with intracranial pressure through significant event analysis. *Brain Inj.* **2019**, *33*, 1032–1038. [CrossRef]

Appendix B

PILOT DATA

This appendix has been published in a peer-reviewed journal:

D.J. Davies, M. Hadis, V. Di Pietro, G. Lazzarino, M. Forcione, G. Harris, **A.R. Stevens**, W.C. Soon, P. Goldberg Oppenheimer, M. Milward, A. Belli, W. Palin. Photobiomodulation reduces hippocampal apoptotic cell death and produces a Raman spectroscopic "signature". *PLoS ONE* 2022 17(3): e0264533. doi: 10.1371/journal.pone.0264533

PLOS ONE

RESEARCH ARTICLE

Photobiomodulation reduces hippocampal apoptotic cell death and produces a Raman spectroscopic "signature"

David J. Davies[1,2]*, Mohammed Hadis[3], Valentina Di Pietro[1], Giuseppe Lazzarino[4], Mario Forcione[1,2], Georgia Harris[5], Andrew R. Stevens[1,2], Wai Cheong Soon[1], Pola Goldberg Oppenheimer[5], Michael Milward[3], Antonio Belli[1,2], William M. Palin[3]

1 Department of Neuroscience and Ophthalmology, Institute of Inflammation and Ageing, University of Birmingham, Birmingham, United Kingdom, **2** National Institute of Health Research Surgical Reconstruction and Microbiology Research Centre, University Hospitals Birmingham' Edgbaston, Birmingham, United Kingdom, **3** Photobiology Research Group, School of Dentistry, College of Medical and Dental Science, Institute of Clinical Sciences, University of Birmingham, Birmingham, United Kingdom, **4** Department of Chemical Sciences, Laboratory of Biochemistry, University of Catania, Catania, Italy, **5** Faculty of Chemical and Biological Engineering, University of Birmingham, Birmingham, United Kingdom

* daviesdj@doctors.org.uk

Check for updates

OPEN ACCESS

Citation: Davies DJ, Hadis M, Di Pietro V, Lazzarino G, Forcione M, Harris G, et al. (2022) Photobiomodulation reduces hippocampal apoptotic cell death and produces a Raman spectroscopic "signature". PLoS ONE 17(3): e0264533. https://doi.org/10.1371/journal.pone.0264533

Editor: Michael R. Hamblin, Massachusetts General Hospital, UNITED STATES

Received: January 19, 2022

Accepted: February 11, 2022

Published: March 3, 2022

Peer Review History: PLOS recognizes the benefits of transparency in the peer review process; therefore, we enable the publication of all of the content of peer review and author responses alongside final, published articles. The editorial history of this article is available here: https://doi.org/10.1371/journal.pone.0264533

Copyright: © 2022 Davies et al. This is an open access article distributed under the terms of the Creative Commons Attribution License, which permits unrestricted use, distribution, and reproduction in any medium, provided the original author and source are credited.

Data Availability Statement: All relevant data are within the paper and its Supporting Information files.

Abstract

Apoptotic cell death within the brain represents a significant contributing factor to impaired post-traumatic tissue function and poor clinical outcome after traumatic brain injury. After irradiation with light in the wavelength range of 600–1200 nm (photobiomodulation), previous investigations have reported a reduction in apoptosis in various tissues. This study investigates the effect of 660 nm photobiomodulation on organotypic slice cultured hippocampal tissue of rats, examining the effect on apoptotic cell loss. Tissue optical Raman spectroscopic changes were evaluated. A significantly higher proportion of apoptotic cells 62.8±12.2% vs 48.6±13.7% (P<0.0001) per region were observed in the control group compared with the photobiomodulation group. After photobiomodulation, Raman spectroscopic observations demonstrated 1440/1660 cm^{-1} spectral shift. Photobiomodulation has the potential for therapeutic utility, reducing cell loss to apoptosis in injured neurological tissue, as demonstrated in this *in vitro* model. A clear Raman spectroscopic signal was observed after apparent optimal irradiation, potentially integrable into therapeutic light delivery apparatus for real-time dose metering.

Introduction and background

Traumatic brain injury (TBI) is a significant contributor to global morbidity and mortality, affecting individuals of all ages [1]. After an initial traumatic injury to the brain, a significant number of neurological cells are lost to apoptosis contributing to a reduction in both neuronal and glial cell populations within the injured brain [2]. Apoptotic cells have been observed both in and around cerebral contusions (areas of necrotic cell death), as well as in brain regions remote to areas of structural pathology [3]. *In vitro* studies have identified that a threshold proportion of apoptotic cells in and around cerebral contusions (66.5% of the observed cellular

Funding: DD received a grant from the Midland Neuroscience Teaching and Research Fund (University of Birmingham Grant Number 1001177) (https://mntrf.org.uk/). The funders had no role in study design, data collection and analysis, decision to publish, or preparation of the manuscript.

Competing interests: The development of this novel concept has resulted in a patent pending application from our group relating to the invasive delivery of PBM, together with the use of temporarily implanted apparatus to establish an optimal dose feedback loop via an optical spectroscopic brain interface (UK Patent Application No 2006201.4). There are no other competing interests to declare, including those relating to employment, consultancy, other patents or products in development. The authors confirm that this does not alter our adherence to all PLOS ONE policies on sharing data and materials.

population) demonstrates a sensitivity of 89.5% and specificity of 66.7% in predicting mortality after severe TBI [3]. Cells undergoing apoptotic transformation (particularly those involved in ascending tracts of oligodendritic lineage [4]) have been observed in traumatic spinal cord injury, spreading to adjacent spinal segments [5], potentially contributing to the reduction in physiological function observed clinically.

Currently, there exist no clinically translated interventional treatments that are aimed at reducing the burden of neurological cell loss during the acute phases of TBI. The majority of clinical management strategies focus on the re-establishment of brain environmental homeostasis [6]: removing active compression, optimising perfusion and oxygenation [7], along with the restoration of functional anatomy. Any new therapeutic approach aimed at reducing the primary burden of cell loss (particularly due to apoptosis within the tissue injury penumbra [3]) has the potential to significantly improve the functional outcome of individuals following TBI.

Photobiomodulation (PBM) or 'low-level light therapy" (LLLT) is the therapeutic application of light for the purpose of facilitating healing and regeneration via any given light source, most frequently light-emitting diodes (LEDs) or a laser. Positive responses have been recorded with the use of light in the wavelength range of 600–1200 nm [8–10], with peak effects observed at approximately 660 nm.

Reduced wound healing time in superficial tissue, accompanied by less pain and inflammation, have been observed as beneficial effects of PBM [11]. Recent investigations have also been demonstrated to increase angiogenesis in wound repair and offer beneficial effects following myocardial infarction [12, 13]. PBM has also been widely used in dentistry due to established benefits of faster oral wound healing and pain relief [14, 15], and most notably with success in treating cancer patients with oral mucositis. Critically, PBM has demonstrated some positive effects in cerebral stroke models through inhibition of the secondary cascade and promoting neurogenesis [16].

A reduction in cell death due to apoptosis has been observed as an effect of PBM in a variety of models. A recent study reported attenuation of TNF/CHX induced apoptosis in squamous endothelial cells [17]. Similar reductions of programmed cell death were observed by a study into gingival fibroblast growth, where irradiated fibroblast colonies lost fewer cells to apoptosis compared with ambient light controls [18]. In vivo studies have also supported these findings, demonstrating attenuation of apoptosis in gastrocnemius myocytes following high intensity exercise in a murine model [19]. Other similar investigations have also observed a reduction of apoptosis in submandibular salivary glands in a diabetic rat model [20].

The exact mechanism by which PBM exhibits these positive biological responses is not fully understood, although it is proposed that the direct or indirect modulation of the enzyme cytochrome c oxidase (COX) is integral to the effect. COX is a large transmembrane protein complex located in the inner mitochondrial membrane [8]. Four metallic centres within its structure act as photoacceptors, transducing photosignals [8, 21]. COX stimulation using red and near-infrared (NIR) light causes the activity of the electron transport chain to increase, ultimately increasing the abundance of adenosine triphosphate (ATP) [8, 21, 22]. It is proposed that photons (of sufficient intensity and number) are absorbed by COX within the mitochondria [8, 22, 23]. This absorption potentiates the oxidative metabolic cascade resulting in beneficial effects of PBM [22, 24]. However, control cell lines and those lacking COX demonstrate cell proliferation [25], suggesting that some effects of PBM are via alternative pathways.

Initial studies investigating the effects of PBM on TBI within animal models have demonstrated potential translatable benefit including reduction in lesion size (up to 50%), improvements in objective neurological function, and reductions in observable trauma-related degeneration [26, 27]. Although not directly considered in these investigations, effects are

likely to be related to the reduction in apoptotic cell loss as demonstrated in non-TBI PBM studies [17, 18, 28].

The intensity (irradiance) and total time of light exposure have long been identified as key factors in the magnitude of the beneficial effect of PBM [29], however, there is little evidence in the literature to indicate the optimum dose for survival benefit in neurological tissue. The range of light intensities (irradiance ($mWcm^{-2}$), fluence (J/cm^2) and the dose (J) discussed in the generic literature leading to clinically significant effects on cell survival and tissue regeneration imply that transcranial delivery of the photons may not deliver a sufficient dose [30]. It may also be the case that the optimal photon dose varies between individual subjects, or different discrete regions of a given target tissue or organ.

Conceptually, the optical apparatus required for tissue photon delivery represent a potential for a simultaneous direct to tissue optical monitoring interface. Through simultaneous optical monitoring, the effect of PBM may be contemporaneously observed using a range of spectroscopic techniques, particularly Raman spectroscopy [31, 32]. Variations over time in the acquired optical spectra may represent a viable method of metering optimal dose and achieving the optimal desired effect.

Raman spectroscopy produces chemically specific optical signatures by utilising the inelastic scattering of coherent light, detecting the shift in wavelengths (cm^{-1}) observed following the energy change between light and matter [33]. Incident photons vibrate the molecules forming the target substance before scattering and the re-captured photons can be collected to form a spectrum of peaks indicating the biochemical structure of the substance [31, 32]. Raman spectroscopy for biological analysis typically use incident wavelengths in the visible/NIR region of the electromagnetic spectrum, with sensitivity to detected photons from biological molecules with wavenumbers in the region of 600–1800 cm^{-1} and 2500–3400 cm^{-1} [34]. Raman spectroscopy is sensitive, rapid and achieved without labelling or strict sample preparation [33]. Optimising the acquisition settings for biological samples would allow for non-destructive diagnoses or monitoring, applicable to intra-cranial access to brain tissue.

Aims

1) To evaluate the potential of 660 nm PBM in reducing the quantity of brain tissue cells lost to apoptosis in a hippocampal organotypic slice culture model (as an *in vitro* TBI model). Here we will also investigate the influence of irradiance, the effect of irradiance and exposure time (total photon dose), and consecutive daily doses on the number of cells initiating programmed cell death within the cultured tissue.

2) To investigate changes in tissue optical (Raman) spectroscopic signature elicited by PBM along with its relation to photon dose, and from this consider if a specific signature in tissue Raman spectrum can be developed as a feedback marker to confirm optimal or adequate tissue dosage.

Materials and methods

1) Sprague-Dawley rat hippocampus organotypic slice model

A hippocampectomy was performed immediately post-mortem on adult Sprague-Dawley rats under Home Office licence, sacrificed via carbon dioxide toxicity. Once performed, 150 μm hippocampal slices were separated (Fig 1). Individual slices were then placed onto polytetrafluoroethylene (PTFE) semi-permeable membranes (4 slices per membrane) incorporated into individual well inserts (Millicell® cell culture inserts, Millipore, PICM03050) fitting into a standard 6 well culture plate (Sigma®, SIAL0516). Glucose fortified B27-supplemented neurobasal medium (sNBA) solution (1 ml) was then added to each well. Plates containing the

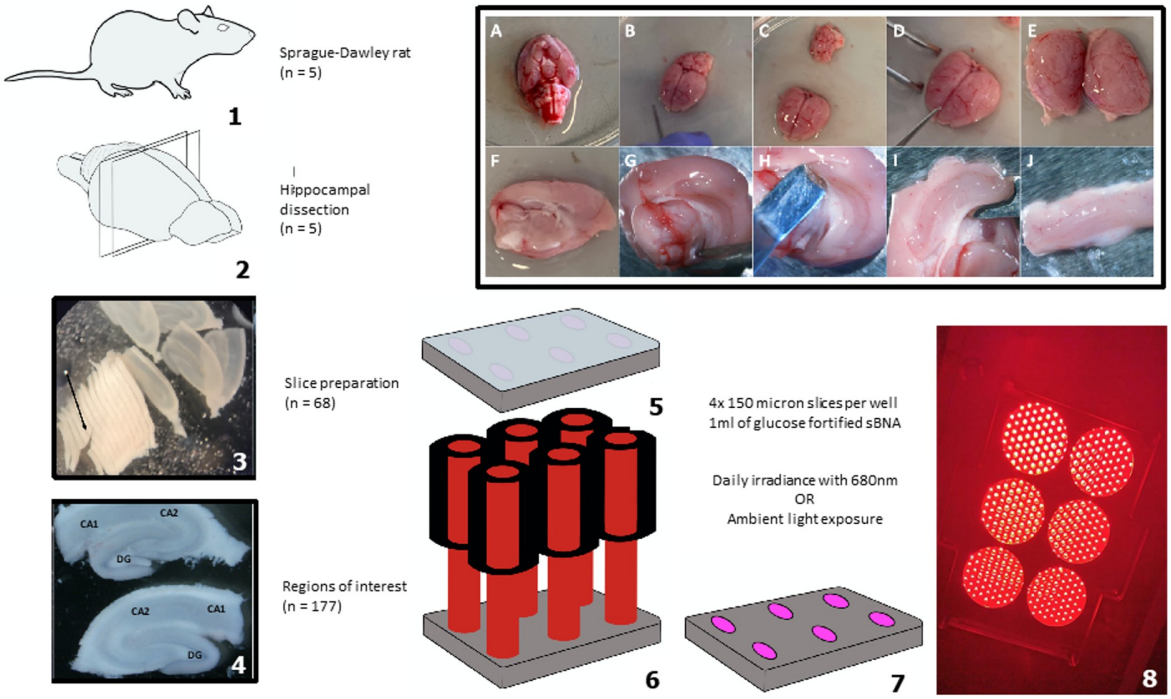


Fig 1. Overview of organotypic hippocampal slice model preparation and administration of PBM. (1) Sprague-Dawley rats were sacrificed; (2) hippocampal dissection (further in top right panel images A-J); (3) manual slice preparation; (4) demonstration of the regions of interest per slice (two slices shown); (5) standard six well culture plate; (6) culture plates exposed to irradiance; (7) culture plates exposed to ambient light; (8) photograph of LED arrangement for irradiance exposure.

https://doi.org/10.1371/journal.pone.0264533.g001

slices were light protected using foil and incubated at 37˚C / 5% CO_2. The initial dissection and slicing of the tissue, particularly the manual slice separation serves as an in vitro analogue of TBI, not requiring the stable culture population and injury calibration of previously described 'stretch' models [35]. A daily visual assessment was undertaken. All subsequent analysis would be carried out on tissue and media harvested from this process, paired control and intervention samples were obtained from the same sacrificed specimens.

2) Photon dose delivery, beam profile and calibration

Therapeutic light of 660 nm wavelength was delivered in a single daily dose using a variable irradiance calibrated LED light source array (BioThor device, Thor Photobiomedicine). This wavelength was selected as it has demonstrated the greatest efficacy within the current limited subject literature [19–24]. Light intensity was controlled using a variable voltage power supply. Irradiance and beam homogeneity were confirmed via UV Vis Spectroscopy and beam profiling respectively.

2.1. Spectrophotometric light characterisation. The BioTHOR plate irradiator was spectroradiometrically characterised using a National Institute of Standards and Technology (NIST) calibrated fiber coupled spectrophotometer (USB400 UV-Vis Spectrometer, Ocean Optics) to obtain information on absolute irradiance and wavelength (Fig 2). Prior to calibration, the spectrometer was assembled with a 200 μM optical fiber and CC3 opal glass cosine corrector (3.9mm diameter). Following calibration, an empty 6-well plate was placed into the plate carrier with an aluminium 'mask' directly below the plate so only the area corresponding to the wells were exposed to light. The cosine corrector of the calibrated fiber was placed centrally into each

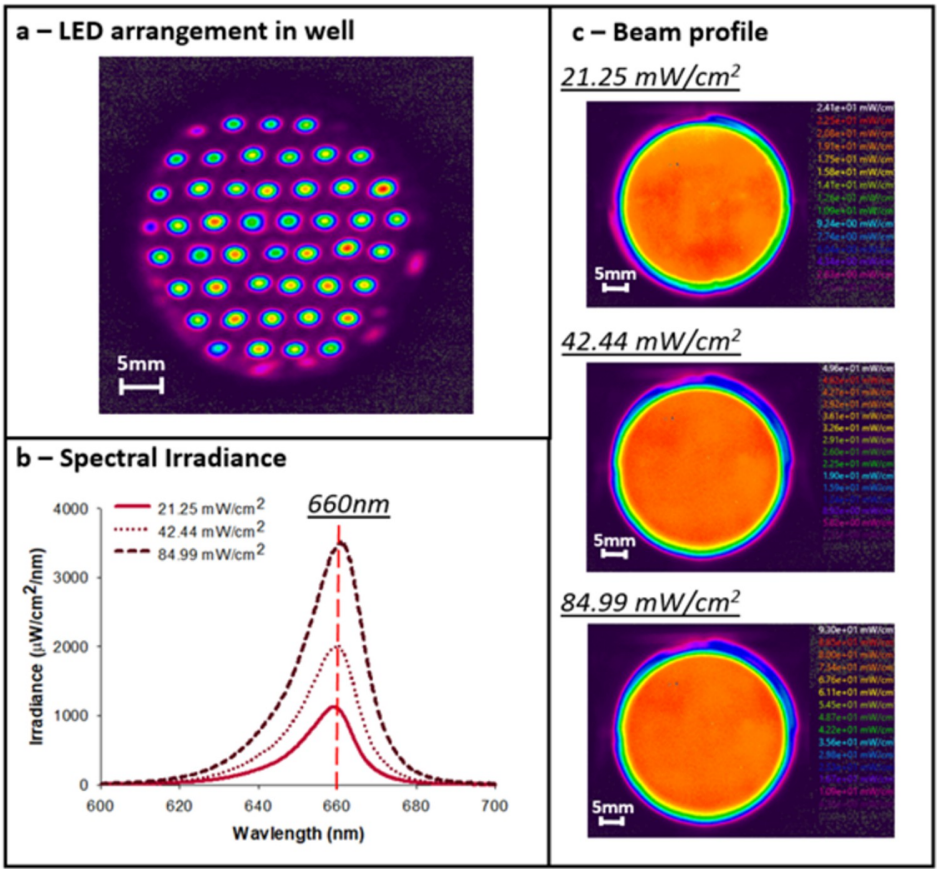


Fig 2. Characterisation of the LED array to confirm spectral irradiance and beam homogeneity. Each well is irradiated by 47 miniature LEDs with Gaussian beam profiles (a). However, at the surface of the 6-well plate a homogenous beam profile is produced due to divergence of the beams from the individual LEDs and scattering at the plate surface. This produces a uniform irradiance with an average irradiance of 21.25 mW/cm^2, 42.44 mW/cm^2 and 84.99 mW/cm^2 for the three tested light intensities (b and c) (measured at tissue level, with a beam diameter equal to well diameter = 34.8mm). Fluence values for 1 min exposure time: LT1 = 1.28 J/cm^2; LT2 = 2.55 J/cm^2; LT3 = 5.10 J/cm^2. Total power output of array (when delivering 42.44 mW/cm^2 at tissue level) = 4.244 W.

https://doi.org/10.1371/journal.pone.0264533.g002

well of the 6- well plate so that the surface of the cosine corrector was in contact with the lower surface of the well to allow the measurement of the amount of light delivered during *in vitro* irradiation of hippocampal slices. Adjustment of the supply voltage to the array to pre-determined values supplied by the manufacturer allowed specific irradiances to be delivered to the plates. The spectral irradiance was recorded using Ocean View software (Ocean Optics, UK) and the absolute irradiance was calculated from the integral of the emission trace.

2.2 Beam profile measurements. The beam profile of the BioTHOR plate irradiator was determined using a CCD based beam profiler camera (Spiricon SP620, Ophir) following optical and linear calibration. The camera was focused onto the clear lower surface of a 6-well plate and beam profiles were measured either with or without a diffuser target screen (Opal glass target screen, Thorlabs) placed between the 6-well plate and light source. For each measurement, an ambient light correction was applied and images were recorded statically to assess the homogeneity of the beam delivered in each well.

2.3 Dosing. A commencing dose of 2 minutes irradiance at 42.4 mW/cm^2 daily was selected. The six well plate containing slices to be treated (intervention plates) was placed on

the source, covered over with an ambient shield. Control plates containing hippocampal slices from the same sacrificed animals (identically and contemporaneously prepared and incubated adjacent to the intervention plates) were placed in ambient light during treatment. All plates were foil shielded as soon as the light therapy was completed and then returned to the incubator.

3) ImmunoFluorescent cell imaging

NucView 488 Caspase-3 was utilised as a fluorescent apoptotic cell marker. Caspase-3 is a key enzyme within the apoptotic pathway, and once activated (as apoptosis is triggered) it cleaves the NucView 488 substrate, liberating the fluorescent product. On the final day of culture, the media within each well was replaced with 1 ml of media containing Nucview 488 (1/200 dilution e.g 5 μl NucView in 995μl glucose fortified sNBA). Plates were then incubated for a further 4 hours. The well media was then replaced with 1 ml 4% paraformaldehyde (PFA) and incubated for 20 minutes shielded from light at room temperature. The membrane inserts containing hippocampal slices then underwent three consecutive washes in phosphate buffered saline (5 minutes per wash). These were then removed from their respective wells and mounted using VECTASHIELD® antifade mounting medium containing 4′,6-diamidino-2-phenylindole (DAPI) for the purpose of additional discreet nuclear marking. A Zeiss axioscope was used for the purpose of fluorescent imaging. Three specific and consistently recognisable regions were imaged on each hippocampal slice, the dentate gyri, and the coru ammonis (CA) regions 1 + 2. Three images were obtained for each region without Z stack: an image showing the total number of cells (DAPI fluorescent blue channel); an image showing only the apoptotic cells (NucView 488 related green channel); and a merged image to observe the relative ratio of these. Images were discarded where image quality was deemed poor or corrupted with artefact or inclusion.

For live cell imaging experiments (investigating the effect of consecutive daily PBM doses), imaging took place daily. Media was replaced each day with 1 ml media containing the Nucview 488 and pure DAPI (5 μl NucView and 1 μl pure DAPI in 994 μl sNBA). Plates were then incubated at 37˚C, 5% CO_2 for 4 hours. Following incubation, images were taken as per the above protocol, however without removal of the membranes or fixation. The fluorescent media was then removed and replaced with sNBA. As a contrast agent for cell nuclei was not applied, only absolute numbers of cells entering (caspase-mediated) apoptosis are obtained. The next PBM dose was then applied where applicable. Plates were then returned to the incubator (37˚C, 5% CO_2).

Images obtained were then analysed and automatic cell counts acquired using ImageJ (NIH, University of Wisconsin, USA). For each slice in all three regions (DG, CA1, CA2), the total cell numbers (DAPI blue channel fluorescence) and apoptotic cells (NucView) were counted providing a percentage ratio of cells that had initiated apoptotic cell death.

4) Tissue Raman spectroscopy

Immediately after the final PBM or control treatment in each individual culture experiment, individual slices retrieved from the culture wells were placed onto an aluminium backing plate (for optical noise reduction) and gentle pressure exerted on the tissue sample directly to create a (visually) homogenous Raman scanning surface of uniform thickness. Spectroscopy was carried out using an inVia™ confocal Raman microscope with incorporated spectrometer (Renishaw, Wotton-under-Edge, UK), The integrated 'WiRE' software package (Renishaw, Wotton-under-Edge, UK) was used for acquisition and image processing. After surface focusing using 20x objective magnification, a 633 nm laser at 100% device specific power was used

to obtain spectra. A total of 3 x 6 second exposures were obtained to formulate the definitive spectrum from each hippocampal slice. Acquisition and processing were carried out in line with previous investigations undertaken [32, 36]. Based on previous investigation the peak intensity at 1440 cm^{-1} and 1660 cm^{-1} were the focus of analysis along with their respective ratios (due to expected variability in raw data absolute quantity).

5) Statistical analysis

Data was assessed for normal distribution (Shapiro-Wilk) and resultantly where data was non-parametric, a Mann-Whitney statistical test was used to ascertain the significance between the two considered continuous variables (intervention and control). A paired student's t-test was utilised for statistical analysis in the case of normally distributed data (effect of PBM on apoptosis in intervention and control samples), with matched intervention/control samples taken from a single sacrificed specimen. A P value < 0.05 was considered statistically significant within this context. Tukey HSD was utilised for multiple comparisons (cumulative effect of daily exposure). Statistical analysis was performed using SPSS (IBM 2019).

6) Animal research

All experimental protocols were approved by the University of Birmingham and performed under the Home Office licence held by our department. All experiments were performed in accordance with relevant guidelines and regulations. Reporting of methods follows the recommendation of the ARRIVE guidelines.

Results

1) Initial effect

An initial control group of 28 slices (82 observed regions of interest (ROI)) was compared with a light irradiated group of 40 slices (95 ROI) from sacrificed animals (n = 5). An initial 2 minutes of PBM at was applied daily for 5 consecutive days at an irradiance of 42.4 mW/cm^2 (LT2). On average, significantly more apoptotic cells 62.8±12.2% vs 48.6±13.7% ($P<0.0001$) per region were observed in the control group compared with the PBM irradiated group (Fig 3). The individual slice with the highest percentage of apoptotic cells (85.6%) occurred within the control group. Conversely, the irradiated group contained the slice with the lowest percentage of apoptotic cells (14.1%). A differential benefit (in terms of proportion of cells lost to apoptosis) was also observed between individual hippocampal regions (Fig 4).

2) Effect of irradiance

To assess the effect of irradiance, 5 day cultures with daily (2 minute) treatments at an irradiance of 21.3 mW/cm^2 (LT1), and 85.0 mW/cm^2 (LT3) were undertaken for comparison with the initial 42.4 mW/cm^2 (LT2). LT1 and LT3 were applied in a total of 20 and 24 hippocampal slices ($n = 57$ and $n = 67$ ROI, respectively) along with 18 contemporaneous control slices ($n = 35$ ROI) from sacrificed specimens ($n = 4$). Within the LT1 treated slices 45.8±12.7% of observable cells underwent apoptosis, significantly less than the 62.8±12.2% observed in the control specimens (Fig 5; $P < 0.0001$). Within the LT2 treated slices the observable apoptotic cell population was 43.9±14.6% and 54.7±11.9% in the LT3 group, both significantly lower than control (Fig 5; $P = 0.0018$ and $P < 0.0001$, respectively).

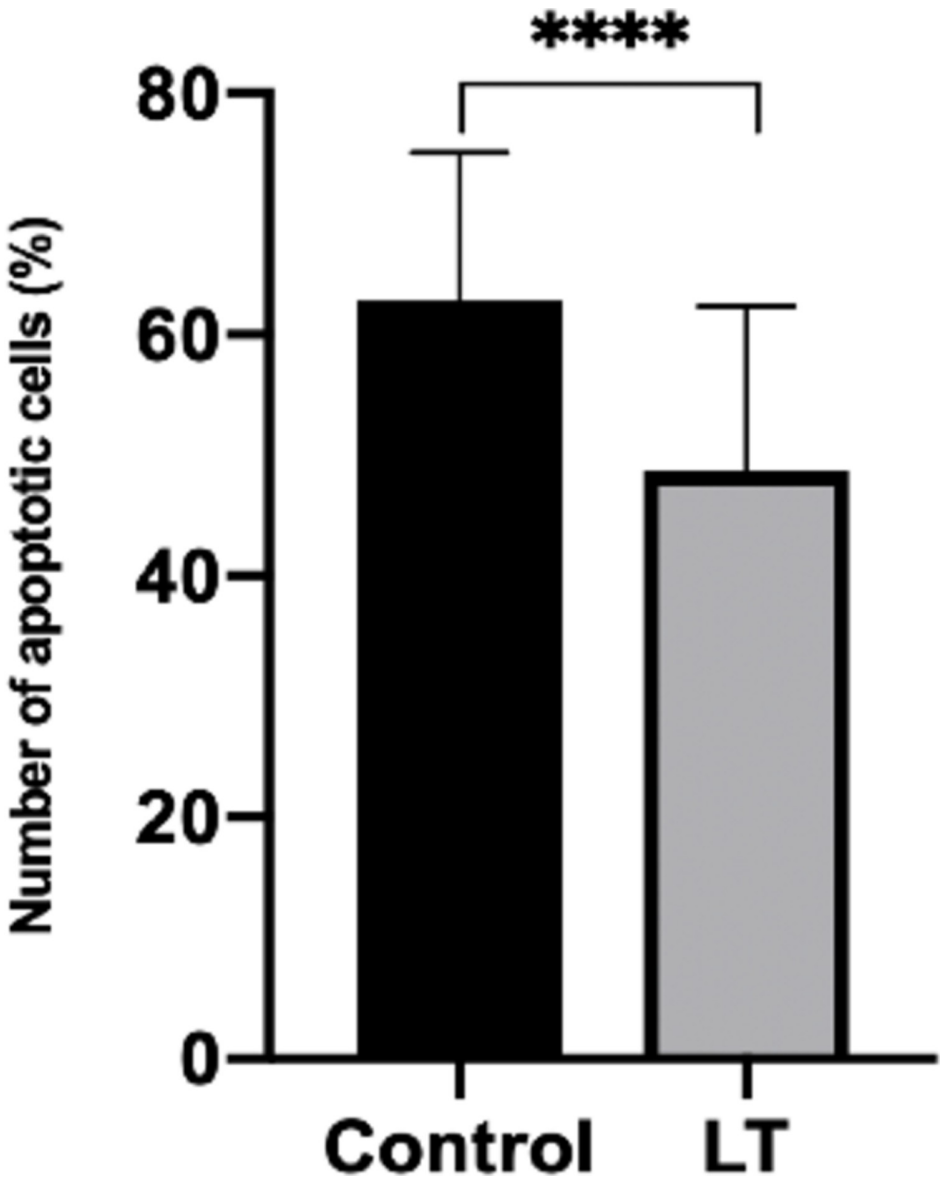


Fig 3. Initial observed effect in the reduction of cell loss to apoptosis. LT = light therapy (PBM). **** denotes $P < 0.0001$, error bars represent standard deviation (SD).

https://doi.org/10.1371/journal.pone.0264533.g003

3) Effect of dose duration

Daily doses of 1 minute, 2 minutes (initial) and 3 minutes were applied to the 5 day slice culture model. In total, 14 slices (n = 41 ROI) received 1 minute of irradiation a day, 14 slices received 2 minutes (n = 39 ROI) and 15 slices (n = 44 ROI) received 3 minutes. The previously ascertained optimal intensity of 42.44 mW/cm^2 was applied, with a contemporaneous control group of 15 slices (n = 43 ROI) cultured from a total of 3 sacrificed specimens (n = 3). The mean proportions of apoptotic cells observed in control slices was 60.2±11.0% compared with 51.6±17.0% in the 1 minute group (P = 0.0066), 54.6±13.5% in the 2 minute group (P = 0.0437), and 61.4±15.2% in the 3 minute group (P = 0.182) (Fig 6).

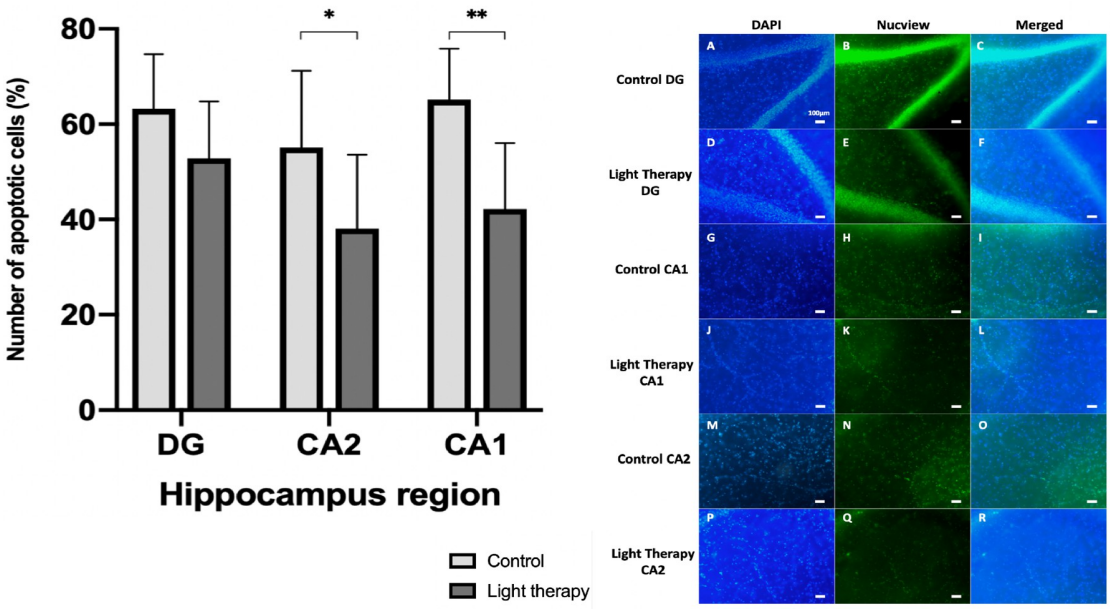


Fig 4. Differential effect of LT2 on the individual hippocampal regions observed. LT2 = 660nm irradiation for two minutes per day over a 5 day culture. ** denotes $P < 0.01$, * denotes $P < 0.05$, error bars represent SD. CA1 = cornu Ammonis 1, CA2 = cornu Ammonis 2, DG = dentate gyrus, DAPI = 4', 6-diamidino-2-phenylindole.

https://doi.org/10.1371/journal.pone.0264533.g004

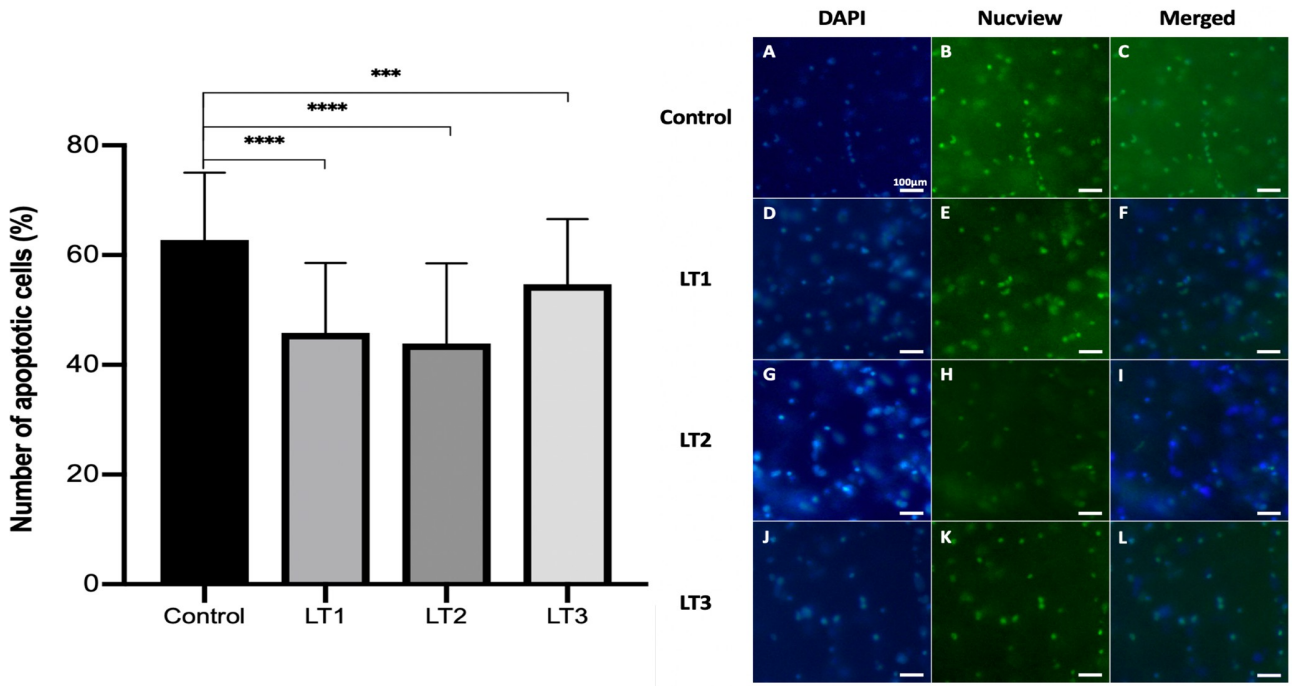


Fig 5. Effect of irradiance—% of apoptotic cells in each group, LT1 = *21.3 mW/cm²*, *LT2 = 42.4 mW/cm²*, LT3 = *85.0 mW/cm²*. **** denotes $P < 0.0001$, *** denotes $P < 0.001$, ** denotes $P < 0.01$, error bars represent SD. DAPI = 4', 6-diamidino-2-phenylindole.

https://doi.org/10.1371/journal.pone.0264533.g005

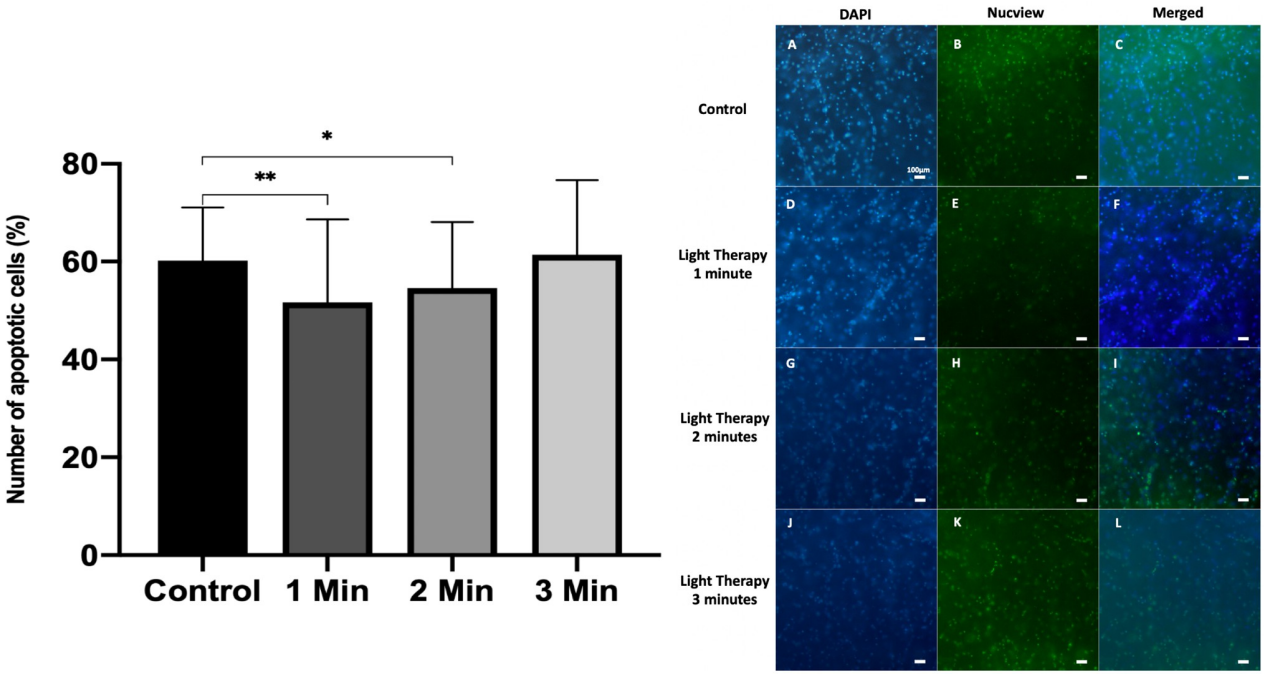


Fig 6. Percentage of apoptotic cells in response to varying light therapy durations, either 1, 2 or 3 minutes per day over 5 days. ** denotes $P < 0.01$, * denotes $P < 0.05$, error bars represent SD. DAPI = 4', 6-diamidino-2-phenylindole.

https://doi.org/10.1371/journal.pone.0264533.g006

4) Cumulative effect of daily doses

A simultaneous 5 day culture with daily live imaging was undertaken with: (1) a control group of 10 slices (no light therapy, $n = 27$ ROI), a 1 day group of 10 slices (receiving one dose of light therapy 0 h after injury and no further doses, $n = 27$ ROI), a 2 day group of 10 slices (receiving two doses of light therapy at 0 h and 24 h after injury then no further doses, $n = 30$ ROI), a 3 day group of 9 slices (receiving three doses of light therapy at 0 h, 24 h and 48 h after injury and no further doses, $n = 25$) and a 4 day group of 10 slices (received four doses of light therapy at 0 h, 24 h, 48 h and 72 h after injury, $n = 28$ ROI). Slices were taken from 4 sacrificed animals ($n = 4$). Daily treatment given was 1 min exposure to LT2.

The control group of slices showed a steady reduction in apoptotic cell death over the 4 day experiment (Table 1). After 2 days, no group of cultured slices demonstrated a significant reduction in apoptotic cells compared with the control. At 3 and 4 days, intervention groups had significant apoptosis reduction compared with the control group ($P = 0.039$ and $P = 0.008$ respectively). A cumulative beneficial effect was demonstrable (Fig 7) on daily doses.

Table 1. Proportion of apoptotic cell loss (%) at 24, 48, 72 and 96 hours in control (no PBM) 1, 2, 3, and 4 consecutive days of PBM.

	24 hrs	48 hrs	72 hrs	96 hrs
Control	67.4±6.10%	64.7±4.02%	63.6±5.60%	62.4±4.00%
1 day	62.6±15.2%	62.1±5.05%	61.3±3.39%	60.4±3.84%
2 day	64.2±5.20%	59.2±8.59%	60.2±3.09%	59.7±3.84%
3 day	62.2±6.84%	58.6±5.54%	56.7±6.05%	56.8±3.83%
4 day	64.7±7.73%	61.8±4.55%	57.1±5.80%	54.7±5.27%

https://doi.org/10.1371/journal.pone.0264533.t001

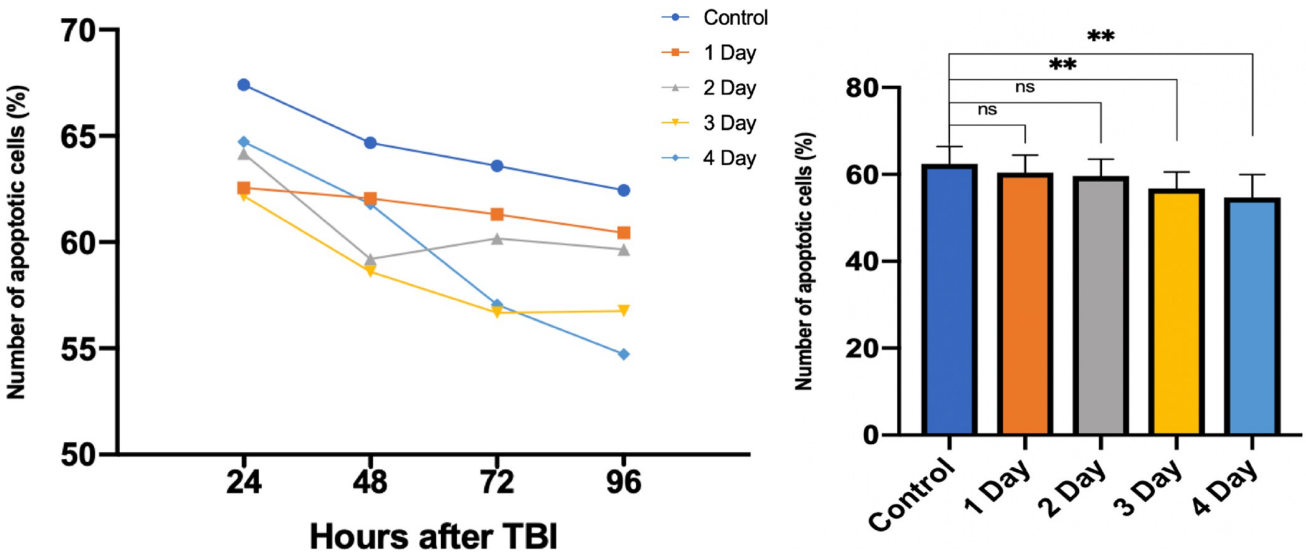


Fig 7. Effect of daily doses of irradiation on cell loss of LT2 (42.4mW/cm^2) for 1 minute per day, for 1 to 4 days. ns denotes no significance, ** denotes $P < 0.01$, error bars represent SD.

https://doi.org/10.1371/journal.pone.0264533.g007

5) Raman spectroscopic signature of effect

After a 5 day organotypic culture, 36 slices underwent Raman spectroscopy (n = 18 control and n = 18 receiving LT2 irradiance therapy for 1 minute per day). For each of the spectra produced, the shift corresponding to the largest peaks in the control condition were 1440±0.7 cm^{-1} and 1659±0.8 cm^{-1}. In the treatment condition, they were at 1440±0.6 cm^{-1} and 1658±0.6 cm^{-1}. For brevity, the peaks in both groups were approximated to 1440 cm^{-1} and 1660 cm^{-1}, respectively. In line with previously undertaken investigations [32, 36] focus centred chiefly on the magnitude of shift at these points in the acquired Raman spectra (Fig 8). Average intensity (peak size) at 1440 cm^{-1} was 1407±187 (au) and 1288±110 in the control and PBM conditions, respectively. The 1660cm^{-1} peak had a mean intensity of 1090±130 in the control samples, and 1291±66 in the treatment samples (Fig 6). There was a significant change in the average 1440/1660cm^{-1} peak ratio between the therapy and control groups (Mann-Whitney U, P = 0.0204), with the ratio increasing from 0.774 in the control group to 1.002 in the therapy group (24.8% relative increase in ratio).

An additional cohort of 14 slices was prepared. 7 of these underwent a 3 day slice culture with daily PBM at LT1 irradiance for 1 minute prior to Raman analysis, with the remaining 7 slices progressing to a 5 day (daily 1 minute LT1) culture before spectroscopic examination in order to observe the progression of the ratio over multiple daily doses. This culture was undertaken with an identical number of matched control slices. Here, an increase in 1440cm/1660 cm^{-1} ratio from the 3 day culture samples vs controls (0.757 vs 0.891; 17.7% increase, P = 0.092) was observed, along with a further increase in the ratio after 5 days. No significant difference was observed between the 1440cm/1660cm^{-1} peak ratios at each therapeutic interval (3 day vs 5 day; P = 0.4).

Discussion

The framework of this series of experiments is based on exploring the possibility of PBM as a clinically viable tool to improve cell survival within the context of moderate to severe TBI, with real-time Raman spectroscopic dose metering. The delivery of such a clinical tool would be

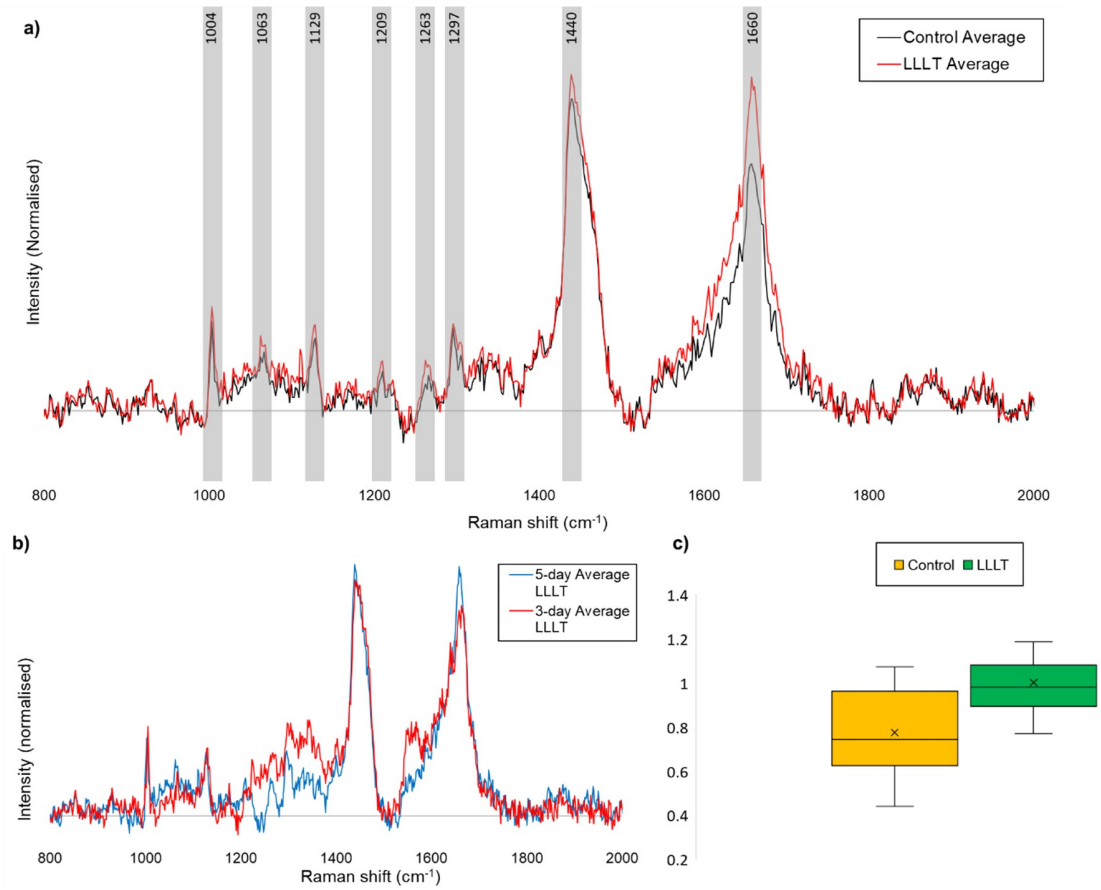


Fig 8. **a)** Comparative figure of average control and average PBM Raman spectra normalised, illustrating the changes in average intensity of the 1440 and 1660 cm^{-1} peaks, and highlighting the assigned, characteristic peaks of rat hippocampus. **b)** Comparative figure of normalised Raman spectra from average 3-day PBM samples and average 5-day PBM samples, no significant difference was observed between the 1660 cm^{-1}/1440 cm^{-1} peak ratios at each therapeutic interval ($p = 0.4$). **c)** Box and Whisker plot illustrating the increase in average peak intensity ratio of 1660 cm^{-1}/1440 cm^{-1}, increasing from 0.774 for control samples to 1.002 for PBM samples ($p = 0.0204$).

https://doi.org/10.1371/journal.pone.0264533.g008

heavily determined by the irradiance and duration of light exposure required to produce a clinically meaningful effect.

Irradiance with 660 nm light has demonstrated a significant improvement in cell survival. An exposure of 1 minute at an irradiance of 42 mW/cm^2 had the greatest decrease in the number of apoptotic cells (an absolute reduction of 18.9%). This work has determined a biphasic pattern of irradiation dose: an increase from approximately 42 mW/cm^2 led to an apparent reduction in effect. However, halving the dose demonstrated a statistically similar effect. Although the range of tested intensities and durations was limited and definitive quantities impossible to deduce, it may be reasonable to consider the optimal irradiance as between 21 and 42 mW/cm^2. However, more investigation would be required to establish this precisely.

Similarly, when assessing the effect of the duration of exposure, 1 minute demonstrated the greatest magnitude of reduction in programmed cell death. Extension of duration to 2 and 3 minutes diminished the observed positive effects. From the observations on intensity and duration, we can infer that it is likely that a certain rate of delivery and/or a total number of absorbed photons will exert the greatest positive effect, although this investigation did not address the effects of exposure reciprocity, i.e. the potential to observe similar benefits for a

prolonged duration at a reduced intensity, or an increased irradiance for a shorter time. These additional required investigations would provide evidence as to whether the total number of photons absorbed was the true proportional variable to effect magnitude.

Live daily image assessment demonstrated a positive cumulative effect of daily application of 1 minute PBM at the optimally established irradiance of approximately 42 mW/cm^2. Daily application led to a progressive reduction in programmed cell death. The reduction in apoptosis within the live daily imaged control samples (reduction in live cell stock within the organotypic slice culture translating to a lower absolute number) was further decreased by the application of daily doses of PBM. When daily applications ceased, the trajectory of reduction returned to that of the control (Fig 5), suggesting that any observed positive effect is transient.

A further observation can be made from the differential benefit between hippocampal regions; the greatest magnitude of effect seemed to be realised by regions of lower mitotic activity and cell turnover [37]. This may have implications on PBM having the greatest benefits in cell preservation in tissues that have naturally low levels of mitosis/cellular division (the cerebral cortex).

Application of red/NIR PBM to neuronal cell culture has a background in the literature, and the findings here correlate with previous study. In SH-SY5Y cells, 635 nm light (18 J) has been shown to reduce mitochondria dependent apoptosis after sodium nitroprusside exposure [38]. Giuliani et al. have previously demonstrated that 670 nm at 0.45 mJ/cm^2 stimulate neurite outgrowth and increased cell viability in conditions of oxidative stress in rat pheochromocytoma cells (PC12) [39]. In primary astrocyte cell culture, 660 nm light at 6 J/cm^2 was found to promote cell proliferation [40]. Using 670 nm light, with Sommer and colleagues demonstrated that PBM significantly increased cell proliferation in amyloid β stressed human neuroblastoma cells [41].

A fundamental limitation of this investigation is the organotypic model utilised. Here we have no quantified injury burden (as would be in previously described 'stretch' models [35]), and rely on the process of preparation together with the naturally suboptimal conditions of the in vitro environment to model the tissue injury. As a result, within the following hours and days, a sustained reduction in the number of cells is expected. The trajectory and 'gradient' of this rate of cell death will be steepend or flattened depending on any additional noxious or nourishing modifications to the culture environment. A quantified and reproducible insult, requiring a prolonged stable (without progressive and terminal loss of surviving cell stock) slice culture [42] was not reliably achievable within our laboratory infrastructure. Unacceptable levels of contamination and sample loss was experienced, leading to inconsistency and smaller data samples.

The Raman spectra recovered and compared between both control and intervention slices revealed a clear signature of tissue response to PBM (as tested at 42 mW/cm^2 intensity for 1 minute per day). All characteristic peaks (identified and assigned in Table 2) are larger in magnitude for the average spectra of PBM samples than control, representing a greater number of protein, lipid, amino acid and glycogen molecular bonds, indicating fewer apoptotic cells. Due to Raman intensity having arbitrary units, and the expected variability in raw data absolute quantity, peak intensity between separate samples are not an ideal source of comparison. The most consistently comparable feature between samples in these spectra is the ratio between the largest peaks: at 1660 cm^{-1} and 1440 cm^{-1}.

The 1660 cm^{-1} peak (Amide I region) is proposed to correspond with the number of protein bonds in the tissue. An increase in this peak intensity (increased presence of protein bonds) as seen in PBM spectra, corresponds with decreasing numbers of apoptotic cells. Conversely, the 1440 cm^{-1} peak is proposed to represent cholesterol bonds, which shows only a modest increase in intensity in PBM compared to control in our samples. Relative stability of the 1440

Table 2. Raman peak assignment for characteristic peaks identified in rat hippocampi spectra [43–47].

Peak Wavenumber (cm^{-1})	Assignment	Origin
1004	ν(C-C) ring	Phenylalanine
1063	ν(C-C) lipids	Phospholipids, Aliphatic side chains
1129	ν_s(COC), ν_s(PO_2), ν(CN), ν(CC)	Glycogen, DNA, Phenylalanine, Lipids, Aliphatic side chains
1209	νPh, δCHC, CH_2 wagging and twisting	Hydroxyproline, Tyrosine, Tryptophan, Phenylalanine
1263	Amide III, CH_2 twisting	Lipids
1297	δ(CH_2) lipids, Amide III	Aliphatic side chains, Lipids
1440	δ(CH_2) lipids and proteins, CH_2 twisting and bending	Cholesterol, Phospholipids, Tyrosine, Proteins
1660	ν(C = C) lipids, C = C stretching Amide I	Tyrosine, Lipids, Proteins, Alpha-helix/random coil

ν = stretching; ν_s = symmetric stretching; δ = in-plane bending, Ph = Phenyl.

https://doi.org/10.1371/journal.pone.0264533.t002

cm^{-1} peak between PBM and control permits its use as a reference point for the 1660cm^{-1} intensity, hence the 1440cm/1660cm^{-1} ratio.

Corresponding survival data was not acquired in this experiment: future investigation incorporating both data streams focusing on potential correlation between the magnitude change/ratio change in these peaks and the proportion of cells initiating apoptotic (and potentially necrotic) cell death is required. The implications of these observations are two-fold: firstly, it would provide a potential avenue for real time monitoring of the effects of PBM within the in vivo and/or clinical setting. Observing a shift in peak ratio may provide insight into when an optimal photon dose of PBM has been delivered, removing the risk of over- or under-dosing which would lead to a reduction in potential positive effect. Secondly, this shift in 1440/1660cm^{-1} ratio may have the potential to provide an independent measurement of brain injury burden and prognostic potential, allowing a real time roadmap of tissue recovery together with information regarding the effectiveness of other therapeutic interventions. Similar approaches have been undertaken previously to quantify the redox state of components in the mitochondrial cytochrome electron transport chain [48]. However, additional work into the optical Raman spectra of tissue irradiated by PBM is required to provide insight into the fundamental effect of light on cellular metabolism, giving a definitive answer to the mechanisms underpinning this photo-cellular effect.

A considerable strength of the present work amongst the literature is the rigorous accuracy in radiometry and dosing [49, 50]. This has been achievable through a collaborative approach between research groups, combining expertise in both photobiomodulation and neural repair. Further cross-disciplinary working has facilitated the integration of optical monitoring techniques into the model, which has demonstrated a spectroscopic "signature" for monitoring dose-effect. This modality for real-time feedback of effect alongside accurate radiometry has allowed development of a system which has the potential to permit therapeutic titration of PBM in a manner which has not been described previously.

Whilst previous work has adopted a transcranial approach to light delivery [16], irradiance within this order, and Raman spectroscopic monitoring, would require a direct-to-brain surface or intra-parenchymal approach at one or more points in order to achieve a meaningful effect. Together with the proposed dosing schedule, and should these observations be confirmed in further in vivo investigation, intracranial access of such a device would be required for sufficient delivery. The integration of an appropriate optical interface into a device delivering the current standard of care is potentially viable, posing a minimal risk burden to the treated individual. The current standard of care for the management of these conditions

involves direct intracranial access, and the placement of an array of catheters into the brain parenchyma substance [51, 52]. Access to this is achieved via burr holes in the skull and is undertaken in all cases meeting the minimum severity requirement [52] with or without the requirement for surgical intervention. Intracranial light delivery in *in vivo* Parkinsonian models has been shown successful previously [53–55], demonstrating feasibility.

The development of this novel concept has resulted in a patent pending application from our group relating to the invasive delivery of PBM, together with the use of temporarily implanted apparatus to establish an optimal dose feedback loop via an optical spectroscopic brain interface (UK Patent Application No 2006201.4). The conceivable optical apparatus required to deliver a meaningful dose of PBM directly onto or into the brain substance (fibre optical), could be utilised for the Raman spectroscopic examination of the brain surface (an emission and detection fibre) and integrated into a single device [56]. As PBM treatment is only potentially required for a short time (1 minute) each day, the scope for establishing a spectroscopic interface to monitoring pathology, metering PBM dose and also tracking the deposition of pharmacological therapeutic agents is an exciting potential prospect for TBI care.

Conclusion

The application of 42 mW/cm^2 of 660 nm light for 1 minute a day has a significant effect on reducing the number of cells lost to apoptosis in the organotypic slice culture considered here. The effects are cumulative daily. A clear Raman spectroscopic signature is observable and may provide a reliable biofeedback mechanism for the metering of optimal dose. The technology to integrate potential direct-to-brain PBM delivery together with real time biofeedback should be the subject of future investigation together with further research into its mechanistic underpinnings.

Acknowledgments

We thank James Carroll, THOR Photomedicine for supplying the BioTHOR device used in this study.

Author Contributions

Conceptualization: David J. Davies, Andrew R. Stevens, Pola Goldberg Oppenheimer, Michael Milward, Antonio Belli, William M. Palin.

Data curation: David J. Davies, Mohammed Hadis, Valentina Di Pietro, Giuseppe Lazzarino, Mario Forcione, Georgia Harris, Andrew R. Stevens.

Formal analysis: David J. Davies, Valentina Di Pietro, Giuseppe Lazzarino, Mario Forcione.

Funding acquisition: David J. Davies.

Investigation: David J. Davies, Mohammed Hadis, Valentina Di Pietro, Giuseppe Lazzarino, Mario Forcione, Georgia Harris.

Methodology: David J. Davies.

Project administration: David J. Davies, Mohammed Hadis.

Resources: Mohammed Hadis, Michael Milward, William M. Palin.

Software: Mohammed Hadis, William M. Palin.

Supervision: Pola Goldberg Oppenheimer, Michael Milward, Antonio Belli, William M. Palin.

Validation: Mohammed Hadis.

Writing – original draft: David J. Davies, Andrew R. Stevens, Wai Cheong Soon.

Writing – review & editing: David J. Davies, Mohammed Hadis, Andrew R. Stevens, Wai Cheong Soon, Michael Milward, William M. Palin.

References

1. Langlois JA, Rutland-Brown W, Wald MM. The epidemiology and impact of traumatic brain injury: a brief overview. J Head Trauma Rehabil. 2006; 21(5):375–8. https://doi.org/10.1097/00001199-200609000-00001 PMID: 16983222
2. Raghupathi R. Cell death mechanisms following traumatic brain injury. Brain Pathol. 2004; 14(2):215–22. https://doi.org/10.1111/j.1750-3639.2004.tb00056.x PMID: 15193035
3. Minambres E, Ballesteros MA, Mayorga M, Marin MJ, Munoz P, Figols J, et al. Cerebral apoptosis in severe traumatic brain injury patients: an in vitro, in vivo, and postmortem study. J Neurotrauma. 2008; 25(6):581–591. https://doi.org/10.1089/neu.2007.0398 PMID: 18363508
4. Beattie MS, Farooqui AA, Bresnahan JC. Review of current evidence for apoptosis after spinal cord injury. J Neurotrauma. 2000; 17(10):915–25. https://doi.org/10.1089/neu.2000.17.915 PMID: 11063057
5. Katoh K, Ikata T, Katoh S, Hamada Y, Nakauchi K, Sano T, et al. Induction and its spread of apoptosis in rat spinal cord after mechanical trauma. Neurosci Lett. 1996; 216(1):9–12. https://doi.org/10.1016/0304-3940(96)12999-2 PMID: 8892379
6. Bullock MR, Chesnut R, Ghajar J, Gordon D, Hartl R, Newell DW, et al. Surgical management of traumatic brain injury. Neurosurgery. 2006; 58(3):16–24.
7. Okonkwo DO, Shutter LA, Moore C, Temkin NR, Puccio AM, Madden CJ, et al. Brain tissue oxygen monitoring and management in severe traumatic brain injury (BOOST-II): a phase II randomized trial. Crit Care Med. 2017; 45(11):1907.
8. Karu TI, Kolyakov SF. Exact action spectra for cellular responses relevant to phototherapy. Photomed Laser Ther. 2005; 23(4):355–61. https://doi.org/10.1089/pho.2005.23.355 PMID: 16144476
9. Hamblin MR. Mechanisms and Mitochondrial Redox Signaling in Photobiomodulation HHS Public Access. Photochem Photobiol. 2018; 94(2):199–212. https://doi.org/10.1111/php.12864 PMID: 29164625
10. Salehpour F, Mahmoudi J, Kamari F, Sadigh-Eteghad S, Rasta SH, Hamblin MR. Brain Photobiomodulation Therapy: a Narrative Review. Mol Neurobiol [Internet]. 2018 Aug 1 [cited 2022 Feb 3]; 55 (8):6601–36. Available from: https://pubmed.ncbi.nlm.nih.gov/29327206/ https://doi.org/10.1007/s12035-017-0852-4 PMID: 29327206
11. Eells JT, Wong-Riley MT, VerHoeve J, Henry M, Buchman E V., Kane MP, et al. Mitochondrial signal transduction in accelerated wound and retinal healing by near-infrared light therapy. Mitochondrion. 2004; 4(5–6):559–67. https://doi.org/10.1016/j.mito.2004.07.033 PMID: 16120414
12. El Gammal ZH, Zaher AM, N. E-B. Effect of low-level laser-treated mesenchymal stem cells on myocardial infarction. Lasers Med Sci. 2017; 32(7):1637–46. https://doi.org/10.1007/s10103-017-2271-1 PMID: 28681086
13. de Medeiros ML, Araújo-Filho I, da Silva EMN, de Sousa Queiroz WS, Soares CD, de Carvalho MGF. Effect of low-level laser therapy on angiogenesis and matrix metalloproteinase-2 immunoexpression in wound repair. Lasers Med Sci. 2017; 32(1):35–43. https://doi.org/10.1007/s10103-016-2080-y PMID: 27649960
14. Sun G, Tunér J. Low-level laser therapy in dentistry. Dent Clin North Am. 2004; 48(4):1061–76. https://doi.org/10.1016/j.cden.2004.05.004 PMID: 15464564
15. Asnaashari M, Safavi N. Application of Low level Lasers in Dentistry (Endodontic). Lasers Med Sci. 2013; 4(2):57–66.
16. Oron A, Oron U, Chen J, Eilam A, Zhang C, Sadeh M, et al. Low-Level Laser Therapy Applied Transcranially to Rats After Induction of Stroke Significantly Reduces Long-Term Neurological Deficits. Stroke. 2006; 37(10):2620–4. https://doi.org/10.1161/01.STR.0000242775.14642.b8 PMID: 16946145
17. Chu Y-H, Chen S-Y, Hsieh Y-L, Teng Y-H, Cheng Y-J. Low-level laser therapy prevents endothelial cells from TNF-α/cycloheximide-induced apoptosis. Lasers Med Sci. 2018; 33(2):279–86. https://doi.org/10.1007/s10103-017-2364-x PMID: 29098460

18. Pansani TN, Basso FG, Turirioni AP., Kurachi C, Hebling J, de Souza Costa C. Effects of low-level laser therapy on the proliferation and apoptosis of gingival fibroblasts treated with zoledronic acid. Int J Oral Maxillofac Surg. 2014; 43(8):1030–4. https://doi.org/10.1016/j.ijom.2014.02.011 PMID: 24656494

19. Sussai DA, Carvalho PDTC De, Dourado DM, Belchior ACG, Dos Reis FA, Pereira DM. Low-level laser therapy attenuates creatine kinase levels and apoptosis during forced swimming in rats. Lasers Med Sci [Internet]. 2010 Jan [cited 2021 Mar 1]; 25(1):115–20. Available from: https://pubmed.ncbi.nlm.nih.gov/19554361/ https://doi.org/10.1007/s10103-009-0697-9 PMID: 19554361

20. Fukuoka CY, Simões A, Uchiyama T, Arana-Chavez VE, Abiko Y, Kuboyama N, et al. The Effects of Low-Power Laser Irradiation on Inflammation and Apoptosis in Submandibular Glands of Diabetes-Induced Rats. Bianchi C, editor. PLoS One [Internet]. 2017 Jan 18 [cited 2021 Mar 1]; 12(1):e0169443. Available from: https://dx.plos.org/10.1371/journal.pone.0169443 PMID: 28099448

21. Karu TI. Multiple roles of cytochrome c oxidase in mammalian cells under action of red and IR-A radiation [Internet]. Vol. 62, IUBMB Life. IUBMB Life; 2010 [cited 2021 Mar 1]. p. 607–10. Available from: https://pubmed.ncbi.nlm.nih.gov/20681024/ https://doi.org/10.1002/iub.359 PMID: 20681024

22. Chung H, Dai T, Sharma SK, Huang YY, Carroll JD, Hamblin MR. The nuts and bolts of low-level laser (Light) therapy. Ann Biomed Eng [Internet]. 2012 Feb [cited 2021 Mar 1]; 40(2):516–33. Available from: /pmc/articles/PMC3288797/ https://doi.org/10.1007/s10439-011-0454-7 PMID: 22045511

23. Gonzalez-Lima F, Rojas. Low-level light therapy of the eye and brain. Eye Brain [Internet]. 2011 Oct [cited 2021 Mar 1]; 3:49. Available from: /pmc/articles/PMC5436183/ https://doi.org/10.2147/EB.S21391 PMID: 28539775

24. Huang YY, Chen ACH, Carroll JD, Hamblin MR. Biphasic dose response in low level lightherapy. Dose-Response [Internet]. 2009 [cited 2021 Mar 1]; 7(4):358–83. Available from: /pmc/articles/PMC2790317/ https://doi.org/10.2203/dose-response.09-027.Hamblin PMID: 20011653

25. Lima PLV, Pereira CV, Nissanka N, Arguello T, Gavini G, Maranduba C, et al. Photobiomodulation enhancement of cell proliferation at 660 nm does not require cytochrome c oxidase. J Photochem Photobiol B [Internet]. 2019 May 1 [cited 2021 Aug 5]; 194:71–5. Available from: https://pubmed.ncbi.nlm.nih.gov/30927704/ https://doi.org/10.1016/j.jphotobiol.2019.03.015 PMID: 30927704

26. Xuan W, Vatansever F, Huang L, Wu Q, Xuan Y, Dai T, et al. Transcranial Low-Level Laser Therapy Improves Neurological Performance in Traumatic Brain Injury in Mice: Effect of Treatment Repetition Regimen. Borlongan C V., editor. PLoS One [Internet]. 2013 Jan 7 [cited 2021 Mar 1]; 8(1):e53454. Available from: https://dx.plos.org/10.1371/journal.pone.0053454 PMID: 23308226

27. Quirk BJ, Torbey M, Buchmann E, Verma S, Whelan HT. Near-infrared photobiomodulation in an animal model of traumatic brain injury: Improvements at the behavioral and biochemical levels. Photomed Laser Surg. 2012 Sep 1; 30(9):523–9. https://doi.org/10.1089/pho.2012.3261 PMID: 22793787

28. Liang J, Liu L, Xing D. Photobiomodulation by low-power laser irradiation attenuates Aβ-induced cell apoptosis through the Akt/GSK3β/β-catenin pathway. Free Radic Biol Med [Internet]. 2012 Oct 1 [cited 2021 Mar 1]; 53(7):1459–67. Available from: https://pubmed.ncbi.nlm.nih.gov/22917976/ https://doi.org/10.1016/j.freeradbiomed.2012.08.003 PMID: 22917976

29. Lanzafame RJ, Stadler I, Kurtz AF, Connelly R, A. T, Brondon P, et al. Reciprocity of exposure time and irradiance on energy density during photoradiation on wound healing in a murine pressure ulcer model. Lasers Surg Med [Internet]. 2007 Jul 1 [cited 2021 Mar 1]; 39(6):534–42. Available from: http://doi.wiley.com/10.1002/lsm.20519 PMID: 17659591

30. Jagdeo JR, Adams LE, Brody NI, Siegel DM. Transcranial Red and Near Infrared Light Transmission in a Cadaveric Model. PLoS One [Internet]. 2012 Oct 15 [cited 2021 Mar 1]; 7(10). Available from: https://pubmed.ncbi.nlm.nih.gov/23077622/

31. Köhler M, MacHill S, Salzer R, Krafft C. Characterization of lipid extracts from brain tissue and tumors using Raman spectroscopy and mass spectrometry. Anal Bioanal Chem [Internet]. 2009 Mar 20 [cited 2021 Mar 1]; 393(5):1513–20. Available from: https://link.springer.com/article/10.1007/s00216-008-2592-9 PMID: 19153721

32. Banbury C, Mason R, Styles I, Eisenstein N, Clancy M, Belli A, et al. Development of the Self Optimising Kohonen Index Network (SKiNET) for Raman Spectroscopy Based Detection of Anatomical Eye Tissue. Sci Rep [Internet]. 2019 Dec 1 [cited 2021 Mar 1]; 9(1):1–9. Available from: www.nature.com/scientificreports https://doi.org/10.1038/s41598-018-37186-2 PMID: 30626917

33. Hanlon EB, Manoharan R, Koo TW, Shafer KE, Motz JT, Fitzmaurice M, et al. Prospects for in vivo Raman spectroscopy [Internet]. Vol. 45, Physics in Medicine and Biology. Phys Med Biol; 2000 [cited 2021 Mar 9]. Available from: https://pubmed.ncbi.nlm.nih.gov/10701500/

34. Shipp DW, Sinjab F, Notingher I. Spectroscopy, Raman; (180.5655) Raman microscopy; (300.6230) Spectroscopy, coherent anti-Stokes Raman scattering; (170.3880) Medical and biological imaging. 2017 [cited 2022 Feb 3]; Available from: http://dx.doi.org/10.1364/aop.XX.XXXXXX

35. Morrison B III, Cater HL, Benham CD, Sundstrom LE. An in vitro model of traumatic brain injury utilising two-dimensional stretch of organotypic hippocampal slice cultures. J Neurosci Methods. 2006; 150 (2):192–201. https://doi.org/10.1016/j.jneumeth.2005.06.014 PMID: 16098599

36. Banbury C, Styles I, Eisenstein N, Zanier ER, Vegliante G, Belli A, et al. Spectroscopic detection of traumatic brain injury severity and biochemistry from the retina. Biomed Opt Express. 2020; 11(11):6249–61. https://doi.org/10.1364/BOE.399473 PMID: 33282487

37. Ferland RJ, Gross RA, Applegate CD. Increased mitotic activity in the dentate gyrus of the hippocampus of adult C57BL/6J mice exposed to the flurothyl kindling model of epileptogenesis. Neuroscience. 2002 Dec 9; 115(3):669–83. https://doi.org/10.1016/s0306-4522(02)00514-6 PMID: 12435406

38. Lim WB, Kim JH, Gook EB, Kim JS, Ko YJ, Kim IA, et al. Inhibition of mitochondria-dependent apoptosis by 635-nm irradiation in sodium nitroprusside-treated SH-SY5Y cells. Free Radic Biol Med [Internet]. 2009 Sep 15 [cited 2022 Feb 3]; 47(6):850–7. Available from: https://pubmed.ncbi.nlm.nih.gov/19545621/ https://doi.org/10.1016/j.freeradbiomed.2009.06.023 PMID: 19545621

39. Giuliani A, Lorenzini L, Gallamini M, Massella A, Giardino L, Calzà L. Low infra red laser light irradiation on cultured neural cells: Effects on mitochondria and cell viability after oxidative stress. BMC Complement Altern Med [Internet]. 2009 Apr 15 [cited 2022 Feb 3]; 9(1):1–10. Available from: https://bmccomplementmedtherapies.biomedcentral.com/articles/10.1186/1472-6882-9-8 PMID: 19368718

40. Yoon SR, Hong N, Lee MY, Ahn JC. Photobiomodulation with a 660-Nanometer Light-Emitting Diode Promotes Cell Proliferation in Astrocyte Culture. Cells 2021, Vol 10, Page 1664 [Internet]. 2021 Jul 2 [cited 2022 Feb 3]; 10(7):1664. Available from: https://www.mdpi.com/2073-4409/10/7/1664/htm https://doi.org/10.3390/cells10071664 PMID: 34359834

41. Sommer AP, Bieschke J, Friedrich RP, Zhu D, Wanker EE, Fecht HJ, et al. 670 nm laser light and EGCG complementarily reduce amyloid-β aggregates in human neuroblastoma cells: Basis for treatment of alzheimer's disease? Photomed Laser Surg. 2012 Jan 1; 30(1):54–60. https://doi.org/10.1089/pho.2011.3073 PMID: 22029866

42. Humpel C. Neuroscience forefront review organotypic brain slice cultures: A review. Vol. 305, Neuroscience. Elsevier Ltd; 2015. p. 86–98. https://doi.org/10.1016/j.neuroscience.2015.07.086 PMID: 26254240

43. Staniszewska-Slezak E, Malek K, Baranska M. Complementary analysis of tissue homogenates composition obtained by Vis and NIR laser excitations and Raman spectroscopy. Spectrochim Acta—Part A Mol Biomol Spectrosc [Internet]. 2015 Aug 5 [cited 2021 Mar 9]; 147:245–56. Available from: https://pubmed.ncbi.nlm.nih.gov/25847786/ https://doi.org/10.1016/j.saa.2015.03.086 PMID: 25847786

44. Sacharz J, Wesełucha-Birczyńska A, Zięba-Palus J, Lewandowski MH, Kowalski R, Palus K, et al. Epileptic rat brain tissue analyzed by 2D correlation Raman spectroscopy. Spectrochim Acta—Part A Mol Biomol Spectrosc [Internet]. 2018 Jan 5 [cited 2021 Mar 9]; 188:581–8. Available from: https://pubmed.ncbi.nlm.nih.gov/28772144/ https://doi.org/10.1016/j.saa.2017.07.046 PMID: 28772144

45. Galli R, Meinhardt M, Koch E, Schackert G, Steiner G, Kirsch M, et al. Rapid Label-Free Analysis of Brain Tumor Biopsies by Near Infrared Raman and Fluorescence Spectroscopy—A Study of 209 Patients. Front Oncol [Internet]. 2019 Nov 5 [cited 2021 Mar 9]; 9. Available from: https://pubmed.ncbi.nlm.nih.gov/31750251/ https://doi.org/10.3389/fonc.2019.01165 PMID: 31750251

46. Muthuselvi C, Pandiaraja SS, Ravikumar B, Athimoolam S, Srinivasan N, Krishnakum RV. FT-IR and FT-Raman Spectroscopic Analyzes of Indeno Quinoxaline Derivative Crystal. Asian J Appl Sci. 2018 Mar 15; 11(2):83–91.

47. Kumar V, Panikar Y, Palafox MA, Vats J, Kostova I, Lang K, et al. Ab-initio calculations, FT-IR and FT-Raman spectra of 2-chloro-6-methyl benzonitrile. Indian J Pure Appl Phys. 2010; 48.

48. Lalonde JW, O'Connor SP, Noojin GD, Gonzales CC, Yakovlev V V., Denton ML. Measuring cytochrome c redox state using resonance Raman spectroscopy to determine metabolic rates in electron transport chain when exposed to light. In: Hamblin MR, Carroll JD, Arany P, editors. Mechanisms of Photobiomodulation Therapy XIV [Internet]. SPIE; 2019 [cited 2021 Mar 1]. p. 18. Available from: https://www.spiedigitallibrary.org/conference-proceedings-of-spie/10861/2508684/Measuring-cytochrome-c-redox-state-using-resonance-Raman-spectroscopy-to/10.1117/12.2508684.full

49. Hadis MA, Cooper PR, Milward MR, Gorecki PC, Tarte E, Churm J, et al. Development and application of LED arrays for use in phototherapy research. J Biophotonics [Internet]. 2017 Nov 1 [cited 2021 Mar 21]; 10(11):1514–25. Available from: https://pubmed.ncbi.nlm.nih.gov/28164460/ https://doi.org/10.1002/jbio.201600273 PMID: 28164460

50. Hadis MA, Zainal SA, Holder MJ, Carroll JD, Cooper PR, Milward MR, et al. The dark art of light measurement: accurate radiometry for low-level light therapy [Internet]. Vol. 31, Lasers in Medical Science. Springer London; 2016 [cited 2021 Mar 21]. p. 789–809. Available from: https://pubmed.ncbi.nlm.nih.gov/26964800/ https://doi.org/10.1007/s10103-016-1914-y PMID: 26964800

51. Tisdall MM, Smith M. Multimodal monitoring in traumatic brain injury: current status and future directions. Br J Anaesth [Internet]. 2007 Jul 1 [cited 2021 Mar 1]; 99(1):61–7. Available from: https://linkinghub.elsevier.com/retrieve/pii/S0007091217347906 https://doi.org/10.1093/bja/aem143 PMID: 17548431

52. Smith M. Monitoring intracranial pressure in traumatic brain injury. Anesth Analg [Internet]. 2008 Jan [cited 2021 Mar 1]; 106(1):240–8. Available from: http://journals.lww.com/00000539-200801000-00042 https://doi.org/10.1213/01.ane.0000297296.52006.8e PMID: 18165584

53. Reinhart F, Massri N El, Chabrol C, Cretallaz C, Johnstone DM, Torres N, et al. Intracranial application of near-infrared light in a hemi-parkinsonian rat model: The impact on behavior and cell survival. J Neurosurg. 2016 Jun 1; 124(6):1829–41. https://doi.org/10.3171/2015.5.JNS15735 PMID: 26613166

54. Moro C, El Massri N, Torres N, Ratel D, De Jaeger X, Chabrol C, et al. Photobiomodulation inside the brain: A novel method of applying near-infrared light intracranially and its impact on dopaminergic cell survival in MPTP-treated mice: Laboratory investigation. J Neurosurg. 2014; 120(3):670–83. https://doi.org/10.3171/2013.9.JNS13423 PMID: 24160475

55. Darlot F, Moro C, El Massri N, Chabrol C, Johnstone DM, Reinhart F, et al. Near-infrared light is neuroprotective in a monkey model of Parkinson disease. Ann Neurol. 2016 Jan 1; 79(1):59–75. https://doi.org/10.1002/ana.24542 PMID: 26456231

56. Mowbray M, Banbury C, Rickard JJS, Davies DJ, Goldberg Oppenheimer P. Development and Characterization of a Probe Device toward Intracranial Spectroscopy of Traumatic Brain Injury. ACS Biomater Sci Eng [Internet]. 2021 Feb 22 [cited 2021 Mar 1];acsbiomaterials.0c01156. Available from: https://pubs.acs.org/doi/10.1021/acsbiomaterials.0c01156. PMID: 33617217

Appendix C

ANTIBODIES

Table C.1: Antibody clones used with dilution, manufacturer and catalogue number

Antigen	Dilution	Supplier	Catalogue No.
GAP43	1:400	Fisher Scientific, Loughborough, UK	33-5000
Laminin	1:400	Sigma, Massachusetts, USA	L9393
NF200	1:400	Sigma, Massachusetts, USA	N4142
Iba1	1:200	Invitrogen, Massachusetts, USA	PA5-27436
Fibronectin	1:200	Sigma, Massachusetts, USA	F3648
GFAP	1:200	Sigma, Massachusetts, USA	G9269
CD11b/c (OX42)	1:100	Abcam, Cambridge, UK	ab1211
(FITC conjugated) CD45	1:200	Biolegend, California, USA	304006
CD68	1:100	Abcam, Cambridge, UK	ab283654
βIII-tubulin	1:400	Sigma, Massachusetts, USA	MAB1637
Cleaved caspase-3	1:200	Cell Signaling Technology, Massachusetts, USA	9661S
Goat anti-mouse IgG (Alexa Fluor 488)	1:400	Fisher Scientific, Loughborough, UK	A-11011
Goat anti-rabbit IgG (Alexa Fluor 594)	1:400	Fisher Scientific, Loughborough, UK	A-11012
Annexin-V (labelled with iFluor 594)	As per manufacturer	Abcam, Cambridge, UK	ab219918

Appendix D

SUPPLEMENTARY IMAGES OF IMMUNOFLUORESCENCE IN TRAUMATIC BRAIN INJURY

In this Appendix, supplementary images of brain slice immunofluorescence from Chapter 4 are presented for all brain areas imaged and reported as quantitative fluorescence.

For all images, experimental details are as described in Chapter 4. For 3 dpi endpoints, PBM was delivered at 810 nm (2 min per day (1 min per hemisphere), 3 day course, 20 mW/cm^2, 2.4J), or with sham PBM. Controls were intact uninjured animals. For 4 wpi, 660 and/or 810 nm used in PBM group (2 min per day (1 min per hemisphere), 3 day course, 20 mW/cm^2, 2.4J). n = 5 per group (n = 4 for control). Representative images taken from one repeat. cc = corpus callosum; Cg1 = cingulate cortex area 1; Cg2 = cingulate cortex area 2; Ch = choroid plexus (within lateral and third ventricles); FL = forelimb area of cortex; Fr1 = frontal cortex area 1; Fr2 = frontal cortex area 2; HL = hindlimb area of cortex; PV-CPu = periventricular region of caudate putamen; GFAP = glial fibrillary acidic protein; NF200 = neurofilament 200; DAPI = 4,6-diamidino-2-phenylindole; TBI = traumatic brain injury; PBM = photobiomodulation, FN = fibronectin; LN = laminin,

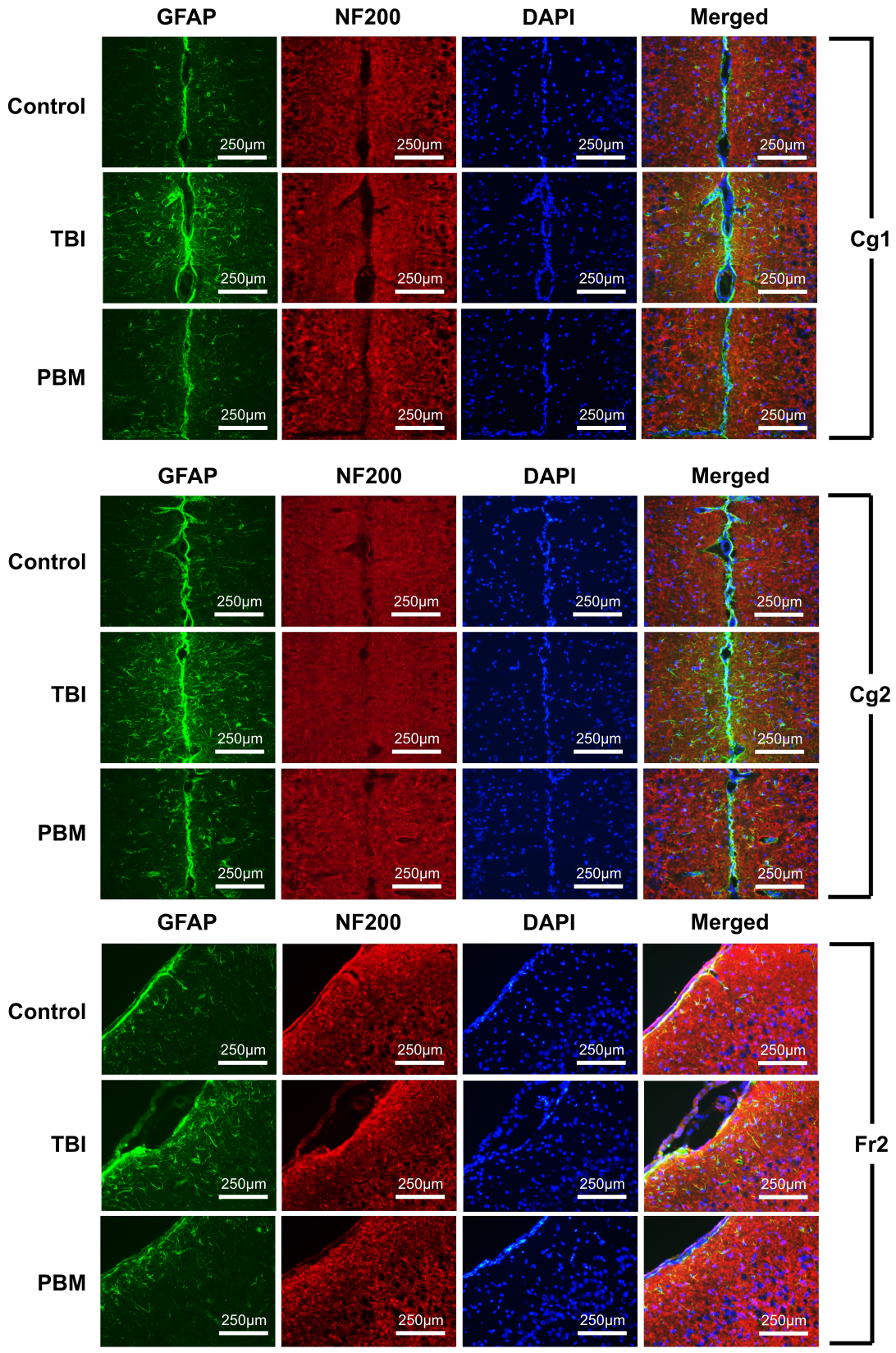


Figure D.1: GFAP 3 dpi Cg1. Cg2, Fr2

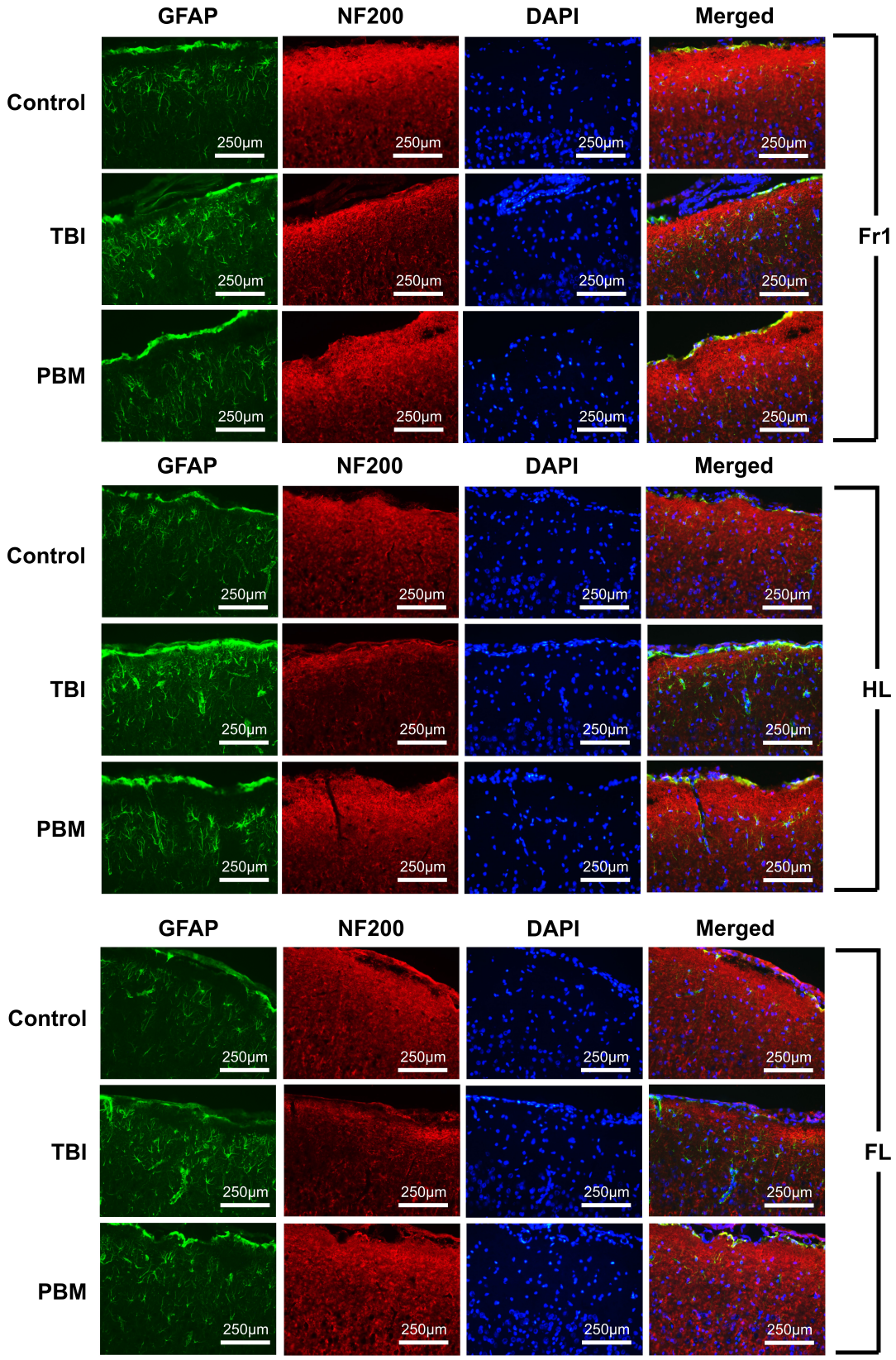


Figure D.2: GFAP 3 dpi Fr1, HL, FL

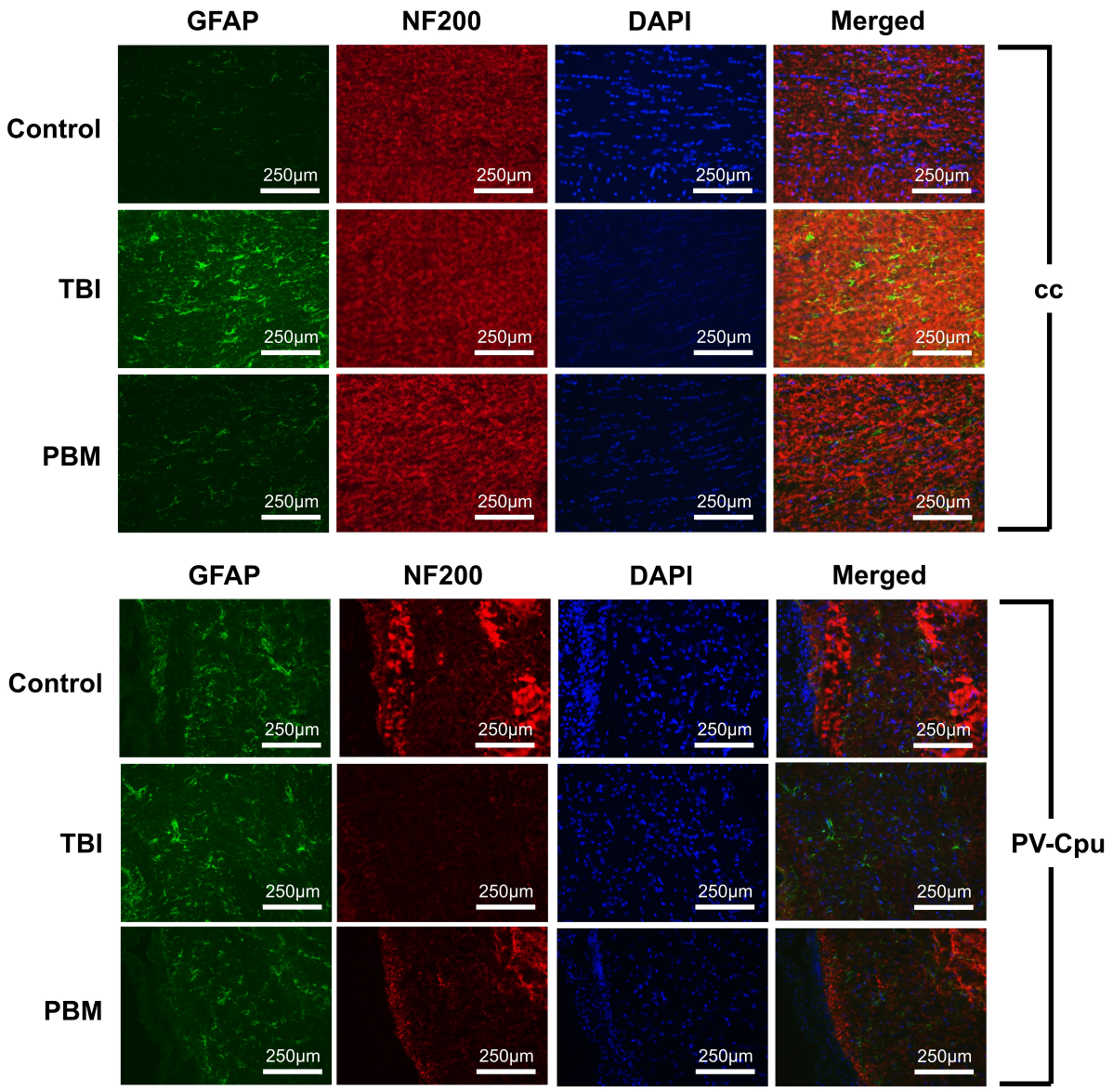


Figure D.3: GFAP 3 dpi cc, PV-CPu

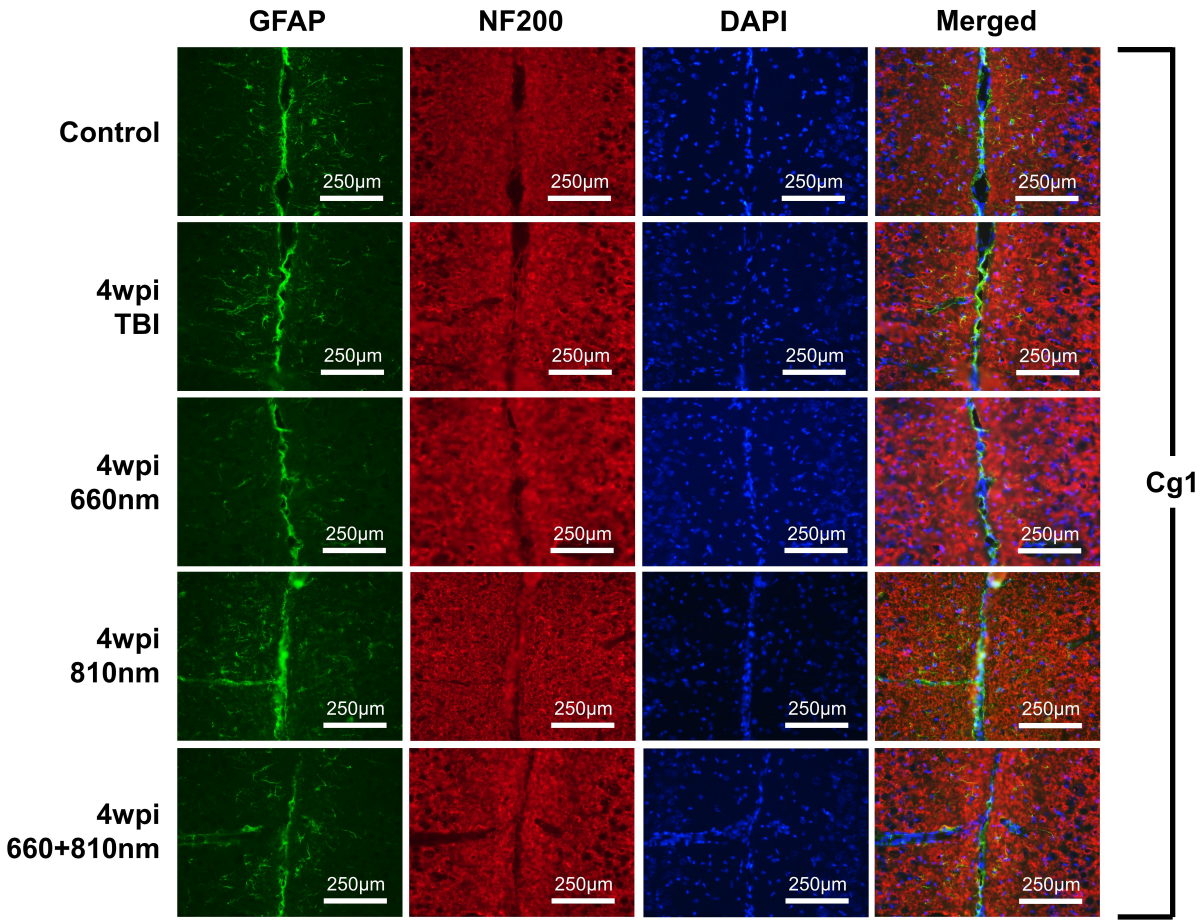


Figure D.4: GFAP 4 wpi Cg1

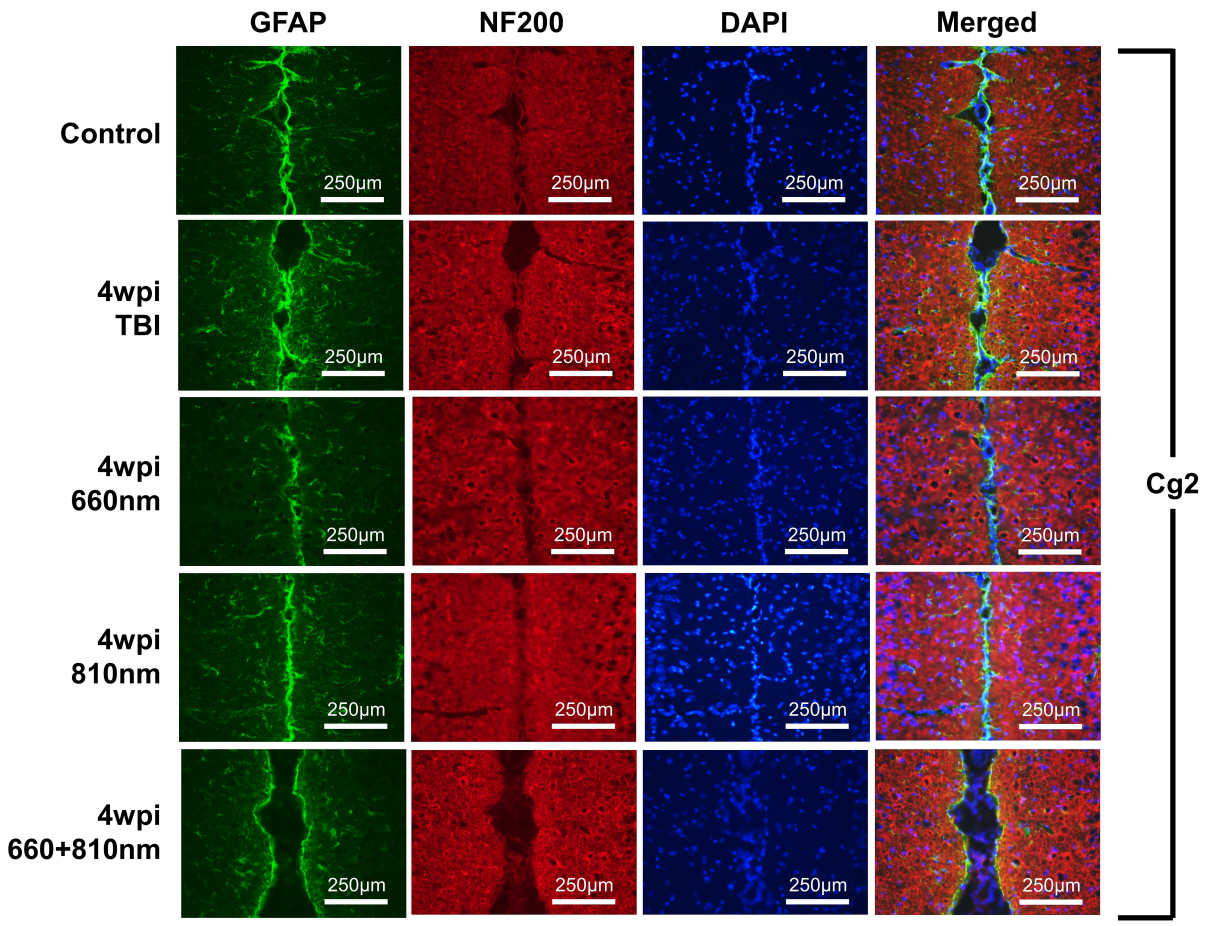


Figure D.5: GFAP 4 wpi Cg2

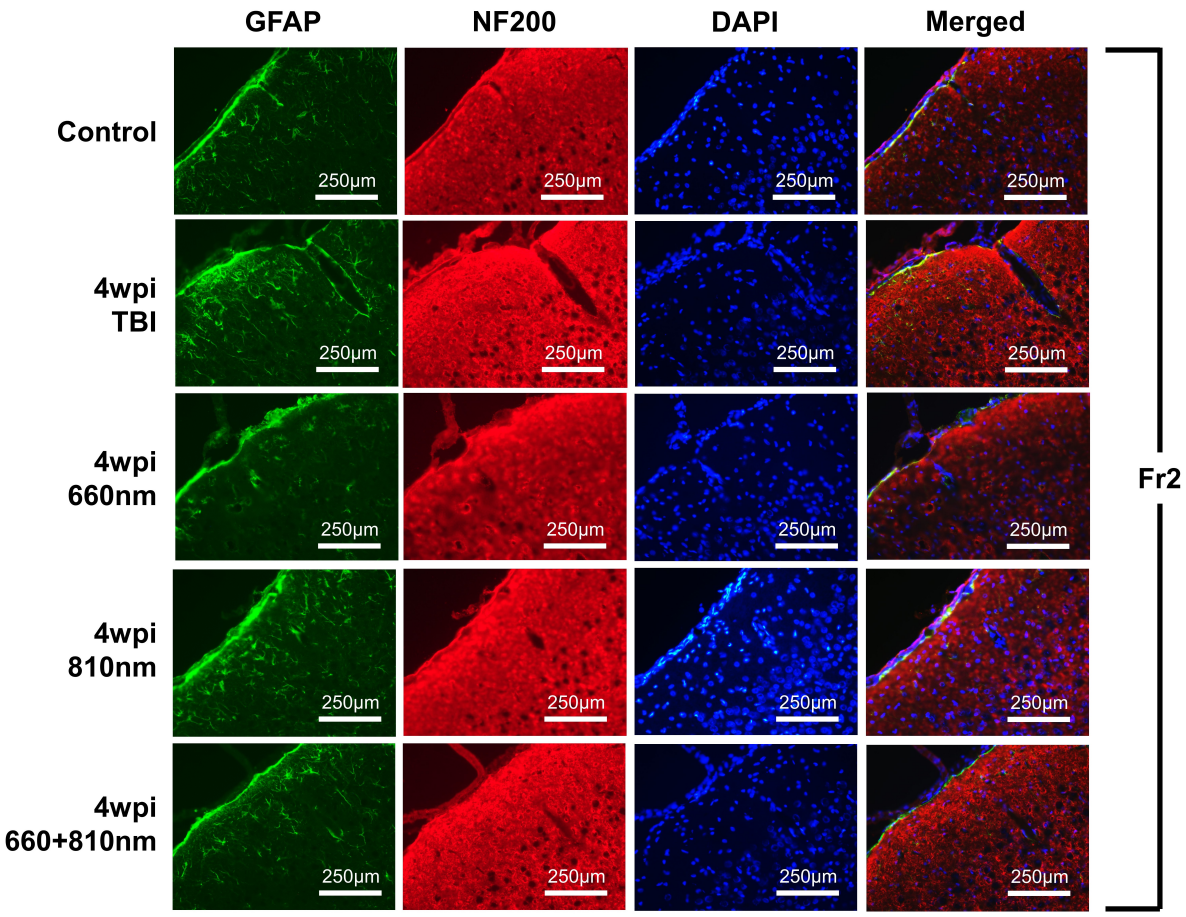


Figure D.6: GFAP 4 wpi Fr2

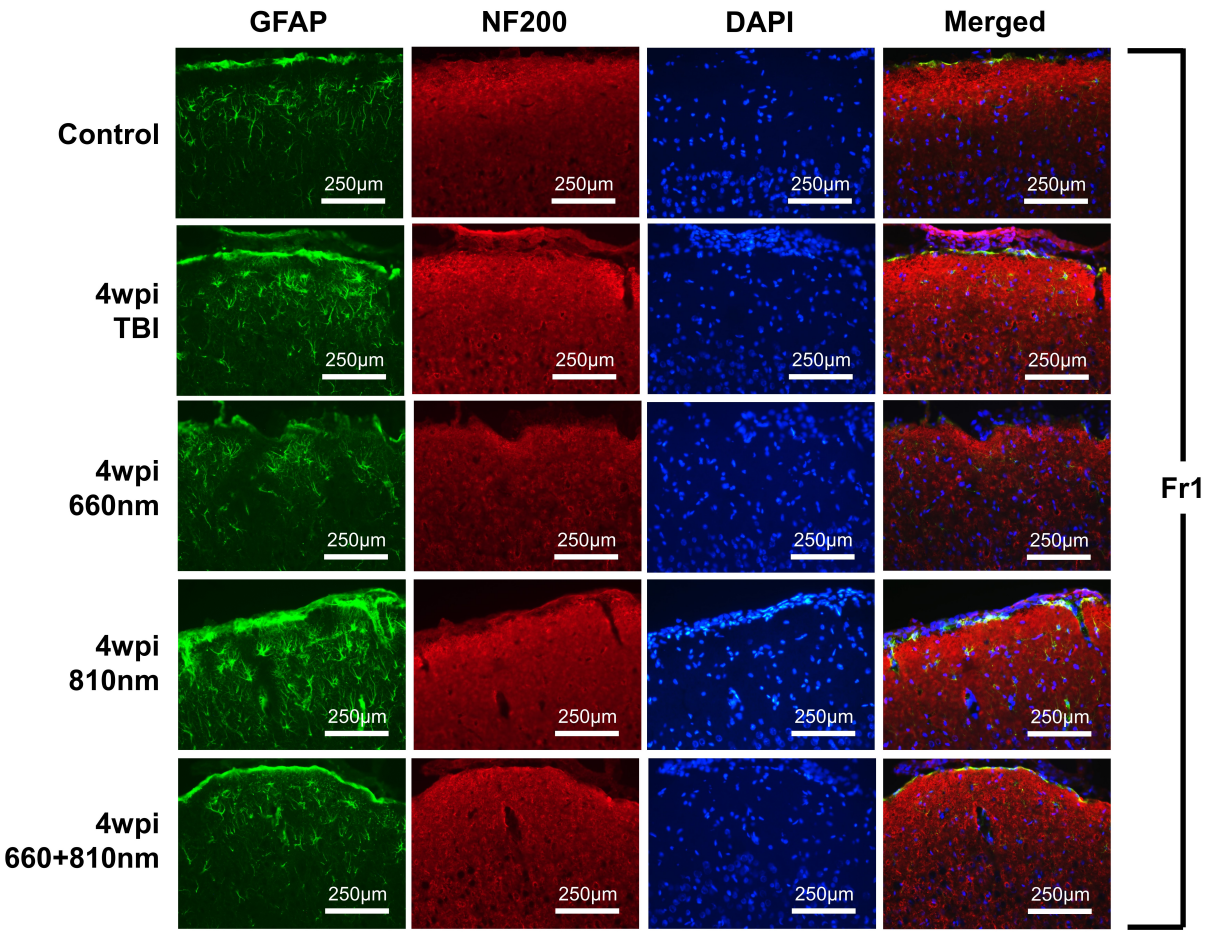


Figure D.7: GFAP 4 wpi Fr1

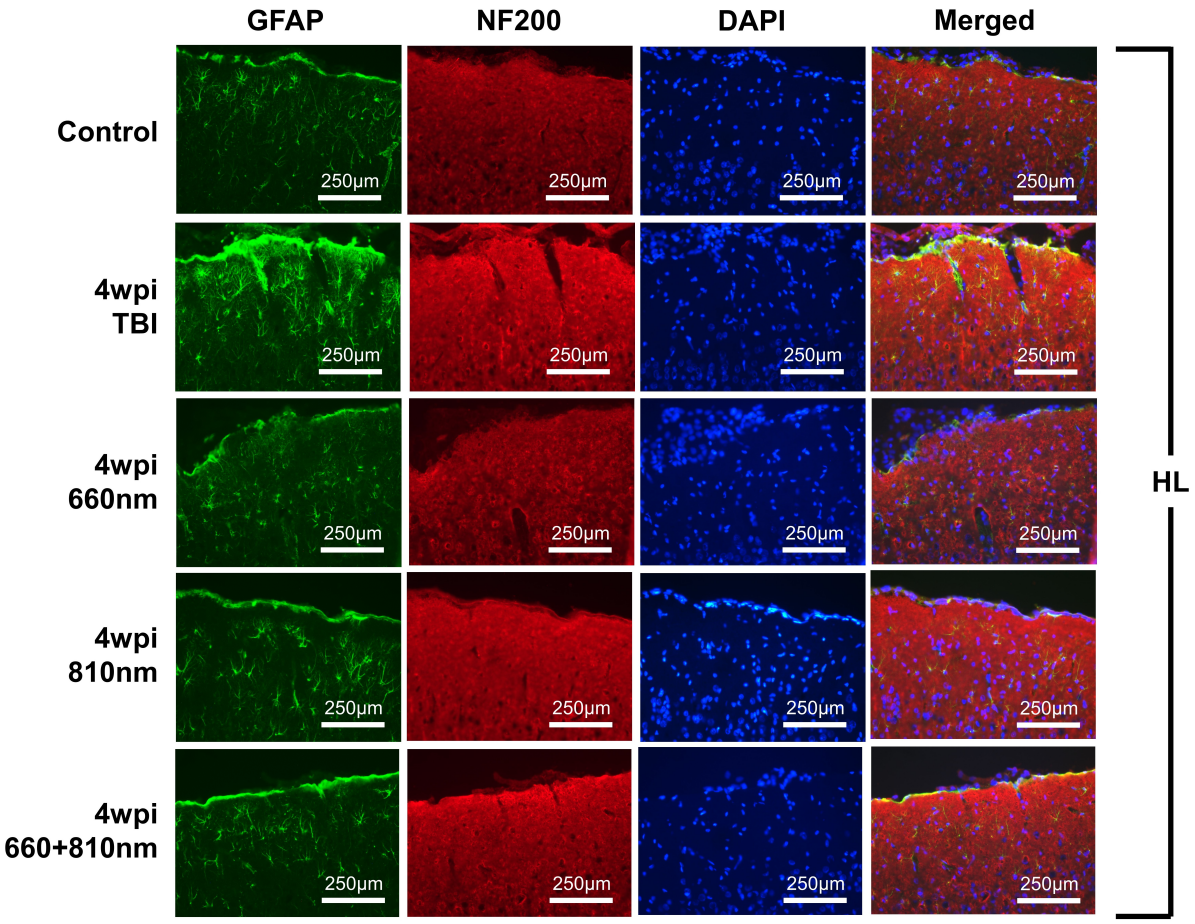


Figure D.8: GFAP 4 wpi HL

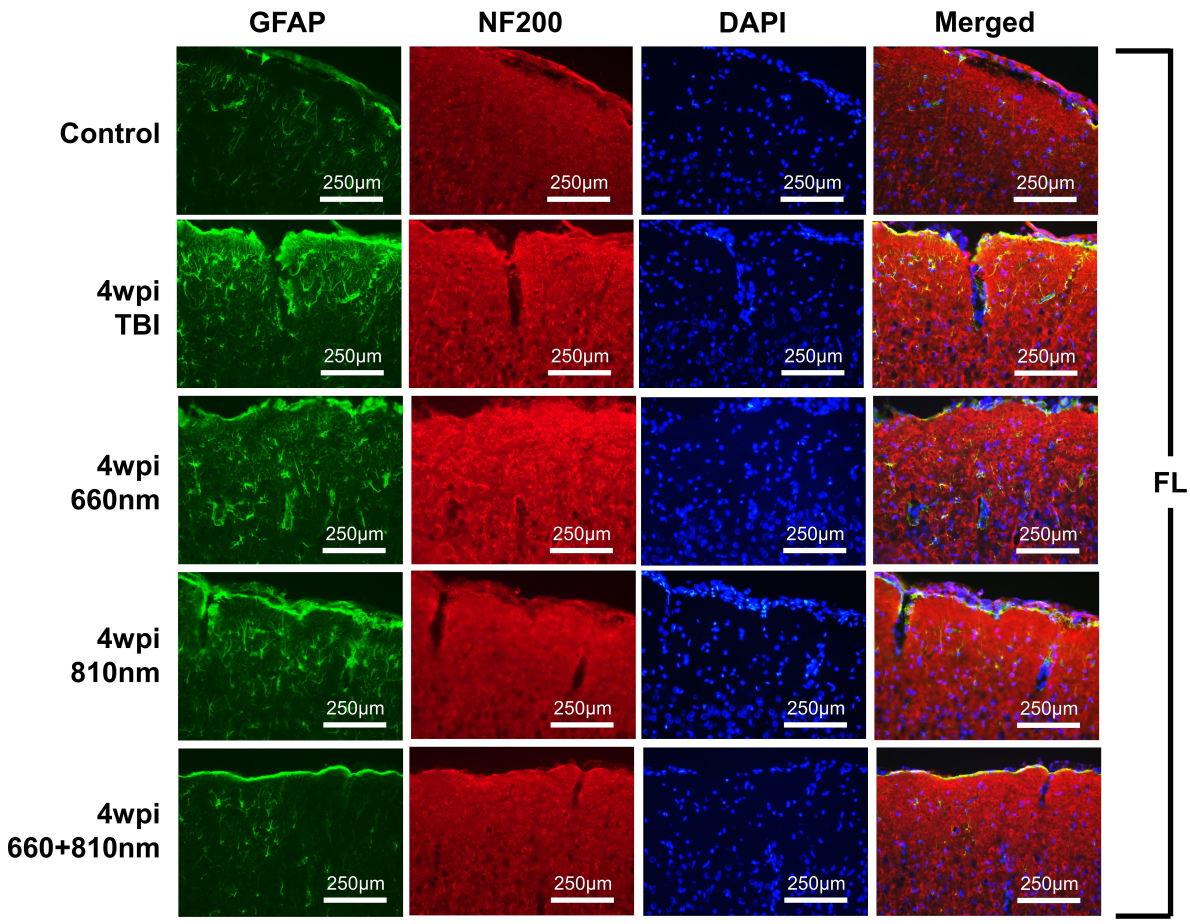


Figure D.9: GFAP 4 wpi FL

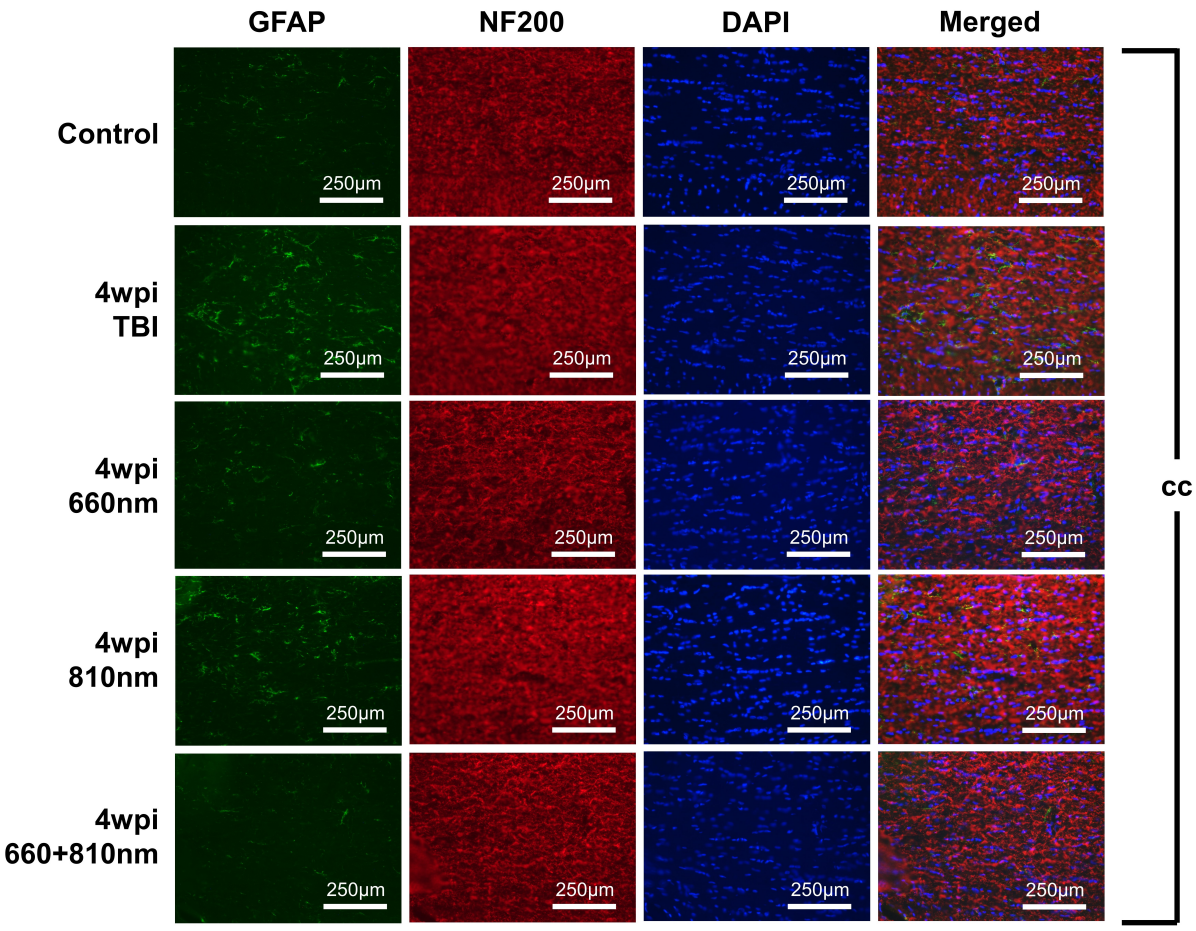


Figure D.10: GFAP 4 wpi cc

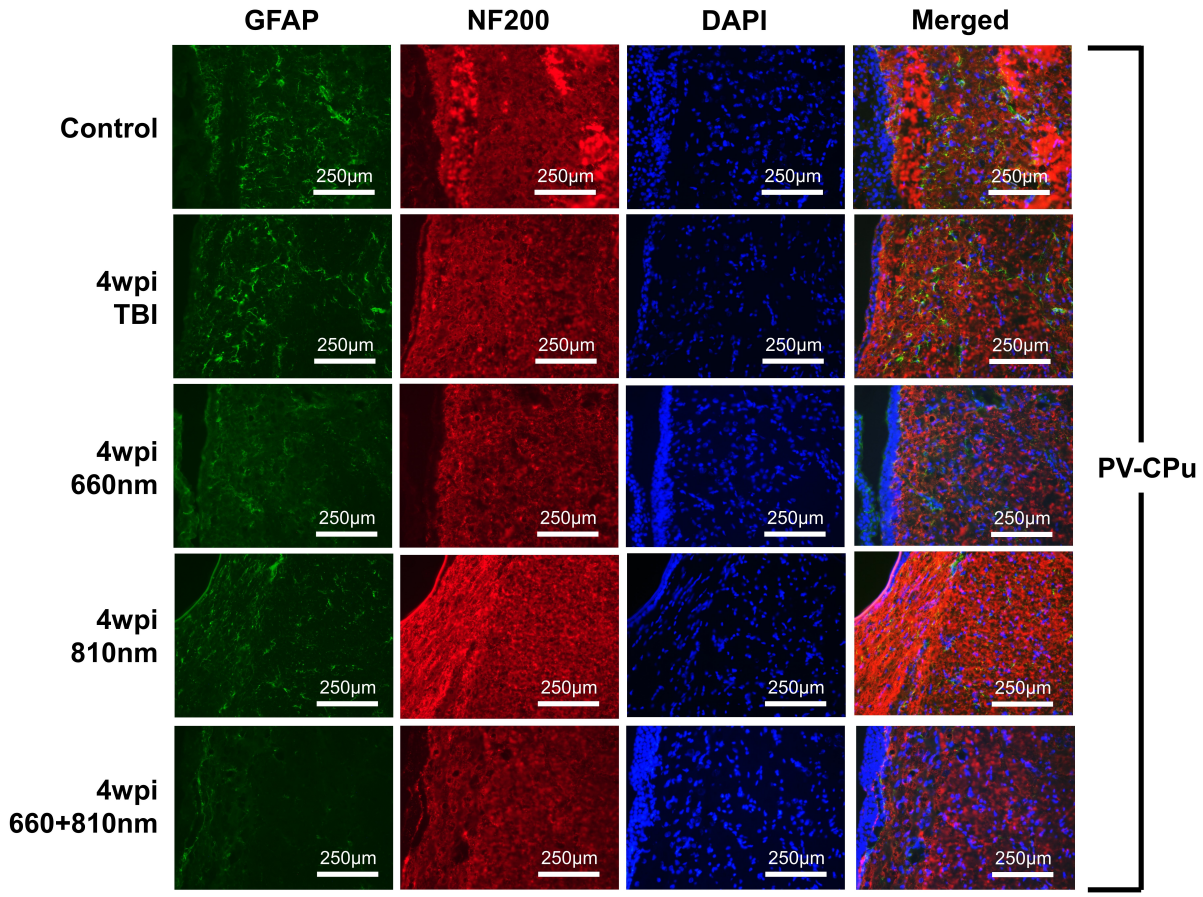


Figure D.11: GFAP 4 wpi PV-CPu

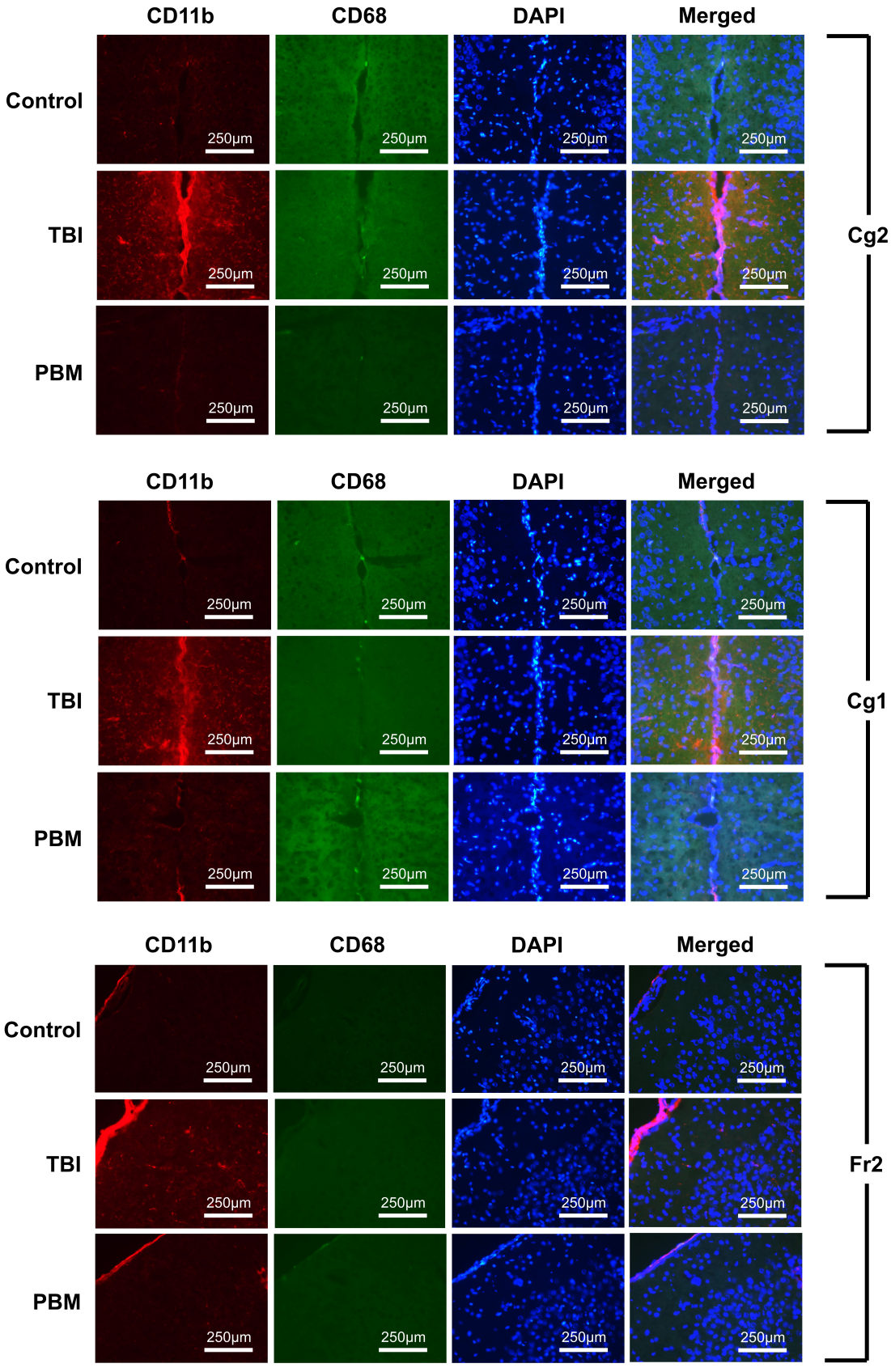


Figure D.12: CD11b/CD68 3 dpi Cg2, Cg1, Fr2

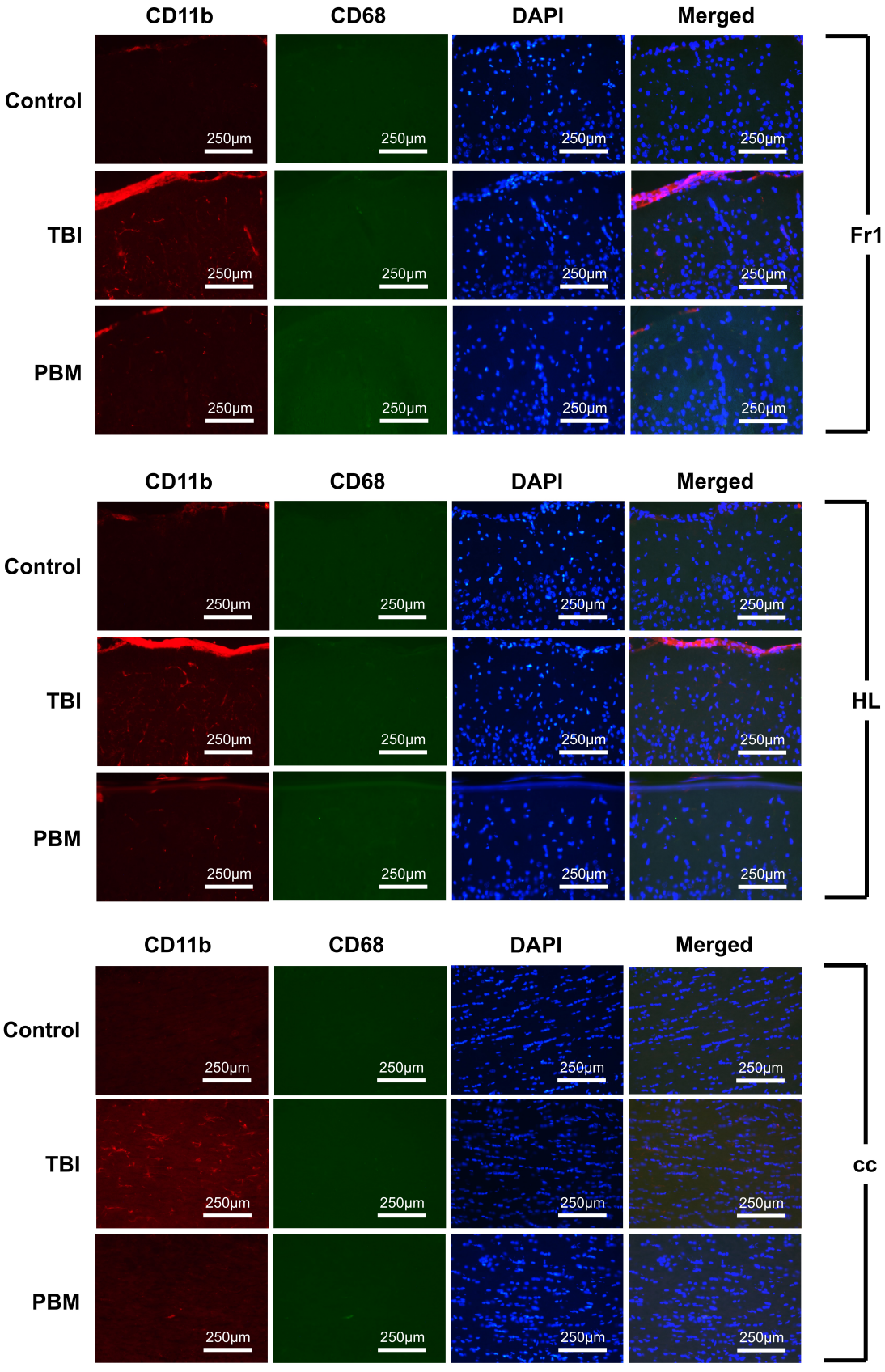


Figure D.13: CD11b/CD68 3 dpi Fr1, HL, cc

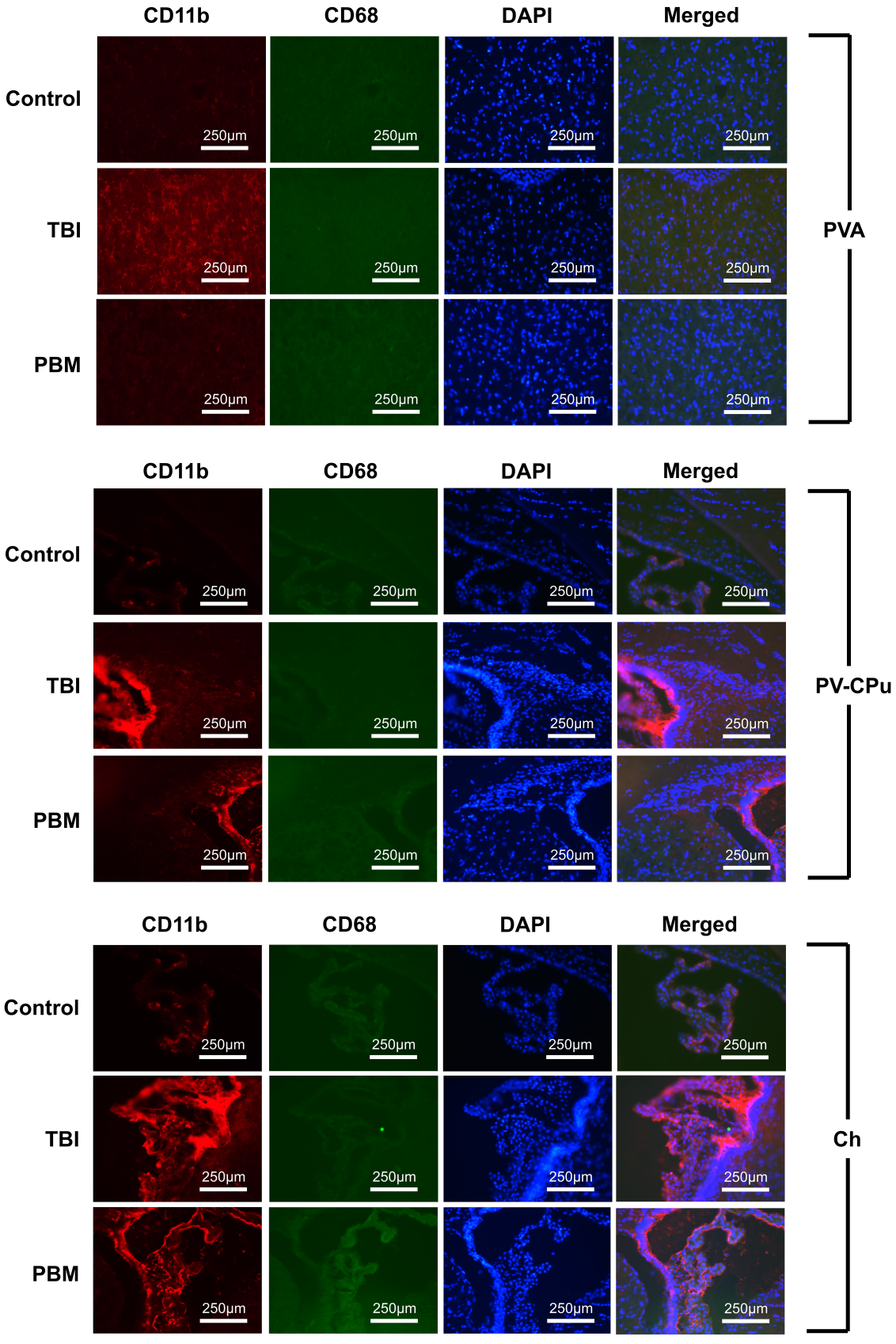


Figure D.14: CD11b/CD68 3 dpi PVA, PV-CPu, Ch

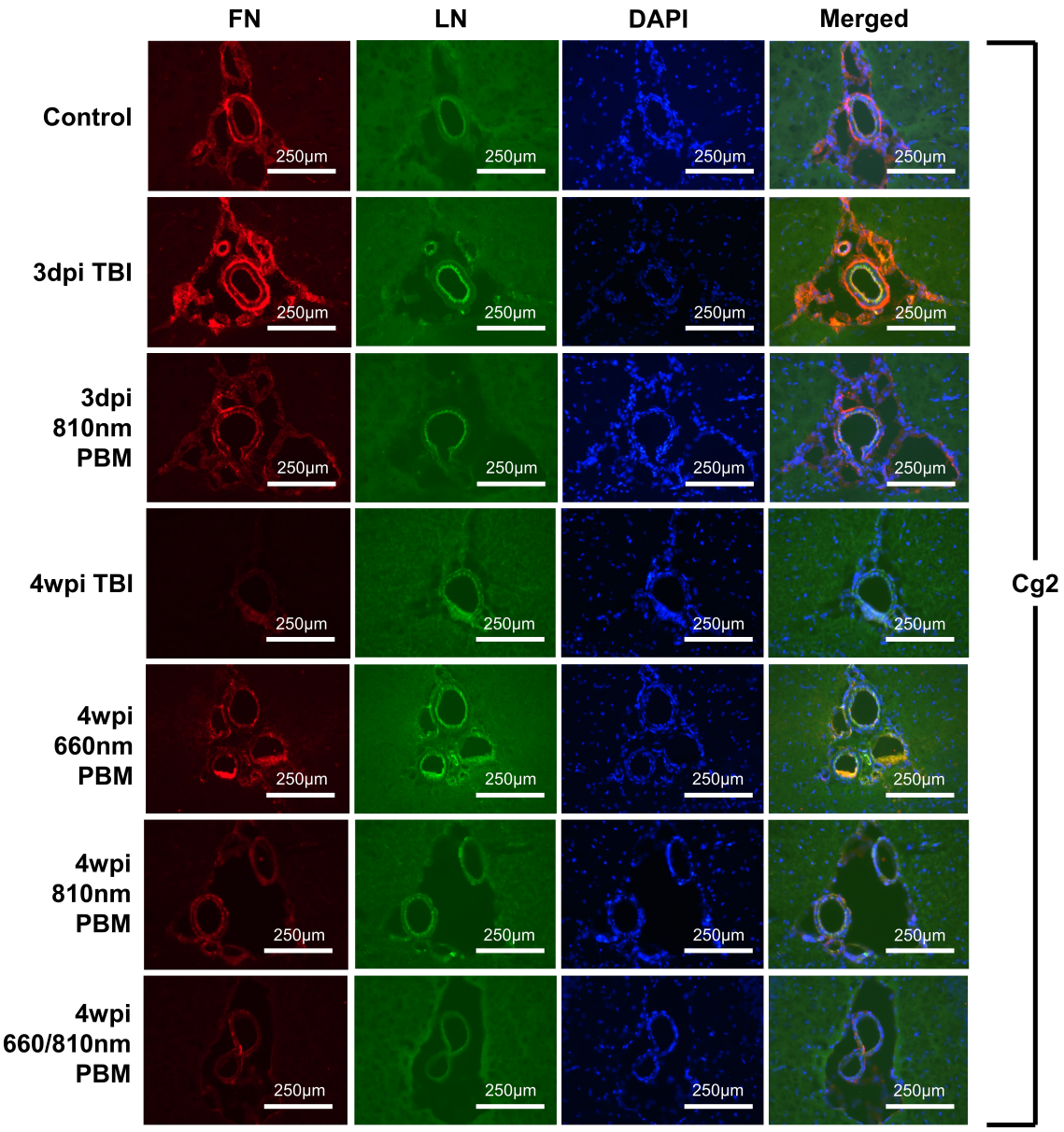


Figure D.15: Laminin/Fibronectin Cg2

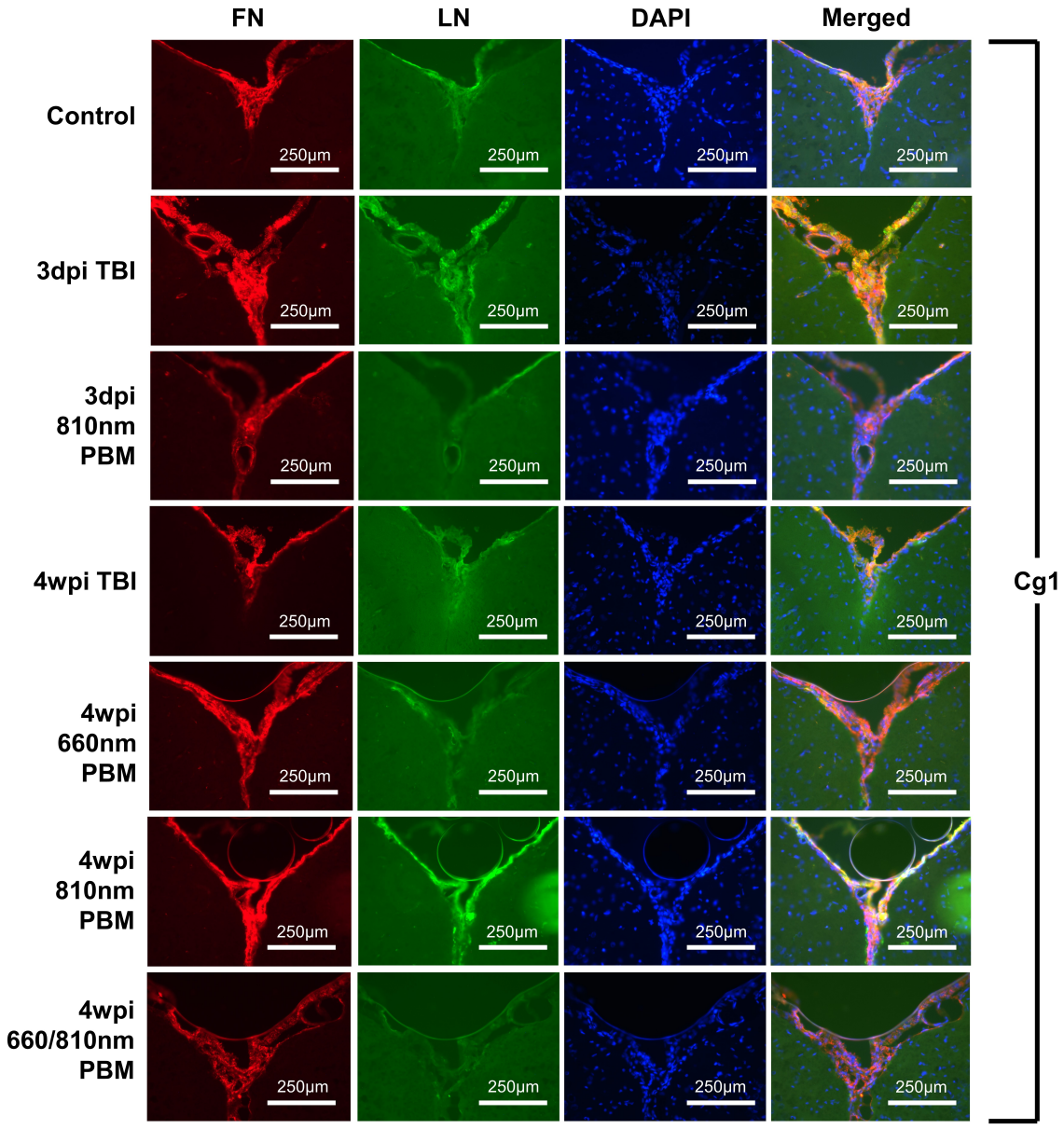


Figure D.16: Laminin/Fibronectin Cg1

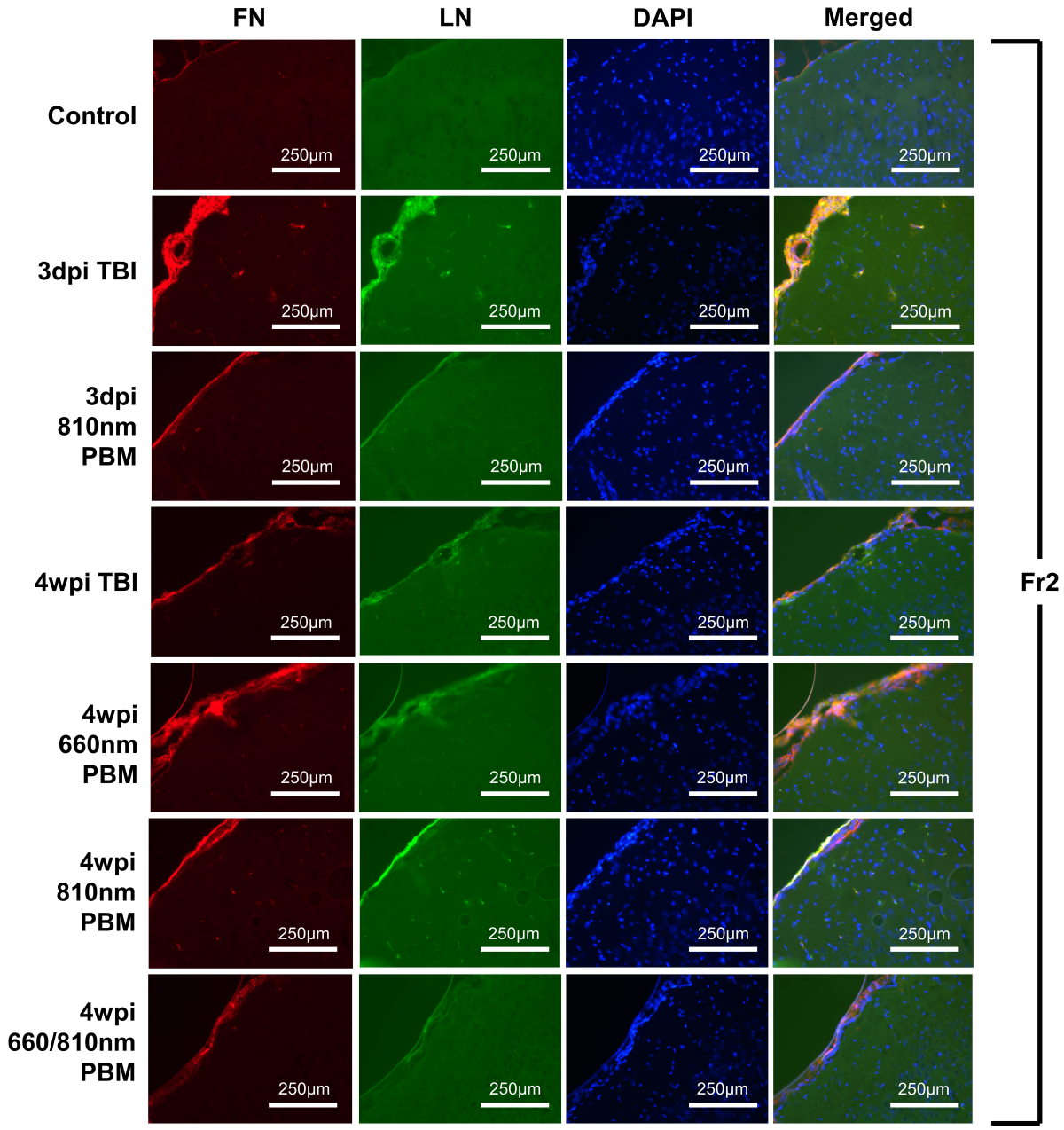


Figure D.17: Laminin/Fibronectin Fr2

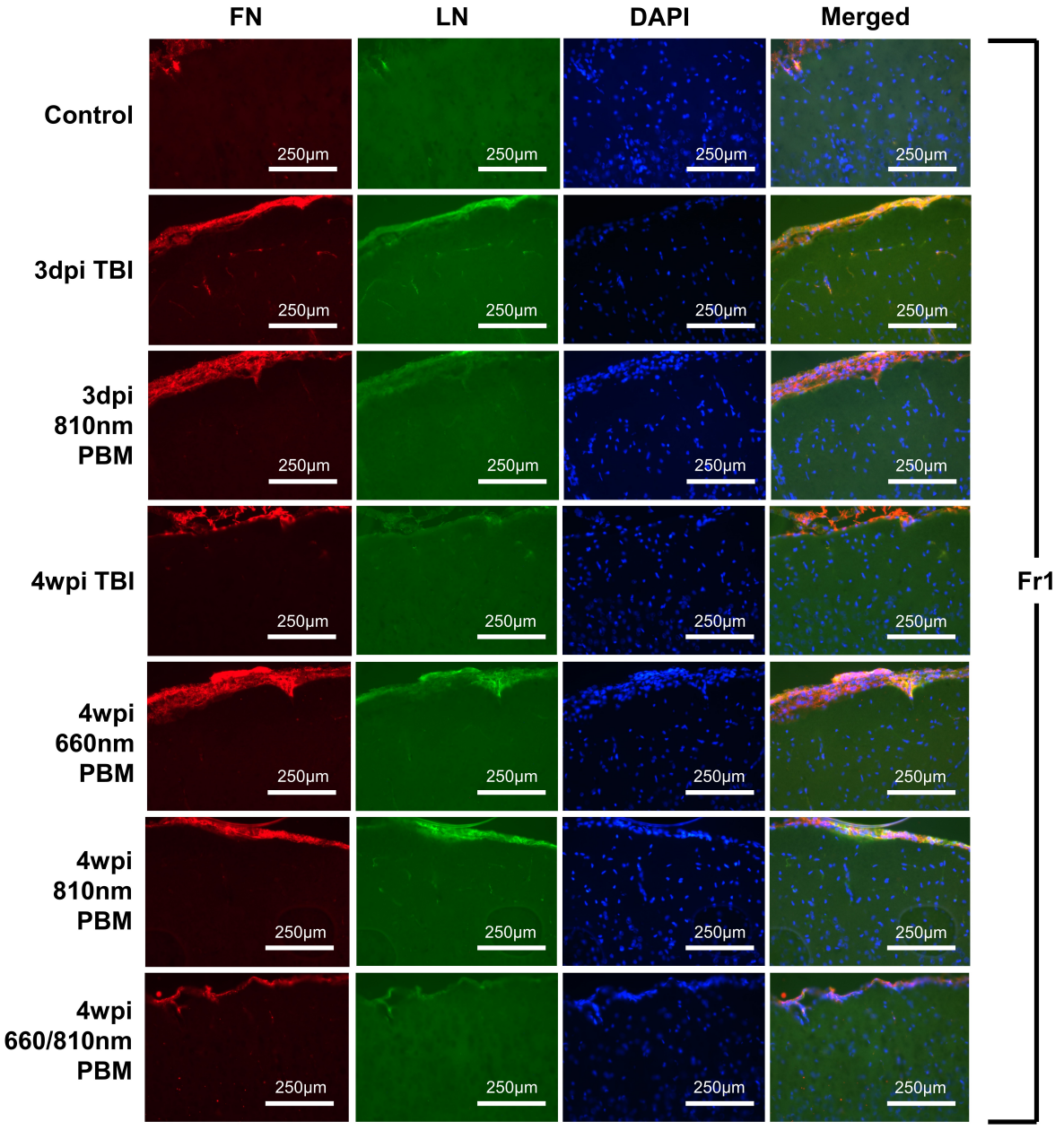


Figure D.18: Laminin/Fibronectin Fr1

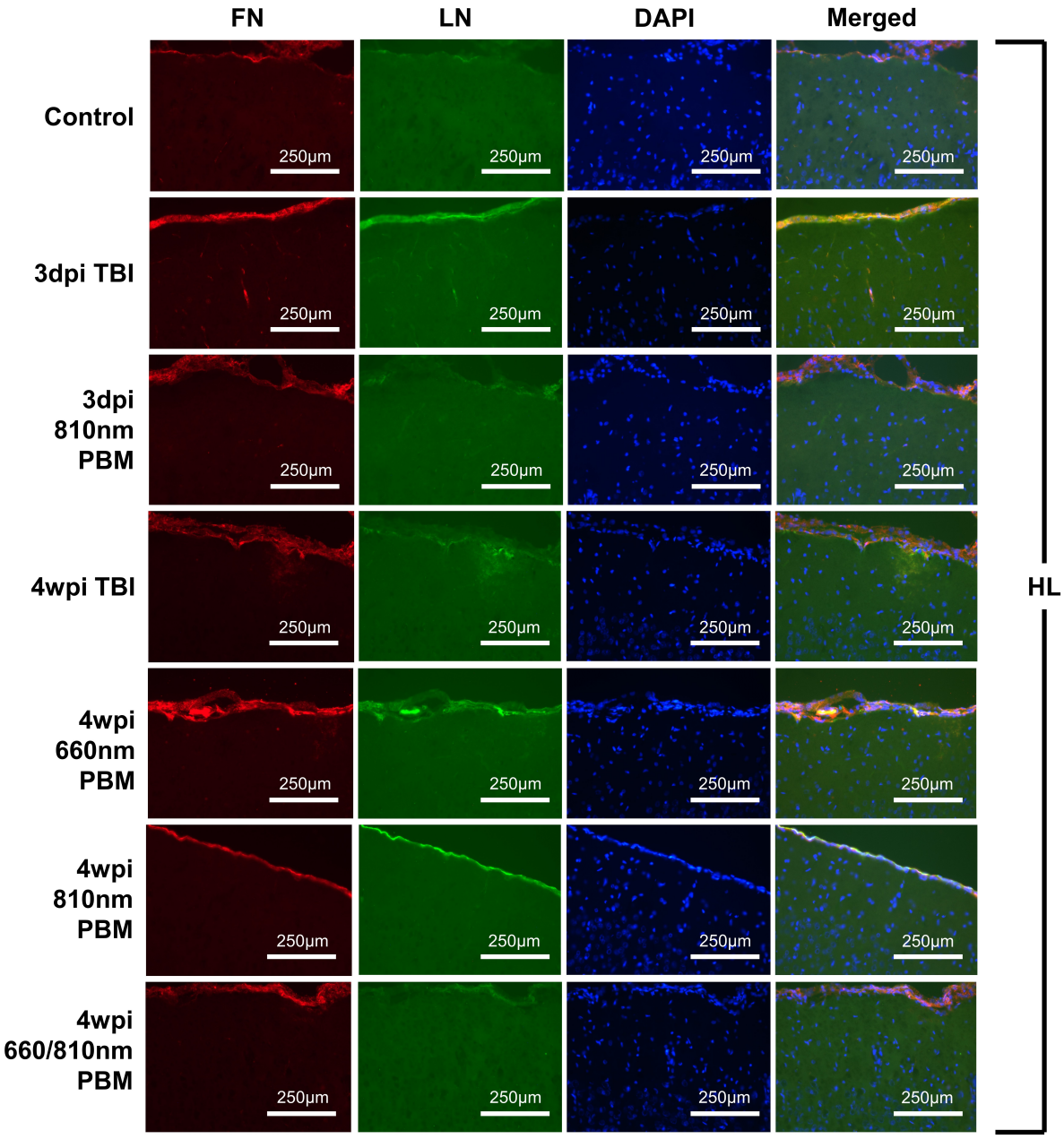


Figure D.19: Laminin/Fibronectin HL

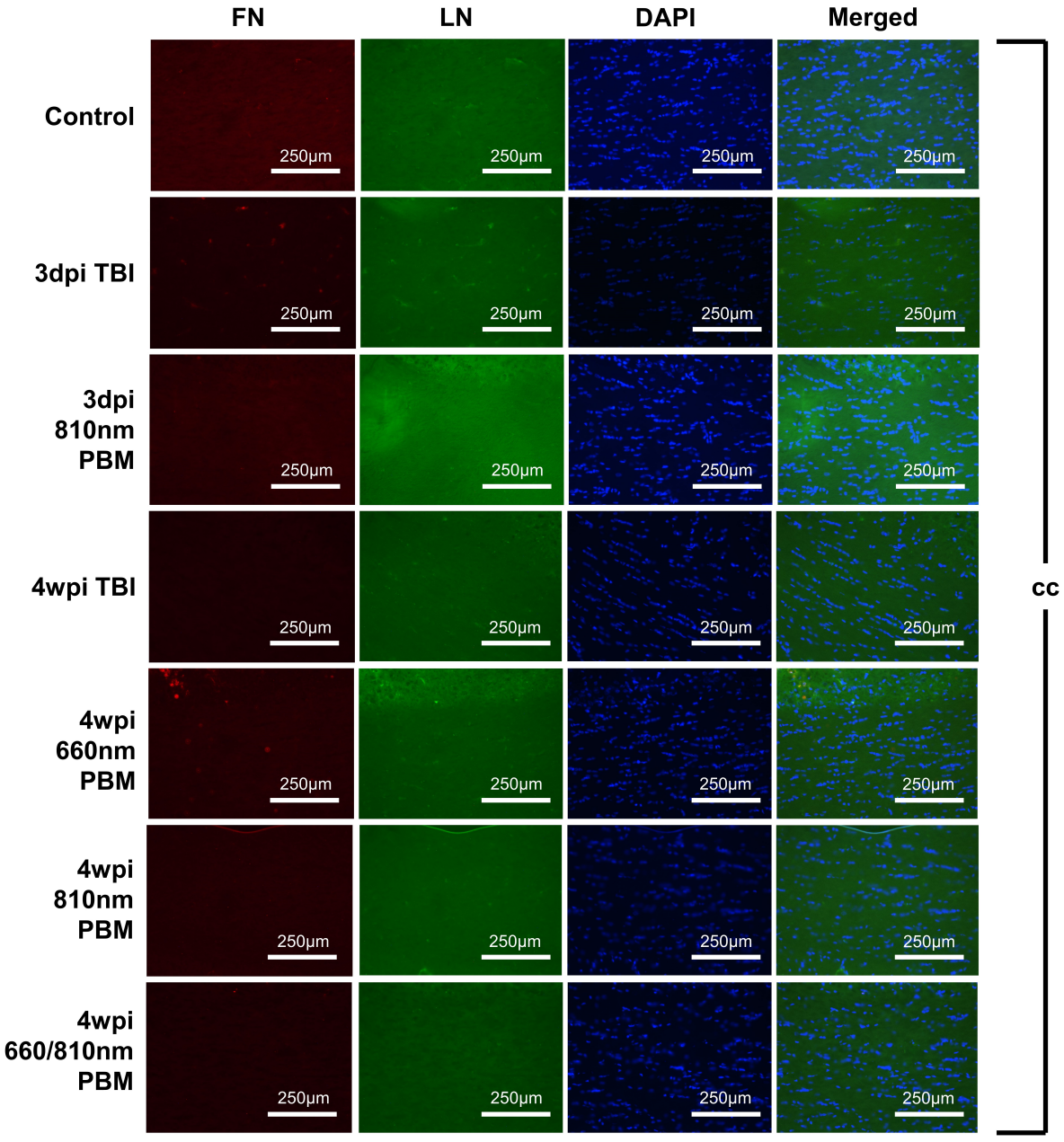


Figure D.20: Laminin/Fibronectin cc

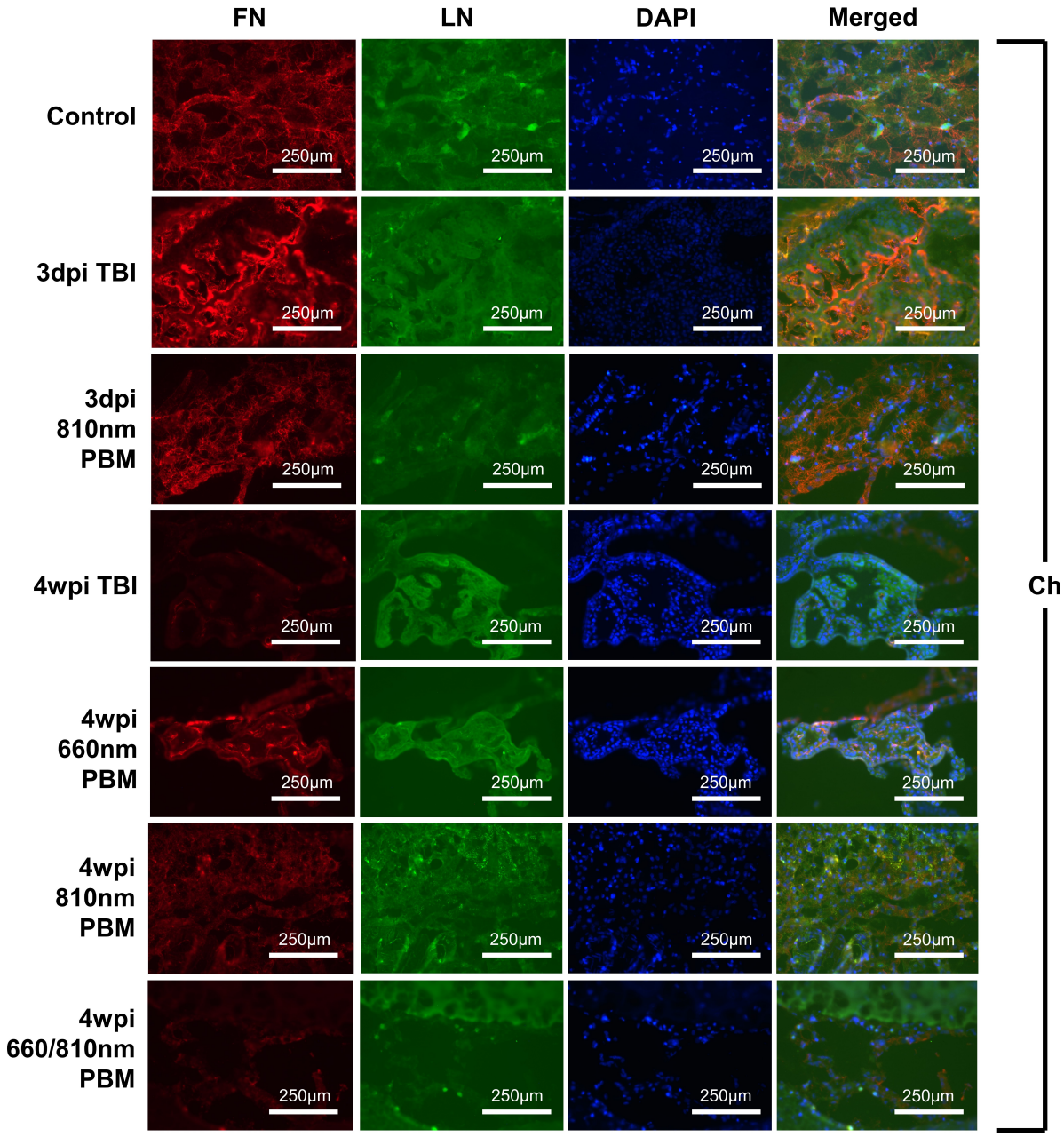


Figure D.21: Laminin/Fibronectin Ch

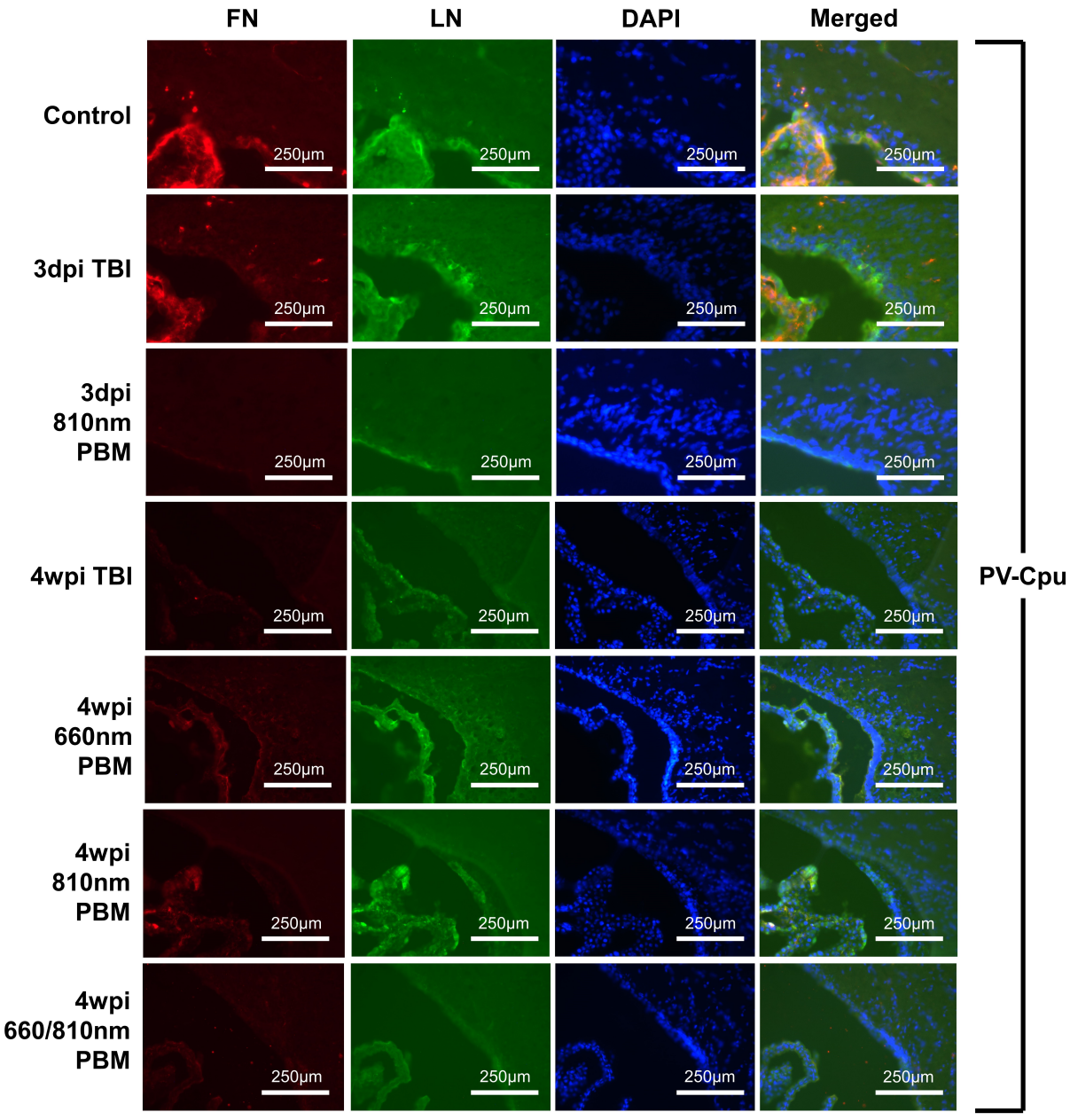


Figure D.22: Laminin/Fibronectin PV-CPu

Appendix E

ADDITIONAL RAMAN SPECTROSCOPY PRINCIPAL COMPONENT ANALYSIS

Raman spectroscopy PCA using individual spectra from mapped scans, with spectra shown (Fig. E.1; comparison of all groups (Fig. E.2); control vs injury (Fig. E.3; and injury vs treatment (Fig. E.4).

Group	n =
C	691
I	588
T	588
Total	1867

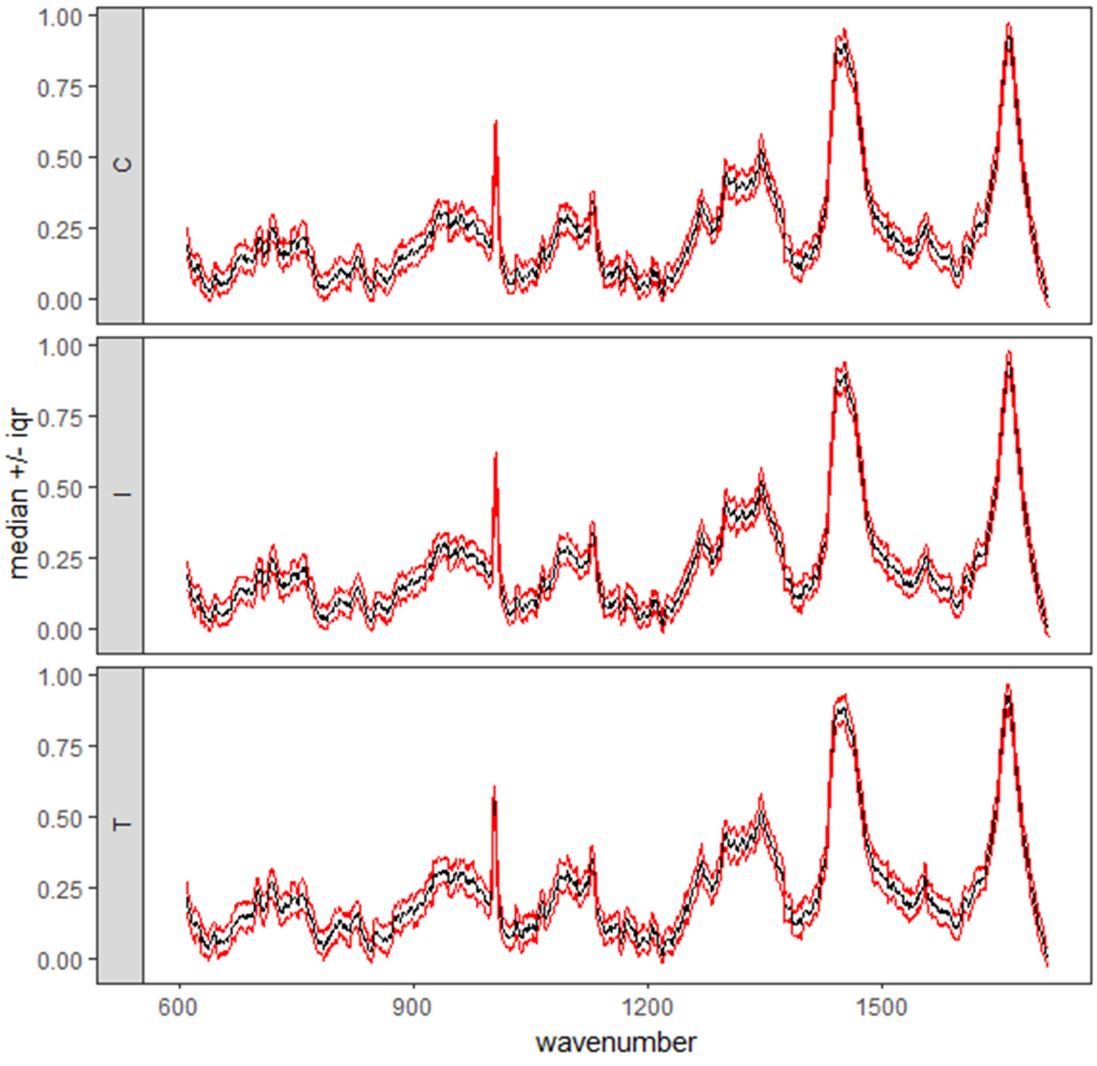


Figure E.1: Fingerprint region of individual spectra from treatment, injury and control groups, black shows median with interquartile range in red. From n = 6 per group, means of 98 1s exposure spectra per specimen, normalised, baseline corrected.

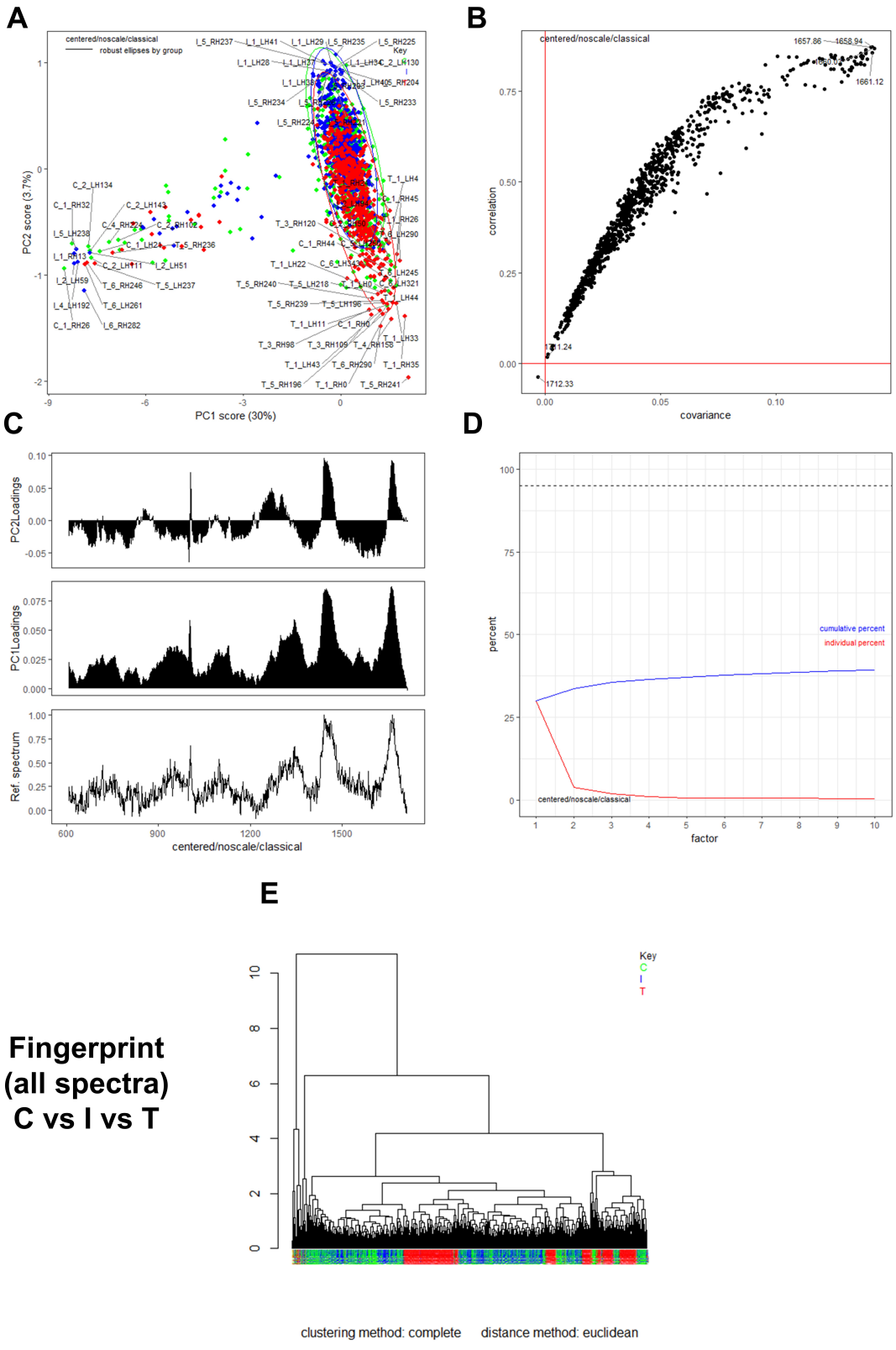


Figure E.2: Caption on next page.

Figure E.2: Figure on previous page. PCA of individual fingerprint region spectra from mapped Raman spectroscopy after TBI (treatment vs injury vs control)Exploratory data analysis of all three groups (T = treatment with PBM; I = TBI with sham treatment; C = control (no injury)). A: Classical principal component analysis (PCA) scores B: s-Plot to identify influential frequencies with identification of the most influential frequency variables. C: Loading plot of PC1 and PC2 against reference spectra. D: Scree plot of 10 PC factors. E: hierarchical cluster analysis (HCA) of PCA scores. n = 6 per group.

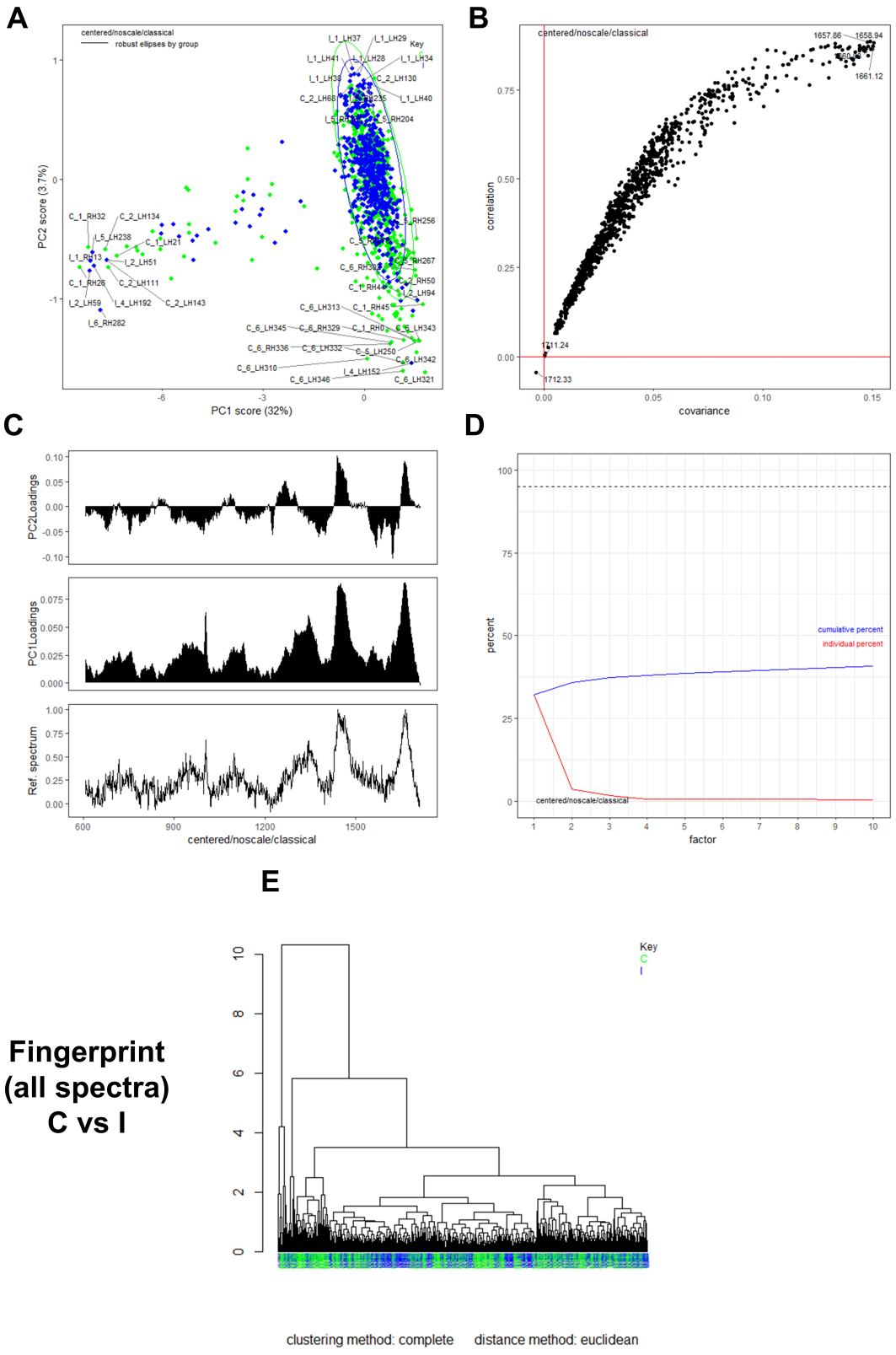


Figure E.3: Caption on next page.

Figure E.3: Figure on previous page. PCA of individual fingerprint region spectra from mapped Raman spectroscopy after TBI (injury vs control). Exploratory data analysis of injury and control groups (I = TBI with sham treatment; C = control (no injury)). A: Classical principal component analysis (PCA) scores B: s-Plot to identify influential frequencies with identification of the most influential frequency variables. C: Loading plot of PC1 and PC2 against reference spectra. D: Scree plot of 10 PC factors. E: hierarchical cluster analysis (HCA) of PCA scores. n = 6 per group.

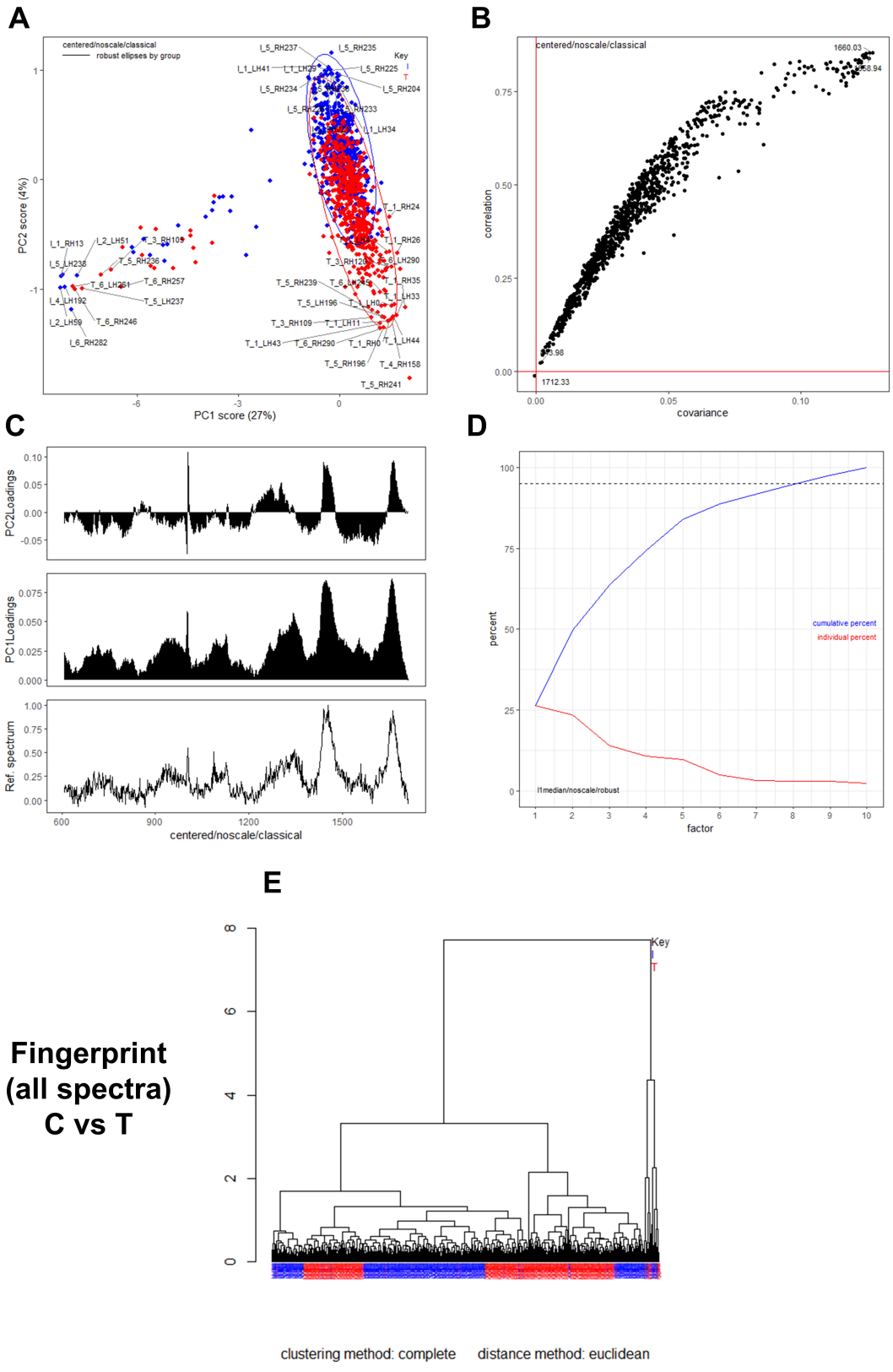


Figure E.4: Caption on next page

Figure E.4: Figure on previous page. PCA of individual fingerprint region spectra from mapped Raman spectroscopy after TBI (treatment vs injury). Exploratory data analysis of treatment and injury groups (T = treatment with PBM; I = TBI with sham treatment; C = control (no injury)). A: Classical principal component analysis (PCA) scores B: s-Plot to identify influential frequencies with identification of the most influential frequency variables. C: Loading plot of PC1 and PC2 against reference spectra. D: Scree plot of 10 PC factors. E: hierarchical cluster analysis (HCA) of PCA scores. n = 6 per group.

Appendix F

METHODOLOGY FOR WHOLE TRANSCRIPTOME SEQUENCING

Further details of sequencing protocol were provided by the company (Qiagen, Holden, Germany):

Library preparation was performed using the QIAseq Stranded Total RNA Library Kit with QIAseq FastSelect rRNA and globin depletion. QIAseq FastSelect rRNA HMR was used to reduce the amount of unwanted RNA species. After first and second strand synthesis, the cDNA was end-repaired and 3' adenylated. Sequencing adapters were ligated to the overhangs. Adapted molecules were enriched using by 16 cycles or PCR and purified by a bead-based cleanup. Library preparation was quality controlled using capillary electrophoresis (High Sensitivity Tape D1000). High quality libraries are pooled based in equimolar concentrations. The library pool(s) were quantified using qPCR and optimal concentration of the library pool used to generate the clusters on the surface of a flowcell before sequencing on a NovaSeq (Illumina Inc.) instrument (2x75, 2x10) according to the manufacturer instructions (Illumina Inc.). Raw data was de-multiplexed and FASTQ files for each sample were generated using the bcl2fastq software v2.20.0.422 (Illumina inc.).

All primary analysis was carried out using CLC Genomics Server 23.0.5. Raw reads were first trimmed to remove potential read-through adapter sequences at the 3'end. Further, reads

were trimmed based on quality scores and ambiguous nucleotides, e.g. due to stretches of Ns. A maximum of 2 ambiguous nucleotides were allowed in a read. The trimmed reads were mapped to mouse ribosomal RNA (rRNA) repetitive unit to get an overview or rRNA content in the samples. However, all reads were mapped to the rat genome Rnor 6.0 with ENSEMBL Rnor 6.0 version 98 annotation.

Appendix G

CRANIAL TRANSMISSION OF PHOTOBIOMODULATION IN CADAVERIC AND PHANTOM MODELS

G.1 Introduction

Cadaveric modelling was used here to explore investigation two specific questions in the application of transcranial PBM: (1) to ascertain the effect of skin pigmentation on transmission of 660 nm PBM to the brain; and (2) to investigate the optical properties of a lipid emulsion-based phantom media (described in Chapter 6), compared to *ex vivo* brain tissue.

G.2 Methods

The methodologies used in this work are described elsewhere in this thesis: profilometry methods are described in Chapter 3; cranial cadaveric modelling is described in Chapter 4; and the preparation of the optical phantom media is described in Chapter 6. Adult 200-250 g Sprague-Dawley (SD) and Lister Hooded rats were used for comparison between low (SD) and high (LH) skin/fur pigmentation of the scalp (fur was shaven prior to profiling).

G.3 Results

Transmission was compared between two breeds of adult rat: Sprague-Dawley (low pigmentation skin) and Lister Hooded (high pigmentation) (n = 4 per group). Transmission was significantly impaired in LH rats compared with SD, in both scalp/skull (Fig. G.1), and scalp/skull/brain preparations (Fig. G.2). Total power and average irradiance across the tested power output values were significantly attenuated through scalp and skull (Fig. G.1). Total power was significantly impaired when including the brain, with a modest reduction in average irradiance values which was not statistically significant (Fig. G.2). D4σ values were not significantly different between species, with or without inclusion of the brain (Fig. G.3).

In SD rats, transmission through brain was compared with transmission through an optical phantom gel. After profilometry with the native brain in situ, brain was removed and the skull used as a mould to cast the liquid phantom gel, to the full depth of the skull cap to equal the depth of brain. In this comparison, there was good correlation between phantom and brain for both total power and average irradiance transmission (Fig. G.4 B/D), though the gross values overall were significantly different across all measured output power values (Fig. G.4 A/C), with greater transmission through phantom, more marked in average irradiance values. D4σ values were also significantly different between the two, with poor correlation and brain demonstrating significantly greater D4σ values. The distribution of the beam profile is qualitatively different between brain and phantom G.5. Based on distribution patterns, anatomical features have an apparent effect on the distribution. Whilst phantom beam profilometry is a clear Gaussian distribution, this pattern is disrupted in the brain, with a strip of greater penetrance and higher intensity observed in the midline (correlating with the position of the falx cerebri).

For use in *in vivo* TBI modelling, transmission values for the cortical surface are given in Table G.1. 63 mW and 228 mW were used as thermpgraphically validated levels of skin surface irradiation which does not result in significant skin surface heating.

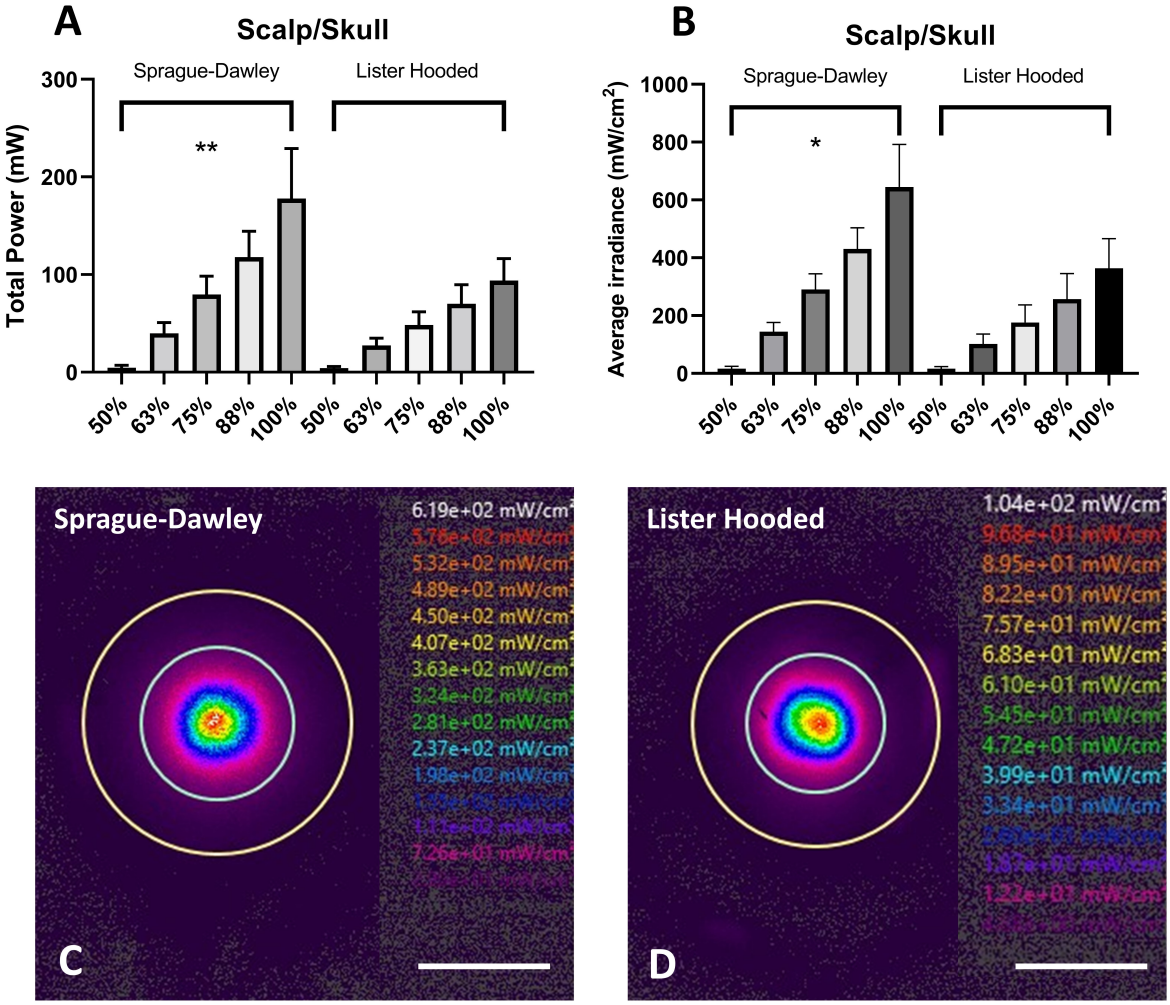


Figure G.1: Skin pigmentation significantly impairs 660 nm light scalp and skull transmission in the cadaveric rat. Comparison of scalp and skull 660 nm PBM penetrance in Sprague-Dawley and Lister Hooded rats. A: comparison of total power; B: comparison of average irradiance; C: beam profile (at 63%) in Sprague-Dawley through scalp and skull; D: beam profile (at 63%) in Lister Hooded. Output values given in percentages of 100% 800 mW output (non-linear). * = $p < 0.05$; ** = $p < 0.01$ (paired t test); scale bar 0.5 cm.

G.4 Discussion

This appendix has demonstrated that skin pigmentation significantly reduces average irradiance values reaching the internal aspect of the skull. Skin pigmentation did not affect distribution (D4σ). This is important to recognise, as this is a further limitation to transcranial PBM due to similarly variable skin pigmentation levels in human populations.

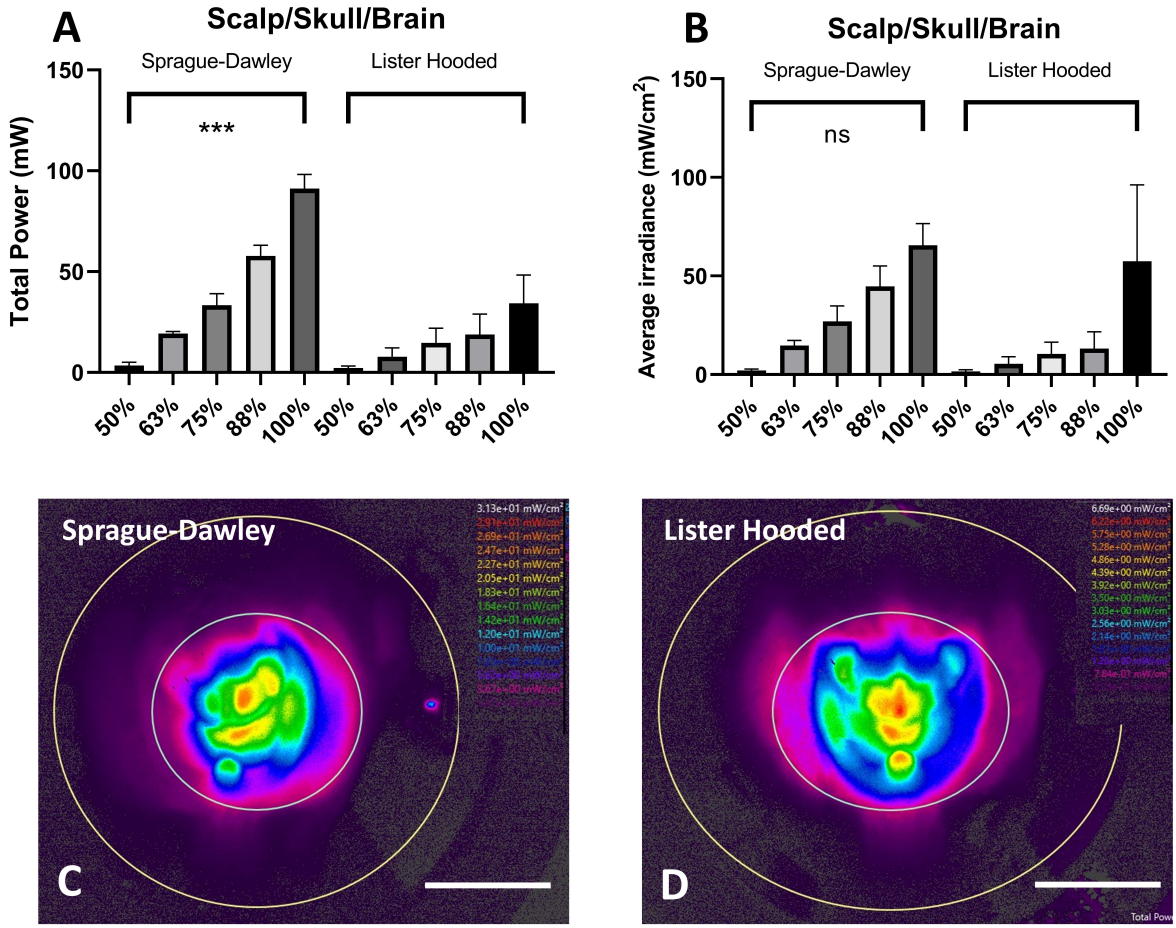


Figure G.2: Skin pigmentation significantly impairs 660 nm light scalp, skull and brain transmission in the cadaveric rat. Comparison of scalp, skull and brain 660 nm PBM penetrance in Sprague-Dawley and Lister Hooded rats. A: comparison of total power; B: comparison of average irradiance; C: beam profile (at 63%) in Sprague-Dawley through scalp, skull and brain; D: beam profile (at 63%) in Lister Hooded. Output values given in percentages of 100% 800 mW output (non-linear). * = $p < 0.05$; ** = $p < 0.01$; *** = $p < 0.001$ (paired t test); scale bar 1 cm.

These results have also demonstrated the optical properties of a lipid-based phantom media in comparison to *ex vivo* brain. This has demonstrated that the two materials have similar patterns in optical transmission, though there are statistically significant differences (phantom permits more transmission, but results in less distribution). This should be considered when interpreting the results of its use in prototyping studies in Chapter 6.

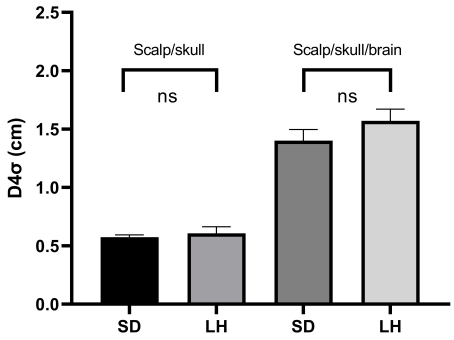


Figure G.3: Skin pigmentation does not significantly affect D4σ values in 660 nm light scalp/skull and scalp/skull/brain transmission in the cadaveric rat. Comparison of scalp, skull and brain 660 nm PBM D4σ values in Sprague-Dawley and Lister Hooded rats, through scalp/skull and scalp/skull/brain dissection preparations; D: beam profile (at 63%) in Lister Hooded. Output values given in percentages of 100% 800 mW output (non-linear). ns = no significant difference (on paired t test).

Table G.1: Values for beam characterisation indices for transmission of 660 nm light to the inner skull surface, with a source placed on the bregma over the scalp. Optical source on scalp is a fibre optic coupled to MD-III 800 mW in a cadaveric model of TBI at two biocompatible power output values. Profilometry camera focused at level of inner surface of skull in a cadaveric model of TBI in an adult Sprague-Dawley rat. All values given ± SEM, n = 3.

Power output (mW)	Total Power (mW)	Average irradiance (mW/cm^2)	Peak irradiance (mW/cm^2)	D4σ (mm)
63 mW	4.7 ± 2.5	16.2 ± 8.8	78.0 ± 35.4	0.58 ± 0.02
228 mW	40.0 ± 10.8	144.4 ± 31.6	590 ± 170.8	0.57 ± 0.02

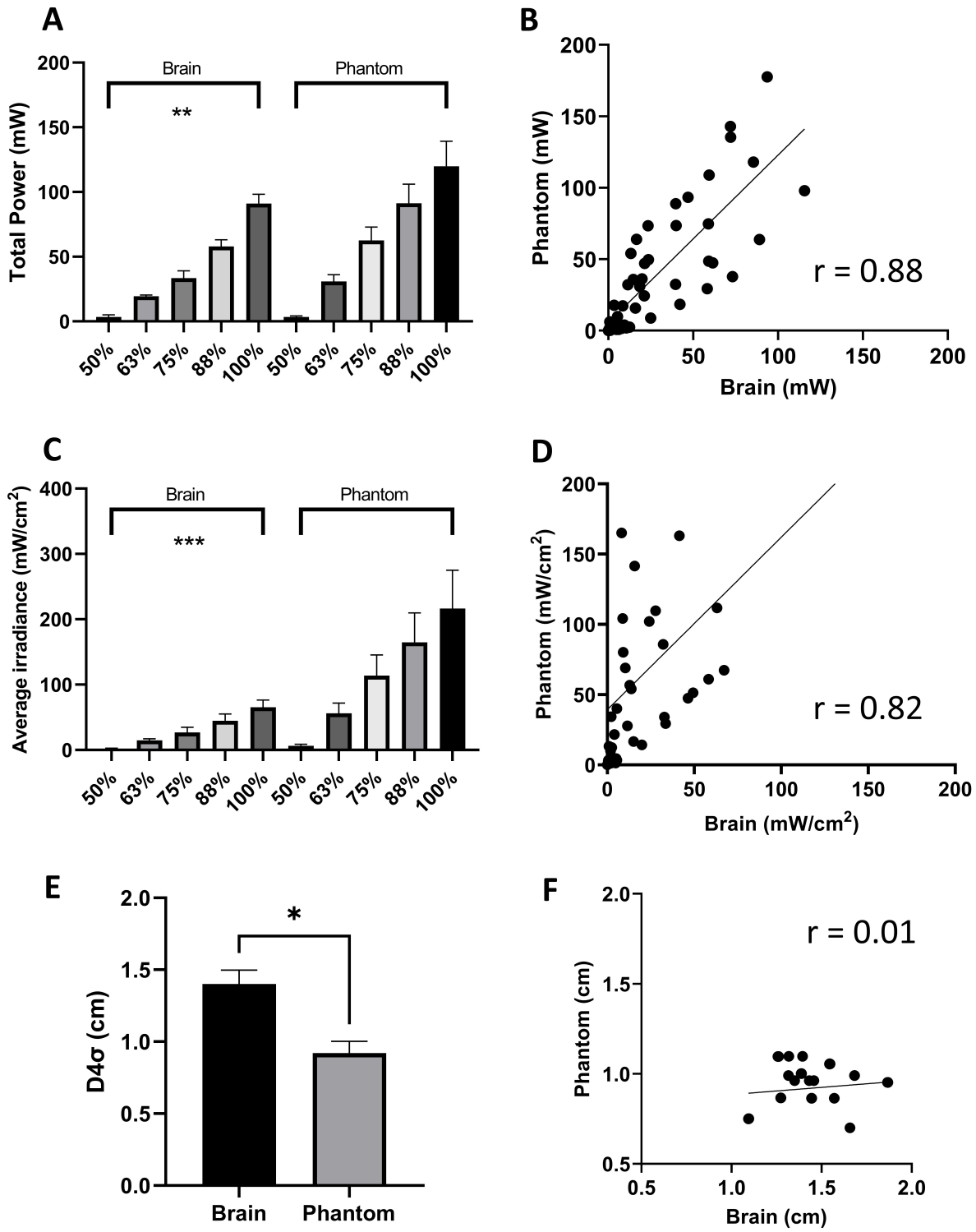


Figure G.4: Caption on next page.

Figure G.4: Total power transmission shows correlation in 660 nm PBM application in brain vs optical phantom, but not average irradiance or D4σ. Comparison of 660 nm PBM penetrance in Sprague-Dawley rats, using either scalp/skull/brain or scalp/skull/phantom. A: comparison of total power; B: correlation of total power between brain and phantom. Confidence intervals - total power brain vs phantom: 0.7877 to 0.9294; C: comparison of average irradiance; D: correlation of average irradiance between brain and phantom. Confidence intervals - average irradiance brain vs phantom: 0.6892 to 0.8927. E: comparison of D4σ; F: correlation of D4σ. Confidence intervals D4σ brain vs phantom: -0.2774 to 0.2948; Output values given in percentages of 100% 800 mW output (non-linear). Error bars represent SD. * = $p < 0.05$; ** = $p < 0.01$; *** = $p < 0.001$. Comparative statistics calculated with paired t test; r values calculated using Spearman correlation coefficients.

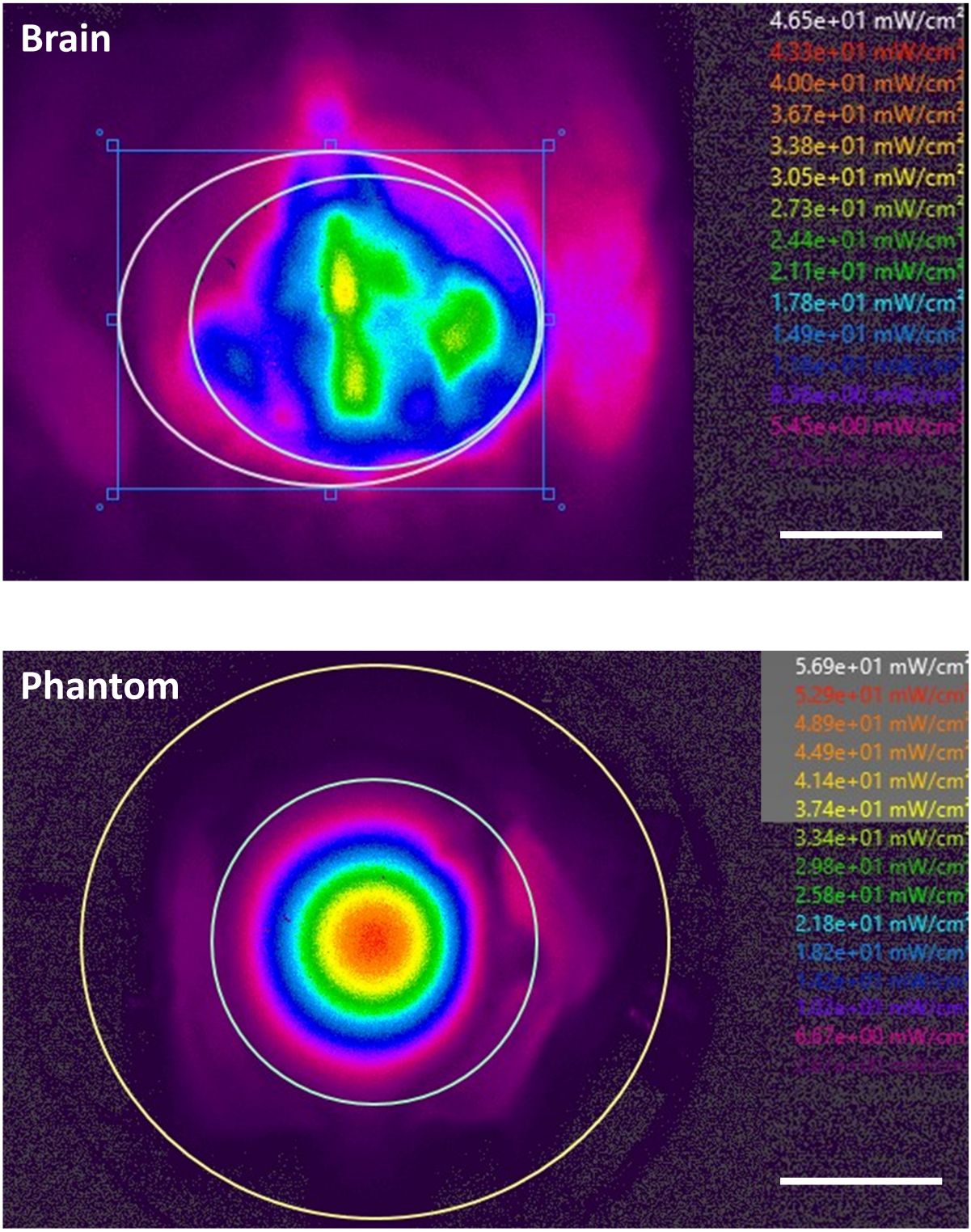


Figure G.5: Profilometry of 660 nm PBM through brain vs phantom. Profilometry was performed using 63% maximum output (800 mW 660 nm laser source) placed upon the bregma, either through native brain, or removed brain replaced with a set optical lipid phantom. Scale bar = 0.5 cm.

Appendix H

PATIENT AND PUBLIC INVOLVEMENT AND ENGAGEMENT

The following reports of patient and public involvement and engagement (PPIE) meetings were prepared by Laura Nice, as a summary of the meetings facilitated by Laura Nice and Jenny Needham, with meeting content presented by the thesis author to members of the Trauma ABC PPIE group.

H.1 Traumatic brain injury device

TrABC Patient & Public Involvement Group
Meeting Notes

Date: Monday 11th October 2021
Time: 10.00am – 12.30pm
Online via Zoom

Chair: Laura Nice (LN), *NIHR SRMRC PPIE Manager*

Presenter: Andrew Stevens (AS)
Neurotrauma Research Fellow, Specialty Registrar Neurosurgery

Present: 10 PPI members with lived experience of trauma, burns and scarring
Hazel Smith (HS), *NIHR SRMRC Project Support Officer*

AS attended the TrABC PPI group meeting for the first time to discuss two upcoming projects and inform his grant applications. AS had sent plain English summaries of the projects to group members beforehand and gave an overview of each topic in turn, allowing for questions and discussion with the group.

PROJECT 1: Using light for treatment and monitoring in severe traumatic brain injury

This project is the development of a device which uses light to treat and monitor the injured brain after severe traumatic brain injury. Light therapy has been shown in laboratory studies to improve recovery after traumatic brain injury. The effect of this therapy can also be detected by "Raman spectroscopy", a highly detailed way of getting information about the brain, which also uses light. The overall project is to develop a device which integrates both technologies into a single system which can be used to deliver light therapy and personalise the dose using the light monitoring.

1.1 What do you think about the project and would you be willing to take part?

- Incredible
- Great
- Fantastic idea
- Amazing technology
- Wish I could join!
- Anything that has the potential to change outcomes is worth trying
- It would be great if this could be used at later stages in head injury recovery
- Absolutely, as I've struggled with focus, sleep, short term memory and concentration despite recovering so well and long term memory being solid

CONFIDENTIAL

- *"Given the situation that the patient will be in, potentially an induced coma anyway, but the thought of having a hole drilled in my head, let alone and even bigger hole …it's just that gulp of air when that's mentioned…we're going to drill a hole in your family members head and here's the big thing we're going to put in it…it's massively scary on top of the already traumatic situation".* This makes the initial sensitive approach to the family very important.

1.2 Questions from the group

The following questions were asked by group members. It may be useful to look back at these questions when you are developing patient/public-facing materials for your project. You could also consider using some of these to develop an FAQ sheet for participants/families.

- How does it work?
- Given that it can be difficult to detect every part of the brain that has been damaged, how does this light manage to do that?
- Why do you use red light?
- Can this treatment be given in the later stages of recovery/post injury?
- How does such a small bolt (shown by AS to the group) reach the whole brain or at least all the damaged areas?
- What are the effects of light reaching or over-exciting non-injured brain tissue?
- Are there any downsides/side effects of the light reaching non-injured areas?
- Currently 25% is the maximum coverage. Is there a point/percentage you are aiming for as the gold standard? E.g., 50%?
- Is this an invasive procedure?
- Do patients have to be unconscious or under general anaesthetic to receive this treatment?
- Has this been tested in animal models?
- How sophisticated is this device and how easy will it be for trauma centres to roll this treatment out?
- How long do you put the red light on for?
- How long does the overall treatment last?
- Is there any possibility to extend the follow-up period to 1 year? E.g., send a letter or questionnaire?
- What is the infection risk of using this red light? (Question sent after the meeting by a group member whose 2 children have both had head injuries – one caused by an infection)
- Do you have ethical approval already?
- Could this benefit patients who have had severe strokes or other neurological injuries?
- What are the implications for the patient/side effects if too much treatment is given?
- What is the cost of the device?
- What material is the device made from?
- Do you have a company that is already involved?

1.3 What do you think about the device being implanted temporarily?

- Best way to conduct it, as it allows treatment to be isolated to clinical setting so life can be as normal as possible for TBI sufferers post discharge

1.3 Considerations for project design

- It was mentioned that it is possible to give too much treatment (time and length). How will you communicate this and reassure families who will be going through a very traumatic, emotional and anxious time?
- How will families be involved in the consent process? If they are not involved in the initial consent, group members felt it was important to inform and explain the study to family members, without causing extra distress in a very difficult time
- Could you offer families the opportunity to speak to one named doctor/nurse throughout the study to give them reassurance and a clear route for answering any further questions?

1.4 Is there anything you think we should consider from a patient perspective when designing this device?

- Could you consider a different colour device? The black makes it look a little scary/clunky/robotic!
- Something on the device to make it more appealing or inviting stickers to be applied by the patient prior to use then sanitised and removed (only if this is not a cost pressure on the use of the kit to the trust).
- Making the device more appealing and engaging here in the first instance could do a lot to take away potential stigma from using it

H.2 Spinal cord injury device

Trauma, Accident, Burns and Critical Care (TrABC)

Patient & Public Involvement Group Meeting

Wednesday 29 March 2023
12-1:30pm
Online via Zoom

Research Lead: Andrew Stevens

Chair: Laura Nice (LN)

Present: AS and 6 PPI Members

Notes: Jenny Needham (JN)

---

1. Summary – A Device for direct Application of Photobiomodulation Therapy in Spinal Cord Injury

Spinal cord injury (SCI) affects 2,500 people per year in the UK alone, and is a cause of severe and lifelong disability. At the moment, there is no therapy which has been shown to improve recovery after injury, and many patients are left with long term problems with mobility, pain, sexual function and control of their bladder and bowel. Photobiomodulation (PBM) is an emerging treatment option, which uses red or near-infrared light at a low-level to improve survival and recovery of spinal cord cells. We have developed a way of delivering PBM directly to the injured spinal cord, and have shown that this improves recovery in laboratory models. The next phase is to produce a fully-functioning device in order to gain CE marking and to be able to use this device to understand whether it improves recovery in humans after SCI.

2. General Questions

2.1 With the device, how would it be put on, what does it look like and how big is it? How significant is the procedure to put on the device?

It is currently in development. Essentially the device doesn't need to be big and can be the same thickness as a Biro pen.

Typically, a piece of bone is removed in surgery which leaves a nice big gap for an implant. It would be put in during the same procedure.

We think it would either be tube structure which would go all the way down and which carries fibres. Or another possibility is a flexible pad which would sit on top of the spinal cord and then connected by some wiring which would come out through the skin. This would be temporary, upto 7 days while the patient is in hospital so it would always be supervised until removed. In terms of removing the device, we're hoping to design it so that it can be easily pulled out and a stitch put it to close the area.

2.2 The device shines a light onto the areas, does it make a noise?

The sources of light (bulb, lamp or laser) would be within a unit outside of the patient. They may make a noise when cooling down (low level humming) but other than that there is no particular noise.

The light is delivered all internally so there wouldn't be anything to see on the outside.

2.3 Does the light regenerate cells or does it create new cells? Do you know why red light works?

From what we have seen in the laboratory it does cause regeneration of the same cells. There are cells that were there originally, have been damaged and are now regenerating to try and repair after injury. It also seems to help cells survive. After a spinal cord injury, cells go into a very stressed state and trigger an internal mechanism so that they die because they feel that they are so stressed they are not going to survive. This treatment has shown that is helps promote those cells to survive.

It does not create new cells. That is one of the big problems in terms of trying to treat traumatic spinal cord injuries. We're born with a particular number of nerve cells. You don't get anymore throughout your life, including after injury.

We don't entirely know why the red light works and it is one of the things I've been trying to improve the knowledge on. Within each cell is a sort of battery called mitochondria which creates all of the energy that cells uses. A key part of the mitochondria which produces that energy is it has a bit of cooper in it which is what absorbs each of those protons of red light. It is only able to absorb and interact with protons that are in a specific part of the spectrum. One of those is red light and the other is near infrared light and within very specific bands. It delivers that additional energy to the mitochondria within these cells. It helps by balancing out how it is and how it is functioning which is good for after injury because the mitochondria go into an energy crisis. Therefore, it is extra effective and triggers the improvements in survival and regeneration. That's how we think it works and why we think it is those certain wavelengths.

2.4 How powerful is the device?

The amount of light required to have this beneficial effect is quite low. It needs to be above the threshold we receive all the time but below the amount that would cause any heating or burning**.**

3. Questions to the group

3.1 What do you think about the project and would you be willing to take part?

CONFIDENTIAL

- Every patient will have a different attitude to the risk. I like the idea of using the pen shape rather than the pad. I like the shape, I feel that it would be more solid, would go in easily and be able to come out easily.
- I like this study because the benefits are clear but also the translational aspects. I would take part.
- For the device, would there be a way for it to be made more sustainable? Would it have to be outsourced outside of the UK?
    - **(AS)** We want to make the disposable part of the device as minimalist as possible. We wouldn't be able to reuse the part implanted into the patient with another patient. Reasons include CJD, Mad Cow Disease. You can't sterilise that kind of disease from the implants. Therefore, we want the device to be as small as possible to reduce plastic and silicon waste. This will also cut costs down. Both of which are important in Med Tech.
- My concern would be having allergic reaction to the implant whilst it is in your body.
    - **(AS)** One of the advantages of using light based therapy is that it is less of a problem than using drugs which can result in unexpected interactions with the body. Silicon is a good product to use as there seems to be very little allergy related to it. This will be all part of the testing and we wouldn't use any material that is a common allergy.

3.2 How would you feel about having extra procedures such as lumbar punctures?

- It isn't going to be for everyone and that needs to be considered, especially as they have been through trauma. It needs to be presented sensitively.

CONFIDENTIAL